

United States Department of Commerce
Technology Administration
Institute of Standards and Technology



NIST Special Publication 839



Technical Digest Symposium on Optical Fiber Measurements, 1992

Sponsored by the National Institute of Standards and Technology
in cooperation with the IEEE Lasers and Electro-Optics Society
and the Optical Society of America



QC
100
U57
839
1992
C.2

The National Institute of Standards and Technology was established in 1988 by Congress to "assist industry in the development of technology . . . needed to improve product quality, to modernize manufacturing processes, to ensure product reliability . . . and to facilitate rapid commercialization . . . of products based on new scientific discoveries."

NIST, originally founded as the National Bureau of Standards in 1901, works to strengthen U.S. industry's competitiveness; advance science and engineering; and improve public health, safety, and the environment. One of the agency's basic functions is to develop, maintain, and retain custody of the national standards of measurement, and provide the means and methods for comparing standards used in science, engineering, manufacturing, commerce, industry, and education with the standards adopted or recognized by the Federal Government.

As an agency of the U.S. Commerce Department's Technology Administration, NIST conducts basic and applied research in the physical sciences and engineering and performs related services. The Institute does generic and precompetitive work on new and advanced technologies. NIST's research facilities are located at Gaithersburg, MD 20899, and at Boulder, CO 80303. Major technical operating units and their principal activities are listed below. For more information contact the Public Inquiries Desk, 301-975-3058.

Technology Services

- Manufacturing Technology Centers Program
- Standards Services
- Technology Commercialization
- Measurement Services
- Technology Evaluation and Assessment
- Information Services

Electronics and Electrical Engineering Laboratory

- Microelectronics
- Law Enforcement Standards
- Electricity
- Semiconductor Electronics
- Electromagnetic Fields¹
- Electromagnetic Technology¹

Chemical Science and Technology Laboratory

- Biotechnology
- Chemical Engineering¹
- Chemical Kinetics and Thermodynamics
- Inorganic Analytical Research
- Organic Analytical Research
- Process Measurements
- Surface and Microanalysis Science
- Thermophysics²

Physics Laboratory

- Electron and Optical Physics
- Atomic Physics
- Molecular Physics
- Radiometric Physics
- Quantum Metrology
- Ionizing Radiation
- Time and Frequency¹
- Quantum Physics¹

Manufacturing Engineering Laboratory

- Precision Engineering
- Automated Production Technology
- Robot Systems
- Factory Automation
- Fabrication Technology

Materials Science and Engineering Laboratory

- Intelligent Processing of Materials
- Ceramics
- Materials Reliability¹
- Polymers
- Metallurgy
- Reactor Radiation

Building and Fire Research Laboratory

- Structures
- Building Materials
- Building Environment
- Fire Science and Engineering
- Fire Measurement and Research

Computer Systems Laboratory

- Information Systems Engineering
- Systems and Software Technology
- Computer Security
- Systems and Network Architecture
- Advanced Systems

Computing and Applied Mathematics Laboratory

- Applied and Computational Mathematics²
- Statistical Engineering²
- Scientific Computing Environments²
- Computer Services²
- Computer Systems and Communications²
- Information Systems

¹At Boulder, CO 80303.

²Some elements at Boulder, CO 80303.

Technical Digest—Symposium on Optical Fiber Measurements, 1992

02100
457
839
1992
0.2

Digest of a symposium sponsored by the
National Institute of Standards and Technology
in cooperation with the
IEEE Lasers and Electro-Optics Society
and the Optical Society of America

September 15-17, 1992
National Institute of Standards and Technology
Boulder, Colorado 80303-3328

Edited by
G. W. Day
D. L. Franzen

September 1992



U.S. DEPARTMENT OF COMMERCE, Barbara Hackman Franklin, Secretary
TECHNOLOGY ADMINISTRATION, Robert M. White, Under Secretary for Technology
NATIONAL INSTITUTE OF STANDARDS AND TECHNOLOGY, John W. Lyons, Director

National Institute of Standards and Technology Special Publication 839
Natl. Inst. Stand. Technol. Spec. Publ. 839, 245 pages (Sept. 1992)
CODEN: NSPUE2

U.S. GOVERNMENT PRINTING OFFICE
WASHINGTON: 1992

For sale by the Superintendent of Documents, U.S. Government Printing Office, Washington, DC 20402-9325

PREFACE

The program for this seventh Symposium on Optical Fiber Measurements has been expanded to two and a half days in order to include a total of 54 papers, 11 invited and 43 contributed.

The invited papers were selected from 43 that were nominated and reviewed by the committee. The contributed papers were selected by the review of the committee from among the 56 submitted.

OTDR technology is an important topic of this Symposium, as it has been in most of the previous ones. Measurements of fiber geometry, which reappeared in 1990 as important topic, continue to be a significant issue. There is increased emphasis on the characterization of optical fiber amplifiers and the measurement of polarization effects. Areas of emerging interest include nonlinear effects in fibers and problems associated with field measurements in systems containing amplifiers and other advanced components.

The Symposium continues to have a strong international character. Eleven countries are represented in the program and more than half of the papers come from outside of the United States.

G.W. Day
D.L. Franzen
Boulder, Colorado
September 1992

Except where attributed to NIST authors, the content of individual sections of this volume has not been reviewed or edited by the National Institute of Standards and Technology. NIST therefore accepts no responsibility for comments or recommendations therein. The mention of trade names in this volume is in no sense an endorsement or recommendation of the National Institute of Standards and Technology.

SYMPOSIUM COMMITTEE

D.L. Franzen, NIST, General Chair

G.W. Day, NIST Program Chair

W.T. Anderson, Bellcore

C. Boisrobert, CNET

N. Channon, York

S. Furukawa, NTT

W.B. Gardner, AT&T Bell Laboratories

R.K. Hickernell, NIST

W.T. Kane, Corning

P.S. Lovely, Photon Kinetics

S.A. Newton, Hewlett-Packard

S. Pollitt, NPL

S.B. Poole, University of Sydney

W.A. Reed, AT&T Bell Laboratories

P.R. Reitz, AMP

C. Saravanos, Northern Telecom

P.G. Suchoski, United Technologies Photonics

CONTENTS

PREFACE

SYMPOSIUM COMMITTEE

Testing strategies for modern fibre network architectures (invited) Nick Lewis, Peter Keeble, David Ferguson, BT Laboratories	1
OTDR measurements through optical splitters Felix P. Kapron, James D. Berardinelli, Bellcore	7
A 1.6- μm -band OTDR using a Raman fiber laser pumped by a Q-switched Er^{3+} -doped fiber ring laser T. Horiguchi, T. Sato, Y. Koyamada, NTT-Ibaraki	11
The effect of OTDR measurement error on fiber uniformity metrics Jane B. Clayton, Andrew L. Ingles, David A. James, Daryl Pregibon, AT&T Bell Laboratories	15
An OTDR based combined end-reflection and backscatter measurement A.F. Judy, AT&T Bell Laboratories	19
Factory measurement solutions to predictable field performance of single- mode fiber optic connectors (invited) Bennett Wong, Halina Kosiorska, Northern Telecom	23
Measurements to assure fiber reliability Hakan H. Yuce, Felix P. Kapron, Bellcore	29
Atomic force microscopy measurements to study optical fiber aging H.H. Yuce, J.P. Kilmer, J.P. Varachi, Jr., Bellcore	33
Fiber microbending test method capable of predicting microbend loss in optical cables Z. Pasturczyk, C. Saravanos, Northern Telecom	37
Measuring method for ribbon fiber skew Ryuichi Matsuoka, Hiroshi Satoh, Nobukazu Kume, Furukawa Electric	41
Review of recent developments in fibre geometry measurements (invited) J. Baines, K. Raine, NPL	45
Fiber cladding diameter measurement by white light interference microscopy P.D. Hale, D.L. Franzen, NIST	51
Accurate measurements of fiber cladding diameter Matt Young, Paul D. Hale, Steven E. Mechels, NIST	55
Measurement of fibre coating geometry by grey-scale analysis Andrew G. Hallam, Julia H. Shaw, York Technology	59

Coating thickness unevenness measurement in fiber drawing process by using reflected light detecting method Akira Inoue, Shuji Shinoki, Yuji Kobayashi, Yasuji Hattori, Sumitomo Electric Industries	63
Development of in-line coating thickness monitor for hermetic carbon coated fiber Yoshinori Ishida, Yukio Kohmura, Shin-ich Arai, Furukawa Electric	67
Measurement of optical nonlinearity of transmission fibers (invited) R.H. Stolen, W.A. Reed, K.S. Kim, K.W. Quoi, AT&T Bell Laboratories	71
Determination of non-linear effective areas for dispersion shifted fibres J.V. Wright, E.S.R. Sikora, BT Laboratories	77
Beam current effects in cathodoluminescence spectroscopy Graham R. Atkins, Mark G. Sceats, Simon B. Poole, University of Sydney	81
Relative dopant concentration profiling of germania, phosphorus and erbium doped silica based optical fibres J.M. Benson, NPL, C.J. Chunnillall, King's College London, J.C. Petersen, Danish Institute of Fundamental Metrology	85
Design and characterization of dispersion compensating fiber (invited) A.J. Antos, Corning	89
Measurement of group effective index of optical fibers and integrated waveguides by the wavelength scan technique S. Morasca, F. Pozzi, C. DeBernardi, CSELT	95
Precision measurement of single-mode fiber group index W.B. Gardner, A.D. Parker, AT&T	99
The direct measurement of highly absorbing bands in optical fibers Robert M. Atkins, AT&T Bell Laboratories	103
Determination of stress optic effect in optical fibers A.J. Barlow, EG&G Fiber Optics, W.H. Ficke, AT&T Bell Laboratories, T. Voots, Photon Kinetics	107
Characterization of integrated optical components (invited) P.G. Suchoski, Jr., United Technologies Photonics	111
Real time measurement of mode partition noise in high speed data modulated laser diodes, in presence of reflections M. Puleo, P. Gambini, E. Vezzoni, CSELT	115
A complete measurement set for high performance optical connectors M. Bottanelli, L. Duca, S. Pitassi, SIRTI	119

A simple and accurate heterodyne technique for the characterization of active and passive narrowband optical filters	
N. Caponio, P. Gambini, R. Hui, M. Puleo, E. Vezzoni, CSELT	123
An automated method for measuring the radius of curvature of an optical fiber	
A.L. Ingles, AT&T Network Systems	127
Recent progress in polarization measurement techniques (invited)	
Brian Heffner, Hewlett Packard	131
Extinction ratio measurements of polarisation maintaining fibre	
Y. Gu, L.J. Poyntz-Wright, York Fibers	137
Accurate measurement of polarization dependent loss over wavelength of single mode optical fiber components	
L.F. Stokes, Hewlett Packard	141
Polarization mode dispersion measurements in optical fibers (invited)	
Yoshinori Namihira, Jun Maeda, KDD	145
Interferometric loop method for polarization dispersion measurements	
Luc Thévenaz, Marc Niklès, Philippe Robert, Swiss Federal Institute of Technology	151
Four interferometric methods for the determination of the birefringence and polarization dispersion of polarization maintaining optical fibers	
Ch. Chojetzki, Kabelmetal-electro, H. Schmitzer, Universität Regensburg, J. Vobian, W. Dultz, DBP Telekom	155
Low coherence reflectometry for the characterization of fiber and planar lightwave circuits (invited)	
Kazumasa Takada, NTT	159
Improved sensitivity for optical low-coherence reflectometry using reference power attenuation	
W.V. Sorin, D.M. Baney, Hewlett-Packard	163
Optical low coherence reflectometry: improving reflectivity accuracy in the presence of chromatic dispersion	
Harry Chou, Hewlett-Packard	167
Standardisation in fibre optic communications: Status and perspectives (invited)	
P. DiVita, M. Artiglia, A. Cavaciuti, M. Potenza, A. Rossaro, CSELT	171
COST 217 intercomparison of OTDR measurements on single-mode fibres	
M. Artiglia, COST 217 Group	179
COST 217 intercomparison of measurements on Er-doped fibres	
P. Kiiveri, COST 217 Group	183

Single-mode fiber geometry and chromatic dispersion: results of interlaboratory comparisons Timothy J. Drapela, Douglas L. Franzen, Matt Young, NIST	187
Moderate-accuracy wavelength standards for optical communications S.L. Gilbert, T.J. Drapela, D.L. Franzen, NIST	191
Characterization of fiber-optic amplifiers (invited) Douglas W. Hall, Corning	195
Chromatic dispersion of erbium-doped fiber amplifier measured by Fourier transform spectroscopy Robert K. Hickernell, Kazumasa Takada, Makoto Yamada, Makoto Shimizu, Masaharu Horiguchi, NTT	201
Noise measurements of erbium-doped optical fibre amplifiers: influence of source excess noise M. Artiglia, CSELT, P. Bonanni, SIRTI, A. Cavaciuti, M. Potenza, M. Puleo, B. Sordo, CSELT	205
Accuracy of noise figure measurement for erbium-doped fiber amplifiers by the optical method T. Kashiwada, M. Shigematsu, M. Nishimura, Sumitomo Electric Industries	209
Automated measurement of gain characteristics of optical fiber amplifiers Douglas R. Cole, Miles E. Vance, Corning	213
Cutoff wavelength measurement precision improvement by curve fitting T.A. Hanson, K.A. Emig, Corning, C.S. Brown, AT&T Bell Laboratories, R.J. Smith, AT&T Network Cable Systems	217
Determination of the LP ₁₁ mode cutoff wavelength from the modal interference pattern K. Abe, Y. Lacroix, Y. Cai, L. Bonnell, National Optics Institute	221
Length and curvature dependence of the effective cutoff wavelength in single-mode fibers measured with an azimuthal filtering technique D. Pagnoux, J.M. Blondy, Institut de Recherche en Communications Optiques et Microondes	225
Mode field diameter and cutoff wavelength profile measurement using dual wavelength OTDR James Warder, Costas Saravanos, Northern Telecom	229
Far field MFD measurements from a reduced far field pattern A. Chiantore, F. Cocchini, D. Cuomo, G. Ferri, Fibre Ottiche Sud	233
AUTHOR INDEX	237

TESTING STRATEGIES FOR MODERN FIBRE NETWORK ARCHITECTURES

Nick Lewis, Peter Keeble, David Ferguson
BT Laboratories

INTRODUCTION

Fibre networks have been used by telecom operators for many years. Up to the present, most fibre based systems have been confined to the core network (communication between central offices). These systems used point to point transmission equipment. Recently, moves have been made to introduce fibre into the access network (central office to customer). These started with the provision to large customers using essentially core network systems. Provision to smaller customers has required the use of different architectures such as passive optical networks [1]. In this paper we look at the testing strategies for these new fibre network architectures.

THE REASONS FOR TESTING

Testing is performed *to ensure that a network bearer can support a transmission system*. If the fibre network is found to be incapable of supporting the transmission network then the network elements are individually tested to discover which of the elements is not performing to the required standard.

The amount of testing that is required in order to satisfy the afore mentioned objective depends on several factors. Firstly, the reliability of components can vary in their susceptibility to their environment and the speed at which they naturally age. This affects how often and in how much detail testing has to be carried out. Secondly, networks are subjected to environmental stresses such as temperature changes, moisture and vibration. They have different amounts of physical protection depending on whether they are ducted, aerial, deep buried or in an area of building activity. Thirdly, the customer is guaranteed a particular quality of serv-

ice quoted as mean time between failure, out of service time or average time to repair a fault. The level of service depends on the speed of repair and the amount of pre-emption of faults. Finally, a network may be shared by many users so that a network fault causes several service faults. All these factors affect the amount of testing and the type of testing that is required in order to instal and maintain a fibre network.

TEST REQUIREMENTS DURING INSTALLATION AND MAINTENANCE

Before addressing the testing strategy for networks, the phases in the network life cycle must identified in which testing is used or where it would be beneficial if it were initiated. The network in this context is defined as the fibre bearer that supports transmission systems (i.e., the part of a transmission link where the traffic is in the optical domain). There are several phases in the life of a network in which testing is an important activity:

- Tests are made on a network that has just been installed in order to commission it. The network is treated as a black box and commissioning entails end to end tests of attenuation at one of more wavelengths. It may also entail tests of fresnel reflections. If the network fails the commissioning tests then the fault and its location are found using fault finding techniques.
- In the situation where a fault has been cured by replacing or repairing a component then the individual component is commissioned. It may also be necessary to perform end to end tests since the distribution of performance of components may

well be defined statistically (depending on the procurement strategy) and it is possible for a network containing only "in-spec" components to be out of specification from end to end.

- Some networks can be physically extended some time after they have been initially installed. These networks are already carrying live traffic so they can not be turned off when commissioning the new parts of the network.
- Fault finding is performed when a fault is reported by a customer, the transmission system that uses the network or a network monitoring system. Fault finding can also be performed after a network has failed its commissioning. The purpose of fault finding is to locate the component of the network that is preventing the overall network from meeting the required specification.
- Network monitoring is not presently performed on the bearer network. It has widely been applied in the transmission systems that use the bearer. The advantage of using it in the bearer is that it may detect faults before they become service affecting (depending on the nature of the fault). They can also give more information on where a fault is located and why it has occurred.

Any test strategy must address the requirements of a network in all of the phases described above. This paper looks at test strategies for both present day fibre optic networks and new types of fibre optic network that are about to be deployed. In particular it looks at some of the tools that have been developed in response to the demands of the new types of network.

TEST STRATEGY FOR PRESENT-DAY NETWORKS

Fibre is widely used in the core network and to serve larger business sites in the access network. These are almost exclusively point to point networks. The test requirements for point to point networks have been studied over many years and are now well understood. They do, however, act as a starting

point from which a test strategy for future network architectures can be developed.

Commissioning

Testing of traditional point to point networks can be carried out using a light-source and a powermeter. This tests only the loss parameter at the system wavelength from one end of the network to the other.

Duplex transmission systems — those that transmit traffic in both directions on one fibre at one wavelength — are sensitive to fresnel reflections but in point to point networks the amplitudes of fresnels are not significant in comparison to the signal amplitude. However, if a check is required then it can be performed with a conventional OTDR.

Testing of the wavelength characteristics may be required where a network bears systems at many wavelenths. WDMs are only used in point to point systems if the transmission system is a diplex system (e.g., 1300nm TX, 1550nm RX). In this case the WDMs are usually incorporated in TX/RX modules in the transmission equipment and not in the network itself. If however the WDM is located in the network then its wavelength parameters can be tested using light sources at different wavelengths.

Fault Finding

The standard test tool for fault finding is the OTDR. This tool has enough resolution to measure backscatter over even the longest fibre. Point losses micro-bending losses and fresnel reflections are all easy to detect and locate with the OTDR. Some OTDRs are now portable enough to be carried in the palm of the hand. Some contain software that detects the more obvious features automatically.

Monitoring

A network is always monitored but usually the monitoring is performed indirectly. The transmission system that uses the network as a bearer will fail when serious network fault arises. If a fault can be proved off the transmission equipment then the fault must be in the fibre network. This is the

monitoring technique used by most present day networks.

The disadvantage of this technique is that the service using the network has been affected before a fault is identified. With direct network monitoring, faults can be found before they become service affecting. (In the UK, copper pairs are monitored every night to see if certain parameters are within limits). One monitoring technique that is sometimes used to test the loss of a network is optical level monitoring. This monitors any changes in the automatic gain control of a transmission system. A level that falls slowly indicates a degrading fault. The problem can be identified before it affects the bit error rate of services.

TEST STRATEGY FOR BRANCHED NETWORKS

Conventional point to point fibre networks have been used very successfully in the core network where the high demands for bandwidth have ideally suited fibre. Now fibre is being employed in the access network where the network requirements are different. Instead of the network nodes being central offices they are individual customers who have a relatively small but somewhat volatile demand for bandwidth.

Passive Optical Networks (PONs) have a multipoint topology that is ideally suited to this type of bandwidth demand [2-5]. PONs use splitters in order to share one network with many users. Power launched at the head-end is divided out by the splitters and only a small portion reaches each remote-end. Similarly only a fraction of the power launched from a remote end reaches the head-end — the splitters are symmetrical. The high loss makes the transmission systems that operate over the network vulnerable to any imperfections so testing is more important for PONs than it is for point to point networks. Testing is more important but it is also more difficult because firstly the end to end network losses are too great for some conventional test tools. Secondly, due to their multipoint topology, PONs require testing to be performed on them whilst live. Thirdly, any test tools used at the head-end perceive all the paths of the network to be

superimposed and finally the short distances involved in the UK access network mean high resolution requirements.

Commissioning

PONs require commissioning tests to be performed at three phases of a network's life. Like point to point networks, a PON requires commissioning after it has been installed to ensure that it can support the transmission systems that will use it, and after a faulty component has been replaced [6,7]. Unlike point to point networks, a PON is not necessarily installed in one go but may be extended at a later date. This network extension must also be commissioned before it can be used.

PONs can be commissioning after the network is first installed by testing the end to end losses between the head end and each remote end using a powermeter and light-source in much the same way as for a point to point network. (Fig.1 shows the link over a PON between the head-end and a remote-end.) However, commissioning after a network repair or a network extension must be performed while the PON is live. The commissioning must not interfere with the traffic on the network nor must the traffic interfere with the commissioning tests.

To commission a network without affecting the transmission system a separate wavelength known as the "maintenance band" can be used. End to end loss measurements can be performed at this wavelength (e.g., 1575nm) while traffic continues unabated at the system wavelength (e.g., 1300) to and from other users on the established parts of the network. The optical receivers in the transmission system have to be fitted with filters so that the light source at the test wavelength does not affect them.

Fault Finding

OTDRs are the best tools for fault finding on point to point networks. Unfortunately conventional OTDRs are unsuited to the fault finding of PONs. PONs exhibit very high end to end losses so most OTDRs can not see beyond a few splitters. Also PONs are multipoint networks so OTDRs connected at the head-end see only an amalgam of all the superimposed paths. Therefore, PONs require

other fault finding methods to be used. One way to find a fault on any network is to directly measure a power loss across it. A light source can be connected at the head-end of the network and tests can be made at various points in the network until a discrepancy is found. This testing method requires two tools; a light-source and a powermeter.

In duplex and diplex systems there is continuous downstream power on all fibres so the transmission wavelength could be used as the light-source. In situations where the network is carrying simplex transmission traffic a separate test light-source can be connected at the head-end. It must be remembered, however, that PONs are multipoint networks and some parts will be unaffected by a fault. It is not acceptable for the transmission system to be turned off in order to find a fault. A light source can be used whilst the network is operating if it uses the maintenance wavelength. In this case a maintenance port that contains a connector and filter must be provided. (The filter prevents test equipment with the wrong wavelength from affecting the transmission system if connected in error.)

A conventional powermeter can not be used because it requires the network to be disassembled in order to make a measurement. This is time consuming and halts the traffic flow. In order that the traffic is not interrupted by the measurement process a non-intrusive clip-on powermeter can be used [8]. The non-intrusive clip-on powermeter is a handheld device that measures the power in a fibre without affecting the traffic.

If the network fault is severe enough to cause service faults then the location of these service faults can implicate the location of the network fault. If the location of a fault can be narrowed to a length of fibre then an OTDR test can be used. The clip-on launch technique used with a standard OTDR enables a test to be performed without breaking into the network. The clip-on launch adaptor consists of an optical amplifier and a clip-on launcher. It can achieve a performance approaching that of a directly connected OTDR whilst allowing uninterrupted traffic.

All clip-on techniques have the disadvantage that the fibre is manhandled from the splice tray. This can induce transitory micro-bending events that interrupt the live traffic. In order to remove this problem a new type of splice tray is being evaluated within BT. This splice tray contains several windows. Clip-on test tools with attachments that engage with these splice tray windows enable a test to be made without moving the splice tray or removing the fibre from it (see Fig.2).

The use of end-on OTDRs to fault find on PONs is not entirely excluded. The problems created by the multipoint nature of PONs can be overcome by connecting an end-on OTDR only at the remote-ends of the network. In this way a unique path is viewable. The problems created by the high end-to-end loss of PONs can be overcome if OTDRs launch more power into the network. The launch power can be increased by using an optical amplifier [5]. This enables the OTDR to resolve the backscatter all the way up the PON and therefore directly detect all features. (Fig.3 shows a schematic of an optically amplified OTDR.) In this application of optical amplifiers all the power is launched into the network — the optical amplifier in the clip-on OTDR was used only to compensate for losses incurred injecting light into and extracting it from the network.

Monitoring

Monitoring of a PON requires a technique that can distinguish between different paths of the network and gather information about the state of each the paths. However, the monitoring tool can only be attached to one part of the PON. If a tool was placed at the a remote-end of a PON then it could only monitor one path. For the tool to monitor all paths then the tool must be at the head-end. This rules out conventional OTDR techniques (even high-power OTDRs) because they can not distinguish the different paths of the PON.

A technique that can distinguish the paths of a PON is remote-end fresnel monitoring. In this technique equipment monitors the reflections from the ends of the network. The amplitude of any

reflection is a measure of the square of the loss between the head-end and the remote-end that has the reflection. The location of a fault can be implied from which end reflections have been affected by a change in amplitude. The reflections from the ends of the networks are produced by the opto-electronic components or filters in the transmission system which must be specified accordingly. The OTDRs are high cost so are shared over many networks. They are connected to these networks via an optical switch (see Fig.4). Pulse OTDR techniques could be used but since the amplitudes of only specific points are monitored, it is an ideal application for a correlating OTDR using a PRBS signal. Note that in order to monitor simplex networks non-intrusively, these systems use their own optical sources in the maintenance band.

TRENDS IN TEST TOOLS

It can be seen from the previous discussion that as new types of fibre network have been developed and used by telecom operators, new types of test tools have had to be developed.

Conventional point to point fibre networks could be commissioned with a light source and powermeter, faults could be found with an OTDR and fibre monitoring was largely unnecessary. Second generation fibre networks present obstacles to the use of some of these tools and require tests that can not be achieved using others.

PONs present three obstacles to conventional test methods; the need for tests to be performed on them whilst live, their high end to end power losses and the multiple paths from the head-end. The first obstacle can be overcome by using a dedicated maintenance band. The other two by using a high-power end-on OTDR or by performing localised tests with a Clip-on OTDR or a Clip-on Powermeter.

The demand for Monitoring is developing at the same time as developments are being made in the network technology. Monitoring can improve the reliability of fibre networks by making the operator aware of degrading faults before they become service affecting. Monitoring tools can be shared over a number of networks using optical

switches. PONs can be monitored by analysing the fresnel reflections that occur or are produced at the ends of PONs.

Test Tools for Future Networks

The architectures of fibre networks are still developing. The most significant new element that will be used in future networks is the optical amplifier. This may be incorporated in a splitter to provide loss-less splitters or it may be spread over the entire network. Other elements that may be used in future fibre networks include comb WDMs modulation dependent passive routers, amplitude dependent passive routers. Networks that are built around these elements will all require new testing strategies and test tools.

CONCLUSION

As modern networks become more complex they require more testing than previous ones and that testing is more difficult to perform. It is anticipated that in future a greater proportion of the cost of networks will be spent on test tools. On the other hand the time that is required for manual testing will be greatly reduced so the whole life cost of the testing strategy will not be increased. The greater automation and monitoring in future strategies will increase perceived reliability and help fibre access systems to out-perform copper access systems in terms of both price and quality.

REFERENCES

1. Hornung S, et al, 1990 "Single-Mode Optical Fibre Networks to the Home", ICC'90.
2. Stern J R, et al, 1987 "Passive Optical Local Networks for Telephony Applications and Beyond", Electronics Letters.
3. Oakley K A, et al, 1988 "Passive Fibre Local Loop for Telephony with Broadband Upgrade" Conference Proceedings ISSL/S, 179-183.
4. Hoppitt C E, et al, 1991 "Operations and Maintenance Experience of the Bishops Stortford Fibre Trial", 3rd Conference on Telecommunications.
5. Hoppitt C E, et al, 1991 "Operations and Maintenance in the Bishop's Stortford Fibre Trial", ISSL/S '91.

6. Finegan T, Hicks A M, 1990 "Prediction for the optical performance of a novel passive branched fibre network", IEE colloquium, London, March 1990.
7. Keeble P J, et al, 1991 "Optical performance specification and measurement of local loop passive optical networks", ICC'91.
8. James S M, et al, 1989 "Clip-on" — A Possible Measurement Technique for Future Optical Networks" IWCS'89, 94-97.
9. Keeble P J, 1990 "Optical time domain reflectometry performance enhancement using erbium doped fibre amplifiers", OE/Fibres'90, September 1990.

FIGURES

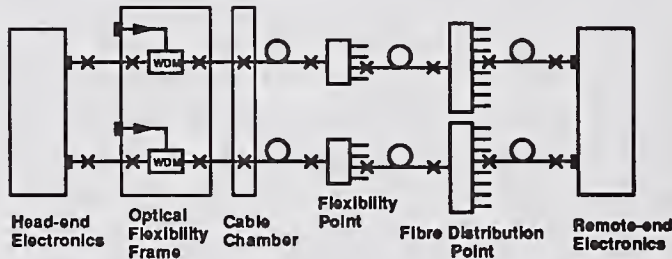


Fig.1 — PON Topology

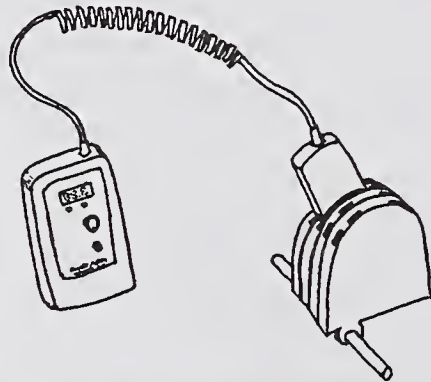


Fig.2 — Clip-on Powermeter and Windowed Splice Trays.

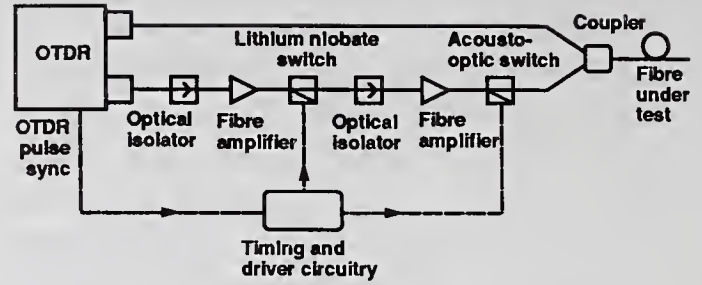


Fig.3 — High power OTDR Schematic

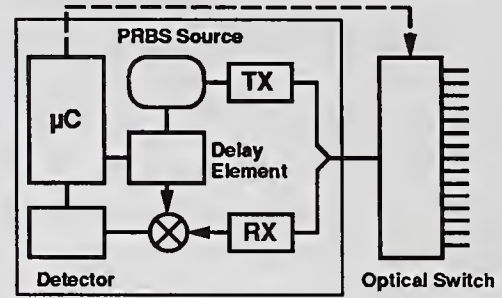


Fig.4 — Routing OTDR Schematic

OTDR Measurements Through Optical Splitters

Felix P. Kapron & James D. Berardinelli

Bellcore
445 South St., MRE-2K140
Morristown, NJ 07962-1910
201/829-5225, FAX 201/829-5965

1. Introduction

In an optical distribution system, a 1-by- N optical splitter can passively route an optical signal from one transmitter to N branch receivers. If there is a fault in a branch, can an OTDR be used at the splitter input to measure fault loss and reflectance? Previous investigations concerned fiber breaks [1] and utilized multi-wavelength OTDRs on splitters with embedded filters [2]. This paper is the first systematic measurement utilizing a standard OTDR for loss and reflectance of a branch fault and conventional splitter.

2. Splitter Properties Measured by an OTDR

2.1 Fiber Backscatter

Consider an OTDR pulse of optical power P (dBm) launched into the splitter input branch at point 1 in Fig. 1. The power backscattered at any point of a fiber depends upon the pulse duration D and is

$$B_D = B + 10 \log_{10} D \quad (1)$$

down from the forward signal [3]. Normalized to a 1 ns pulse duration, the single-mode fiber backscatter coefficient B is about -80 dB around 1310 nm, and about -82 dB around 1550 nm [3]. In Fig. 2, the OTDR reading for point 1 is

$$P_1 = 1/2 (P + B_D) \quad (2)$$

(The OTDR reading halves the dB power, and for relative power we ignore any additive constant.)

2.2 Splitter Losses

As it passes through the splitter, the pulse power suffers an excess loss E (positive dB). Then the power divides among the N branches so that the level entering any one branch at point 2 just after the splitter has been reduced by the intrinsic splitting loss

$$S = -10 \log_{10} \frac{1}{N} = 3 \log_2 N \quad (3)$$

The insertion loss of the splitter between points 1 & 2 is the sum

$$L_s = E + S \quad (4)$$

At point 2, power $(P - L_s + B_D)$ backscattered from each fiber re-enters the splitter, and experiences the excess and splitting losses again. However, the latter is canceled out by all branch fibers now contributing to total backscatter, so the effective recombination (inverse splitting) loss is zero. Thus the OTDR reading for point 2 is

$$P_2 = 1/2 (P - L_s + B_D - E) \quad (5)$$

The apparent insertion loss L_{as} is the OTDR reading drop from point 1 to point 2 in Fig. 2:

$$L_{as} = P_1 - P_2 = E + 1/2 S \quad (6)$$

We have used Eqs. (2), (5), & (4). From Eqs. (6) & (4) one has the calculated insertion loss

$$L_s = L_{as} + \frac{3}{2} \log_2 N \quad (7)$$

2.3 Splitter Reflection

If R_s is the splitter reflectance (negative dB), then at point s at the peak of the splitter reflection trace in Fig. 2, the fiber-backscattered linear power corresponding to $2P_1$ of Eq. (2) adds to the splitter-reflected linear power corresponding to $(P + R_s)$. The OTDR reading is then

$$P_s = 5 \log_{10} \left[10^{\frac{P_1}{5}} + 10^{\frac{P + R_s}{10}} \right] . \quad (8)$$

The pulse height above backscatter is

$$H_s = P_s - P_1 = 5 \log_{10} \left[1 + 10^{\frac{R_s - B_D}{10}} \right] , \quad (9)$$

using Eqs. (8) & (2). Along with Eq. (1) this gives the calculated splitter reflectance

$$R_s = B + 10 \log_{10} \left[\left[10^{\frac{H_s}{5}} - 1 \right] D \right] . \quad (10)$$

This is the standard formula [3] for a localized reflectance, shown here to be valid for a splitter.

3. Branch Fault Properties Measured by an OTDR

3.1 Branch Fault Loss

Call A dB the fiber attenuation between point 2 and point 3 just before the fault, and L_f dB the fault loss between point 3 and point 4 just after the fault. Power budgeting as above shows that the OTDR reading of Fig. 2 for one branch at point 4 is

$$P_4 = P_1 - L_s - A - L_f . \quad (11)$$

To this must be added the signals from the $N - 1$ branches with no faults. Using Eq. (11), the total OTDR signal just after the fault is

$$P_{4t} = P_4 + 5 \log_{10} \left[1 + (N - 1) 10^{\frac{L_f}{5}} \right] . \quad (12)$$

The total signal from just before the fault is P_{3t} , i.e. P_{4t} with $L_f = 0$. The apparent fault loss detected by the OTDR is the drop

$$L_{af} = P_{3t} - P_{4t} = 5 \log_{10} \left[\frac{N}{(N - 1) + 10^{\frac{-L_f}{5}}} \right] . \quad (13)$$

(For a break one has $L_f = \infty$.) Solving leaves the calculated fault loss

$$L_f = -5 \log_{10} \left[N \left(10^{\frac{-L_{af}}{5}} - 1 \right) + 1 \right] . \quad (14)$$

3.2 Branch Fault Reflectance

At point 3 the backward power is $(P - L_s - A + R_f)$ due to fault reflectance R_f and $(P - L_s - A + B_D)$ due to fiber backscatter. As before, tracing the linear powers back to the OTDR gives the reading

$$P_f = P_2 - A + 5 \log_{10} \left[1 + 10^{\frac{R_f + B_D - S}{10}} \right] . \quad (15)$$

The height of the fault reflection is

$$H_f = P_f - P_{3t} . \quad (16)$$

Using Eqs. (16), (15), (2), & (8), the calculated fault reflectance is found to be

$$R_f = S + B + 10 \log_{10} \left[\left[10^{\frac{H_f}{5}} - 1 \right] D \right] . \quad (17)$$

4. Experimental Measurements

4.1 Test Setups

Both 1-by-2 and 1-by-4 uniform optical splitters were used in separate setups, each similar to Fig. 1. The OTDR pulse spatial width was about 50 m, so all features were resolvable from each other. All branches were terminated reflectively or non-reflectively, with no differences in results.

4.2 Splitter Properties

In each setup with the splitter in place, the OTDR trace showed that $H_s = 0$, so there were no apparent splitter reflections. The concurrent apparent splitter loss L_{as} was obtained in each case, and Eq. (7) leads to a calculated insertion loss L_s . The actual insertion losses were determined with a loss testset. The results for the 1-by-2 setup are given in Table 1; those for the 1-by-4 setup are in Table 4. The calculated and actual loss values are in agreement to within measurement error bounds for the 1-by-2 splitter, but the correlation is only fair for the 1-by-4 splitter.

4.3 Splice Properties

The apparent splice losses L_{af} were determined from the setups of Fig. 1, and Eq. (14) resulted in calculated splice losses L_f . With the splitter removed in each setup, direct single-direction OTDR measurements were made on the splices of the faulty branches. These showed larger features compared to those in the above traces. Again, losses summarized in Table 2 for the 1-by-2 splitter agreed within error bounds, but the 1-by-4 results in Table 5 were not as favorable.

The apparent reflection peaks H_f with the splitter and the actual peaks without the splitter are given in Tables 3a (1-by-2) & 6a (1-by-4). These were used in Eq. (17) to obtain the calculated and actual fault reflectances given in Tables 3b (1-by-2) & 6b (1-by-4). Agreement is good in both cases.

5. Conclusions

We have given a procedure by which an OTDR can be used at the input port of a 1-by- N uniform splitter to measure the losses and reflectances of the splitter and of any faults in the output branches. A theory outline was followed by experiments with 1-by-2 and 1-by-4 splitters. With higher split ratios, faults are expected to become more difficult to measure accurately.

6. References

- [1] I. Sankawa et al., *IEEE Photon. Technol. Lett.*, vol. 2, no. 10, pp.766-768 (Oct. 1990)
- [2] H. Yanagawa et al., *Tech. Digest OFC'92*, paper FA4, p. 263 (Feb. 1992)
- [3] F. Kapron, et al., *IEEE/OSA J. Lightwave Technol.*, vol. 7, no. 6, pp. 1234-1241 (Aug. 1989)



Figure 1. Schematic of a splitter connected to an OTDR, defining several points at which power levels are referenced.

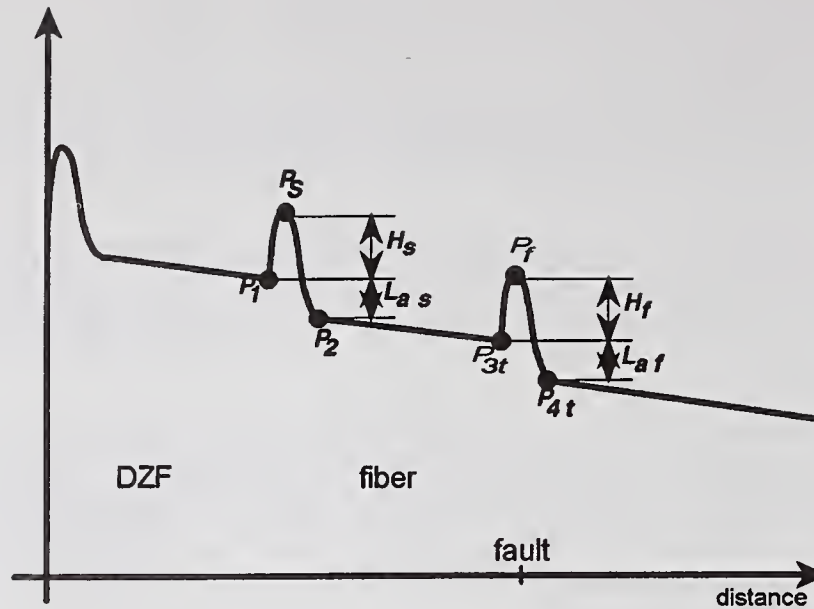


Figure 2. Schematic of an OTDR trace, with the reference points corresponding to Figure 1. (In practice, points P_2 and P_{4t} are extrapolated backward by the OTDR to account for pulse width.)

Table 1: 1x2 Splitter Loss (to ± 0.2 dB)

Apparent	Calculated	Actual
1.62	3.12	3.50

Table 2: 1x2 Splice Loss (to ± 0.05 dB)

	Apparent	Calculated	Actual
Splice #1	0.26	0.56	0.48
Splice #2	0.32	0.69	0.60

Table 3a: 1x2 Reflection Peaks (to ± 0.1 dB)

	Apparent	Actual
Splice #1	7.60	8.46
Splice #2	8.20	9.22

Table 3b: 1x2 Reflectances (to ± 0.4 dB)

	Calculated	Actual
Splice #1	-28.0	-29.3
Splice #2	-26.8	-27.2

Table 4: 1x4 Splitter Loss (to ± 0.2 dB)

Apparent	Calculated	Actual
3.18	6.18	7.50

Table 5: 1x4 Splice Loss (to ± 0.1 dB)

	Apparent	Calculated	Actual
Splice #1	0.14	0.62	0.46
Splice #2	0.20	0.94	1.52

Table 6a: 1x4 Reflection Peaks (to ± 0.1 dB)

	Apparent	Actual
Splice #1	6.74	8.72
Splice #2	5.16	7.70

Table 6b: 1x4 Reflectances (to ± 0.4 dB)

	Calculated	Actual
Splice #1	-26.9	-28.8
Splice #2	-30.3	-30.9

A 1.6- μm -band OTDR using a Raman fiber laser pumped by a Q-switched Er^{3+} -doped fiber ring laser

T. Horiguchi, T. Sato, and Y. Koyamada

NTT Telecommunication Field Systems R&D Center
Tokai, Ibaraki-ken, 319-11 Japan

1. Introduction

Optical time domain reflectometers (OTDR) operating at 1.6- μm -band are a very important diagnostic tools for maintaining optical fiber transmission lines. This is because the 1.6- μm -band OTDR can find faults caused by fiber bending with a higher sensitivity than OTDRs whose wavelength is the same as that of existing optical transmission systems, 1.3 or 1.55 μm [1]. In addition, the 1.6- μm -band OTDR has the potential to investigate in-service subscriber lines of 1.3/1.5 μm WDM system in the planned.

One approach to extending the dynamic range of an OTDR is to use fiber amplifiers or lasers. Of those currently available, the Raman fiber amplifier or laser is the most promising for the 1.6- μm -band OTDR [2,3]. A Raman fiber amplifier or laser requires a pump source at a wavelength that is one Stokes shift shorter than the required amplification or lasing, but with significantly greater power. Until recently, however, there was no light source with sufficiently high power yet small enough to incorporate in a 1.6- μm -band OTDR for practical use. Fortunately, the Er^{3+} -doped fiber amplifier or laser has now been developed which is compact, operates at around 1.55 μm as the pump for a 1.6- μm -band light signal and produces high peak pulse powers.

In our previous 1.6- μm -band OTDR [3], a Raman fiber amplifier was used which was pumped by the output of an Er^{3+} -doped fiber amplifier. The output peak power of the Er^{3+} -doped fiber amplifier was limited to about 1.5 W, which made it necessary to use a long Raman fiber of 20 km. In addition, the output peak power of the Raman fiber amplifier was limited to 0.2 W. As a result, the dynamic range of the OTDR was 25.7 dB with a relatively poor spatial resolution of 100 m.

In this paper we report a 1.6- μm -band OTDR with higher performance which is based on a Raman fiber laser pumped by a Q-switched Er^{3+} -doped fiber ring laser.

2. Experiments

2.1 Q-switched Er³⁺-doped fiber ring laser and Raman fiber laser

The experimental set-up of the 1.6- μm -band OTDR, which includes a Q-switched Er³⁺-doped fiber ring laser and a Raman fiber laser, is shown in Fig.1. The Q-switched laser had a ring cavity in which a 10 m Er³⁺-doped fiber with an Er³⁺ concentration of 1800 ppm was pumped at 25 mW by a 1.48 μm laser diode through a 1.48/1.55 μm WDM fiber coupler. A polarization-independent optical isolator was inserted into the ring cavity to attain unidirectional lasing. Q-switching was performed by a mechanical chopper in the cavity. The trace of the output pulse of the Q-switched fiber laser is shown in Fig.2(a), indicating a pulse duration of 170 ns and a peak power of as high as 16 W. The output pulse was then launched into a Raman fiber as a pump. The Raman fiber was a specially prepared single-mode fiber, whose Raman gain was enhanced by raising the relative index difference of the fiber to 1.8 % by doping its core and cladding with GeO₂ [4] and F, respectively. The optimum length of the Raman fiber was determined as 1.5 km, by observing the fiber length at which the backward Rayleigh scattering of the stimulated Raman scattering due to the 16 W input pulse in the Raman fiber reaches its maximum power. The transmitted pulse was filtered with a long-wave-pass filter to eliminate the unwanted 1.55 μm pulse and obtain a 1.6- μm -band pulse. The waveform of the generated pulse of the stimulated Raman scattering is shown in Fig.2(b). Its duration and peak power were 150 ns and 5.5 W, respectively, which are a significant improvement on the results in [2]. Figure 2(c) shows the trace of the pump pulse transmitted through the Raman fiber. It can be seen that the pump pulse was significantly depleted. Figure 3 shows output pulse spectra from both the Q-switched Er³⁺-doped fiber ring laser and the Raman fiber laser. Their center wavelengths were 1557 and 1672 nm, respectively. The wavelength difference was in good agreement with the Stokes shift in silica optical fibers [5].

2.2 OTDR experiments

The experimental set-up of the 1.6- μm -band OTDR is shown in Fig.1. A 1.6- μm -band probe pulse from the Raman fiber laser was launched into a 66 km single-mode fiber which was composed of 6 fiber spools, each about 11 km long, spliced in series. The input peak power of the probe pulse was reduced to 1.2 W to suppress the stimulated Raman scattering in the test fiber itself. The backscattered Rayleigh scattering was received by an InGaAs avalanche photo-

diode (APD) through a 50/50 fiber coupler and an acoustooptic switch (AO-SW). The AO-SW was used to prevent strong near-end Rayleigh backscattering from entering the APD as this would otherwise distort the signal waveform when measuring the weaker Rayleigh backscattering from the far-end of the test fiber. The backscattered signal received by the APD was digitized and averaged with a digital processing system. The probe pulses have jitter caused by fluctuations in the revolution speed of the mechanical chopper blade. Therefore a timing signal was produced from a portion of each probe pulse and supplied to the AO-SW and the digital processing system to synchronize them.

Figure 4 shows a backscattered signal waveform which was measured with a receiver bandwidth of 6 MHz and the 2^{16} signal integrations. The dynamic range of the 1.6- μm -band OTDR, which can be evaluated from the difference between the near-end Rayleigh scattering level and the noise floor, was 24.5 dB. The spatial resolution was confirmed to be 20 m by measuring the step-wise change in backscattered power from the splice points. These results imply that the OTDR has approximately the same dynamic range and 5 times better spatial resolution than the previously reported OTDR [3]. The average loss of the test fiber including 5 splices was estimated to be 0.30 dB/km from the backscattered signal trace of Fig.4. This value is in good agreement with results obtained by the cut-back method.

3. Conclusion

We have demonstrated a 1.6- μm -band OTDR utilizing a Raman fiber laser pumped by a Q-switched Er^{3+} -doped fiber ring laser. The dynamic range of the OTDR was 24.5 dB with a spatial resolution of 20 m. This performance is superior to that of commercially available 1.3 or 1.55 μm OTDRs. The demonstrated OTDR is also able to operate at 1.55 μm by utilizing the output from a Q-switched Er^{3+} -doped fiber ring laser as the OTDR probe pulses.

References

- [1] Y. Koyamada, N. Ohta, and N. Tomita, "Basic concepts of fiber subscriber loop operation systems," in *Proc. Int. Conf. Commun.*, 1990, vol.4, pp.1540-1544.
- [2] T. Horiguchi, T. Sato, and Y. Koyamada, "Stimulated Raman amplification of 1.6- μm -band pulsed light in optical fibers," *IEEE Photon. Technol. Lett.*, vol.4, no.1, pp.64-66, 1992.
- [3] T. Sato, T. Horiguchi, and Y. Koyamada, "A 1.6 μm band OTDR using a synchronous Raman fiber amplifier," to be published in the August 1992 issue of *IEEE Photon. Technol. Lett.*
- [4] S. Sudo, T. Hosaka, H. Itoh, and K. Okamoto, "High- Δn , small-core single-mode fibers for efficient nonlinear optical effects," *Electron. Lett.*, vol.22, no.16, pp.833-835, 1986.
- [5] R. H. Stolen, "Nonlinearity in fiber transmission," *IEEE Proc.* vol.68, no.10, pp.1232-1236, 1980.

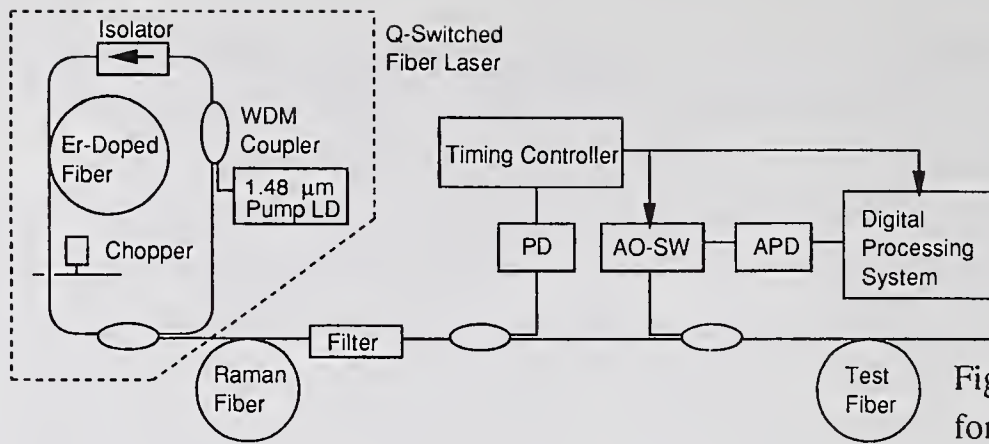


Fig.1 Experimental arrangement for 1.6- μ m-band OTDR.

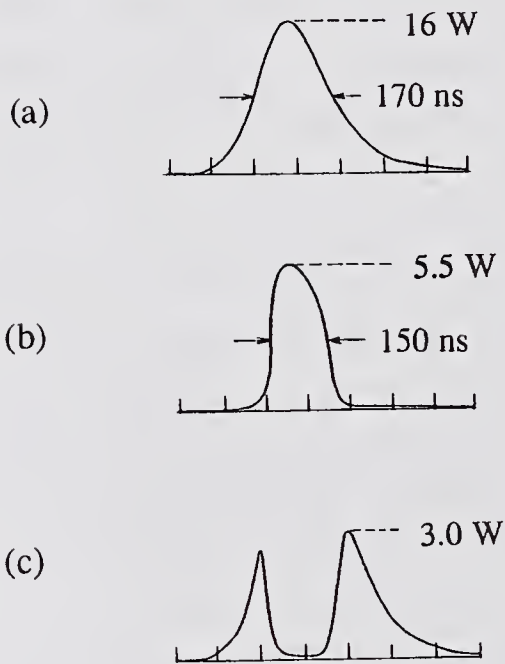


Fig. 2 Fiber laser data. (a) Pump pulse from Q-switched fiber laser, (b) output pulse from Raman fiber laser, (c) pump pulse after depletion. Time scale is 100 ns/div.

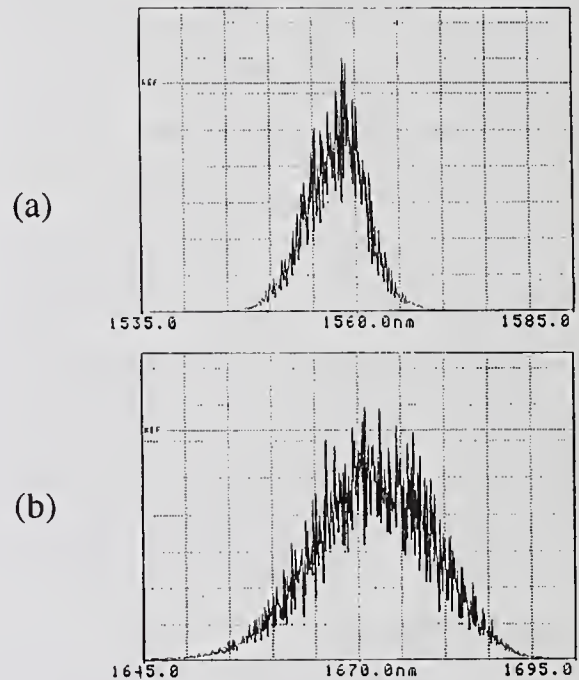


Fig. 3 Spectra of (a) Q-switched fiber laser and (b) Raman fiber laser. Horizontal scale is 5 nm/div.

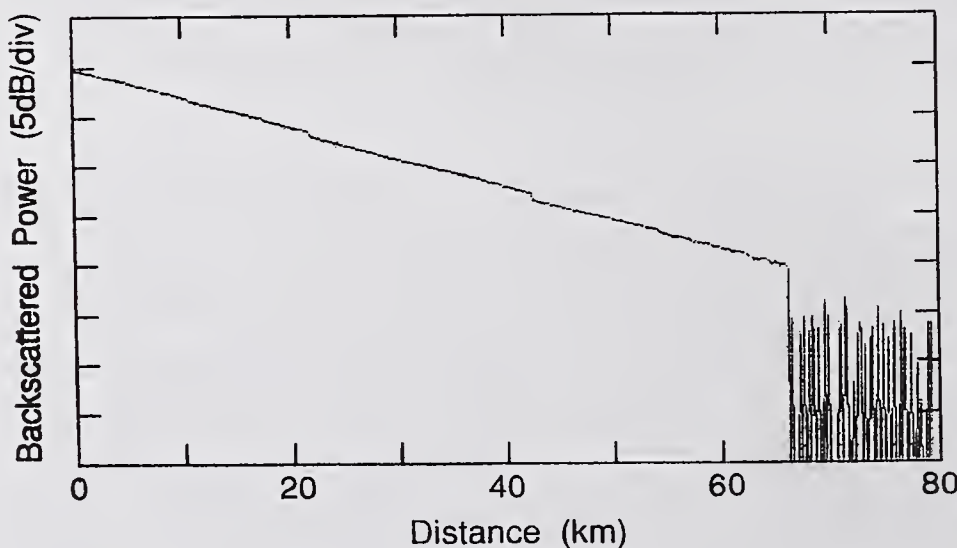


Fig. 4 Rayleigh backscattered power from a 66 km fiber.

The Effect of OTDR Measurement Error on Fiber Uniformity Metrics

Jane B. Clayton, Andrew L. Ingles, David A. James*, Daryl Pregibon*

AT&T Bell Laboratories

Norcross, GA 30071, *Murray Hill, NJ 07974-2070

1. INTRODUCTION

The Optical Time Domain Reflectometer (OTDR) which uses backscattered signals to measure power loss along the fiber length and provides the basis for quantifying fiber uniformity is known to produce backscattered measurements which are more variable the farther signals travel into a fiber; this increase in measurement variability adversely affects the reliability of widely used nonuniformity metrics such as maximum individual segment loss (MISL) and the difference between MISL and average loss (AVG).

Results from an experiment characterizing the dependence of OTDR measurement variability on laser power unit, pulse width, and number of signal averages show the primary determinants of OTDR measurement variability are plugin and pulsewidth. The significance of these results is demonstrated in terms of the metric MISL-AVG.

2. EXPERIMENTAL ARRANGEMENT

Plugin type (high power versus low power), pulse width (25, 50, 250m), and number of signal averages (39, 100, 150, 200) were varied in a statistically designed experiment. A full factorial design was suggested since little prior information on potential interactions was available, and this resulted in 24 (2×3×4) separate experimental conditions.

A single 30 km test fiber was used in our experiment, for which 100 OTDR traces were generated in succession. Elapsed time for each set of traces was approximately 20 minutes (per wavelength). The 24 sets of 100 traces (each either 579 or 2313 data points long, depending on the pulse width) are the basis for the subsequent analysis.

3. DATA PROCESSING

3.1 Estimating Effects of OTDR Settings on OTDR Variation

We examine the role of OTDR measurement variability on uniformity metrics by analyzing the variance of OTDR measurements rather than directly analyzing the variance of derived metrics. Since the accuracy and precision of the latter depends on the former, we do not lose any flexibility in doing so. What we gain is important insight into the relationship of OTDR measurement variability and position along the fiber length.

OTDR measurement variability is quantified at each condition by simply computing the sample standard deviation of the 100 repeat measurements by position. This results in 24 standard deviation traces which were smoothed using the lowess algorithm.^[1] These smooth standard deviation traces capture the salient global relationship of measurement variation on fiber position. Since narrow pulse traces contain measurements every 12.5m as opposed to every 50m for the medium and wide pulses, we addressed the problem of unequal number of measurements by interpolating the smoothed traces every kilometer to obtain 30 variances per test condition.

We use an analysis of variance model^{[2] [3]} to quantify the relationship between OTDR measurement variability and the experimental conditions. The model can be concisely written as:

$$Y(p) = X\beta(p) + E(p)$$

where Y denotes the response variable, X the matrix of coded experimental conditions, β the effects of varying parameter settings, and E the (independent) error terms with mean zero. The notation " (p) " conveys the fact that in our analysis each element of Y is a trace, i.e. a function of position " (p) " along the fiber. This induces position dependence on the effects $\beta(p)$ and the error terms $E(p)$, but not on the coded experimental conditions X .

In our analysis, the logarithm of the interpolated smoothed standard deviation traces served as the response variable since it better satisfies the assumptions underlying the analysis. The particular parameterization we chose for the effects is given in Table 1.

4. DATA ANALYSIS

Figure 1 depicts the standard deviation of power measurements (in dBs) at positions 5, 15, and 30km (indicated at

the upper right-hand corner on each panel) for 1310nm and 1550nm. Intermediate positions can be obtained by linear interpolation. On each panel, the horizontal line represents the overall average; the factors are displayed along the horizontal axis, and the labels depict the average standard deviation at that level of the factor. Note that averages for plugin are based on 12 observations each, those for pulse width on 8 observations, and those for number of signal averages on 6 observations. Wide pulsewidths lead to relatively uniform OTDR measurement variability. For narrow and medium pulse widths, 39 signal averages leads to noticeable increased baseline variation. Also a strong effect due to the power of the test unit (plugin) at 1550nm is observed.

Figures 2 and 3 display the standardized effects¹ by position for 1310nm and 1550nm. These plots exploit the continuity along fiber length of the raw data as a means to summarize estimated effects. At 1310nm, the only clear factor driving measurement variability is pulse width. Other factors pale in comparison. At 1550nm, plugin is also important, and a small interaction between plugin and pulse is exhibited. The salient feature of the figures is the position dependence (or lack thereof) of the estimated effects. For example at 1550nm, although pulse and plugin are the largest two effects, they are increasingly so deeper into the fiber. In contrast, changing the number of averages from 39 times to 100 or more times is marginally important and not position dependent.

While this analysis suggest that plugin power is important only at 1550nm, we believe it to be important at both wavelengths. The wider pulse widths contain higher power and we see consistent pulse width effects at both wavelengths, suggesting higher power is important at 1310nm and 1550nm. And upon further examination of the data, we determined that there was essentially no difference in output power level between the "low" and "high" power plugins at 1310nm; consequently, we should not have expected to see a plugin effect at 1310nm. The difference between the actual output power levels was only observed at 1550nm. This misclassification of plugin type arose out of relying on the manufacturer's specification of "minimum output power" to characterize the plugins (the "low power" plugin had higher power than its specification guaranteed). Future experiments will classify plugin type based upon actual output power measurements.

5. EFFECT ON DERIVED UNIFORMITY METRICS

5.1 Modelling 'Perfect' Fiber

OTDR measurement variability in these experimental data deviates from measurement variability on a perfect fiber in at least two ways: deviations due to nonuniformity in the test fiber and deviations caused by changes in the laser's power output over the course of the experiment. To estimate "intrinsic" OTDR measurement variability, we estimated fiber nonuniformity and laser drift from the experimental data and corrected for them as follows.

Let P denote the matrix of power measurements for a given fiber at a given wavelength such that P_{ij} is the measured power at position j for the i th repeat. Let r_i denote the mean of the i th row and c_j the mean of the j th column. Average fiber loss at position j , $pred(j)$, can be determined by the least squares fit of average power (c_j) on position (j). Fiber nonuniformity defined as the deviation of actual power from predicted power over the fiber is given by:

$$c'_j = c_j - pred(j), \quad j = 1, \dots, 579 \text{ or } 2313.$$

Assuming laser power is constant for each trace, laser drift, r'_i , is defined as the deviation of power from the average power over the course of the experiment:

$$r'_i = r_i - mean(r_i), \quad i = 1, \dots, 100.$$

We model "perfect" fiber from test fiber by simply subtracting the estimated laser drift from each trace (i.e., row) and the estimated fiber nonuniformity from each column:

$$P'_{ij} = P_{ij} - r'_i - c'_j.$$

This process yields 100 "perfect" fibers with identical average loss and OTDR launch power. These cannot have arisen as OTDR measurements since the OTDR scales integer measurements by machine constants that effectively rounds measured power to the nearest 0.01 dB or 0.02 dB. The final operation we perform to mimic OTDR measurements on "perfect" fiber thus entails rounding to the desired precision.

1. The precision of the coefficients β_i varies with the number of factor levels in the corresponding term (see Table 1); the standardized effects, however, have constant precision.

5.2 Assessment of Parameter Settings on Uniformity Metrics

The measurement variability affects the operating characteristics of derived metrics, such as MISL, in two important ways: by changing the mean value and changing the spread (variance) about the mean. We now show how the best and the worst settings translate into expected behavior of derived metrics on perfect fiber.

Upon "manufacturing" 100 perfect fiber OTDR traces as described earlier, 100 pseudo-traces are constructed by sampling (by position) the power measurements. Another 100 pseudo-traces are similarly constructed, and these are "folded" to mimic 100 bidirectional (outside-in, inside-out) true attenuation traces. Each true attenuation pseudo-trace is decomposed into individual 1 km sectional loss (ISL) values. The desired metric (MISL-AVE) is computed for each ISL trace along with position of the MISL.

Figures 4 and 5 display the results of this procedure at 1310nm and 1550nm at the optimal parameter settings (wide pulse, high plugin, and 100 averages). The top panel shows the variation in the one-kilometer ISLs as a function of position; the vertical lines centered on the means depict two- σ bars. There is a slight increase in the length of the two- σ bars at the fiber ends for 1310nm. This translates into a slight nonuniformity in the distribution of MISL locations towards the fiber ends. The induced distributions of MISL-AVG for 1310nm and 1550nm are unimodal with varying degrees of asymmetry. As emphasized by us earlier, the distribution of MISL-AVE is not centered on zero, even for perfectly uniform fiber.

In comparison, Figures 6 and 7 display the corresponding results at the worst parameter settings (narrow pulse, low power, 39 signal averages). The differences are striking, not only in the final distribution of the derived metric MISL-AVE (which has shifted to the right and has larger spread), but more so in the ISL trace and the distribution of MISL position. In effect, the fiber ends completely dominate the distribution of this metric when the parameter settings are not "optimally" set.

6. CONCLUSIONS

OTDR measurement variability is minimized on existing OTDR devices, especially deeper into the fiber, by using 100 signal averages and wide pulse widths. Signal averages in excess of 100 times is marginal. Testing at wider pulsewidths reduces measurement variability at the expense of reducing testing resolution and this tradeoff will need to be considered before standardizing test procedures. High power plugin is shown to be important at 1550, and we suspect this to be the case for 1310 as well.

7. REFERENCES

1. Chambers, J. M., W. S. Cleveland, B. Kleiner, and P. A. Tukey. (1983). Graphical Methods for Data Analysis. Belmont, CA; Wadsworth International Group.
2. Box, G. E. P., W. G. Hunter, and J. S. Hunter. (1978). Statistics for Experimenters, New York. Wiley and Sons.
3. Chambers, J. M. and T. Hastie (editors). (1992). Statistical Models in S. Pacific Grove, CA. Wadsworth.

TABLE 1		
Terms	Coefficients	Proportional to
Main Effects		
Intercept	β_0	average response over all test conditions
plugin	β_1	average response at High plugin – average response at Low plugin
pulse1	β_2	average response at Medium pulse – average response at Wide pulse
pulse2	β_3	average response at Narrow – average response at Medium and High
navg1	β_4	average at 150 – average at 200
navg2	β_5	average at 100 – average at 150 and 200
navg3	β_6	average at 30 – average at 100, 150, and 200
Two-way Interactions		
plugin by pulse1	β_7	average pulse1 at High – average pulse1 at Low
plugin by pulse2	β_8	average pulse2 at High – average pulse2 at Low
plugin by navg1	β_9	average navg1 at High – average navg1 at Low
plugin by navg2	β_{10}	average navg2 at High – average navg2 at Low
plugin by navg3	β_{11}	average navg3 at High – average navg3 at Low
pulse1 by navg1	β_{12}	average navg1 at Medium – average navg1 at Wide
pulse2 by navg1	β_{13}	average navg1 at Narrow – average navg1 at Medium and Wide
pulse1 by navg2	β_{14}	average navg2 at Medium – average navg2 at Wide
pulse2 by navg2	β_{15}	average navg2 at Narrow – average navg2 at Medium and Wide
pulse1 by navg3	β_{16}	average navg3 at Medium – average navg3 at Wide
pulse2 by navg3	β_{17}	average navg3 at Narrow – average navg3 at Medium and Wide
Three-way Interactions		
plugin by pulse1 by navg1	β_{18}	average pulse1 by navg1 at High – average pulse1 by navg1 at Low
plugin by pulse2 by navg1	β_{19}	average pulse2 by navg1 at High – average pulse2 by navg1 at Low
plugin by pulse1 by navg2	β_{20}	average pulse1 by navg2 at High – average pulse2 by navg2 at Low
plugin by pulse2 by navg2	β_{21}	average pulse2 by navg2 at High – average pulse2 by navg2 at Low
plugin by pulse1 by navg3	β_{22}	average pulse1 by navg3 at High – average pulse1 by navg3 at Low
plugin by pulse2 by navg3	β_{23}	average pulse2 by navg3 at High – average pulse2 by navg3 at Low

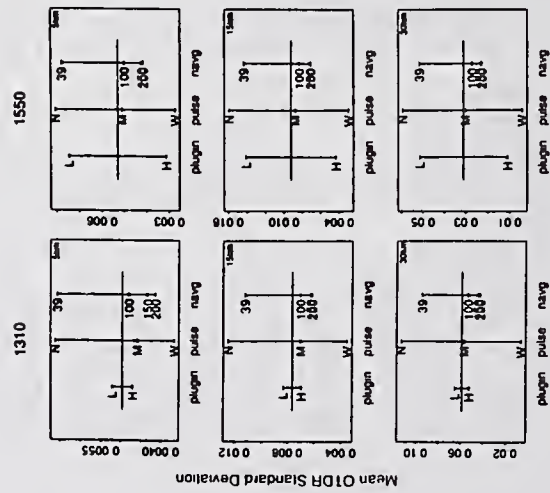


Figure 1

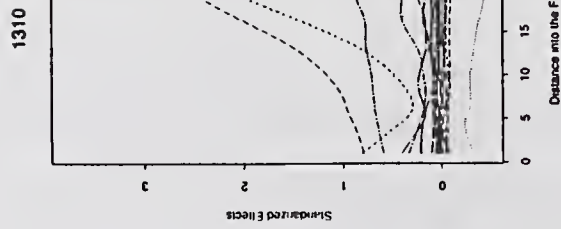


Figure 2

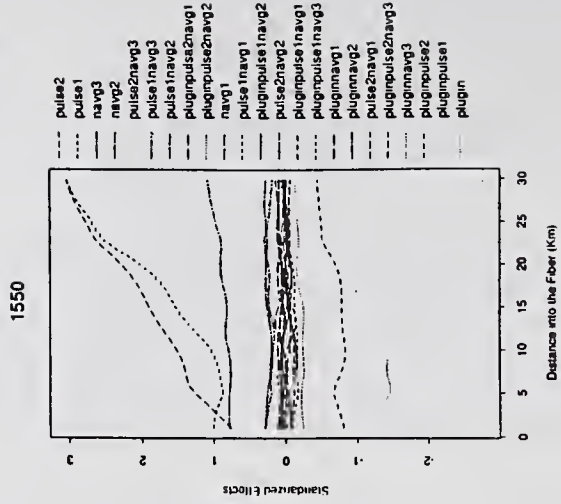


Figure 3

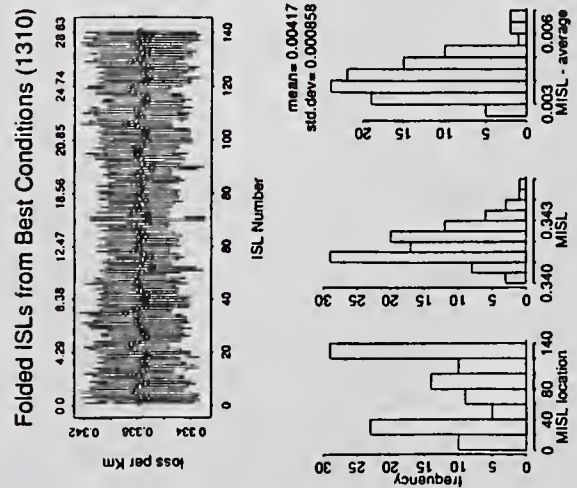


Figure 4

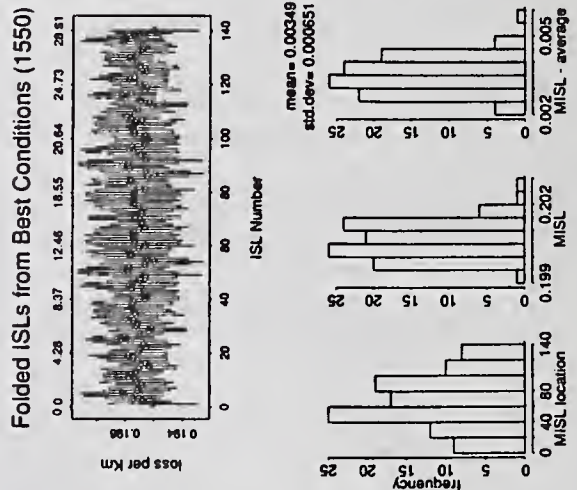


Figure 5

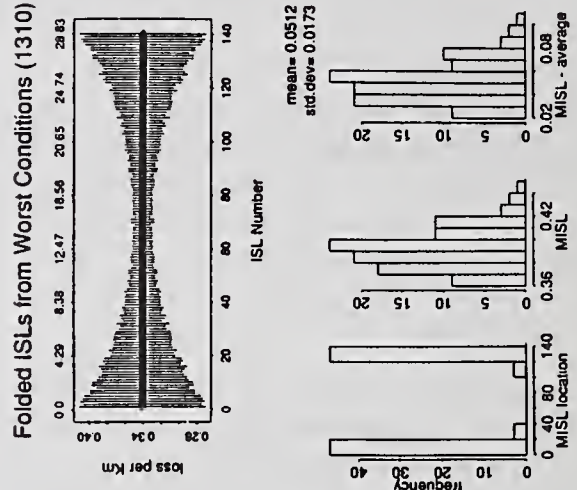


Figure 6

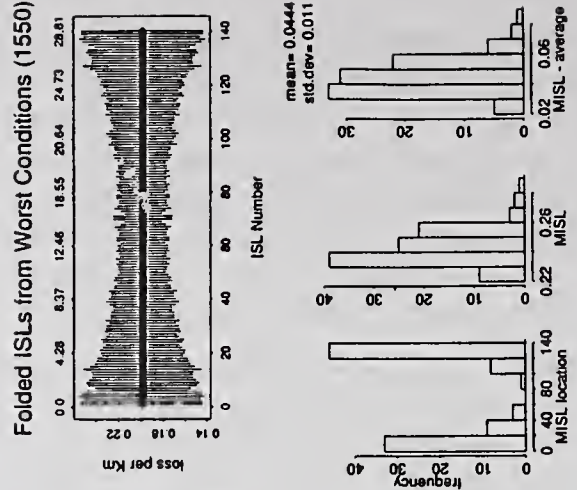


Figure 7

An OTDR Based Combined End-Reflection and Backscatter Measurement

A. F. Judy

AT&T Bell Laboratories
Norcross, Georgia 30071

1. INTRODUCTION. Because of Rayleigh scattering, optical fibers will reflect a portion of any transmitted light back toward the input. The amount of this fiber backscatter (FBS) is important to determine. It is needed for measuring splice and connector reflections with an OTDR, for predicting the total feedback and double Rayleigh backscatter for transmission system design, and for measuring the uni-directional OTDR splice loss between dissimilar fibers.

For step-index fiber profiles, the amount of FBS can be theoretically calculated but the accuracy is limited by uncertainties in the fiber parameters. For more complicated profiles even the theoretical solution is uncertain. So a reliable measurement methodology is needed. This paper describes an OTDR based method called the combined end-reflection and backscatter (CERBS) technique. It is an inherently repeatable means for measuring FBS with potentially traceable accuracy.

2. DEFINITIONS AND THEORY. The amount of FBS is measured by the pulse reflectance, R_{bs} . This is defined as the ratio of captured reflected power to the total pulse power, both evaluated at the scattering location within in the fiber. R_{bs} depends on wavelength, the fiber's index profile, and the optical input signal. For a narrow rectangular pulse it is: ^[1]

$$R_{bs} = S\alpha_R PW, \quad (1)$$

where α_R is the total Rayleigh scattering per unit length, S is the fraction of scattering captured by the fiber, and PW is the spatial pulse width, i.e. the temporal width multiplied by half the group velocity. For non-rectangular pulses, PW is the width of the rectangular pulse whose energy and peak power equals that of the actual pulse. ^[2] PW is assumed small enough that the fiber loss between the leading and trail edges is negligible.

To calculate R_{bs} , the parameter S must be known. For a step-index fiber this is: ^[3]

$$S = \frac{3}{8} \left[\frac{\lambda}{\pi n_{co} \omega_o} \right]^2 \quad (2)$$

where: λ is the wavelength, n_{co} is the refractive index of the fiber core, and ω_o is the spot size (which also depends on λ). For other than step-index profiles, equation (2) approximately holds if ω_o for the "equivalent step index" ^[4] is used. But the accuracy of this approximation is unevaluated and an experimental measurement method is required to find R_{bs} .

3. CERBS MEASUREMENT METHOD. The CERBS measurement method (Figure 1) uses the principle of creating a reference reflection (R_{ref}) at the fiber's end, measuring it, and measuring R_{bs} with respect to it. Each of these three steps is described below.

3.1 CREATING THE REFERENCE REFLECTION. A large end-reflection can be generated by perpendicularly placing the fiber-end against a front-surface mirror with a high, but not necessarily known, reflectance. This is most easily done by terminating the fiber with a rotary-mechanical-splice ferrule and using the polishing fixture to hold the ferrule perpendicular to the mirror. A cleaved fiber-end, similarly positioned, should also work. Any non-flatness of the fiber end or non-perpendicularity to the mirror is unimportant because, as described below, the end-reflection is actually measured.

It is common to use the glass-air Fresnel reflection at an unterminated fiber-end as a "known" R_{ref} of -14.7 dB. As will be shown, this is not always a repeatable method.

3.2 MEASURING THE REFERENCE REFLECTION. The CERBS method attains its accuracy by actually measuring R_{bs} . This is done with an OTDR by considering the mirror as a splice and measuring the 'splice loss'. That is, when viewed on the OTDR, the mirror will appear (Figure 2) as a reflection with FBS both preceding it and following it.^[5] The FBS that follows it is the reflection of the fiber that precedes it. It is generated by the OTDR pulse reflecting in the mirror and, as it propagates back towards the OTDR, continuing to be backscattered. This 'backscatter' actually travels in the forward direction (away from the OTDR) until it too hits the mirror and is reflected towards the OTDR. When it reaches the OTDR its time delay will be greater than the round-trip delay to the mirror so it appears to follow the mirror. Likewise, its amplitude will be reduced (in decibels) by $2R_{ref}$. So R_{ref} is found by measuring the difference between the FBS before and after the mirror (points B and C in Figure (2), less the intervening fiber loss). This is exactly what the OTDR 'splice loss' measurement performs.

Three cautions must be observed in implementing this technique. First, the 'splice loss' measurement may not be accurate unless the OTDR has a masking feature. This feature suppresses the mirror's large Fresnel reflection that could cause the OTDR to distort the FBS that follows the mirror. Second, there must be no other large reflections in the system, e.g. the OTDR panel connector, the optical attenuator, etc.. Other large reflections, even if they are not near the mirror, can introduce errors by generating either ghost reflections or additional double-reflected FBS. Third, the reference reflection must be large ($> -5dB$). Smaller reflections cause too large a loss at the mirror for accurate OTDR measurement.

3.3 MEASURING THE DIFFERENCE BETWEEN R_{ref} and R_{bs} . Since the difference between R_{ref} and R_{bs} can be 50 dB or more, it probably cannot be directly measured on the OTDR. Even if it could, one would have to verify the OTDR's accuracy over such a large range. For both reasons, a calibrated optical attenuator is placed (Figure 1) between a reference fiber and the fiber under test. With the attenuator at its minimum loss, one measures the loss difference (L_{AB}) on the OTDR between the FBS at the end of the two fibers (Points A and B in Figure 2). Then the attenuator is increased an amount ATT until the end reflection is about the same level as point B (see Figure 3), and the OTDR loss difference (L_{AD}) between the reference FBS and R_{ref} (points A and D in Figure 3) is measured. The R_{bs} is then given by:

$$R_{bs} = 2(R_{ref} + L_{AD} - L_{AB} - ATT) \quad [dB]$$

4. RESULTS. Using a commercial OTDR with a PW of 102 meters (1 μs), we measured both ends of nine dispersion-shifted fibers at both 1.31 and 1.55 μm . Each fiber-end was terminated with three different reference reflections. They were:

- (1) A first-surface mirror (FSM) with a nominal 100% (0 dB) reflectance, and a measured R_{ref} that ranged from -0.06 to -0.80 dB.
- (2) A neutral density filter (NDF) with a nominal density of 2.0, and a measured R_{ref} that ranged from -1.4 to -3.0 dB.
- (3) The glass-air reflection (GAR) which is assumed to be -14.7 dB. Since the glass-air reflectance is less than -5 dB, its true value could not be measured.

The test's repeatability can be gauged by comparing the results for each reference reflection at both wavelengths. Any variations between the parameters of the eighteen fiber-ends should cause proportional effects at the two wavelengths. This was observed (Figures 4 and 5) for the FSM and NDF but not for the GAR (Figure 6). Thus the inherent repeatability of the CERBS method is high only when R_{ref} is actually measured, as is the case for the FSM and NDF.

The second repeatability test is to compare, at a given wavelength, the results for the three reference reflections. At 1.31 μm it is seen that the NDF and FSM data are highly correlated (Figure 7) but the GAR and FSM are not (Figure 8). Similar results occurred at 1.55 μm .

The final R_{bs} statistics for all eighteen fiber ends is shown below:

Reference Reflection	1.31 μm		1.55 μm	
	\bar{x} (dB)	σ (dB)	\bar{x} (dB)	σ (dB)
FSM	-46.2	.31	-49.8	.45
NDF	-46.1	.30	-49.7	.48
GAR	-46.1	.48	-49.2	.58

where \bar{x} is the mean and σ is the standard deviation. For each wavelength, the FSM and NDF statistics are practically identical but the GAR results have a larger standard deviation and, at 1.55 μm , a different mean. This demonstrates again the reliability of the CERBS measurement when the R_{ref} is actually measured and the uncertainty that is introduced by assuming a known glass-air reflection.

5. *THEORY AND MEASUREMENTS COMPARED.* Both the theory and data show that R_{bs} is a function of wavelength. The measured mean values at 1.31 and 1.55 μm differ by 3.6 dB of which theory predicts 2.9 dB is caused by the λ^4 dependence of α in equation (1) and the remainder is consistent with S wavelength dependence. Although not obvious from equations (1) and (2), theory predicts that variations in fiber parameters will cause a greater change in S at 1.55 μm than at 1.31. This causes the non-unity slopes in Figures (4-6) and the larger σ at 1.55 μm in Table 1. In fact, the slopes in Figures (4) and (5) indicate which fiber parameters are varying. Numerical analysis shows that small variations in fiber core radius and n_{co} will yield slopes of .21 and .71, respectively. The measured slopes of 0.66 and 0.61 (whose difference is not statistically significant) appear to be dominated by n_{co} variations. However, no attempt was made to confirm this with independent measurement of core radius and n_{co} .

6. *CONCLUSIONS.* The CERBS measurement method is shown to be both repeatable and easily implemented. Excellent agreement is obtained between different reference reflections, providing they are large enough for OTDR measurement. Using a glass-air reflection is less reliable, at least when attempted with polished ferrules.

REFERENCES

1. A. H. Hartog and M. P. Gold, "On the Theory of Backscattering in Single- Mode Optical Fibers," *J. Lightwave Tech.*, LT-2, 76, pp. 76-82, 1984.
2. F. P. Kapron, E. A. Thomas and J. W. Peters, "OTDR Measurements of Optical Return Loss," *Technical Digest Symposium on Optical Fiber Measurements*, NBS Publication 748 (Boulder CO), pp. 35-38, 1988.
3. E. Brinkmeyer, "Analysis of the backscattering method for single- mode optical fibers," *J. Opt. Soc. Am.*, vol. 70, no. 8, pp. 1010-1012, 1980.
4. V. A. Bhagavatula, "Estimation of Single-Mode Waveguide Dispersion using an Equivalent-Step-Index Approach," *Electron. Lett.*, vol. 18, no. 8, pp. 319-320, 1982.
5. E. L. Buckland and M. Nishimura, "Bidirectional OTDR Measurements Utilizing an Improved Folded-Path Technique," *Technical Digest Symposium on Optical Fiber Measurements*, NBS Publication 748 (Boulder CO), p. 15-18, 1988.

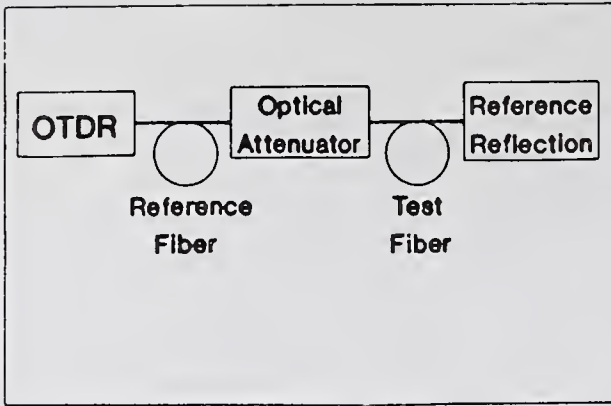


Figure 1. CERBS Test Configuration.

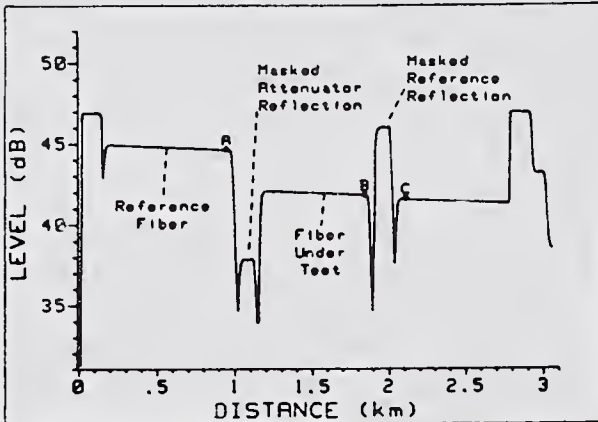


Figure 2. OTDR display with 0 dB attenuation.

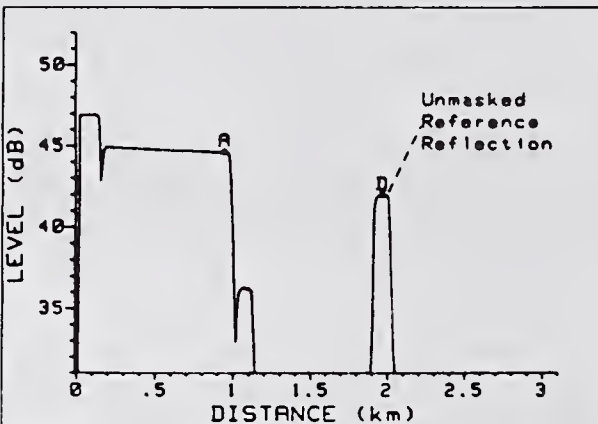


Figure 3. OTDR display with 25 dB attenuation.

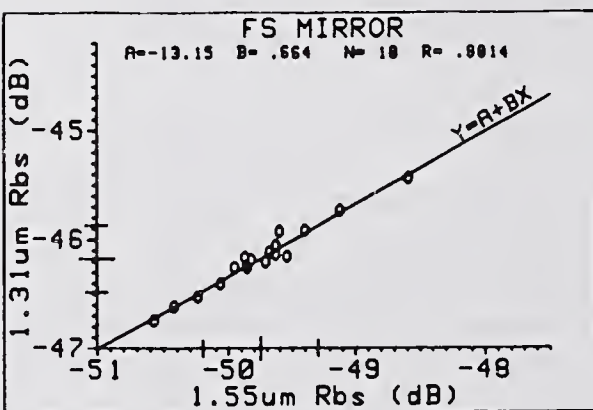


Figure 4. FSM comparison at 1.31 and 1.55 μm.

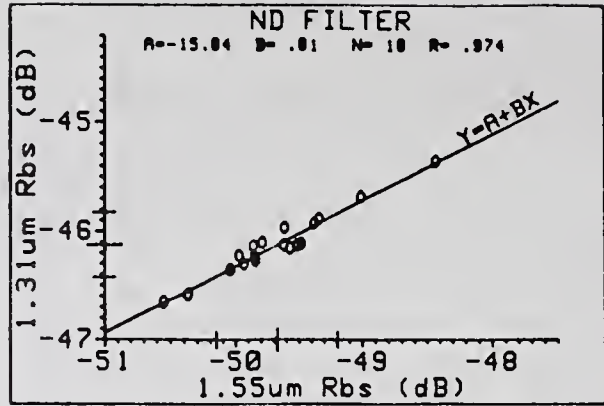


Figure 5. NDF comparison at 1.31 and 1.55 μm.

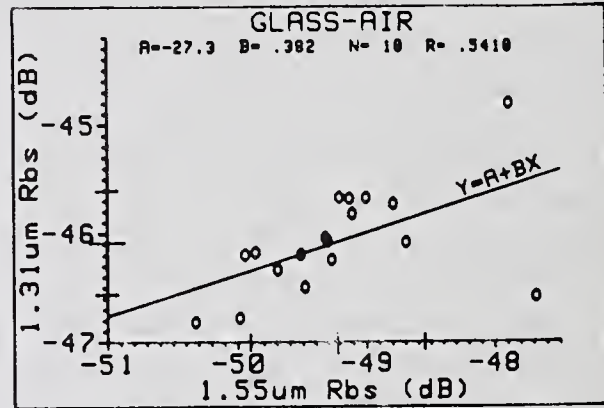


Figure 6. GAR comparison at 1.31 and 1.55 μm.

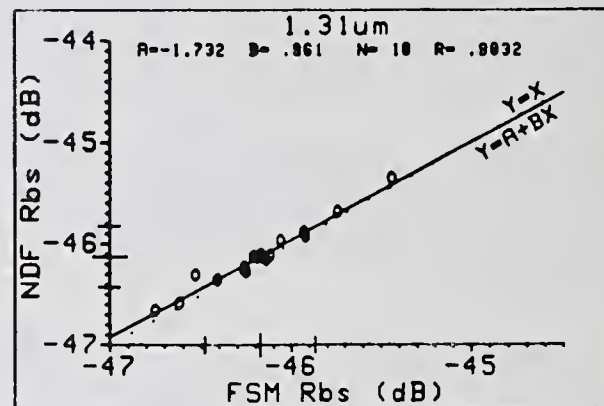


Figure 7. Comparison of FSM and NDF at 1.31 μm.

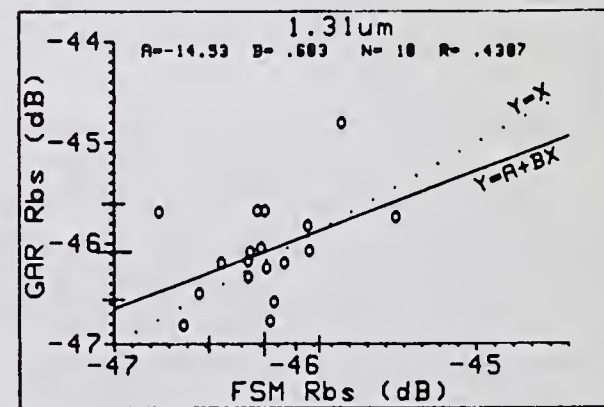


Figure 8. Comparison of FSM and GAR at 1.31 μm.

Factory Measurement Solutions to Predictable Field Performance of Single-Mode Fiber Optic Connectors

by

Bennett Wong, Halina Kosiorska

Northern Telecom Canada Limited

Optical Cable Plant

P.O. Box 807, Saskatoon, Saskatchewan, Canada S7K-3L7

1.0 Introduction

Modern fiber optic systems are designed with ever decreasing margins in terms of loss and reflections. In addition, high traffic densities require the systems to be both stable and reliable. These demands drive manufacturers to design and produce connectors with optimized performance. A number of test methods are used to verify performance during design and manufacture, but connectors measured in the factory may give different results in the field. This is because factory measurements are performed using setups and conditions that are different from those of installed connections. Also, as standards organizations are yet to complete their work on optical and mechanical intermatability, products from different suppliers may not be fully compatible.

2.0 Optical Performance

The three elements that contribute to insertion loss are fiber parameters, connector parameters, and manufacturing process. In the category of fiber parameters, geometry plays the most important role, while index and mode-field mismatch are of less significance. For the connector, geometry is again of primary concern. In particular, it is the diameter and eccentricity of the ferrule microhole that has the greatest impact to insertion loss. Finally, the manufacturing process must produce fiber and ferrule endfaces with controlled profiles and pristine finishes. Through careful measurement and matching of components, and process optimization, insertion losses of better than 0.5 dB are achievable in field connections.

Reflection at a connector interface is a function of index matching and scattering. If an air gap exists at the connection plane, a return loss of 14 dB results due to the air-glass mismatch. A common approach to promoting fiber contact is to polish the ferrule endface into a spherical profile. This allows the axis of the two connection ferrules to readily mate, and routinely produces connectors with return losses in the range of 30 dB. Higher return loss - in the range from 40 to 50 dB - is attained by eliminating high-index layers¹ and scattering sites at the fiber end-face. A special class of connectors, utilizing a combination of physical contact and angled fiber endfaces^{2,3}, can achieve return losses in excess of 60 dB.

The most common straight-ferrule connectors use a combination of precision alignment and physical contact to achieve low insertion loss and high return loss. However, the factory specified values often do not match those experienced in the field, due to the methods in which the factory measurements are performed. As will be described in the following sections, predicting field performance of connectors requires knowledge of other parameters as well.

2.1 Fiber and Connector Parameters

Connector eccentricity error results from fibers and ferrules with non-ideal geometry. Commercially available fibers have a worst-case eccentricity of 1 μm and a diameter tolerance of $\pm 2 \mu\text{m}$. Connector

ferrule microholes are typically 1 μm larger than the fiber diameters, in order to facilitate assembly. Eccentricity of the microhole is specified to within 1 μm . The ferrule diameter is less critical because the adapter sleeve element effectively compensates for small diameter variations. In the extreme case of tolerance build up, there can be an offset as large as 8 μm between the two fiber cores in the connection, giving rise to an insertion loss of over 13 dB (Figure 1). In connectors designed for physical contact, eccentricity combined with vertex offset can lead to fiber separation. Vertex offset is defined as the distance between the apex of the spherical ferrule profile and the fiber axis. An air gap between the fibers can severely degrade both the insertion and return loss performances. Furthermore, the separation causes interference to occur within the gap, so that wavelength drift or changes in the gap spacing (Figure 2) will result in transmitted and reflected power fluctuations.

During manufacture, the overall offset in connectors is controlled through fiber and ferrule geometry measurements. Accurate determination of the diameter, non-circularity, and eccentricity values permits components to be pre-selected and matched prior to assembly, thereby improving consistency and yield. Once the fiber-ferrule assembly is complete, a measurement of the overall eccentricity provides insight to the expected insertion loss of the connector, while vertex analysis is used to deduce return loss (Figure 3). Fiber geometry measurement with sub-micron accuracy and precision is achieved with grey scale⁴ and interferometric^{5,6} methods. Ferrule geometry is tested using optical and mechanical techniques^{7,8}, with slightly lower accuracy and precision.

Geometry measurements can also help to reduce the impact of connector eccentricity through a concept known as keying⁹. Here, the eccentricity direction of each fiber-ferrule assembly is measured and identified. In the final assembly operation, the ferrules are mounted into connector bodies with the eccentricities aligned to a consistent direction. For connectors that use oblique endfaces to achieve ultra-low return loss, keying is imperative to ensure proper contact and alignment. In this case, the keying feature fixes the orientation of the end-angle. The endface angle and orientation are found using beam deflection¹⁰ or optical microscopes. Connector keying is a simple solution to improving factory yield and field performance, but as there is presently no industry standard defining the keying mechanism or keying angle, performance is guaranteed only if all the parts in a connection are from the same manufacturer.

Factory insertion loss¹¹ and return loss^{12,13,14} are measured by mating the test connector to a reference connector. The reference connector has overall eccentricity and vertex offset close to zero, so repeatable test results are obtained regardless of the test connector's eccentricity direction. In the field, two mated connectors may have their eccentricities pointing in the same or in opposite direction. These extremes can produce insertion losses as low as zero, or as high as four times the factory specified maximum. As for return loss, the factory value gives no guarantee whatsoever of field performance. This is because a connector with finite vertex offset may make fiber contact with a reference connector having zero vertex offset, but not with any other connector with non-zero vertex offset (Figure 4). To predict return loss in the field, the ferrule vertex offset and radius of curvature must also be specified. These values are found using interferometric^{15,16} techniques.

In the factory, the various test acceptance criteria can be adjusted to meet any required worst-case installed performance. However, the feasibility and extent of this practice depend on the actual customer requirements. For example, if the worst-case acceptable insertion loss is very low, it will be necessary to impose extremely stringent factory screening limits, thus increasing the rejection rate and cost of the product. A more lenient approach is to specify typical field performance, which would allow for some instances of marginal connections. The system designer must select the tolerance level for borderline connections, based on the system margin and number of connections in each link. The manufacturer can then apply statistical modeling¹⁷ to the factory measured loss distributions to estimate the field performance distribution (Figure 5).

2.2 Polishing Process

The polishing operation generates the proper ferrule end-face shape and finish for the connector. Even if connectors are made with zero eccentricity and vertex offset, a poor finish on the fiber can still render unacceptable insertion and return losses. An non-optimized process may also cause over-polishing and high index layers. An over-polished connector is characterized by the fiber being recessed from the ferrule tip (Figure 6) because of the different rates of abrasion between the two materials. Recess, even in the order of a few microns, is sufficient to prevent fiber contact and therefore give poor return loss performance. High-index layers are formed due to compaction of the fiber during polishing, and can degrade return loss by several decibels in contacting connections.

The end finish of connectors is inspected after the polishing process using simple microscopes. Scratches, debris, and epoxy smears are easily detected in this fashion¹⁸. Since the surface finish of the fiber contributes to the intrinsic loss of a connector, it affects a factory connection to the same extent as a field connection. Therefore, factory loss testing is sufficient to prevent field failures caused solely by poor finish. If over-polishing is present in a connector, direct return loss testing with a reference connector alone is insufficient to guarantee field performance. This situation is similar to that of vertex offset, where an over-polished connector may make contact with a reference connector in the factory, but not with other over-polished connectors in the field. Over-polishing can be measured with sub-micron resolution using the same techniques as for vertex offset and radius of curvature^{15,16}, and field performance is further assured by limiting this parameter. High-index layers are detected by monitoring changes in return loss as the ferrule end is chemically etched.

3.0 Mechanical Performance

The majority of equipment in which connectors are installed do not allow the cable leading from the connector to exit in a straight path. In addition, the connector must withstand any pulling, bending, or twisting of the cable during installation and removal. As such, the connector must provide some form of strain relief. The strain relief mechanism is critical to a connector's performance (Figure 7), and is designed to restrict the bending radius of the cable so that bending induced losses are minimized. Manufacturers incorporate mechanical testing in developing connectors, and apply sufficient margin to their designs to guarantee field performance.

A number of EIA/TIA test methods are available for verifying the mechanical performance of connectors. These tests quantify a connector's design with respect to cable flexing¹⁹, retention²⁰, twisting²¹, strength²², and installation²³. In addition to the standard test procedures, manufacturers often test connectors according to Bellcore requirements²⁴, which includes addition procedures for cable proof and loading stability tests.

4.0 Reliability

Connector testing is not limited to optical or mechanical parameters. A number of techniques also exist for studying reliability. In designing a connector, a manufacturer must perform extensive testing in harsh environments to study and understand the long term reliability of the product. These tests help to identify process or component related deficiencies, so that improvements can be implemented to reduce the risk of in-service failures.

Depending on the design, components in a connector may place unusual stresses on the fiber when it is subjected to vibration, thermal variations, or aging. Any of these effects may induce high loss or even fiber breakage. Connector stability and reliability are determined through accelerated environmental tests such as humidity aging²⁵, heat aging²⁶, and temperature cycling²⁷. Durability is checked by a series of impact²⁸, vibration²⁹ and re-mating³⁰ tests.

When fiber breaks occur, fracture analysis³¹ can highlight problems such as stripping tool damage, sharp edges in the ferrule, or epoxy incompatibility. Fiber breaks are located using high-resolution OTDR or X-ray³² methods.

For physical contact connectors, a substantial axial pressure exists at the fiber ends due to the small contact area. Over time, the epoxy bond fixing the fiber to the ferrule may fail, resulting in the fiber recessing³³ into the ferrule and eventual loss of contact. Fiber recess is identified by interferometric techniques^{16,17}, while the epoxy bond, as part of the connector assembly, is tested during reliability testing.

5.0 Summary

High-performance connectors are typified by more than just low insertion loss and high return loss. Today's applications also require connectors to be robust and reliable. From a manufacturer's perspective, designing a connector to satisfy these requirements means being able to accurately characterize the determining parameters. Many excellent methods have been established for measuring connector optical, mechanical, and reliability performance. These tests allow each manufacturer to design for - and impose limits on - factors that affect field performance. However, this gives predictable in-service performance only if the connectors are from the same manufacturer. To ensure performance when multiple vendors are involved, the connector industry must agree on acceptable limits for important parameters such as vertex offset, ferrule end-face radius of curvature, and over-polishing, and resolve outstanding issues on optical and mechanical compatibility. This work is currently the focus within international standards organizations such as EIA/TIA, IEC, and CCITT.

6.0 References

1. J. B. Clayton, G. M. Alameel, G. F. DeVeau, "Low-reflection polish for ferrule-based mechanical splices and straight-tip connectors," OFC '89, Houston, 1989, paper ThJ4, p 166.
2. W. C. Young, V. Shah, and L. Curtis, "Loss and reflectance of standard cylindrical-ferrule single-mode connectors modified by polishing a 10° oblique endface angle," IEEE Photonics Technology Letters, Vol. 1, No. 12, December, 1989, pp 461-463.
3. N. Suzuki, "Physical contact technology suppresses light reflected from connectors," JEE, April, 1991, pp 76-80.
4. EIA/TIA-455-176, "Method for measuring optical fiber cross-sectional geometry by automated grey-scale analysis," in approval.
5. EIA/TIA-455-92, "Optical fiber cladding diameter and noncircularity by Fizeau interferometry," in approval.
6. EIA/TIA-455-93, "Optical fiber cladding diameter and noncircularity by non-contacting Michelson interferometry," in approval.
7. Z. Pasturczyk, B. Wong, C. Saravanos, "Fiber optic connector geometry test station," International Wire and Cable Symposium Proceedings 1989, pp 623-625.
8. M. Ueki, Y. Hattori, "Accurate measurement of structural parameters of single fiber connector ferrule," OFC '91, San Diego, 1991, paper ThA1, p 137.
9. Y. Ando, "Statistical analysis of insertion loss improvement for optical connectors using the orientation method for fiber-core offset," IEEE Photonics Technology Letters, Vol. 3, No. 10, October 1991, pp 939-941.
10. EIA/TIA-455-57A, "Optical fiber end preparation and examination," Appendix A.
11. EIA/TIA-455-171, "Attenuation by substitution measurement -- for short-length multimode graded-index and single-mode optical fiber cable assemblies."
12. EIA/TIA-455-107, "Return loss for fiber optic components."
13. EIA/TIA-455-8, "Measurement of splice or connector loss and reflection using an OTDR," in approval.

14. S. K. Das, A. F. Judy, G. M. Alameel, R. M. Jopson, T. F. Adda, "Reflectance measurement in lightwave systems: A comparison of various techniques," Technical Digest, Symposium on Optical Fiber Measurements, pp 25-30, 1988.
15. Z. Pasturczyk, T. Chepyha, C. Saravanos, H. Wood, "Test methods for fiber optic connector parameters directly affecting return loss," Technical Digest, Symposium on Optical Fiber Measurements, pp 163-166, 1990.
16. K. Creath, "Step height measurement using two-wavelength phase-shifting interferometry," Applied Optics, Vol. 26, No. 14, 15 July 1987, pp 2810-2816.
17. H. Kosiorska, B. Wong, C. Saravanos, "Statistical method for predicting connector loss in the field using factory measurements," OFC '91, San Diego, 1991, paper ThA2, p 138.
18. R. P. Drexel, J. A. Nelson, J. Schnecker, "New approaches to termination," Photonics Spectra, March 1988, pp 101-106.
19. EIA/TIA-455-1A, "Cable Flexing for Fiber Optic Interconnecting Devices"
20. EIA/TIA-455-6B, "Cable Retention Test Procedure for Fiber Optic Cable Interconnecting Devices."
21. EIA/TIA-455-36, "Twist Test for Fiber Optic Connecting Devices."
22. EIA/TIA-455-185, "Strength of Coupling Mechanism for Fiber Optic Interconnecting Devices."
23. EIA/TIA-455-187, "Engagement and Separation Force Measurement of Fiber Optic Connector Set."
24. Bellcore TR-TSY-000326, Issue 2, "Generic Requirements for Optical Fiber Connectors and Connectorized Jumper Cable."
25. EIA/TIA-455-5, "Humidity Test Procedure for Fiber Optic Connecting Devices."
26. EIA/TIA-455-3, "Procedure to Measure Temperature Cycling Effects on Optical Fibers, Optical Cable, and Other Passive Fiber Optic Components."
27. EIA/TIA-455-4, "Fiber Optic Component Temperature Life Test."
28. EIA/TIA-455-2, "Impact Test Measurements for Fiber Optic Devices."
29. EIA/TIA-455-11, "Vibration Test Procedure for Fiber Optic Connecting Devices and Cables."
30. EIA/TIA-455-21, "Mating Durability for Fiber Optic Interconnecting Devices."
31. W. R. Wagner, "Extrinsic fiber damage and its effect on the reliability of optical fiber connectors and splices," SPIE Vol. 1850, Fiber Optic Components and Reliability, 1991, pp 168-185.
32. T. Wei, D. J. Cotter, B. T. Devlin, W. D. Koenigsberg, "Nondestructive evaluation of optical fiber splices and connectors," OFC '92, San Jose, 1992, paper Th11, p 226.
33. R. Ziebol, H. Roberts, B. Daniel, "Permanent fiber withdrawal in fiber optic connectors," 8th Annual NFOEC, Washington, D.C., 1992, pp 211-230.

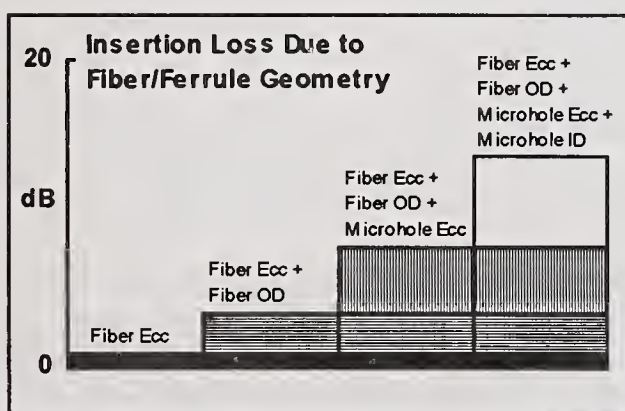


Figure 1. Connector insertion loss contribution due to accumulation of fiber and ferrule geometry errors.

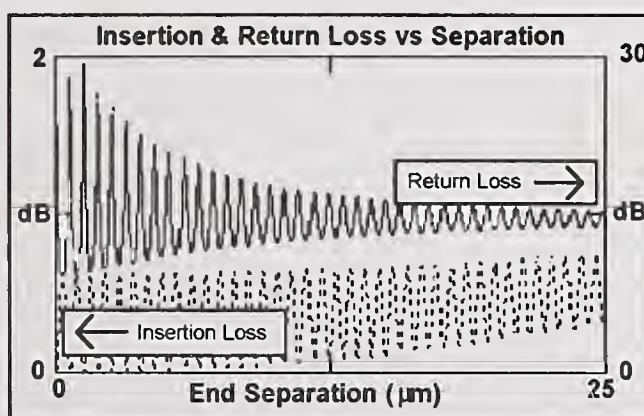


Figure 2. Insertion loss and return loss as a function of fiber separation. Oscillations are due to interference between the fiber ends.

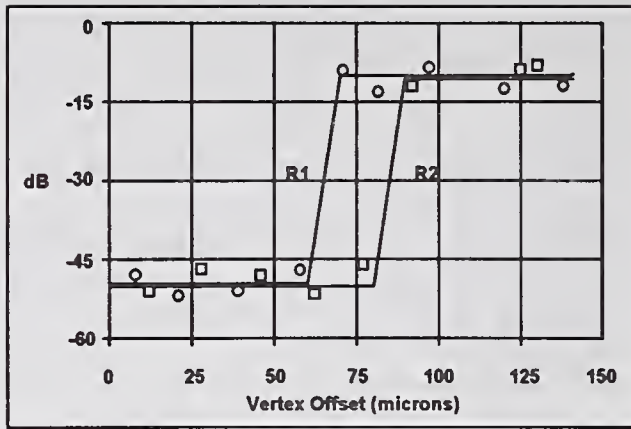


Figure 3. Effect of radius of curvature and vertex offset on return loss. $R1 < R2$.

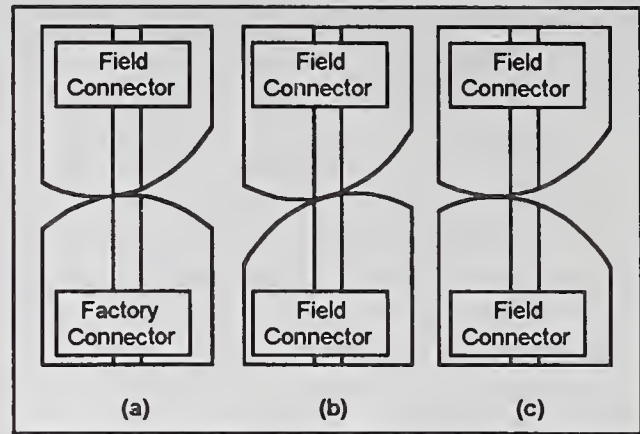


Figure 4. A connector makes full contact during factory testing (a) and in some instances, in a field connection (b). However, contact may not be achieved (c) if the radius of curvature and vertex offset are not controlled.

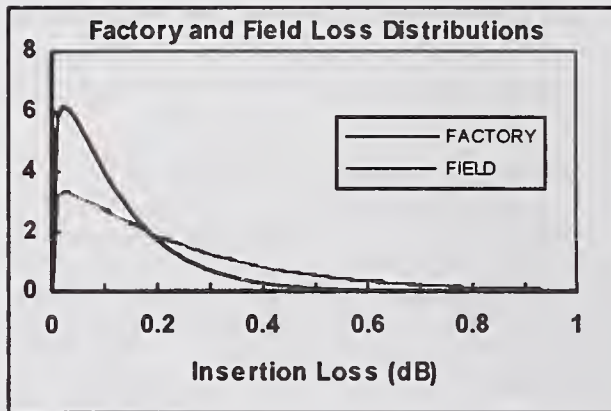


Figure 5. Insertion loss distributions for factory and field (random) connections.

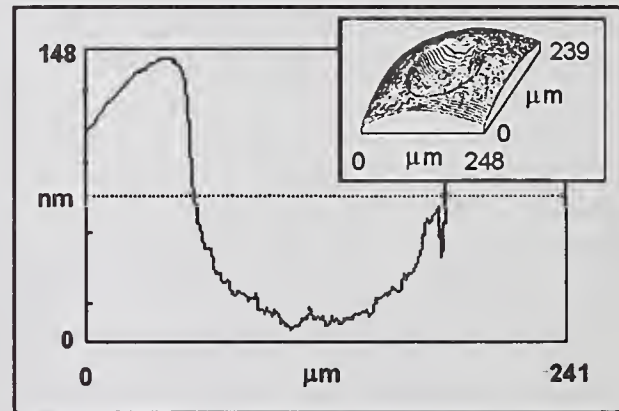


Figure 6. Profile measurement showing fiber over-polishing.

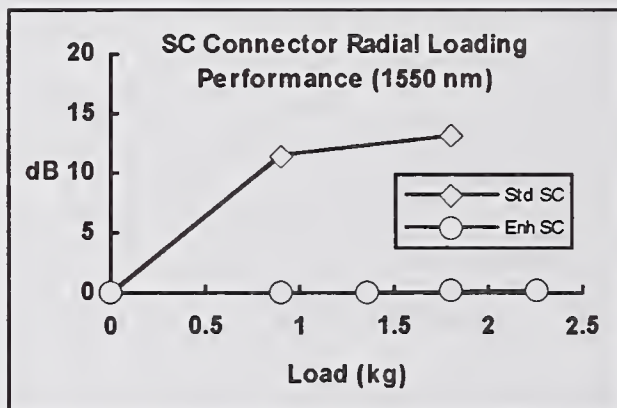


Figure 7. Cable bending-induced loss of standard and enhanced SC connectors.

Measurements to Assure Fiber Reliability

Hakan H. Yuce & Felix P. Kapron

Bellcore

445 South St., Morristown, NJ 07962-1910

1. Fiber Environment

More than 10 Mkm of optical fiber has been installed in the U.S., some for a period approaching 15 years. To date, very few mechanical failures have been reported that are not related to a catastrophic cable cut, fire, or earthquake. Most of the few failures are associated with defects in the fibers or cables. Some failures are due to gradual fiber weakening under an extreme environmental condition (e.g., cable tension, constant steam), or are due to handling the fiber at some termination point such as a splice or connector. Why then is there an increasing interest in measuring fiber mechanical properties more accurately? Why are stricter mechanical specifications being imposed on fiber? What new specified parameters and measurements are necessary? This paper attempts to answer these questions.

Consider that until now most fiber has been used for trunking applications in which long lengths of fiber cable are in a benign underground or underwater environment, with rather few terminations. As fiber permeates closer to the customer, however, distribution cable lengths are shorter, and they are subject to increased handling at more close-packed termination points both during installation and during network rearrangements. The fiber cable must endure a wider range of above-ground temperatures, continuous vibrations in some applications, and terminations possibly exposed to humidity and corrosive materials. Yet costs must be kept low, with few repairs required.

2. New Measurement Standards

The issues of fiber strength, aging, and lifetime have been addressed in the research literature for some time [1]. So what's new? The above need for enhanced reliability requirements and the prospect of additional fiber specifications have made it necessary to "fine tune" the measurement techniques so that results are reproducible amongst testing facilities. Since this has commercial implications, precise measurement standards are becoming necessary.

Several national and international standards organizations have recently become involved in testing for mechanical reliability. In the U.S., this is resulting in several ANSI FOTPs (Fiber Optic Test Procedures) [2-7] generated by fiber users and suppliers within the Telecommunications Industry Association. An advantage of standards is that the mechanical properties of different fibers can now be directly compared with each other in ways agreed to by the industry. Another is that estimates can be made of fiber reliability (e.g., lifetime for a given service stress, or allowable stress for a desired lifetime) in different service conditions.

A common field situation occurs when the fiber is subjected to a longterm residual applied stress, as within a cable or in a bends in a splice housing or on a payout bobbin. Three measurement deployment conditions, somewhat relating to field deployments, are longitudinal tension with a gage length of about 1 m [2-4], mandrel-wrap uniform bending, or two-point bending of a few cm of fiber between parallel plates [3, 6]. A particular crack fails when its decreasing inert strength during service or during a test falls below the applied stress at that instant.

3. Fatigue Measurements

To be able to predict fiber lifetime, there needs to be a means of measuring it. One method is *static fatigue* under constant applied stress [2, 3]. It would seem straightforward to obtain the times-to-failure as a function of several constant stresses, and then to extrapolate to smaller in-service stresses and longer expected lifetimes. However, the distribution of flaws in a fiber is statistical both in position and in

strength. To take this into account, first measure the random failure times of many fiber samples at a fixed applied stress. With a static fatigue measurement this is usually done in the worst-case environment that the fiber is expected to experience, with failure times of days to months. Then plot the cumulative failure probability F for these times on scaled Weibull paper to obtain the form of Fig. 1, where the slope m_s is related to the ratio of mean over standard deviation for the distribution. Sometimes the plot consists of two (or more) straight-line segments, characteristic of two (or more) flaw types. How to take this into account is still under study.

Repeat the measurements for several values of applied stress. The values of m_s should not change much, but plot the median failure times t_{median} vs. these stresses as per Fig. 2. This yields the (static) stress-corrosion coefficient n_s (typically around 20), and an intercept $t_f(1)$. The testing parameters of gage length, m_s , n_s , $t_f(1)$ and the parameters of service length, service stress, and acceptable failure probability can then be used in formulas [7] to estimate fiber lifetime or safe stress.

The above procedures can take a long time. Moreover, fiber aging can take place during the tests, and the above crack parameters (apart from strength) will change. (This is starting to be addressed in a series of draft FOTPs.) More convenient *dynamic fatigue* measurements are often used [4-6]. Here controlled ambient conditions are common, so relating these to any more severe in-serve conditions is uncertain. Moreover, any environmental aging must take place prior to the tests.

Similar to the above, first measure the random failure stresses of many fiber samples at a fixed applied stress *rate*. Then plot the cumulative failure probability F for these stresses on scaled Weibull paper to obtain the form of Fig. 3; again, the slope m_d may have more than one value. Repeat the measurements for several values of applied stress rates, and plot the median failure stresses σ_{median} vs. these stress rates as per Fig. 4. This yields the (dynamic) stress-corrosion coefficient n_d , and an intercept $\sigma_f(1)$. The testing parameters of gage length, m_d , n_d , $\sigma_f(1)$ and the parameters of service length, service stress, and acceptable failure probability can then be used in similar formulas [7] to estimate fiber reliability.

4. Prooftesting Measurements

Prooftesting is a basic screening that virtually all commercial fiber is subjected to as a part of the manufacturing process. Figure 5 shows the stress history in which a proofstress is applied sequentially along the full length of fiber [8]. The "measurement" aspects of the test are generally limited to determining the lengths of the surviving fiber. Unfortunately, it cannot be guaranteed that in the surviving lengths there are no cracks with strengths below the proofstress level. Although this is the case at the end of the dwell portion, further weakening occurs during unloading. Revisions are likely to occur in the FOTP to limit this effect. In addition to the proofstress, the final minimum strength depends upon the unload time, the stress-corrosion coefficient, and the crack "B-value". This last quantity is elusive, and some controversy exists in the literature about how to measure it. Meanwhile, prooftesting also distorts the Weibull failure distribution [9]. Although lifetime formulas appear in the literature [9], studies in standards groups have not yet progressed sufficiently to allow a recommendation having commercial impact.

5. Lifetime Prediction Example

Dynamic tensile fatigue measurements were made on standard 125- μm diameter fused silica fiber coated with a 250- μm UV-curable polyurethane acrylate. The environment was $30 \pm 1^\circ\text{C}$ and $85 \pm 5\%$ relative humidity. Strain rates ranged from 0.01 %/min to 10 %/min. At a gage length of 0.5 m, 31 samples were tested at each rate, as per Fig. 3, to obtain the median failure stress σ_{median} and m_d for each rate. The lowest value of 30 for the latter was used. These median failure stresses were plotted against the applied stress rate as per Fig. 4 to obtain the intercept and an n_d value of 19.6.

Service conditions of 1 km and an allowed failure probability of 10^{-6} were assumed in the lifetime formulae. Figure 6 shows the results, where a lb-force equals about 53 kpsi (common prooftest levels range from 50 to 200 kpsi.) Based on these measurements and calculation, the fiber will survive several decades so long as the service stress does not exceed $2\frac{1}{2}$ lb-force. Fiber aging in harsh environments,

which will alter the parameter values (apart from strength) is not accounted for.

6. Conclusions

This paper has outlined why increased demands are being put on the mechanical properties of fiber, and what standards-sponsored measurement techniques can be used to obtain required mechanical parameters. Much work remains to complete these techniques and to relate the parameters to reliability calculations. A useful example has been given of measurement results and the resulting estimates of lifetime vs. applied stress.

7. References

- [1] Review by J. E. Ritter, Jr., in *Fracture Mechanics of Ceramics* vol. 5, pp. 227-251, ed. by R. C. Bradt et al (Plenum Press, N.Y., 1981), and references therein.
- [2] *Procedure for Measuring the Static Fatigue of Optical Fiber in Tension*, FOTP proposed.
- [3] *Procedure for Measuring the Static Fatigue of Optical Fiber in Two-Point Bending*, FOTP-97.
- [4] *Method for Measuring Dynamic Fatigue of Optical Fibers by Tension*, FOTP-76.
- [5] *Method for Measuring Dynamic Tensile Strength of Optical Fibers*, FOTP-28.
- [6] *Method for Measuring Dynamic Fatigue of Optical Fibers by Two-Point Bending*, FOTP-90.
- [7] *Power-Law Theory of Optical Fiber Reliability*, EIA/TIA draft.
- [8] *Fiber Tensile Proof Test Method*, FOTP-31.
- [9] Review by V. A. Bogatyryov et al., *Optical Eng.*, vol. 30, no. 6, pp. 690-699 (June 1991), and references therein.

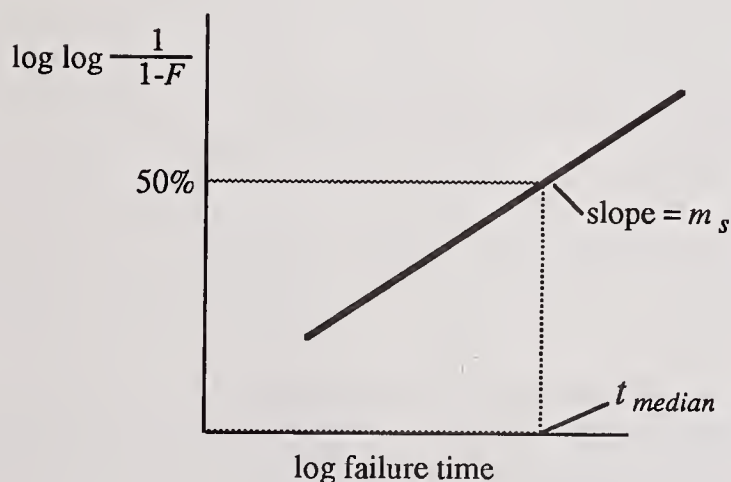


Figure 1: Schematic plot of static Weibull failure probability versus lifetime.

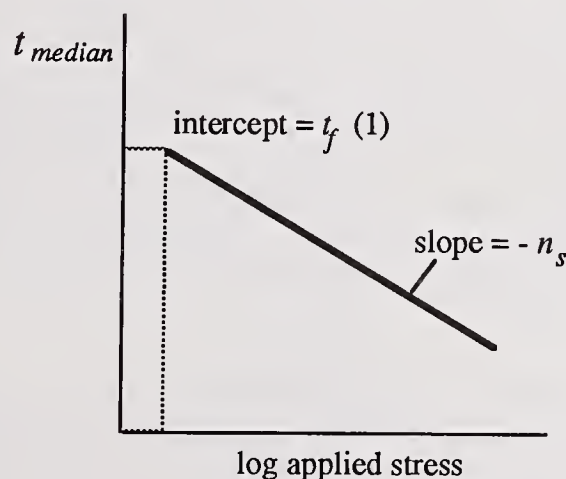


Figure 2: Schematic plot of failure time versus applied stress.

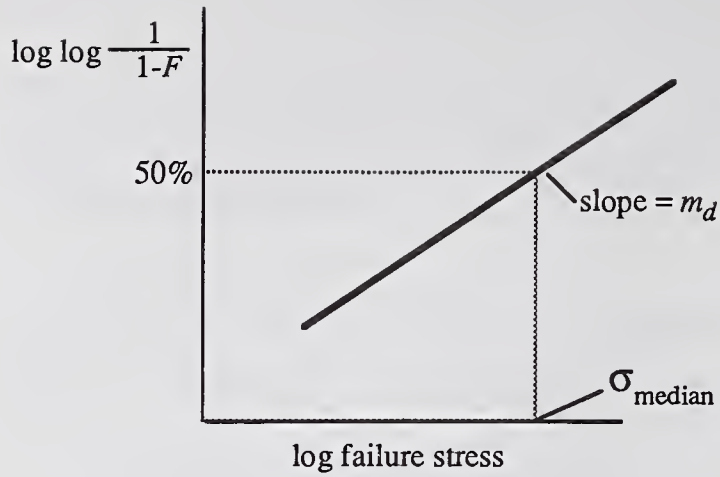


Figure 3: Schematic plot of dynamic Weibull failure probability versus failure stress.

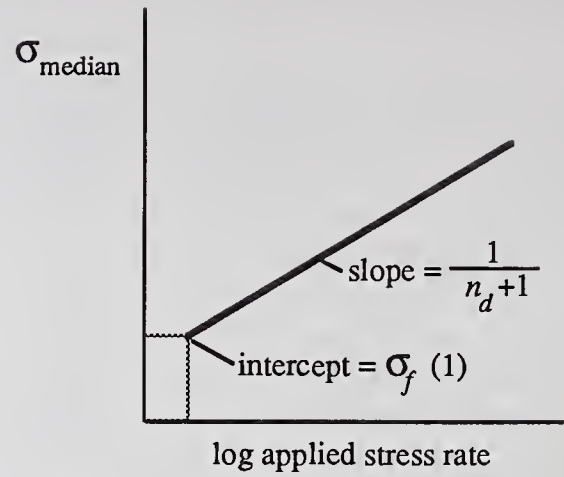


Figure 4: Schematic plot of failure stress versus applied stress rate.

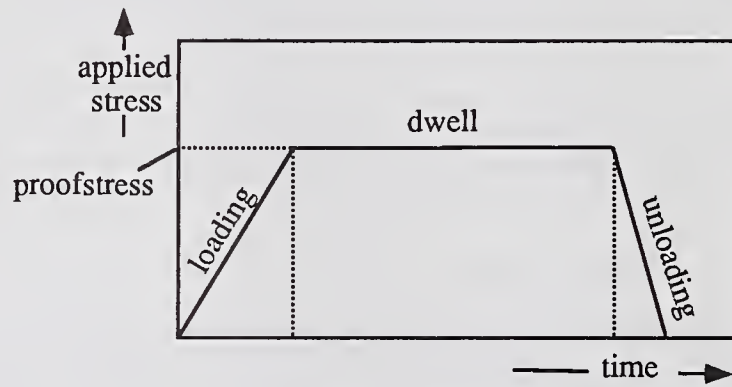


Figure 5: The proofstress cycle

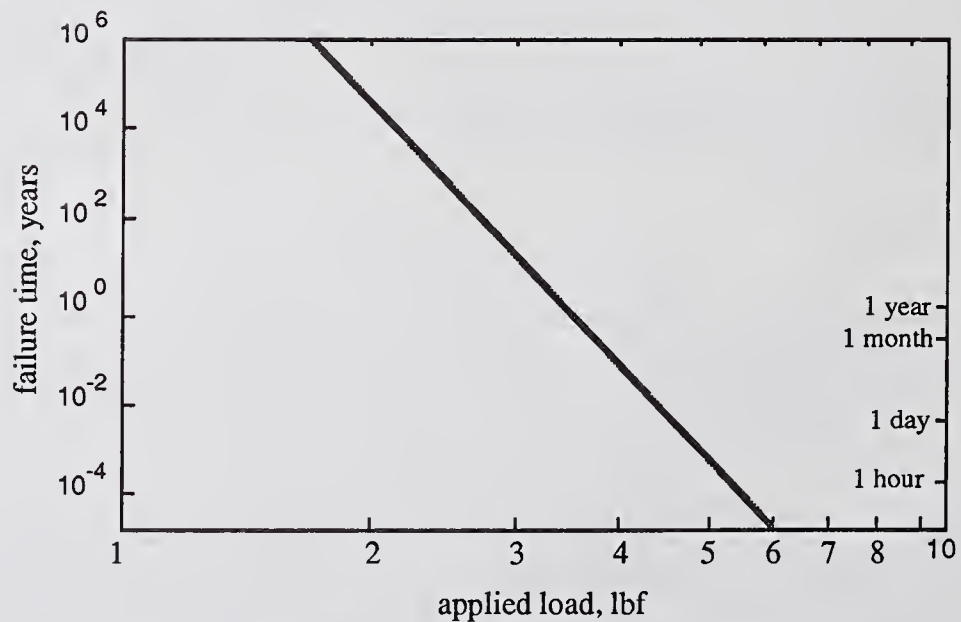


Figure 6: Lifetime predictions from dynamic fatigue experiments

Atomic Force Microscopy Measurements to Study Optical Fiber Aging

H. H. Yuce, J. P. Kilmer and J. P. Varachi, Jr.

*Bellcore
445 South Street, Morristown, NJ 07962*

INTRODUCTION

The critical mechanical properties of optical fibers are strength, fatigue resistance, and zero-stress aging behavior. Understanding the effect of the chemical environment under zero stress on the subsequent fracture strength of fibers is important because fibers in service are likely to encounter water and other chemical species while deployed closer to subscriber premises. Zero-stress aging refers to the loss of strength of high-strength glass fibers in the absence of stress in some corrosive environments such as water.

In this work, the strength of fibers aged under zero-stress conditions has been measured and compared to the surface roughness of the fibers. The roughening of the fibers from corrosion was measured with atomic force microscopy (AFM) at intervals during aging duration. This paper shows that AFM measurements can be used to image the surface of silica fibers at a nanometer scale, opening fundamental understanding of the aging behavior of fibers.

2. EXPERIMENTAL PROCEDURE

Two commercially available silica optical fibers fibers 1 and 2, with a nominal glass diameter of 125 μm coated with UV-cured acrylate polymer to an overall diameter of 250 μm , were used. Fibers 1 and 2 were subjected to aging in both 85 °C deionized water buffered at pH 7 and 85 °C, 85% RH for 1 day, 1 week, 1 month and 3 months at zero-stress. The aged and unaged fibers were then examined by two techniques.

A computer controlled, two-point bending apparatus was used to determine the strength of the aged and unaged fibers. The test apparatus (see Fig. 1) consists of two parallel platens, one fixed and one moving, between which a fiber loop is bent until it breaks¹. The moving platen is driven by a computer controlled stepper motor; the rate of closure can be varied so that the maximum stress in the fiber loop changes at a constant rate². Fiber failure is sensed by an acoustic transducer which signals the computer to stop the moving platen and record the platen separation at the failure. The stress at failure is calculated from the platen separation, the elastic modulus of the glass, and the dimensions of the fiber. Because the effective gage length is less than 20 μm ³, the probability of measuring a fiber sample containing a large flaw is very small, so the results tend to be uniform and unimodal. The technique is suitable for measuring strengths in different environments since the fiber sample and jaws can be immersed in the environment of interest. Since there are no gripping problems, uncoated fibers can be also tested. For these experiments, the fiber strengths were measured in deionized water buffered at pH 7 and held at 23°C. Strength tests were made on 31 samples from each aging condition. Sufficient preconditioning in the test environment was imposed on all fibers prior to testing.

The surface morphology the fibers in this study was characterized with a commercially available atomic force microscope. It has given atomic resolution images of both conductors⁴ and nonconductors⁵. The AFM was invented⁶ in 1986 shortly after the development of the scanning tunneling microscope (STM)⁷. The AFM offers the added advantage over the STM or the scanning electron microscope (SEM) that the sample need not be a conductor. Mechanically, the AFM consists of a stylus that is attached to a cantilever. The surface is scanned under the stylus and the cantilever is deflected as the stylus interacts with the surface. The stylus may be in direct contact with the surface or may be vibrated above it. The latter method has been used to image magnetic domains⁸ and charge distributions⁹.

Images are produced by measuring the deflection of the cantilever. Three techniques for measuring

the deflection include: (1) tunneling to the back of the cantilever (the tunneling technique)^{6,10}, (2) measuring the phase change of light from an optical fiber reflected off the back of the cantilever (the optical fiber interference technique)⁸, and (3) measuring the change in angle of light reflected off the back of the cantilever (the optical lever technique)^{11,12}

Our AFM combines a microfabricated cantilever¹³ with the optical lever technique. It operates as follows (refer to Fig. 2): a Si_3N_4 cantilever with integrated tip, is allowed to gently touch the surface. A small surface feature deflects the cantilever by a small distance δz , which causes a laser beam reflecting off the cantilever to deflect by an angle of $2\delta z/L$, where L is the length of the cantilever. ϕ is the angle between the surface and the cantilever; for us ϕ is 15° . This deflection of the reflected beam is detected as a change in the difference between light falling on separate segments of a two- or four-segment photodiode. We can operate the microscope either by measuring the deflection (variable deflection mode) or by using a feedback system to keep the deflection constant (constant force mode). The constant force mode was used for all of the images in this paper.

There are certain advantages to using the constant force mode. They are (1) the heights of the surface features are accurately measured and (2) the repulsive force, from a few atoms at the tip of the stylus, can be held constant at a low value (as small as 2×10^{-10} N for this paper). This repulsive force plus the spring force of the cantilever counterbalances the attractive van der Waals force between the stylus and the surface. Theoretically, the AFM can be operated with a vanishingly small repulsive force by offsetting the attractive van der Waals force with the spring force of the cantilever¹⁴.

The microfabricated cantilevers¹³ that we used were 100 or 200 μm long with spring constants of order 0.1 N/m . The photodiode detector was approximately 4 cm from the cantilever. The sample is placed on top of an xyz translator¹⁵ and is enclosed in a sample cell that can be sealed with an O ring. Sealing the sample cell allows us to deposit a variety of liquids or gases onto the sample. For this paper, all the samples were imaged in air. None of the samples required any special preparation. We used xyz translators with three different scan widths: 5 and 0.1 μm . Using different translators allowed us to image with tremendous resolution (0.3 nm laterally and 0.1 nm vertically), depending upon the sample. Scanning frequencies were in the range of 5 to 100 Hz with the higher frequencies for smaller scan widths. The coating was removed before AFM examination by dipping the fiber briefly in hot (200 $^\circ\text{C}$) H_2SO_4 and rinsing in distilled water. To ensure representative results, several samples from each aging condition were used. Each sample was also examined with at least two different AFM tips, minimizing the possibility of misinterpreting tip-induced artifacts in the images.

RESULTS AND DISCUSSION

The median strength values of unaged and aged fibers are shown in Figure 3. The median strength values for both aged and unaged fibers are shown in Figure 4 as a function of the depth of surface roughness obtained from the AFM cantilever tip motion. Figures 3 and 4 show that the median strength of fibers decreases and surface roughness of glass increases with increasing aqueous aging, particularly with Fiber 1. The surface roughness of the fibers increased with increasing aging time and was more dramatic in liquid water than in humidity.

Figure 5 show the AFM images of Fiber 1 where (a) is the glass surface of the unaged fiber and (b) is the surface of the fiber aged for 1 month at 85 $^\circ\text{C}$ and 85% RH. The roughening that occurred during the aging process is evident in this figure. The roughened surface showed an increase in amplitude and wavelength of surface contour with increasing aging time, consistent with earlier predictions¹⁶ and findings¹⁷⁻²⁰

In summary, we have compared the strength and morphological properties of aged and unaged fibers. The images in this study demonstrate the versatility of atomic force microscopes. The AFM provides a new tool for studying long-term mechanical reliability of optical fibers.

REFERENCES

1. P.W. France et al., *J. Mater. Sci.* **15**, 825(1980).
2. H. H. Yuce, et al., *Proc. Seventh Int. Conf. on Integrated Optics* **2** 44(1989).
3. M. J. Matthewson, C. R. Kurkjian, *J. Am. Ceram. Soc.*, **69** [11] 815(1986).
4. G. Binnig, et al., *Europhys. Lett.*, **33**, 1281(1987).
5. T. R. Albrecht and C. F. Quate, *J. Appl. Phys.*, **62**, 2599(1987) .
6. G. Binnig, et al., *Phys. Rev. Lett.*, **12**, 930(1986).
7. G. Binnig, et al., *Phys. Rev. Lett.*, **49**, 57(1982) .
8. H. J. Mamin et al., *Phys. Rev. Lett.*, **53**,1563 (1989).
9. J. E. Stern, et al., *Appl. Phys. Lett.* **53**, 2717(1988).
10. Marti, et al., *J. Vac. Sci. Technol.* **A6**, 287(1988).
11. N. M. Amer and G. Meyer, *Bull. Am. Phys. Soc.* **33**, 319(1988).
12. G. Meyer and N. M. Amer, *Appl. Phys. Lett.* **53**, 1045(1988).
13. T. R. Albrecht and C. F. Quate, *J. Vac. Sci. Technol.*, **A6**, 271(1988).
14. A. L. Weisenhorn, *Appl. Phys. Lett.* **54**, 2651(1989).
15. D. P. E. Smith and G. Binnig, *Rev. Sci. Instrum.* **57**, 2630(1986).
16. M. J. Matthewson, C. R. Kurkjian; *J Amer Ceram Soc* **71**; 177 (1988).
17. H.H. Yuce, et al., OFC' 90 Postdeadline Paper, Paper PD14, (1990).
18. R. S. Robinson and H. H. Yuce; *J Amer Ceram Soc* **74**, [4]; 814 (1991).
19. H. H. Yuce, et al., *Trans Glasses for Electronic Applications*, (in print)
20. H. H. Yuce, et al., OFC' 92 Postdeadline Paper, Paper PD21, (1992).

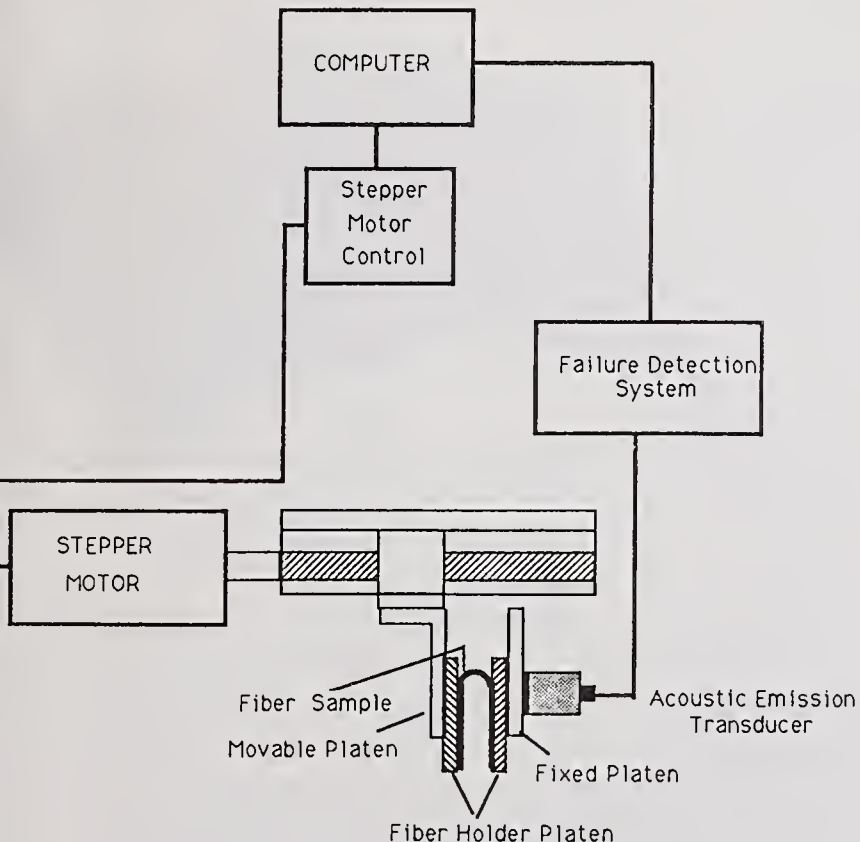


Figure 1: Schematic diagram of two-point bending unit

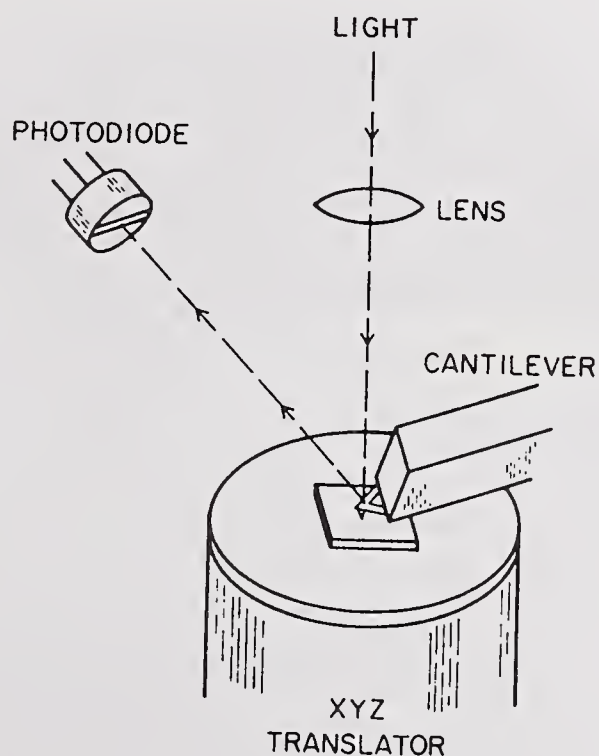


Figure 2: Schematic diagram of AFM

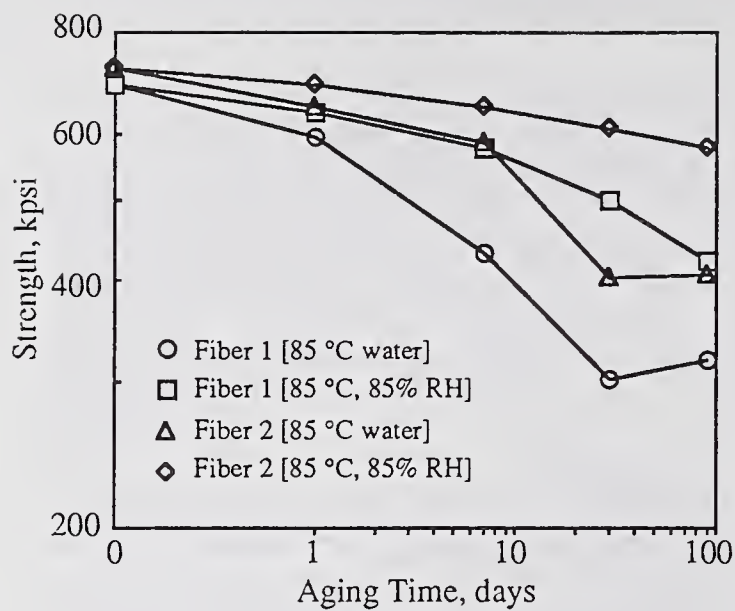


Figure 3: Strength degradation after aging

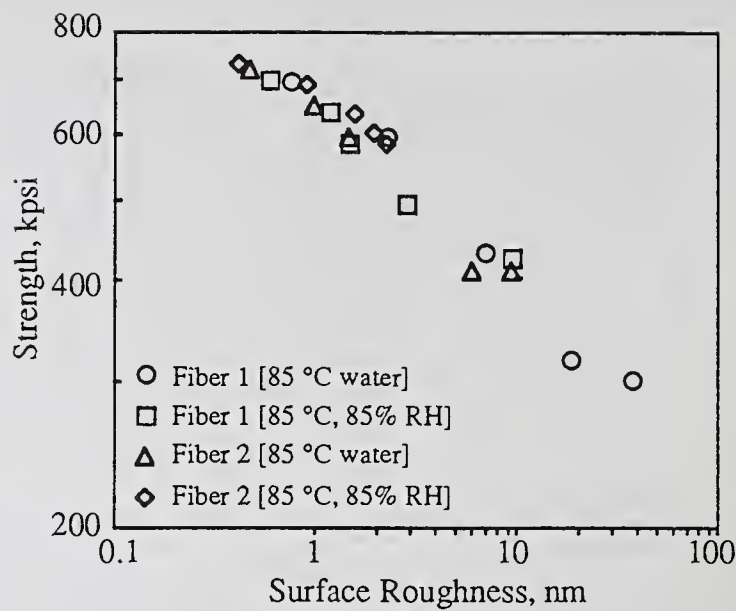
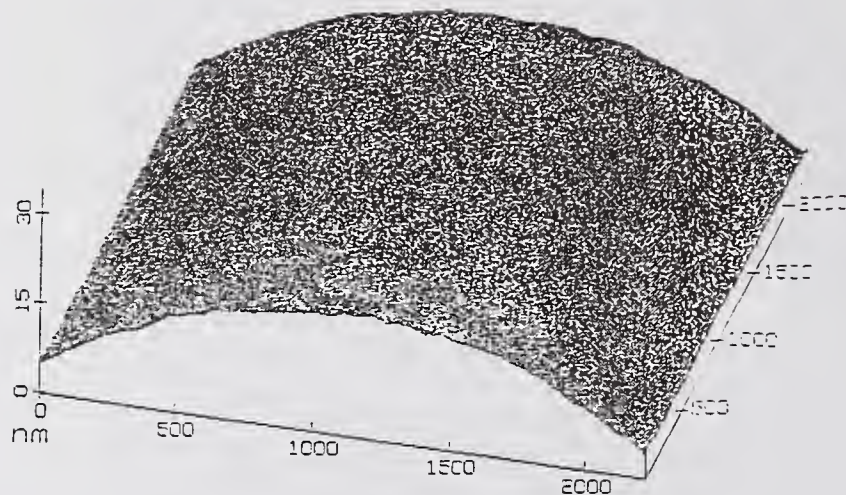
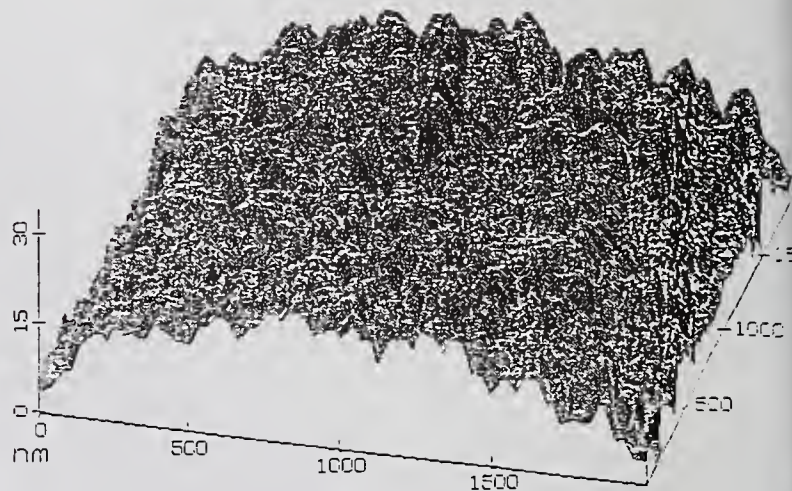


Figure 4: Strength versus surface roughness



(a)



(b)

Figure 5: AFM image of surfaces of fiber 1 (a) unaged (b) aged at 85 °C and 85% RH for a month

Fiber Microbending Test Method Capable of Predicting Microbend Loss in Optical Cables

Z. Pasturczyk C. Saravanos

*Optical Cable Plant, Northern Telecom Canada Ltd.
Saskatoon, Saskatchewan, S7K 3L7*

1.0 Introduction

Fiber attenuation caused by small, randomly distributed perturbations along the axis of an optical fiber is known as microbending loss. This microbending can be an important loss mechanism of cabled fibers, and may dominate the overall loss if the fiber and cable designs are not properly optimized. For cables at room temperature the microbending loss is usually negligible. As the temperature decreases the fiber coating stiffens, while the cable material contracts, allowing microbending effects to be transferred through the coating to the glass fiber. At very low temperatures the microbending loss increases rapidly and performance discrepancies of various fiber types and coatings become apparent. It is important for a cable manufacturer and end user to be able to determine microbend sensitivity of an optical fiber as a function of temperature, especially at low temperatures. By developing the proper test method, it is possible to use uncabled fiber to predict the microbending loss of a cabled fiber.

The microbending loss is a strong function of the fiber design and the coating material. Even though the fiber design can reduce this loss significantly, the issue of protecting the fiber axis from external lateral loads, is entirely up to the fiber coating. Dual coatings due to their nature offer two levels of protection. A soft cushioning layer surrounding the fiber and hard protective shell on the outside. Protection provided by single coatings is a compromise between cushioning and shielding effects. The test method presented in this paper determines how much protection against external forces is offered by a given coating over the relevant cable operating temperature range.

Over the years the industry has developed two approaches to test the microbend induced loss based on the fiber length. The respective examples of long and short length tests are the basket weave ^[1] and FOTP-68 also known as the sandpaper test method ^[2]. The former one works well at room temperature only and is not suitable at extreme temperatures or over a wide temperature range. The sandpaper test is not very repeatable and, for that reason, was recently rescinded by the TIA coating subcommittee. Various test methods have been developed since, based on short fiber length principles ^[3]. Even though the repeatability of these methods has improved they have one common problem. The loss induced by these tests in a short piece of fiber exceeds by orders of magnitude the worst case microbend loss per unit length measured in cabled fibers. There are two different loss mechanisms in these short and long fiber tests. A plastic deformation of the coating, in short fibers, is known to cause a drastic increase in microbending loss ^[4]. In long fibers, the coating is never deformed beyond its elastic limit. Only in this latter case does the loss mechanism, and the resulting microbending loss, correspond to the actual cable-induced fiber loss.

2.0 Proposed Test Method

The proposed test method is based on the well known basket weave method [1]. The optimum fiber length is 2.5 kilometers. Shorter lengths give noisy results, while longer ones do not offer any further improvements. The fiber is wound on a drum made of pure silica. The choice of the material was made to guarantee its thermal compatibility to the optical fiber and assure minimum fluctuations of the winding tension with temperature. The fiber was wound on a 111 mm diameter drum with 2 mm pitch and under 70 g of tension. It should be noted that the diameter of the pure silica drum is large enough to eliminate any macrobend induced loss.

Once on the drum, the fiber is placed inside a temperature chamber with one fiber end cleaved and the other spliced to a 1550 nm OTDR. The temperature of the chamber is cycled between -40°C and $+80^{\circ}\text{C}$ at a rate of one degree per minute. The slow rate is necessary to prevent tension transients due to temperature gradients between winding layers. The OTDR and the temperature chamber are computer controlled. Every two minutes the computer receives the OTDR trace as well as the temperature readout. The traces are processed by truncating 250 m from each end of the fiber and measuring the attenuation of the middle 2 km section. Nonlinear portions of the OTDR trace, corresponding to underwrap (next to the smooth drum surface) or overwrap layers (not restrained from the top) are thus ignored. The middle section is always linear. The fiber attenuation data are plotted versus temperature as shown in Figure 1.

3.0 Test Results

The measurement repeatability has been verified by rewinding and retesting the same fiber. The results were repeatable to within ± 0.03 dB/km over the temperature range of -40°C to $+80^{\circ}\text{C}$. Even better repeatability of ± 0.02 dB/km was observed when the same fiber went through several temperature cycles without rewinding. The fact that the induced loss mechanism is completely reversible indicates that there is no permanent (plastic) deformation of the coating. Subsequent visual examination of the fiber confirmed this finding.

Figure 1 shows the microbend sensitivity of three commercially available fibers. Fibers 1 and 3 are dual coated while fiber 2 is single coated. Only low temperature attenuations are shown because for all the fibers tested the loss above $+20^{\circ}\text{C}$ was constant. At room temperature fiber 2 is the most sensitive to microbending and fiber 3 the least. The coating of fiber 3 provides almost perfect protection against microbending. The 0.2 [dB/km] attenuation of fiber 3 is typical for 1550 nm and ideal winding conditions. As the temperature decreases fiber 3 becomes more sensitive to microbending. Below -20°C its attenuation is significantly higher than the attenuations of fibers 1 and 2. The reason for this behavior is due to reduced thermal stability of its coating system. The coating material at low temperatures becomes stiff and the cushioning effect disappears.

The dual coating of fiber 1 provides low microbend sensitivity over a wide temperature range. This type of dual coating outperforms single coating (fiber 2) at all temperatures. The slightly higher attenuation of fiber 1 as compared to fiber 3 at temperatures above 0°C are made up for by the improvement at low temperatures. The small difference at room temperature does not necessarily mean that the coating of fiber 1 is stiffer to start with. As mentioned in the introduction, fiber design and mode field diameter affect microbend sensitivity to a certain degree. Differences in the form of constant offset were observed

between two fiber samples having identical coatings, and were caused by variations in the fiber parameters.

The cable performance of fibers 1 and 2 was tested by putting 12 one kilometer lengths of each fiber type into a loose tube cable. Each tube contained equal count of both types of fibers to eliminate potential tubing differences. The attenuation of each fiber was measured as the temperature of the cable was cycled from -60°C to $+60^{\circ}\text{C}$. The data acquisition was performed according to Section 2.0. The low temperature range was extended in order to compensate for the higher microbending loss induced by tight winding on the glass drum. Lowering the temperature increased both, the cable-induced microbending loss and fiber sensitivity to microbending.

The results of the cabled fiber experiment are shown in Figure 2. Each data point represents an average of 12 fibers. The curves fitted to the data have similar shape and relative position as the corresponding curves shown in Figure 1. Inside the cable, the dual coated fiber (1) showed lower microbend loss than the single coated fiber (2) with the improvement being more prominent at low temperatures. In addition, the performance of fiber 1 was more consistent as seen from the standard deviation that was added to the mean value and shown in Figure 2 as a thin line. It is seen that the attenuation of cabled fiber is not as repeatable as the proposed test method. The microbending loss mechanism inside a cable is more complex and difficult to reproduce rendering the results of a single fiber test not representative.

4.0 Conclusions

The test method for determining fiber sensitivity to microbending over a wide temperature range has been proposed and evaluated. The applied loss mechanism does not deform the fiber coating beyond the elastic limit. Excellent repeatability of ± 0.03 dB/km for temperatures from -40°C to $+80^{\circ}\text{C}$ was achieved. Much less repeatable cable-induced loss requires testing of many samples to draw valid conclusions. The good correlation between the results of this test and cable test over a wide temperature range makes it possible to predict performance of fibers inside the cable. This test method is an economical tool for quick evaluation of new fiber coatings. Considerable fiber performance shortcomings, impossible to detect at room temperature, are now possible to identify and quantify for the critical low temperature region.

5.0 References

- [1] A. Tomita, P.F. Glodis, D. Kalish, P. Kaiser, "Characterization of the bend sensitivity of single-mode fibers using the basket-weave test", *Tech. Digest - Symposium on Optical Fiber Measurements 1982*, Boulder CO, NBS S/P 641, pp. 89-92, 1982.
- [2] FOTP-68 "Optical Fiber Microbend Test Procedure", ANSI/EIA-455-68-1988.
- [3] P.A. Sutton, J.L.L. Roberts, A.T. Summers, A. Phoenix, D. Rees, "Development of a non-destructive test for microbend loss mechanisms in cabled fiber", *International Wire & Cable Symposium Proceedings 1989*, Atlanta GA, pp. 450-455, 1989.
- [4] Y. Katsuyama, Y. Mitsunaga, C. Tanaka, T. Waki, Y. Ishida, "Optical loss stability of a fiber cable under lateral force and optimum design of the coated fiber structure", *Appl. Opt.*, vol. 21, pp. 1337-1341, 1982.

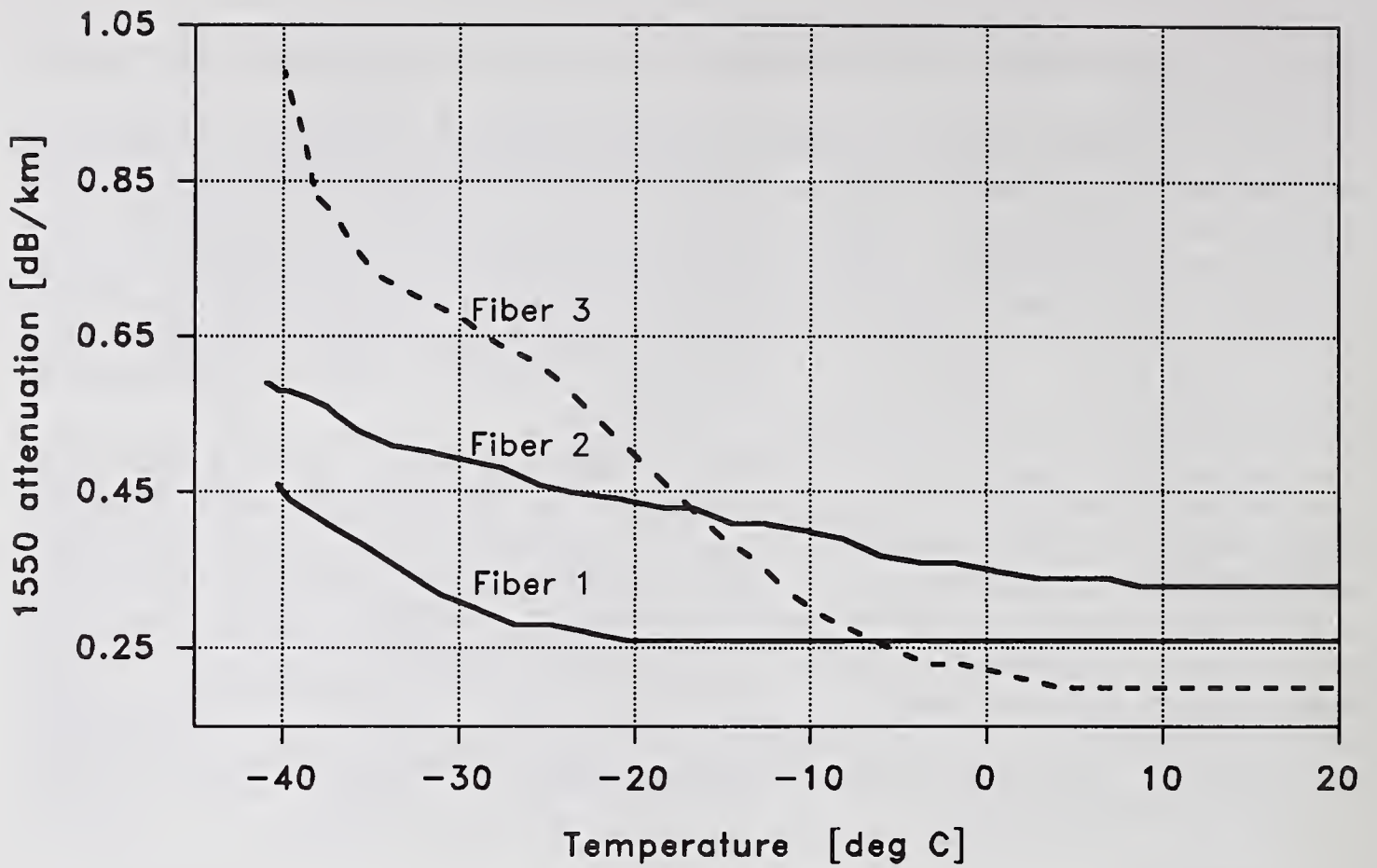


Figure 1. Microbend Loss of Fibers on Glass Drum

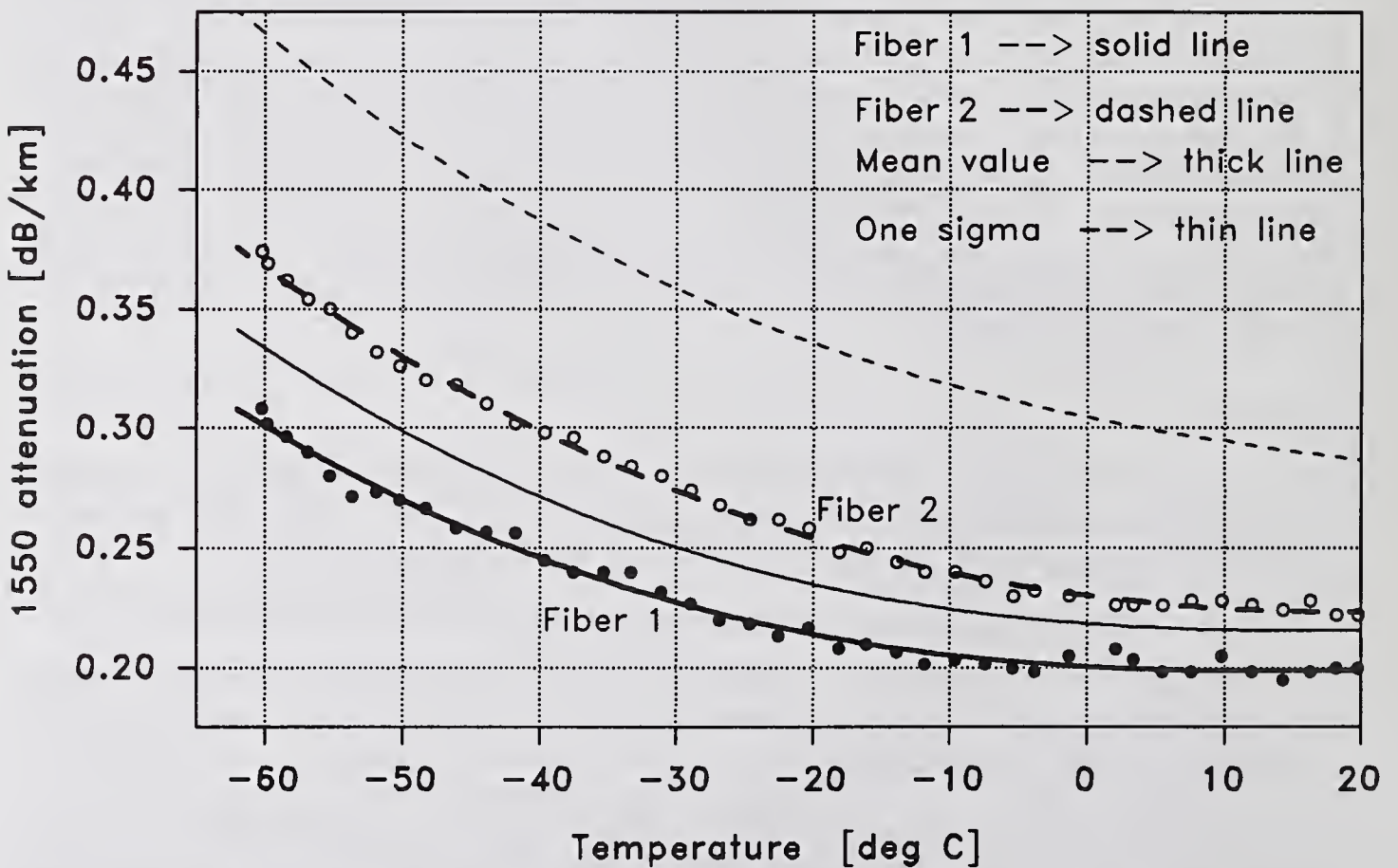


Figure 2. Performance of Fibers inside a Cable

Measuring Method for Ribbon Fiber Skew

Ryuichi Matsuoka, Hiroshi Satoh, and Nobukazu Kume

The Furukawa Electric Co.,Ltd.
Opto-Technology Laboratory

I. BACKGROUND

Recently, optical parallel transmission methods between computers have been studied by various fields from the viewpoint of transmitting and processing large volumes of information. The delay time difference (skew) of signals between optical fibers has become an important factor in optical parallel transmission, requiring the skew to be minimized. In this respect, ribbon fiber is most suitable among various types of optical fiber. The phase shift and pulse delay methods in measuring skews of ribbon fiber have been compared and the result of the comparison have been studied as reported below.

II. SKEW FACTOR ANALYSIS

The following three factors can be listed as the causes for skews which occur with ribbon fiber:

1. Difference in signal propagation time caused by fiber parameter deviation.
2. Difference in residual distortion during ribbon fiber manufacture.
3. Difference in physical length caused by structural non-uniformity of ribbon fiber.

II -1. Skew Caused by Fiber Parameter Deviation.

Using optical fiber parameters, the fiber delay time t can be given by the following expression:

$$c t = \frac{d\beta}{dk} = N_2 \left(1 + \Delta \frac{d(\nu b)}{d\nu} \right) \quad (1)$$

where β is a propagation constant, b is a normalized variable of β , ν is a normalized frequency, N_2 is a cladding group refractive index, and Δ is the relative refractive index difference. This means that the ribbon fiber skew is decided by differences of the Δ value and the value of $d(\nu b)/d\nu$ of each core.

II -2. Skew by Residual Distortion of Ribbon Fiber During Manufacture.

Residual distortion differences between cores are caused by difference of supply-back tensions of uncoated fibers during the manufacture of ribbon fiber. The skew Δt between cores in ribbon fiber of length L applied with distortion ε_1 and ε_2 ($\ll 1$) can be expressed as follows.

$$\Delta t = (\kappa - 1)(\varepsilon_1 - \varepsilon_2) \frac{NL}{c} \quad (2)$$

where κ is a photo-elasticity coefficient.

II -3. Skew by Structural Non-uniformity of Ribbon Fiber.

Physical lengths of optical fibers coiled on a bobbin or drum differ due to distortion applied to cores if ribbon fiber has curves or misalignment. The misalignment dimension d of the ribbon fiber is estimated and the value of skew caused by misalignment based on the diameter r of the take-up bobbin (drum) is calculated. The skew Δt between cores can be calculated as follows if the photo-elastic effects are taken into consideration:

$$\Delta t = \Delta L \times \frac{\kappa N}{c} = \frac{\kappa d L N}{c r} \quad (3)$$

III. SKEW MEASURING METHOD

Fundamentally, the ribbon fiber skew is measured by a method similar to that applied to measuring chromatic dispersions of SM optical fibers. Utilizing the apparatus for measuring chromatic dispersions, instead of changing of wavelength, fibers to be measured are changed in succession to obtain relative skews among fibers. As in chromatic dispersion measurement, skews can be measured by the phase shift method (frequency domain method) and pulse delay method (time domain method). A comparative study of the two methods has been made as follows.

III -1. Phase Shift Method

The light sinusoidally modulated in power is driven into the optical fiber, and the light emitted from the fiber is converted into an electrical signal by a photodetector. The phase angle difference of this output light to a reference signal is measured for each fiber and determine the ribbon fiber skew.

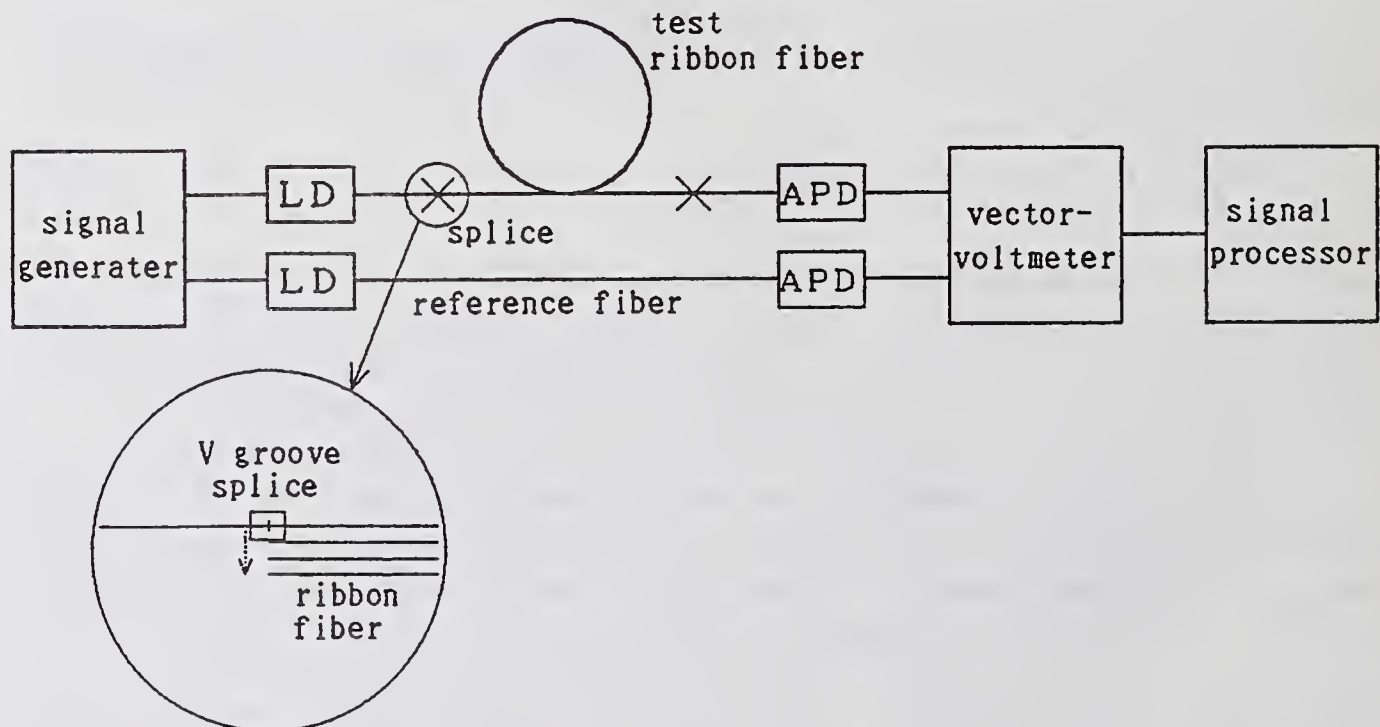


Figure 1 Apparatus for measuring ribbon fiber skew by the phase shift method.

III -2. Pulse Delay Method

Skews are measured by the pulse delay method by the directly measuring the signal delay time. An electrical signal generated by a pulse generator is converted into an optical pulse by a laser diode (LD) and injected into the optical fiber to be measured and the light emitted from the measurable fiber is reconverted into an electrical pulse by an avalanche photodiode (APD). The time and electrical level are measured by an oscilloscope. Delays are caused such as responses by the pulse generator, LD and APD. However, skews between fibers can be measured by changing optical fibers to be measured in succession.

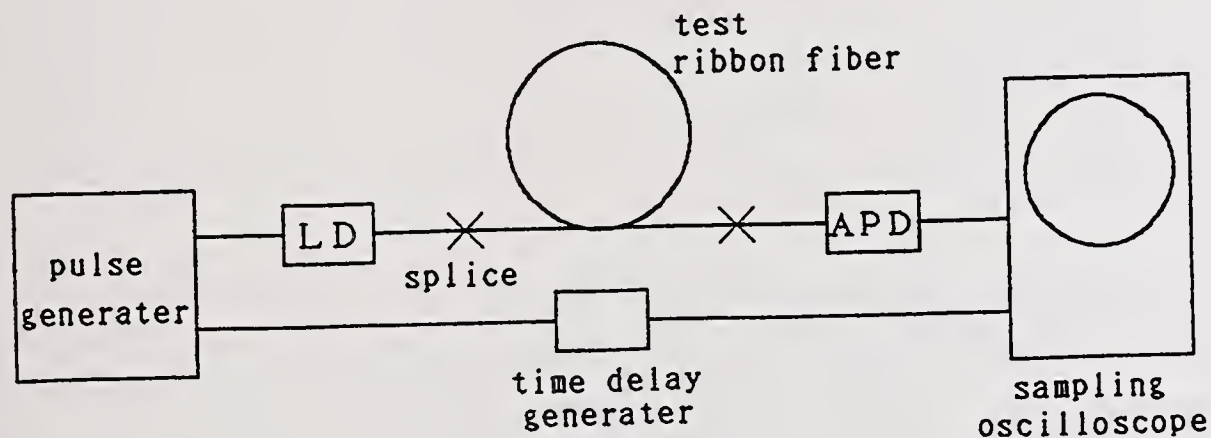


Figure 2 Apparatus for measuring ribbon fiber skew by the pulse delay method.

IV. STUDY OF MEASUREMENT RESULTS

Skews on the same ribbon fiber were measured to compare the accuracy of the two skew measuring methods, namely, the phase shift and pulse delay methods. Figure 3 and 4 show the results of skew measurement on 4-core SM ribbon fibers 100m in the length by the phase shift and pulse delay methods. The results of the two methods were nearly identical except in deviation of measured values. The deviation of measured values in three times by the phase shift method was 13ps, compared with maximum 37ps by the pulse delay method. The two measuring methods seemed to differ in terms of measurement accuracy.

Deviations of skew values by the two measuring methods were compared by extensively changing the measurable lengths from 1000m to 10m in the length to evaluate the accuracy of the two measuring methods. (See Figure 5.) The measured skew values of ribbon fibers longer than 100m coincided with those of ribbon fibers 100m in length, and those deviations also were small. Deviations of measured skew values per 100m naturally increased when the measurable fiber length was shorter than 100m. Deviations of measured skew values were generally larger with the pulse delay method than with the phase shift method, indicating that the pulse delay method would not be suitable for measuring fibers shorter than 100m in length.

Measurement by the phase shift method involves processing of electrical signals in a narrow band near a modulating frequency (200MHz) and the signal to noise ratio of the measurement system can be increased relatively so that measurement can be accurate. The pulse delay method is better than the phase shift method in terms of measuring absolute values of the delay time. However, the measurement system of it requires a high-speed response and time resolution to the order of several picoseconds. As a result, effects of jitter by each measuring equipment are expected to increase relatively. The measurement system of the phase shift method is easy to operate and the cost of it will be low compared with that of the pulse delay method. Taking these factor into consideration, the phase shift method appears to be better than the pulse delay method in measurement of ribbon fiber skews.

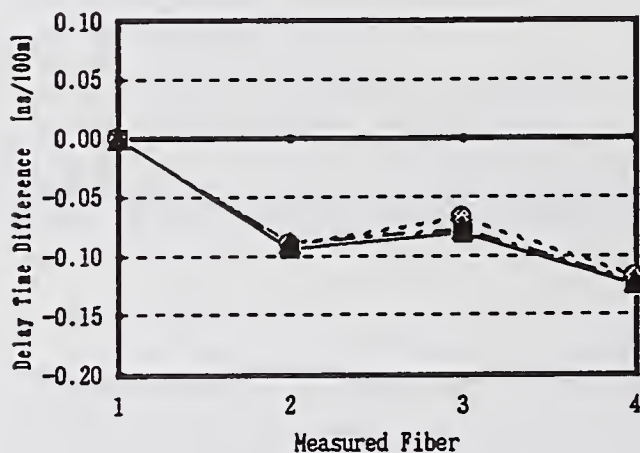


Figure 3 Phase Shift Method

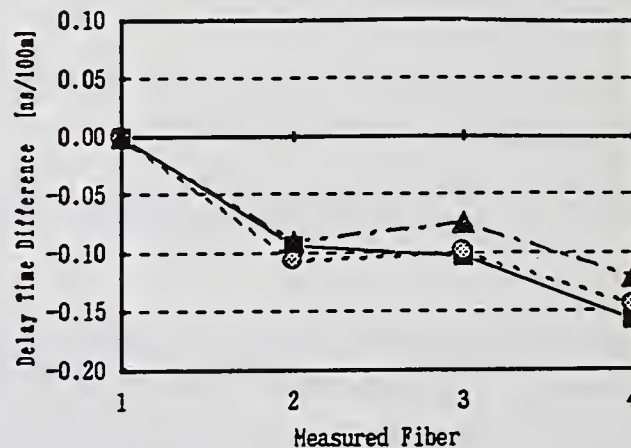


Figure 4 Pulse Delay Method

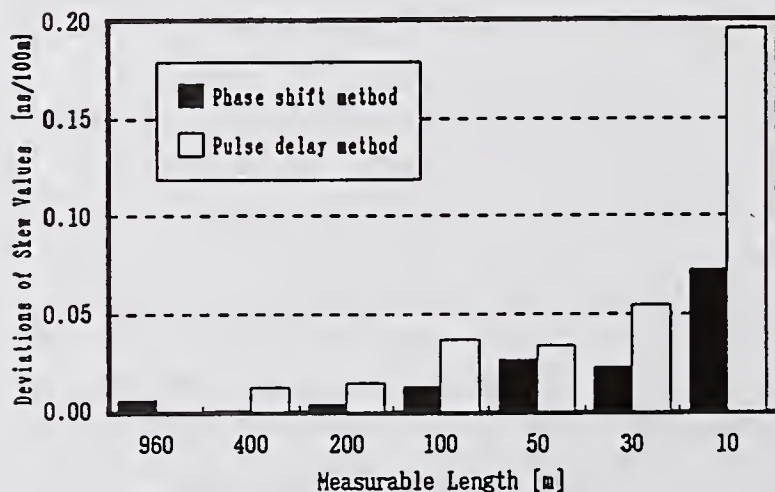


Figure 5 Deviations of Skew Values

REVIEW OF RECENT DEVELOPMENTS IN FIBRE GEOMETRY MEASUREMENTS.

J. Baines, K. Raine

National Physical Laboratory
Division of Mechanical and Optical Metrology
Queens Road
Teddington
Middlesex, TW11 0LW
U.K.

REQUIREMENTS

Present specification requirements are for fibre diameter to be determined to $\pm 2\mu\text{m}$ with the possibility that this will be reduced to $\pm 1\mu\text{m}$ in the future. If we apply the calibration standard rule of thumb then the standards laboratories are thus required to make measurements with uncertainties of about $0.1\mu\text{m}$.

The standard deviation of grey scale mean diameter measurements is typically 50nm and this has recently led to a demand from the instrument manufacturers for a calibration uncertainty of better than $0.1\mu\text{m}$. This contrasts with the view of the fibre manufacturers who see little evidence to justify a tightening of the specification that may follow from improved measurement procedures.

The grey scale instrument has become the most widely used in industry because of reliability and operator independence. Also used, but less widely, are the refracted and transmitted near field, side view and image shearing methods. All of these instruments require calibration and the standards laboratories have investigated other methods, usually less convenient, which are directly traceable to national length standards.

WORK OF THE STANDARDS LABORATORIES

Philosophically the units of length are not important provided everybody uses the same unit. Since we require a

reference artifact or physical property it is best if the unit is one which is easily realised; hence the use of the micrometre which can be easily obtained from the wavelength of laser sources.

At the National Institute for Standards and Technology (NIST), Matt Young, Steven Mechels and Paul Hale are using a Mireau white light interferometer, a contact micrometer and a scanning confocal microscope. These instruments use interferometers for length measurement and the overall uncertainty of the diameter measurement is 50nm (3σ). They plan to start selling transfer standard fibres by the summer of this year.

At the National Physical Laboratory (NPL) we make traceable measurements with a Michelson white light interferometer, an image inverting microscope and a scanning confocal microscope; in all cases the position of the sample stage is measured with a length measuring interferometer. The edge setting offset of the image inverting microscope is traceable to scanning electron microscope measurements made with interferometrically measured stage movement. We have some small doubts about the uncertainty of the scanning confocal microscope; in our instrument, which has a standard deviation of about 6nm, the measured diameter has a small dependence, amounting to 30nm, on the pinhole size. As far as we are aware this is not predicted by the theory.

At present these methods are used to calibrate an image shearing microscope which is more convenient to use but it requires some care to achieve the $0.15\mu\text{m}$ uncertainty we typically quote when selling transfer standards.

The early indications are that the calibration stability of grey scale instruments is good to about 0.1% over a period of months. We are therefore developing a high resolution grey scale instrument to provide cheap calibrations to customers with uncertainty of 50nm or better. The instrument uses a high resolution camera in which the pixel size corresponds to less

than $0.15\mu\text{m}$ in the object plane. We have performed sampling calculations to show that with a 0.65 numerical aperture objective this instrument should produce a diffraction limited edge, between about 20% and 80% edge intensity levels, leading to increased precision and a true edge location at the 25% intensity level with coherent illumination of the object.

We have compared measurements on two fibres using our image shear results with some results from NIST using the contact micrometer. The agreement on diameter measurement for a fibre with a non-circularity of 0.3% was $0.01\mu\text{m}$ but for one with a non-circularity of 1.5% it was only $0.08\mu\text{m}$. Further work is being done to try to resolve this discrepancy. There is an ongoing exchange of information between the two laboratories to ensure that calibration methods and reference materials are widely acceptable with a high degree of confidence.

We have continued the investigation into using chromium on glass masks for calibrating grey scale instruments to see under what circumstances it is possible to obtain an accurate extension, rather than just scale, calibration. Joint work between the authors and Dave Levitt of BT has shown that it is possible to calibrate back-lit grey scale instruments directly, with an uncertainty of $0.1\mu\text{m}$ or better, using a chrome circle without the need to determine the edge setting offset using a fibre.

INTERCOMPARISONS

The first CCITT round robin in 1989 [1] showed that there are short range variations in fibre diameter of the order of $0.2\mu\text{m}$. More recently John Colton and Andy Hallam at York Technology showed a worse case variation of about $2.5\mu\text{m}$ over lengths of 0.5 metre within their data set [2]. It is therefore clear that a meaningful comparison between different laboratories can only be

made if all participants measure the same cleaved ends, unless it can be shown that longitudinal variations are insignificant.

In order to try to preserve fibres during storage and transportation for intercomparisons, Photon Kinetics have developed a retractable fibre holder which it is hoped will protect the fragile cleaved end from the attentions of Carriers and Customs officials.

In the US the Telecommunications Industry Association (TIA) has organized an intercomparison of grey scale cladding diameter measurements amongst 8 participants with NIST as the coordinating laboratory and it is intended that the results will be presented by Tim Drapela at this meeting.

Within the European Cooperation in Science and Technology framework, COST 217 organized a round robin between 12 participants using the side-view, grey scale, transmitted near field, contact micrometry, image shear and refracted near field techniques. For this intercomparison NPL circulated a fibre with diameter variations along its length of less than $0.15\mu\text{m}$. The results confirmed that such instruments are capable making measurements with an uncertainty of $0.15\mu\text{m}$ when used with suitable calibration artifacts and measurement procedures although the refracted near field measurements showed excessive non-circularity as has been observed in earlier studies [3].

A second CCITT round robin was proposed last year and preparations are under way to enable this to be started soon.

STANDARDS COMMITTEE ACTIVITY

Committees and working groups of the different standards organizations have been active in various areas. A task group has been set up under IEC TC86 WG4 to produce a calibration procedure document for cladding geometry measurements but this

work is still at an early stage. One area of concern is the current plethora of existing and emerging standards in this area and the sometimes conflicting definitions of quantities to be measured. For instance, cladding non-circularity is defined differently in CCITT and TIA documents and, in the case of multimode core diameter the so-called 'k factor' level at which measurements are made is specified in EIA FOTP 58 as 2.5% but in CCITT G651 as 5%, unless otherwise specified.

Also of current interest is the type of algorithm most suitable for filtering and form-fitting to fibre edge data used in the analysis of grey scale images. Fourier analysis, best fit ellipse and cubic spline fits are all under consideration by the TIA and CCITT. The performance of each algorithm depends on the shape of the fibre and on the angular extent of any cleave damage present. Andy Hallam and Neil MacFarlane of York Technology have cleaves made with different cleave tensions to investigate the robustness of the algorithms. They found that as the amount of cleave damage, or hackle, on the fibre end increased a difference of $1\mu\text{m}$ between the filtered ellipse and the Fourier algorithms was seen. Further, a cubic spline developed by Tom Hanson of Corning showed a bias of between 0.5% and 1% in non-circularity on these data sets. However, Tom has recently shown that the spline fit may be modified to eliminate this bias. In its current draft form the TIA test procedure FOTP 176 allows the user to opt for any algorithm which passes a defined quality of fit test.

NEW MEASUREMENT NEEDS

All of the above has referred to the geometry of bare fibres. However, in the last year there has been interest in developing traceable calibration methods for measurements of diameter, thickness and concentricity of fibre coatings with an uncertainty of $0.5\mu\text{m}$ for the primary coating diameter. This has led to the development of new commercial instruments with

different calibration requirements.

The increasing use of ribbon cables is leading to demands for accurate X-Y coordinate measurements of the positions of individual fibres within the cable. It would appear that requirement will be for an uncertainty of about $0.5\mu\text{m}$ in 1cm for ribbon fibre.

CONCLUSIONS

Standards labs are now capable making fibre diameter measurements with an uncertainty of less than about $0.1\mu\text{m}$ or better. At present we typically measure eighteen diameters each with an individual uncertainty of $0.15\mu\text{m}$ but we hope to reduce this to less than $0.1\mu\text{m}$ in the near future. NIST plans to provide reference test materials certified to 50nm by the summer of 1992.

Recent work indicates that back-lit grey scale systems can be directly calibrated with an uncertainty of $0.1\mu\text{m}$ or better with an opaque chromium disk.

The dependence of the fibre diameter measurement on the curve fitting routines and the type of cleave damage is not fully satisfactory if accurate measurements are to follow accurate calibration, whether by a reference fibre or a chromium mask.

REFERENCES

CCITT Study Group XV, "Results of a round-robin study into the measurement of the geometrical properties of single-mode fibres", September 1989.

J. R. Colton, A. G. Hallam, "Measurements on the uniformity of fibre cladding geometry", in OFMC Optical Fibre Meas. Conf. Digest, York, September 1991, pp127-131.

J. G. N. Baines, A. G. Hallam, K. W. Raine, N. P. Turner, "Fibre diameter measurements and their calibration", J. Lightwave Tech., vol.18, no.8, September 1990, pp1259-1268.

Fiber Cladding Diameter Measurement
by White Light Interference Microscopy

P. D. Hale and D. L. Franzen

National Institute of Standards and Technology
Electromagnetic Technology Division
325 Broadway, Boulder, Colorado 80303

Measurement of fiber cladding diameter with an overall uncertainty of $0.1 \mu\text{m}$, or less, has been an ongoing project at NIST for the past three years. The main purpose of this project is to produce standard reference fibers for calibration of gray scale video microscopes. To help evaluate the systematic errors of any one technique, we have constructed three absolute measurement systems: a scanning confocal microscope, contact micrometer, and white light interference microscope.

The white light interference microscope uses a Mirau interference objective with a single surface in contact with the fiber. We chose a Mirau objective over the Michelson objective used in previous works [1,2] because of its stability, ease of operation, and higher magnification. Single-surface contact was chosen because a knowledge of the fiber index profile is not required [1] and material dispersion is avoided.

The system was constructed from commercial metallurgical microscope parts and uses bright-field illumination from a halogen lamp, a binocular eyepiece, and a CCD array video camera with $400\times$ overall magnification. The camera is connected to a video analyzer and monitor. An optical flat is held perpendicular to the optical axis ($\pm 100 \mu\text{rad}$) with a high quality mirror mount on a precise three-axis translation stage. The position of the flat is monitored by a commercial interferometer with 1.2 nm least count. The interferometer, translation stage, and video analyzer are all controlled by computer, and repeated measurements can be made automatically (Fig. 1).

The mirror mount has been modified to hold a standard NIST fiber holder along with a cantilevered brass weight which holds the fiber against the optical flat. The fiber holder positions the fiber on top of the flat and can be interchanged among all three NIST measurement systems. The brass weight has a semi-circular cross section and is thin enough to fit between the fiber and objective with the curved side toward the fiber. It has a 0.76 mm slot through which the fiber and flat are viewed (Fig. 2). The weight can be oriented using two precise $1/4\text{-}80$ screws so that even pressure is applied to the fiber from both contact points. The weight deforms the fiber by about $0.5 \mu\text{m}$, but the deformation is localized to a region within $20 \mu\text{m}$ of the edge of the slot. Measurements of the fiber diameter are made $380 \mu\text{m}$ from both fiber-weight contacts. Contact between fiber and flat is verified within 100 nm by viewing contact white light interference fringes analogous to Newton's rings. Surface contamination larger than 25 nm on or adjacent to the fiber can be detected using colored fringes.

The top surface of the fiber or flat is located by scanning the stage and recording white light fringes using the video analyzer while the position of the stage is monitored. The central fringe of the interferogram is then fitted to a parabola to average out random fluctuations in intensity and position tracking (Fig. 3). The region of the video image to be sampled is

located using a set of cross hairs on the video monitor. Since the field of view is a few fiber diameters in extent, no lateral motion of the translation stage is required during a measurement. To measure the diameter of a fiber, the flat is located, the top of the fiber is located, and the difference is calculated. The flat is then relocated and the difference is again calculated. The average of these two measurements is one datum which has been corrected for linear drift. When this measurement is repeated without fiber replacement, the standard deviation of the measured mean diameter is about 10 nm. When the fiber is removed and replaced between measurements the uncertainty becomes 25 nm (all uncertainties are reported as 3σ).

Placement of the cross hairs on top of the fiber is subject to digitizing and random errors. Slight offset of the cross hairs makes the measured fiber diameter too small. A 40 \times Mirau objective was used to estimate the magnitude of this effect. Six measurements on a control fiber were made alternating with measurements using the 20 \times objective. The 40 \times objective gave values 6 ± 12 nm larger than the 20 \times objective. If probability distributions for placement of the cross hair are the same for both objectives, the mean offset of the measured diameter using the 40 \times objective is 4 times smaller than the offset for the 20 \times objective. Then, the correction factor is $(4/3)\times 6$ nm or 9 ± 15 nm. All subsequent measurements include this additive correction factor, giving a total uncertainty of 30 nm.

Finally we have compared measurements on fibers using the white light interference microscope, a contact micrometer [3], and a scanning confocal microscope [4]. Measurements were made by different operators without prior knowledge of each others' results. The diameter of each fiber was measured at two specific angular orientations, thus giving a comparison of eight measured diameters (Fig. 4). Results of the interference microscope and scanning confocal microscope are plotted with respect to the contact micrometer. The mean difference between the contact micrometer and interference microscope was -1 nm and the rms difference was 15 nm. Similarly, the difference between the contact micrometer and the scanning confocal microscope was 16 nm and the rms difference was 29 nm.

Matt Young and Steven Mechels made the measurements with the contact micrometer and the scanning confocal microscope, and provided many useful insights on precise fiber measurements. Contribution of NIST, not subject to copyright.

References

- [1] K.A. Emig, "A comparison of interferometric techniques for fiber cladding diameter measurements," NIST Spec. Publ. 792, Technical digest-Symposium on optical fiber measurements, 1990, ed. by G. W. Day and D. L. Franzen, pp. 135-138, 1990.
- [2] M. J. Saunders, "Noncontact interferometric determination of the outside diameter of optical fibers," NBS Spec. Publ. 748, Technical digest-Symposium on optical fiber measurements, 1988, ed. by G. W. Day and D.L. Franzen, pp. 149-152, 1988.
- [3] M. Young, "Fiber cladding diameter by contact micrometry," Digest, Optical Fiber Measurement Conf., York, U.K., 1991, pp. 121-126 (NPL, Teddington, Middlesex, England).
- [4] S. Mechels and M. Young, "Scanning confocal microscope for accurate dimensional measurement," SPIE, Vol. 1660, 1992, in press.

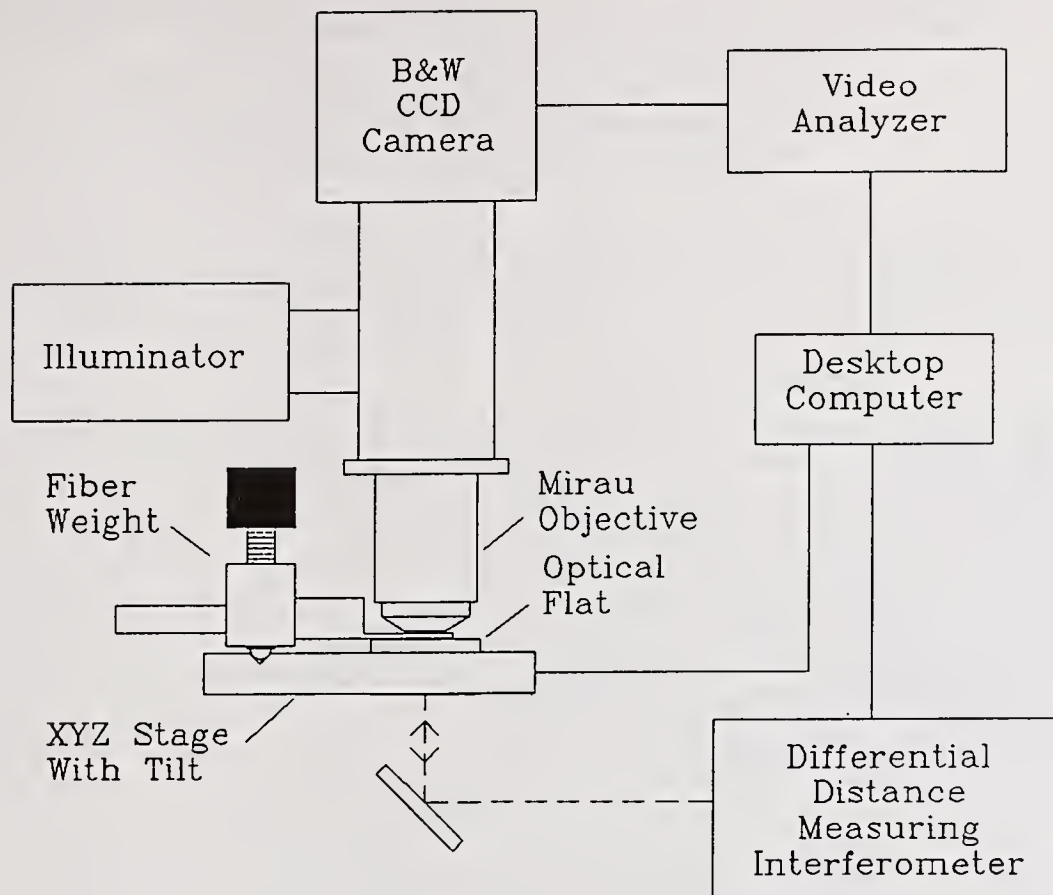


Fig. 1. White light interference microscope system based on Mirau objective.

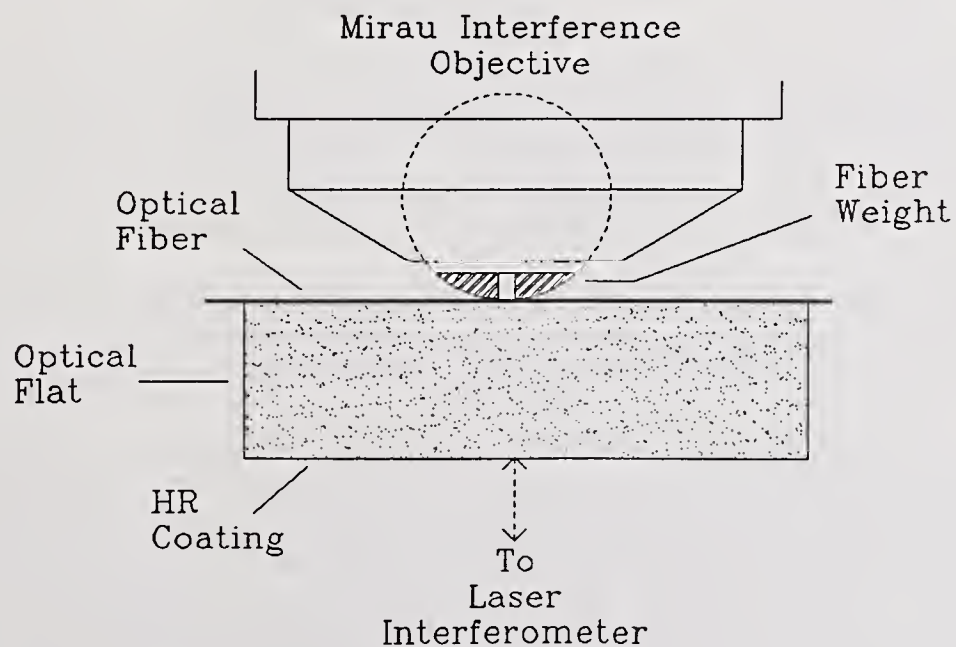


Fig. 2. Schematic of fiber held in contact with optical flat.

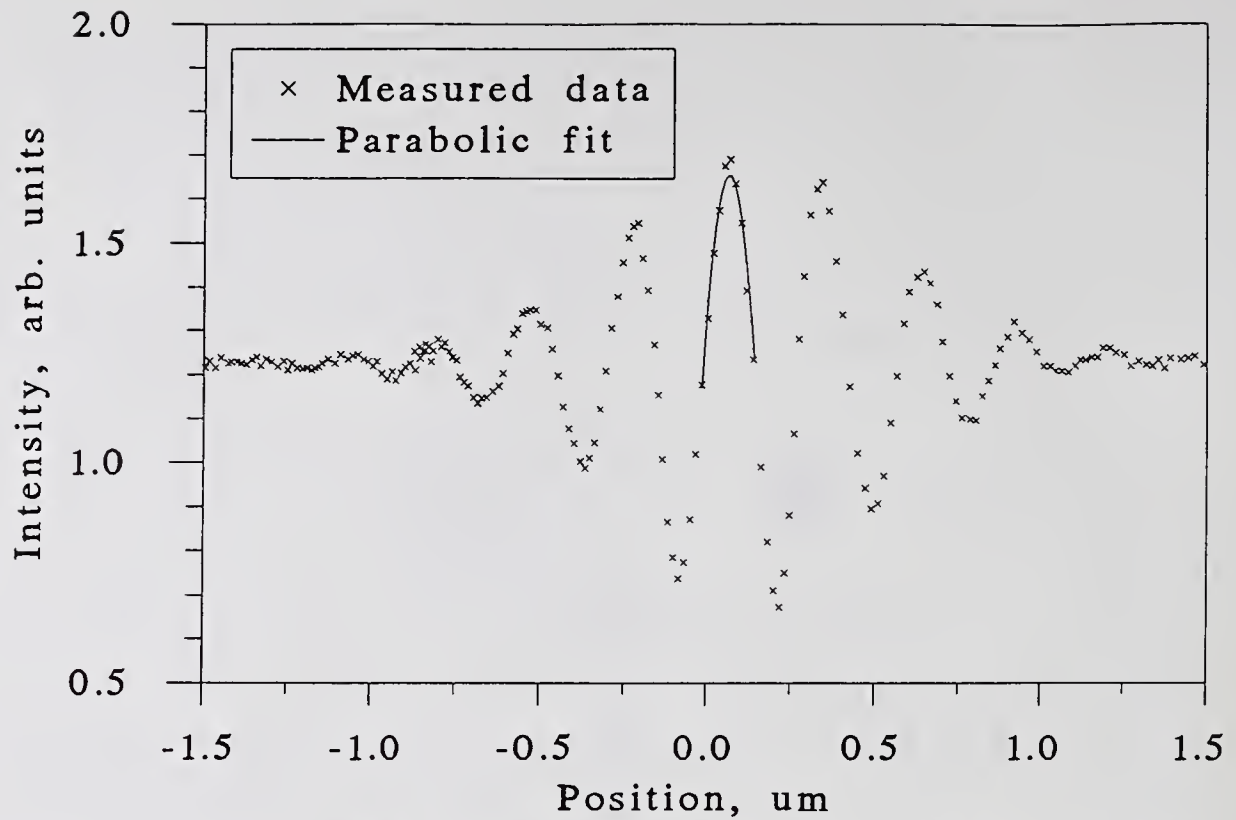


Fig. 3. White light interferogram with parabolic best fit to central fringe.

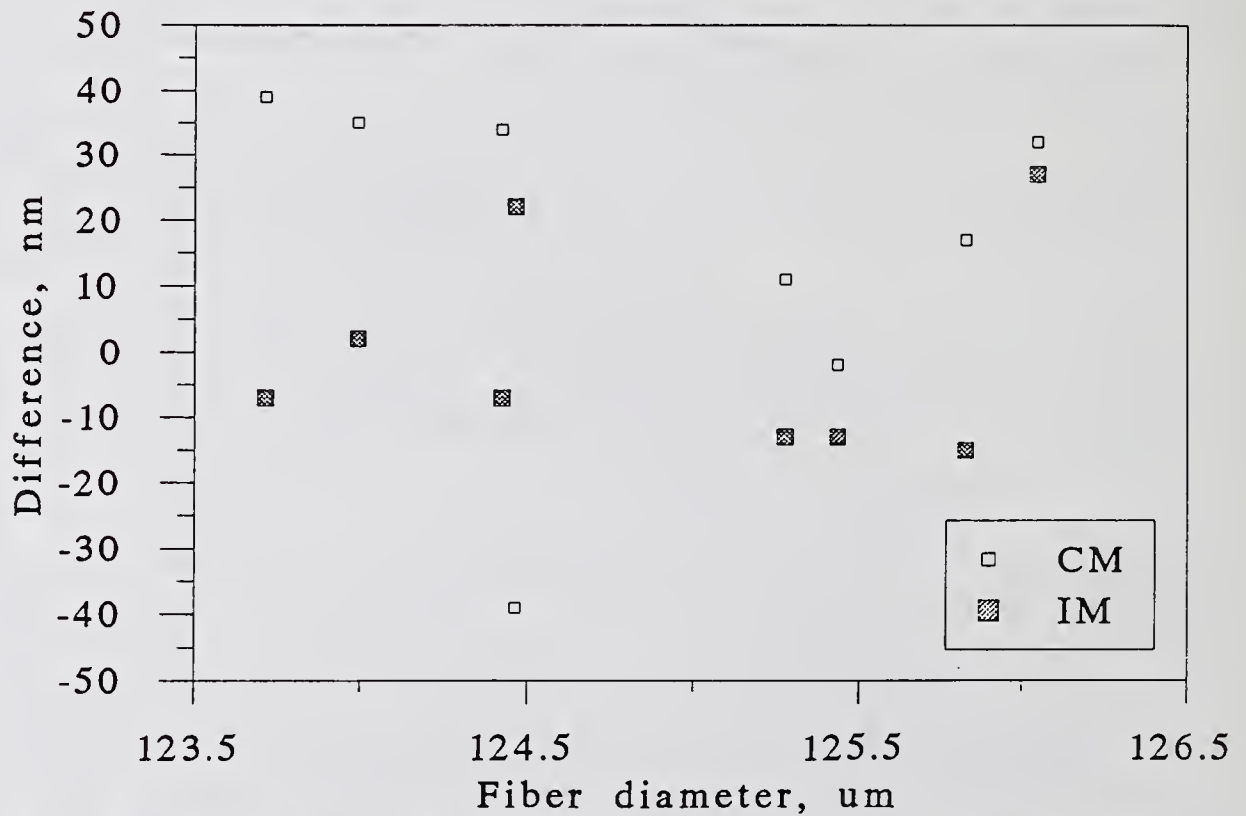


Fig. 4. Comparison of interference microscope (IM) and scanning confocal microscope (CM) with respect to contact micrometer. Measurements of fiber diameter were made at two angular orientations on four fibers.

ACCURATE MEASUREMENTS OF FIBER CLADDING DIAMETER

Matt Young, Paul D. Hale, and Steven E. Mechels
U. S. National Institute of Standards and Technology
325 Broadway, Boulder, Colorado 80303

This paper reports the development of an artifact standard for video microscopes devoted to measuring optical fiber geometry [1]. Specifically, we have developed three devices, a contact micrometer, a scanning confocal microscope, and a white-light interference microscope, that are capable of absolute measurements with accuracy between 50 and 100 nm.

A video microscope dedicated to fiber geometry is called a gray scale system by the Telecommunications Industry Association (TIA). Gray scale systems are typically used to determine the outer, or cladding, diameter of a cleaved fiber end; the ovality or noncircularity of the cladding; and the decentering, or concentricity error, between the core and the cladding. Measurements of ovality and decentering do not require absolute accuracy, but cladding diameter must be measured within $0.1 \mu\text{m}$ or so in order to manufacture efficient connectors that do not require manual adjustment. Measurements made with video microscopes, however, may well suffer from a systematic error of a few-tenths micrometer [2]. The TIA subcommittees we work with therefore requested that NIST develop an artifact standard for calibrating the gray scale systems. (The National Physical Laboratory in the U. K. has a similar program [3].) The subcommittees were, however, reluctant to accept any standard other than an optical fiber because the measured result is a function of illumination and because reflection from a metal film displays phase shifts that are not present in reflection from a glass edge [1,4].

In this paper, we will describe the contact micrometer, scanning confocal microscope, and white-light interference microscope that we have set up to measure the cladding diameter within $0.1 \mu\text{m}$ or less. Because of the ease of using the micrometer, it will become the instrument that we use regularly to prepare standards. Because of the need for accuracy (as opposed to precision or repeatability), however, we require the other methods to verify the accuracy of the micrometer.

Contact micrometer

We acquired a contact micrometer from our laboratory in Gaithersburg, Maryland. The micrometer consists of a stationary, cylindrical *anvil* and a flat, moving *spindle* (Fig. 1). Both are steel and have been polished with hard laps in an optical shop. The spindle is aligned so that the polished end is accurately parallel to the anvil. It rides horizontally on an air bearing and is pressed against the fiber with a known force. Its position is measured by a commercial interferometer that has a least count of 1.25 nm [5].

The fiber and the anvil make a point contact, so there is measurable compression at that point. The compression depends on the elastic constants of the materials and can in principle be calculated from a standard formula. The calculated value is then used as a correction to the measurement.

To test the formula, we measured the diameter of different fibers and steel thread wires as a function of the force the spindle exerts on the fiber. If the formula is correct, the measured diameter will be constant, independent of force. Possibly because we do not know the elastic constants of the materials accurately, the measured diameter is not constant (see Fig. 2). The formula does, however, display the correct functional dependence on force: force to the two-thirds power. Therefore, instead of relying on the compression calculated by the formula, we measured the diameters of a number of fibers as a function of force and calculated the slopes of curves similar to the "Raw data" curve in Fig. 2 in order to extrapolate to the values of the diameters in the absence of force on the fiber. Fortunately, all the fibers we tested gave the same slope, within experimental uncertainty.

The statistical uncertainty of measuring the slope gives rise to a systematic uncertainty of the diameter of about 3 nm (1σ). Additionally, the random uncertainty of a single set of 6 measurements is typically about 12 nm. Finally, a random uncertainty of 8 nm results from the roughness of the anvil. Other uncertainties we have been able to identify are less than 1 nm. Adding the random uncertainties in quadrature and then adding the systematic uncertainty arithmetically, we find that the overall uncertainty of the measurements is about 17 nm. We take the overall uncertainty of any measurement to be ± 3 times this value, or ± 50 nm.

Confocal Microscope

We constructed a stage-scanning confocal microscope (Fig. 3) that also uses a commercial interferometer to measure position [4]. The imagery in a confocal microscope is highly coherent, unlike that in a conventional video microscope. We can therefore find the true location of the edge by calculating the amplitude image and seeking its inflection point (this procedure is equivalent to finding the 25 % intensity point).

To help assess the accuracy of our instrument, we first measured widths of chrome-on-glass lines that had previously been calibrated by our laboratory in Gaithersburg. Our measurements agree with the Gaithersburg measurements within about 30 nm, though the sign of the disagreement depends on whether the line is clear or reflecting [4].

We measured diameters of carefully cleaved fibers and found a random uncertainty of 40 nm (3σ). Taking care not to rotate the fibers, we measured the diameters of the same fibers with the contact micrometer. The results are plotted as open squares in Fig. 4, which shows the arithmetic difference between the two measurements as a function of the diameter measured by the micrometer. That is, the horizontal line represents the micrometer measurements, and the points represent differences from those measurements.

On average, the confocal microscope measurements exceed the micrometer measurements by 20 nm; this is approximately the increment by which the confocal microscope measurements exceeded the Gaithersburg measurements of reflecting metallic lines. We cannot explain this discrepancy and do not know whether it represents a systematic uncertainty in the confocal microscope. The single outlying point in Fig. 4 is a measurement taken on a fiber that we think had very high stress and may have become deformed when it was cleaved, but that is a subject for another time.

Interference microscope

We also constructed a white-light interference microscope which uses a Mirau interference objective and a partial contact method for locating the fiber surfaces [6]. We chose a Mirau objective over the Michelson objective used in previous works [7,8] because of its stability, ease of operation, and higher magnification. We chose a partial contact method because, otherwise, we would have to know the index profile of a test fiber in order to perform absolute measurements [8].

The system consists of a commercial metallurgical microscope with bright-field illumination and a video monitor. An optical flat is held parallel to the Mirau objective, and the fiber is held against that flat by a semi-circular brass weight that contains a slot through which the fiber and flat are viewed. The position of the flat is monitored with a commercial interferometer. The white-light fringes are monitored with a video analyzer. All data acquisition and motion control are automated. Contact between fiber and flat is verified by viewing white-light fringes analogous to Newton's rings; a separation of ~ 100 nm can be detected by examining the central dark fringe visually. In addition, particles with diameters of the order of 25 nm can be detected by viewing white-light fringes from the Mirau objective.

Measurements are made by observing white-light fringes from the top of the fiber and then from the flat. If the fiber is not removed, the random uncertainty (1σ) of a set of measurements is about ± 3 nm; the uncertainty increases to ± 8 nm when the fiber is removed and replaced between measurements.

We used the interference microscope to measure the diameters of the same set of fibers we described with regard to Fig. 4. We had to remove the fibers from their holders and remount them, so we remeasured their diameters with the micrometer, in case there had been rotation when the fibers were remounted. We show the results as closed squares in Fig. 4; the mean difference between the interference microscope and the micrometer is a few nanometers.

Discussion

We estimate the overall uncertainty (3 standard deviations of the mean) of the micrometer as 50 nm; of the confocal microscope as 40 nm; and of the white-light interference microscope as 30 nm. The interference microscope and the micrometer agree remarkably well, whereas the confocal microscope may display an additional systematic error of 20 nm. The microscopes are hard to use, so, as of the time of this writing (May, 1992), we are preparing to use the micrometer to characterize Standard Reference Materials that will shortly be made available from our offices in Gaithersburg [9].

Ted Doiron of NIST, Gaithersburg, Maryland, designed and constructed the micrometer. This paper is based on a paper presented at the 1992 Conference on Precision Electromagnetic Measurements and is a condensation of the paper to be published in the proceedings of that conference. Contribution of NIST, not subject to copyright.

References

- [1] M. Young, Standards for optical fiber geometry measurements," Natl. Inst. Stand. Technol. Spec. Publ. 792, *Technical digest--Symposium on optical fiber measurements, 1990*, ed. by G. W. Day and D. L. Franzen, pp. 129-133, 1990.
- [2] S. Mechels and M. Young, "Video microscope with sub-micrometer resolution," *Appl. Opt.*, vol. 30, pp. 2202-2211, 1 June 1991.
- [3] A. Collyer, K. W. Raine, and J. G. N. Baines, "Investigation into the use of a scanning confocal microscope as a primary measurement method for determining optical fiber diameter," *Digest, Optical fiber measurement conference*, York, U.K., pp. 143-146, 1990.
- [4] S. Mechels and M. Young, "Scanning confocal microscope for accurate dimensional measurement," *Proc. Soc. Photo-Optical Instrum. Engrs.*, vol. 1660, 1992, in press. S. Mechels and M. Young, "Scanning confocal microscope for precise measurement of optical fiber diameter," *Proc. Soc. Photo-Optical Instrum. Engrs.*, vol. 1556, pp. 164-170, 1991.
- [5] M. Young, "Fiber cladding diameter by contact micrometry," *Digest, Optical fiber measurement conference*, York, U.K., pp. 123-126, 1990.
- [6] P. D. Hale and D. L. Franzen, "Fiber cladding diameter measurement by white light interference microscopy," this conference.
- [7] K. A. Emig, "A comparison of interferometric techniques for fiber cladding diameter measurements," Natl. Inst. Stand. Technol. Spec. Publ. 792, *Technical digest--Symposium on optical fiber measurements, 1990*, ed. by G. W. Day and D. L. Franzen, pp. 135-138, 1990.
- [8] M. J. Saunders, "Noncontact interferometric determination of the outside diameter of optical fibers," Nat. Bur. Stand. (U.S.) Spec. Publ. 748, *Technical digest--Symposium on optical fiber measurements, 1988*, ed. by G. W. Day and D. L. Franzen, pp. 149-152, 1988.
- [9] National Institute of Standards and Technology, Office of Standard Reference Materials, Room B311, Chemistry Building, Gaithersburg, Maryland 20899; 301-975-6776. Refer to SRM 2520, Optical Fiber Diameter Standard.

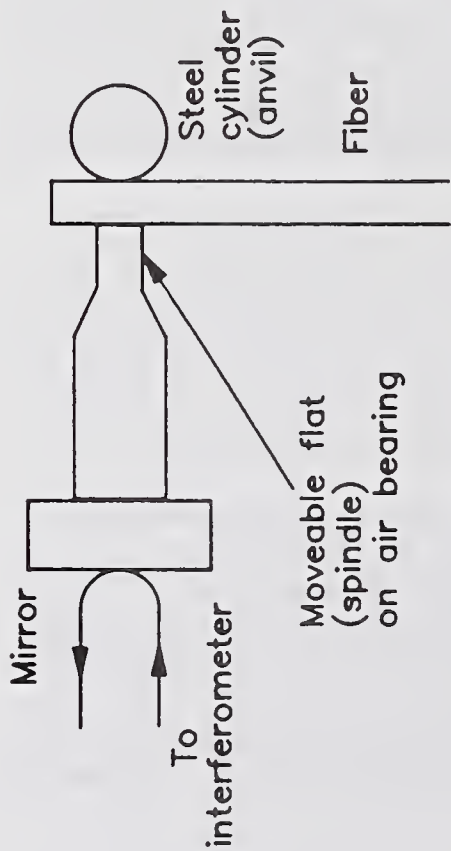


Figure 1. Contact micrometer. The moveable spindle is pressed against the fiber with a known force, and the position of the spindle is monitored interferometrically.

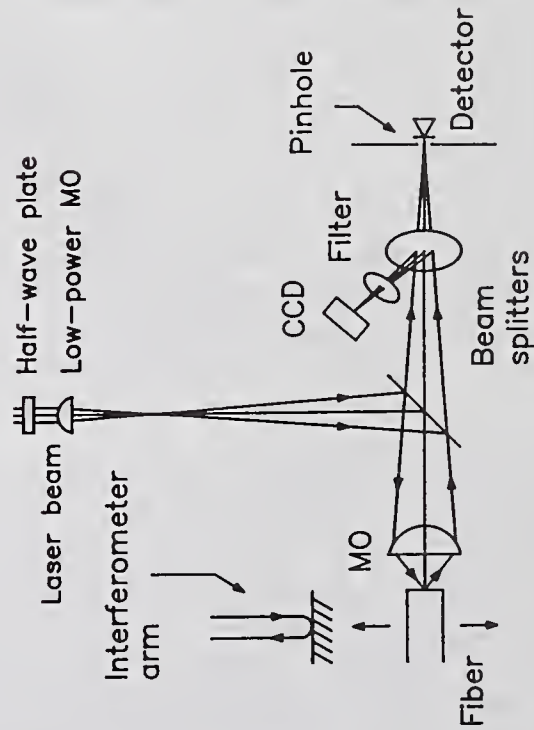


Figure 3. Scanning confocal micrometer. The fiber is scanned vertically and its position is monitored interferometrically.

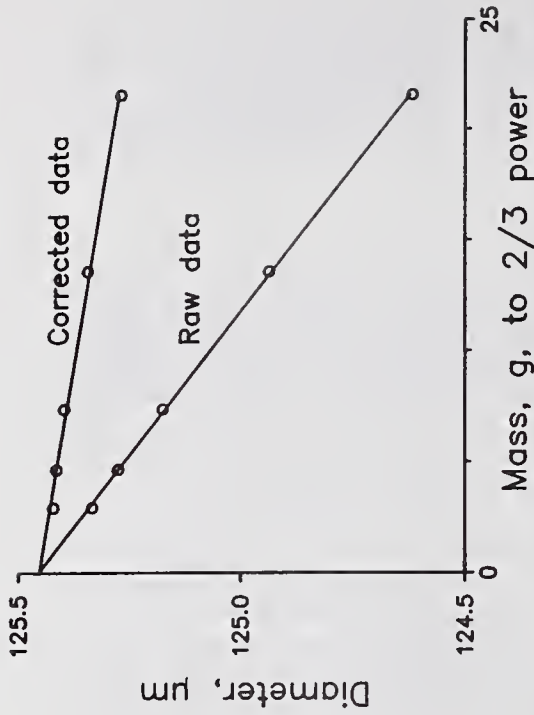


Figure 2. Measured diameter as a function of force (mass) to the two-thirds power. The slope of the best-fit line marked "Raw data" is used to determine the diameter of the fiber.

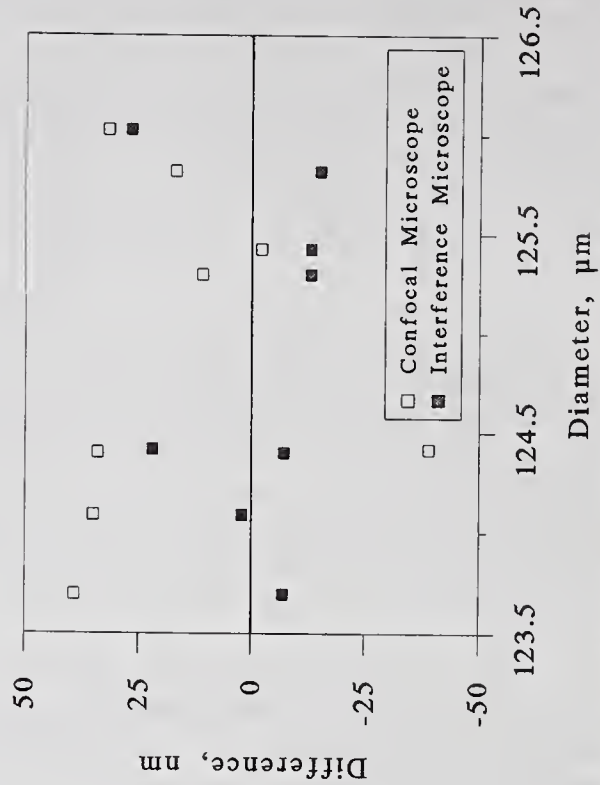


Figure 4. Diameter measurements made with the two microscopes (squares) compared with the contact micrometer (horizontal line).

MEASUREMENT OF FIBRE COATING GEOMETRY BY GREY-SCALE ANALYSIS

Andrew G Hallam, Julia H Shaw

York Technology Ltd, School Lane,
Chandlers Ford, Hants, S05 3DG. UK

INTRODUCTION To preserve the mechanical strength of newly-pulled optical fibres it is usual to apply one or more protective polymer coatings to the fibre. Generally two coating layers are applied; the inner coating to strip out cladding-modes and also minimise microbending effects, the outer coating to provide mechanical and chemical protection.

The thickness of the coatings is important to ensure the fibre's mechanical and optical performance. The concentricity of the coatings is particularly important in the manufacture of ribbon cable. The established method (1) for measuring the geometry of fibre coatings consists of positioning the fibre in an oil filled cell, at right angles to the axis of a microscope, and measuring the positions of the coating boundaries using a filar eyepiece. The measurement repeatability of this method can no longer be considered adequate in the light of recent improvements in fibre glass geometry measurement technology (2) where repeatabilities of 0.1 μ m are routinely achieved. A new method has therefore been developed, based on established grey-scale analysis techniques.

EXPERIMENTAL APPARATUS An intensity profile obtained using a conventional microscope illumination system is shown in figure 1. A CCD camera was used to record the image profile. The positions of the coating and cladding boundaries are difficult to locate accurately and the image is not suitable for computer analysis. In order to improve visibility of the boundaries a measurement system employing dark-field illumination has been developed. Here the illumination is arranged so that it is outside the collection numerical aperture, NA, of the imaging objective. Thus when no fibre is present no light reaches the camera. When a fibre is inserted into the cell light is deviated by the fibre into the collection NA of the objective and an image is formed at the camera. Figure 2 shows the intensity profile obtained from a double-coated fibre. The image consists of six bright peaks corresponding to the coating and cladding boundaries. The peaks are sufficiently sharp to allow computer optimisation and analysis.

The experimental set-up is shown schematically in figure 3, where the central component of the system is a novel wedge-shaped prism. Illumination at 850nm, provided by a large core fibre, is collimated by a lens, and directed on to the front surfaces of

the prism. Light from the upper face, in the diagram, is refracted downwards and then reflected by Total Internal Reflection upwards towards the measurement cell. Similarly for light incident in the lower half of the diagram. The two beams cross in the centre of the cell, which is filled with oil, and emerge through the front window of the cell with an NA which is outside that of the imaging objective. The presence of a fibre in the cell causes the light paths to be deviated, by the processes of refraction and reflection, into the collection NA of the optical system. An image is thus formed which consists of a series of bright peaks corresponding to the coating and cladding boundaries.

The practical implementation of this technique is shown in figure 4. A plastic moulded collimating lens is located on the projections at the wedged end of the prism. The measurement cell itself is demountable to allow easy access for cleaning with an O-ring seal and spring-clip retainers. The fibre is inserted into the cell through a precision ferrule and is further located by a second blind ferrule at the bottom of the cell. In order to fully characterize the geometry of the coating, provision is also made to rotate the fibre about its axis. The prism itself is manufactured from perspex.

Further advantages of this technique are that the camera allows a section of fibre about 0.5mm long to be seen on the monitor, allowing the cleanliness of the cell to be assessed. Also the presence of bubbles, which sometimes occur in fibres at the interface between the inner coating and the cladding, can readily be seen and their positions measured. Secondly, the system needs no special imaging optics, the prism assembly can be used on commercial grey-scale instruments.

MEASUREMENT PROCEDURE AND DATA ANALYSIS The geometrical parameters of importance are the diameters and non-circularities/ovalities of the coating layers, and the concentricities with respect to the cladding. From these parameters the thickness of the coating layers may also be determined. The measurement procedure is as follows. The fibre is inserted into the cell and located in the alignment ferrules. The focus position is then optimised by analysing scan data from the camera. Measurements are made at 30 degree intervals resulting in a series of edge points for each boundary. Ellipses are fitted to the sets of edge points giving the diameters and non-circularities of each coating, and the concentricities are computed from the relative centre positions of the ellipses. The complete measurement, including re-optimisation of the focus for each fibre position, takes less than 90 seconds.

RESULTS Some typical repeatability data are shown in figure 5. The mean and maximum standard deviations, SD, from 9 sets of

measurements are shown, where each set consists of 12 re-insertions of the fibre under test. The mean SD on the diameter of each layer was better than 0.2um with a worst case of 0.33um. The mean SD on the concentricity of each layer was better than 0.25um with a worst case of 0.41um. These results are a significant improvement on the conventional filar eyepiece method.

From the coating geometry values the thickness of the coatings may also be determined. Measurements on a range of fibres have shown some fibres with variations of up to 9um in the thickness of the outer coating and 11um in the inner coating.

CALIBRATION To calibrate the side-view measurement system, reference fibres or glass rods of certified diameters may be used. In order to determine the effect of measuring fibres coated with different materials a series of fibres from 11 manufacturers was obtained. The refractive index of the inner and outer coatings of these fibres were then measured using the refracted near-field method. It was found that the use of 3 calibration fibres, or glass rods, enabled a calibration accuracy on outer diameter of 0.6um to be achieved over the range of fibres investigated.

It was found that the calibration factor for the inner coating diameter could be determined from the calibration factor for the outer coating. This is due to the fact that the refractive index differences between the inner and outer coatings on the range of fibres measured were similar. An accuracy on inner coating diameter of approximately 1um may be achieved

The measurement of non-circularity is self-calibrating as it is a ratio measurement. Concentricity calibration depends on only nominal dimensional calibration of the optical system.

SUMMARY A practical system for fibre coating geometry measurement based on the established side-view method has been described. The new implementation makes use of computerised control and data processing techniques to achieve typical repeatabilities of 0.2um on diameter and 0.25um on concentricity.

REFERENCES

(1) Fibre Optics Test Procedure FOTP-173. 'Coating Geometry Measurement for Optical Fiber, Side-View Method', TIA/EIA, 2001 Pennsylvania Avenue, N.W., Washington, D.C. 20006-1813, USA.

(2) 'The First International Fibre Geometry Round Robin', Kane W.T., 'Optical Fibre Measurement Conference', York UK, Sept 1991.

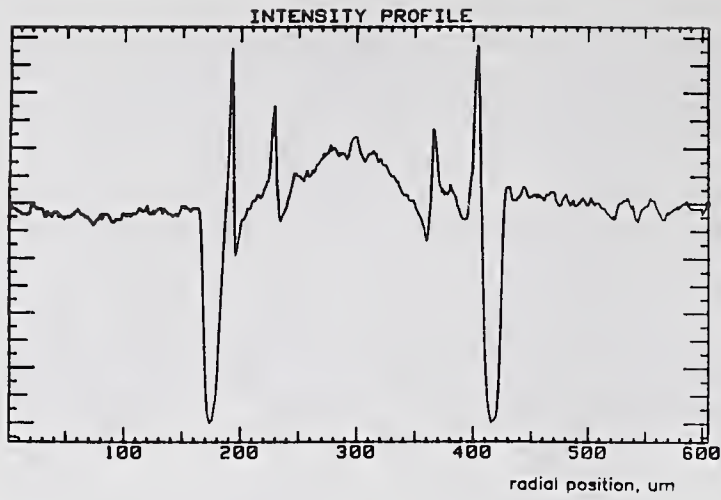


Fig 1. Conventional intensity profile.

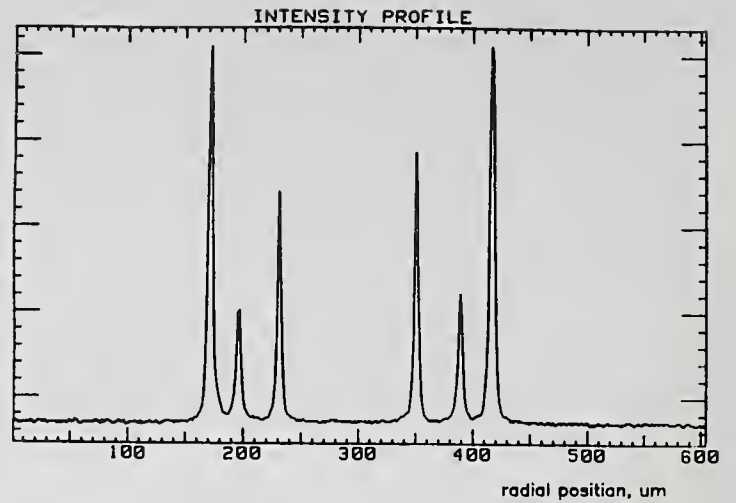


Fig 2. Dark-field intensity profile.

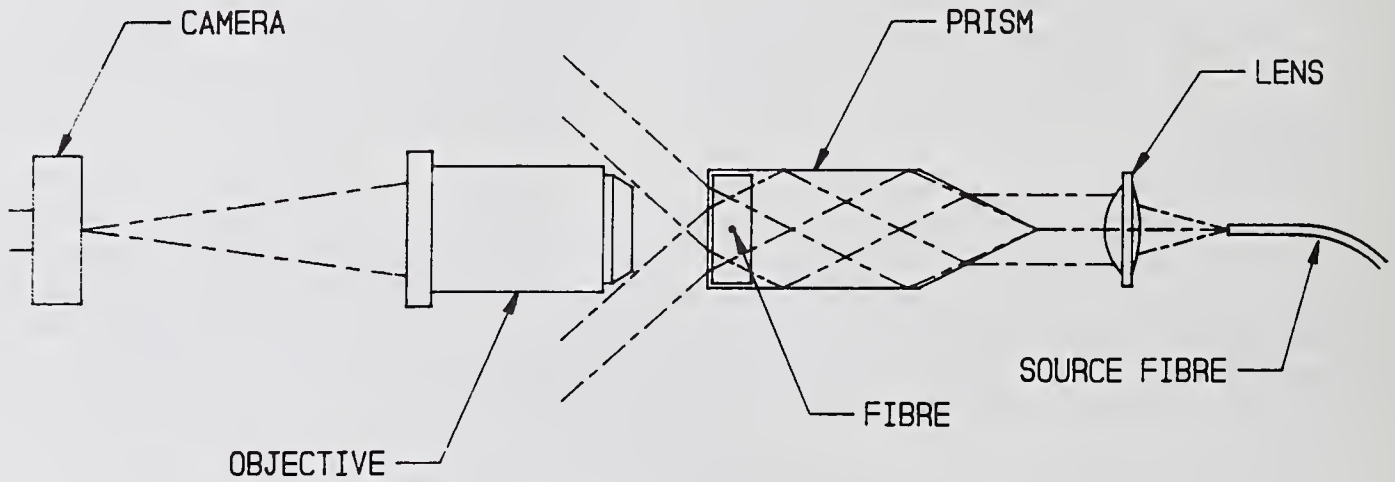


Fig 3. Optical set-up of the side-view system.

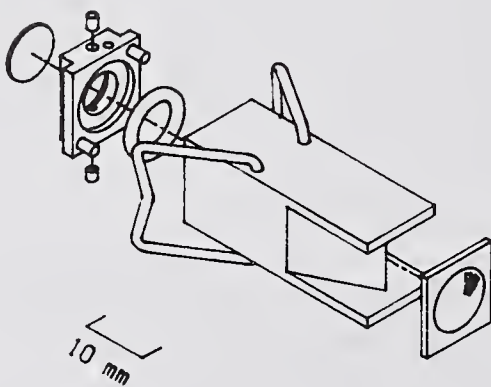


Fig 4. View of prism components.

Parameter	Mean std dev	Max std dev
outer coating diam	0.17 μ m	0.33 μ m
inner coating diam	0.16 μ m	0.33 μ m
cladding diam	0.11 μ m	0.24 μ m
outer coating non-circ	0.15%	0.37%
inner coating non-circ	0.23%	0.44%
cladding non-circ	0.15%	0.23%
outer coating conc	0.15 μ m	0.26 μ m
inner coating conc	0.23 μ m	0.41 μ m

Fig 5. Repeatability of side-view system.

Coating Thickness Unevenness Measurement in Fiber Drawing Process by using Reflected Light Detecting Method

Akira Inoue, Shuji Shinoki, Yuji Kobayashi, Yasuji Hattori
Sumitomo Electric Industries, Ltd.
1, Taya-cho, Sakae-ku, Yokohama, 244, Japan

Introduction

Optical fiber is coated with resin immediately after fiber-drawing in order to keep its tensile strength and improve its endurance to environment. The coating state strongly influences the transmission characteristics of a fiber, for example temperature resistance and pressure resistance. So it is necessary to monitor the coating state in the fiber-drawing process and to control fiber-drawing condition upon the variation of the coating state.

B.R.Eichenbaum introduced coating thickness unevenness measuring method by monitoring forward scattering patterns⁽¹⁾. In this method, coating thickness unevenness around a optical fiber is measured by illuminating a side wall of a fiber under drawing with a laser beam and detecting a forward scattering light pattern. This method is available in the case that the light passing through both the resin portion and the glass portion and the light passing through only the resin portion can be discriminated from each other (Fig.1(a)). When the coating diameter is small and the resin portion is thin, there exists no light that passes through only the resin portion and the coating thickness unevenness can't be measured (Fig.1(b)). In this paper, we describe a new coating thickness unevenness measuring technique by detecting reflected light from a fiber under drawing. Using this technique, coating thickness unevenness of a fiber which has a thin resin layer can be measured.

System Configuration

Fig.2 shows the system configuration of the new coating thickness unevenness measuring system. An linearly polarized He-Ne laser and two reflected light detecting sections are located so that their optical axes are perpendicular to the longitudinal axis of the coated optical fiber under drawing. The direction of laser beam's polarization is set perpendicular to the longitudinal axis of the fiber. Light detecting sections are set symmetrically with respect to the fiber and their optical axes are perpendicular to the optical axis of the He-Ne laser. Reflected light beams from the fiber are detected by CCD cameras with electronic shutters which are controlled by a personal computer and monitored images of the reflected light beams are simultaneously stored

by image freezers. Each light detecting section has a diaphragm at the focal plane of the receiving lens so as to limit its light-receiving numerical aperture and enlarge its depth of focus. Diameters of the fiber with resin portion and without resin portion are measured by laser scanning micrometers and measured diameters are sent to the personal computer.

Principle

Fig.3 shows a cross sectional view of an optical fiber which consists of a glass portion and a surrounding resin portion. The side wall of the fiber is illuminated with parallel light. Light beams A and B, which are reflected on the outer surface of the resin portion and the boundary surface between the glass portion and the resin portion respectively, are detected to measure a distance d of reflected light beams. r_1 , r_2 express the radius of the glass portion and the resin portion respectively. n_0 , n_1 express the refractive index of the ambient area of the coated optical fiber and that of the resin portion respectively. If the center of the resin portion is selected as the origin of the x-y coordinate system, coordinates of a reflection point P_0 of the light beam A and a exit point P_3 at which the light beam B exits from the resin portion are calculated as follows.

$$P_0 = (r_2/\sqrt{2}, r_2/\sqrt{2})$$

$$P_3 = (\sqrt{r_2^2 - (r_2/\sqrt{2} - d)^2}, r_2/\sqrt{2} - d)$$

The coordinate of the reflection point $P_2(P_{2x}, P_{2y})$ of the light beam B on the boundary surface satisfies the following equation.

$$P_{2y} = P_{3y} + \tan(\theta_3 - \theta_2) * (P_{2x} - P_{3x})$$

$$\text{where } \theta_3 = \tan^{-1}(P_{3y}/P_{3x})$$

$$\theta_2 = \sin^{-1}(n_0 * \sin \theta_3 / n_1)$$

If it is assumed that the coordinate of the incident point P_1 , at which the light beam B is incident on the resin portion, is $(r_2 * \cos \omega, r_2 * \sin \omega)$, θ_0, θ_1 satisfy the following equations.

$$\theta_0 = \pi / 2 - \omega$$

$$\theta_1 = \sin^{-1}(n_0 * \sin \theta_0 / n_1)$$

$$\theta_1 = \theta_0 - \tan^{-1}((P_{1x} - P_{2x}) / (P_{1y} - P_{2y}))$$

$$= \theta_0 - \tan^{-1}((r_2 * \cos \omega - P_{2x}) / (r_2 * \sin \omega - P_{2y}))$$

The center C_s of the glass portion is located on a bisector of an angle formed at the reflection point P_2 by the incident light and reflected light, and is spaced from P_2 by a distance of r_1 . Therefore, the coordinate of C_s is expressed as follows.

$$C_s = (P_{2x} - r_1 * \cos \phi, P_{2y} - r_1 * \sin \phi)$$

$$\text{where } \phi = \{ \tan^{-1}((P_{1y} - P_{2y}) / (P_{1x} - P_{2x})) + \tan^{-1}((P_{3y} - P_{2y}) / (P_{3x} - P_{2x})) \} / 2$$

The coordinate of C_s is expressed in the same manner as above by using the distance d' of reflected light beams A' and B' which are reflected

to the opposite direction. If n_0 , n_1 are known, the coordinate of C_e can be calculated from above mentioned equations by measuring r_1 , r_2 , d , d' . The distance between the origin and C_e correspond to the eccentricity of the center of the glass portion from the center of the resin portion. Coating thickness unevenness is calculated from this value of the eccentricity and the radii r_1 , r_2 .

Experimental Results

To estimate the accuracy of the measured coating thickness unevenness, test fibers with coating thickness unevenness were manufactured and their coating thickness unevenness were measured in the fiber-drawing process by using the reflected light detecting method and after fiber-drawing by using a microscope. The diameters of the fibers are from $170\mu\text{m}$ to $210\mu\text{m}$. To get the clear image of the reflection point on the outer surface and on the boundary surface, high angular selectivity and large depth of focus are needed to the light detecting system. To achieve these, the numerical apertures of the receiving lenses are limited to 0.11 by the diaphragms. This value of numerical aperture corresponds to $25\mu\text{m}$ of the depth of focus. To eliminate the degradation of the monitored image caused by the vibration of the fiber, electronic shutters of the CCD cameras are driven at the speed of $1/2000\text{sec}$.

Fig.4 compares the coating thickness unevenness measured after fiber-drawing by using a microscope with that measured in the fiber-drawing process by using the reflected light detecting method. The coating thickness unevenness is expressed as a ratio of a minimum thickness of the resin portion to a maximum thickness of that around the glass portion. The difference between the coating thickness unevenness measured in fiber-drawing process and that measured after fiber-drawing process is less than 10% .

Conclusion

A new technique to measure an optical fiber's coating thickness unevenness in fiber-drawing process has been developed. The accuracy of coating thickness unevenness measurement is better than 10%. Using this technique, coating thickness unevenness is measured by detecting reflected light from the fiber, so it is available for a fiber which has a thin resin layer.

Reference

- (1). B.R. Eichenbau, "The Centering of Optical Fiber Coatings by Monitoring Forward Scattering Patterns", Bell System Technical Journal, Mar. 1980.

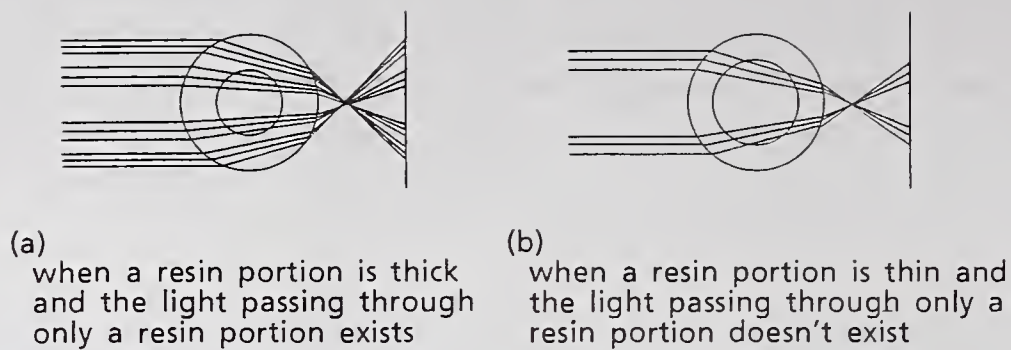


Fig.1 Light passing through a coated optical fiber

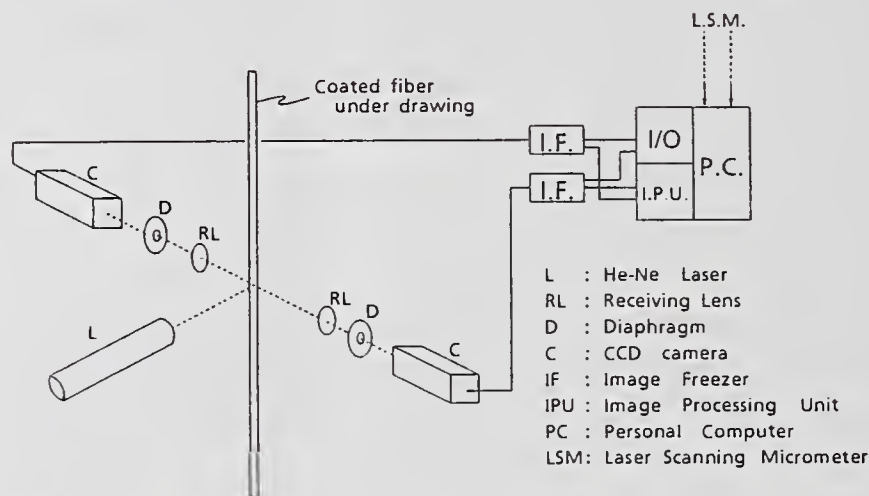


Fig.2 System configuration of the coating thickness unevenness measuring system

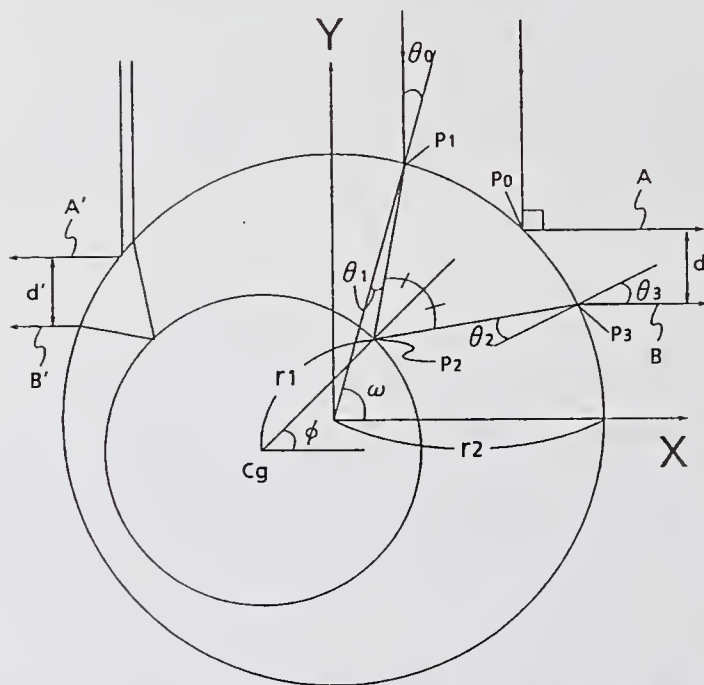


Fig.3 Reflection on the outer surface of the resin portion and on the boundary surface between the resin portion and the glass portion

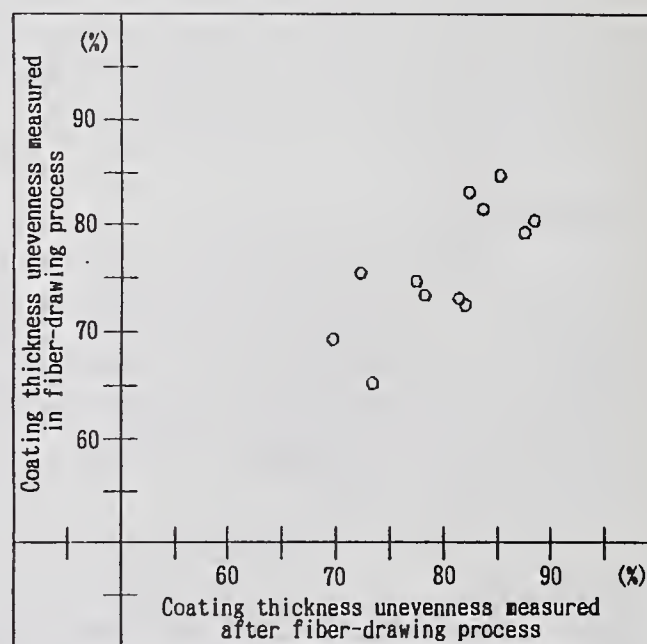


Fig.4 Coating thickness unevenness measured after fiber-drawing process and measured in fiber-drawing process

DEVELOPMENT OF IN-LINE COATING THICKNESS MONITOR FOR HERMETIC CARBON COATED FIBER

Yoshinori Ishida, Yukio Kohmura, Shin-ich Arai
The Furukawa Electric Co.,Ltd.
R&D Department Plant & Facilities Division
6,Yawata-kaigandori,Ichihara,Chiba,290,Japan
Tel.+81-436-42-1631 Fax.+81-436-41-6218

Introduction

Recently a hermetic carbon coated fiber(HCF) has been investigated intensively to suppress of hydrogen-induced losses and to improve the fatigue behavior. Hermetic coating consists of an amorphous carbon which is deposited on the fiber surface with thermal chemical vapor deposition during fiber drawing. After carbon coating, polymer coating is formed on it, and then the fiber is wound up at high speed as shown in Fig.1-(a).

The aforementioned features of HCF depends upon the thickness of the amorphous carbon coating. So, from the point of quality control, it is very significant to measure the thickness of the full-length of fiber.

Because amorphous carbon is a conductor, the thickness of carbon coating has relation to electrical resistance. So far, we have measured the electrical resistance experimentally after stripping the polymer coating. However, it is not a useful method for production because it is a destructive measurement. We must develop a new method which can be applied to a production line and enables the measurement of the thickness continuously.

Therefore, we have developed a thickness measurement technique for carbon coating beneath the polymer coating by using the eddy current measurement method.

Measurement technique

It is a common practice to analyze the change in complex impedance of an electromagnetic circuit which is constituted by a pickup coil and a work, in the area of the eddy current measurement of a metal wire and a metal tube. Amorphous carbon of HCF can be regarded as a super thin film tube. Assuming that the quality of thin film, namely conductivity, and diameter of fiber are constant, the complex impedance is correlative only with the thickness of coating. We expect that we can measure the thickness of carbon coating by the change in complex impedance. However there are some problems practically, and we must solve them. Firstly, the fiber diameter is very thin, the thickness of carbon coating is very thin (several tens of nanometers), and the pickup signal is very weak. Secondly, because of high running speed of fiber, mechanical vibration of fiber is large. And finally, because of high sensitivity measurement, it is difficult to keep the zero position during a long measurement.

We have solved aforementioned problems by the following method. We used MHz order high frequency for the weak pickup signal. We vibrated a pickup coil mechanically at a constant frequency to disregard the vibration of fiber and keep the zero position electrically. This is because we ascertained experimentally that the phase angle of impedance is determined only by electrical resistance in spite of vibration of the fiber and coil. Besides, we could compensate the zero position using the OFF signal condition when a coil separates from a fiber. As a result, we could measure stably the thickness of carbon coating for a long time.

Fig.1-(b) shows a schematic diagram of a measuring system. High frequency signal from oscillator excites a pickup coil which constitutes a part of bridge circuit. Simultaneously, a phase shift circuit converts the signal to two signals which have phase differences, 0° and 90° . The pickup signal which has the information of carbon coating thickness is detected by a phase detector with two phase difference signals. Each of detected signals corresponds to an imaginary part and a real part of complex impedance.

Results of measurement

Fig.2 shows a result of measurement obtained by using this measurement method. It is plotted in a complex plane. The electrical resistance of the samples were already measured by another method. It shows that there is high correlation between the phase angle of impedance and the electrical resistance. When a coil separates from a fiber, a signal is treated as the origin. When a coil approaches a fiber, a signal apart the origin and moves in a constant direction.

Fig.3 shows the relation between electrical resistance and phase angle of impedance. In this case, the phase angle means a relative value to a standard sample. By convert in the electrical resistance to the thickness of carbon coating in Fig.3, Fig.4 was obtained. Presently the minimum measurable thickness is 17.6nm, and the resolution is $\pm 1.0\text{nm}$ (for the thickness 17.6nm).

Fig.5 shows a result of a practical measurement in fiber drawing process. Total drawing length was 15Km. During the drawing, we changed the production condition for two times. The thickness of carbon coating and its fluctuation under each condition are shown in the following.

condition	thickness (nm)	fluctuation (nm)
1	23.6	± 0.6
2	35.6	± 1.2
3	26.4	± 1.0

We could find a big fluctuation of measured values in Fig.5 at the end of condition 3. This fluctuation was caused by stopping the thickness control at the end of drawing. Since the control was stopped, the reactor pressure was affected by adhered carbon inside the reactor.

In this way, we are now able to control conditions necessary to keep the coating thickness constant. Those conditions are, for example, flow rate of gases, pressure of reactor, and fiber drawing speed etc.,.

Conclusion

We have developed an in-line and continuous coating thickness measurement technique by using eddy current measurement method. The measurement of phase angle of impedance and the vibration of a pickup coil are key factors. In this way, we could realize the stable measurement of carbon coating thickness. Presently, the minimum measurable thickness is 17.6nm, and the resolution is $\pm 1.0\text{nm}$ (for the thickness 17.6nm).

Using this thickness measurement technique, we can guarantee the features of HCF along the full-length of fiber.

Reference

- 1) K.Hirabayasi et al., " Characteristics of carbon coated optical fibers and cables", IEICE JAPAN, OCS 91-16, P43-48, 1991
- 2) " Handbook of non-destructive test", Edited by Association of Non-Destructive Test

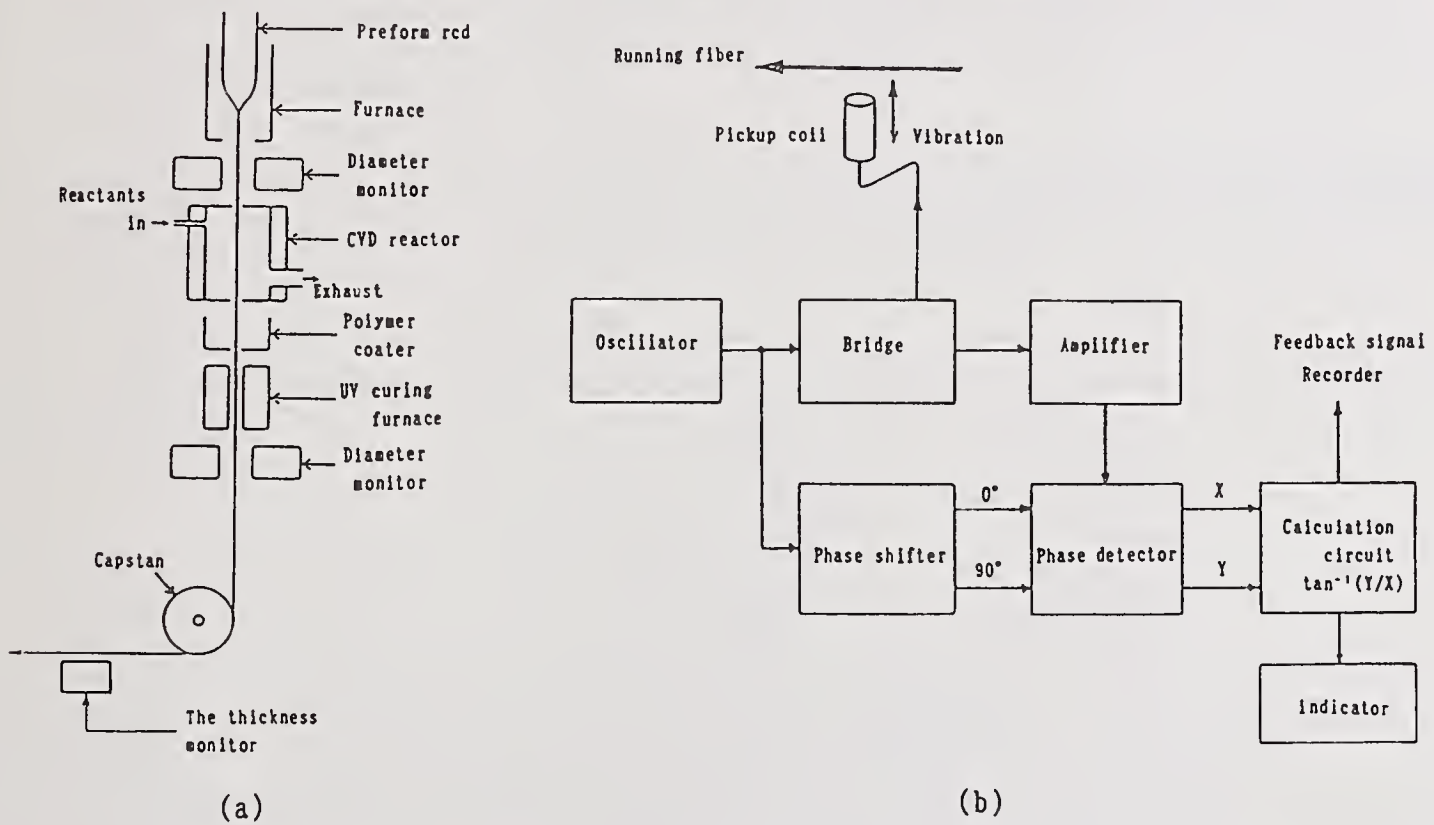


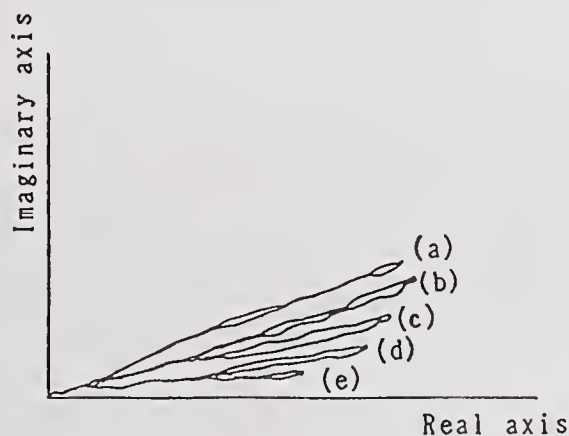
Fig.1 Schematic diagram of HCF drawing process (a), and monitor system (b)

Fig.2

Output of electrical resistance in a complex plane.

Electrical resistance ($\text{K}\Omega/\text{cm}$)

- (a) 4.6 (b) 6.6
- (c) 9.3 (d) 18.7
- (e) 26.6



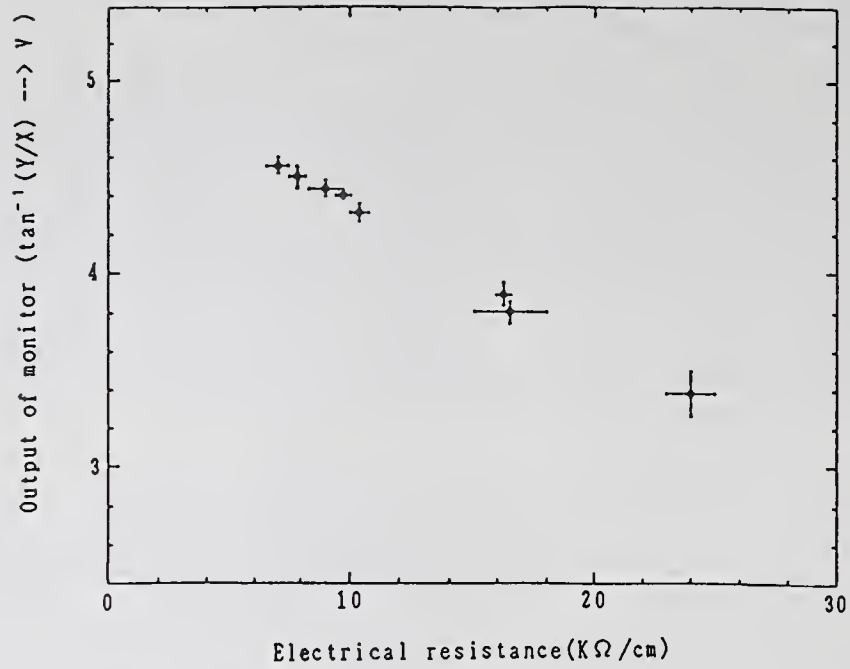


Fig.3 Output of monitor versus electrical resistance.
Output of monitor is converted by a function of $\tan^{-1}(Y/X)$.

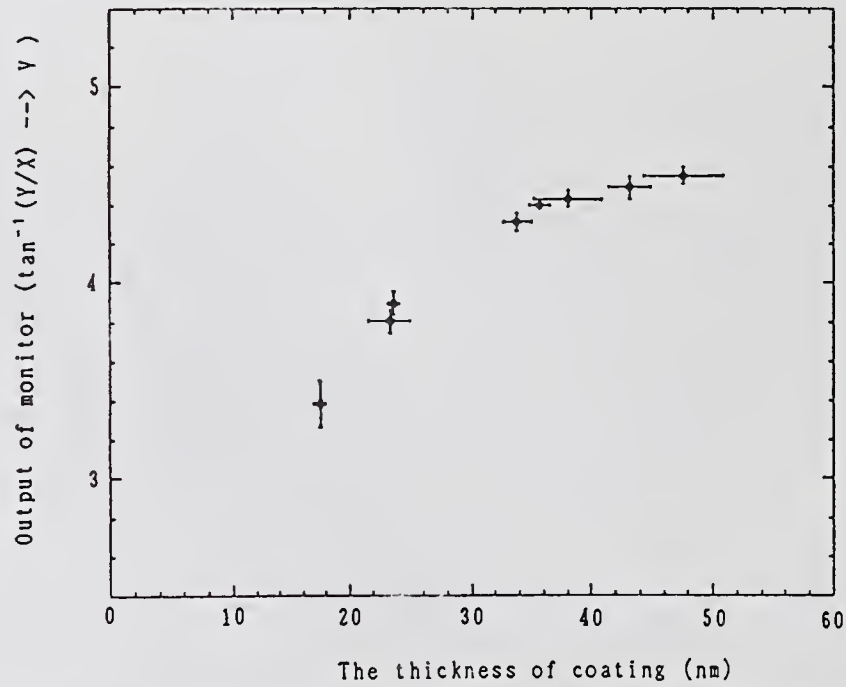


Fig.4 Output of monitor versus the thickness of coating.

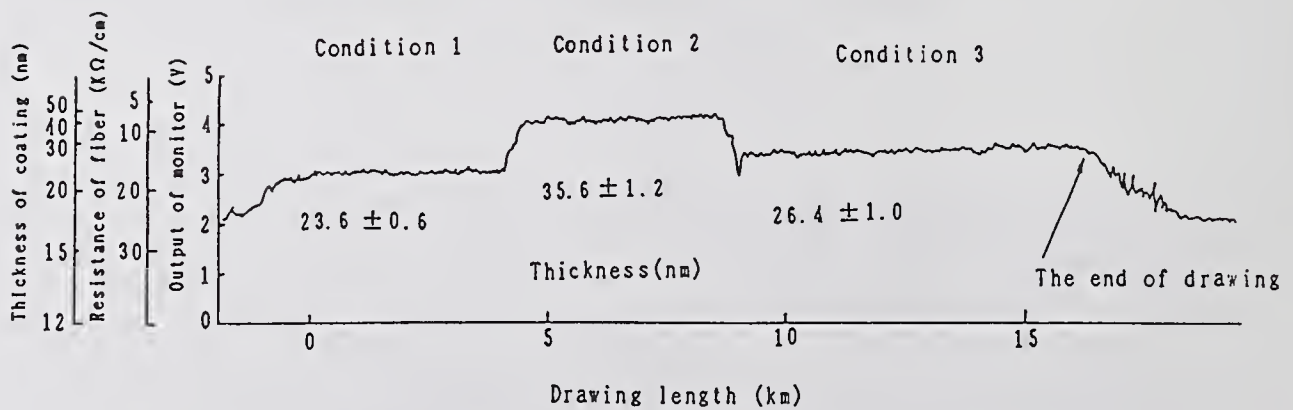


Fig.5 A result of measurement in fiber drawing process.

Measurement of Optical Nonlinearity of Transmission Fibers

R. H. Stolen^{*}, *W. A. Reed*⁺, *K. S. Kim*^{*} and *K. W. Quoi*⁺
AT&T Bell Laboratories
Holmdel^{*}, NJ 07733 and Murray Hill⁺, NJ 07974

1. ABSTRACT

The optical nonlinearity of a fiber is represented by the ratio of an effective nonlinear coefficient divided by an effective core area. This ratio has been determined for transmission fibers at 1.55 μm by using self-phase modulation measurements in combination with mode-intensity calculations. The nonlinear index of silica can be extracted and is in good agreement with earlier measurements in bulk silica.

2. INTRODUCTION

Optical nonlinearities limit the maximum power which can be transmitted through an optical fiber transmission system[1]. This was not a serious limitation until optical amplifiers permitted the design of ultralong transmission spans. It has therefore now become important that an accurate value for the nonlinearity be available to the system designer.

The magnitude of the nonlinearity in the fiber depends on the nonlinear coefficient of the material, the power in the fiber, and the mode confinement. We discuss here the basic issues related to measuring these quantities in transmission fibers. We will also argue that the measurement of the fundamental nonlinear coefficient in a fiber will produce a more accurate value than previous techniques using bulk samples.

3. BACKGROUND

The optical nonlinearity of concern is a tiny increase of the refractive index, n , with optical intensity. This can be written as:

$$\begin{aligned}n &= n_0 + \delta n(I) \\ \delta n(I) &= n_2 I \\ \delta \Phi &= \frac{2\pi \delta n L}{\lambda}\end{aligned}\tag{1}$$

where n_2 is the nonlinear coefficient, λ is the vacuum wavelength, I is the optical intensity and $\delta \Phi$ is the phase shift.

The nonlinear index shows up as an intensity-dependent phase shift ($\delta \Phi$). Even though the nonlinear effect is extremely small it doesn't take much power to produce a significant phase shift as the length L becomes large. For example, a laser focused in a piece of silica glass requires a peak power of 10 MW to produce a π phase shift. This drops to 20 mW of average power in a 70 km fiber transmission span between repeaters. For the longest projected span using optical amplifiers (9000 km) a π phase shift is produced by an average power of only 150 μW .

The effect of the nonlinear phase shift is to produce a spectral broadening. The simplest way to treat this broadening is to look at the phase along an optical pulse. The phase will be delayed at the pulse maximum relative to the wings. A phase modulated pulse has a broader spectrum than an ideal transform-limited pulse. Although not immediately obvious, an equivalent approach is to treat the problem as a four-wave mixing between all the spectral components of the input pulse. This generates new frequencies which spectrally broaden the pulse. In general, the phase picture is most useful for optical pulses, while the four-wave mixing approach is

more useful when discrete wavelengths are present such as in wavelength multiplexing.

The deleterious effects of nonlinear spectral broadening usually show up because of the simultaneous presence of group-velocity-dispersion (GVD). GVD by itself broadens the pulse temporally while the nonlinearity broadens the pulse spectrally. Increased spectral width then increases the temporal broadening by GVD. This necessitates much greater precision in the control of GVD for a long fiber span. In amplified systems there is also four-wave mixing between the signal and amplifier spontaneous emission[2]. The output pulse is now not only longer but looks quite noisy. However, in spite of these complications, it appears that a useful rule of thumb for the onset of trouble is still a π phase shift over the system length.

The effect of all this on a lightwave system is to create a minimum in the bit error rate as the power increases. In a linear system, the errors always drop as optical power goes up. The inclusion of nonlinearities results in an increase in the bit-error rate at high powers. There is now a minimum in the bit-error rate as a function of power. Thus there is a maximum average power that can be injected into a system which in turn places a severe limitation on amplifier spacing (See Fig. 2). Problems will also appear with wavelength multiplexing.

4. FIBER ISSUES

There are two issues that must be addressed before n_2 can be measured in a fiber. First, the intensity (mode power) is not constant across the fiber core, and second, the nonlinear coefficient is not necessarily the same in the core and the cladding because of different glass compositions. This is illustrated in the Fig. 3 where we show an idealized index profile for a dispersion-shifted fiber along with the mode intensity.

To obtain the phase shift as a function of power it is necessary to average, in some way, over the intensity profile. This is possible because there has to be a single value for the phase of a single frequency in a single mode of the fiber. The average takes the form:

$$\delta\Phi = \frac{2\pi n_2 L}{\lambda} \frac{\int I^2(r) r dr d\theta}{\left[\int I(r) r dr d\theta \right]^2} = \frac{n_2 P}{A_{\text{eff}}} \quad (2)$$

This average takes the form of an overlap integral with the dimensions of 1/area. Conveniently, this effective area is fairly close to the actual core area of the fiber[1,3].

Since the cores of fibers are usually doped with germanium and the nonlinear coefficient of Ge:silica is higher than for pure silica, n_2 is a function of radius which must be included inside the integral of Eq. (2). The result is that a fiber must be characterized by both an effective nonlinear coefficient and an effective area. The phase shift out of the fiber then becomes:

$$\delta\Phi = \frac{2\pi}{\lambda} \left[\frac{n_2}{A} \right]_{\text{eff}} PL \quad (3)$$

From the equation it can be seen that it is the ratio $(n_2/A)_{\text{eff}}$ that is important for system design, and knowledge of the individual quantities is not required.

5. METHOD OF MEASURING $(n_2/A)_{\text{eff}}$

The method chosen for measuring $(n_2/A)_{\text{eff}}$ is that of self-phase modulation which is illustrated in Fig. 4[3]. A transform limited optical pulse is coupled into a single-mode fiber and the spectrum is observed at the output. As input power is increased, the spectrum takes on various easily identified patterns. The maxima and minima of the central peak occur at integer orders of $\pi/2$. Self-phase modulation can be viewed as an interferometer where the shifted phase at the pulse maximum is referenced to the phase of the weaker pulse tails.

The power is obtained by measuring the average power out of the fiber and correcting for the end reflection. To get the peak power, a separate measurement of pulse shape and width is made. The errors in the measurement can be further reduced by plotting phase shift vs power for a wide range of powers.

One might think that the major uncertainty would come from the extraction of the peak power from the measurement of average power. Fortunately there turns out to be a secondary check on this number. An independent value for peak power can be obtained from a knowledge of the phase shift and the $1/e$ spectral width of the broadened pulse[4].

The ideal measurements are made in fibers that are short enough to neglect loss and dispersion. It is, of course, possible to use numerical simulation to include these effects in the analysis.

6. MEASUREMENTS ON ACTUAL FIBERS

The actual measurements of $(n_2/A)_{\text{eff}}$ are made using either the 1.318 μm or 1.3385 μm line of a mode-locked Nd:YAG laser. For the measurements reported here we used the 1.3385 μm line although the 1.318 μm line will be used in future measurements. It is logical to ask why not try to work near 1.55 μm since this is the wavelength of interest for system application? The reason is that the Nd:YAG laser is a convenient and available source of relatively high-power stable transform-limited pulses. The test fibers are typically 250 meters long so that loss is negligible. Peak powers of more than 50 W are required so that several orders of $\pi/2$ can be seen in a fiber of this length. Pulse lengths around 100 ps are relatively easy to measure and are not affected by dispersion in a 250 m fiber. The measurements also require an isolator to eliminate degradation of the mode locked pulses by light reflected from the front face of the fiber.

An independent calculation of effective area is necessary to translate the results for $(n_2/A)_{\text{eff}}$ from 1.3 μm to 1.55 μm . The measured refractive index profile of the fiber is used as the input to a computer program that models the optical transmission properties of the fiber and the validity of the model output is checked by comparing calculated and measured far field patterns[5]. The effective area is calculated at both 1.3 μm and 1.55 μm and the ratio is used to convert the measured value for $(n_2/A)_{\text{eff}}$ to the desired wavelength of 1.55 μm . The ratio of effective areas is not particularly sensitive to the germanium doping of the core or uncertainties in the index profile. There is also good reason to believe that any frequency dependence of n_2 between 1.3 and 1.55 μm is negligible.

A secondary goal of this work is to determine a value for n_2 of pure silica. This ties into a large body of existing work on the nonlinear index of bulk glasses which is driven by the self-focusing problem in high-power lasers[6]. One of the central results of this earlier work is a relation between n_2 and two-photon absorption[7] which is similar to the Kramers-Kronig relation relating linear absorption and refractive index. It is this relation which leads us to believe that the frequency dependence of n_2 is well understood and is negligible over the range 1.3 - 1.55 μm . The existing studies of bulk materials have produced good relative values of n_2 for various materials but the absolute uncertainty is around $\pm 15\%$. We believe that the present fiber measurements have the potential of giving a value for n_2 of silica with an accuracy of $\pm 5\%$. The ultimate limitation is the power measurement.

To extract the absolute value for n_2 of silica requires considerably more precision in the effective area than is needed for the simple ratio of area between 1.3 and 1.55 μm . Also, a correction for the Ge-doping of the core becomes essential. Fortunately, there are some data on the variation of the third-order susceptibility (χ_3) for germanium concentrations between pure silica and pure germania[8]. The third-order susceptibility of pure germania is four times that of silica and the concentration dependence lies somewhere between linear and quadratic. The nonlinear index is proportional to χ_3 and the relation between refractive index and Ge concentration is known[9]. Thus, given the index profile, we can generate a reasonable estimate for $n_2(r)$. We represent $n_2(r)$ as $n_2 f(r)$ where $f(r)$ is the increase of the nonlinear index due to the germania, and n_2 is the nonlinear index of pure silica. We have also used several forms of $f(r)$ in an attempt to use the n_2 results to gain

information about the effect of Ge concentration on n_2 . In the end, if everything is correct, we should extract the same value for n_2 from measurements on different fibers of widely differing doping levels. The overall accuracy is not yet sufficient to obtain any meaningful information but the different forms of $f(r)$ provide support for our confidence in the accuracy of the ratio of effective areas between 1.3 and 1.55 μm . The different forms of $f(r)$ have almost no effect on the ratio; in fact, neglecting the effect of Ge on n_2 altogether ($f(r) = 1.0$) has less than 1% effect on the ratio of the effective areas.

Measurements on three fibers are shown in Table I. One fiber (Std.) is a standard transmission fiber with λ_0 at 1.31 μm . The other two fibers (DS1 and DS2) are dispersion shifted ($\lambda_0 = 1.55 \mu\text{m}$). The first column is $(n_2/A)_{\text{eff}}$ measured at 1.3385 μm . Columns 2-4 contain the effective areas calculated from the measured index profiles assuming that the n_2 for germania is equal (+), twice (++), and three times (+++) the n_2 of silica. The last three columns contain the n_2 's, which are the product of the measured ratio and the calculated effective areas.

Table I
Effective Areas and n_2 at 1.3385 μm

	$(n_2/A)_{\text{eff}}^{\#}$ $\times 10^{-18} \text{ cm}^2/\text{W}\cdot\mu\text{m}^2$	Effective Area			n_{2+}	n_{2++}	n_{2+++}
		+	++	+++	$\times 10^{-16} \text{ cm}^2/\text{W}$		
Std.	4.13	59.6	57.8	56.1	2.46	2.38	2.32
DS1	8.07	32.0	29.9	28.0	2.58	2.41	2.20
DS2	6.99	33.5	31.4	29.7	2.34	2.19	2.08

Notes:

measured value

+, ++, +++: assuming n_2 for GeO_2 is 1, 2, and 3 times n_2 of silica

The calculated wavelength ratios of the effective areas, $A_{1.55}/A_{1.3385}$ are 1.17, 1.48 and 1.46 respectively for the three fibers assuming n_2 is the same for germania and silica. As can be seen, the values for n_2 for silica at this point are consistent to about 10% but little can be said about the n_2 for germania. It is clear that additional measurements are required if our goal of $\pm 5\%$ is to be achieved.

The effect of polarization must be included when comparing n_2 as measured in a fiber to n_2 as measured in bulk glass. Typically, bulk measurements are made with linear polarization while standard telecommunications fibers average over all possible states of polarization. The ratio between the fiber and bulk values for n_2 should be 8:9[10]. Our experimental result for 1.3 μm becomes $2.62 \times 10^{-16} \text{ cm}^2/\text{W}$ which is obtained by converting the n_{2++} data of Table I to linear polarization. This compares to the accepted value for bulk silica of $2.74 \times 10^{-16} \text{ cm}^2/\text{W}$ at 1.064 μm [6].

7. STANDARD METHODS FOR MEASURING $(n_2/A)_{\text{eff}}$

There is a growing desire by people in the area of systems design and modeling for a standard method for measuring $(n_2/A)_{\text{eff}}$ in a non-laboratory environment. The present method is not particularly suitable for this application. We suggest two possible approaches. One method would use standard techniques to measure the index profile of the fiber and $(n_2/A)_{\text{eff}}$ would then be calculated using the known value for n_2 of silica, the effect on n_2 of the Ge doping, and the A_{eff} calculated from the index profile. A convenient experimental method would use a comparison with a standard fiber of known $(n_2/A)_{\text{eff}}$. This method would modulate a 1.55 μm cw laser and observe the growth of the modulation sidebands due to four-wave mixing[11]. A comparison between the test and reference fibers combined with a measurement of output powers would give $(n_2/A)_{\text{eff}}$.

8. SUMMARY

Using self-phase modulation measurements in combination with mode- intensity calculations we have obtained a value for the nonlinearity of transmission fibers at 1.55 μm . The value of the nonlinear index for silica which we obtain is in good agreement with earlier measurements in bulk samples. The present uncertainty is estimated to be $\pm 10\%$ which we anticipate can be reduced to around $\pm 5\%$ by projected improvements in various aspects of the measurements.

9. REFERENCES

- [1] R.H. Stolen, "Nonlinearity in fiber transmission", IEEE J. Quantum Electron, **QE-68**, 1232 (1980); D. Marcuse, A.R. Chraplyvy, and R.W. Tkach, "Effect of fiber nonlinearity on long distance transmission", J. Lightwave Tech. **9**, 121 (1991); G.P. Agrawal, "Nonlinear Fiber Optics", (Academic Press, N.Y., 1989).
- [2] D. Marcuse, "Single-channel operation in very long nonlinear fibers with optical amplifiers at zero dispersion", J. Lightwave Tech. **6**, 356 (1991).
- [3] R.H. Stolen and Chinlon Lin, "Self-Phase Modulation In Silica Optical Fibers", Phys Rev. **A14**, 1948 (1978).
- [4] C.H. Lin and T.K. Gustafson, "Optical pulsewidth measurement using self-phase modulation", IEEE J. Quantum Electron. **8**, 429 (1972).
- [5] W. J. Stewart, "Optical Fiber and Preform Profiling Technology", IEEE J. Quant. Electron. **QE18**, 1451 (1982); and W. T. Anderson and D. L. Philen, "Spot Size Measurements for Single-Mode Fibers - A Comparison of Four Techniques", J. Lightwave Tech. **LT-1**, 20 (1983).
- [6] D. Milam and M. J. Weber, " Measurement of nonlinear refractive- index coefficients using time-resolved interferometry: Application to optical materials for high-power neodymium lasers", J. App. Phys. **47**, 2497 (1976).
- [7] M. Sheik-Bahae, "Dispersion of bound electronic nonlinear refraction in solids", IEEE J. Quantum Electron. **27**, 1296 (1991).
- [8] W.E. Torruellas, "The optical cubic susceptibility dispersion of some transparent thin films", Ph.D. Thesis, Univ. of Arizona (1990).
- [9] J. W. Fleming, "Material Dispersion in Lightguide Glasses", Electron. Letters **14**, 326 (1978).
- [10] S.G. Evangelides, L.F. Mollenauer, J.P. Gordon, and N.S. Bergano, "Polarization multiplexing with solitons", J. Lightwave Tech. **10**, 28 (1992).
- [11] R.W. Tkach, Private communication

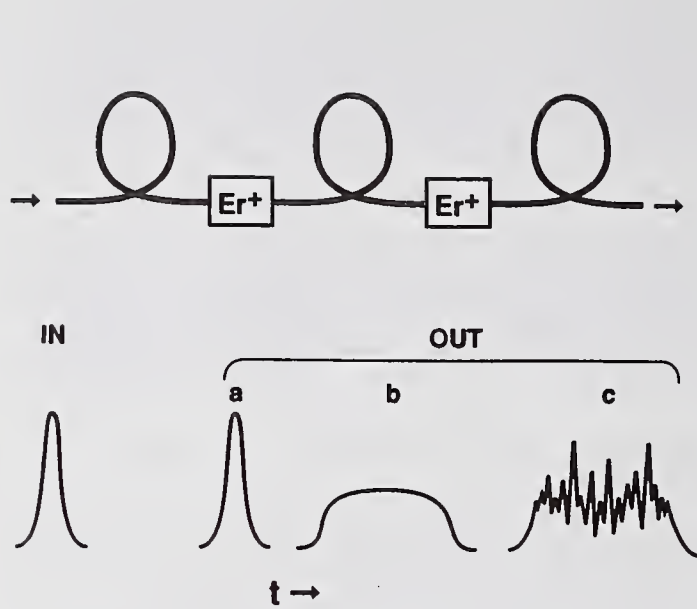


Fig 1. Optical pulse in and out of a fiber for: a. SPM but no GVD; b. SPM plus GVD; c. SPM plus GVD plus mixing with amplifier noise.

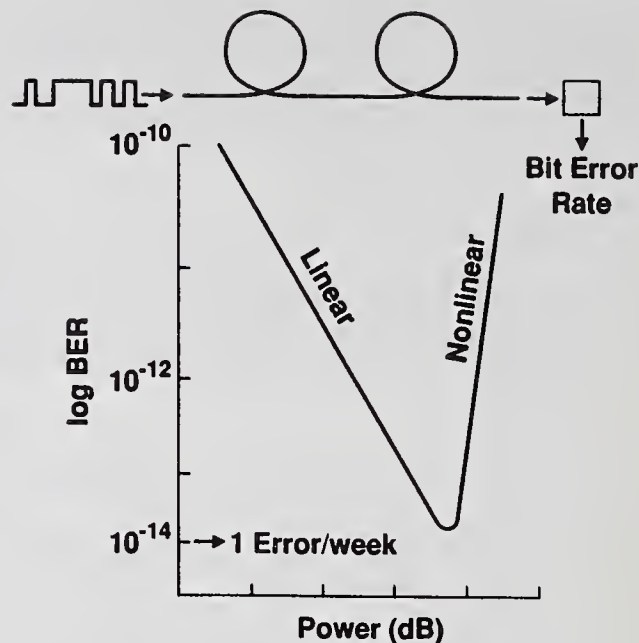


Fig 2. Bit error rate vs. optical power in the presence of nonlinearity.

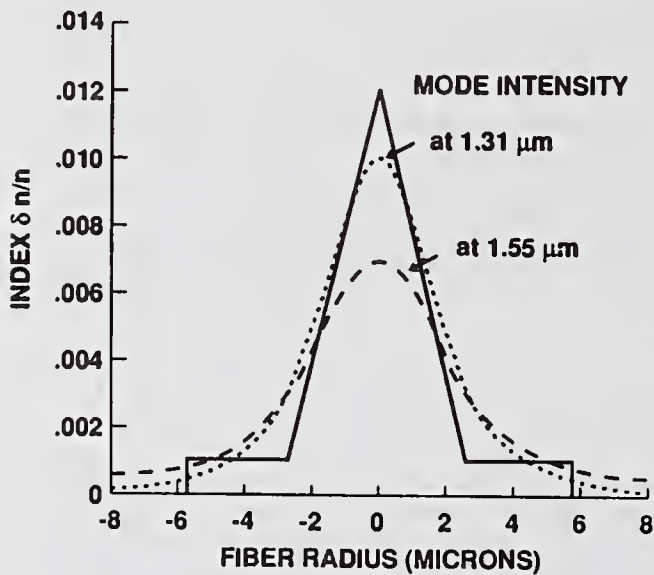


Fig 3. Index profile and mode intensity for an idealized dispersion-shifted fiber.

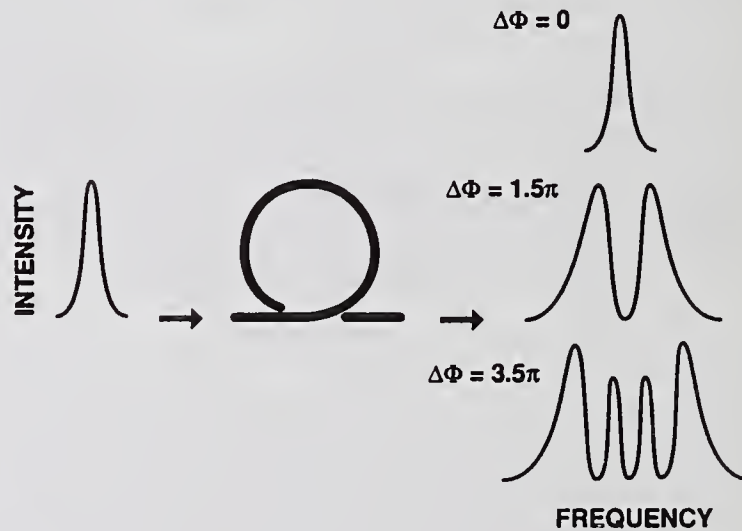


Fig 4. Spectral output of self-phase modulated pulse for different peak powers.

Determination of Non-linear Effective Areas for Dispersion Shifted Fibres

J V Wright and E S R Sikora
BT Laboratories, Martlesham Heath
Ipswich, IP5 7RE, UK

1. Introduction

The non-linear effective area of a fibre is an important parameter for any system where optical non-linearities become important. These will include: long haul optically amplified systems operating with NRZ formats such as those proposed for the Atlantic and Pacific Oceans and any soliton systems. In general, we observe that the refractive index of silica fibre is dependent on the intensity of the optical signal according to

$$n = n_1 + n_2 I \quad (1)$$

where n_2 is the non-linear Kerr coefficient with a value of $3.2 \times 10^{-20} m^2/W$. Although the non-linear term is very small compared to the conventional refractive index term, n_1 , a significant non-linear phase shift can accumulate over the very long distances experienced in transoceanic cable systems. This is given by

$$\phi = \frac{2\pi n_2 I z}{\lambda} = \frac{2\pi n_2 P(t) z}{\lambda A_{eff}} \quad (2)$$

where z is the total distance and λ is the optical wavelength. The non-linear effective area, A_{eff} , allows the transmitted optical power, $P(t)$, with units of watts to be converted into the intensity, I , with units of watts per square meter. We can see that the non-linearity is proportional to the product

$$n_2 \frac{P(t)}{A_{eff}}$$

and so for a given power level, a fibre with the smaller value of effective area will experience the greater non-linearity. For a long haul NRZ system we will wish to minimise the non-linearity since this is responsible for various system impairments and so it is desirable to use as large a value of A_{eff} as practicable. However, non-linearity is essential for soliton systems where A_{eff} now determines the exact optical power required to support correct soliton operation. Even in the case of long haul soliton systems, it may still be desirable to utilise a large value of A_{eff} since this will require a larger optical power to support the soliton and thus improve the resultant signal to noise ratio.

2. Non-linear Effective Area

The non-linear effective area is given by

$$A_{eff} = \frac{\left[\int_0^\infty |F(r)|^2 dA \right]^2}{\int_0^\infty |F(r)|^4 dA} \quad (3)$$

where $F(r)$ is the field distribution of the fundamental mode of the fibre at radius r [1]. The integration is over the entire cross-sectional area of the fibre with $dA = 2\pi r dr$. For example, if we make a gaussian approximation such that

$$F(r) = \exp\left(-\frac{r^2}{w_0^2}\right) \quad (4)$$

where w_0 is the $1/e$ width of the field, ie the spot-size radius, then the effective area can be integrated analytically to give $A_{eff} = \pi w_0^2$. In the case of a typical dispersion shifted fibre with a spot-size diameter of $8.10 \pm 0.65 \mu m$ [2], we should expect $A_{eff} \approx 52 \pm 8 \mu m^2$. However, the field shape is never quite gaussian, particularly for a dispersion shifted fibre where the refractive index profile is deliberately designed to control the variation of spot-size with wavelength. For the detailed design and assessment of potential transoceanic systems, we require to know the exact value of A_{eff} and also its likely variations. In previous work, A_{eff} has been measured for step-index fibres using measurements of Raman gain. However, in this paper we will determine A_{eff} from the refractive index profiles measured for a range of commercially available dispersion shifted monomode fibres. This will require establishing the exact field shape for a selection of fibres so that (3) can be used to give the effective areas.

2.1 Measured profiles

The refractive index profile has been measured on twelve different samples of Corning dispersion shifted fibre. An example of one measurement is shown in Figure 1 showing a distinctive triangular shaped core with triangular shoulders. The profiles have been digitised and used as an input to a finite element program which can establish the field shape of a mode given a circularly symmetric refractive index profile, $n(r)$. However due to experimental limitations, the measured profiles are not strictly symmetrical and so two separate data sets were derived from each profile measurement, representing the profiles on the left and right-hand sides of each fibre axis. For this process, the fibre axis was selected at a point where the profile and its mirror image achieved the greatest overlap over the central triangular region.

The calculation of A_{eff} and hence the refractive index profile is required at a wavelength corresponding to the erbium gain peak, say $1555nm$. However, the profile measurements were made with a helium-neon laser and so the measured index differences were corrected by a simple factor of 0.982. This was determined from the ratio of δn between germania-doped and pure silica fibre at the wavelengths of 1555 and $633nm$, see Table 1 which has been compiled from data contained in [3].

TABLE 1. Refractive index of silica and germania doped silica

	633nm	1555nm
Si	1.45756	1.44439
Ge	1.47907	1.46552
δn	.02151	.02113

2.2 Calculation

The field shapes for all twelve fibres were evaluated at $1.555 \mu m$ using the wavelength corrected refractive index profiles. Using profiles on both the left and right hand sides of the fibre axes gave a total of twenty four field shapes. The effective areas were then calculated from (3) using numerical quadrature and the results shown in Table 2. The difference between the left and right hand profiles is tabulated as Δ and most likely gives an indication of the measurement accuracy rather than the fibre geometry. An unbiased estimate of the variance on each measurement is $\Delta^2/2$ which can be summed over the twelve fibres to give an average standard deviation of $0.9 \mu m^2$. A histogram of these results is shown in Figure 2 which shows a distribution with $A_{eff} \approx 60 \pm 5 \mu m^2$. This variation is considerably larger than that expected from the standard deviation and suggests that this is caused by a real variability from fibre to fibre. Particularly as there is one isolated peak at $\approx 72 \mu m^2$ which is attributed solely to fibre E.

TABLE 2. Estimates of A_{eff} at $1.555\mu m$

Fibre Id.	Effective area μm^2		$\Delta \mu m^2$
	Left profile	Right profile	
A	59.5	60.6	1.1
B	62.8	63.6	0.8
C	57.2	56.4	0.8
D	62.4	61.5	0.9
E	73.0	72.8	0.2
F	57.9	58.1	0.2
G	55.3	57.0	1.7
H	59.7	63.0	3.3
I	61.2	61.4	0.2
J	60.5	62.0	1.5
Y	56.7	58.8	2.1
Z	58.9	61.0	2.1

2.3 Discussion

The variability in observed values of A_{eff} is broadly in agreement with the initial estimate from the gaussian approximation. However, the mean value of $60\mu m^2$ is somewhat larger than that expected from the gaussian approximation. This is not surprising since the field shape varies as the Bessel function $K_0(wr)$ within the cladding which decays far less rapidly than a gaussian. Figure 3 shows the field shape for the left profile of fibre A superimposed on its refractive index profile. This shows the important feature that the field shape is *picked up* by the shoulders of the index profile for a dispersion shifted fibre when λ is increased towards the dispersion zero, λ_0 , again resulting in non gaussian behaviour. The difference between the calculated field shape and the gaussian approximation is also shown in Figure 3 by plotting the gaussian which matches the calculated field at the $1/e$ radius

3. Conclusions

Non-linear effective areas have been determined for a number of commercially available dispersion shifted monomode fibres directly from their measured refractive index profiles. These show values of A_{eff} which are somewhat larger than those expected by applying the gaussian approximation to the spot-size. There is a real variability from fibre to fibre with a standard deviation of $5\mu m^2$ but this is not inconsistent with the published variability in the spot-size. Finally, it is interesting to note that fibres such as E can produce such large values of A_{eff} since it would be beneficial if every fibre could be made like this. The interplay between large A_{eff} and other fibre parameters is being investigated.

4. References

- [1] Nonlinear Fibre Optics: G P Agrawal, Academic Press, 1989.
- [2] Corguide® Product Information: SMF/DS CPC3 Single-Mode Dispersion-Shifted Optical Fibre (Issue 9/88).
- [3] Material dispersion in light-guide glasses: J W Fleming, Electron. Lett. 14, p326, 1978.

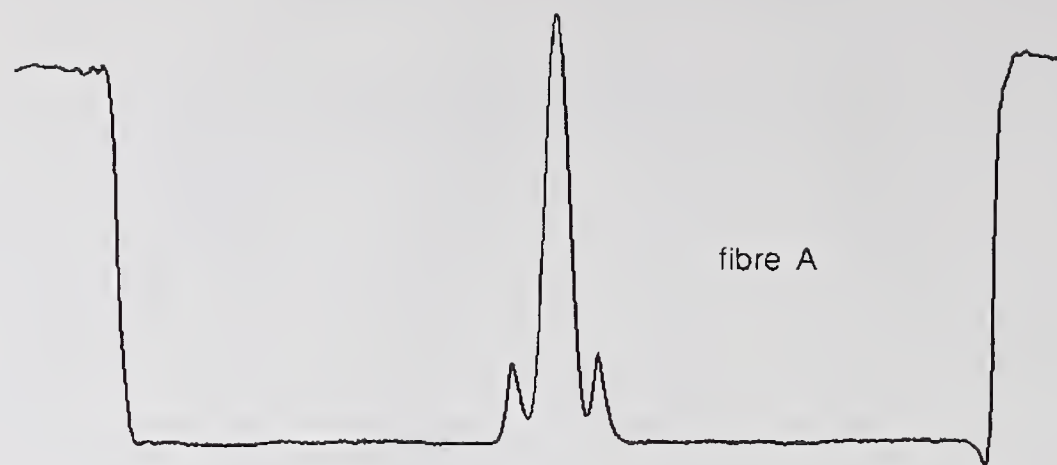


Fig. 1 Refractive index profile for dispersion shifted fibre

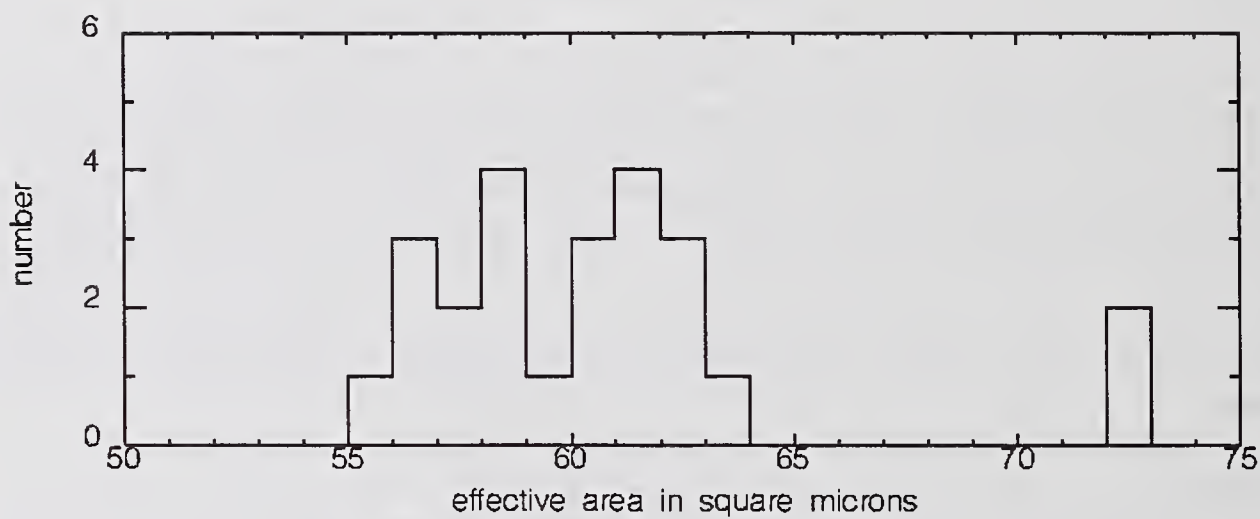


Fig. 2 Histogram of effective areas

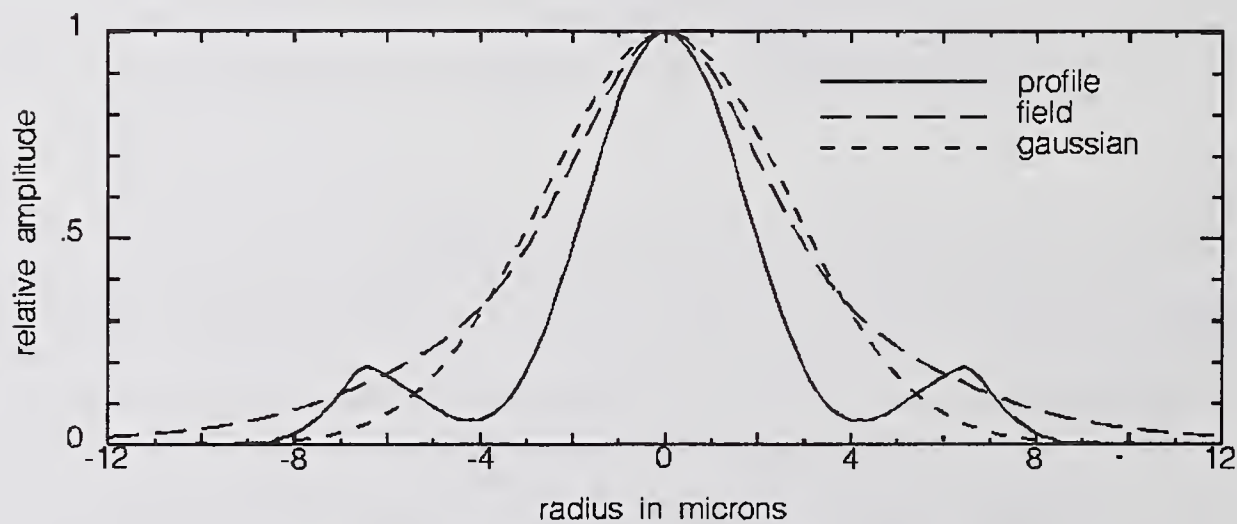


Fig 3. Field shape of dispersion shifted fibre

Beam current effects in Cathodoluminescence Spectroscopy

Graham R Atkins, Mark G Sceats* and Simon B Poole

Optical Fibre Technology Centre
University of Sydney , NSW 2006, Australia

Abstract

Cathodoluminescence spectra of germanosilicate and silicate glass in MCVD and VAD preforms are presented, and the major peaks assigned to E' and the so-called drawing-induced defects. The effects of the electron microscope beam current on the spectra obtained is analysed and limitations observed.

Introduction

It is well known that bonding defects in the glass network structure have an important influence on both the linear¹ and non-linear² transmission properties of optical fibres. More recently, such defects have been shown to play a role in the formation of gratings by both visible³ and ultraviolet⁴ excitation. However the identification and the mechanism of formation of such defects is not well understood. The most common probe of defects in optical fibres has been by optical spectroscopy in the fibre or preform. However, the majority of results in this area give little or no **spatial** information regarding the location of the defects.

We have recently shown^{5,6} that the spatial distribution of GeE' defects in germanosilicate optical fibres and preforms can be accurately and simply profiled using cathodoluminescence⁷ (abbreviated to CL). Here, the preform sample is placed in an electron microscope and irradiated with low-current electron beams with a (typically) 20kV accelerating voltage. The technique (Fig. 1) enables the determination of not only the CL but also other information such as the secondary and backscattered electron emission which allows an accurate location of the region under investigation.

We have also shown⁶ that the addition of phosphorus as a co-dopant greatly reduces the E' concentration, whilst other co-dopants, such as boron or fluorine, reduce the concentration of the so-called 'drawing-induced defects'⁸ However, since it is known⁹ that the use of high-current electron beams can damage silica glasses sufficiently to cause compaction of the glass to produce waveguides, it is important to understand the effect that the electron beam current may have on the sample under investigation. We report here the results of a study to understand these effects in which a sample of germanosilicate glass is subject to repeated measurements and the change in the observed spectrum recorded. The results show that, at the low beam currents typically used in these measurements, there is negligible effect on the cathodoluminescence spectrum.

Experiment

The CL spectra presented here were obtained using a Jeol 35C scanning electron microscope (SEM) equipped with an Oxford Instruments *monoCL* dedicated CL spectroscopy system. The CL emitted by the sample was collected by a paraboloidal mirror, passed through a grating monochromator and detected with a Hamamatsu R2228 photomultiplier tube (with a multialkali extended red photocathode, range 300 to 900 nm, peak response 650 nm). A schematic of the system is shown in Figure 1; note that the electron beam passes through a hole in the paraboloidal mirror. For purposes of clarity, the spectra shown here were not corrected for detector response; however the quoted band positions and widths were obtained from the corrected spectra. This point has been discussed in detail elsewhere⁸. The CL was excited by a 20 kV electron beam, with beam current of approximately 1 nA. The effect of the beam current on the CL spectra was monitored by acquiring and comparing a series of spectra obtained with the above beam current, but with different exposure times.

Results and Discussion

A CL spectrum of MCVD germanosilicate glass (Si:Ge ratio approximately 10:1) is shown in Figure 2(a). Two bands are observed: a large band at 425 nm, FWHM 55 nm, assigned to the *GeE'* defect, and a smaller band at 650 nm, FWHM 65 nm, assigned to the *GeDID* defect. Similar spectra are obtained from pure silica glass, although the strength of both the *SiE'* and *SiDID* CL signals are considerably weaker due to the better stoichiometry of pure silica glass. The broad, weak band at around 800 nm, which is visible in Fig 2(a) has not been assigned but appears to be present only in germanium-doped glass.

It has been shown that co-dopants and fabrication conditions affect the CL spectra, and these changes have yielded a great deal of information regarding the defects and their transformations^{6,8}. As an example of the information which can be obtained by this technique, the CL spectrum of boron co-doped germanosilicate glass is shown in Figure 2(b). It can be seen that the presence of boron has removed the *GeDID* band and shifted the *GeE'* band to 410 nm.

Figure 3 shows a series of four CL spectra collected sequentially from the same region of germanosilicate glass. The spectra each took approximately five minutes to collect, so that the total exposure time was around 20 minutes. It can be seen that while there is a slight decrease in the intensities of both bands, the changes are not significant. The bands have clearly maintained their integrity, and no new bands have appeared as a result of electron beam damage. The small reduction in CL intensity may be due either to the emission being absorbed by the deposition of surface contamination (a common problem in electron microscopy), or to actual physical transformations of the defect species. This question is under continuing investigation.

Conclusions

The cathodoluminescence spectrum of germanosilicate glass in MCVD preforms has been presented. Two broad bands were observed and assigned: a strong violet band centred at 425 nm, assigned to the GeE' defect; and a weak red band centred at 650 nm, assigned to the Ge drawing-induced defect. The influence of co-dopants, such as boron, on the defects present can also be determined by this technique. Finally, the effects of electron beam exposure on the measured defect profiles have been investigated and shown to be insignificant at the beam currents used in the measurement technique.

Acknowledgments

GRA acknowledges the support of the Australian Postgraduate Research Award. This work was carried out with funding from Siemens Ltd, through a Generic Industrial Research and Development (GIRD) program. AOTC is acknowledged as a Sponsor of the Optical Fibre Technology Centre.

References

1. L. J. Poyntz-Wright, M. E. Fermann and P. St-J. Russell "Nonlinear transmission and color-center dynamics in germanosilicate fibers at 420-540 nm", *Opt. Lett.* **13**, 1023-1025, (1988).
2. U. Osterburg and W. Margulis, "Dye laser pumped by Nd:YAG laser pulses frequency doubled in a glass optical fiber", *Opt. Lett.* **11**, 516-518, (1986).
3. K. O. Hill, Y. Fujii, D. C. Johnson and B. S. Kawasaki, "Photosensitivity in optical fiber waveguides: Application to reflection filter fabrication", *Appl. Phys. Lett.* **32**, 647-649, (1978).
4. G. Meltz, W. W. Morey and W. H. Glenn, "Formation of Bragg gratings in optical fibers by a transverse holographic method", *Opt. Lett.* **14**, 823-825, (1989).
5. G. R. Atkins, S. B. Poole, M. G. Sceats, H. W. Simmons and C. E. Nockolds, "Defects in optical fibres in regions of high stress gradients", *Electron. Lett.* **27**, 1432-1433, (1991).
6. G. R. Atkins, S. B. Poole, M. G. Sceats, H. W. Simmons and C. E. Nockolds, "The influence of co-dopants and fabrication conditions on germanium defects in optical fibre preforms", *IEEE Photon. Technol. Lett.* **4**, 43-46, (1992).
7. A. D. Trigg, "A high efficiency cathodoluminescence system and its application to optical materials", *Scan. Elect. Microsc.* **1985/III**, 1011-1022, (1985).
8. G.R. Atkins, Z. H. Wang, D. R. McKenzie, M. G. Sceats, S. B. Poole and H. W. Simmons, "Control of Defects in Optical Fibres - a Study Using Cathodoluminescence Spectroscopy" *Submitted to IEEE Journal of Lightwave Technology*.
9. D. Barbier, M. Green, and S. J. Madden, "Waveguide fabrication for integrated optics by electron beam irradiation of silica", *IEEE J. Lightwave Technol.* **9**, 715-720, (1992).

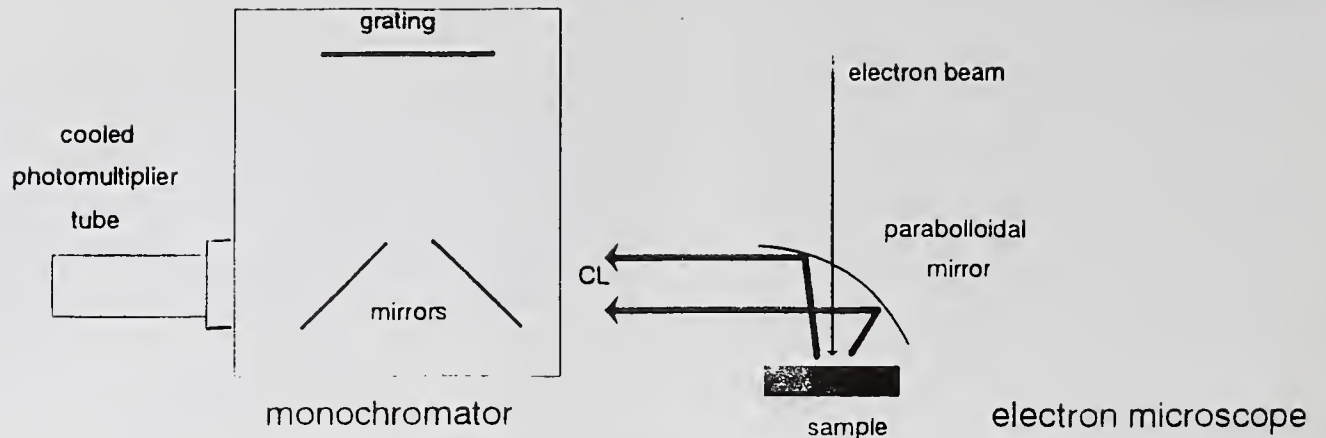


Figure 1. Experimental arrangement for cathodoluminescence.

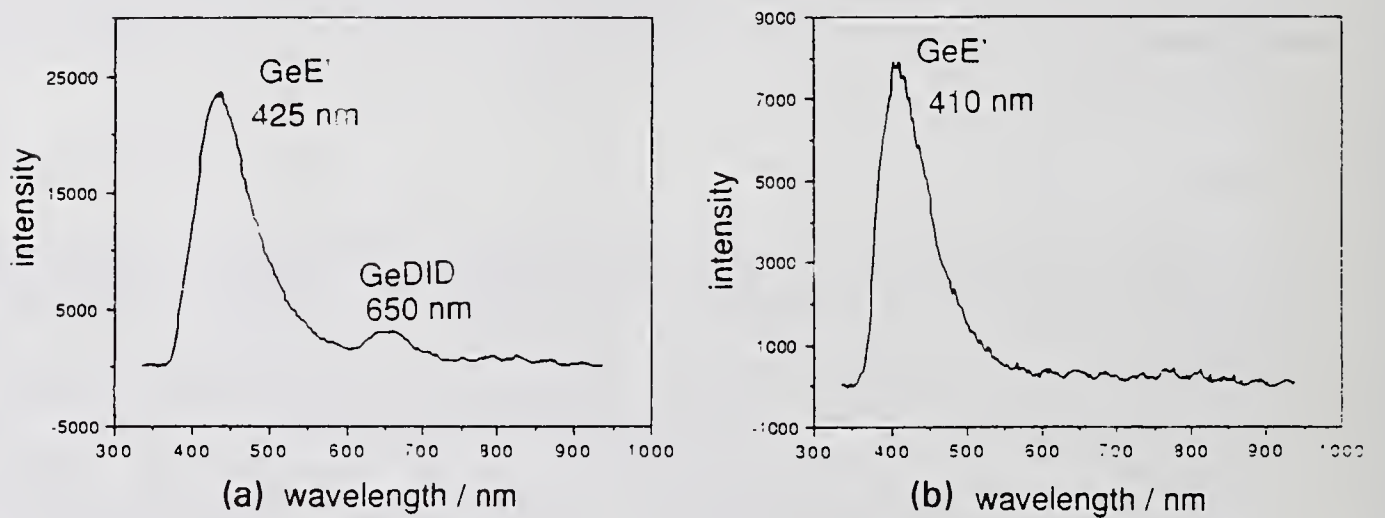


Figure 2. Cathodoluminescence spectra of (a) germanosilicate glass and (b) boron co-doped germanosilicate glass.

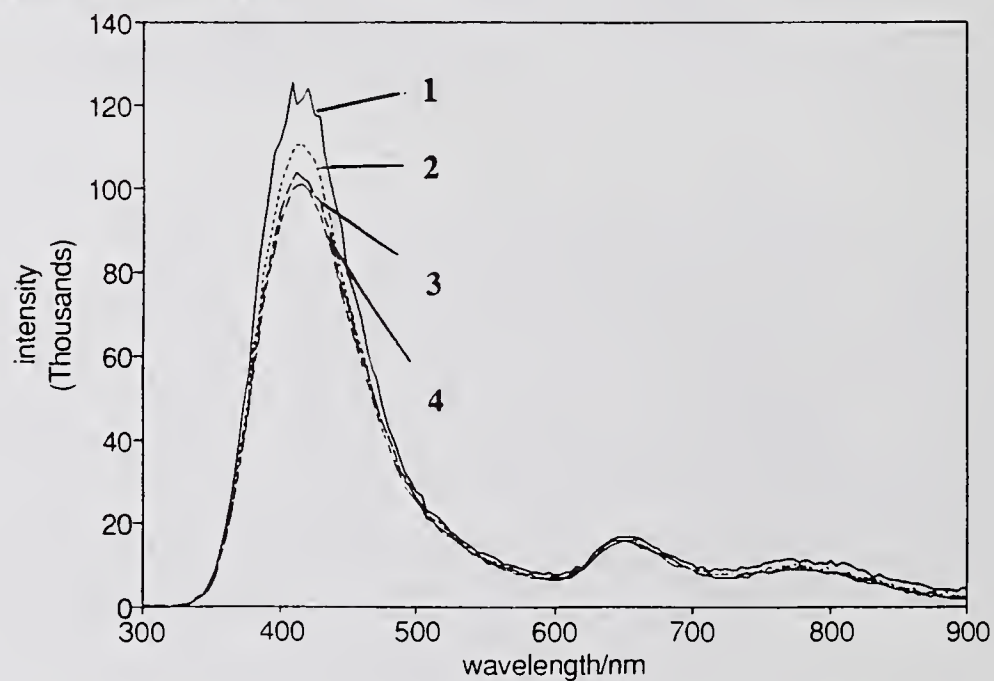


Figure 3. Successive cathodoluminescence spectra of germanosilicate glass. Curve 1 is the initial measurement and curve 4 is the final spectrum.

RELATIVE DOPANT CONCENTRATION PROFILING OF GERMANIA, PHOSPHORUS AND ERBIUM DOPED SILICA BASED OPTICAL FIBRES

J M Benson^{1*} and C J Chunnillal² and J C Petersen³

¹Division of Quantum Metrology, National Physical Laboratory, Queen's Road, Teddington, Middlesex TW11 0LW, UK

²Department of Physics, King's College London, Strand, London WC2R 2LS, UK

³Danish Institute of Fundamental Metrology, Bldg 307, Lundtoftevej 100, 2800 Lyngby, Denmark

1. Introduction

The propagation properties of an optical fibre critically depend on the material nature of the glass from which it is manufactured. The majority of optical fibres are made from silica glass, which is doped to produce the raised refractive index core, the profile of which can be manipulated to modify the dispersion properties of the fibre. Deviation from the optimum dopant profile seriously degrades the fibre's operation. Therefore, it is important to measure dopant profiles of fibre after manufacture. In addition, the fibre core can be doped in order to produce fibre lasers and amplifiers. For efficient operation of these active devices, the mode shape of the pump laser must overlap efficiently with the concentration profile of the active component. Also, for accurate modelling of active fibres, a detailed knowledge of the spatial distribution of the active component is required. The techniques of micro-Raman and micro-fluorescence spectroscopies are ideal for obtaining these profiles, as they are non-destructive and can be used on the fibre as opposed to the preform. This paper presents relative dopant profiles from multimode and single mode telecommunications fibre as well as preliminary results of relative concentration profiles of rare earth ions in the cores of erbium and praseodymium doped fibre.

2. Experiment

Optical fibre slices were prepared from standard telecoms fibre, 50 μm thick and flat to better than 1 μm across the whole diameter of the fibre. Raman spectra were recorded using a Dilor XY multichannel spectrometer with a microscope attachment and 488 nm laser radiation. A stepper stage enabled precise movement of the fibre samples, allowing spatial resolution on the 1 μm scale. Refractive index profiles were measured interferometrically [1].

Slices from active fibres were not available at the time of measurement therefore these fibres were profiled from the side. The laser was focused at the core/cladding interface and the fibre stepped horizontally in 1 μm steps, such that the laser sampled a diameter of the core. Fluorescence spectra were recorded for each fibre position. It was assumed to a first approximation that the focal position of the laser did not vary with fibre position.

3. Results

3.1 Standard Fibre

Fig.1 shows Raman spectra measured at 2 μm intervals across the diameter of a slice from a typical multimode telecommunications fibre. These spectra can be understood in terms of Raman scattering from silica, with varying amounts of germania (GeO_2) and P_2O_5 doping [2]. The dominant feature for P_2O_5 doping which is at approximately 1325 cm^{-1} , is associated with $-\text{P}=\text{O}$ stretching [2] and can be profiled using band intensities. The case for germania profiling is more complex. Silica glass is understood in terms of strong coupling between SiO_4 tetrahedra [3], leading to the band-like Raman spectra. The replacement of Si atoms by Ge atoms therefore affects the entire spectrum, modifying some features more than others. This means that a more precise technique is required to measure the profiles. Factor analysis [4] has been found to be effective in extracting the germania profile.

Fig. 2 shows the relative concentration profiles of germania and P_2O_5 obtained by factor analysis of the spectra in Fig. 1, along with the measured refractive index profile of the fibre. There is close correlation between the germania profile and the refractive index profile as expected because the fibre is doped with germania to raise the refractive index of the core region. The sharp dip in the refractive index profile is mirrored in the germania profile, although reduced resolution makes it less prominent. A uniform distribution of P_2O_5 is observed which is consistent with its purpose to modify the mechanical properties rather than the optical properties of the fibre. Profiles for a number of different types of optical fibre have been measured [5].

Fig.3 shows the measured variation of germania across the core of a step index single mode fibre extracted from Raman spectra using factor analysis.

3.2 Active Fibre

Because of the nature of the rare earth ions within a silica fibre, distinct Raman features associated with these dopants are not observed. However, characteristic fluorescence spectra, associated with transitions within the 4f manifold of the Er^{3+} and Pr^{3+} ions can be measured.

Fig. 4 and Fig. 5. show the fluorescence features associated with the $^2\text{H}_{11/2}, ^4\text{S}_{3/2} - ^4\text{I}_{15/2}$ transitions in Er^{3+} and $^1\text{D}_2 - ^3\text{H}_4$ transition in Pr^{3+} respectively. Saturation of these fluorescence features has not been observed for the 10 mW laser excitation power used in this experiment and therefore the relative intensity of these features is proportional to the concentration of the respective rare earth at each sampling position across the core of the fibre.

Fig. 6 and Fig. 7 show the relative rare earth concentration profile for the erbium and praseodymium doped fibres respectively. In both cases the rare earth is observed to be localised within the core region.

4. Conclusion

The techniques of micro-Raman and micro-fluorescence spectroscopies have been demonstrated to be useful tools in the characterisation of dopant variations in both passive and active fibres. Improved spatial resolution is required for the accurate measurement of small-cored active fibres. This will be achieved by the use of a confocal microscope.

5. References

1. K Raine, J Baines and D Putland, *J Lightwave Tech.* **7**, 1162 (1989).
2. N. Shibata, M Horigudhi and T. Edahiro, *J. Non-Cryst. Solids* **45**, 115 (1981).
3. P. N. Sen and M. F. Thorpe, *Phys. Rev.* **B15**, 4030 (1977).
4. H. Martens and T Naes, *Multivariate Calibration*, John Wiley & Sons Ltd, London
5. J Benson and C J Chunnillal, *Proceedings of the Fibre Optics Measurement Conference*, York, UK (1991).

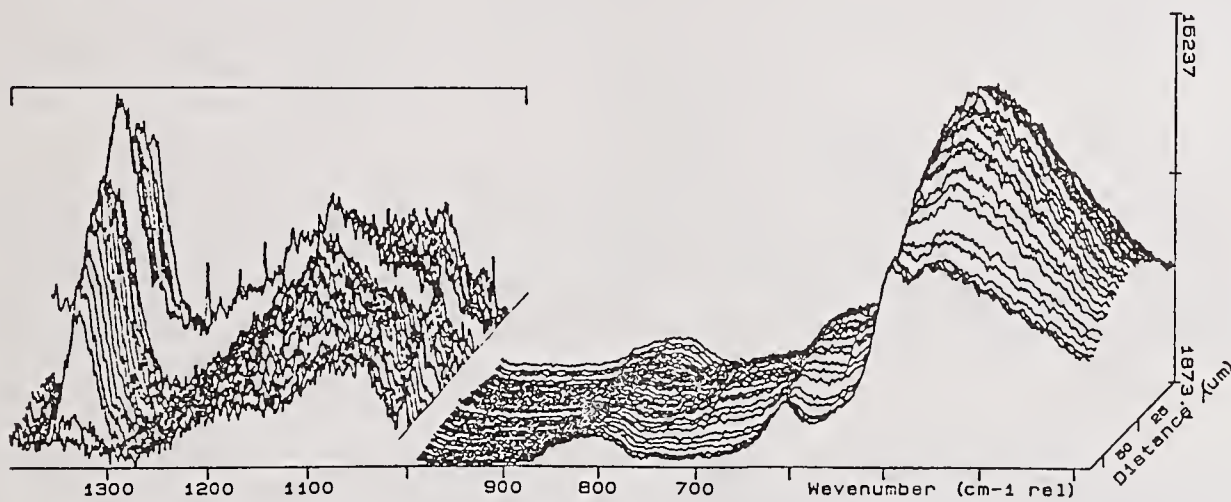


Fig. 1. Spatially resolved Raman spectra recorded at 2 μm intervals across the core of a multimode fibre slice

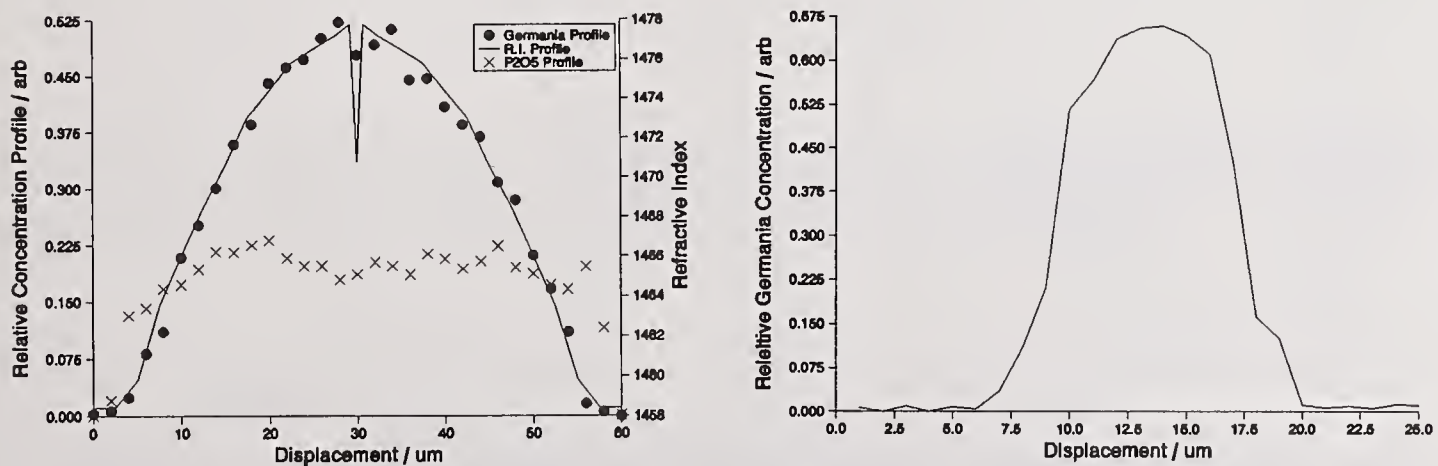


Fig. 2. GeO_2 , P_2O_5 and refractive index profiles of a multimode fibre. Fig. 3. GeO_2 profile of a single mode fibre.

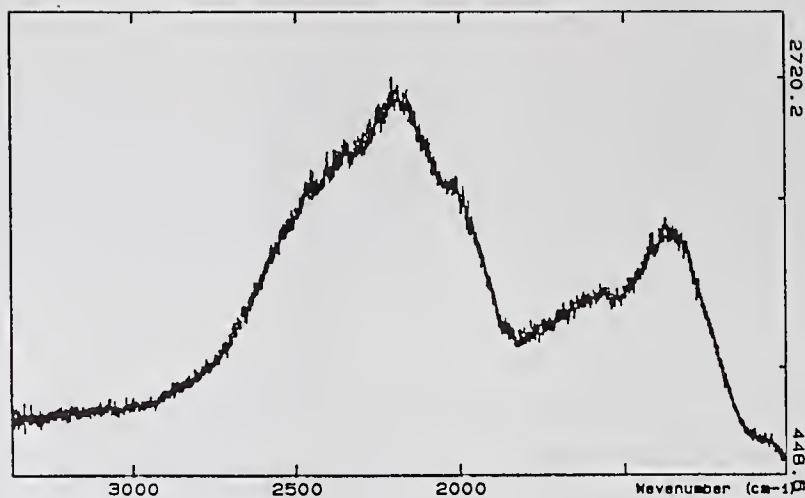


Fig. 4. Fluorescence spectrum associated with ${}^2H_{11/2}, {}^4S_{3/2} - {}^4I_{15/2}$ transitions in erbium doped fibre.

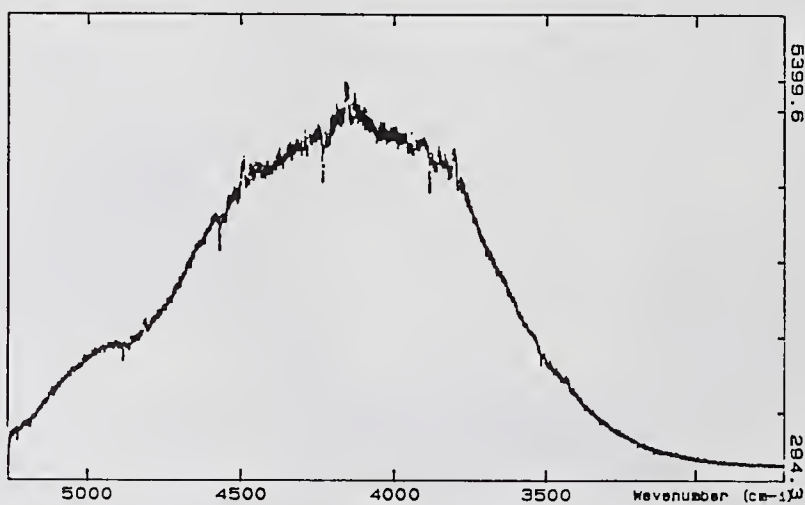


Fig. 5. Fluorescence spectrum associated with ${}^1D_2 - {}^3H_4$ transition in praseodymium doped fibre.

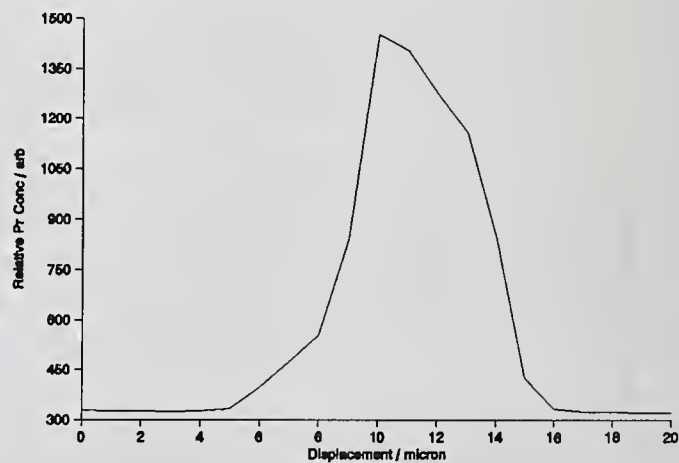
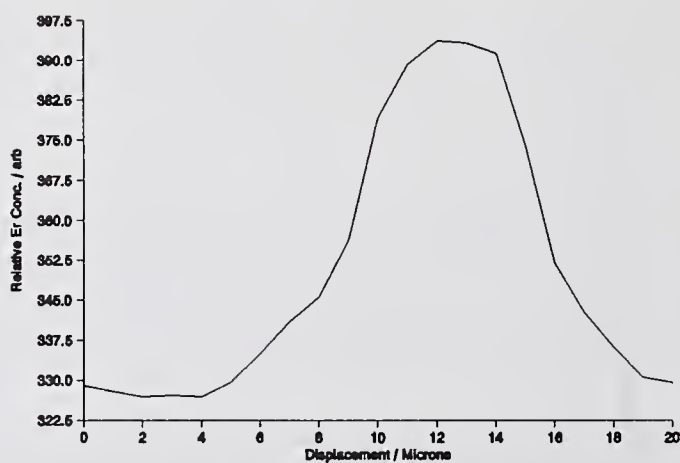


Fig. 6. Relative distribution of Er in the core of Er doped fibre. Fig. 7. Relative distribution of Pr in the core of Pr doped fibre.

Design and Characterization of Dispersion Compensating Fiber

A.J. Antos
Opto-Electronics Group, Corning Incorporated
Corning, NY 14831

Abstract

Dispersion compensation provides a method for upgrading 1310 nanometer (nm) optimized systems to run at 1550 nm. Design criteria for an all-optical, fiber-based method are presented together with optical results. System tests demonstrating 10 Gbit/s performance over 150 kilometers (km) of standard single-mode fiber (SMF) also are shown.

Introduction

Erbium-doped fiber amplifiers (EDFAs) have reduced the importance of loss as a key system design limitation. One issue associated with EDFAs is the need for operation in the 1550 nm window. The best solution for new installations is the use of dispersion-shifted fibers. However there is a very large installed base of fiber optimized for 1310 nm operation. These systems are dispersion limited at 1550 nm except for short lengths and low bit rates. To fully utilize the flexibility of EDFAs in already installed systems and to realize high data rates over long unrepeated lengths, a technique to compensate for the chromatic dispersion of the fiber is required.

There are several solutions to this problem; they can be roughly divided into active and passive classes. The active solutions include external modulation [1], narrow line-width sources, and prechirp techniques [2,3]. Passive solutions include dispersion compensation using the large waveguide dispersion of the LP₁₁ mode [4] and dispersion compensation directly by the LP₀₁ mode [5-7]. The balance of this paper concentrates on dispersion compensation by the LP₀₁ mode with some comparison to the LP₁₁ dispersion compensation method.

Theory and Design

The dispersion compensator concept is shown in Figure 1a and b. Figure 1b shows that after travelling through 100 km of standard singlemode fiber, a 1550 nm signal has broadened by 1.7 ns/nm. The signal is fed into the dispersion compensator (DC) module, consisting of a length of dispersion compensator fiber and an EDFA to make up for the extra loss. The total dispersion of the system can be written as: where l_{SMF} and l_{DC} are the lengths of the standard fiber and dispersion compensating fiber,

$$\Delta\tau = D_{SMF}l_{SMF} + D_{DC}l_{DC},$$

respectively. The system is perfectly compensated when $\Delta\tau = 0$. The larger the negative dispersion of the DC fiber, the shorter the length of fiber that is required to compensate for a given link length. The length-dependent loss (not including splice losses) of the system can be written as:

$$\begin{aligned} Loss &= \alpha_{SMF}l_{SMF} + \alpha_{DC}l_{DC} \\ &= (\alpha_{SMF} - (\alpha_{DC}/D_{DC}) D_{SMF}) \times l_{SMF} \\ &= (\alpha_{SMF} - D_{SMF}/FOM) \times l_{SMF} \end{aligned}$$

where $FOM = DDC/\alpha_{DC}$. The figure of merit (FOM) defines the efficiency of the DC fiber. The loss due to the DC fiber is made up by the EDFA. Because EDFAs have certain limitations to the amount of gain available, a larger negative FOM denotes a better fiber.

Another key parameter is the dispersion slope around 1550 nm. One can imagine a flat or even an inverted dispersion slope which, when concatenated to the SMF fiber, produces a flatter total system dispersion, facilitating wavelength division multiplexing at several wavelengths around 1550 nm. Unfortunately, the dispersion slope of the DC fiber required for total system dispersion flattening is not easily achieved in practice.

Several profile designs have been explored to achieve large negative dispersion. Computer modeling was done to predict optical properties, especially dispersion as a function of key profile parameters. Table 1 lists five classes of fibers and the potential fiber properties achieved by each. Fiber 1 is a high delta step-index fiber. Fibers 2, 3, and 4 all are of a segmented core profile design. At 1550 nm dispersions of between 0 to -85 ps/nm/km have been demonstrated. The FOM for these fibers range between -100 and -140 ps/nm/dB. Figure 2 shows both attenuation and dispersion as a function of wavelength for a selected fiber. As can be seen from this figure, the dispersion of this fiber at 1550 nm is -77 ps/nm²/km and the dispersion slope is inverted at -0.015 ps/nm/km.

Fiber 5 is an early attempt at dispersion compensation [4] that uses the dispersion of the LP₁₁ mode to compensate for the dispersion of the standard fiber. Although light propagating in the LP₁₁ mode in this fiber experiences the largest effective negative dispersion, the FOM is much smaller than the other fibers. Clearly this is the result of high attenuation in this fiber; it is unknown whether this is intrinsic. This technique also has issues associated with polarization dispersion and the need for complete LP₁₁ to LP₁₁ mode conversion.

System Tests

Two key fiber and EDFA tests have been completed using the LP₁₁ DC module. The first [6], shown schematically in Figure 3, involved DC fiber that had -65 ps/nm/km dispersion and an attenuation of 0.48 db/km at 1550 nm. To compensate for the dispersion resulting from 150 km of standard single-mode fiber, 39 km of DC fiber was used. The loss of the DC fiber was overcome by an EDFA. Two other EDFAs were used to overcome the loss of the transmission fiber. A uniform-grating DFB laser diode was the optical source; the laser was driven with a 10 Gbit/s NRZ waveform. Eye patterns of the optical waveform after 0 km, after 12 km without dispersion compensation and after 150 km with dispersion compensation are shown in Figure 4. Without dispersion compensation the system is inoperable after 12 km of SMF fiber. However, with the fiber-based optical compensator, a receiver power penalty of less than 1 dB was obtained after 150 km of SMF fiber as shown in the BER graph of Figure 5. A second test [7] was done, demonstrating the simultaneous transmission of both 1310 and 1550 nm wavelengths over 60 km of SMF fiber with a 1310/1550 WDM at the 2.5 Gbit/s SONET rate.

In summary, the concept of dispersion compensation using a simple all-optical, fiber-based method has been demonstrated. 10 Gbit/s has been transmitted through 150 km of standard single-mode fiber at 1550 nm. This technique for upgrading already installed systems optimized to run at 1310 nm has many potential applications from long-haul telephony systems and interoffice networks to AM video for cable TV.

Acknowledgments

The author would like to thank Alcatel Network Systems and Bellcore for their assistance@ in doing the systems tests. The author also would like to thank D. Smith and D. Hall for computer modeling and useful discussions.

References

- [1] A.H. Gnauck, et al., "Optical Equalization of Fiber Chromatic Dispersion in a 5 Gbit/s Transmission System," *IEEE Photonics Technology Letters*, vol. 2, no. 8, pp. 585-587.
- [2] N. Henmi, et al., "10 Gb/s, 100 km Normal Fiber Transmission Experiment Employing a Modified Prechirp Technique," Paper TuO2, *Technical Digest, Conf. on Optical Fiber Comm., 1991*.
- [3] A.D. Ellis, et al., "Dispersion Compensation in 450 km Transmission System using Standard Fibre," *Electronic Letters*, vol. 28, No. 10, pp. 954-955.
- [4] C.D. Poole, et al., "Broad-Band Dispersion Compensation Using the Higher-order Spatial-mode in a Two-mode Fiber," Paper PD13, *Technical Digest, Conf. on Optical Fiber Comm., 1991*.
- [5] Chinlon Lin, H. Kogelnik, and L.G. Cohen, "Optical-pulse Equalization of Low Dispersion Transmission in Single-mode Fibers in the 1.3-1.7 μm Spectral Region," *Optical Letters*, vol. 5, no. 11, Nov. 1980.
- [6] M.J. Dugan, et al., "All Optical Fiber-Based 1550 nm Dispersion Compensation in a 10 Gbit/s, 150 km Transmission Experiment over 1310 nm Optimized Fiber,"- Paper PD14, *Technical Digest, Conf. on Optical Fiber Comm., 1992*.
- [7] H. Izadpanah, et al., Dispersion Compensation for Upgrading Interoffice Networks Built with 1310 nm Optimized SMF Using an Equalizer Fiber, EDFA's and 1310/1550 nm WDM," Paper PD15, *Technical Digest, Conf on Optical Fiber Comm., 1992*.

Table 1. Dispersion Compensating Fiber Properties

Fiber Type	Dispersion (ps/nm/km)	Dispersion Slope (ps/nM ² /kM)	Nominal Attenuation (dB/km)	Figure of Merit (FOM) (ps/nm/dB)
<u>Single-mode Propagation</u>				
F 1	-45 to -60	0.07	0.4	112 -150 [7]
F 2	-55 to -80	0.0	0.5	110 -160 [6]
F 3	-60 to -80	-0.01-.02	0.6	100 -133
F 4	-80 to -100	0.07	0.6	133 -200
<u>LP₁₁ Mode Propagation</u>				
F 5	1 60 to -240		4.9	33 - 50 [4]

Applications - SMF Upgrade

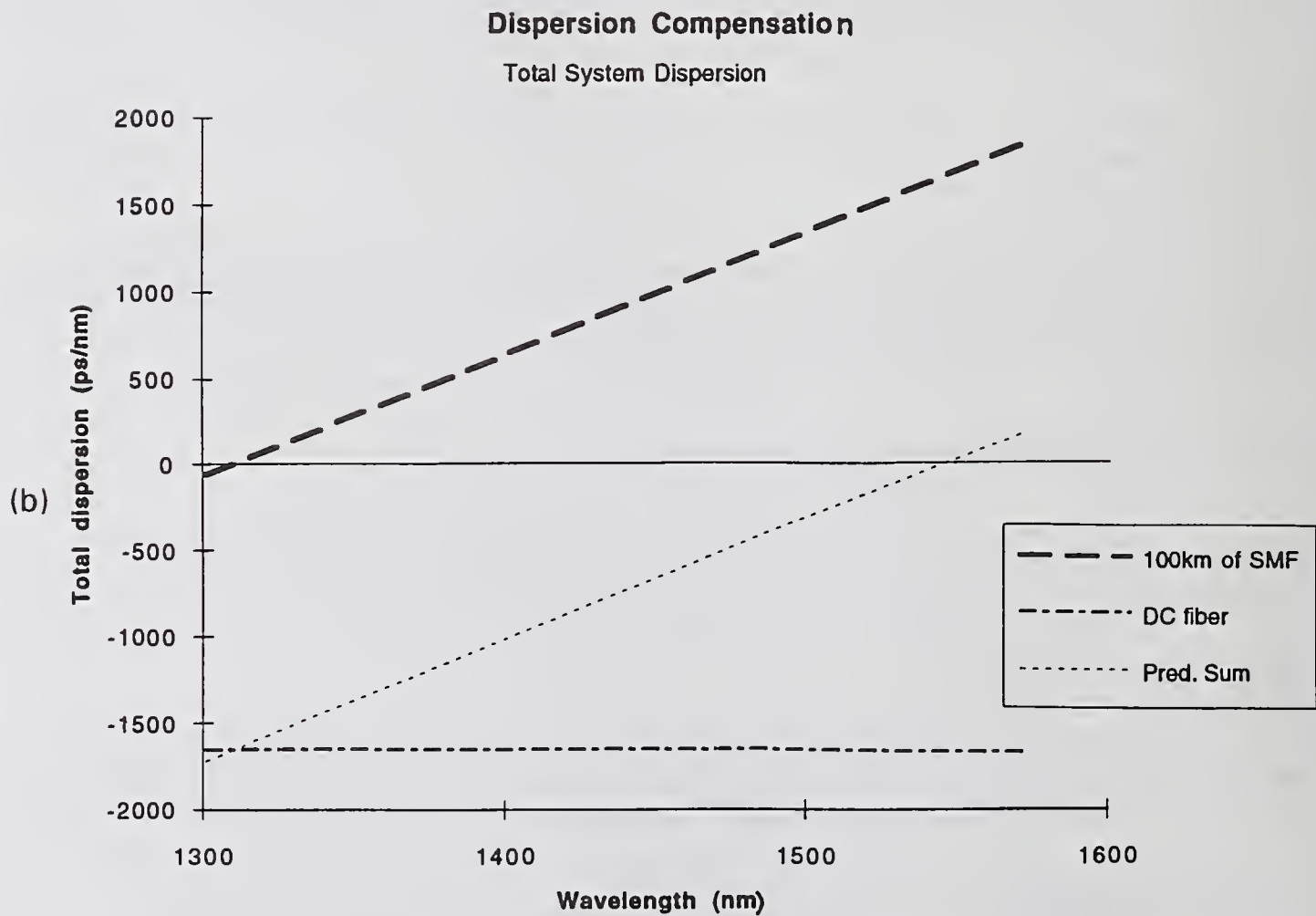
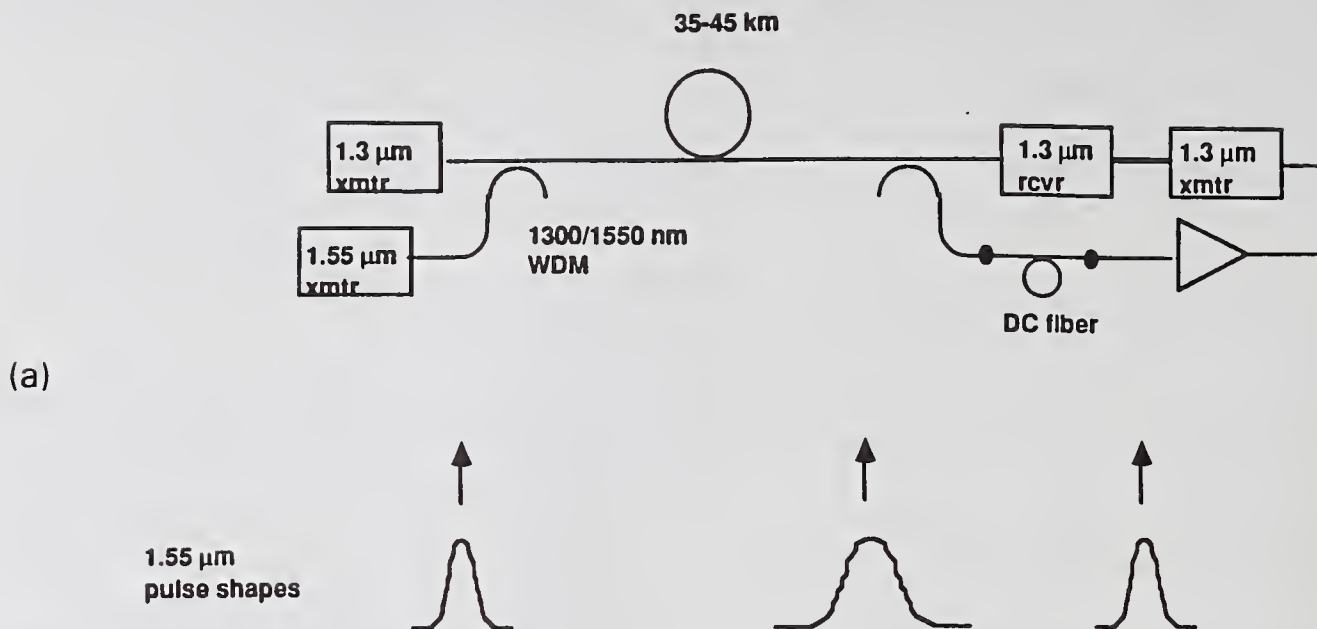


Figure 1. Dispersion compensator concept.

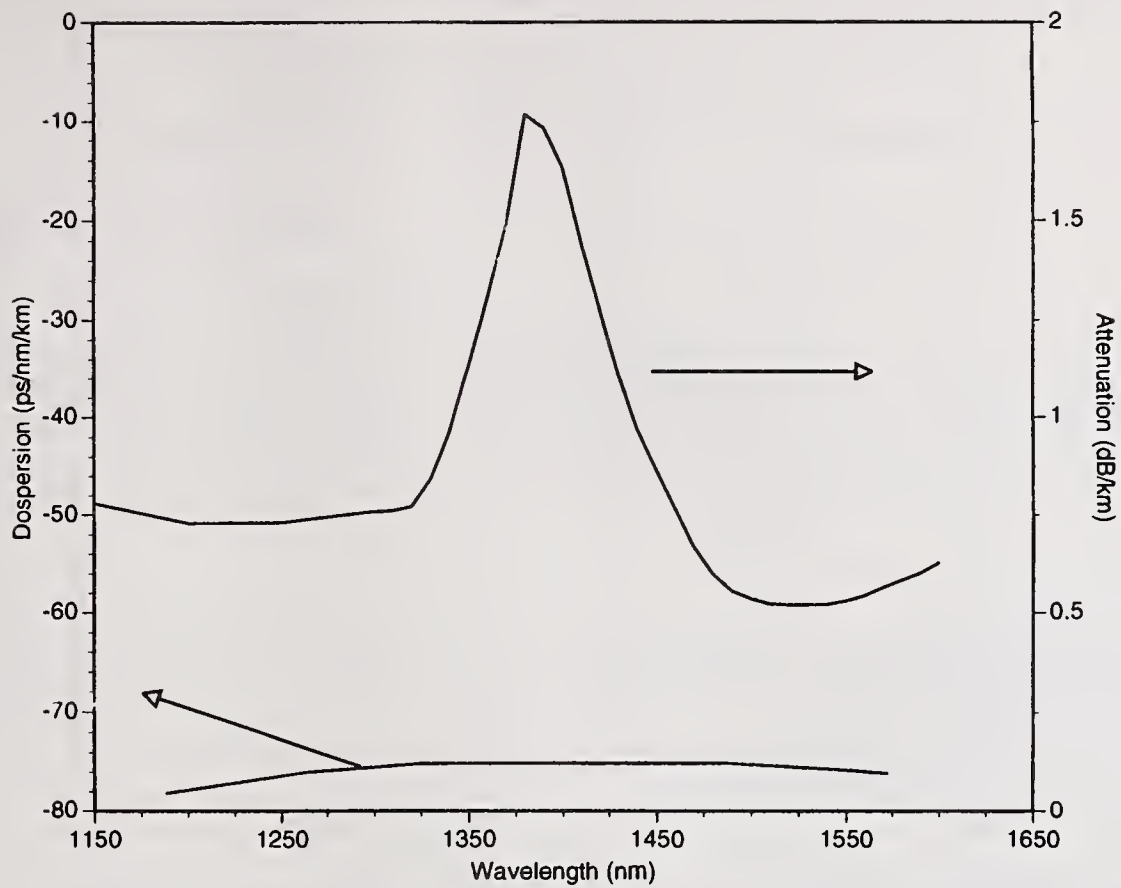


Figure 2. Dispersion and attenuation of dispersion compensating fiber.

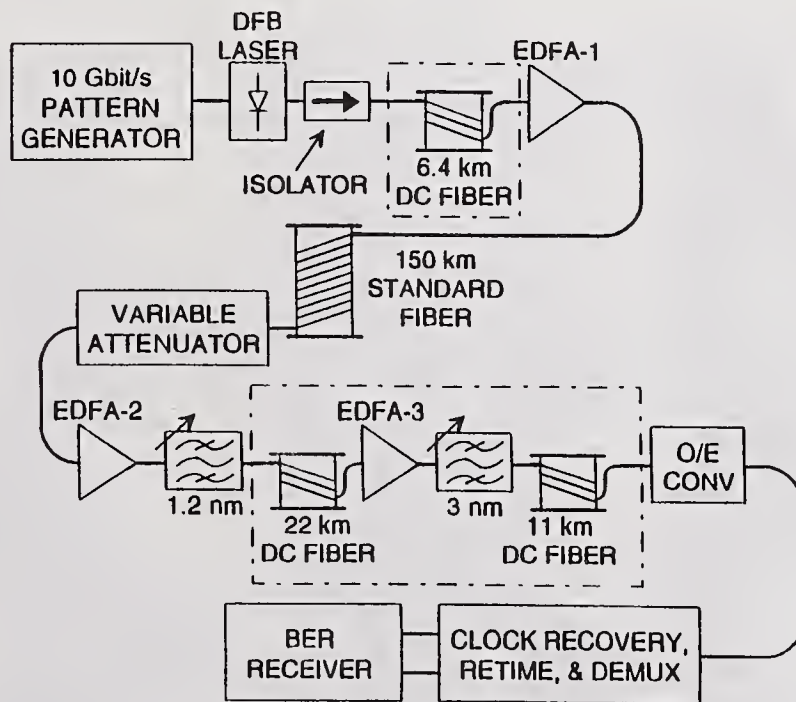


Figure 3. Block diagram of experimental set-up.

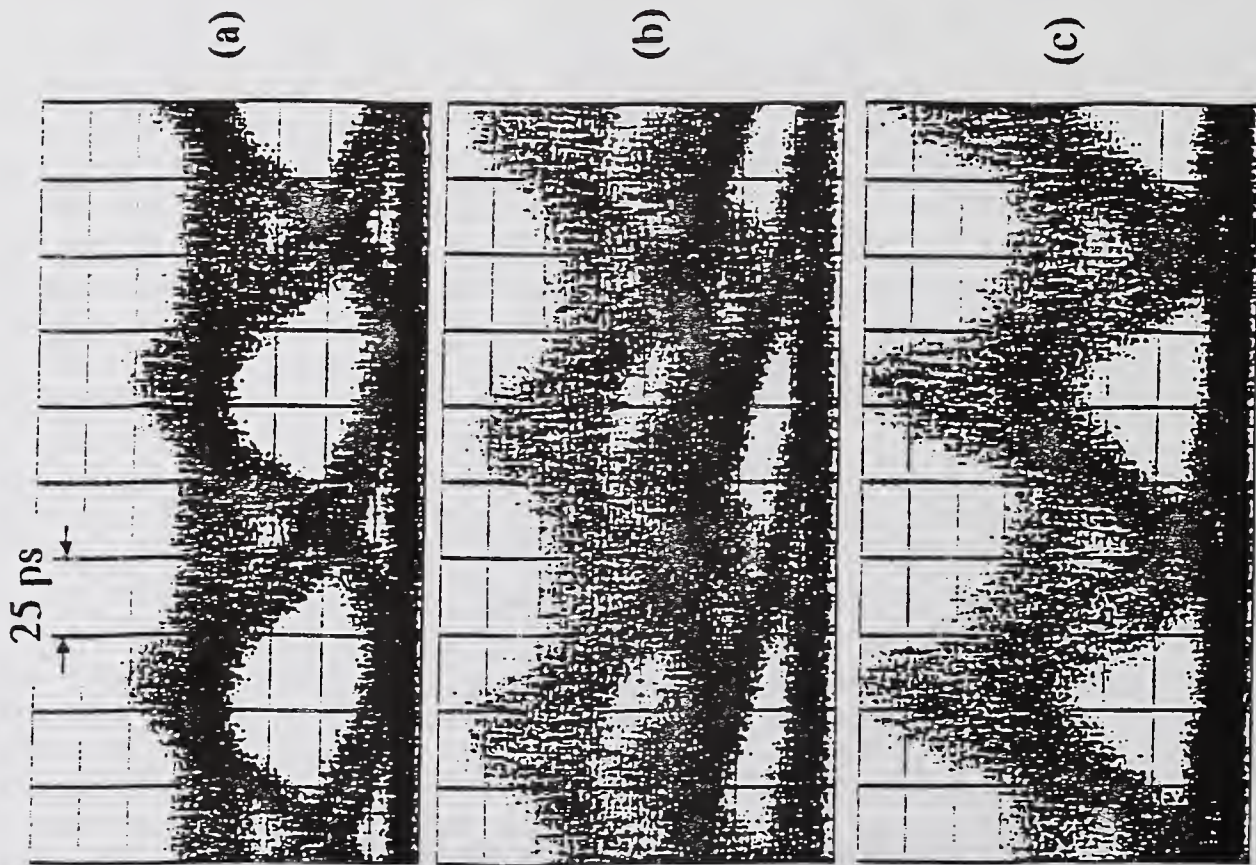


Figure 4. Optical eye patterns: (a) Zero km, no compensation; (b) 12 km, no compensation; (c) 150 km, with compensation.

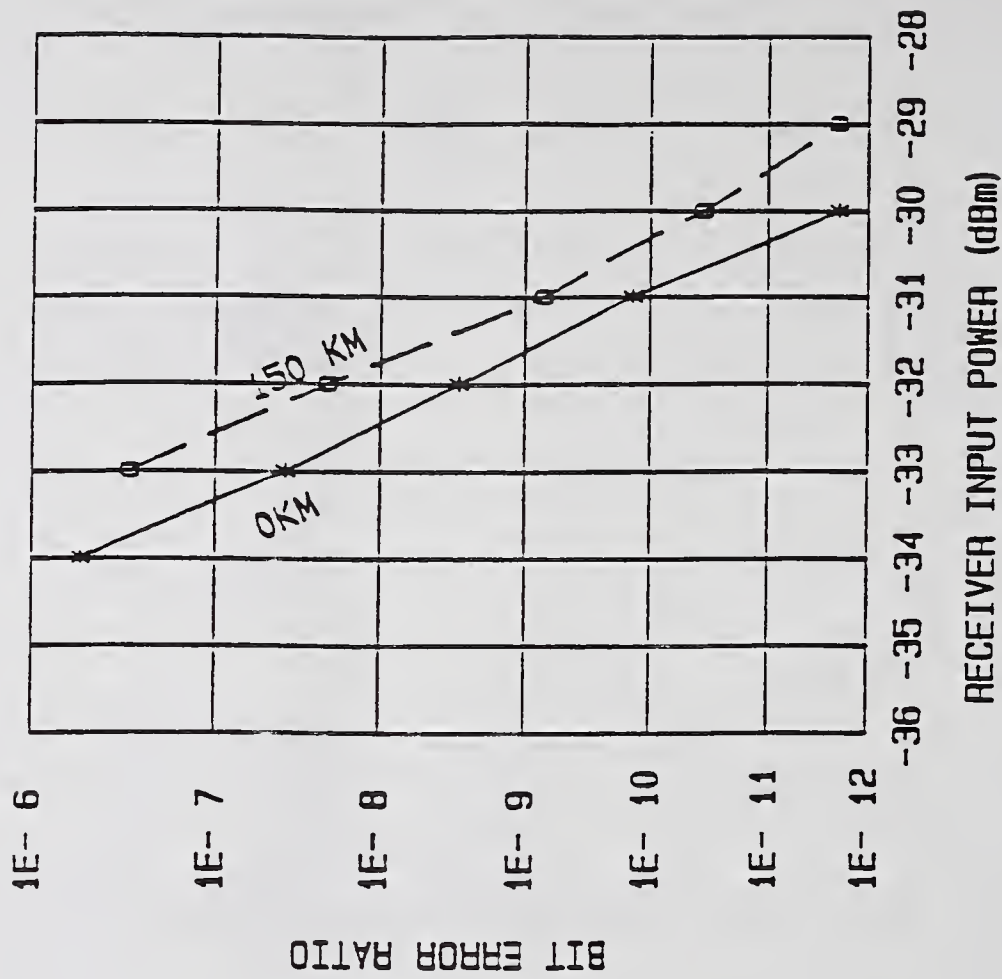


Figure 5. BER performance through zero km and through compensated 150 km path.

MEASUREMENT OF GROUP EFFECTIVE INDEX OF OPTICAL FIBERS AND INTEGRATED WAVEGUIDES BY THE WAVELENGTH SCAN TECHNIQUE

S. Morasca, F. Pozzi, C. De Bernardi
CSELT S.p.A. - Via G. Reiss Romoli 274 - 10148 Torino, Italy

ABSTRACT

The technique of Fourier analysis of the spectral transmission function of a resonant cavity formed by a waveguide has been applied for the first time to single-mode optical fibers and semiconductor waveguides, to determine directly the group effective indices of the guided modes. On single-mode fibers, accuracy to four decimal places is demonstrated, and for the integrated guides differences between TE and TM indices are also evidenced.

1. - Introduction

The determination of the effective indices of the guided modes has a fundamental role in waveguide technology: precise values of these parameters are needed both for the design of optical guided-wave devices, and to test the validity of the theoretical models used to calculate the waveguide propagation constants from the geometrical and material parameters of the guide; this applies to optical fibers as well, with added applications, e.g. to calibrate the distance scale of OTDR instruments.

A technique based on a wavelength scan of a resonant cavity, formed by the guide under measurement, was introduced to this purpose [1] and has been successfully implemented. In the present work we report experimental results obtained on single mode fibers and InP/InGaAsP optical waveguides. The method is particularly suitable for semiconductor waveguides, whose cleaved facets provide sufficient reflectivity without any further preparation, but can be used on any type of waveguide. Its accuracy is discussed, as well as evolutionary lines for further improvements.

2. - Principle of the technique

The transmittance T of a Fabry-Perot resonator as function of the incident wavelength λ has a well known form [2], which for a lossy medium can be expressed as:

$$T = C \frac{e^{-\alpha L}}{1 + R^2 e^{-2\alpha L} - 2R e^{-\alpha L} \cos \frac{4\pi L n}{\lambda}} \quad (1)$$

where α is the cavity internal loss, L its length, n the refractive index of the medium filling the cavity, R the cavity mirror reflectivity and C a constant.

The period P of eq. (1) depends only on λ , L and n (provided that α and R are not rapidly varying with λ), and is given by the following relationship:

$$P = \frac{\lambda^2}{2L(n - \lambda \frac{dn}{d\lambda})} \quad (2)$$

where the medium dispersion has been taken into account. From eq. (2) the group index $n_g = (n - \lambda \frac{dn}{d\lambda})$ can be obtained as a function of P and λ , if L is also known. Using a tunable, narrow linewidth laser source it is easy to cover a large number of periods of the cavity, while monitoring the wavelength by means of a wavemeter, and therefore to determine adequately

the period itself; in the case of a waveguide, the effective indices n_{eff} and $n_{\text{eff } g}$ of the guided mode substitute indices n and n_g respectively.

A Discrete Fourier Transform algorithm is particularly suitable to determine P , when the sampled points are irregularly distributed [3], as in this case; the analysis provides the power density in the frequency spectrum of the cavity transmission function, so that peaks appear corresponding to its periodic terms; actually, several peaks may appear, due to the harmonics of the fundamental period, to terms coming from the distribution of sampled points, and to their sums and differences. Since the terms from the sampling distribution can be calculated, or a first approximation of the significant period is already known, the peak corresponding to the real cavity term can be univocally determined. For samples of centimeter size, the cavity length L can be easily measured to about $\pm 1 \mu\text{m}$, so that the effective index can be accurately calculated.

3. - Experimental set-up

The experimental configuration we have used [4] is shown schematically in Fig. 1: a tunable laser source (in this case an external-cavity, grating-tuned semiconductor laser diode) is coupled to the guide under measurement via a collimator-polariser-focuser system; a portion of the power emitted by the source goes to a wavemeter (with a resolution of 1 pm) to provide continuous monitoring of the source wavelength, while another fraction provides a reference power signal for normalization of the power transmitted by the guide; this transmitted power is collected by a microscope objective and read by a power meter. The entire set-up is under computer control, for data acquisition and processing. The presently available laser source has a linewidth below 200 kHz and is usefully tunable in the range 1.52 to 1.58 μm , although rather discontinuously due to laser mode jumps; for guide lengths of about 1 centimeter this amounts to thousands of periods of the corresponding resonant cavity, which allow a very precise period determination. On the other hand, over such a wide wavelength range the chromatic dispersion may be significant (e.g. for semiconductors), and the corresponding "chirp" on P would degrade its determination; therefore, the whole spectral interval is divided into subsections of less than 10 nm, so that an appropriate balance between dispersion and Fourier analysis baseline is realised; in this way $P(\lambda)$ and the guide group dispersion are obtained as well.

A modification of this set-up is also used, in which a current-tuned DFB laser is used in place of the external-cavity source; although presently the tuning range, at a rate of 9.6 pm/mA, is only about 0.2 nm and corresponds to a few periods of the cavity, the dense spectral sampling attained allows the determination of a first-approximation value for the period itself and hence an independent check of the analysis on the wider spectral baseline.

4. - Results and discussion

The technique has been applied to short sections (25 to 35 mm, measured to within 1 μm) of standard single mode fiber; to enhance the fiber reflectivity, a thin (6 nm) gold layer was coated on the end faces. The results from different lengths ($n_{\text{eff } g} = 1.4682 \pm 0.0003$ around 1.555 μm) are in excellent agreement with the declared value for the fiber, and their uncertainty indicates the present level of accuracy of the method; measurements over subsections of the 1.52+1.58 μm range evidence the group dispersion clearly.

The application to integrated waveguides has been tested on InGaAsP/InP guides having a Moderately Diluted Multi Quantum Well Structure (MD-MQW), schematically shown in Fig. 2 (this structure has the purpose to effectively "dilute" the InGaAsP refractive index by the lower-index InP, to get a low core-cladding index difference and therefore a better modal match to optical fibers). Guides 3 to 10 μm wide have been measured, about 15.1, 8.4 and 6.7 mm long, obtained by cleavage of a single chip; the individual guide lengths have been measured to better than 2 μm . A typical wavelength scan is shown in Fig. 3: although no periodic behaviour is apparent in the distribution of points, due to the low sampling density (less than one point per period), the period shows up prominently in the corresponding frequency power spectrum, reported in Fig. 4. An average effective group index $n_{\text{eff } g}(\text{TM}) = 3.394 \pm 0.002$

around 1.555 μm has been measured, with no significant difference between different guide widths. On the other hand, a conspicuous, repeatable difference is observed between TE and TM indices, about 0.009 ± 0.002 , evidencing a marked guide birefringence; scans over subintervals of the available 1.52-1.58 μm window show clearly the group chromatic dispersion effect as well, with a decrease from 3.410 to 3.393 (TE polarisation) between 1.535 and 1.575 μm . Work is in progress on other waveguides, both on glass and on other semiconductor structures.

The present high level of accuracy (about 10^{-4} for fibers and 10^{-3} for semiconductor waveguides) is a significant improvement in the effective index determination, compared to the previously available results. At the moment it is limited mainly by the following factors: *a)* low sampling density due to the currently available tunable laser (it provides only 5 to 15 stable wavelengths per nanometer); *b)* power instability of the used laser; *c)* thermal and mechanical drifts (e.g. creep of piezo positioners) of the set-up during the measurement time (currently about 30 min, mostly due to the settling time of the source); *d)* resolution of the available wavemeter. In fact, the latter parameter should be much smaller than the cavity wavelength spacing, and thus its value of 1 pm poses an upper limit of few centimeters to the usable cavity length.

For fibers, increasing the sample length to decimetric values would enhance the measurement accuracy in two ways: increasing proportionately the number of periods and the associated resolution of the Fourier analysis over a given spectral interval, and reducing the relative error on the measure of the sample length.

For the case of integrated waveguides, the current uncertainty can be attributed mainly to the higher impact of the thermal and mechanical drifts during the measurement.

Improvements under investigation include the use of stable, multielectrode semiconductor lasers, rapidly and continuously current-tunable over a few nanometers, to reduce the effect of factors *a)*, *b)* and *c)*, and concurrent refinements on cavity length measurements; improving also the resolution of wavelength measurements, enhancements in accuracy by nearly an order of magnitude are expected, for both fibers and integrated waveguides.

5. - Conclusions

A new, simple technique has been tested for the measurement of the effective group index of both single-mode fibers and integrated optical waveguides. The method, based on a Fourier analysis of the transmission function of a resonant cavity composed by the guide or by a short (a few centimeters) fiber section, has a demonstrated accuracy up to the fourth decimal place, detecting the difference in group index for fibers between 1.52 and 1.58 μm . Furthermore, the method has margins for further improvements by at least an order of magnitude, limited mostly by the spectral characteristics of tunable lasers, while the simplicity of the method allows a routine determination of the group index even for each fiber reel. As to integrated guides, the accuracy limits are set mainly by their overall length and longitudinal uniformity, and are expected to improve one extra decade from the current third decimal place.

Acknowledgements

The authors wish to thank G. Galliano for the useful discussions, D. Re for coating the fiber samples, G. Schiavini and A. Stano for fabricating and providing the semiconductor guides.

References

- [1] C. De Bernardi, S. Morasca, "Waveguide loss and effective indices determination by optical frequency scan integrated resonant cavities", VI Symposium on Optical Fiber Measurements, Boulder, NIST Special Publication N° 792, pp. 67-70, 1990.
- [2] M. Born, E. Wolf, "Principles of optics", 5th Ed. (Pergamon Press, London 1975), pp. 323-329.
- [3] E.P. Belserene, "Rhythms of a variable star", Sky & Telescope, pp. 288-290, Sept. 1988.
- [4] Patent pending.

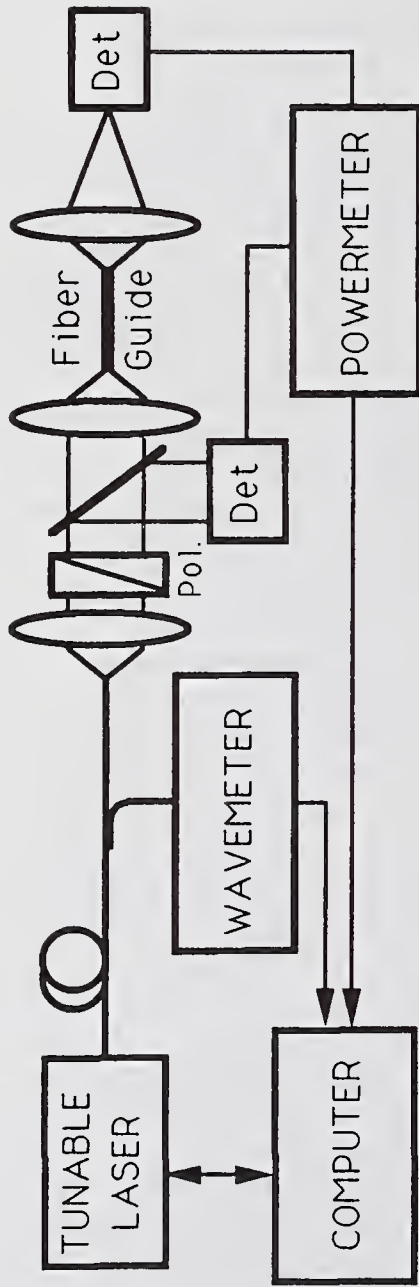


Fig. 1 - Schematic of the experimental set-up.

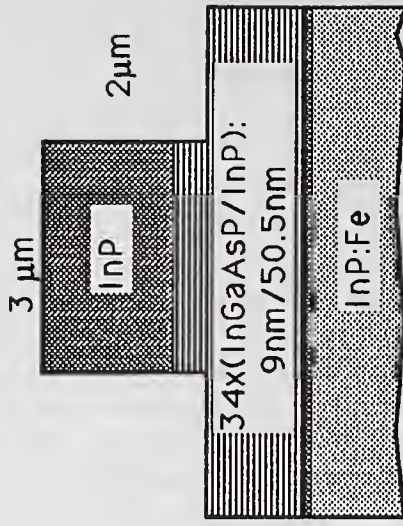


Fig. 2 - Schematic cross section of a MD-MQW semiconductor waveguide.

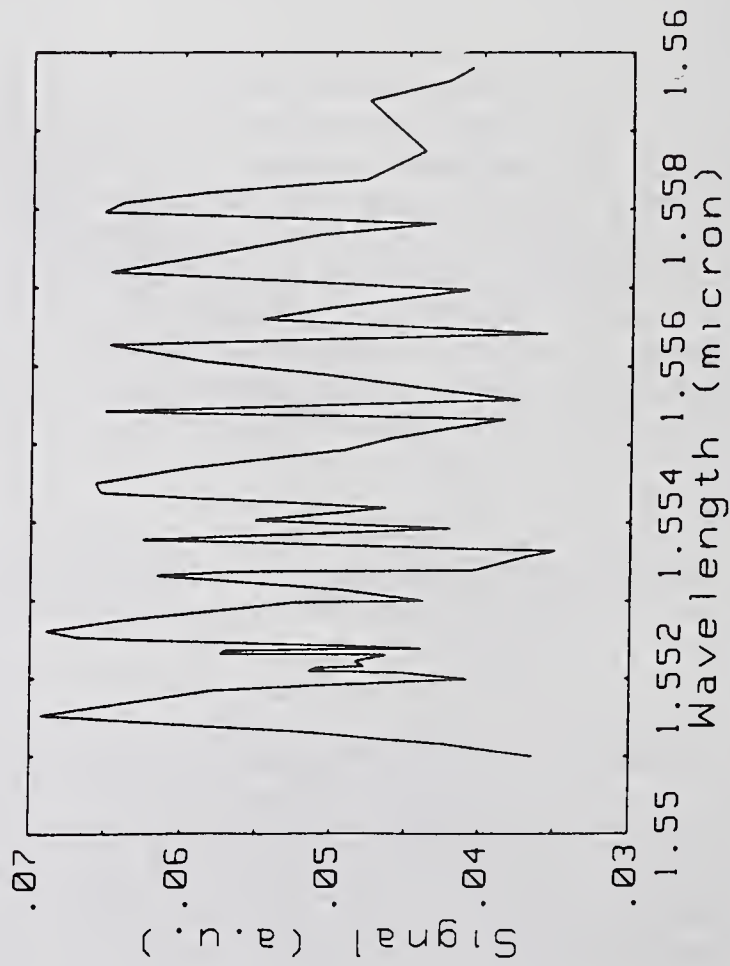


Fig. 3 - Transmission characteristics of a MD-MQW semiconductor waveguide 8.445 mm long and 6 μm wide.

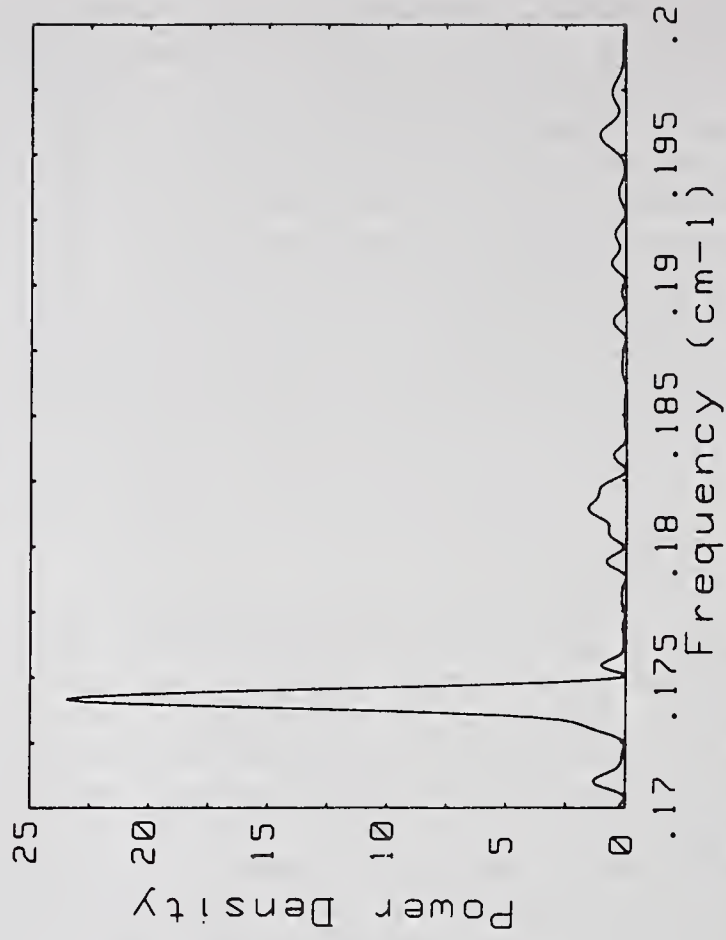


Fig. 4 - Power density spectrum of the signal shown in the previous figure; the main peak corresponds to a cavity period of 0.17418 cm^{-1} , leading to an effective group index of 3.399.

PRECISION MEASUREMENT OF SINGLE-MODE FIBER GROUP INDEX

W. B. Gardner

A. D. Parker

AT&T
2000 Northeast Expressway
Norcross, GA 30071

1. INTRODUCTION

Single-mode fiber attenuation is frequently measured and reported with an uncertainty of .001 dB/km. The fiber length is usually measured with an Optical Time Domain Reflectometer (OTDR). If one wishes to keep the uncertainty in this length measurement from contributing significantly to the uncertainty in a $.350 \pm .001$ dB/km loss measurement, then the group velocity V_g of the fundamental mode must be known to better than ± 1 part in 350, say to $\pm 0.07\%$. Since the group index N is c/V_g (where c is the speed of light in vacuum), this implies that N must also be known to an accuracy of $\pm 0.07\%$, which is $\pm .001$. Methods having this capability have been reported.¹⁻⁵ However, these methods generally require facilities which are not readily available, such as IR fiber interferometers,^{1,2} 50 meter benchmarks surveyed with 2 mm accuracy,³ or nanosecond modulation of broad-band sources.^{4,5} Because N will in general be different for each fiber design from each supplier, there is a need to make frequent precision measurements of N to keep pace with evolving fiber designs and the increasing accuracy of attenuation measurements. This paper shows how the desired accuracy can be achieved using only an OTDR and a suitable fiber winder.

2. MEASUREMENT METHOD

The time t for a round trip transit of a fiber of length L is given by $t = 2L/V_g$. The group index is then $N = ct/2L$. $\pm .001$ accuracy in N can be achieved with sufficiently careful measurements of t and L .

A fiber approximately 1.2 km in length was wound in a single layer onto a metal drum whose circumference was measured to be 878.0 ± 0.5 mm, using a precision steel rule as the length reference. The number of turns was recorded to a fraction of a turn by an optical encoder during winding. The encoder was mounted on the winder's headstock to avoid errors due to slippage in belts and pulleys.

The transit time t was measured by an OTDR whose pulse width was 3 nsec. A point on the reflected pulse 3 dB down from the peak was chosen to represent the fiber end. By judicious choice of matching fluids, the reflection from the far end of the 1.2 km test fiber could be made equal in magnitude to the reflection from the end of the 600 m fiber test lead that was spliced to the test fiber. In this way, the transit time reproducibility was ± 0.1 nsec, which corresponds to ± 1 cm. To check for calibration errors, one of the fibers was measured on two different OTDR's. With the group index set to 1.47, the two OTDR's gave lengths of 1220.01 m and 1220.11 m. This uncertainty is listed as iii) in Sec. 4.

3. WINDING TENSION

The fiber tension during winding was measured to be 35 gm. After the measurements, several of the fibers were paid off the metal drum into a loose pile. The transit time was then re-measured with the fiber in this "zero-tension" condition. The decrease in transit time was typically 0.04%, which calls for the N measured under tension to be increased by .02%. The $\pm .01\%$ uncertainty in this correction is item vi in Sec. 4. After winding a fiber onto the drum, the drum radius measurement was repeated over the wound fiber. The increase in this radius equalled the coated fiber diameter to within $\pm .03\%$. This is item ii in Sec. 4, and indicates that compression of the coating and/or drum due to the winding tension is small.

4. ERROR ANALYSIS

This section summarizes the known sources of error. The impact of each is given in parenthesis as a percent of the measured group index.

- i. Circumference of empty drum ($\pm .06\%$)
- ii. Uncertainty in the distance of the fiber core from the drum surface ($\pm .03\%$)
- iii. OTDR Calibration ($\pm .01\%$)
- iv. Reproducibility of OTDR length measurement by the Sec. 2 procedure ($\pm .001\%$)
- v. Change in the transit time due to a $\pm 5^\circ\text{C}$ change in the fiber temperature (calculated from Ref. 6) ($\pm .005\%$)
- vi. Uncertainty associated with a 35 gm winding tension (see Sec. 3) ($\pm .01\%$)
- vii. ± 25 cm uncertainty in fiber length resulting from multiple end preparation ($\pm .02\%$)
- viii. ± 30 nm uncertainty in the OTDR laser wavelength ($\pm .006\%$)

Assuming that the above errors are uncorrelated, an rms addition gives a total uncertainty of $\pm .07\%$ or $\pm .001$ in the measured group index.

5. MEASUREMENT RESULTS

The results of applying this technique to seven AT&T single-mode fibers are given in Table I. The apparent fiber-to-fiber variations are explainable by the $\pm .001$ measurement uncertainty. Actual fiber-to-fiber variations have been shown¹ to be on the order of .0003. For comparison, Table II gives some previously reported group index values. As expected, the group index is always lowest near the zero-dispersion wavelength.

Table I — Group indices of conventional single-mode (SM) and dispersion-shifted (DS) single-mode AT&T fibers. The 1σ uncertainty of all values is .001.

<u>Fiber</u>	<u>N (1.31 μm)</u>	<u>N (1.55 μm)</u>
SM #1	1.468	1.469
SM #2	1.466	1.467
SM #3	1.467	1.468
SM #4	1.467	1.468
DS #1	1.470	1.469
DS #2	1.471	1.470
DS #3	1.471	1.470

Table II — Some previously reported group index values. Only the measurements in Ref. 1 were performed on AT&T fibers.

<u>Fiber</u>	<u>N (1.31 μm)</u>	<u>N (1.55 μm)</u>
SM (Ref. 1)	1.4659	1.4666
SM (Ref. 3)	1.4675	1.4681
DS (Ref. 3)	1.4718	1.4711
DS (Ref. 7)	--	1.475
Z-Fiber (Ref. 7)	--	1.462

6. ACKNOWLEDGMENTS

The authors are grateful for the assistance of C. W. Jackson, J. A. Hudson, and R. B. Kummer.

REFERENCES

1. M. J. Saunders and W. B. Gardner, "Interferometric Determination of Dispersion Variations in SM Fibers", *J. Lightwave Tech.*, Vol. 5, pp. 1701-1705 (1987).
2. Y. Namihira, Y. Iwamoto, T. Murakami, and S. An, "High Speed and High Accurate SM Fiber Dispersion Measuring Equipment Using Modified Interferometric Method", *NIST Symp. on Optical Fiber Measurements*, Boulder, Sept. 9-10, 1986, pp. 19-22.
3. J. J. Carr, S. L. Saikkonen, and D. H. Williams, "Refractive Index Measurements on SM Fiber as Functions of Product Parameters, Tensile Stress, and Temperature", *NIST Symp. on Optical Fiber Measurements*, Boulder, Sept. 11-12, 1990, pp. 59-62.
4. M. Horiguchi, Y. Ohmori, and T. Miya, "Evaluation of Material Dispersion Using a Nanosecond Optical Pulse Radiator", *Appl. Opt.*, Vol. 18, pp. 2223-2228 (1979).
5. L. Thevanaz and J. P. Pellaux, "Group Delay Measurement in SM Fibers with True Picosecond Resolution Using Double Optical Modulation", *J. Lightwave Tech.*, Vol. 6, pp. 1470-1475 (1988).
6. L. G. Cohen and J. W. Fleming, "Effect of Temperature on Transmission in Lightguides", *Bell Sys. Tech. J.*, Vol. 58, pp. 945-951 (1979).
7. Y. Namihira, Y. Horiuchi, H. Wakabayashi, T. Oshimi, K. Kitagawa, and T. Ooka, "155 km Long-Range OTDR Measurement at 1.55 μm Wavelength Region", *NIST Symp. on Optical Fiber Measurements*, Boulder, Sept. 20-21, 1988, pp. 11-14.

THE DIRECT MEASUREMENT OF HIGHLY ABSORBING BANDS IN OPTICAL FIBERS

Robert M Atkins
AT&T Bell Laboratories
Murray Hill
NJ 07974

Abstract

A technique has been developed to directly measure the attenuation of optical fibers even in the region of very highly absorbing bands. An example is given of the measurement of the UV spectrum of a singlemode germanosilicate core fiber between 200nm and 300nm, where the absorption band at 241nm due to GeO shows attenuation of ca. 230dB/mm.

Introduction

Conventional cut-back techniques for measuring the optical attenuation of fibers become impractical when optical losses become greater than a few dB/cm. Though it is in principle possible to fusion splice a very short section of test fiber into a longer length of non-attenuating fiber, the extreme temperatures involved in the fusion splice can radically alter the concentration of some highly attenuating species. Some species present in fibers can give rise to optical absorptions as high as several hundred dB/mm and thus attenuation can only be measured on fiber lengths of several hundred microns. One such species, whose measurement will be discussed in detail in this paper, is GeO, formed by the reduction of GeO₂ in germanosilicate fibers, which has an intense UV absorption band near 241nm^[1]. GeO is of particular importance in view of its reported role in the formation of UV written refractive index gratings in optical fibers^[2]. Fusion splicing results in very high levels of GeO at the splice and so cannot be used in the measurement of GeO in short lengths of fiber. The alternative splicing techniques developed and reported here have enabled direct, accurate measurements to be made in fiber test lengths as short as 40μm with attenuation values >400dB/mm and at wavelengths as short as 190nm.

Experimental

This technique relies on the precise alignment of a very short section of the fiber to be measured (typically <200μm) with two pigtail fibers. The test section can be fabricated by cutting and polishing short sections of fiber, or with some care, such short sections can be cleaved directly saving a considerable amount of time and effort. The pigtail fibers must be transparent over the wavelength range of interest. In this case, since GeO absorbs in the short wavelength UV, with a peak near 241nm, the pigtail fibers must be UV transparent and thus pure silica core fibers must be used. The fiber section to be measured and the pigtail fibers are precisely aligned by placing them in a "V" groove etched into a small silicon block as shown in figure 1. The accuracy with which silicon can be etched ensures a straight and uniform "V" groove. It is also essential that both test and pigtail fibers have low eccentricity in order to ensure core alignment,

and that the core size and numerical aperture of the pigtail fiber is no larger than that of the test fiber in order to ensure that light is launched only into the test fiber core. For fibers with small cores it was found necessary to fabricate non-standard small core silica fibers for use as pigtails. In order to obtain minimum splice loss an index matching fluid is required. In this case, since measurements were required down to 190nm, the index matching fluid must not only match the index of silica (ca 1.55 at 200nm), but must also be transparent down to 190nm, at least for path lengths of the order of the gaps in the mechanical splice, i.e. $<10\mu\text{m}$. Though not a perfect match, cyclohexane was found to work quite well in this role. Alternative materials are cyclooctane, cyclooctanol and bromoform, though these materials, while providing a slightly better index match, have higher short wavelength optical absorptions as well as potentially higher toxicity and in practice have no advantage over cyclohexane. The volatility of cyclohexane may mean that repeated applications are required if measurement times are more than a few minutes. The assembly of pigtail and test fibers was secured in place in the silicon "V" groove by means of a spring loaded cover glass. Index matching fluid is drawn into the splice region by capillary action.

To obtain the absorption spectrum of the test fiber the system shown in figure 1 was used. Light from a monochromator, illuminated by a 75W Xe arc lamp, was launched into one of the fiber pigtails. To avoid problems associated with the chromatic aberrations and optical absorption of lenses, the light was launched into the fiber by simply placing it at the exit slit of the monochromator. The light exiting from the second fiber pigtail was launched into a second monochromator by positioning the fiber at the entrance slit. The purpose of this second monochromator was to eliminate fluorescence radiation from the test fiber. The two monochromators were set to track each other in wavelength during measurements. Light exiting the second monochromator was detected using a thermoelectrically cooled photomultiplier tube. The same procedure was then repeated, but this time using only a length of pigtail fiber equal to the total length of the two pigtails used in the first experiment. The ratio of these two measurements can then be used to determine the loss of the test section of fiber. It may be necessary to make small offset adjustments to take into account wavelength independent losses (such as splice losses). If measurements on the test section of fiber are extended into a wavelength region at which losses (as determined by other measurement techniques) are known, then corrections for wavelength independent losses can be made with confidence.

A few words of caution are appropriate in the discussion of these measurements. GeO is well known to fluoresce at ca. 400nm when illuminated near its absorption bands at 241nm and 330nm. For high accuracy measurements it is of critical importance to ensure that no fluorescence radiation reaches the detector, and that no light can bypass the test fiber section via propagation by cladding modes. In a typical measurement of a high GeO fiber optical transmission at 241nm of a $150\mu\text{m}$ test section falls to a very low level (ca. 35dB below the launched light level). If any extraneous light falls on the detector (either from light propagating in cladding modes, or fluorescence from the core itself) considerable underestimation of the peak attenuation will result, sometimes without an obvious distortion of the resultant peak shapes. Such problems have lead erroneous reports of the UV absorption spectrum of optical fibers^[3], later corrected when these problems were addressed^[4]. A check that such problems are not distorting experimental results can be made by measuring the attenuation per unit length of several

different lengths of test fiber. If the attenuation per unit length is not constant, it is a very strong indication of measurement problems due to propagation of light via cladding modes or core fluorescence. If this occurs it may be necessary to use pigtails with a smaller core diameter, lower eccentricity and/or to improve the filtering of fluorescence radiation.

Results

An examples of measurements made using the technique described here is given in figure 2 which shows the absorption spectrum of an AT&T Tethered Vehicle fiber (a single mode fiber with a $6.5\ \mu\text{m}$ core containing about 10 mole% germania). The small fiber core required the fabrication of pure silica core pigtail fibers with a core diameter around $5\ \mu\text{m}$ for accurate measurement. The GeO peak near 241nm was measured on a $160\ \mu\text{m}$ length of fiber and is seen to be ca. 230dB/mm. Despite efforts to minimize errors due to the effects discussed previously, an earlier reported measurement made using larger core pigtail fibers evidently suffered from some propagation of light via cladding modes and the resulting reported loss value of 80dB/mm for the GeO band in an AT&T Tethered Vehicle fiber was significantly too low^[5]. After the formation of a refractive index grating in the fiber by 242nm UV exposure, the absorption spectrum of the fiber showed considerable changes as shown in figure 2. Analysis of such changes can give insight into the mechanisms involved in grating formation^[6].

Conclusions

A technique has been presented which allows absorption measurements to be made in very highly attenuating fibers. The specific application of the measurement of GeO in fibers has been described, though the technique is generally applicable to any highly attenuating species. The technique has the advantage over fusion splicing that the fiber is not subjected to high temperature extremes which can radically affect the fiber attenuation under some circumstances.

Acknowledgements

The author would like to thank K. T. Nelson, D. DiGiovanni, J. W. Fleming, F. V. DiMarcello, W. A. Reed, A. Moesle, R. G. Huff, V. Mizrahi and K. L. Walker for their assistance in this project.

References

- 1 - M. J. Yuen, Appl. Opt. 21, 136 (1982).
- 2 - G. Meltz, W. W. Morey and W.H. Glenn, Opt. Lett. 14, 823 (1989).
- 3 - D. L. Williams, S. T. Davey, R. Kashyap, J. R. Armitage and B. J. Ainsle, Appl. Phys. Lett. 59, 762 (1991).
- 4 - D. L. Williams, S. T. Davey, R. Kashyap, J. R. Armitage and B. J. Ainsle, Elect. Lett. 28, 369 (1992).
- 5 - R. M. Atkins, Opt. Lett. 17, 469 (1992).
- 6 - R. M. Atkins and V. Mizrahi, Paper JTua3, Technical Digest, Conference on Lasers and Electro-Optics, May 10-15, 1992, Anaheim, CA.

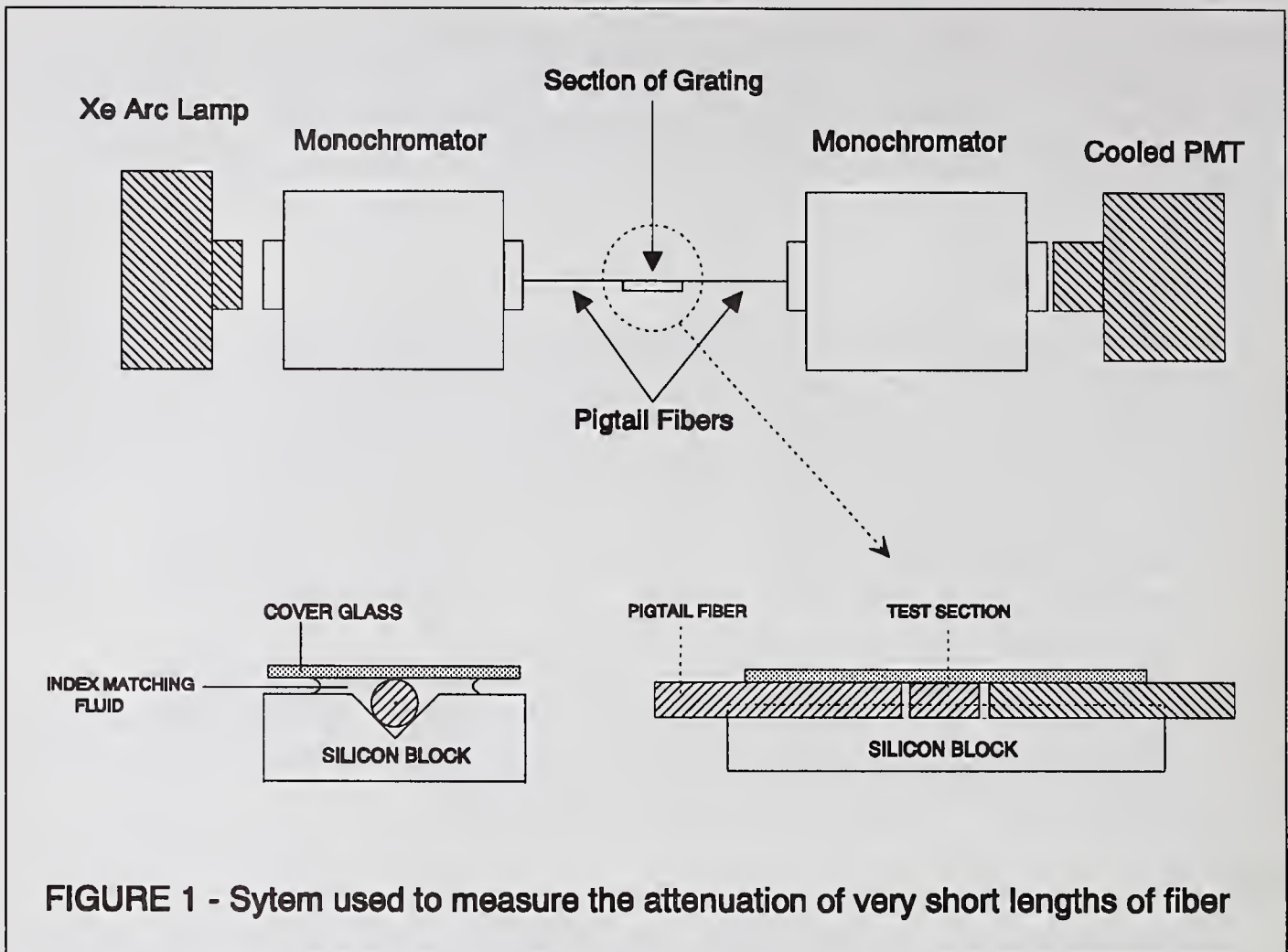


FIGURE 1 - System used to measure the attenuation of very short lengths of fiber

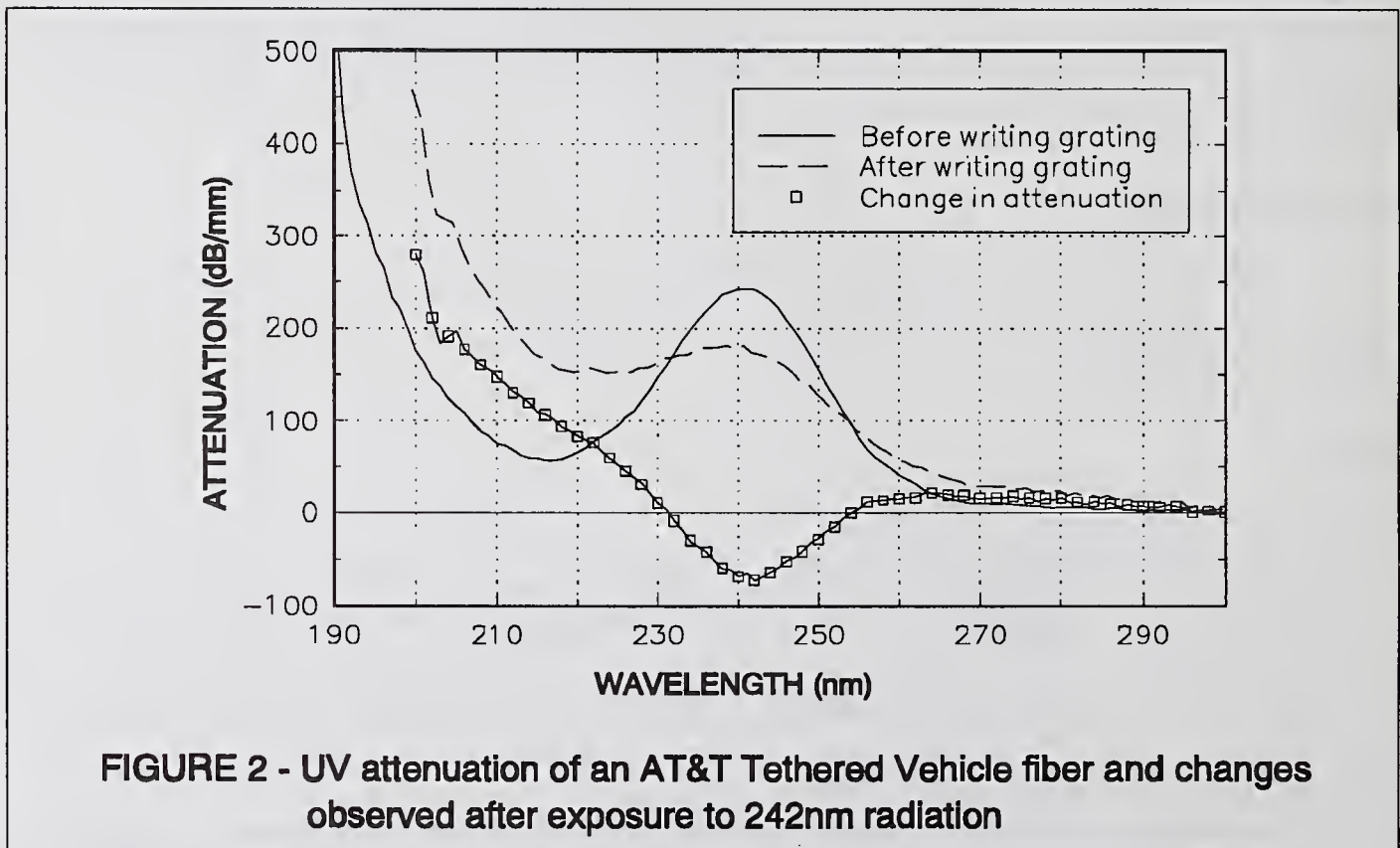


FIGURE 2 - UV attenuation of an AT&T Tethered Vehicle fiber and changes observed after exposure to 242nm radiation

DETERMINATION OF STRESS OPTIC EFFECT IN OPTICAL FIBERS

A J Barlow*, W H Ficke**, T Voots***

* EG&G Fiber Optics, Wokingham, UK

** AT&T Bell Laboratories, Norcross, GA, USA

*** Photon Kinetics, Beaverton, OR, USA

Introduction

Qualifying a fiber cable design, to verify that premature failure caused by excessive fiber strain will not occur during cable service, requires the accurate determination of its fiber strain/ cable load characteristics. Measurement of this characteristic typically involves using a phase shift method [1] to observe the change in optical propagation delay of the fiber [2] in a loaded cable. Conversion of the delay change to a physical fiber strain (or elongation) requires two constants: the fiber group index [3] and its stress-optic characteristic [4], [5].

In this paper, a refined phase shift method to accurately determine the "stress-optic correction factor" is presented. The new method uses standard fiber strain measurement and tensile test equipment.

The propagation delay change $\delta\tau(\lambda)$ of a strained fiber of initial gauge length L and group index $N(\lambda)$ at wavelength λ , is given by [4]:-

$$\delta\tau(\lambda) = (N(\lambda) \cdot \delta L + L \cdot \delta N) / c \quad \text{--(1)}$$

where: $\delta\tau(\lambda)$ is the relative delay change in the fiber when strain ϵ is applied;

δL is the physical elongation of the fiber;

δN is the term representing the stress-optic effect on the group index $N(\lambda)$ due to axial tension;

c is the speed of light in vacuo.

Applying stress-optic theory [4], equation (1) becomes:-

$$\delta\tau(\lambda) = N(\lambda) \cdot \delta L \cdot K / c \quad \text{--(2)}$$

$$\text{where: } K = \left[1 - \frac{N(\lambda)^2 \cdot \{ p_{12} - \sigma(p_{11} + p_{12}) \} }{2} \right] \quad \text{--(3)}$$

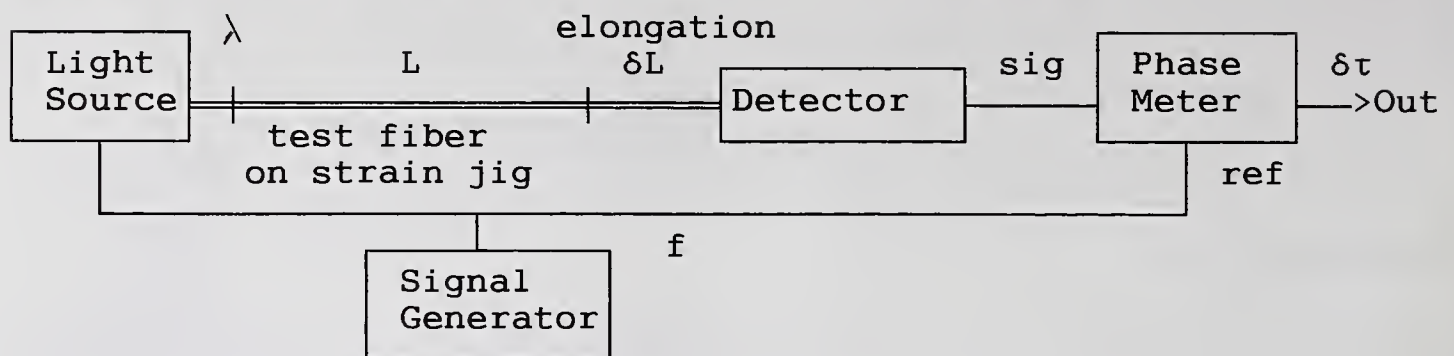
K is the "stress-optic correction factor" for a fiber under axial tension. Other correction factors would be needed to correct any thermo-optic [4], [5] or pressure effects on N [4].

The strain ϵ is then given by:-

$$\epsilon = \delta L / L = \frac{\delta\tau(\lambda) \cdot c}{(N(\lambda) \cdot L)} \cdot (1/K) \quad \text{--(4)}$$

Group index N and the associated stress-optic correction factor K both directly affect strain measurement accuracy. Evaluation of K using fused silica values [4] of $P_{11}=0.121$, $p_{12}=0.27$, $\sigma=0.17$, and $N=1.468$ yields a value of $K=0.78$. However, it is the object of this work to experimentally determine the actual K value for a typical single mode unshifted fiber to high accuracy.

Determination of The Stress Optic Correction Factor



By definition, K can only be determined [4] by straining a fiber and measuring δL , δT using standard tensile test jigs [2] (see figure above). It would be desirable to minimise measurement uncertainty, since the K value obtained will likely be used systematically and repeatedly in subsequent fiber tests. Obviously, the fiber used in the determination should be of the same type as the fiber used in the cables under investigation.

Similarly, the fiber should be tightly buffered (eg Nylon or Hytrel), in order that a deterministic strain can be applied, at the same time ensuring negligible slippage at the anchoring points. The fiber leads to and from the measurement instrumentation must be kept short to minimise the effect of delay changes arising from these leads. We assume that K is almost constant up to a few percent strain [5]. To avoid potential non-linear elasticity effects at high strains, the fiber length L must be sufficiently large to provide sufficient δL and $\delta\tau$ at only moderate percentage strain levels.

Assuming the use of a phase shift based measurement system, the phase (delay) detector must be well calibrated and of sufficient linearity. In many such systems, the phase detection linearity may only a percent or so [3]. The Quadrature Phase shift method [1] widely used in the industry greatly reduces this to levels that are negligible for normal tensile measurements. However, for the purpose of determining K or N [3], some means of circumventing any phase meter non-linearity is required.

The proposal of this paper is to circumvent the non-linearity and other error of the phase detection system by using a simple modification [4] of the existing technique. Basically, by always operating the phase meter at the same (zero, or null) phase point, nonlinearity is never invoked. Operation in this mode may for example, be obtained using an electrical variable phase shifter inserted into the phase meter reference path, but such devices are themselves generally non-linear. Alternatively, a variable air-path optical delay line fitted in the optical measurement system could bring the phase meter indication back to zero for any $\delta\tau$, the delay line length yielding $\delta\tau$. Such a method is not easily adapted to routine use. Instead, a third possibility is proposed.

The normal response curve of any phase meter repeats every 2π of phase change, no matter what the linearity or scale factor error of the phase meter is within the 2π range. Hence if the elongation δL is increased such that the delay change $\delta\tau$ is

always close to one period of the source modulation frequency f (i.e. the phase change is always close to 2π), the effect of any non-linearity or scale factor error in the phase meter is greatly diminished. In effect, the phase meter reading is only taken close to two identical fixed points on the phase meter curve for both the unstrained and strained fiber measurements. We set out to show that this simple variation incorporated into the technique yields excellent accuracy and precision of K using standard commercial instrumentation.

Results and Discussion

An unshifted standard telecommunication single mode fiber (AT&T) with a 0.9mm Hytrel jacket was used. The phase shift measurement system used was a standard, unmodified commercial strain measurement unit (EG&G SPL3 / PK 2300), capable of automatically measuring $\delta\tau$ with a precision better than 1ps. A wavelength of 1310nm and source linewidth of 4nm was used. The fiber strain jig used conformed to the requirements of TIA FOTP-33/-38 [2].

First, the fiber group index $N(\lambda)$ was determined using the cut-back method, again modified as above [3] for increased precision. N was found to be 1.468 ± 0.001 by this method [3], at a temperature of 23 degrees Celsius.

The fiber was placed onto the strain jig, using several loops wrapped around each 50cm-diameter mandrel, one of which was movable. The separation between the mandrels and the total fiber gauge length were approximately 17m and 215m respectively. The mandrel movement relative to a fixed calibrated graduated scale was determined using an anti-parallax sight marker on the mandrel stage, from which δL was calculated.

A small, arbitrary amount of initial tension was applied to ensure all fiber loops were taut and that slippage and other movement on the mandrels (which would result in non-linear take up of the tension when the mandrel initially moves) was negligible. The strain measurement cycle was started and the fiber load gradually increased until a total of approximately 2π incremental phase change (in this case corresponding to 20.000ns) had developed due to the fiber elongation. At a point close to 2π phase change, the corresponding $\delta\tau$ and δL values were simultaneously recorded. The total elongation was of the order of 5 m, giving a 2-3% strain level, well below the proof test level for this fiber. The stress-optic correction factor, K , was determined from equation (2) using the N value obtained previously.

Several measurements of K were performed to establish the repeatability of the method. Results are summarised below:

Fiber	unshifted, single mode
Group Index	1.468 ± 0.001
Temperature	23 ± 2 °C
Wavelength	1310 ± 0.05 nm
Linewidth	4nm

Number of measurements	= 20
Mean K value	= 0.8074
Std Deviation	= 0.0044

The random uncertainty in K is made up of contributions from δL ($\sim 15\text{mm}$) and $\delta\tau$ (1ps), and residual slippage on the mandrels. The Systematic uncertainty in K (0.003) largely originates from the mechanical measurement of δL , with smaller contributions from $\delta\tau$ and N. δL uncertainty could be significantly improved by using electronic or opto-electronic methods of detecting the mandrel movement.

Thus the stress optic correction factor for this fiber is 0.807 ± 0.009 , to 95% confidence. This value compares with the value predicted above (0.78). In a single mode fiber of a different construction, group index measurements versus strain [5] gave a derived value for K of 0.816 ± 0.04 at 1295 nm. Further results will be presented at the conference.

Conclusion

A simple modification of the existing phase shift method for measuring stress-optic correction factor in single mode optical fibers has been described. The modified method appears to offer a substantial improvement in uncertainty over the standard implementation of the phase shift method [1], [4] or comparable time delay techniques [5]. The improvement has been achieved by arranging for the phase detection system used to be operated close to a fixed phase value, in order to avoid inherent phase detection non-linearities. The fixed phase value is accomplished by arranging the fiber elongation to be approximately that length of fiber that produces one complete 2π phase shift, a length typically of the order of five meters.

Using commercial equipment commonly available in cable/ fiber manufacturing plants, where most strain measurements are made, a 95% confidence interval of correction factor K of 0.009 has been obtained, a value limited mainly by the mechanical determination of the fiber elongation. Such an uncertainty ($\sim 1\%$) will permit more accurate determination of cable strain performance and thereby help to improve cable design and quality control.

References

- 1) A Barlow, "Quadrature Phase Shift Technique For Measurement of Strain, Optical Power Transmission, and Length in Optical Fibers", Jnl. Lightwave Technology, 7, 1989, pp1264-1269.
- 2). EIA/TIA-455-33 'Fiber Optic Cable Tensile Loading and Bending Test', and EIA/TIA-455-38 'Measurement of Fiber Strain in Cable Under Tensile Load'.
- 3) A J Barlow, S Dodd and N Ives, "Measurement of Group Index using Fiber Cut Back" OFMC Proceedings, 1991, pp. 16-19.
- 4) M Brininstool, "Measuring longitudinal strain in optical fibers", Optical Engineering, 26, 1987, pp1112-1119.
- 5) J J Carr, S L Saikkonen and D H Williams, "Refractive Index Measurements on Single-mode Fiber as Function of Product Parameters, Tensile Stress and Temperature", Proc. Tech. Digest Symp. on Optical Fiber Measurements, Boulder CO, USA, 1990, pp. 59-62.

CHARACTERIZATION OF INTEGRATED OPTICAL COMPONENTS

PAUL G. SUCHOSKI, JR.

UNITED TECHNOLOGIES PHOTONICS
1289 BLUE HILLS AVENUE
BLOOMFIELD, CT 06002
(203) 769-3012

United Technologies Photonics (UTP) currently offers a family of integrated optic products for application in guidance systems, CATV distribution, antenna remoting, telecommunications, and instrumentation. The devices are fabricated on x-cut LiNbO_3 using the annealed proton exchange (APE) process and are available with either single mode or polarization-maintaining fiber pigtailed. Devices are available for operation at 830, 1320, and 1550 nm wavelengths.

Due to the relative immaturity of this technology, standardized test procedures do not exist for LiNbO_3 integrated optical components. Thus, it has been necessary for UTP to work with customers to develop a set of test procedures for characterizing those device parameters that impact system performance. As a component manufacturer, UTP is faced with the challenge of developing a minimum test set that will guarantee that all devices meet specifications. The test set must be relatively easy and inexpensive to implement as well as being suitable for automation. At the same time, the test set must be accurate enough to provide the customer and the manufacturer with useful data that can be used for statistical process control, future device design iterations, and system modeling.

In this report, we initially list the critical specifications for the various devices along with typical performance values. We then describe the test set that has been developed for each device type. Detailed descriptions of the various tests will be presented at the conference and are available as appendices to this report.

Fiber Optic Gyro (FOG) Circuits

A three-port FOG circuit consists of a Y-junction power splitter with independently-addressable phase modulators on each output arm. The device is pigtailed with polarization-maintaining fiber on all three output ports. Critical performance parameters and typical performance are listed below:

Insertion loss	2.0-3.5 dB
Split ratio	52:48 to 48:52
Polarization extinction	60-75 dB
Polarization crosstalk (waveguide-fiber interfaces)	-30 to -40 dB
Back reflections	<-60 dB
Half-wave voltage	3-4 Volts
Intensity modulation	0.01-0.05 %

FOG systems are typically configured using broadband sources such as ELEDs or SLDs. Due to the limited power of these sources, it is difficult to make accurate measurements on FOG circuits. We therefore opt to use high-power (10 mW) multimode laser diodes at 830, 1320, and 1550 nm for the measurements. The only parameter that is impacted by source spectral width is the intensity modulation which is typically 2-5 times lower when measured with a broadband source. Thus, the intensity modulation measurements made using a multimode laser diode source represent worst-case values.

The following test set is used to characterize the FOG circuits:

1. Launch optical power into the input fiber. Measure the power from the two output fibers (P1 and P2). The split ratio is defined as $P1/(P1+P2):P2/(P1+P2)$.
2. Measure polarization crosstalk of the two output fibers using a strain-free colimating objective and a polarizer.
3. Measure the half-wave voltage of the two phase modulators by interfering the optical signals from the two output fibers.
4. Measure the intensity modulation by driving each phase modulator with a 2000 Hz sinusoid of amplitude $(\pm) 2V_{pi}$.
5. Measure the polarization extinction of the device.
6. Using the cut-back method, measure the insertion loss which is defined as $(P1+P2)/P_{in}$.
7. Excite one of the output fibers. Measure the polarization crosstalk of the input fiber.

Phase Modulators

Phase modulators are provided with polarization-maintaining fiber on the input and either polarization-maintaining or single mode fiber on the output. Critical performance parameters and typical performance are listed below:

Insertion loss	2.0-3.5 dB
Polarization crosstalk	-30 to -40 dB
Back reflection	<-60 dB
Half-wave voltage	Depends on wavelength and frequency response
Intensity modulation	0.01-0.05%

The following test set is used to measure the phase modulators. High-power multimode laser diodes are used as the light sources.

1. Launch optical power into the input fiber. Measure polarization crosstalk of the output fiber.
2. Measure the intensity modulation of the device with a 2 kHz (+-) 10 Volt sinusoidal signal.
3. Measure the half-wave voltage of the device by interfering the fiber output with a reference optical beam.
4. Using the cut-back method, measure the insertion loss of the device.
5. Launch power into the output fiber. Measure the polarization crosstalk of the input fiber.

UHF Intensity Modulators

Two types of UHF intensity modulators are currently offered: Mach Zehnder interferometers with input and output Y-junctions; and Y-fed balanced bridge modulators with an input Y-junction and an output 3-dB directional coupler. The devices have both high-speed (600 and 860 MHz 1-dB points) and bias electrodes. The Mach Zehnder output power varies sinusoidally with applied voltage while the YBBM provides two complementary optical outputs that vary sinusoidally with applied voltage. The devices are typically pigtailed with polarization-maintaining input fiber and single mode output fiber. Critical performance parameters and typical performance are listed below:

Insertion loss	3.0-4.5 dB
On/off extinction	25-40 dB
Back reflection	<-60 dB
Frequency response	-1 dB >600, 860 MHz
Flatness	0.5 dB amplitude, 2 degrees phase
Half-wave voltage	4-5 Volts

The following test set is used to characterize the UHF modulators:

1. Launch power into the input fiber. Measure power from the output fiber(s) while applying a DC voltage to the bias port. Adjust the DC voltage to obtain minimum and maximum output powers. On/off extinction is defined as P_{\max}/P_{\min} .
2. Measure the half-wave voltage of the bias and RF electrodes.
3. Measure the frequency response (amplitude and phase) using a network analyzer. Extreme care must be taken in this measurement since device flatness is comparable to or better than the best available electronic test gear.
4. Using the cut-back method, measure the insertion loss of the device, which is defined as P_{\max}/P_{in} .

Microwave Intensity Modulators

The microwave intensity modulators are similar to the UHF intensity modulators except that traveling-wave electrodes are utilized to achieve bandwidths (-3 dB electrical) of 3, 8, 12, and 18 GHz. The critical performance parameters and test procedures are similar to the UHF modulators with the exception that

1. the swept frequency technique is used to measure the frequency response and
2. S_{11} is measured using a network analyzer.

Conclusions

It is important to note that the test sets described above are performed as final tests on every packaged, pigtailed component that is delivered by UTP. Since it is difficult to integrate into production, back reflection is currently not measured on every device. It is experience that back reflection is consistently <-65 dB and is insensitive to device design and fabrication conditions. The low back reflection is obtained by polishing the optical fibers at 15 degrees and the LiNbO_3 device at 10 degrees so that the back reflection is well outside the collection apperture of the optical fiber.

In addition to the tests described above, there is extensive testing, inspecting, and tracking of parts and materials associated with quality control that is performed during device fabrication and assembly.

M. Puleo, P. Gambini, E. Vezzoni

CSELT - Centro Studi E Laboratori Telecomunicazioni S.p.A. - Torino - Italy

Abstract

A measurement set-up is described that allows the real time observation of the instantaneous optical spectrum of a multimode laser diode, modulated by a data stream; statistical analysis on the temporal evolution of this spectrum leads to the evaluation of the mode partition coefficient k , in realistic operating conditions. Different lasers have been evaluated, with high speed (622 Mbit/s) modulation, evidencing the effects of data pattern and optical reflections.

Introduction

The power distribution among the different longitudinal modes of a multimode laser diode continuously fluctuates, while keeping constant the total power. This behaviour is a severe cause of impairment for system performance at high bit rates, when the different wavelengths experience different propagation conditions due to chromatic dispersion [1]. To characterize the spectral behaviour a mode partition coefficient k was defined as follows [1]:

$$k^2 = \frac{\sum_i \sum_{j>i} (\overline{a_i a_j} - \overline{a_i} \overline{a_j})}{\sum_i \sum_{j>i} (\overline{a_i a_j})} \quad \text{for } i \neq j \quad (1)$$

where $a_{i,j}$ are the instantaneous amplitudes of each mode, normalized to the total emitted power at a given time; the summation being carried out over all modes.

A few methods have been proposed so far to characterize this parameter: some of them separately measure the fluctuations of the different modes, neglecting, under proper assumptions, the cross-correlation terms [1]; other techniques simultaneously observe all modes, by applying pulsed modulating waveforms to the laser source [2].

The proposed technique allows the simultaneous, real time observation of several longitudinal modes of the laser spectrum corresponding to a selected bit, while the source is continuously modulated by a pseudorandom bit stream at 622 Mbit/s; the average and cross-correlation terms $\overline{a_i}$ and $\overline{a_i a_j}$, needed to apply (1), are then easily derived. The mode partition noise coefficient has been measured under different operating conditions, as a function of bias current, bit pattern and external optical reflections.

Experimental set-up

The experimental set-up is schematically shown in fig. 1. The laser under test is temperature controlled, biased by a high stability current source and modulated by a 622 Mbit/s PRBS data stream. A controlled optical reflection is provided by a variable back-reflector, in order to check the device sensitivity to external reflections; uncontrolled reflections from the following optical set-up are rejected by a polarization independent pigtailed isolator. The modulated optical signal is then fed to a LiNbO₃ Mach-Zehnder intensity modulator, acting as an optical gate, which allows beam transmission for a short time interval only (8 ns gating time, corresponding to 5 bit times of the 622 Mbit/s modulating signal, has been used in the experiment), synchronously with the data sequence entering the gate. The output beam is collimated on a diffraction grating, which spreads the light coming from the different modes in different directions; a suitable lens system with variable magnification (zoom) then focuses each beam on an array of 5 equally spaced fibres, positioned by a V-grooved silicon substrate. The zoom is adjusted so that each fibre collects the light coming from a single, different mode of the laser. The optical system works as a multiple output grating monochromator, whose output resolution is set by the core diameter of the collecting fibre. As the fibre spacing is fixed at 160 μm , and the fibre core diameter is 50

μm , a wavelength resolution of about 0.3 nm is obtained (which should be large enough to accept mode spreading due to wavelength chirp).

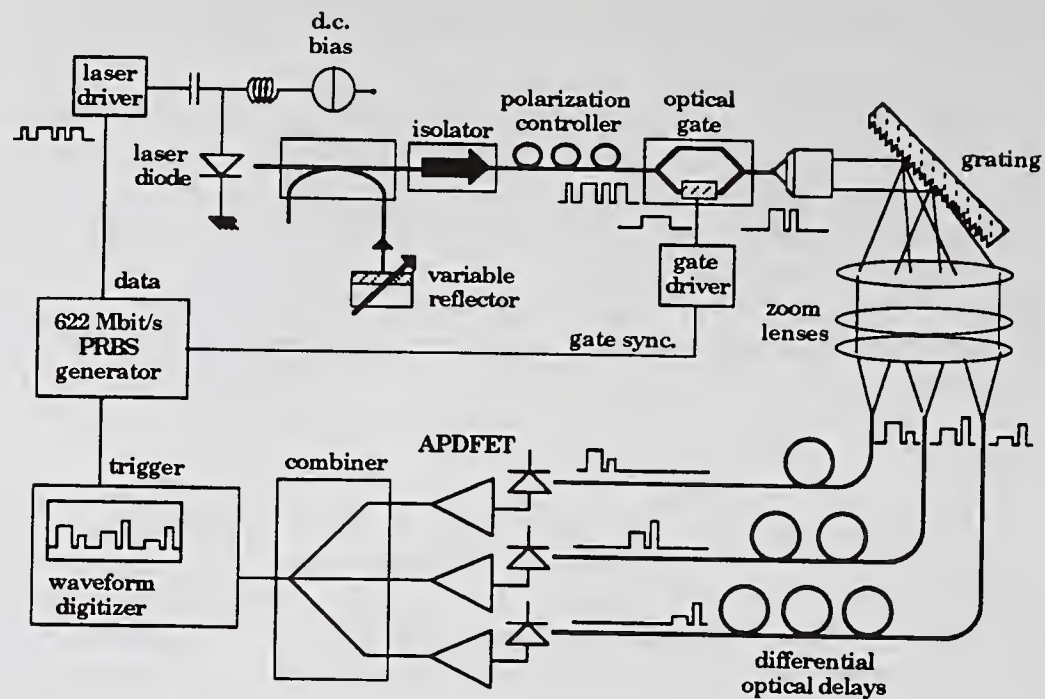


Fig.1 - Experimental set-up

At each fibre input in the array, the same (gated) pulse sequence, with different wavelengths, is present simultaneously; to avoid the need of multichannel waveform acquisition, the fibre lengths in the array are different, such that the differential delay (one gating period plus a guard interval of 2 ns) allows to detect the same sequence at different wavelengths, without overlapping. After detection and amplification by low noise APDFET receivers, the pulse sequences are electrically combined and then displayed by a single channel waveform digitizer (Tektronix 7912AD), operating in single shot mode; the simultaneous temporal evolution of the 5 observed modes, inside the 8 ns gate period, is then displayed in a single sweep of the digitizer; due to the synchronous operation of the data and gate generator circuitry, the laser spectral behaviour corresponding to any particular data sequence in the PRBS stream can be observed. The waveform digitizer is then connected to a workstation, to performs data acquisition and processing. Multiple acquisitions can be carried out in a relatively short time (400 ms/sweep), allowing a further statistical analysis of the measurement data.

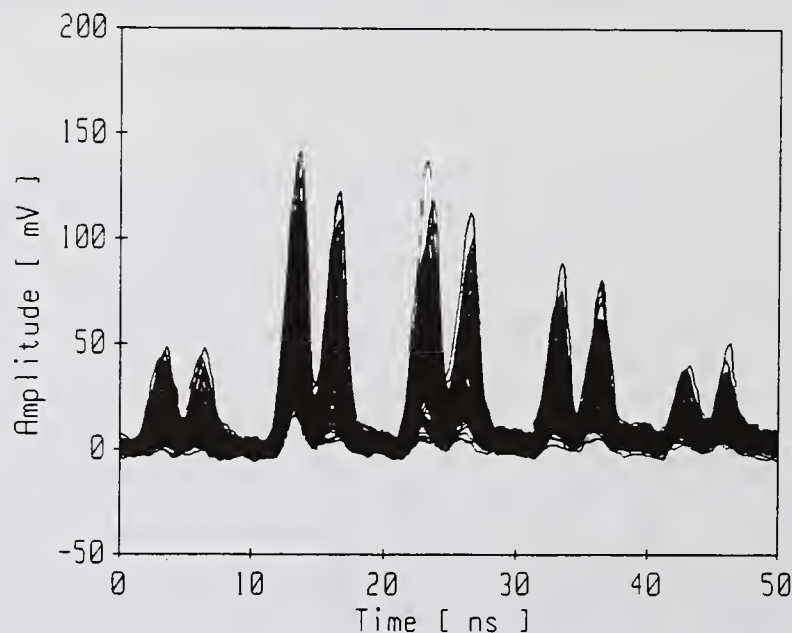


Fig.2 - Waveforms acquired in 100 consecutive sweeps, corresponding to a 01010 bit sequence extracted from a $2^{15}-1$ bits long PRBS

The overall bandwidth of the receiver and digitizing system is higher than 500 MHz, thus allowing the observation of very fast amplitude fluctuations; the waveforms acquired in 100 consecutive sweeps, corresponding in this particular case to a 01010 bit sequence extracted from the $2^{15}-1$ bits long PRBS, are displayed in figure 2; these data are then corrected for the gate and receiver pulse responses, (previously measured using a fast DFB laser source), and the amplitude of each mode at the same instant is computed. Some optical spectra, corresponding to the peaks of the first and second "1" (upper and lower row respectively) of consecutive waveforms taken from the display of fig. 2, are shown in fig. 3.

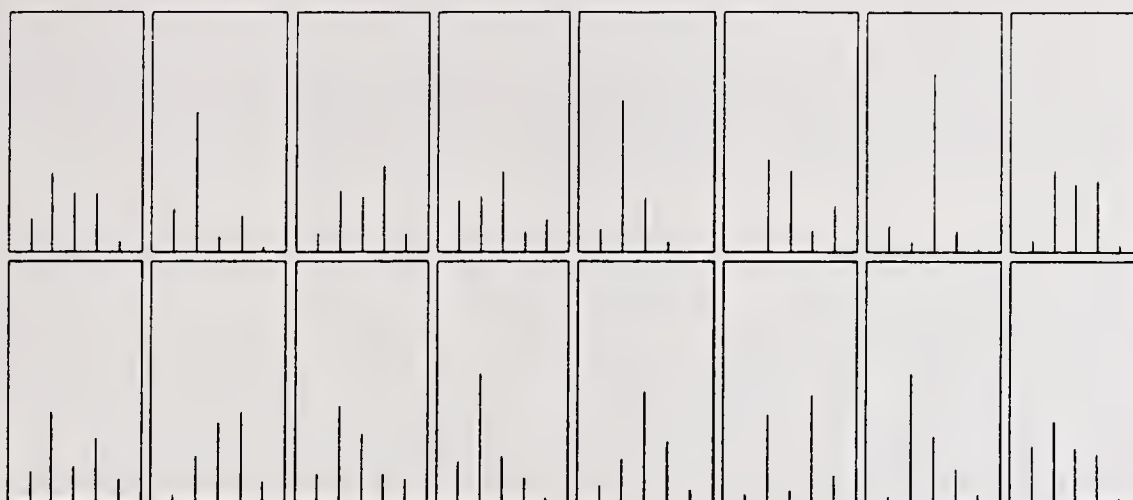


Fig.3 - Measured laser optical spectra, corresponding to mark peaks in the 01010 sequence

Repeated observations of the instantaneous spectrum allow to carry out a statistical analysis on the spectral behaviour of the laser under test; the mode partition coefficient k is then evaluated by applying (1).

It should be noted that the operation of the laser under test is not affected by the measurement procedure, nor special modulation waveforms are required; this spectral analysis could be carried out even at the output of standard optical transmitters, provided that a suitable timing signal for the gate operation is available.

Results

Different Fabry-Perot devices have been evaluated in realistic operating conditions. A commercial pig-tailed laser diode (#1) has been measured first.

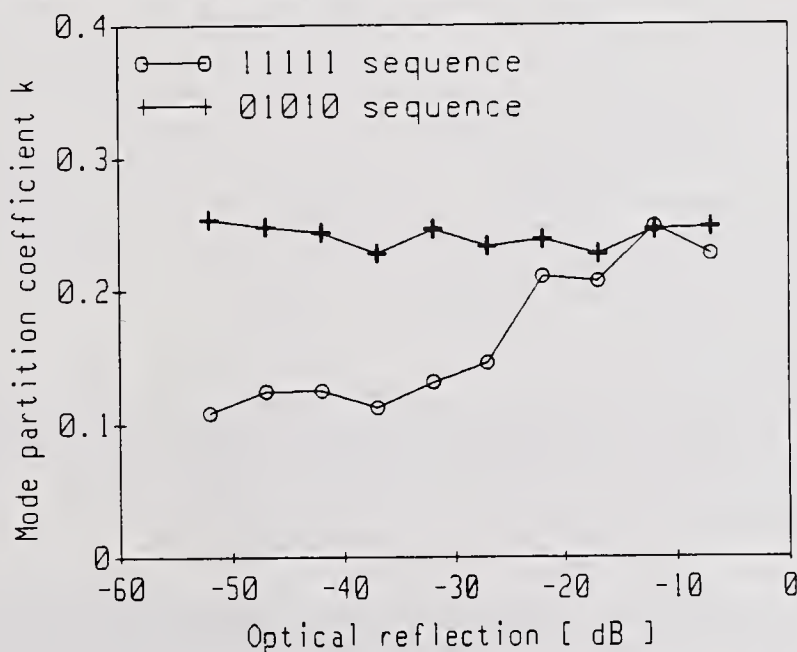


Fig. 4 - Measured values of the k parameter vs. optical reflection for laser#1, and for: a) a long sequence of marks, and b) a 01010 sequence, extracted from the PRBS pattern.

This device has a relatively narrow optical spectrum, with few significant modes. It is biased at threshold and modulated with a data stream at 622 Mbit/s; the peak-to-peak driving current is 40 mA and the peak output power is about 1 mW. The measured values of k are reported in fig. 4, as a function of the optical reflection level, corresponding to a long sequence of 1s (a) and a 01010 sequence (b), respectively, extracted from the PRBS pattern. At low reflection levels the mode partition coefficient is lower for sequence a), when the laser is kept turned on for a long time, than for sequence b), where the source is continuously switched on and off; as the reflection level increases the two curves converge to higher values of k ($0.3 \div 0.4$).

A different laser (#2), with broader spectrum, has been tested as well, with comparable results. The change of the mode partition coefficient with bias current is shown in fig. 5 for reflection values of -8 and -40 dB; as expected k increases when the laser is biased below threshold and is relatively stable above threshold. As the measurement was carried out in correspondence of many transitions, reflections have little effect on k value.

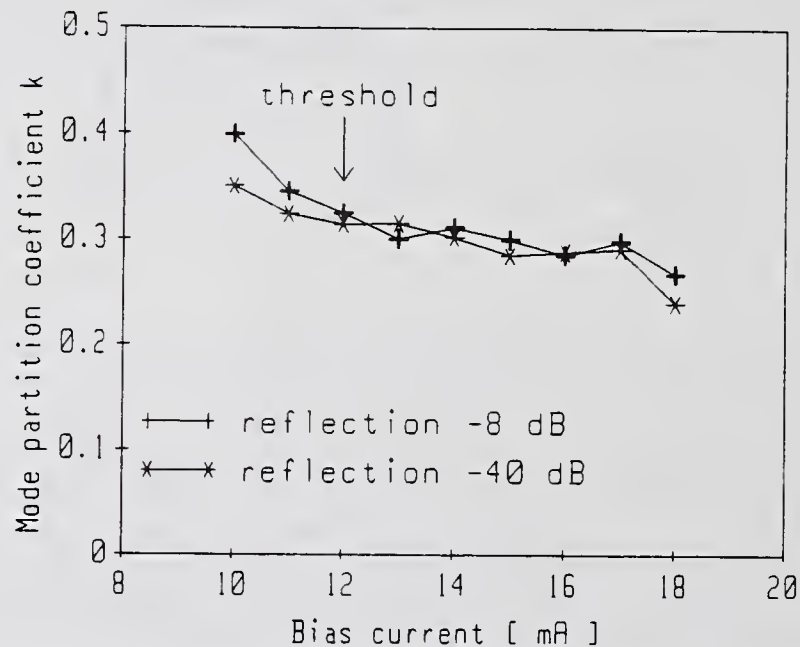


Fig. 5 - Variation of the mode partition coefficient, k , with the bias current of laser #2

Conclusions

A specialized set-up for the real time measurement of the instantaneous spectrum of a laser diode, operating in realistic modulation conditions and in presence of optical reflections, has been developed. Statistical processing of the acquired spectra has led to the evaluation of the mode partition coefficient, k . Different multimode devices have been investigated; a strong pattern dependence of the k coefficient was found at low reflection levels, while at higher reflection levels k is less affected by data pattern.

This technique can be applied as well to investigate mode partitioning effects between the main and the highest side-modes in nominally single mode DFB laser diodes; higher dynamic range can be obtained by using EDFAs.

Acknowledgements

The authors gratefully acknowledge Dr. B. Sordo for his helpful assistance and Dr. M. Potenza for useful discussions. This work has been supported by SIP and Italtel-SIT.

References

- [1] K. Ogawa, R.S. Vodhanel - Measurement of mode partition noise of laser diodes- IEEE Journal of Quantum Electronics. Vol. QE-18, No 7, July 1982, pp. 1090,1093.
- [2] I.D. Henning, D.A. Frisch - Real time measurement of semiconductor laser spectra IEEE Journal of Lightwave Technology, Vol. LT-1, No 1, March 1983.

A COMPLETE MEASUREMENT SET FOR HIGH PERFORMANCE OPTICAL CONNECTORS

M. Bottanelli, L. Duca, S. Pitassi

SIRTI S.p.A., Cables and Optical Technologies,
Via G. Vida 19, 20127 Milano, ITALY

ABSTRACT

This paper illustrates how to assemble and characterize high performance connectors by means of a complete measurement set on connector parts and mounted connectors. Some of these measurements are known and are reported here for completeness only, while other ones are new or very little experimented.

INTRODUCTION

The development of optical telecommunication systems has a strong impact in the implementation of very accurate and effective optical passive components. In recent years, the growing of the [bit rate] \times [distance] product towards higher and higher values has forced connector manufacturers to improve dramatically the quality of their products.

Nowadays, a good single-mode optical connector ensures less than 0.2 dB insertion loss and more than 40 dB return loss. High performances can only be obtained by a perfect matching between the two fibers involved in the connection. Sub-micrometric precisions are therefore required in measuring and mounting the main parts of connectors, and manufacturers need the availability of fast, high precision measuring set-ups.

Figure 1 shows the scheme of a modern cylindrical single-mode interconnection [1]. Two fibers are inserted and glued into two ferrules and polished to obtain high quality end surfaces. The two ferrules are then coupled into an alignment sleeve and pushed axially one against the other by the action of two calibrated springs. In this situation, the transverse offset between the fiber cores, being the main cause of loss, is due to the composition of the following parameters:

- the eccentricity between the fiber core and the fiber cladding;
- the clearance between the fiber cladding and the ferrule hole;
- the eccentricity of the ferrule hole.

Additionally, the transverse offset between the top of the ferrule end face convexity and the theoretical axis of the connection is another contribution to the global transverse offset. This convexity is a necessary result of the polishing procedure to improve the physical contact between the fibers.

FIBER GEOMETRICAL PARAMETERS AND MEASUREMENTS

For connector manufacturers, the cladding diameter and the core-cladding concentricity error are the main geometrical parameters of a fiber. In 1989, the First International Fibre Geometry Round Robin [2] suggested a $125 \pm 1 \mu\text{m}$ and $0.5 \mu\text{m}$ upper limit respectively as the future target specifications for these parameters; but it also showed high interlaboratories measurement sigma and a substantial need for calibration and transfer standards. Recent years researches are giving interesting results especially in the field of calibration standards ([3], [4], [5]), while it has not been yet determined the best measurement method among the possible ones. Recently, the "Gray Scale" method, which uses incoherent illumination, video microscopy and image digitalization, seems to receive manufacturers' attentions, especially because of its intrinsic simplicity and usefulness. Figure 2 illustrates, for instance, a reproducibility test for a Gray Scale set-up, calibrated by a high precision reticle, with very good result obtained in a short measuring time. At present, the Gray Scale method is classified among the CCITT alternative test methods, even without the approval of specific algorithms [6], waiting for the results and suggestions of the next CCITT Fibre Geometry Round Robin. In the meantime, Gray Scale method, contact micrometry, manual selection of the ferrule with respect to fiber diameter and autocentering epoxy resins are simultaneously used to limit the effect of the clearance between the fiber cladding and the ferrule hole, while the current quality of the fibers ensures fiber core-cladding concentricity error mean value of about $0.3 \mu\text{m}$.

FERRULE GEOMETRICAL PARAMETERS AND MEASUREMENTS

Many ferrule geometrical parameters may be considered, but only a few ones are really important because of their direct impact on the optical performances of connectors; among these the outer diameter, the hole diameter

and the hole eccentricity are the most important ones.

A large difference between the two ferrule outer diameters may not only influence the global transverse offset in a connection, as stated above, but also increase dramatically tilt angle losses by widening the alignment sleeve in a non uniform way. For such reasons, a tight tolerance of $\pm 0.5 \mu\text{m}$ on the nominal value is nowadays recommended for this parameter. Figure 3 illustrates a fast and effective optical set-up for ferrule outer diameter measurement. The ferrule is held by a precision mandrel, turned around its axis and shifted forward and backward in the light band of a laser scanning gauge by micropositioning motors. A whole accurate mapping of the ferrule cylinder can thus be obtained in a very short time. Figure 4 illustrates a reproducibility test for this set-up, considering the maximum ferrule outer diameter only.

In measuring ferrule eccentricity, the main difficulties consist in the ratio of 1 to about 20 between the hole and the ferrule diameter, and their different focal planes due to the frontal chamfering. Many different methods have been proposed to overcome these difficulties ([7], [8], [9], [10]), but nowadays it seems to be impossible to obtain good resolution measurements without turning the ferrule around its axis. Figure 5 shows the scheme and the principle of an optical set-up for ferrule eccentricity and hole diameter measurement. The ferrule hole is back-lighted, the ferrule is turned six times on a V-groove and the spot projected by the hole is taken for each of the different positions. The hole diameter is the mean value of the six spot diameters; the eccentricity is the radius of the circumference fitting the six spot centers. Figure 6 illustrates a reproducibility test for this set-up, with very good results.

GEOMETRICAL PARAMETERS OF POLISHED FERRULES AND RELEVANT MEASUREMENTS

The optical parameters and the stability of the PC (Physical Contact) connection between two mated ferrules, polished in the convex shape, mainly depends on three geometrical parameters ([11], [12]):

- eccentricity between the top of the ferrule end face convexity and the ferrule axis (convexity vertex eccentricity);
- fiber withdrawal with respect to the spherical surface best fitting the ferrule end face;
- curvature radius of the ferrule end face;

Such three parameters are subjected to some restrictions in order to preserve the PC of the fibers. In fact, if two ferrules with high convexity vertex eccentricity are connected to each other, the fiber ends could be separated by an extra gap above the fiber withdrawals, resulting in poor return loss and insertion loss performances. Besides the geometrical parameters of the ferrule, however, the quality of the PC strongly depends on the compression forces between the fibers and the elasticity characteristics of the ferrule material.

Both mechanical and optical methods can be used to control those geometrical parameters. The vertex eccentricity can be measured by a Michelson interferometer supported by a signal controller processing the image of the interference patterns. The most important source of inaccuracy is the angular offset between the ferrule axis and the interferometer axis. This error can even introduce a measurement variability of a few tens of microns (a typical vertex eccentricity mean value is about $20 \mu\text{m}$). If the ferrule axis and the interferometer axis are parallel, the geometrical locus described by the center of the fringes with the rotation of the ferrule is a circumference centered on the ferrule axis. The radius of this circumference is the vertex eccentricity: in other words, the vertex eccentricity measured value is the same for every angle of rotation. Let's suppose that the ferrule has its axis tilted of an angle δ in comparison with the interferometer axis. From simple geometrical considerations, the locus of the center of the fringes, obtained by rotating the ferrule, is an ellipse with the center shifted of a quantity $R \cdot \sin \delta$ with respect to the fiber center (R being the curvature radius of the ferrule end face). Because of the small value of δ , the ellipse can be approximated with a circumference whose radius represents the vertex eccentricity without angular errors. Following these considerations, a measurement set-up based on a Michelson interferometer has been developed by which it is possible to turn the ferrule around its axis, to determine the convexity vertex positions and to fit them with a circumference. The radius of this circumference is the real vertex eccentricity. This procedure improves measurement accuracy above $2.5 \mu\text{m}$. Figure 7 shows a final plot for a vertex eccentricity measurement: the biggest circumference is the fiber, while the smaller one is the circumference fitting three different convexity vertex positions for three

different rotations of the ferrule.

Fiber withdrawal and ferrule end face curvature radius can be measured by a mechanical contact profilometer. The measurement cord, followed by the sensitive pick-up, is usually 500 μm long. Figure 8 shows the typical transverse profile of a ferrule end face after polishing procedure: the irregular line is the surface profile along the measurement cord, while the straight line is its mathematical average; the fiber end face is about 0.04 μm above this line. Withdrawals lower than 0.1 μm are necessary for optimum return loss performance.

CONCLUSIONS

The main geometrical parameters of cylindrical optical connectors and a complete measurement set on these parameters have been described from the connector manufacturer's point of view. Less than 0.2 dB insertion loss and more than 40 dB return loss can be obtained by few, fast and very effective measurement set-ups.

ACKNOWLEDGEMENTS

We would like to thank U. Rossi and E. Serafini for their invaluable remarks and suggestions.

REFERENCES

- [1] M. Bottanelli, E. Serafini
MISURA DEI PARAMETRI GEOMETRICI
DI CONNETTORI OTTICI CILINDRICI
Atti del 2° Convegno Nazionale
"Strumentazione e Metodi Ottici"
- Firenze (ITALY) - 25÷27 May
1992 - pp. 281÷284
- [2] J. G. N. Baines, A. G. Hallam, K.
W. Raine, N. P. Turner
FIBER DIAMETER MEASUREMENTS AND
THEIR CALIBRATION
Journal of Lightwave Technology,
vol. 8, No. 9, September 1990,
pp. 1259÷1267
- [3] W. T. Kane
THE FIRST INTERNATIONAL FIBRE
GEOMETRY ROUND ROBIN
Optical Fibre Measurement
Conference - York (UK) - 17÷18
September 1991 - Conference
Digest - pp. 119÷122
- [4] M. Young
FIBER CLADDING DIAMETER BY
CONTACT MICROMETRY
Optical Fibre Measurement
Conference - York (UK) - 17÷18
September 1991 - Conference
Digest - pp. 123÷126
- [5] A. Collyer, K. W. Raine, J. G. N.
Baines
INVESTIGATION INTO THE USE OF A
SCANNING CONFOCAL MICROSCOPE AS A
PRIMARY MEASUREMENT METHOD FOR
DETERMINING OPTICAL FIBRE
DIAMETER
Optical Fibre Measurement
Conference - York (UK) - 17÷18
September 1991 - Conference
Digest - pp. 143÷146
- [6] CCITT TEMPORARY DOCUMENT 39
(XV/5)
Geneva - 4÷15 May 1992 - Report
of the expert meeting on Q.11/XV
- pp. 1÷2
- [7] G. Warnes, C. A. Millar
A STUDY OF CORE CONCENTRICITY
ERROR MEASUREMENTS
- SPIE vol. 468 - Fibre Optics
'84 (Sira) 1984 - pp. 138÷144
- [8] T. Tanabe, A. Ushirogawa, M.
Takashima
HIGHLY ACCURATE MEASURING
EQUIPMENT FOR THE OPTICAL
CONNECTOR FERRULE
Measurements, vol. 4, No. 1,
Jan.-Mar. 1986, pp. 23÷27
- [9] Z. Pasturczyk, B. Wong, C.
Saravanos
FIBER OPTIC CONNECTOR GEOMETRY
TEST STATION
International Wire & Cable
Symposium Proceeding 1989, pp.
683÷626
- [10] M. Ueki, Y. Hattori
ACCURATE MEASUREMENT OF
STRUCTURAL PARAMETERS OF SINGLE
FIBER CONNECTOR FERRULE
OFC '91 - Thursday, February 21,
p. 137
- [11] T. Shintaku, R. Nagase, E. Sugita
CONNECTION MECHANISM OF PHYSICAL-
CONTACT OPTICAL FIBER CONNECTORS
WITH SPHERICAL CONVEX POLISHED
ENDS
Applied Optics, vol. 30, No. 36,
December 1991, pp. 5260÷5265
- [12] Z. Pasturczyk, T. Chepyha, C.
Saravanos, H. Wood
TEST METHOD FOR FIBER OPTIC
CONNECTOR PARAMETERS DIRECTLY
AFFECTING RETURN LOSS
Symposium on Optical Fiber
Measurements, 1990 - Technical
Digest - NIST Special Publication
792 - pp. 163÷166

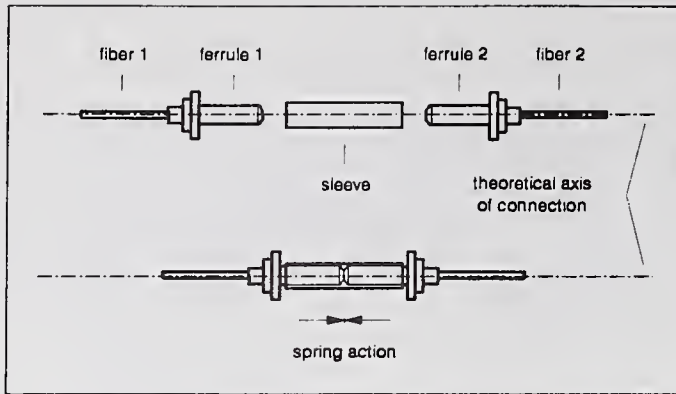


Fig. 1 - Scheme of a modern cylindrical single-mode interconnection

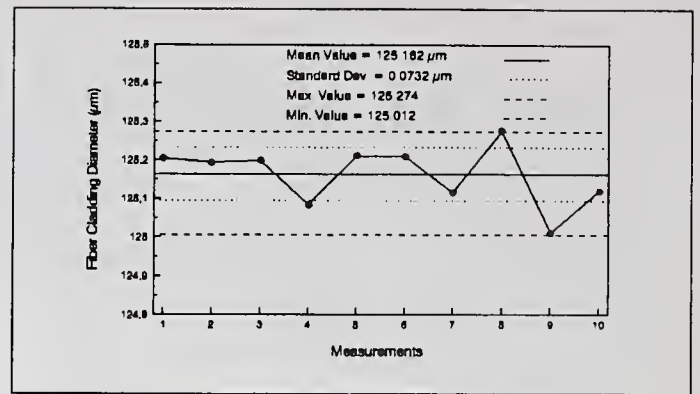


Fig. 2 - Reproducibility test for a Gray Scale optical set-up

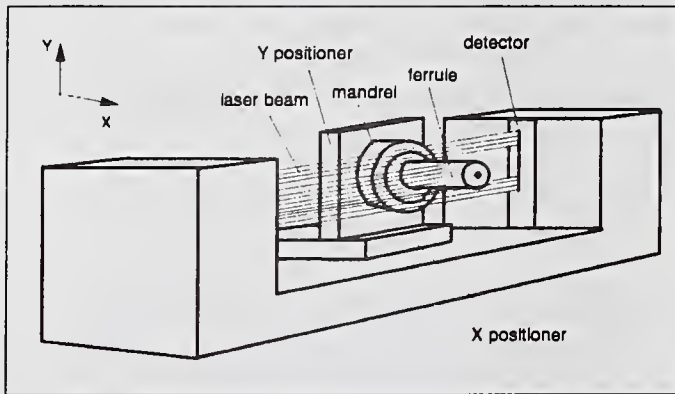


Fig. 3 - Scheme of a set-up for ferrule outer diameter measurement

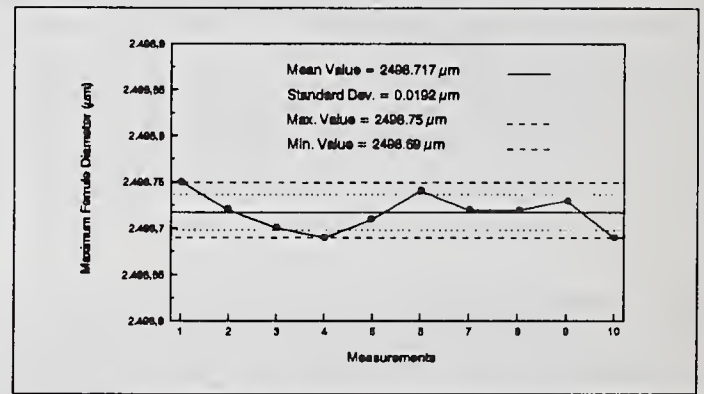


Fig. 4 - Reproducibility test for the measurement set-up showed in fig. 3

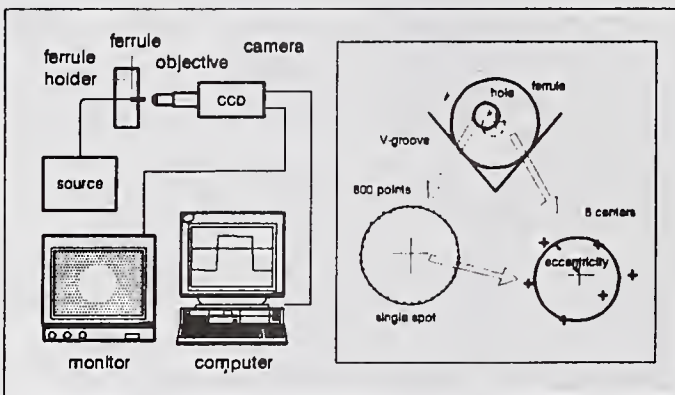


Fig. 5 - Scheme and principle of an optical set-up for ferrule eccentricity and hole diameter measurement

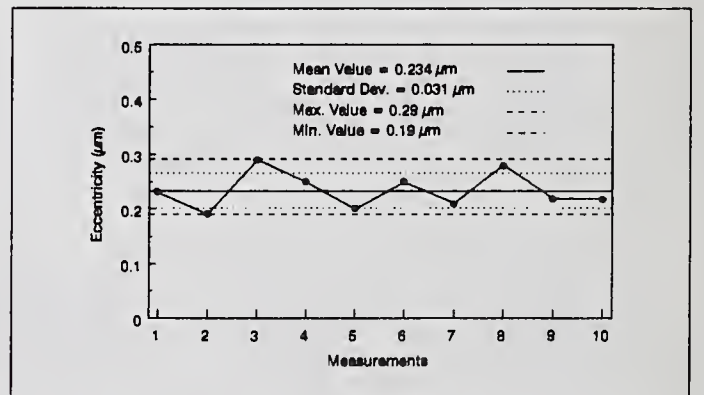


Fig. 6 - Reproducibility test for the measurement set-up showed in fig. 5

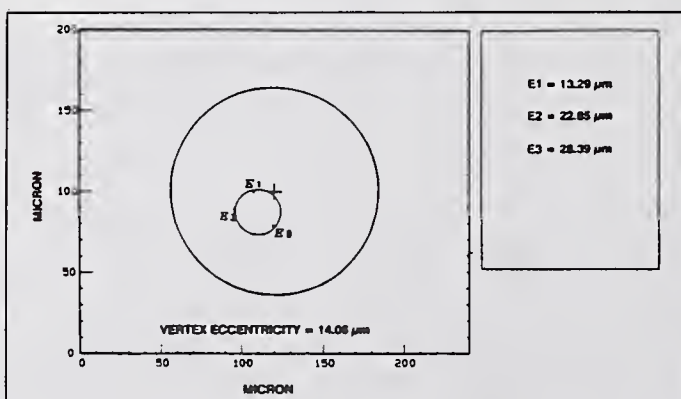


Fig. 7 - Final plot for a convexity vertex eccentricity measurement

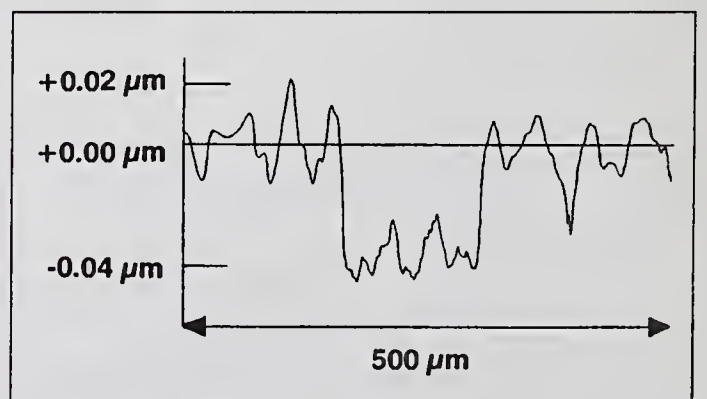


Fig. 8 - Typical transverse profile of a ferrule end face after polishing procedure

A SIMPLE AND ACCURATE HETERODYNE TECHNIQUE FOR THE CHARACTERIZATION OF ACTIVE AND PASSIVE NARROWBAND OPTICAL FILTERS

N. Caponio, P. Gambini, R. Hui, M. Puleo, E. Vezzoni

CSELT - Centro Studi E Laboratori Telecomunicazioni S.p.A.
Via G. Reiss Romoli, 274
10148 TORINO - ITALY

ABSTRACT

An effective technique has been developed to characterise the spectral transmission of narrowband (\approx GHz) fiber-coupled optical filters, both passive and active. The measurement principle is based on optical heterodyne detection of the emission of a frequency-swept source, passing through the filter under test. This allows the straightforward and accurate identification of the sweep frequency.

INTRODUCTION

High density wavelength division multiplexed (HDWDM) optical transmission systems, operating with channel spacings in the order of a few tens GHz or less, result in the efficient exploitation of the wide transmission bandwidth available in single mode optical fibres [1]. Channel selection can be performed directly in the optical domain by means of an optical filter, followed by a direct detection receiver. Passive tunable filters based on Fabry-Perot or Mach-Zehnder interferometers have been proposed and used, as well as active tunable filters based on DFB or DBR structures [2].

The precise knowledge of the shape of the filter transmission curve is essential for an accurate design of the receiver and for system performance evaluation. To characterise the transmission curve of these narrow-bandwidth filters, conventional grating spectrometers cannot be used, due to their limited resolution. A usual technique is based on sweeping the optical frequency of a single wavelength, narrow-linewidth laser source across the wavelength range of interest, and on measuring the transmitted power after the filter. Yet, when a laser diode is used as a current-tunable source, the relationship between emission wavelength (or frequency) and injection current is usually unknown and nonlinear, and therefore an in-line frequency monitor with sub-GHz resolution (etalon, wavemeter...) has to be used, to scale the optical frequency.

In this paper an alternative and effective technique for the accurate spectral characterisation of optical narrowband filters, allowing direct frequency reading, is proposed and demonstrated; experimental results for narrowband (\approx GHz) passive Fabry-Perot and active DFB filters are presented.

PRINCIPLE OF OPERATION AND EXPERIMENTAL SET-UP

Fig. 1 shows a schematic of the measurement set-up that has been implemented; two narrow linewidth, wavelength matched and temperature controlled DFB lasers are biased with low noise current generators. Their emission is fed to a 2x2 fibre coupler; high performance optical isolators are used to prevent spectral instabilities due to backreflections. The emission wavelength of laser #1 is fixed, while a sawtooth

modulation current is fed to laser #2, resulting in a swept emission wavelength. The device under test (i. e. the filter) is inserted between laser #2 and the corresponding input branch of the coupler. The transmission response of the filter (i.e. the amplitude vs. frequency information) is simply obtained from the beat signal at the output of the photodiode, displayed by means of a RF spectrum analyser (SA). A fiber polarisation control is used to match the state of polarization of the two fields on the photodetector, to achieve the maximum heterodyne detection efficiency. Although it could be possible to synchronize the start of the sweep of the SA and of the DFB laser frequency, it would be however difficult to have an exact time coincidence of the beat frequency and of the SA central frequency, due to the above mentioned DFB nonlinear frequency vs. current behaviour. For this reason we have chosen two very different sweep times for the SA (τ_{sa}) and for the laser frequency (τ_l). Two choices are possible: either $\tau_{sa} \gg \tau_l$ or $\tau_{sa} \ll \tau_l$. In both cases the ratio between τ_{sa} and τ_l should be much larger than the number of points to be displayed on the SA screen (typically 801). In the second case the SA is used in the "peak-hold" mode. We usually adopt the first approach as it gives cleaner traces, not being subject to the "worst case" noise.

In the present set-up the beat linewidth of the sources exceeds the SA resolution bandwidth (3 MHz), causing a signal decrease. The use of very narrow linewidth lasers [3], would easily overcome this problem.

To calibrate the measurement set-up, the small power and linewidth variations due to the DFB laser current sweep and the frequency response of the set-up are obtained in a separate measurement, bypassing the filter.

The upper limit to the optical frequency span depends on the laser tuning characteristics and on the frequency response of the spectrum analyser and photodetector. In the present set-up it is limited to 22 GHz (≈ 0.2 nm at $1.55 \mu\text{m}$) by the SA. If necessary, this limitation can be overcome by performing different measurements in different, adjacent windows; this can be simply obtained by step tuning the source wavelengths adjusting their temperatures. In this way the tuning characteristic and the spectral response of three-electrode DFB filters has been measured over more than 60 GHz.

The sensitivity of the measurement is mainly limited by the thermal noise of the receiver and spectrum analyzer. It could be improved, if required, by a lock-in technique, as described in [4]; chopping the "local oscillator" beam would eliminate the spontaneous emission noise, in the case of active filters.

It must be noted that the main advantage of this technique is the accurate determination of the frequency, which results in the accurate evaluation of the lineshape of the filter under test.

EXPERIMENTAL RESULTS

Figure 2 shows the measured transmission characteristic of a Fibre Fabry-Perot filter (FWHM width: 2.9 GHz), resulting in a regular, symmetrical response. Fig. 3 refers to the transmission characteristic of a bulk-optics fiber-coupled tunable etalon, which, suffering from spurious reflections at the interfaces, gives a highly distorted shape.

The measurement of active filters is performed inserting a variable optical attenuator and another polarization control before the filter in the set-up. Fig. 4 shows the spectral gain characteristic of a Distributed FeedBack (DFB) laser amplifier (FWHM width: 5.1 GHz), biased just below the lasing threshold. The shape is asymmetrical, as predicted by theory for moderate input powers.

CONCLUSIONS

In conclusion, a simple and accurate technique for the characterisation of narrowband optical filters, based on optical heterodyne detection of a frequency-swept source, has been demonstrated. This approach allows an easy identification of the (relative) sweep frequency by the RF spectrum analyser, which results in the precise

evaluation of the filter transmission shape. Both passive (Fabry-Perot) and active (DFB lasers biased below threshold) filters have been characterized.

ACKNOWLEDGEMENTS

This work has been partially supported by SIP and Italtel.

REFERENCES

- [1] H. Toba, K. Oda, K. Nakanishi, N. Shibata, K. Nosu, N. Takato, M. Fukuda, "100-channel optical FDM transmission/distribution at 622 Mbit/s over 50 km", Proc. OFC'90, paper PD1, 1990
- [2] G. Magari, H. Kawaguchi, K. Oe, Y. Nakano, M. Fukuda, "Optical signal selection with a constant gain and gain bandwidth by a multielectrode distributed feedback laser amplifier", Appl. Phys. Lett., Vol. 51, No 24, pp. 51-52, 1987
- [3] J. Charil, A. Ougazzaden, J.C. Bouley, H. Nakajima, A. Gloukhian, J. Landreau, A. Mircea, "Sub-MHz spectral linewidth in 1.5 μm strained quantum well DFB BRS LDs", Proc. 17th ECOC - 8th IOOC, pp. 641-644, 9-12 sept. 1991
- [4] M. Puleo, P. Gambini, E. Vezzoni, "Characterisation of laser diode intensity noise at microwave frequencies with high sensitivity", SPIE Vol. 1175, Coherent Lightwave Communications, pp.24-32, 1989

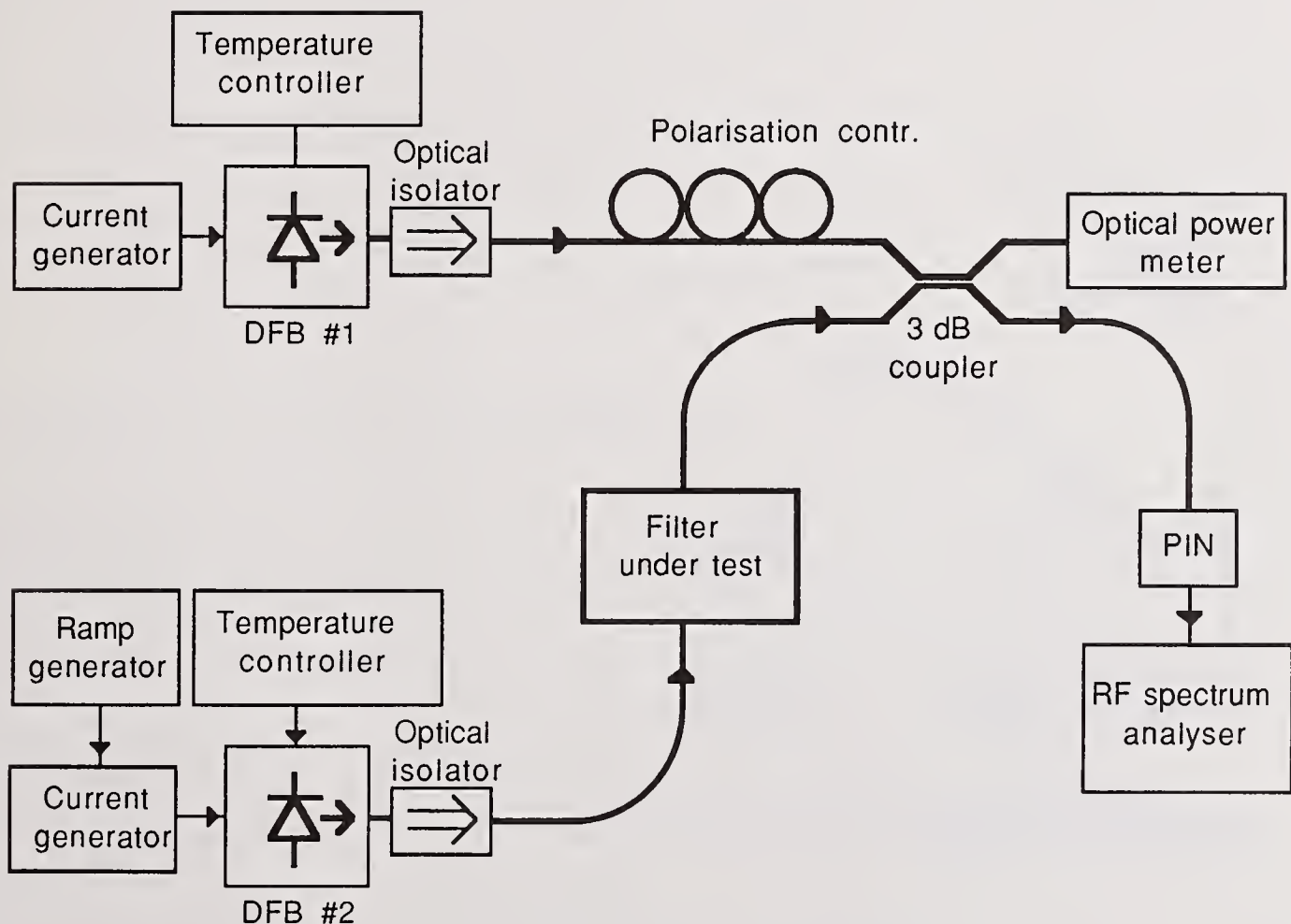


Fig. 1: Experimental set-up for the characterisation of narrowband optical filters.

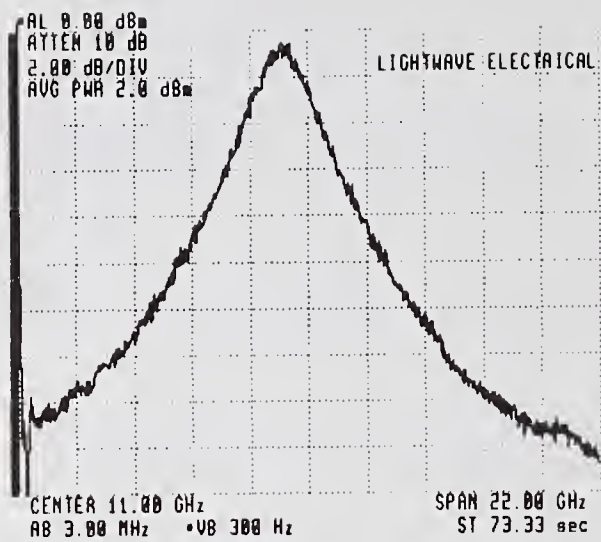


Fig. 2: Measured transmission characteristic of a fiber Fabry-Perot filter.

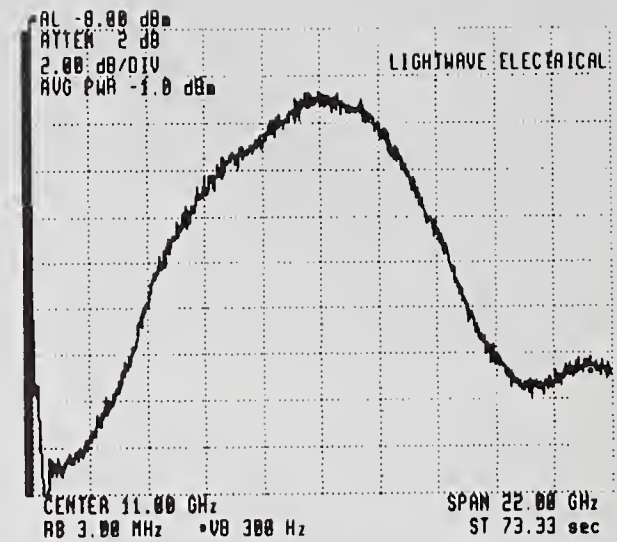


Fig. 3: Measured transmission characteristic of a fiber coupled bulk-optics Fabry-Perot etalon.

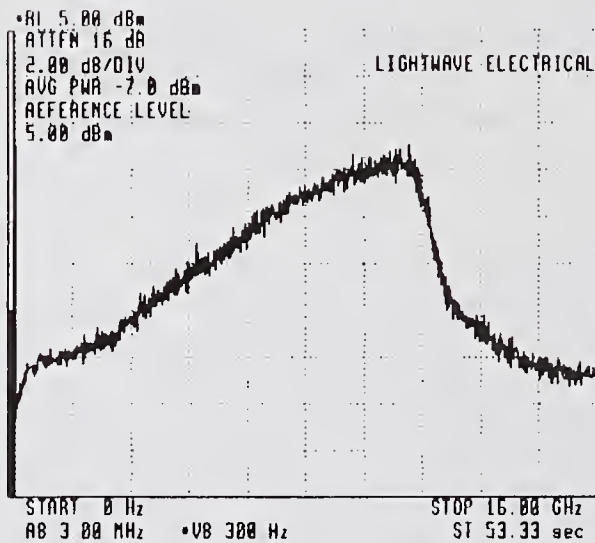


Fig. 4: Measured transmission characteristic of a DFB filter/amplifier.

An Automated Method for Measuring The Radius of Curvature of An Optical Fiber

A. L. Ingles
AT&T Network Systems
Norcross, GA

INTRODUCTION

An uncoated, unconstrained length of optical fiber can have sufficient curvature to cause alignment problems in automated mass fusion splicing equipment. The mass splicing techniques, which require the simultaneous alignment of as many as 24 fiber ends (12 splices), can tolerate limited offset between fiber ends. This paper describes a system for use in factory production which quickly and accurately measures the radius of curvature of a fiber, from which the maximum offset at any length can be calculated.

DESCRIPTION OF THE METHOD

Typically, a mass fusion splicer has an unconstrained distance of about 3 mm and can tolerate a fiber end which is offset about 3.5 microns from where a perfectly straight fiber would be. By accurately determining the radius of curvature of the fiber, we can insure this condition is met. The technique is to measure the fiber's offset from a straight line at a point 20 mm from where the fiber becomes unconstrained. The principle of the method is shown in Figure 1. By rotating the fiber 360 degrees and viewing the fiber transverse to the axis of rotation, the maximum offset y is obtained. The radius of curvature of the fiber (R) is then

$$R = (x^2 + y^2) / (2 * y) . \quad (1)$$

DESCRIPTION OF THE HARDWARE IMPLEMENTATION

The system consists of a computer, a CCD camera, a light source, a stepping motor, and a fixture to hold the sample. A diagram of the system is shown in Figure 2. A fixed ceramic ferrule with an inside diameter of 127 microns is used to hold the fiber during rotation. The fiber sample, 6 inches long with 4 inches of coating mechanically removed, is inserted into the end of the ferrule. The sample is then rotated one full revolution stopping every 9 degrees to analyze a backlighted transverse image of the uncoated fiber at a distance, $x=20\text{mm}$, from the point where the ferrule allows the fiber to bend freely.

Precision fiber centers obtained from the analysis represent a series of y values. The set of fiber centers is analyzed in two ways.

First a simple calculation of one half the separation of the highest and lowest center positions is the offset, y , in equation 1 above. Also, y is obtained by fitting a sine wave to the centers. Very little difference has been observed between the two methods.

The computer controls the stepping motor and analyzes the video image. A video frame memory card is used to capture the images from the camera. Sample preparation and insertion takes about 20 seconds while the rotating and analysis take 10 seconds.

ACCURACY AND REPEATABILITY

Ideally a measurement system should have accuracy and repeatability a factor of 20 smaller than the the limit or range of interest. In this case, we want to insure that the offset is less than 3.5 microns at 3 mm, so we need accuracy and repeatability to be less than $\pm .175$ microns at 3 mm.

The magnification of the video imaging system and the distance from the end of the ferrule to the point of measurement are the two parameters which must be accurately set and maintained to insure an accurate measurement. Methods have been developed to insure that both of these requirements are met.

To determine the magnification of the system a stage micrometer is scanned and analyzed with a computer program. The error associated with this determination of the magnification is $\pm .16$ %, so that an offset of $y = 10$ microns would have an uncertainty of $\pm .016$ microns. This equates to an uncertainty at 3 mm of $\pm .00036$ microns.

To set the measurement distance, a special calibration rod has been fabricated. The rod, which has a small transverse hole in it, is inserted into the fixture at the opposite end from the ferrule. The end of the rod touches the end of the ferrule and the hole is located $20 \pm .01$ mm from the end of the rod. The fixture is adjusted so that the hole is in the center of the video image. This is accurate to better than ± 10 microns, which can contribute $\pm .040$ microns maximum error in the offset at 20 mm. At a distance of 3 mm from the end of the ferrule this equates to $\pm .0009$ microns, which is insignificant. Adding these two sources of error we get a total $\pm .0013$ microns of uncertainty. This is well within our desired limits.

An experiment was performed to determine the measurement repeatability. Twenty five samples were measured on the test system and then retested. Figure 3 shows the data in a control chart format.

From these results the one sigma error of measurement is calculated to be +/- 1.28 microns offset for a 20 mm measurement distance. Since the y^2 term in equation 1 is much smaller than x^2 , the error at 3 mm is

$$\begin{aligned} \text{error}_{3\text{mm}} &= (1.28) * (3^2 / 20^2) \\ &= .03 \text{ microns} \end{aligned}$$

Thus, in total, the three sigma uncertainty due to accuracy and repeatability is $3 * \sqrt{.001^2 + .03^2} = +/- .1$ microns.

SUMMARY

A system has been developed and implemented in production which measures fiber curvature with accuracy and repeatability sufficient to insure the desired product performance. The technique is simple and measurement time is about 30 seconds including sample preparation.

ACKNOWLEDGMENTS

I would like to acknowledge S. A. Jacobs for providing the sine wave fitting algorithm, and S. L. Pelts, J. M. Palmquist and C. L. Bice for helpful consultations.

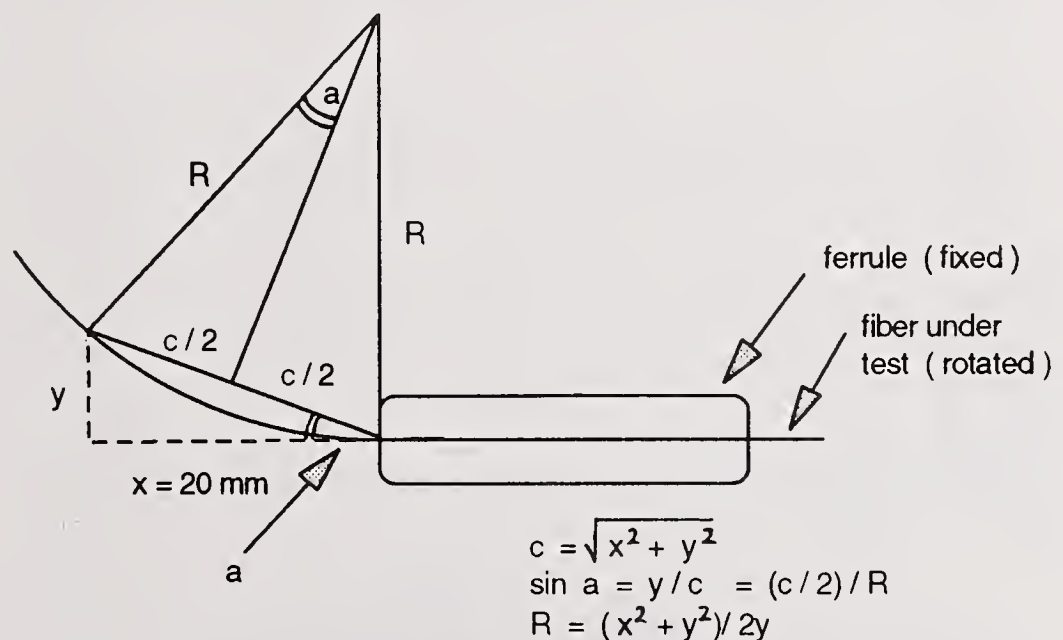


Figure 1. Measurement Method

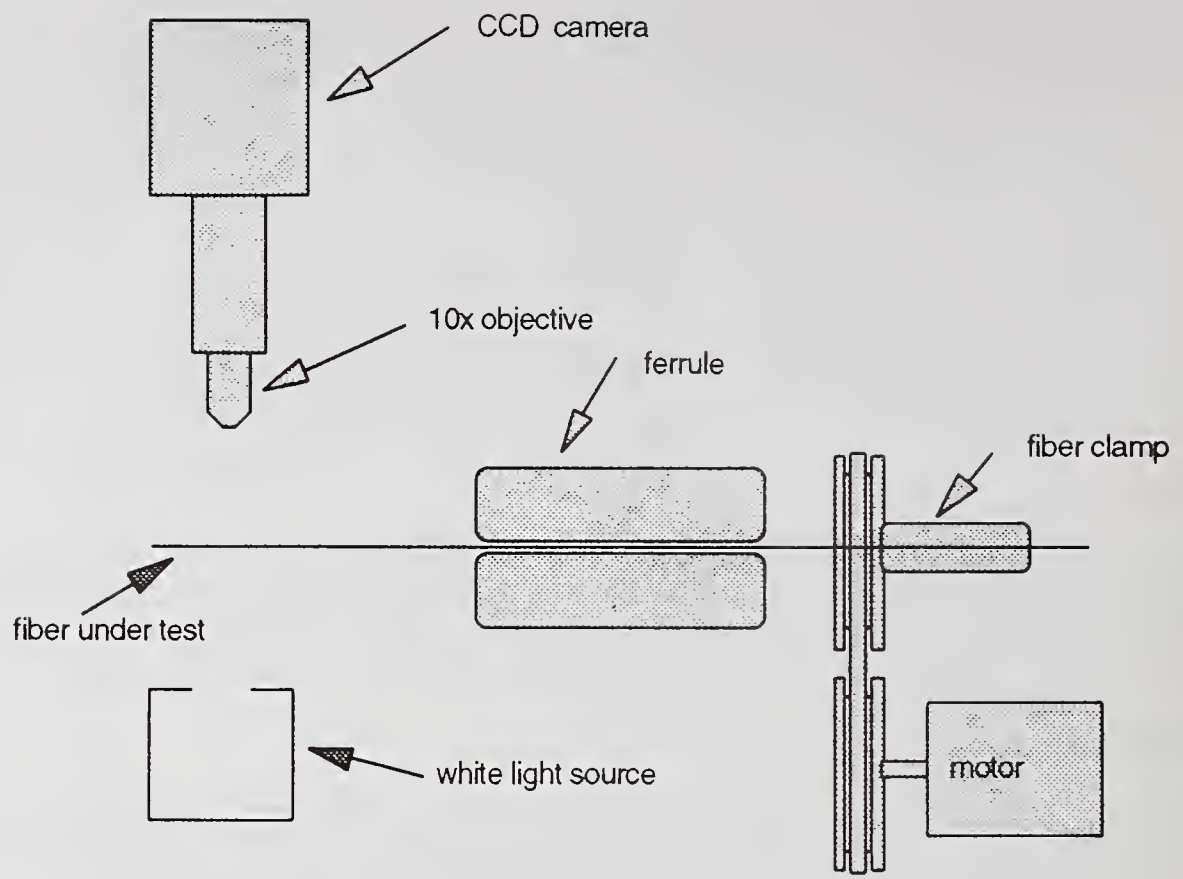


Figure 2. System Block Diagram

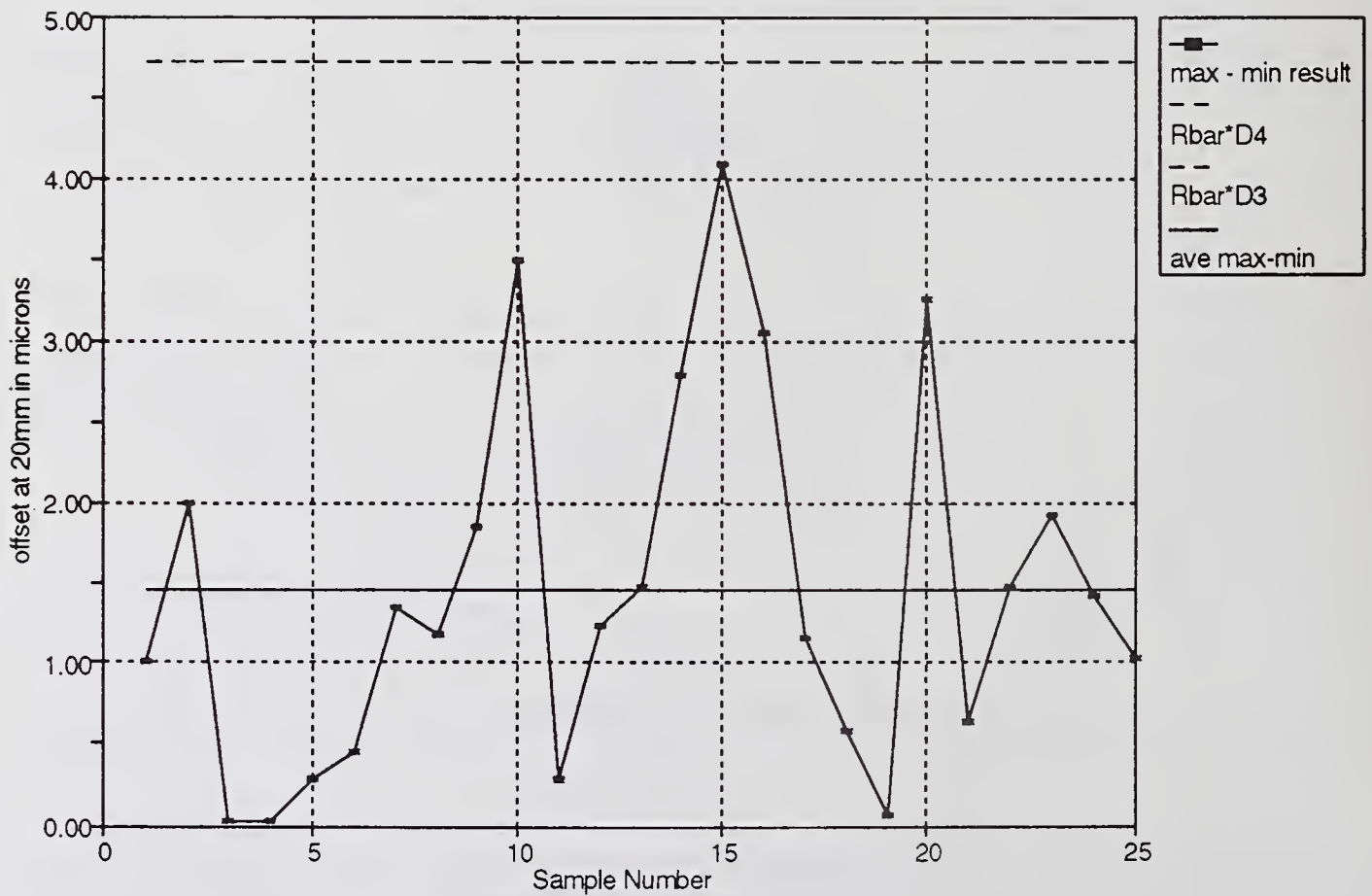


Figure 3. Range Chart

Recent Progress in Polarization Measurement Techniques

Brian L. Heffner

Hewlett-Packard Laboratories, 3500 Deer Creek Road 26M, Palo Alto, CA 94303-0867

Introduction

Attempting to measure polarization through single-mode fiber might at first seem foolish: Aside from the problem of getting the light of interest into a single-mode fiber, any real fiber will significantly transform the state of polarization (SOP) of the light passing through it, and that transformation will change as the fiber is flexed. In spite of these constraints, a fiber-based polarimeter has proven extremely useful for a wide variety of measurements. In many applications the light of interest is only available through a fiber, and many measurements are insensitive to the constant, unitary polarization transformation presented by a stationary fiber. When it is necessary to measure a SOP in an absolute coordinate system, a linear polarizer can be used to establish a known reference frame on the laboratory bench-top, in effect calibrating out the effects of the fiber to the polarimeter.

The capabilities of a polarimeter are dramatically augmented by the addition of a simple polarization synthesizer. The synthesizer allows stimulus-response measurement of devices and networks, allowing calculation of Jones matrices and complete characterization of linear, time-invariant networks. This capability, along with automated operation and fiber connectors, can make polarization measurements comparable to microwave measurements in their levels of convenience, flexibility, speed and sophistication of analysis.

Measurement of Stokes vectors

Accuracy, convenience and measurement speed are of primary importance to the usefulness of Stokes vector measurements, especially when a large number of Stokes vectors are required, for example, to characterize polarization dispersion as a function of wavelength. Measurement of a SOP is traditionally performed by rotating a waveplate and a polarizer to four pairs of angular orientations to obtain four optical intensities transmitted through the polarizer. These intensities form a vector which is linearly related to the SOP. Alternatively, by splitting the optical beam into four beams (Fig. 1), the same four optical powers can be measured in parallel through a suitable set of fixed polarizing filters, allowing measurement of the complete SOP at speeds limited only by electronic data acquisition.

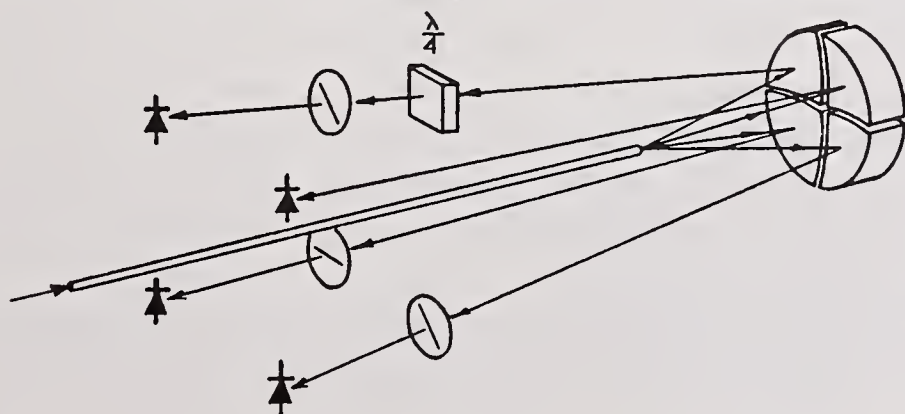


Figure 1 A four-detector polarimeter. A divided concave mirror images the output of a single-mode fiber onto four photodiodes through a set of fixed polarizing filters.

Measurement of Jones matrices

R. C. Jones gave an explicit algorithm for experimentally determining the forward transmission Jones matrix \mathbf{T} of an unknown linear, time-invariant optical device [1]. The restriction of time invariance applies only to the polarization transformation caused by the device, and does not include the absolute optical phase delay, so this technique can be used to characterize fiber networks even when the phase delay through the fiber is drifting during the measurement.

Any Jones vector \mathbf{v} can be completely specified by a magnitude, an absolute phase, and a unit vector $\hat{\mathbf{v}}$ which locates the SOP on the Poincare sphere. To measure the Jones matrix of a device, a stimulus optical field of linear polarization parallel to the x axis is first generated, and the resulting response unit vector $\hat{\mathbf{h}}$ is measured through the device. Similarly, stimulus fields of linear polarization parallel to the y axis, and parallel to the bisector of the angle between the positive x and y axes result in response unit vectors $\hat{\mathbf{v}}$ and $\hat{\mathbf{q}}$, respectively. Three complex ratios independent of the intensities of the three stimulus fields can now be formed from the x and y components of $\hat{\mathbf{h}}$, $\hat{\mathbf{v}}$, and $\hat{\mathbf{q}}$: $k_1 = \hat{h}_x / \hat{h}_y$, $k_2 = \hat{v}_x / \hat{v}_y$, and $k_3 = \hat{q}_x / \hat{q}_y$. A fourth ratio $k_4 = (k_3 - k_2) / (k_1 - k_3)$ is then found. To within a complex constant β , the transmission Jones matrix \mathbf{T} is then given [1] by

$$\mathbf{T} = \beta \begin{bmatrix} k_1 k_4 & k_2 \\ k_4 & 1 \end{bmatrix}. \quad (1)$$

Measurement of polarization-dependence of the loss through a device

The polarization dependence of the gain or loss through a DUT is often measured by monitoring the output power of the DUT with a polarization-independent detector or optical power meter while the input SOP is deliberately varied over all possible values. This technique can try the patience of the measurement technician and suffers two fundamental limitations. One is the difficulty of arbitrary SOP generation, as the control inputs to a polarization transformer do not relate to the output SOP in a simple way. Moreover, the output intensity of a SOP synthesizer is usually a weak function of the control inputs, and this variability in intensity translates directly into errors in measurement of the polarization dependence of transmission. A second, more serious disadvantage is the necessity of a search algorithm. At constant power, the state of a purely polarized source (i.e. with unit degree of polarization) has two degrees of freedom, so the synthesized SOP must be varied over a two-dimensional space while searching for the global minimum and maximum transmission. The search algorithm must not mistakenly identify local extrema of transmission as the desired global values. Other sources of error include polarization sensitivity of the power meter, unstable source amplitude or unstable device transmission, and, unless a separate polarizer is used, partial polarization of the source.

These problems yield to an efficient solution once it is recognized that the global minimum and maximum intensity transmission coefficients T_{\min} and T_{\max} through a DUT

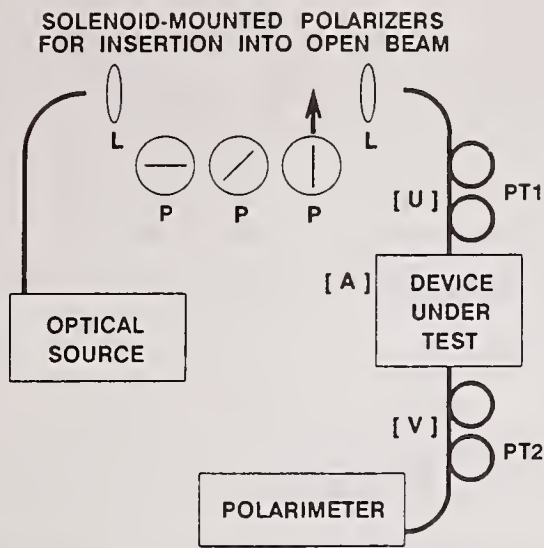


Figure 2 Apparatus used for singular value calculation of polarization-dependent transmission. L: lens; P: linear polarizer; PT: polarization transformer.

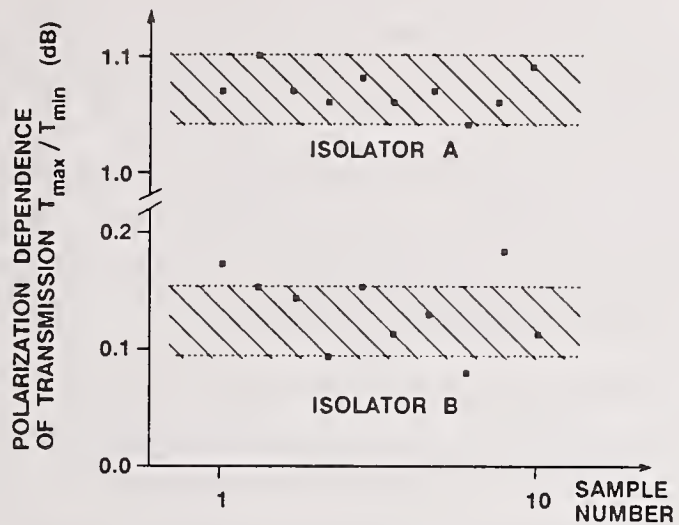


Figure 3 Measurements of two pigtailed optical isolators. Shaded areas indicate the manually measured values including uncertainty of ± 0.03 dB; plotted points are singular value measurements for different settings of PT1 and PT2.

over all SOPs can be determined without resorting to a search over polarization space. The polarization responses to only three input SOPs completely determine the polarization sensitivity of a linear, time-invariant optical device. Although not generally recognized, it can be shown [2] that T_{\min} and T_{\max} are given by the squares of the singular values of the Jones matrix associated with the DUT.

Suppose the only access to the device under test is through fiber pigtailed (Fig. 2). While direct measurement of the device matrix \mathbf{A} is then impossible, the matrix $\mathbf{B} = \mathbf{V}\mathbf{A}\mathbf{U}$, where \mathbf{U} and \mathbf{V} are unitary Jones matrices representing the pigtailed, is easily determined to within a complex scalar constant β using (1) and the method previously described. Because its loss is independent of polarization, each pigtail can be represented by a unitary Jones matrix times a scalar. Having measured $\mathbf{C} = \beta\mathbf{B}$, we can compute the singular values $s_i(\mathbf{C}) = |\beta| s_i(\mathbf{B})$. Finally, using the fact that singular values are invariant under unitary transformation, we obtain an expression for the polarization dependence of transmission in terms of the singular values of the measured Jones matrix \mathbf{C} :

$$\frac{T_{\min}}{T_{\max}} = \frac{s_1^2(\mathbf{A})}{s_2^2(\mathbf{A})} = \frac{s_1^2(\mathbf{B})}{s_2^2(\mathbf{B})} = \frac{s_1^2(\mathbf{C})}{s_2^2(\mathbf{C})} \quad (2)$$

Experimental results comparing the manual method to the singular value method for measurement of the polarization sensitivity of two optical isolators with single-mode fiber pigtailed are shown in Fig. 3. The shaded areas indicate the manually measured polarization sensitivity of the two test devices using the apparatus of Fig. 1, including a measurement uncertainty of ± 0.03 dB caused by residual polarization dependence of the power meter and slight drifts in the intensity of the polarized source. The singular value measurement

was performed ten times for each device, with both the input and output polarization transformers shown in Fig. 2 randomly reset for each of the ten measurements to present a different unitary polarization transformation before and after the device each time a Jones matrix was measured. The grouping of the plotted measurement points experimentally verifies the invariance of the singular value ratio over a variety of unitary input and output transformations, demonstrating that the polarization transformations caused by the pigtailed do not impair measurement accuracy.

Measurement of polarization mode dispersion

Thorough characterization of the optical components intended for high-speed transmission links requires accurate, repeatable measurement of polarization mode dispersion (PMD). PMD is completely characterized by a wavelength-dependent, three-dimensional polarization dispersion vector, or equivalently by the specification of a pair of principal states of polarization (PSP) and a differential group delay $\Delta\tau$ as a function of wavelength.

A general device or network has associated with it a pair of input principal states $\hat{\mathbf{x}}(\omega)$ which, as the SOP is held constant while the optical frequency ω is changed a small amount, result in a pair of output principal states whose unit vectors are invariant to first order over ω . For a general transmission Jones matrix $\mathbf{T}(\omega)$, we can express an output principal state as a magnitude $\sigma(\omega)$ and absolute phase $\phi(\omega)$ times a unit vector $\hat{\mathbf{y}}(\omega)$ which specifies the SOP of the output PSP:

$$\mathbf{y}(\omega) = \mathbf{T}(\omega) \hat{\mathbf{x}}(\omega) = \sigma(\omega) e^{i\phi(\omega)} \hat{\mathbf{y}}(\omega). \quad (3)$$

$\sigma(\omega)$ and $\phi(\omega)$ may vary with ω , but $\hat{\mathbf{y}}(\omega)$ is frequency-invariant to first order by definition of the output PSP. If the network is not perfectly polarizing, its transmission matrix \mathbf{T} is nonsingular and the input can be expressed in terms of the output as $\hat{\mathbf{x}} = \mathbf{T}^{-1} \mathbf{y}$. Using primes to denote differentiation with respect to ω , differentiation of (3) leads to the eigenvalue relation

$$\sigma e^{i\phi} \hat{\mathbf{y}}' = \left[\mathbf{T}' \mathbf{T}^{-1} - \left(\frac{\sigma'}{\sigma} + i\tau_g \right) \mathbf{I} \right] \mathbf{y} = 0, \quad (4)$$

where $\hat{\mathbf{y}}'$ is set to zero because it locates the output PSP. The imaginary parts of the eigenvalues of the matrix product $\mathbf{T}' \mathbf{T}^{-1}$ are the group delays associated with the PSPs, and the differential group delay $\Delta\tau = \tau_{g,1} - \tau_{g,2}$ which leads to PMD is given by the difference of the imaginary parts of the two eigenvalues.

Measurement of \mathbf{T}' and \mathbf{T} , including measurement of the absolute phase, would allow direct calculation of the two group delays and $\Delta\tau$, but in practice two restrictions are imposed by the Jones matrix measurement technique previously described. Instead of measuring \mathbf{T}' directly, we must approximate it as $\mathbf{T}' \approx [\mathbf{T}(\omega + \Delta\omega) - \mathbf{T}(\omega)] / \Delta\omega$ for a finite $\Delta\omega$. If the frequency interval $\Delta\omega$ is small enough so that each output PSP suffers nearly the same loss at ω and $\omega + \Delta\omega$, then $\sigma' \Delta\omega / \sigma \approx 0$ and (4) can be rewritten as

$$\left[\mathbf{T}(\omega + \Delta\omega) \mathbf{T}^{-1}(\omega) - (1 + i\tau_g \Delta\omega) \mathbf{I} \right] \mathbf{y} = 0. \quad (5)$$

The second restriction arises from the fact that $\mathbf{T}(\omega + \Delta\omega) \mathbf{T}^{-1}(\omega)$, and therefore its associated eigenvalues ρ_1 and ρ_2 , can be determined only to within a complex constant, preventing determination of the two group delays individually. When $\tau_g \Delta\omega$ is small we can approximate the eigenvalues as $\rho_k = 1 + i\tau_{g,k} \Delta\omega \approx \exp(i\tau_{g,k} \Delta\omega)$, and the differential group delay $\Delta\tau$ can be expressed as [3]

$$\Delta\tau = |\tau_{g,1} - \tau_{g,2}| = \left| \frac{\text{Arg}(\rho_1 / \rho_2)}{\Delta\omega} \right|, \quad (6)$$

where ρ_1 and ρ_2 are the eigenvalues of $\mathbf{T}(\omega + \Delta\omega) \mathbf{T}^{-1}(\omega)$ and Arg denotes the argument function. In fact, the requirement that $\tau_{g,k} \Delta\omega$ be small can be substantially relaxed: Since all the fundamental measurements are completely insensitive to absolute optical phase, only the quantity $\Delta\tau \Delta\omega$ need be small enough to allow an exponential approximation of the eigenvalues. The exponential approximation is exact when the loss of the DUT is independent of polarization, in which case only the condition $\Delta\tau \Delta\omega < \pi$ need be satisfied in order to avoid the ambiguities of the multiple-valued argument function

The experimental apparatus is shown in Fig. 4. A tunable laser source was directed through the polarization synthesizer and through the DUT to the polarimeter through short lengths of single-mode fiber which are assumed to introduce negligible polarization dispersion. At any given optical frequency ω_n , the polarization synthesizer generated three stimulus SOPs and the polarimeter measured the corresponding three response SOPs, resulting in a Jones matrix $\mathbf{T}(\omega_n)$ given by (1). The process is repeated for each ω_n in a sequence from $n=1$ to $n=N$. $N-1$ values of $\Delta\tau$ at frequencies $(\omega_n + \omega_{n-1})/2$ are then calculated from the eigenvalues of successive matrix products $\mathbf{T}(\omega_n) \mathbf{T}^{-1}(\omega_{n-1})$ using (6). The eigenvectors of $\mathbf{T}(\omega_n) \mathbf{T}^{-1}(\omega_{n-1})$ locate the output PSP as a function of frequency.

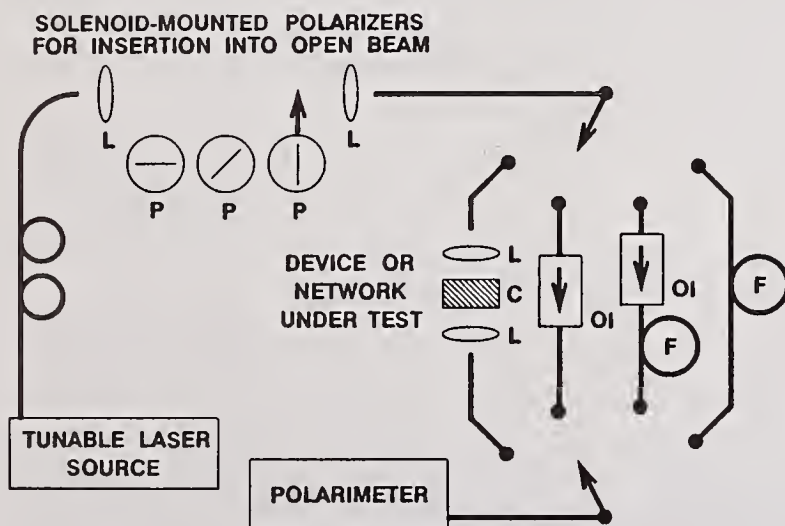


Figure 4 Apparatus used for measurement of polarization mode dispersion by Jones matrix eigenanalysis. L: lens; P: linear polarizer; C: crystal sample; OI: optical isolator; F: 2-km single-mode fiber.

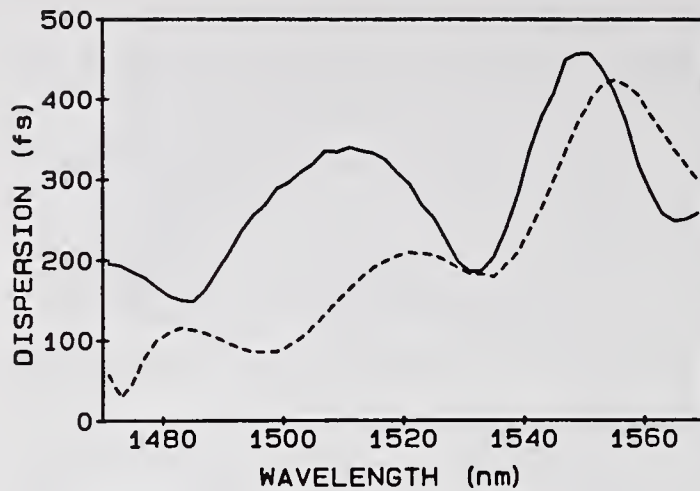


Figure 5 Differential delay of a 2-km spool of fiber measured at two different temperatures.

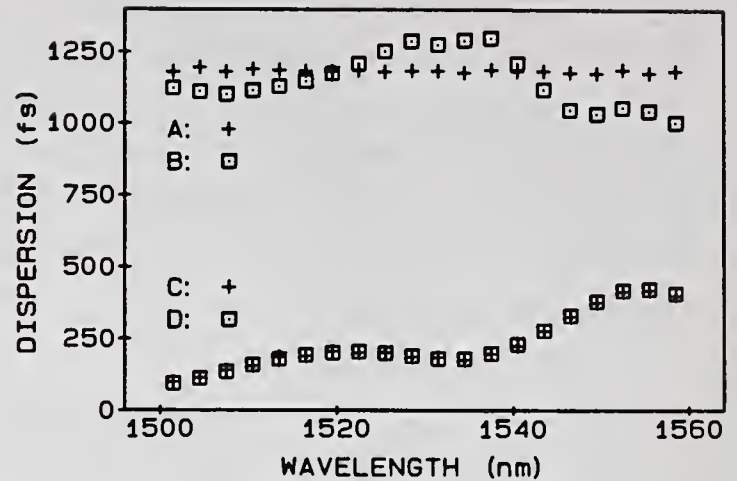


Figure 6 Differential delay measured using a similarity technique. A: isolator; B: isolator and 2-km fiber; C: fiber measured through isolator using similarity technique; D: fiber alone.

Summary

A fiber-based, automated approach to polarimetry can greatly reduce the tedium of polarization measurement while offering speed, ruggedness, accuracy and convenience. Addition of a simple polarization synthesizer allows complete stimulus-response measurement of the polarization-transforming properties of linear devices and networks, affording powerful characterization and analysis capabilities. Measurement of a Jones matrix depends on no assumptions about the device or network under test except that it must be linear and its polarization transformation must be constant over a period of several seconds.

This system makes possible two new analysis techniques which offer unique measurement advantages. Singular value calculations provide a deterministic, analytically complete means to characterize the variation in transmission of devices such as isolators or directional couplers over all SOPs. By eliminating the search over polarization space it allows a completely specified test suitable for comparisons and standards. Jones matrix eigenanalysis offers measurement of both differential group delay and orientation of the PSP as a function of optical frequency, providing a complete measurement of polarization mode dispersion. This technique affords temporal accuracy of a few percent down to a limit of several femtoseconds, even for networks exhibiting polarization-dependent loss.

References

- [1] R. C. Jones, "A new calculus for the treatment of optical systems. VI. Experimental determination of the matrix," *J. Optical Soc. Am.*, **37**, pp. 110 - 112, 1947.
- [2] B. L. Heffner, "Deterministic, analytically complete measurement of polarization-dependent transmission through optical devices," *IEEE Photonics Technol. Lett.*, PTL-4, 1992.
- [3] B. L. Heffner, "Automated measurement of polarization mode dispersion using Jones matrix eigenanalysis," submitted to *IEEE Photonics Technol. Lett.*

EXTINCTION RATIO MEASUREMENTS OF POLARISATION MAINTAINING FIBRE

Y. GU, L.J. POYNTZ-WRIGHT

York Fibers Ltd., York House, School Lane,
Chandler's Ford, Hampshire SO5 3DG, U.K.

INTRODUCTION

Polarisation maintaining (or high birefringence) fibre is an important component in many optical communication and sensor applications, including fibre optic gyroscope systems^[1]. However, agreement has yet to be reached as to how fibre performance should be specified. On exciting only one of the two orthogonal, linearly polarised modes, the fibre is capable of sustaining the transmission of stable, linearly polarised light over long lengths. How well the fibre performs depends not only on the fibre birefringence but also other factors such as coating properties and the severity of external perturbations.

While the beat length characterises the intrinsic birefringence of the fibre, in practical terms a more useful parameter is the overall polarisation holding ability of the fibre. The degree of cross-talk between the two polarised modes is commonly specified by the h-parameter^[2], a measure of the average rate at which power in the excited polarisation mode is coupled to the orthogonal mode. Alternatively, the ratio of the powers in the two modes can be expressed in dB, known as the extinction ratio. However, the validity of quoting extinction ratio or h-parameter measurements to describe commercially available fibres has been questioned due to the large dependence on external stresses. Failure to pay attention to this point results in an h-parameter specification which is not a test of the quality of the fibre, but of the winding conditions.

Here we present results of an investigation into the repeatability of extinction ratio measurements, and the effects of winding conditions.

EXPERIMENT

A schematic of the measurement station is shown in Figure 1. A Glan-Thompson polariser is used at the input, and a Woolaston beam splitter at the output, both of which have extinction ratios of greater than 50 dB. The source used is a super luminescent

diode, with a central wavelength of 820nm and bandwidth of 35nm. Using this arrangement, extinction ratios in fibre can be measured up to 39 dB (although figures of up to 60dB can be obtained when measuring fibre polarisers).

A YORK FK-11 cleaver was used in all the experiments in order to ensure the quality and repeatability of the fibre ends. The alignment technique is the standard iterative approach of searching for the best cross-talk ratio, and rotating the polariser through increasingly small steps (the use of the beam splitter at the output simplifies this considerably). With this method the angular position of the input axes can be defined with an accuracy of better than 10 minutes.

To assess the repeatability of the system, a 500m length of HB800, wound on a 164mm drum under constant tension, was measured a number of times without altering the winding conditions. The results of a set of 5 measurements for each eigenaxis excitation had a mean value of 27.3 dB, with a standard deviation of 0.34 dB. The system could be improved by replacing the polariser at the input which deviates the beam slightly, resulting in varying launch conditions between measurements. This is believed to be the main cause of errors in our results.

The same length of fibre was then rewound onto different diameter mandrels, under varying tensions. The mandrels ranged from 60mm to 300mm diameter, and winding tensions from 20g to 60g. A set of measurements for each eigenaxis was taken for each of the winding conditions. The results are summarised in Table 1.

DISCUSSION

The experimental results presented in Table 1 show that the standard deviation for the majority of measurements did not exceed 0.44 dB. This is only slightly higher than the system repeatability, indicating that the winding conditions are constant and that coils can be produced repeatably.

It can also be seen from Table 1 that the extinction ratio values vary significantly with winding conditions. As expected, the higher the tension, the greater the cross-talk. There is also a large dependence on coil diameter, the extinction ratio of the 68mm diameter coils being on average 11 dB lower than that of the 320mm diameter coils.

It is also observed that the effects of winding tension are not so significant for larger diameters. In fact, the values obtained for the 320mm diameter coil are similar to the free standing value of 35.5 dB. Thus these measurements on the larger drum are a better indication of the inherent fibre quality than tighter coils.

It should be noted that all these measurements were undertaken using mandrels of the same material. It is expected that different results would be obtained for, say, an aluminium mandrel compared to a similar one covered in foam. Therefore, although the results are repeatable, they can only be used to compare fibres wound under exactly the same conditions. It would be extremely difficult to extrapolate any results to determine fibre performance under any other conditions, and so can in no way be used to guarantee performance of a fibre for a particular application.

CONCLUSIONS

The results presented here show that it is possible to measure the polarisation holding ability of a fibre repeatably. However, great care has to be taken when quoting h-parameter or extinction ratio measurements to describe commercially available fibres, since they are only appropriate for the conditions under which the measurement was conducted. From the end-users point of view it is desirable for fibre manufacturers to standardise on measurement conditions if any comparisons are to be made.

REFERENCES

- [1] R.A.Bergh, H.C.Lefevre, and H.J.Shaw, Journal of Lightwave Tech., **LT-2**, 1984, pp91-107.
- [2] S.C.Rashleigh, Journal of Lightwave Tech., **1**, 1983, pp312-331.

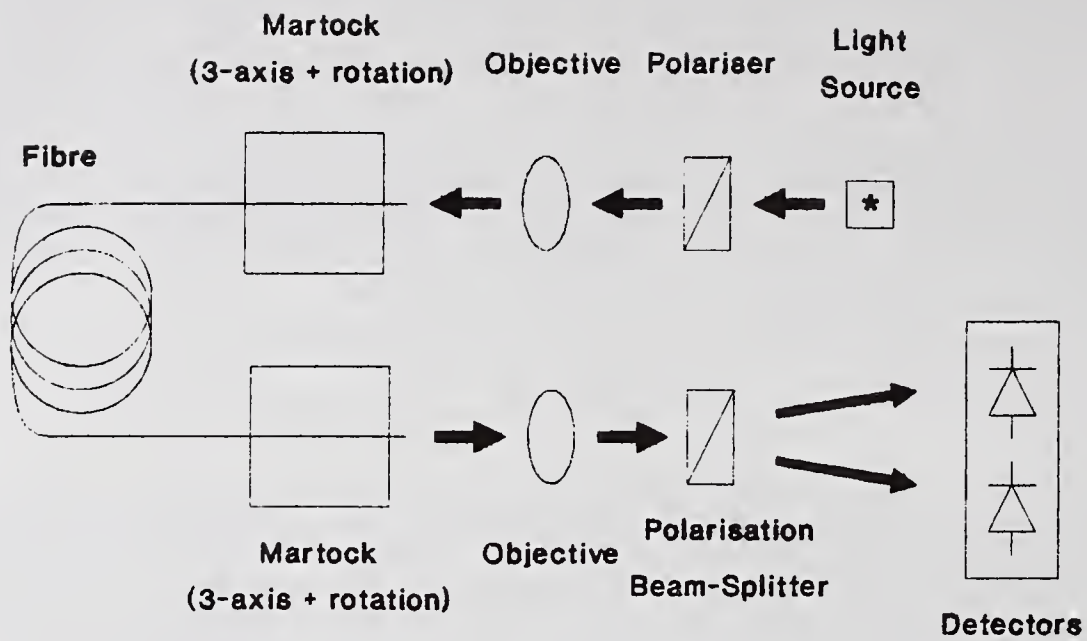


Figure 1. Schematic of Measurement Arrangement

<i>Coil Winding Conditions</i>		<i>Ext. Ratio</i>	
<i>Spool Dia (mm)</i>	<i>Tension (g)</i>	<i>Mean (dB)</i>	<i>Std Dev (dB)</i>
320	56	34.0	0.67
	22	34.7	0.23
164	56	27.8	0.44
	32	30.6	0.34
	22	31.3	0.39
68	56	21.4	0.40
	32	25.3	0.40
	22	26.6	0.41

Table 1. Experimental Results

ACCURATE MEASUREMENT OF POLARIZATION DEPENDENT LOSS OVER WAVELENGTH OF SINGLE MODE OPTICAL FIBER COMPONENTS

L. F. STOKES

HEWLETT-PACKARD COMPANY
ROHNERT PARK, CALIFORNIA

Introduction

Polarization dependent loss (PDL) is defined as the maximum *change* in insertion loss, expressed in dB units, of an optical fiber component as the input polarization is varied over all possible states. Accurate PDL measurements have become important recently. A long haul fiber transmission system, for example, may contain many fiber components between transmitter and receiver. Each component may have a very small polarization dependent loss. However, cumulative effects could produce a large fluctuation in received power as polarization randomly varies with the environment. Consequently, it is desired to measure the very low (0.1 dB or lower) polarization dependent loss of each component.

Traditionally, a polarized laser has been used as a source to measure PDL. The laser polarization is varied with a polarization state controller located before the component under test, and power exiting the component is measured. The ratio (difference in dB units) between the maximum and minimum power is the polarization dependent loss. This technique can be used with a wavelength tunable laser to measure PDL over wavelength, although it is quite time consuming if many wavelength points are desired. The technique described in this paper uses a white light source and an optical spectrum analyzer (OSA) to quickly measure PDL over wide wavelength ranges (greater than that possible with a single tunable laser) with great precision.

Optical Source

White light sources coupled to single mode fiber cannot begin to match the intensity of lasers coupled to single mode fiber. To illustrate this, consider a black body radiator (such as a hot lamp filament) imaged to the end of an optical fiber. The traditional Planck black body radiation law can be modified [1] to show that the maximum optical power in the fiber per spatial mode per unit optical frequency, dP/df , is

$$dP/df = ehf/[\exp(hf/kT) - 1]$$

where e is the material emissivity (≤ 1), h is Planck's constant, f is the optical frequency, k is Boltzmann's constant, and T is the black body temperature in deg K. Take $f = 231$ THz (1300 nm wavelength), $df = 178$ GHz (1 nm bandwidth), $e = 0.3$ for a tungsten filament, and $T = 3300$ deg K. With the above formula, we calculate a power per spatial mode of 0.294 nW for the 1 nm bandwidth. Equivalently, at 1300 nm, we have a power spectral density of

0.294 nW/nm, or -65.3 dBm/nm, in single mode fiber. It should be noted that the power spectral density calculated here is for one polarization only, as if a lossless polarizer were inserted between the lamp and the optical fiber. In general, single mode fiber supports two polarization modes, and the power spectral density will be 3 dB greater (-62.3 dBm/nm) without a polarizer present.

Optical Spectrum Analyzer

The very small amount of power available from a white light source is not a deterrent to accurate PDL measurements over wavelength because of the new generation of high sensitivity optical spectrum analyzers. For example, the HP 71451A has a typical sensitivity (noise level) of -90 dBm at 1300 nm, independent of resolution bandwidth. A PDL measurement with 1 nm resolution would have about -65 dBm signal and 25 dB dynamic range available. The noise is about 0.3% of the signal, and represents a PDL measurement uncertainty of 0.014 dB. A PDL measurement with 10 nm resolution would have 10 times the signal (-55 dBm) and 35 dB dynamic range.

Measurement Technique

The simplest PDL measurement using a white light source and an optical spectrum analyzer would be configured as follows: An unpolarized single mode fiber white light source would be followed by a single mode fiber polarizer, a single mode fiber polarization state controller, the component under test, and finally the optical spectrum analyzer. The OSA sweeps over the wavelength range of interest using the desired resolution bandwidth. Simultaneous MAX HOLD and MIN HOLD traces are selected, and the polarization state controller is adjusted, over many OSA sweeps, until no larger MAX or smaller MIN can be found over wavelength. Finally, subtracting (in dB units) the MIN trace from the MAX trace gives the desired PDL over wavelength. Note that no source flatness calibration is necessary, as it is common to both traces.

A major problem with the above measurement technique is that the PDL of both the component under test *and the OSA* has been measured. Typically, OSA's have a polarization sensitivity of at least 0.5 dB (due to polarization dependence of diffraction gratings). This sensitivity limits the PDL sensitivity and accuracy to 0.5 dB. Indeed, replacing the component under test with a short section of single mode fiber, and performing the above measurement, will yield the polarization sensitivity over wavelength of the OSA.

To avoid this problem, the OSA monochromator is placed directly after the unpolarized white light source, as shown in Figure 1. The fiberized output of the OSA monochromator, now partially polarized due to the polarization sensitivity of the grating, passes through the fiber polarizer. As long as this piece of fiber is relatively short (eg., 1 meter) and is not disturbed during the measurement (so as not to change whatever state of polarization is incident on the polarizer), the polarization dependence of the OSA will be common to both the MAX and MIN traces. Trace subtraction will eliminate this dependence leaving just the PDL of the component under test.

One minor drawback to this technique is that no OSAs are presently available with single

mode fiber at the monochromator output. Consequently, multimode fiber is used between the white light source and the monochromator input, and between the monochromator output and the polarizer. The output of the polarizer is single mode fiber. The same power of -65 dBm/nm (minus the monochromator insertion loss) is available as a signal, and the same dynamic range exists. However, some speckle will be present, due to the multimode/single mode fiber interface, which gives a variation of power over wavelength. Again, this variation is common to both MAX and MIN traces and is eliminated with trace subtraction.

Measurement Results

Figures 2 and 3 show the precision of this PDL technique. A 3 meter section of single mode fiber was chosen as the component under test, and it should have no PDL. Figure 2 shows the MAX and MIN traces virtually overlapping. About 10 monochromator sweeps were taken, while the polarization state controller was adjusted continuously looking for MAX and MIN response. Total measurement time was 400 seconds. Note the 1 dB power variation over wavelength due to speckle described above. Figure 3 shows the subtraction of the two traces of Figure 2. The lowest measurable PDL is limited by the residual of 0.05 dB in this case. The residual results from the speckle pattern variation in time, the insertion loss variation of the polarization state controller, and the polarization dependence of the photodetector.

Figures 4 and 5 show PDL of a 1310 nm "polarization independent" isolator. The MAX and MIN traces of Figure 4 took about 10 sweeps to generate, again representing 400 seconds measurement time. Figure 5, the trace subtraction of Figure 4, shows a PDL of 0.27 to 0.39 dB over the 100 nm span. Again, note how the speckle effect is common to both traces of Figure 4, and subtracts out quite well.

Summary

A simple, accurate method of measuring polarization dependent loss over wavelength has been described. A low cost white light source and a high sensitivity optical spectrum analyzer allow quick (a few minutes) determination of very low polarization dependent loss over wavelength to high accuracy.

Acknowledgements

The author appreciates helpful discussions and assistance from J. P. Hamilton-Gahart and J. R. Stimple.

References

1. W. R. Trutna, Jr., Hewlett-Packard Laboratories, personal communication.

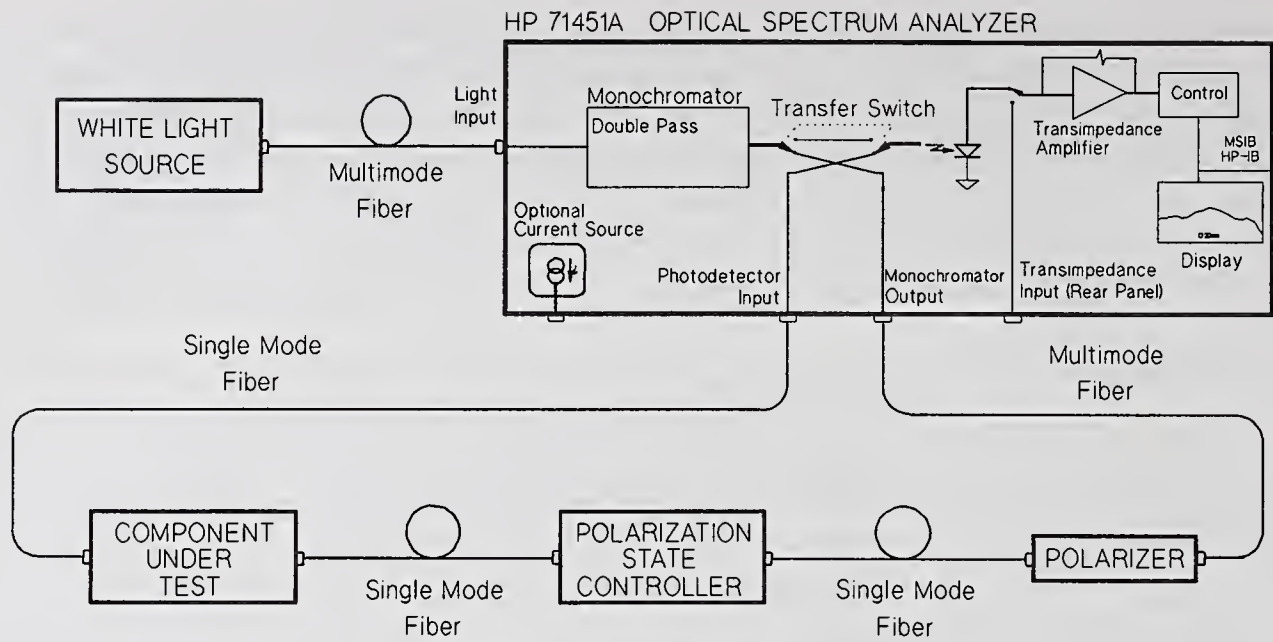


Fig. 1. PDL measurement configuration.

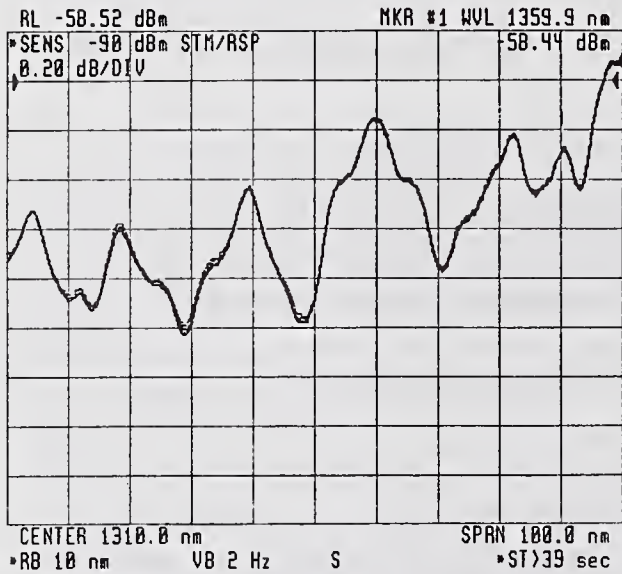


Fig. 2. MAX and MIN traces of fiber.

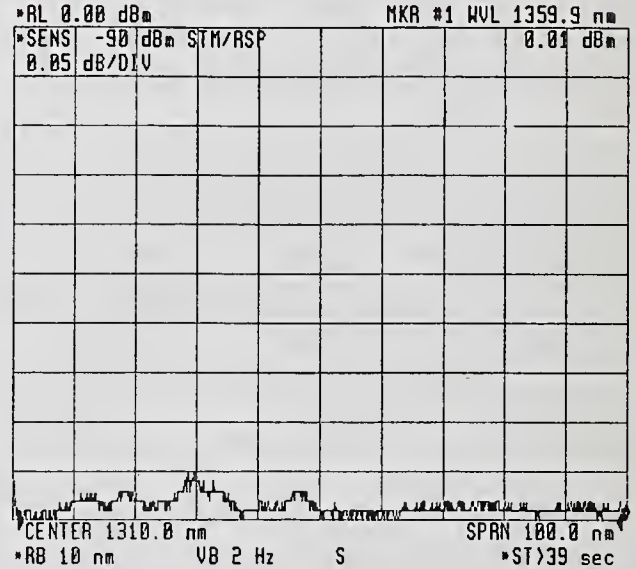


Fig. 3. PDL sensitivity.

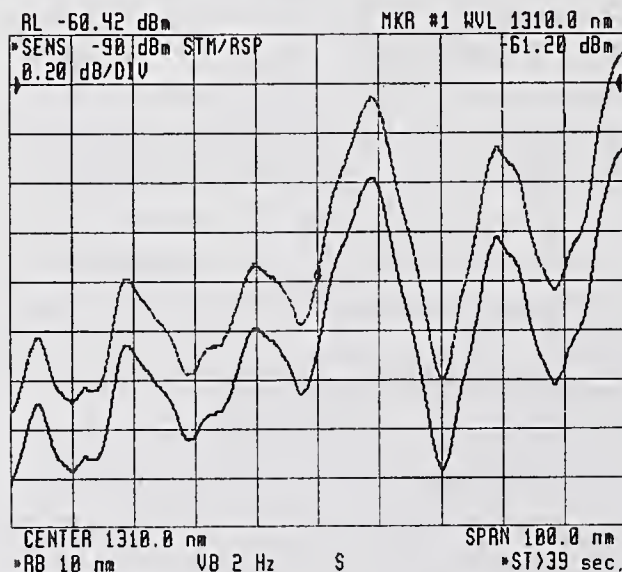


Fig. 4. MAX and MIN traces of isolator.

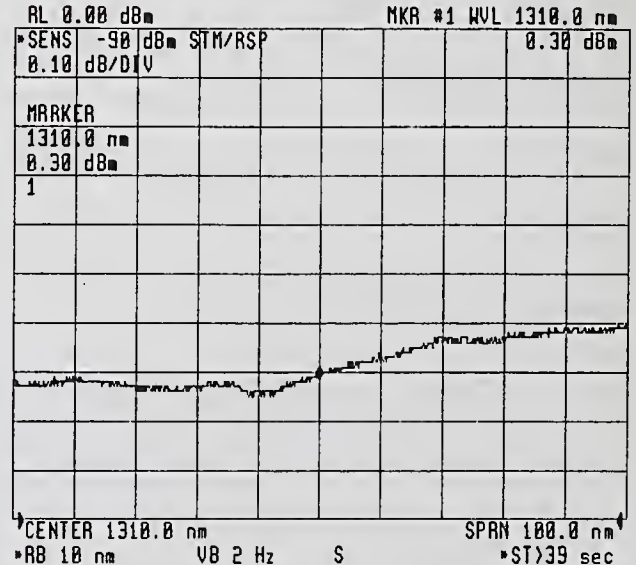


Fig. 5. PDL of isolator.

POLARIZATION MODE DISPERSION MEASUREMENTS IN OPTICAL FIBERS

Yoshinori NAMIHIRA and Jun MAEDA (*)

KDD R&D Laboratories,
2-1-15, Ohara, Kamifukuoka, Saitama, 356 Japan

I. INTRODUCTION

In the single-mode optical fibers (SMFs), there exists a modal birefringence due to geometrical core deformation and external stress which give rise to polarization mode dispersion (PMD). The PMD may set a limit to the use of ultra high bit rate long haul optical fiber amplifier systems, especially when the chromatic dispersion effects become very small by tuning the signal wavelength near the zero-chromatic dispersion wavelength. So far, the PMD has been measured by mainly two different procedures. One is the time domain measurement and the other is the frequency domain measurement. The former method is based on the interferometric [1]-[3] and pulse methods [3],[4]. The latter method is based on the evolution of the states of polarization (SOP) as a function of the frequency (wavelength) and measures the differential group delay (or PMD) τ between the principal SOP [3]-[6].

This paper presents the comparison of various PMD measurement technologies ; (1) Interferometric, (2) Optical pulse, (3) Fixed analyzer, (4) Poincaré sphere, and (5) SOP- PMD measurement methods, respectively.

II. TIME DOMAIN PMD MEASUREMENTS

A. Interferometric PMD Measurement Method

Fig.1 shows the experimental set-up for the highly accurate interferometric PMD measurement method [1]-[3]. The principle of the measurement is based on the Michelson interferometer [1]-[3]. The interferenced output optical powers (visibility curves) can be obtained if the group-delay difference between the two orthogonal polarized waves is within the coherence time of a light source. The center wavelength of semiconductor laser amplifier (SLA), the spectral line width and single-mode fiber pigtail output power were $\sim 1.548 \mu\text{m}$, $\sim 80 \text{ nm}$ ($\sim 10 \text{ THz}$) and $\sim -15 \text{ dBm}$, respectively. The measurement accuracy is depending on the mechanical accuracy ($\sim 1.0 \mu\text{m}$) of optical delay line, and the PMD measurement accuracy is $\sim 0.003 \text{ ps}$ [2]. The PMD τ is given by [2]

$$\tau = 2d / c \quad (1)$$

where, $2d$ and c are the optical path length ($= 2d$; two times of delay line moving length d) and the light velocity in free space, respectively.

The example of the interferometric PMD measurements of the polarization independent optical isolator and the $1.3 \mu\text{m}$ optimized SMF ($L \cong 10 \text{ km}$) are shown in Figs.2-(a) and (b), respectively. In Fig.2, it is confirmed that a small PMD values of $\sim 0.012 \text{ ps}$ of the polarization independent

(*) : University of Electro-Communications, Chofu, Tokyo, 182 Japan

optical isolator can be measured successfully by using the interferometric PMD measurement method. Also, it is found that there is great difference between the two visibility curves of Figs. 2-(a) and (b). Many interference points in the visibility pattern of the SMF are interpreted as a results of the random polarization mode couplings along the fiber length. The other results are summarized in Table 1.

B. Optical Pulse PMD Method

Fig. 3 represents the experimental set-up for the optical pulse PMD measurement method. In the PMD method, a pulsed DFB-LD and an optical sampling oscilloscope were used. Incident polarization with rotation angle of 45° was launched into the fiber under test. The output optical pulse was split into two pulses (fast and slow waves). The interval of the two optical pulses is equivalent to the averaged PMD value. Fig.4 shows an example of PMD measurement result of the polarization maintaining fiber (PMF 2, $L \cong 200$ m). The PMD is found to be ~ 44 ps (~ 0.22 ps/m) as shown in Table 1. The measurement accuracy depends on the optical pulse width, and its value is ~ 15 ps when the pulsed DFB-LD was used in the experiment.

III. FREQUENCY DOMAIN PMD MEASUREMENTS

A. Fixed Analyzer PMD Measurement Method using Optical Spectrum Analyzer

Fig. 5 shows the experimental set-up for the fixed analyzer PMD measurement method using optical spectrum analyzer (OSA). The PMD measurement results of the PMF4 ($L \cong 6.4$ m) and the SMF ($L \cong 10$ km) are shown in Fig.6-(a) and (b), respectively. The interval of the peak to peak powers is equivalent to the phase difference of 2π . The PMD τ is expressed as

$$\tau = N(1/\Delta f) = N(\lambda_1 \lambda_n / c \Delta \lambda) \quad (2)$$

where, N , Δf , and $\Delta \lambda$ represent the numbers from peak at λ_1 (f_1) to peak at λ_n (f_n), the frequency difference ($f_n - f_1$) and the wavelength difference ($\lambda_n - \lambda_1$), respectively. The PMF4 (Fig.6-a) shows almost periodic curve, meanwhile the SMF (Fig.6-b) indicates somewhat irregular periods. The other results are summarized in Table 1.

B. PMD Measurement Methods using Stokes Analyzer

In the PMD measurement method using a real time Stokes analyzer, there are two different PMD measurement methods such as conventional Poincaré sphere method [3],[5]-[8], and new SOP method.

B.1 Poincaré Sphere PMD Measurement Method

A schematic diagram of the experimental set-up for the PMD measurement using a real time Stokes analyzer [3],[8] is shown in Fig.7. A tunable $1.55 \mu\text{m}$ external cavity semiconductor laser (ECL) with a spectral linewidth of ~ 65 kHz at $1.55 \mu\text{m}$ was used as a light source. The wavelength was tuned by adjusting the angle of the external-grating automatically. It is possible to measure in $1.51 \sim 1.59 \mu\text{m}$ wavelength range at 0.2 nm (~ 25 GHz) wavelength steps corresponding to the longitudinal mode spacing of the laser diode (LD). The SOP can be determined by the Stokes parameters (S_0 , S_1 , S_2 and S_3). S_0 , S_1 , S_2 and S_3 relate to the total optical power, the linear polarization of $\theta = 0^\circ$, the linear polarization of $\theta = 45^\circ$ and the right circular polarization, respectively. In Fig.8, (o) and (x) are SOP arcs of measured values due to PMD as a function of wavelength λ . Here, Pa-a' is principal SOP [8].

The PMD τ is given by [8]

$$\tau = (\Delta\phi/2\pi)(1/\Delta f) = (\Delta\phi/2\pi)(\lambda_1\lambda_n/c\Delta\lambda) \quad (6)$$

where, $\Delta\phi$ is the phase difference (Stokes vector arc on the Poincaré sphere). Figs. 8 -(a) and (b) show the example of Poincaré sphere representation of PMF4 ($L \cong 6.4$ m) and SMF ($L \cong 10$ km). PMF4 (Fig.8-a) shows almost periodic curve, meanwhile the SMF (Fig.8-b) indicates somewhat irregular periods. The other results are summarized in Table 1.

B.2 SOP PMD Measurement Method

After the polarization fluctuation was measured by Stokes analyzer (or Rotatable analyzer) , it can be transformed into the SOP curve as a function of wavelength (frequency); The SOP is expressed as

$$\text{SOP} = (1 - \eta^2)/(1 + \eta^2) \quad (7)$$

$$\text{where, } \eta = \tan [0.5 \tan^{-1} \{ S_3 / \sqrt{S_1^2 + S_2^2} \}]$$

Here, η is the polarization ellipticity, S_1 , S_2 and S_3 are Stokes parameters. In Fig.9, the peak to peak of SOP curves is equivalent to the phase difference of π . The PMD τ is given by

$$\tau = (N/2)(1/\Delta f) = (N/2)(\lambda_1\lambda_n/c\Delta\lambda) \quad (8)$$

VI. CONCLUSIONS

The comparison of the various PMD measurement methods is shown in Table 1. From Table 1, it was found that the following results;

(A) Birefringent optical devices (PMFs etc.) ; (1) Not a great difference was remarked among all PMD measurement methods. (2) Interferometric method was best for optical components having very small PMD values because of highest measurement accuracy (~ 0.003 ps). (3) Optical pulse method was useful for only large PMD values ($\geq \sim 15$ ps).

(B) Optical fibers (SMF, DSF and DFF) ; (1) The time domain methods (Interferometric and Optical pulse method) were not useful due to SOP fluctuations during measuring time. (2) The PMD values of the Interferometric method were slightly smaller than those of the Frequency domain methods. (3) In the Frequency domain methods, the PMD values of the Poincaré sphere method are slightly scattered than those of the SOP method. (4) Although, PMD values of the Fixed analyzer method were slightly larger than those of the SOP method, these two methods (Fixed analyzer method and SOP method) were better than the Poincaré sphere method for PMD measurements in optical fibers. Finally, we would like to thank Dr. K. Ono, Dr. T. Yamamoto and Dr. Y. Kushiro and Mr. H. Wakabayashi of KDD R&D Labs for their encouragement, and also thank Mr.T. Kawazawa of KDD R&D Labs. for his cooperation.

REFERENCES :

- [1] Y. Namihira et al., : IEEE, Photonics Letters, Vol.1, pp.329-331, Oct.,1989.
- [2] Y. Namihira et al., : J. of Optical Communications, Vol.12, No.1, pp.1-8, 1991.
- [3] Y. Namihira et al., : IEICE of Japan, Technical Report, OCS90-56, pp.31-38, 1990.
- [4] C. D. Poole et al., : Optics Letters, Vol. 13 pp.155-157, 1988.
- [5] C. D. Poole et al., : IEEE, JLT, Vol.6, No.7, pp.1185-1189, 1988.
- [6] N. S. Bergano et al, : IEEE, JLT, Vol.5, No.11, pp.1618-1622, 1987.
- [7] D. Andresciani et al., : Optics Lett., Vol.12, No.10, pp.844-846, 1987.
- [8] Y. Namihira et al., : Electron . Lett., Vol.28, No.9, pp.881-883,1992.

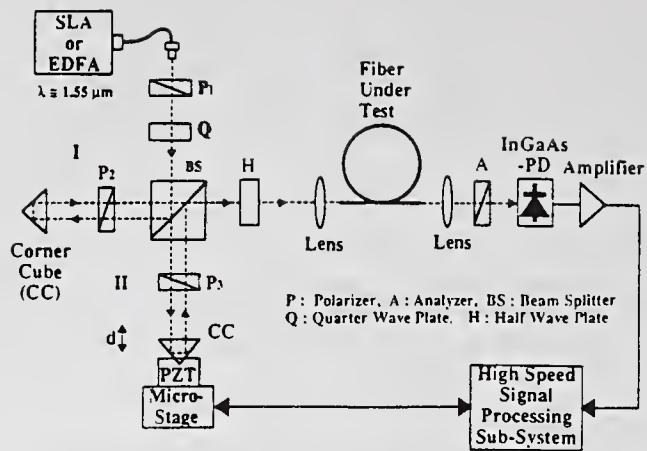


Fig. 1 Experimental set-up for Interferometric PMD measurement method

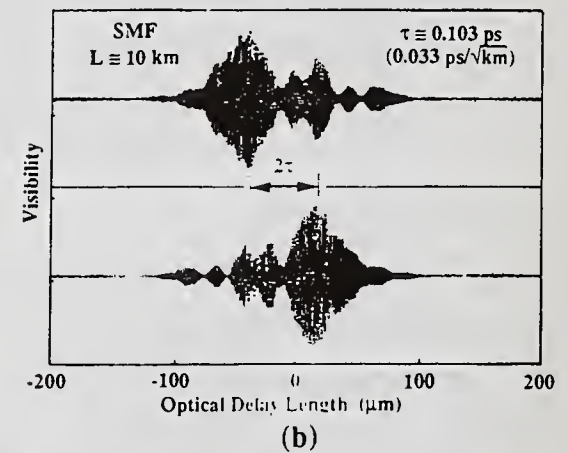
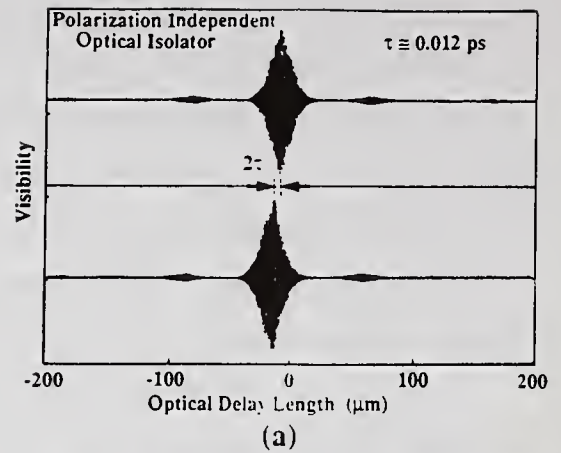


Fig. 2 Interferometric PMD measurement results in (a) Polarization independent optical isolator, (b) SMF ($L \cong 10$ km)

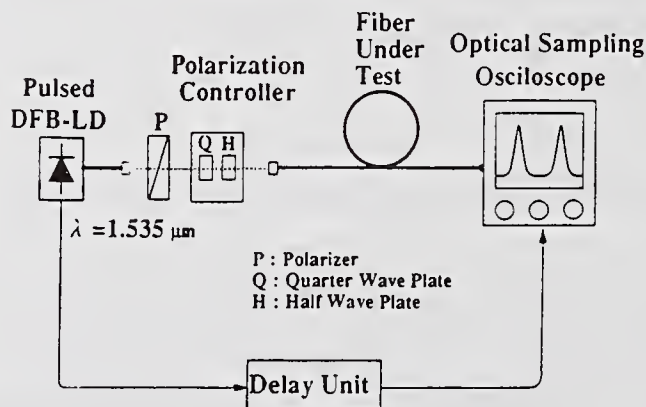


Fig. 3 Experimental set-up for Optical pulse PMD measurement method

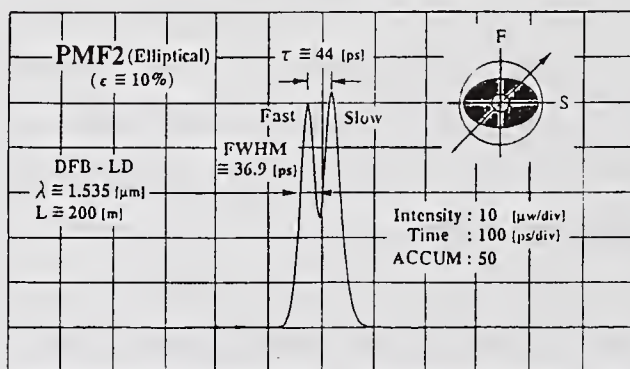


Fig. 4 Optical pulse PMD measurement results in PMF2 ($L \cong 200$ m)

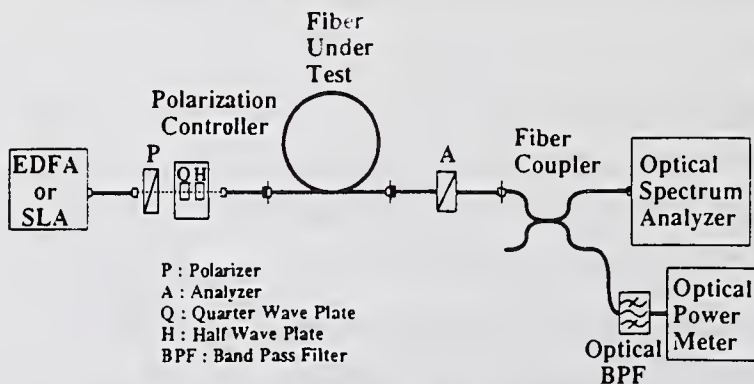


Fig. 5 Experimental set-up for Fixed analyzer PMD measurement method using Optical spectrum analyzer (OSA)

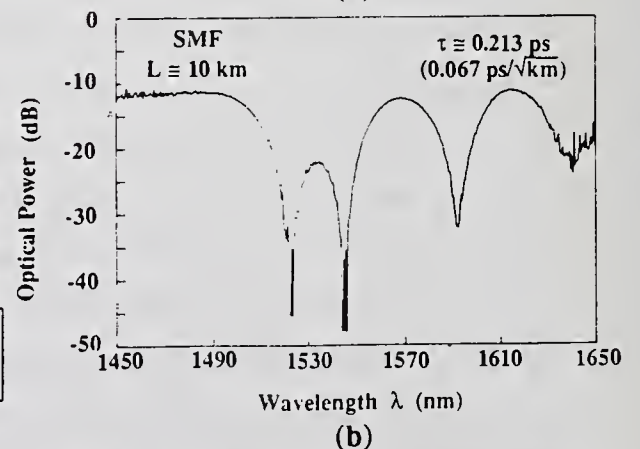
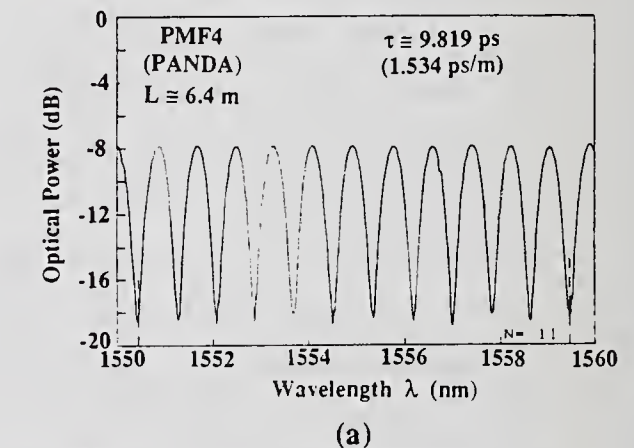


Fig. 6 Fixed analyzer PMD measurements in (a) PMF 4 ($L \cong 6.4$ m), and (b) SMF

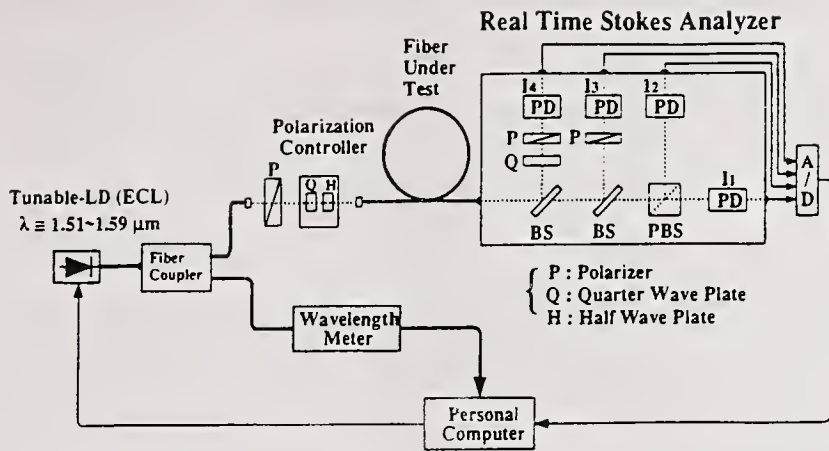


Fig.7 Experimental set-up for PMD measurement method using Real time Stokes analyzer

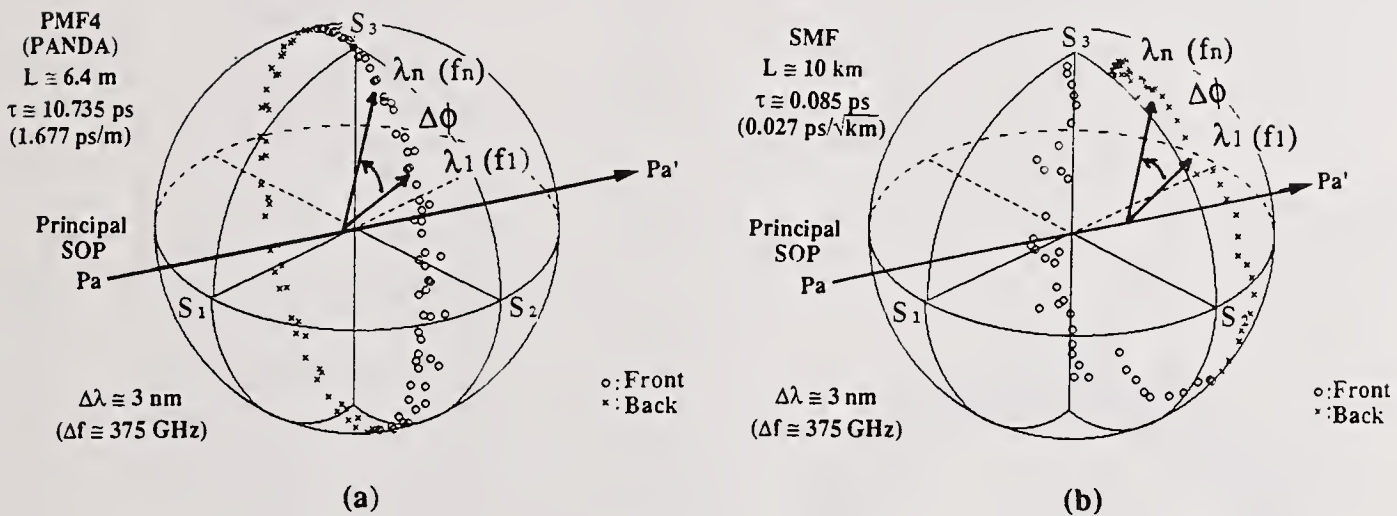


Fig.8 Poincaré sphere representation of PMD measurements in (a) PMF 4 ($L \approx 6.4\text{m}$) and (b) SMF ($L \approx 10\text{km}$)

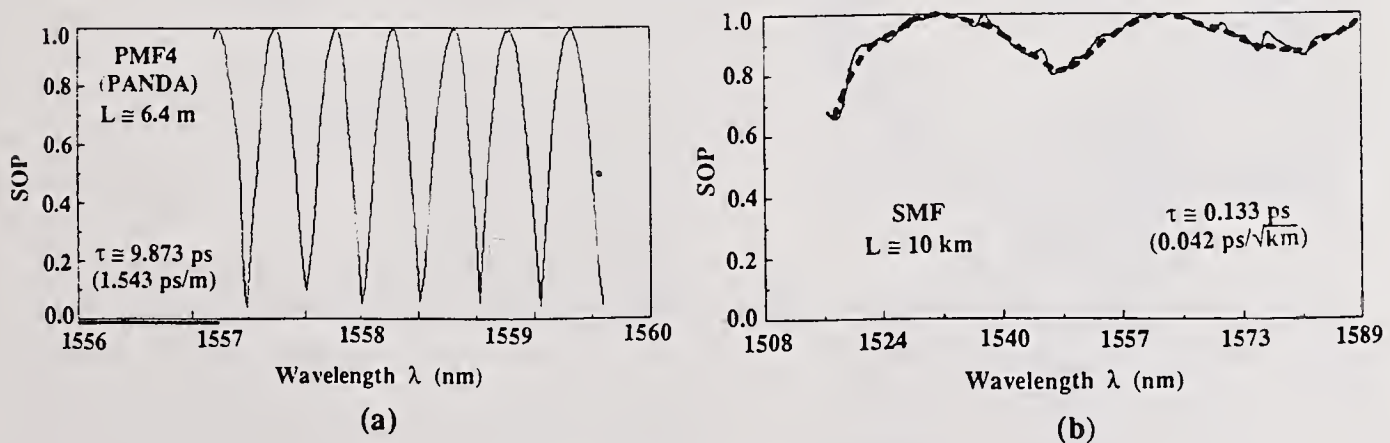
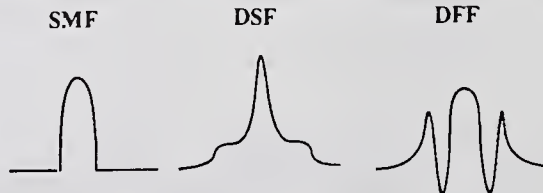
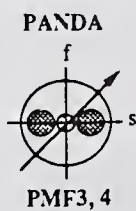
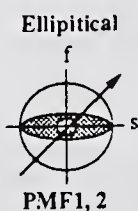


Fig.9 State of polarization (SOP) representation of PMD measurements in (a) PMF 4 ($L \approx 6.4\text{m}$) and (b) SMF ($L \approx 10\text{km}$)

Table 1. Comparison of Various PMD Measurement Methods

	Time Domain		Frequency Domain		
PMD Measurement Methods	Interferometric Method	Optical Pulse Method	Fixed Analyzer Method	Poincare' Sphere Method	SOP Method
Optical Source	SLA or EDFA LED	Pulsed-LD	EDFA or SLA LED	Tunable-LD (ECL) or DFB-LD (Temperature Control)	
Equipments	Michelson Interferometer	Optical Sampling Oscilloscope	Optical Spectrum Analyzer	Stokes Analyzer	Stokes Analyzer or Rotatable Analyzer
Measurement Accuracy	$\geq \sim 0.003$ ps	$\geq \sim 15$ ps	$\geq \sim 0.05$ ps	$\geq \sim 0.05$ ps	$\geq \sim 0.025$ ps
Polarization Independent Optical Isolator	$\tau \cong 0.012$ ps	—	—	—	—
PMF1 (L \cong 0.245 m)	$\tau \cong 0.048$ ps (0.196ps/m) $\sigma \cong 0.001$ ps	—	$\tau \cong 0.051$ ps (0.208 ps/m) $\sigma \cong 0.001$ ps	$\tau \cong 0.056$ ps (0.229 ps/m) $\sigma \cong 0.002$ ps	$\tau \cong 0.051$ ps (0.208 ps/m) $\sigma \cong 0.003$ ps
PMF2 (L \cong 0.646 m)	$\tau \cong 0.134$ ps (0.207 ps/m) $\sigma \cong 0.002$ ps	$\tau \cong 44.0$ ps (0.220 ps/m) (L \cong 200 m)	$\tau \cong 0.135$ ps (0.209 ps/m) $\sigma \cong 0.001$ ps	$\tau \cong 0.128$ ps (0.198 ps/m) $\sigma \cong 0.004$ ps	$\tau \cong 0.139$ ps (0.215 ps/m) $\sigma \cong 0.002$ ps
PMF3 (L \cong 0.64 m)	$\tau \cong 0.970$ ps (1.516 ps/m) $\sigma \cong 0.002$ ps	—	$\tau \cong 0.969$ ps (1.514 ps/m) $\sigma \cong 0.001$ ps	$\tau \cong 0.842$ ps (1.316 ps/m) $\sigma \cong 0.003$ ps	$\tau \cong 0.972$ ps (1.522 ps/m) $\sigma \cong 0.004$ ps
PMF4 (L \cong 6.4 m)	$\tau \cong 9.772$ ps (1.503 ps/m) $\sigma \cong 0.003$ ps	—	$\tau \cong 9.792$ ps (1.506 ps/m) $\sigma \cong 0.019$ ps	$\tau \cong 10.538$ ps (1.621 ps/m) $\sigma \cong 0.284$ ps	$\tau \cong 9.772$ ps (1.503 ps/m) $\sigma \cong 0.141$ ps
DFF (L \cong 6.4 km)	$\tau \cong 0.345$ ps (0.136ps/ $\sqrt{\text{km}}$) $\sigma \cong 0.001$ ps	—	$\tau \cong 0.368$ ps (0.145ps/ $\sqrt{\text{km}}$) $\sigma \cong 0.008$ ps	$\tau \cong 0.294$ ps (0.066ps/ $\sqrt{\text{km}}$) $\sigma \cong 0.006$ ps	$\tau \cong 0.251$ ps (0.099ps/ $\sqrt{\text{km}}$) $\sigma \cong 0.006$ ps
SMF (L \cong 10 km)	$\tau \cong 0.094$ ps (0.030ps/ $\sqrt{\text{km}}$) $\sigma \cong 0.006$ ps	—	$\tau \cong 0.175$ ps (0.055ps/ $\sqrt{\text{km}}$) $\sigma \cong 0.004$ ps	$\tau \cong 0.160$ ps (0.051ps/ $\sqrt{\text{km}}$) $\sigma \cong 0.012$ ps	$\tau \cong 0.130$ ps (0.041ps/ $\sqrt{\text{km}}$) $\sigma \cong 0.007$ ps
DSF (L \cong 20 km)	$\tau \cong 0.110$ ps (0.025ps/ $\sqrt{\text{km}}$) $\sigma \cong 0.041$ ps	—	$\tau \cong 0.264$ ps (0.059ps/ $\sqrt{\text{km}}$) $\sigma \cong 0.005$ ps	$\tau \cong 0.184$ ps (0.041ps/ $\sqrt{\text{km}}$) $\sigma \cong 0.013$ ps	$\tau \cong 0.224$ ps (0.050ps/ $\sqrt{\text{km}}$) $\sigma \cong 0.006$ ps
Application	PMFs, Birefringent - Optical-Components, and Short-Optical-Fibers (SMF, CSF,DSF,DFF) etc.	Long-PMFs, High-Birefringent-Optical-Components etc.	Optical Fibers (SMF, CSF, DSF, DFF), PMFs, Optical Components and Optical Amplifier Systems etc., <div style="border: 1px solid black; padding: 5px; width: fit-content; margin: 5px auto;"> PMF : Polarization Maintaining Fiber SMF : Standard Single Mode Fiber CSF : Cutoff Shifted Fiber DSF : Dispersion Shifted Fiber DFF : Dispersion Flattened Fiber SOP : State of Polarization SLA : Semiconductor Laser Amplifier EDFA : Er-Doped Fiber Amplifier </div>		



Interferometric Loop Method for Polarization Dispersion Measurements

Luc Thévenaz, Marc Niklès, Philippe Robert

EPFL, Metrology Laboratory, Swiss Federal Institute of Technology of Lausanne

CH-1015 Lausanne, Switzerland

Abstract: A novel method for polarization dispersion measurements using an interferometric loop is presented. It can be achieved using a particularly simple setup and provides a representation of the probability distribution of the polarization dispersion.

Introduction

A single-mode fiber is not truly single-mode since it can propagate two degenerate modes that are orthogonally polarized. Weak residual birefringence together with environmental perturbations makes the polarization degeneracy to be actually removed leading to pulse broadening or Polarization Mode Dispersion (PMD). The combined effects of weak birefringence and mode coupling due to external perturbations result in a stochastic behavior of the polarization dispersion and consequently of the output polarization state. The so-called principal states, a particular set of orthogonal polarization states, experience the maximum propagation delay and are therefore very convenient for the description of PMD [1-5]. Dynamic equations show that polarization in fibers is a randomly varying quantity and its probability density function is a Maxwell distribution [2,4,5].

Several methods have been reported so far for the measurements of PMD in long single-mode fibers. A technique using a tunable laser source and analyzing paths over the Poincaré sphere provides a measurement of the instantaneous polarization dispersion [6,7]. This requires repeated measurements to obtain the delay statistical distribution. Another technique uses interferences produced by a low-coherence source to map the actual distribution of possible delays [8], so that a single measurement yields the delay statistical distribution and makes the determination of the PMD expectation value possible.

In this contribution we report a novel method that enables the measurement of PMD using a particularly simple setup, without polarizing elements or retardation plates. A single measurement also provides the PMD expectation value.

Theoretical background

In an interferometric loop, counterpropagating lightwaves propagate along the same optical path, so

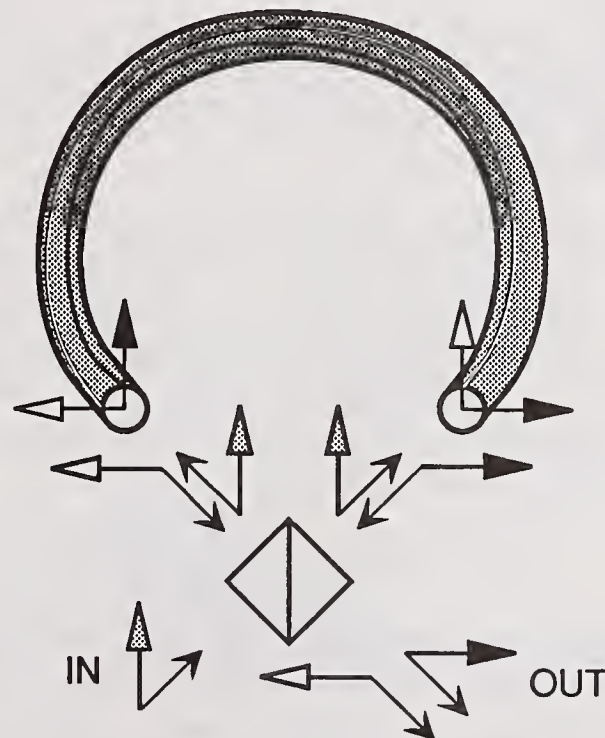


Fig.1 Example of non-reciprocal propagation in an interferometric loop through a 90 deg twisted linearly birefringent fiber.

that the propagation phase difference is zero at the recombination point for any optical path length, except when light experiences a non-reciprocal effect such as Sagnac effect (rotation) or Faraday effect (magnetic field).

A non-reciprocal propagation may also occur when the optical medium is birefringent. Our measurement method uses this property to evaluate the PMD.

For instance a linearly birefringent fiber experiencing a 90 deg twist in the loop gives rise to a complete non-reciprocal propagation, as shown in Fig.1. This way, light from the same input polarization state splits and propagates along two distinct polarization modes of the fiber. Their phase difference $\delta\phi$ is given by

$$\delta\phi = \frac{2\pi}{\lambda} \Delta n L$$

where L is the fiber length and Δn the birefringence. This phase difference may actually be changed by varying the wavelength λ , so that a succession of constructive and destructive interferences is observed when the wavelength is scanned, resulting in a periodic variation of the interferometer output intensity. For a given fiber length L , the higher the birefringence Δn , the faster the periodic variations, so that the period measurement straightforwardly yields the value of PMD. Actually this period is simply calculated by performing a Fourier transform.

For a long standard single mode fiber, the random nature of PMD makes the expression for interference intensity more difficult to be carried out. In addition, the set of principal states depends on the propagation direction. After some lengthy calculations using Jones calculus, the interferometer output intensity turns out to be for any input light polarization state:

$$I_{out} = I_o \left[1 + \cos^2\theta \cos 2\phi - \sin^2\theta \sin\left(\frac{2\pi}{\lambda} \Delta n L\right) \right]$$

where θ and ϕ are the angles defining the rotation on the Poincaré sphere to perform the vector base change from the principal states for one direction to the set of principal states for the other direction. When the wavelength is scanned, Δn is expected to be constant only over a limited range, so that interference periodicity randomly varies over the spectrum. The wavelength scan

makes the fiber experience a great number of polarization situations, so that it may be equivalent to an ensemble average, provided that the statistical distribution is unchanged over the spectrum. With this assumption the distribution obtained by performing the Fourier transform is a measure of the actual PMD statistical distribution. The angles θ and ϕ also vary when the wavelength is changed, but it was demonstrated elsewhere that they don't fluctuate at a higher rate than PMD[3,4], so that their fluctuations induce variations of the output intensity with longer periods. The resulting distribution function of delays has still to be determined, even though its asymptotic nature is expected to be Gaussian.

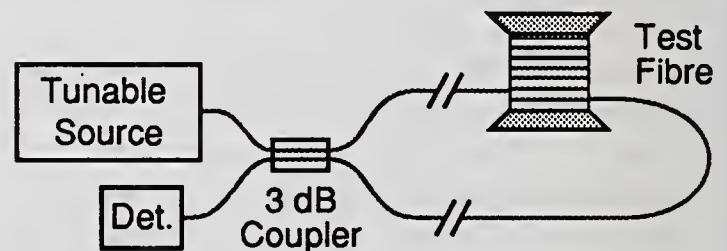


Fig.2 Block diagram of the interferometric loop method.

Experimental results

The interferometer output intensity does not depend on the input light polarization as stated above, so that neither polarization preparation nor tuning is required using polarizing elements or retardation plates. Consequently, even unpolarized light may be used. The optical circuit is therefore particularly simple, as shown in Fig.2. The only needed optical component is a 3dB single mode coupler, that has to be preferably wavelength-independent.

The most critical element is the tunable source. Three configurations were actually tested:

- A white light halogen lamp, whereas detection is performed using an optical spectrum analyzer. This configuration provides the largest wavelength coverage, a very uniform and smooth spectrum, but has a poor dynamic range. It is also low-cost and quite suitable for the measurement of less than 10-km fibers [9].

- A set of LEDs, detection still performed using an optical spectrum analyzer. The dynamic range is larger, enabling the measurement of up to 30-km fibers. The drawback is a narrower and less uniform spectral coverage.

- A tunable external cavity laser diode. This advanced configuration enables the best performances, with an ideal dynamic range and a convenient spectral coverage. However it suffers from the drawback of the present high cost of such a source.

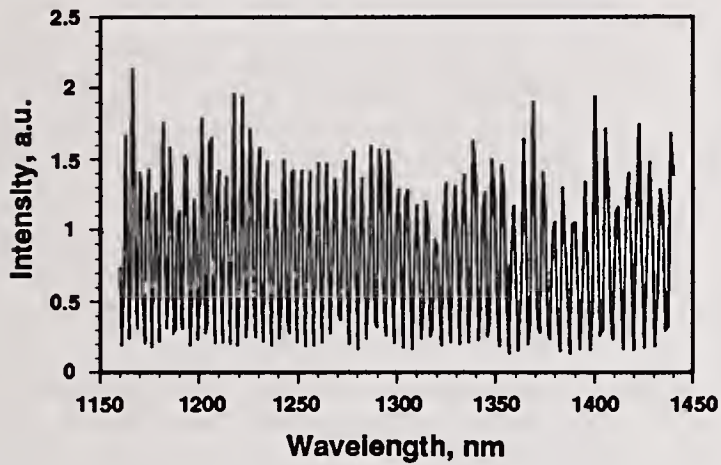


Fig.3 Interferometric loop output intensity as a function of wavelength. The loop is a 0.5m highly birefringent fiber.

The results obtained using any of these three configurations were identical. As a first test, a sample of 0.5 m highly birefringent fiber was measured, using a

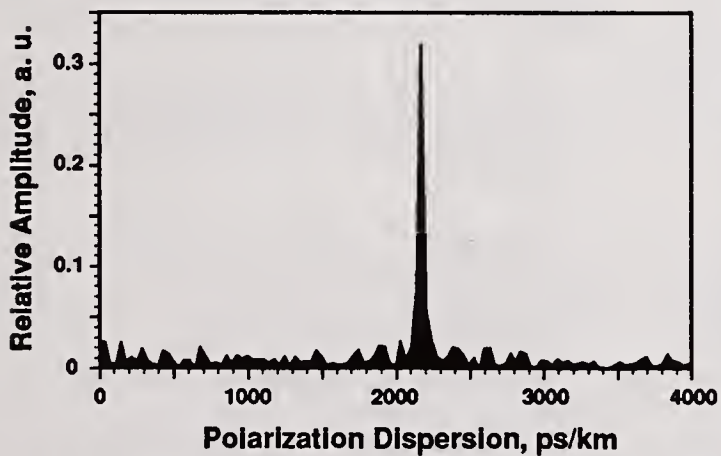


Fig.4 Fourier transform of the measurements shown in Fig.3. One frequency is dominant, corresponding to the polarization dispersion value.

configuration equivalent to Fig.1. The output intensity periodically varies as the wavelength is scanned, as shown in Fig.3. The interference contrast was observed to change from a maximum to a minimum value when either fiber end was rotated. The period of the intensity spectral variations is obtained by performing a Fourier transform, so that the PMD corresponds to the peak position in the transformed distribution, as shown in Fig.4.

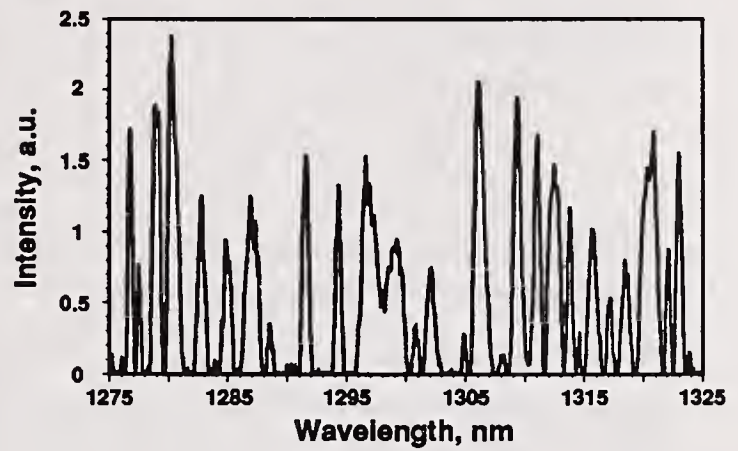


Fig.5 Interferometric loop output intensity as a function of wavelength. The loop is a 3600m standard single mode fiber.

The observed intensity variations are quite different when a several kilometers standard single-mode fiber is measured, as shown in Fig.5. The delay between polarization modes is wavelength-dependent making the

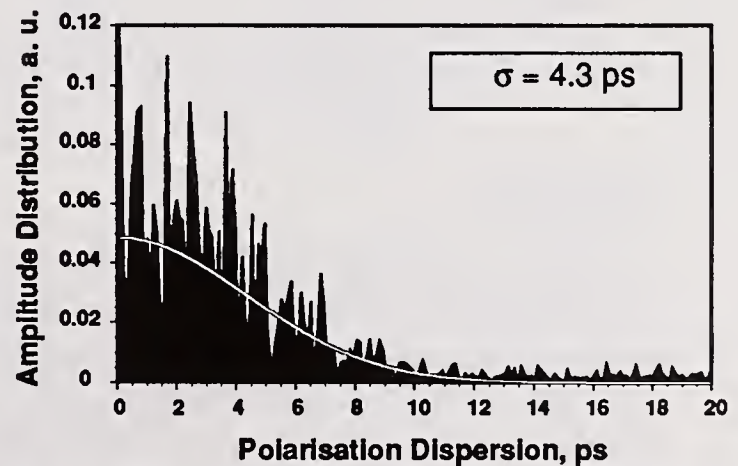


Fig.6 Fourier transform of the measurements shown in Fig.5. The obtained Gaussian-like distribution is directly related to the statistical distribution of polarization dispersion.

period of intensity variations to fluctuate over the spectrum. The Fourier transform of such a measurement is not just one peak, but a distribution of numerous peaks, as shown in Fig.6. With the "wavelength scan" = "ensemble average" assumption, this distribution is a close representation of the actual delay statistical distribution.

The minimum observable delay corresponds to an interference period equal to the spread of the measurement spectral range, so that the larger is this spread, the better is the resolution. Hence:

$$\delta\tau_{min} = \frac{\lambda_{max}\lambda_{min}}{c(\lambda_{max}-\lambda_{min})}$$

where λ_{min} , λ_{max} are the lower and upper bounds of the measurement wavelength range, respectively.

On the other hand, the maximum observable delay is bounded by the source spectral width, because this delay must remain shorter than the coherence time in order to observe interferences. Hence

$$\delta\tau_{max} = \frac{\lambda^2}{c \Delta\lambda}$$

where $\Delta\lambda$ is the spectral width and λ the center wavelength ($\Delta\lambda$ corresponds to the minimum wavelength step when using a tunable laser source). Actual obtained figures are shown in the table below:

Source	$\delta\tau_{min}$	$\delta\tau_{max}$
White lamp	0.008 ps	1.4 ps
LEDs	0.016 ps	9.6 ps
Tunable laser	0.075 ps	375 ps

Conclusion

Reproducibility tests were successfully carried out using this method and the scattering of the obtained PMD expectation value was below 10%, even though the fiber was displaced between the measurements and the intensity versus wavelength curves look totally different. Results were also compared to those obtained using another measuring technique [10] and the agreement was excellent for expectation value below 1ps. For larger values, great differences are observed and

are still unexplained. This method has the great advantage to be very easy to implement, because most of the setup elements are available in any optics lab, so that most of them can already afford the implementation of this technique.

References

- [1] C. D. Poole, R. E. Wagner, *Phenomenological Approach to Polarization Dispersion in long Single-Mode Fiber*, Electron. Lett., **22**, pp 1029-1030.
- [2] F. Curti, B. Daino, G. de Marchis, F. Matera, *Statistical Treatment of the Evolution of the Principal States of Polarization in Single-Mode Fiber*, IEEE J. Lightwave Technol., **8**, pp 1162-1166.
- [3] S. Betti, F. Curti, B. Daino, G. de Marchis, E. Iannone, F. Matera, *Evolution of the Bandwidth of the Principal states of Polarization in Single-Mode Fiber*, Opt. Lett., **16**, pp 467-469.
- [4] C. D. Poole, J. H. Winters, J. A. Nagel, *Dynamical Equations for Polarization Dispersion*, Opt. Lett., **16**, pp 372-374.
- [5] G. J. Foschini, C. D. Poole, *Statistical Theory of Polarization Dispersion in Single-Mode Fiber*, IEEE J. Lightwave Technol., **9**, pp 1439-1456.
- [6] D. Andresciani, F. Curti, F. Matera, B. Daino, *Measurement of the group-delay difference between the principal states of polarization on a low-birefringence terrestrial fiber cable*, Opt. Lett., **12**, pp 844-846.
- [7] C. D. Poole, N. S. Bergano, R. E. Wagner, H. J. Schulte, *Polarization Dispersion and Principal States in a 147-km Undersea Lightwave Cable*, IEEE J. Lightwave Technol., **6**, pp 1185-1190.
- [8] N. Gisin, J.-P. von der Weid, J.-P. Pellaux, *Polarization Mode Dispersion of Short and Long Single-Mode Fibers*, IEEE J. Lightwave Technol., **9**, pp 821-827.
- [9] L. Thévenaz, Ph. Robert, *Simple method for Polarization Dispersion Measurements in Long Single-Mode Fibres*, Proc. ECOC '90 (Amsterdam), Vol.1, pp. 581-584.
- [10] L. Thévenaz, M. Niklès, N. Gisin, Ph. Robert, *Overall Polarization Dispersion after Propagation through Different Fibres*, Proc. EFOC/LAN '91 (London), pp 156-158.

**Four interferometric methods for the determination of the
birefringence and polarization dispersion of polarization
maintaining optical fibers**

Ch. Chojetzki, Kabelmetal-electro, Stadthagen
H. Schmitzer, Universität Regensburg
J. Vobian, W. Dultz, DBP Telekom
Germany

Polarization-maintaining optical fibers are destined to gain importance in optics and optical communications since they combine the properties of a waveguide with those of a mechanically stable two-beam interferometer. Interferometric measuring techniques are the most precise in physics. Thus they suggest themselves, to characterize polarization-maintaining optical fibers with respect to their physical parameters.

The transmission behaviour of these fibers is determined by polarization dispersion, but since this parameter depends on the character of the spectral and temporal features of the transmitted optical information flow, the birefringence is the primary physical quantity in spite of the fact that it combines waveguide and material properties in an obscure blend.

Unfortunately, instead of the birefringence $B(\lambda)$ the beat length $L_B(\lambda)$ has been adopted to characterize polarization-maintaining fibers in optical communications

$$L_B = \frac{\lambda}{B(\lambda)}, \quad B(\lambda) = n_s - n_f, \quad c_{s,f} = \frac{c}{n_{s,f}}. \quad (1)$$

c_s, c_f are the phase velocities and n_s, n_f the refractive indices of the slow and fast axis of the fiber. L_B has an intrinsic dependence on the wavelength λ , while the birefringence B only depends weakly on λ . To introduce pulse propagation in this picture, the modified beatlength L_{B^*} and the modified birefringence B^* are defined with respect to the group velocities $v_{gs,f}$

$$L_{B^*} = \frac{\lambda}{B^*}, \quad B^*(\lambda) = n_{gs} - n_{gf}, \quad v_{gs,f} = \frac{c}{n_{gs,f}}. \quad (2)$$

Equations (1) and (2) are connected by the dispersion relation for the wave vector $k(\lambda)$

$$v_{gs,f} = \frac{d\omega}{dk_{s,f}}, \quad k_{s,f} = \frac{2\pi n_{s,f}}{\lambda}. \quad (3)$$

From (1), (2) and (3)

$$B^* = \frac{1}{c} \left(B - \lambda \frac{dB}{d\lambda} \right) = - \frac{\lambda^2}{c} \frac{d(B/\lambda)}{d\lambda}. \quad (4) \quad (4)$$

can be derived /1/. Equation (4) allows the calculation of the modified birefringence B^* , when the spectral dependence of the birefringence $B(\lambda)$ is known.

We compare four different experimental techniques to measure beatlength and modified beatlength of a polarization-maintaining optical fiber. The pressing method (P), see Fig. 1 above, uses the Lyot-filter principle /2/. Linearly polarized light (parallel to one of the two orthogonal polarization axes) is launched into the polarization-maintaining fiber under test. A pressing wheel couples light coherently into the second channel of the fiber. At the end of the fiber the two polarization modes are resolved by a polarizer and interfere. During the movement of the wheel along the fiber, a detector shows alternate constructive and destructive interference maxima and minima at a distance of one beatlength $L_B(\lambda)$.

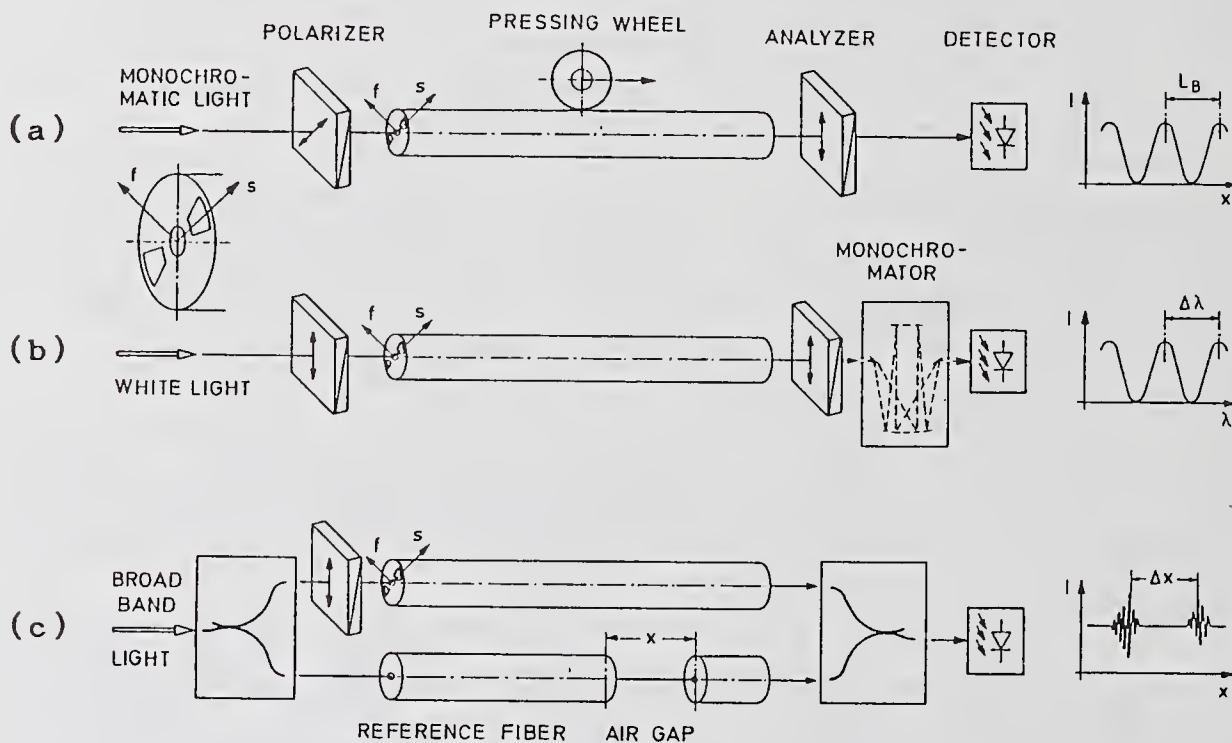


Fig. 1 Measurement set-up of the

- (a) pressing method (P)
- (b) wavelength-scanning method (WLS)
- (c) Mach-Zehnder interferometric method (MZI)

The wavelength scanning method (WLS), see Fig 1 in the center, is also based on the Lyot-filter principle. In this case the length l of the Lyot filter element is fixed, and the wavelength of the light is changed. The number of beats in fiber piece l changes with wavelength

$$N = \frac{l(n_f - n_s)}{\lambda} = \frac{l \cdot B}{\lambda} \quad (5)$$

and this becomes apparent in a periodic detector reading with period $\Delta\lambda$. It was shown that $\Delta\lambda$ determines the modified beatlength L_{B*}

$$L_{B*} = \frac{1}{\lambda} \Delta\lambda \quad (6)$$

The WLS-method allows the easy measurement of the modified beatlength L_{B*} and the modified birefringence B^* in a wide spectral region. Unfortunately, it needs one additional measurement of the beatlength $L_B(\lambda)$ with the pressing method at a single wavelength to determine the beat length $L_B(\lambda)$ from (4) and (1) by integration, since the integration constant has to be known. This supplementary measurement with a different method can be avoided if the number N of beats L_B of the Lyot filter element is changed in a known way by introducing a birefringent plate with a definite retardation in the optical path behind the fiber. From the shift $d\lambda$ of the maximum N can be determined

$$N = \frac{\lambda}{d\lambda} \quad (7)$$

From equation (5) we get the birefringence B . We call this the modified wavelength scanning method (MWLS).

The last technique we discuss is the Mach-Zehnder interferometric method (MZI) /3/, see Fig. 1 below. The white light interference fringes of the light from the two polarization channels of the polarization maintaining fiber with the light from a normal single mode reference fiber are determined with a variable air gap. The distance Δx is equal to the optical path length difference $l \cdot B^*(\lambda)$ of the polarization-maintaining fiber. As in the case of the WLS-method, one measurement with the pressing method is necessary to determine B and L_B .

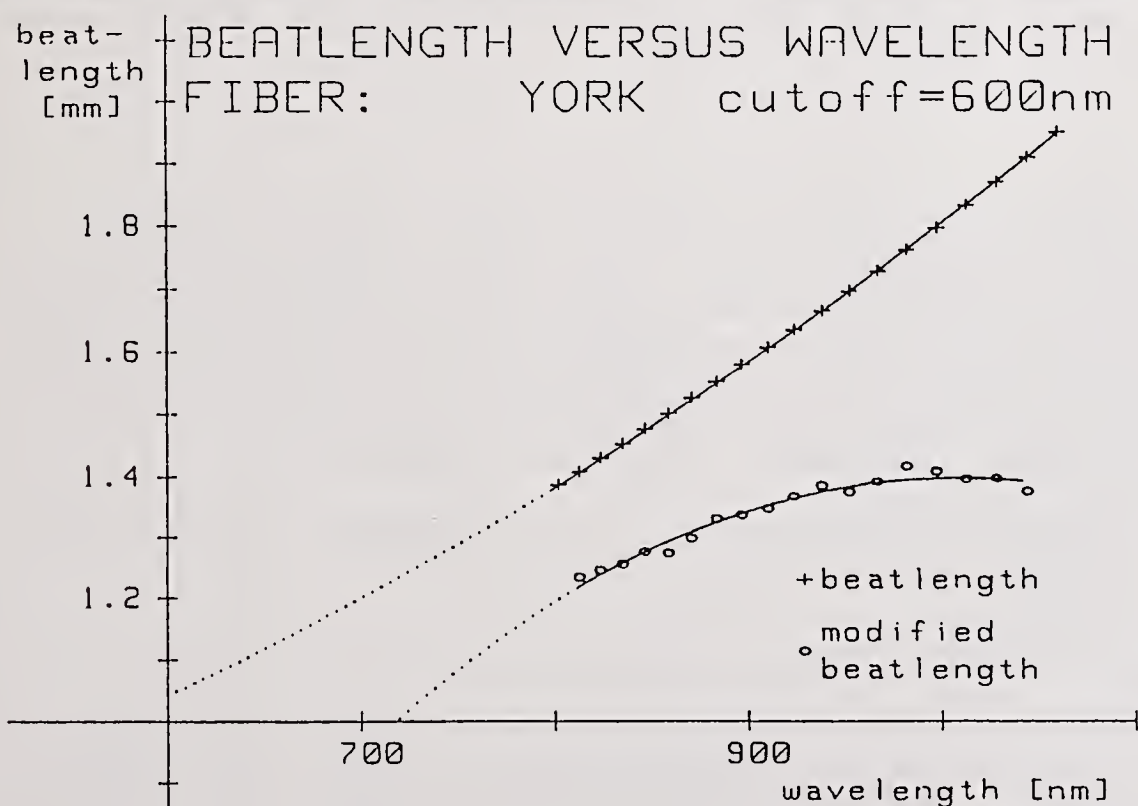


Fig. 2 Spectral dependence of the beatlength and the modified beatlength of a YORK bow-tie fiber

In Table 1 the measurement results of the modified beatlength L_B^* and birefringence B^* (3 polarization-maintaining fibers of COST 217) obtained by means of the WLS and MZI method are compared. An excellent agreement can be stated, with the exception of the AT&T fiber.

	$\lambda = 1300 \text{ nm}$				$\lambda = 1500 \text{ nm}$			
	L_B^* in mm	L_B^* in mm	$B^* \cdot 10^{-4}$	$B^* \cdot 10^{-4}$	L_B^* in mm	L_B^* in mm	$B^* \cdot 10^{-4}$	$B^* \cdot 10^{-4}$
	MZI	WLS	MZI	WLS	MZI	WLS	MZI	WLS
PANDA fiber	3.01	2.99	4.32	4.34	3.42	3.405	4.39	4.41
YORK Bow-tie fiber	1.97	1.99	6.60	6.53	2.25	2.25	6.67	6.67
PM fiber AT & T	5.58	5.72	2.33	2.27	6.46	6.44	2.35	2.33

Table 1 Comparison of the test results of the modified beatlength and birefringence of the MZI- and WLS method

We demonstrate the high precision of these interferometric techniques on a YORK-fiber with a cutoff wavelength of 600 nm. As an example, the beatlength and the modified beatlength of this fiber which were measured with the wavelength scanning method together with the pressing method are shown in Fig. 2. Note the interesting opposite behaviour of the phase and the group beatlength, the latter becoming constant above 950 nm.

This study was partly performed in the framework of the COST 217/241 action.

References:

- /1/ CH. CHOJETZKI, J. VOBIAN, W. DULTZ; J. Opt. Comm. 1992
- /2/ K. TAKADA, J. NODA, R. ULRICH; Appl. Optics, 24 (1985) p. 4387
- /3/ J. VOBIAN, W. DULTZ; Proc. Interferometry 89, Warsaw (1989), SPIE Volume 1121, p. 325

Low Coherence Reflectometry for the Characterization of Fiber and Planar Lightwave Circuits

Kazumasa TAKADA
NTT Opto-electronics Laboratories,
Tokai, Ibaraki-ken, 319-11, Japan

Abstract: Micrometer-resolution low coherence reflectometry has been demonstrated using high-power broadband sources. We describe recent advances in the field with particular attention to characterization of the fiber and planar lightwave circuits.

Introduction: Recent progress in planar lightwave circuit (PLC) technology [1] requires a nondestructive diagnostic method that can provide, for example, a loss level diagram and the backreflection distribution in a PLC. Micrometer-resolution reflectometry shows promise as a solution to PLC diagnosis. Fontaine et al. first demonstrated the micrometer-resolution reflectometry using ultrashort light pulses and the optical intensity correlation technique based on second harmonic generation [2]. Due to the limited dynamic range, the most promising reflectometry technique for PLC diagnosis is now considered to be optical low coherence reflectometry (OLCR) [3-5] using a CW broadband source. We describe the performance of OLCR and its application to waveguide characterization.

Performance of OLCR: The basic OLCR configuration, consisting of a broadband source and a Michelson interferometer with a movable arm, is shown in Fig. 1 [6]. The output light is split into a reference and a probe light. The probe light is launched into the waveguide under test. The backreflected light from the test waveguide is combined with the reference light. The intensity of the beat signal is measured for reflection measurement, while an interferogram is used for dispersion measurement. Optical modulation is often applied to either the reference or reflected light using a piezoelectric stretcher or an optical frequency shifter to reduce the noise at the lower frequency.

The main factors limiting the sensitivity of the OLCR are excess photon noise, beat noise and shot noise. The excess photon noise of the reference light is removed by using the balanced detection technique [6-8]. Fresnel reflection produces beat noise due to beating of the various Fourier components within the reference and reflected light spectra [9]. Figure 2 shows the measured minimum detectable reflectivity at unit bandwidth versus total mean photocurrent at four different Fresnel reflections R from the test waveguide. The source was the 1.3- μm InGaAs superluminescent diode [10]. At $R = 0$ the minimum reflectivity decreases by 10 dB/decade of current, indicating that the shot noise limited the sensitivity. The optimum value was -140 dB at a 3 Hz detection bandwidth. As R increases, the reflectivity approaches a definite noise floor. A reduction in the facet reflection with matching oil or AR coating is indispensable for shot-noise limited operation.

Spatial resolution depends on the reflection distribution profile. With point-like distribution, the resolution is determined by the coherence length divided by the waveguide refractive index [3]. Typical values for LED's and SLD's range from 15-40 μm . With Rayleigh backscattering, coherent jaggging occurs owing to the speckle-like phenomenon induced by the number of scattered waves contributing to the detected signal [11]. The signal is randomly jagged according to the law of Rayleigh distribution and does not change with external perturbations. Signal smoothing, which reduces the resolution, can reveal the desired profile for waveguide diagnosis. Figure 3 shows one example of the revealed backscattering signal profile for a bent portion of the fiber. The actual resolution determined by smoothing was 400 μm . There is a 3 dB change in intensity after the signal propagates through the bent portion, thus indicating a bending loss of 1.5 dB.

Reflection Profiles: Reflection profiles for an integrated GaAs Mach-Zehnder interferometer [12], and straight and curved silica-based waveguides [13] have been measured. Figure 4 describes the results for the GaAs interferometer. Backreflection at the splitting section (Y) and Fresnel reflections at both facets (F and B) are observed, from which the average loss coefficient and the coupling coefficient are estimated. The profile for a curved (3-mm-radius) silica glass waveguide is shown in Fig. 5, where the light is launched from the end of region A into the waveguide. The intensity decreases by 5 dB during the back-and-forth propagation from region A to region C, indicating a transmission loss of 2.5 dB. Rare-earth-doped superfluorescent fiber sources provide an output power in a range of more than 10 mW and a spectral linewidth of more than 10 nm [14,15]. An OLCR coupled to the source has achieved a minimum detectable reflectivity of less than -140 dB [16,17], as shown in Fig. 6. The dynamic range is 25 dB, indicating that a waveguide loss of up to 12 dB can be evaluated. Such a large dynamic range is required for semiconductor waveguides without injection current, or with absorbed regions.

Dispersion Measurement: Fourier transform spectroscopy has long been known to be a powerful tool for measuring the dispersive properties of bulk optical samples [18]. Recently, dispersive spectroscopy has been applied to the measurement of guided wave properties, including chromatic dispersion [19] and the location of index discontinuities with fraction of a wavelength precision [20]. Based on the principles of Fourier spectroscopy, the phase of the Fourier transform of the dispersive interferogram is equal to the optical phase difference between the two arms in the interferometers. The second derivative of the phase spectrum with respect to the wavenumber leads to the chromatic dispersion spectrum. Measuring the phase slope of the Fourier components in the frequency domain makes it possible to locate the positions of reflections with nanometer precision even in the presence of sample dispersion. Precise dispersion measurement requires that the interferogram be sampled without distortion. Coherent laser light is launched into the interferometer and separated at the

output with a wavelength-division multiplexer. Clock pulses for interferogram sampling are generated by zero crossings of an ac-coupled high coherence interference signal [21]. Since the signal and reference light are co-propagating, distortion of the sampled interferogram due to temperature changes and scanning arm vibrations is minimal.

Conclusion: Recent progress in optical low coherence reflectometry (OLCR) for nondestructive waveguide diagnosis has been described. High-power broadband sources such as rare-earth-doped superfluorescent fiber sources provide sensitivity in the -140 dB range and a dynamic range of more than 25 dB in Rayleigh backscattering measurement. Most of the problems regarding OLCR have now been overcome and its practical application to the diagnosis of fiber and planar lightwave circuits will provide useful information for circuit development.

Acknowledgment: The author would like to express his sincere thanks to M. Nakahara, M. Horiguchi, K. Yukimatsu and A. Himeno for their continuous encouragement.

References

1. N. Takato, K. Jinguji, H. Toba, and M. Kawachi, *IEEE J. Lightwave Technol.* 6, 1003-1010 (1988).
2. J. J. Fontaine, J. -C. Diels, C. J. Wang, and H. Sallaba, *Opt. Lett.* 6, 405-407 (1981).
3. R. C. Youngquist, S. Carr, and D. E. N. Davies, *Opt. Lett.* 12, 158-160 (1987).
4. K. Takada, I. Yokohama, K. Chida, and J. Noda, *Appl. Opt.* 26, 1603-1606 (1987).
5. B. L. Danielson, and C. D. Whittenberg, *Appl. Opt.* 26, 2836-2842 (1987).
6. H. H. Gilgen, R. P. Novak, R. P. Salathe, W. Hodel, and P. Beaud, *IEEE J. Lightwave Technol.* 7, 1225-1233 (1989).
7. K. Takada, K. Yukimatsu, M. Kobayashi, and J. Noda, *Appl. Phys. Lett.* 59, 143-145 (1991).
8. M. Kobayashi, H. F. Taylor, K. Takada, and J. Noda, *IEEE Photon. Technol. Lett.* 3, 564-566 (1991).
9. K. Takada, A. Himeno, and K. Yukimatsu, *Appl. Phys. Lett.* 59, 2483-2485 (1991).
10. H. Nagai, Y. Noguchi, and S. Sudo, *Appl. Phys. Lett.* 54, 1719-1721 (1989).
11. K. Takada, A. Himeno, and K. Yukimatsu, *Opt. Lett.* 16, 1433-1435 (1991).
12. R. P. Novak, H. H. Gilgen, R. P. Salathe, W. Hodel, P. Beaud, J. Schutz, and H. P. Weber, in *Tech. Dig. Symp. Opt. Fiber Meas.*, 1988, 7-10.
13. K. Takada, N. Takato, J. Noda, and Y. Noguchi, *Opt. Lett.* 14, 706-708 (1989).
14. I. N. Duling III, W. K. Burns, and L. Goldberg, *Opt. Lett.* 15, 33-35 (1990).
15. H. Fevrier, J. F. Marcerou, P. Bousset, J. Auge, and M. Jurczyk, *Electron. Lett.* 27, 261-263 (1991).
16. K. Takada, M. Shimizu, Y. Yamada, A. Himeno, and K. Yukimatsu, *Electron. Lett.* 28, 29-30 (1992).
17. W. V. Sorin, D. M. Road, and S. A. Newton, in *Tech. Dig. Opt. Fiber Sens.* 1992, PD7.
18. J. Chamberlain, *The Principles of Interferometric Spectroscopy*, John Wiley & Sons, Chichester 1979.
19. P. -L. Francois, M. Monerie, C. Vassallo, Y. Durtteste, and F. R. Alard, *IEEE J. Lightwave Technol.* 7, 500-513 (1989).
20. B. L. Danielson, and C. Y. Boisrobert, *Appl. Opt.* 30, 2975-2979 (1991).
21. K. Takada, M. Kobayashi, and J. Noda, *Appl. Opt.* 29, 5170-5176 (1990).

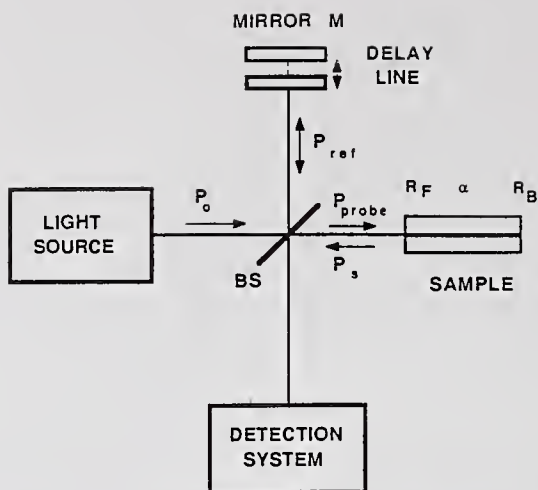


Fig.1. Schematic arrangement of OLCR (Ref. 6). R_F, R_B : end reflection coefficients.

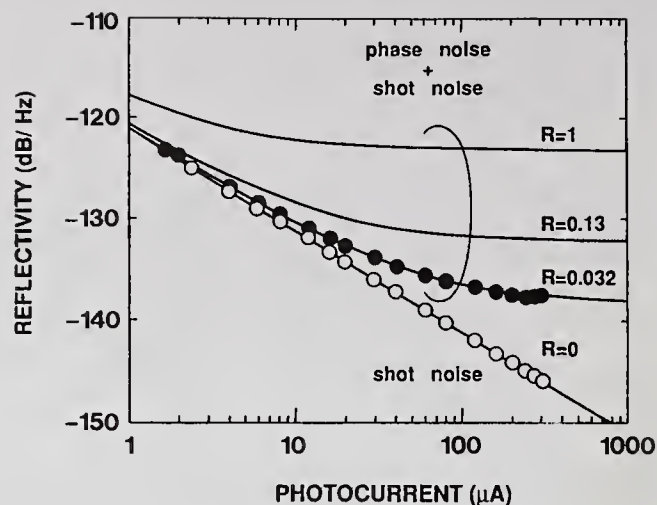


Fig.2. Minimum detectable reflectivity vs total mean photocurrent. Points represent experimental values.

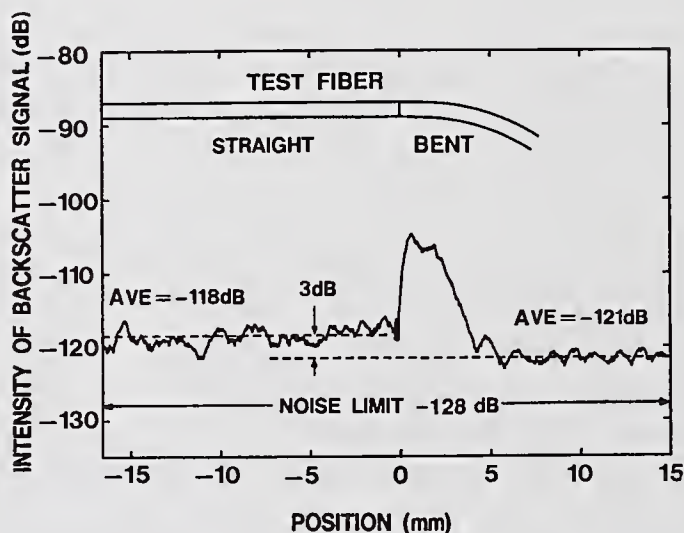


Fig.3. Backscatter signal change by fiber bending.

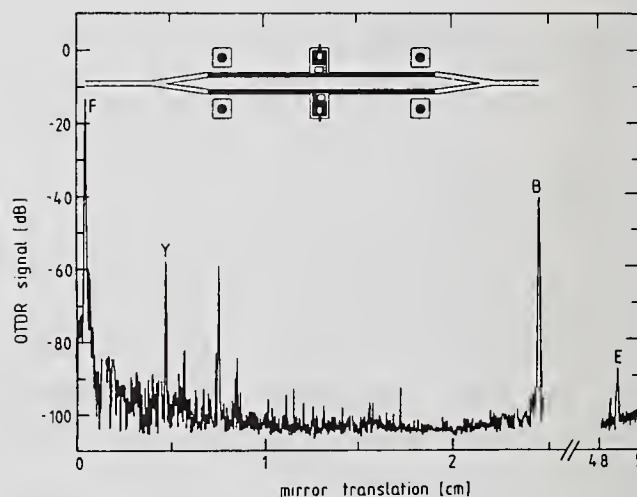


Fig.4. Backscatter signal from GaAs Mach-Zehnder interferometer (Ref.12).

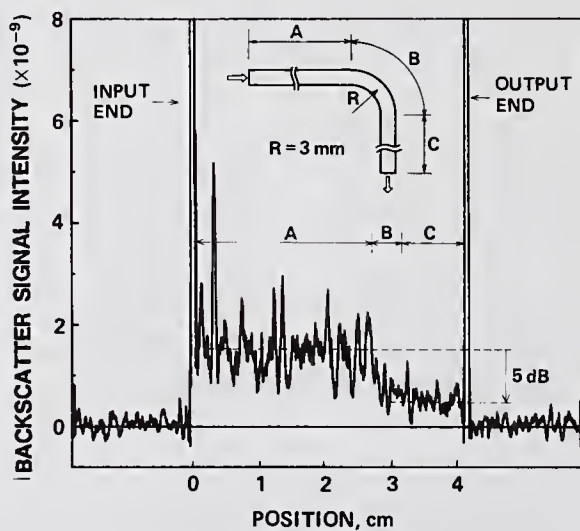


Fig.5. Backscatter signal from curved silica-based waveguide.

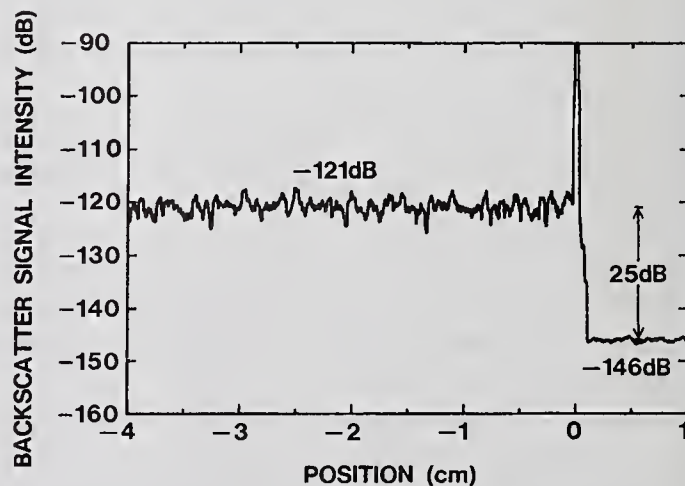


Fig.6. Backscatter signal from fiber in index matching oil.

Improved Sensitivity for Optical Low-Coherence Reflectometry using Reference Power Attenuation

W. V. Sorin and D. M. Baney
Hewlett-Packard Laboratories
3500 Deer Creek Road, Palo Alto, California 94303

Introduction

Optical Low-Coherence Reflectometry (OLCR) is a measurement technique capable of spatially resolving optical reflections separated by tens of microns with reflection sensitivities demonstrated as low as -148 dB [1]-[3]. Initial work consisted of a simple Michelson interferometer with a variable time delay in one arm [4]. It was soon realized that reflection sensitivities obtained using the simple Michelson interferometer were limited by the intensity noise associated with low-coherence sources. Minimum reflection sensitivities were set by intensity noise and did not improve as source power was increased. Using a more complex interferometer arrangement, it was later shown [2] that sensitivity limitations due to intensity noise can be removed. This arrangement consisted of a combined Michelson and Mach Zehnder interferometer allowing use of a balanced receiver to subtract out the intensity noise [1]-[3].

In this paper a simple modification to a Michelson interferometer based OLCR is proposed allowing for improvement of reflection sensitivities to a value similar to that achieved using the more complex balanced receiver approach. The main concept for the modification is the reduction of intensity noise at the optical detector via reference path attenuation. As will be shown, this improves the detected signal to noise ratio (SNR).

Theory

The Michelson interferometer with incorporated reference path attenuation is shown in figure 1. The interferometric beating between reflected powers from the reference and DUT (device under test) arms of the interferometer is detected as a function of the position of the translatable retroreflector. The following expression shows how the signal to noise ratio (SNR) of the photocurrent depends on the reflected powers from each arm.

$$SNR \propto \frac{P_{REF} P_{DUT}}{P_{REF} + K_I P_{REF}^2 + K_T}$$

The reflected powers incident onto the photodetector, P_{DUT} and P_{REF} are from the upper DUT and lower reference arms, respectively. This result assumes that $P_{DUT} \ll P_{REF}$ which is usually the case when attempting to obtain the greatest reflection sensitivity. The three terms in the denominator represent the shot noise, the intensity noise (RIN), and the receiver noise contributions, respectively. The parameters K_I and K_T are constants independent of the actual powers returning to the receiver. For reference powers on the order of $1 \mu\text{W}$ or more, the source intensity noise term $K_I P_{REF}^2$ becomes dominant. For this condition, the above expression shows that the signal to noise

ratio can be improved by attenuating the reflected reference power. This effect occurs since the detected noise decreases at a faster rate than the interferometric signal.

Figure 2 shows a plot of how the signal to noise ratio degrades as the returning reference power is varied using the attenuation method illustrated in figure 1. It is assumed that $P_{DUT} \ll P_{REF}$ for all values of P_{REF} . The shot noise limit is the best SNR that can be obtained for a given source power. Figure 2 assumes a receiver noise equivalent to the thermal noise from $1 \text{ M}\Omega$, a photodiode responsivity equal to 1 A/W , and a source RIN equal to -121 dB/Hz . For large values of the returning reference power, it can be seen that a 10 dB attenuation of P_{REF} equates to a 10 dB improvement in the SNR. Eventually, as P_{REF} is made too small, the receiver noise starts to become dominant and the SNR decreases with increased attenuation. The optimized value for the reference power occurs when the noise contributions due to the receiver and source RIN become equal. For the case when the above assumption of small P_{DUT} is not valid, then the best SNR occurs for $P_{DUT} \sim P_{REF}$. In this case, additional methods designed to remove the intensity noise should not be too useful since the effects of phase noise [5] should be of a similar value.

Experiment

Figure 1 describes the experimental arrangement used to demonstrate the sensitivity improvement possible using reference power attenuation. The low-coherence signal was obtained from an erbium doped fiber noise source. An unpolarized output power of 16 mW was generated at $1.55 \mu\text{m}$ with a spectral width of about 20 nm . The source RIN was measured to be -121 dB/Hz at the detection frequency of 20 KHz . The polarization controller in the lower reference arm was adjusted to maximize the interference signal at the photodetector. Attenuation of P_{REF} was achieved by adjusting the spacing between two angle polished fibers. The DUT consisted of a fiber cleaved at an angle to minimize the reflectivity from the fiber end. A phase modulator was used to translate the Doppler beat frequency to about 20 KHz to avoid the increased intensity noise that occurs at lower detection frequencies.

The measurement sensitivity with and without attenuation of the reference power is shown in figure 3. The upper and lower curves correspond to reference powers of $P_{REF} = 2 \text{ mW}$ and $P_{REF} = 200 \text{ nW}$ respectively. The increased reflectivity of the lower curve, for distances of less than 70 mm , corresponds to Rayleigh backscattering (RBS) from the DUT fiber. For the upper curve, corresponding to no attenuation, the RBS is completely masked by intensity noise. The difference in sensitivity of about 34 dB is in good agreement with that predicted from figure 2. The spatial resolution within the optical fiber was measured to be $20 \mu\text{m}$, which for the RBS level of -120 dB gives a normalized value of -73 dB/m for the DUT fiber. Data points were measured at $5 \mu\text{m}$ intervals and each 100 points were spatially averaged to reduce amplitude uncertainty. A reflection sensitivity of -134 dB as shown by the lower curve was achieved in a 30 Hz detection bandwidth. A sensitivity penalty of 5 dB was also present due to the detection scheme that measured the strength of the first order Bessel function of the sinusoidally phase modulated Doppler frequency. Taking the bandwidth difference and detection scheme into account, this sensitivity result is approximately equal to that obtained using the more complex balanced detection technique [1],[3].

Summary

This reference power attenuation technique offers several advantages over the more complex balanced detection technique. First, for a given translation range of the retroreflector, this new technique allows the use of a Michelson interferometer which gives twice the measurement range since the reference signal experiences a double pass through the corner cube retroreflector. Second, since only one receiver is required, accurate balanced detection does not have to be maintained and the implementation of a polarization diversity receiver is much easier.

By attenuating the reference power in a simple Michelson interferometer based OLCR, it has been shown that reflection sensitivity can be improved to values similar to that obtained using more complex approaches requiring two balanced receivers. Using this technique, a 34 dB improvement in reflection sensitivity was demonstrated when using a high power erbium doped fiber noise source.

References

- [1] W. V. Sorin and D. M. Baney, "Measurement of Rayleigh backscattering at 1.55 μm with a 32 μm spatial resolution," *Photonics Tech. Lett.*, vol. 4, 374 (1992).
- [2] K. Takada, K. Yukimatsu, M. Kobayashi and J. Noda, "Rayleigh backscattering measurement of single-mode fibers by low coherence optical time-domain reflectometer with 14 μm spatial resolution," *Appl. Phys. Lett.*, vol. 59, p. 143, 1991.
- [3] K. Takada, M. Shimizu, M. Yamada, M. Horiguchi, A. Himeno and K. Yukimatsu, "Ultrahigh-sensitivity low coherence OTDR using Er^{3+} -doped high-power superfluorescent fibre source," *Electron. Lett.*, vol. 28, p. 29, 1992.
- [4] B. L. Danielson and C. D. Whittenberg, "Guided-wave reflectometry with micrometer resolution," *Appl. Opt.*, vol. 26, p. 2836, 1987.
- [5] K. Takada, A. Himeno and K. Yukimatsu, "Phase-noise and shot-noise limited operations of low coherence optical time domain reflectometry," *Appl. Phys. Lett.*, vol. 59, p. 2483, 1991.

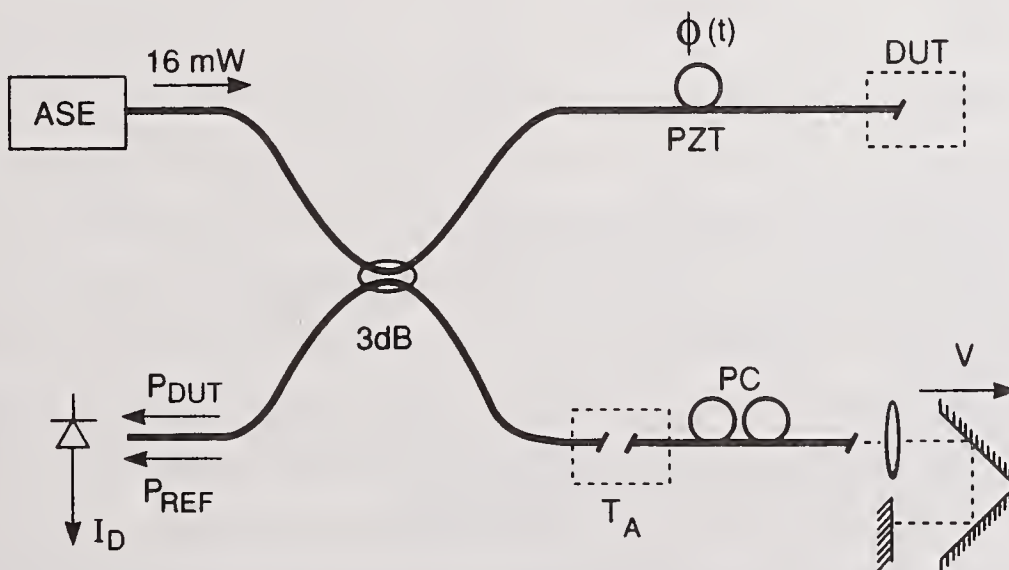


Figure 1. Experimental set-up for OLCR measurements using the reference path attenuation technique. PC: polarization controller, PZT: piezoelectric phase modulator, T_A : optical transmission of attenuator.

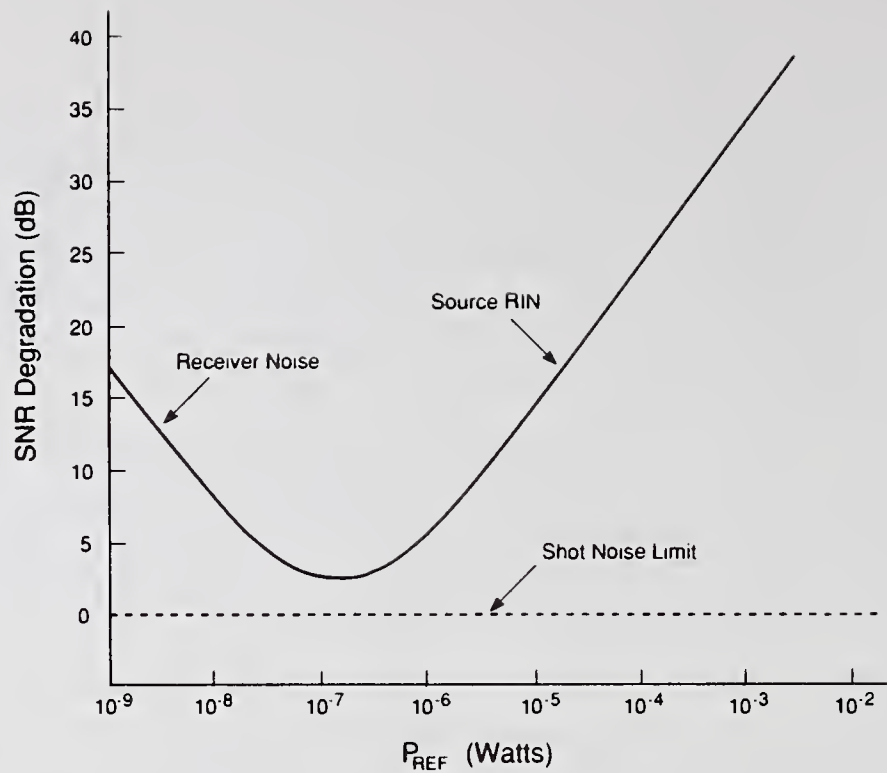


Figure 2. The effect of reference power on OLCR noise performance as limited by source intensity noise and receiver thermal noise.

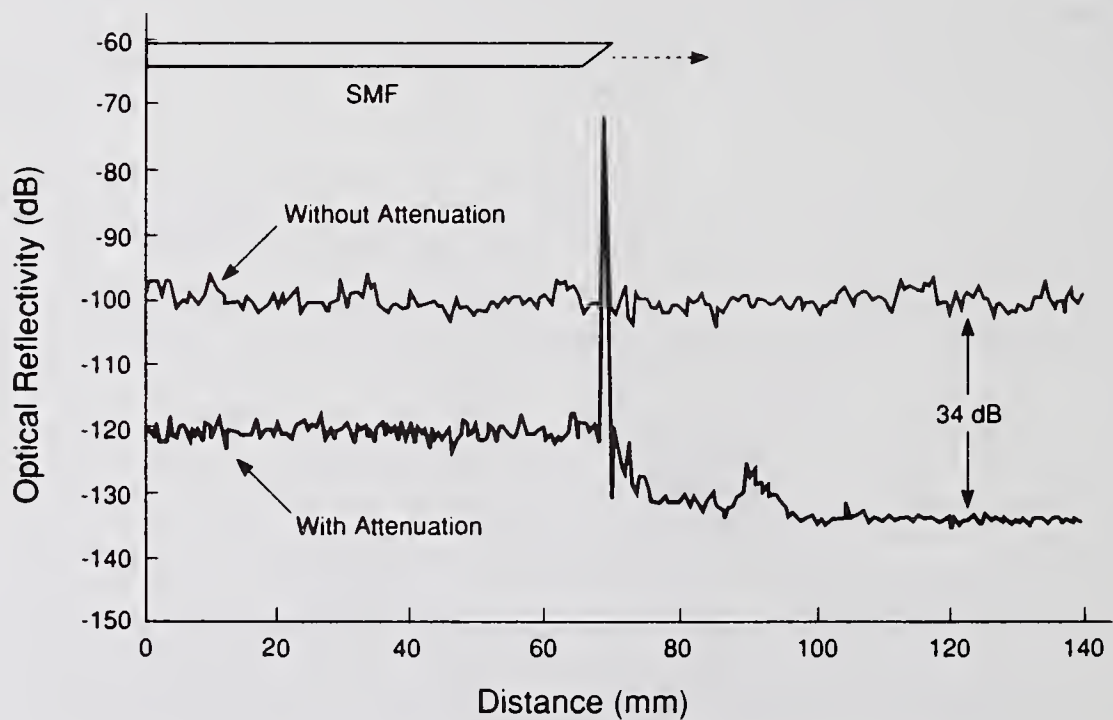


Figure 3. OLCR measurement of optical backscatter near the end of a cleaved single-mode fiber (SMF) with and without reference power attenuation. Detection bandwidth = 30 Hz, source limited resolution = 20 μm , resolution after spatial averaging = 340 μm .

Optical Low Coherence Reflectometry: Improving Reflectivity Accuracy in the Presence of Chromatic Dispersion

Harry Chou
Hewlett-Packard Co.
1400 Fountaingrove Parkway
Santa Rosa, CA 95403

Introduction

Optical low coherence reflectometry (OLCR), also known as white light interferometry, is an important non-destructive technique for probing small optical devices.[1-3] Its main advantages are high resolution and excellent dynamic range. In a typical system, chromatic dispersion can play an important role due to the broadband source needed to achieve high resolution. A mismatch between the dispersion properties of the two arms of the interferometer will result in the broadening of the interferogram and a reduction in its peak magnitude. This can lead to an error in the measurement of reflectivity if the peak magnitude is used to calculate reflectivity. A number of researchers have examined the effects of chromatic dispersion in OLCR.[4-7] The general problem of recovering the true signal from the dispersion-broadened signal has been treated by Brinkmeyer et. al.[4,5] In this paper, we present data on the dependence of the reflectometer signal as a function of the length of dispersion mismatch, and demonstrate reasonable agreement with a Gaussian model. We have used this model to improve the accuracy of reflectivity measurements.

Experimental Apparatus

The experimental setup is a Michelson interferometer, as shown in Fig. 1. Only the 1550 nm source (an edge-emitting light emitting diode) is used in this work. A 3-dB directional coupler splits the light into the reference and test arms of the interferometer. The light exiting the reference arm fiber is polarized by a polarizer and collimated by a lens. The collimated beam is reflected from a flat gold mirror after going through a corner cube, which is movable to provide 400 mm of maximum delay. In the receiver arm, a polarization diversity receiver is used to reduce the sensitivity of the interference signal to the polarization transformations of the test arm fiber. This is achieved by first setting up the polarization split in the receiver such that the optical power returned from the reference arm alone is about equally divided between the two orthogonal polarizations of the receiver. Then the interferograms of the two polarization channels are envelope-detected, digitized, and mathematically

combined to produce a peak value proportional to the reflectivity of the interface under study. Chromatic dispersion, however, will decrease this peak value and lead to an apparently lower reflectivity if uncorrected.

Experimental Results

To obtain the variation of the peak signal with length of dispersion mismatch, a set of four fiber cables of different lengths with polished ends was used to sample four points along the 400 mm range of the interferometer. The fiber ends had been measured in a power meter-coupler setup to have a return loss of -14.73 ± 0.085 dB. The cables were then each connected to the test port of the reflectometer and the reflectivity signal was measured. In each case, the connection loss at the test port and the change in the power returned from the reference arm were also measured and taken into account. The peak signal measured for the shortest cable was taken to be 0 dB and all the others were referenced to it. To check for consistency, the same measurement was made on three systems of the same block diagram, and the data are shown in Fig. 2.

Model

We model the free-space coherence envelope of the optical field as a Gaussian with a full $1/e$ width of W_0 . After going through a dispersive medium, the pulse is broader in width and lower in peak amplitude.[8] The quantity of interest is the peak magnitude squared of the correlation function between the unbroadened and dispersion-broadened optical fields, since it is used to compute the reflectivity. By carrying out the calculation of the correlation function, we obtain the following dependence

$$S(L) = \frac{2W_0\sqrt{W_0^2 + (2DL\Delta\lambda)^2}}{\sqrt{[2W_0^2 + (2DL\Delta\lambda)^2]^2 + (2DLW_0\Delta\lambda)^2}}$$

where L is the length of the dispersion mismatch, $S(L)$ the apparent reduction in reflectivity due to dispersion broadening ($S(0)=1$), D the dispersion coefficient, and $\Delta\lambda$ the full width at half maximum of the source spectrum. W_0 is related to $\Delta\lambda$ by

$$W_0 = 2 \frac{\sqrt{2 \ln 2}}{\pi} \frac{\lambda^2}{\Delta \lambda} \frac{1}{c}$$

where λ is the peak wavelength of the source and c the free-space speed of light. The following parameter values yielded a good fit to the experimental data:

$$D = 17.5 \text{ ps}/(\text{nm} \cdot \text{km})$$

$$\Delta \lambda = 60 \text{ nm}$$

as shown in Fig. 2. These are reasonable values for the sources and fibers used in these measurements.

Conclusions

We have demonstrated reasonable agreement between experimental data and a Gaussian model to account for the dependence of the peak signal of a low coherence reflectometer on the length of dispersion mismatch. We have used this model to improve the accuracy of reflectivity measurements.

Acknowledgement

The author wishes to thank Wayne Sorin and Steve Newton for helpful discussions and Howard Booster and Roger Wong for their support.

References

1. K. Takada, N. Takato, J. Noda, and Y. Noguchi, *Optics Lett.* **14** 706 (1989)
2. B.L. Danielson and C.D. Whittenberg, *Applied Optics* **26** 2836 (1987)
3. R.C. Youngquist, S. Carr, and D.E.N. Davies, *Optics Lett.* **12** 158 (1987)
4. E. Brinkmeyer and R. Ulrich, *Electron. Lett.* **26** 413 (1990)
5. A. Kohlhaas, C. Fromchen, and E. Brinkmeyer, *J. Lightwave Technology* **9** 1493 (1991)
6. P. Merrit, R.P. Tatam, and D.A. Jackson, *J. Lightwave Technology* **7** 703 (1989)
7. P.-L. Francois, M. Monerie, C. Vassalo, Y. Durteste, and F.R. Alard, *J. of Lightwave Technology* **7** 500 (1989)
8. A. Yariv, *Optical Electronics*, Third Ed., p. 42 (Holt Rinehart & Winston, Orlando, 1985)

HP 8504A OVERALL BLOCK DIAGRAM

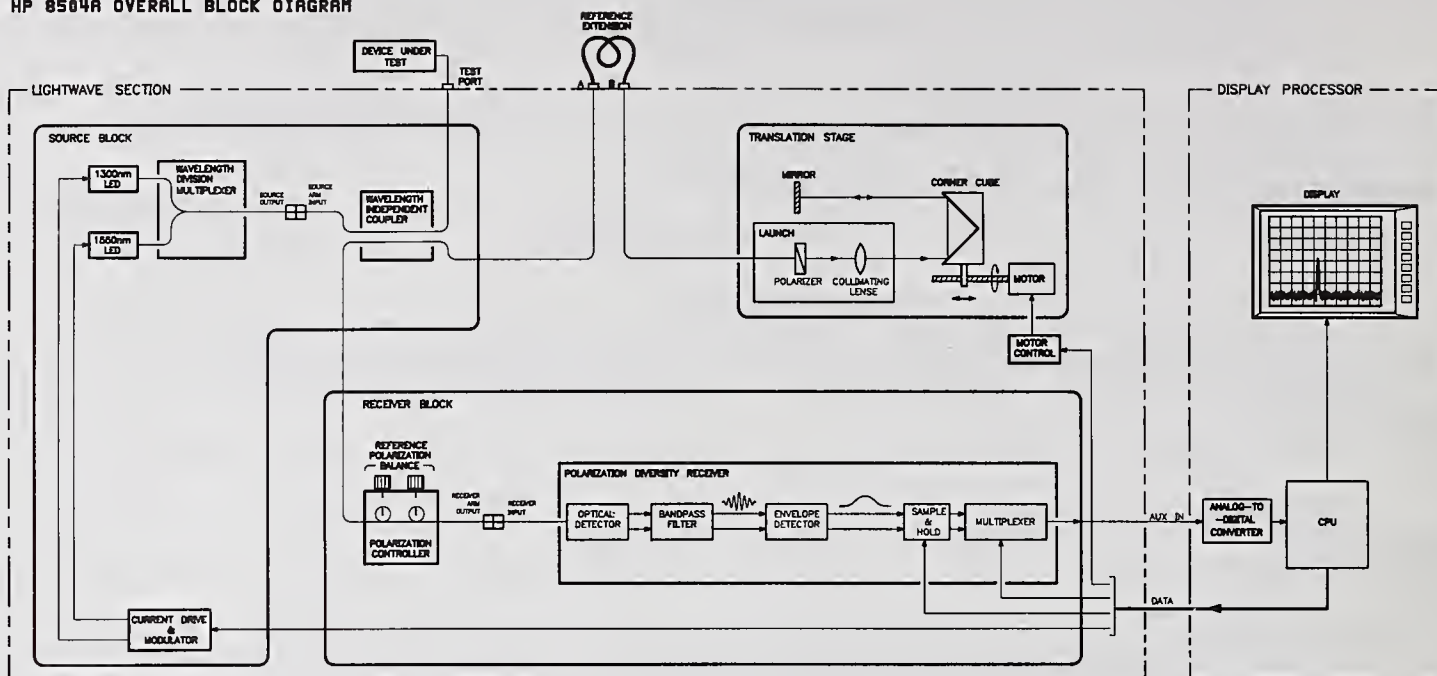


Fig. 1 Schematic of the experimental apparatus.

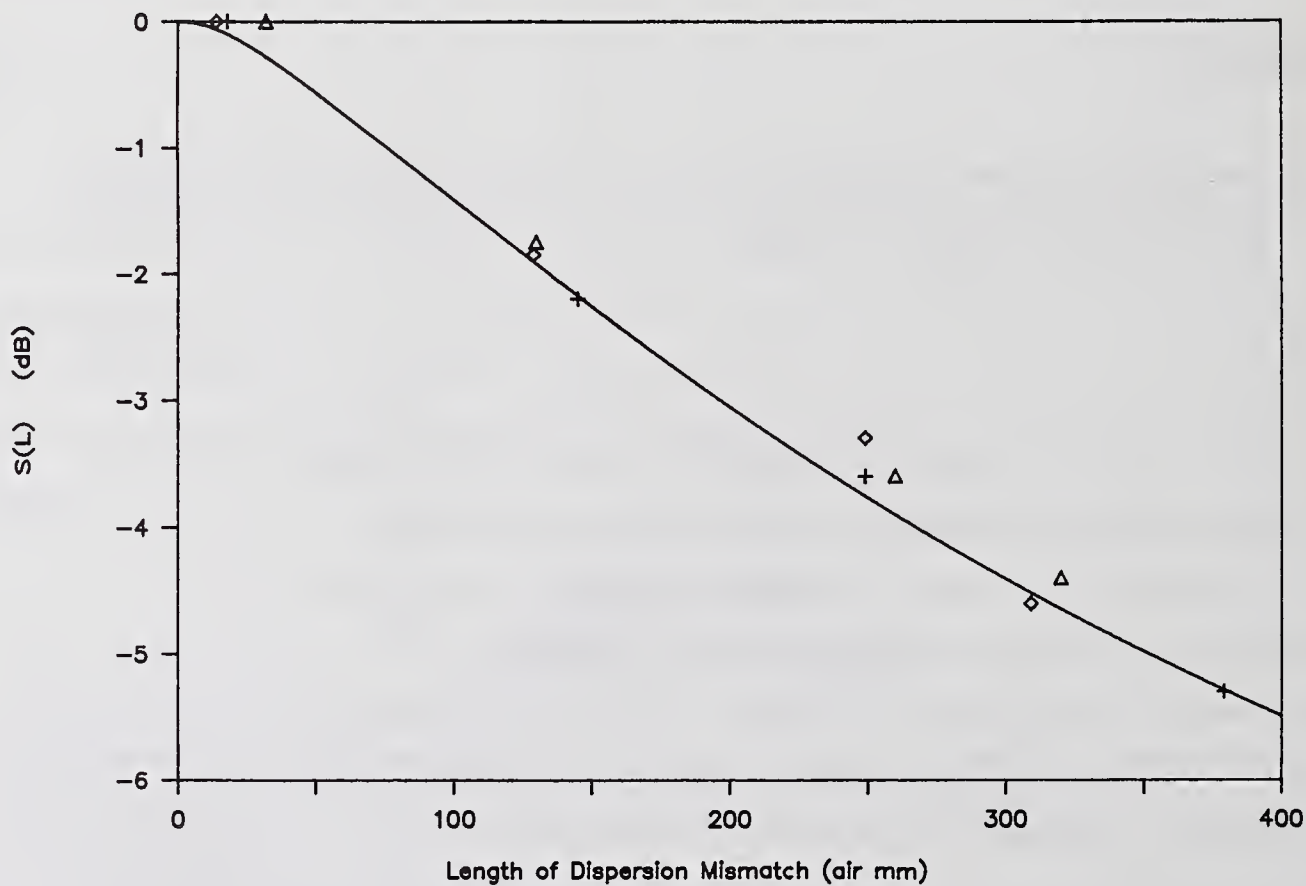


Fig. 2 Dependence of the reflectivity signal on the length of dispersion mismatch. The data points are for three systems of the same block diagram as shown in Fig. 1.

STANDARDISATION IN FIBRE OPTIC COMMUNICATIONS: STATUS AND PERSPECTIVES

P. Di Vita, M. Artiglia, A. Cavaciuti, M. Potenza, A. Rossaro
CSELT - Via G. Reiss Romoli, 274 Torino (Italy)

Abstract

The activity of standardisation in the field of fibre optic communications is reviewed with emphasis on new developments in optical fibres, optical amplifiers and on new trends in the telecommunication network.

1. Introduction

Standardisation is one of the major aspects for the development of every industrial field, since it mirrors the confrontation and the agreement between customers and manufacturers requirements and brings to a rational and widespread diffusion of the industrial products. This is particularly true in the field of fibre optic communications where developments are going increasingly rapid. New applications for optical components and new functions and enhanced capabilities for the optical network are coming to light. New network architectures can be introduced thanks to the availability of optical amplifiers and particularly Optical (active) Fibre Amplifiers (OFAs) with their high efficiency and versatility. Standardisation of components and subsystems represents a key condition for a rational development of the optical network all over the world.

The aim of this activity is two-fold: specify the physical parameters featuring the performance of each device and characterize it in terms of such quantities through a univocally defined and well assessed set of measurements. This in turn will allow the optimized interfacing of the various components and the exploitation of the full system capabilities and would be of great help in designing the systems themselves. On the other hand it is also evident that a premature full standardisation could, to a certain extent, prevent the proper evolution of the technology. With the rapid pace of development of optical communications it is not always easy to understand where the proper border between research and standards should be placed. This is the hard task of the standardisation bodies, who should reach the ideal trade-off between these two opposite needs.

To understand the importance and complexity of this problem, it is worth mentioning the groups of standardisation bodies at international level (see Figs. 1 and 2) such as the CCITT (Com. XV) and IEC (TC 86). These groups are supported by some regional bodies, such as the EIA/TIA and the T1 Committee in the USA, the TTC of Japan, the Asian ISDN Council in the Far East (although primarily commerce oriented) and in Europe the ETSI (stc TM1) and the Cenelec/CECC (WGs 26, 27, 28) that bring to the attention of the international community the needs emerging from local demands that have to be harmonised in the framework of a global project and in the meantime provides a mean of diffusing the standards agreed upon at international level. Last but not least, standardisation bodies also represent a forum for confronting and harmonising the requirements of such differently motivated interests as those of users and suppliers of industrial products. Important working tools for the standardisation activity are studies carried out by individual companies and institutions as well as interlaboratory comparisons at regional and international levels, which have been of great help in identifying the characterisation parameters and the crucial aspects of the pertaining test methods.

In the following section we shall review the present status of standardisation activities in the field of single-mode fibres including the latest developments. Section 3 will treat possible lines of evolution of the optical network motivated by the introduction of optical amplification. Finally, Section 4 will briefly cover some aspects of system and component standardisation issues.

2. Standardisation of single mode fibres

The preferred physical carrier in today telecommunication systems is the single-mode fibre (SMF) with its very low attenuation and huge bandwidth. Standardisation of SMF is in progress since the middle of 70s and has reached a good level of maturity. As a result, relevant documents [1-6] on SMFs have been published which unambiguously define proper parameters featuring the fibre behaviour, give accurate descriptions of their test methods and fix recommended range of values.

Within SMFs, CCITT actually gives recommendations for three types of fibres: SMFs dispersion optimized around 1310 nm covered by Recommendation G.652 [2]; dispersion shifted SMFs, dispersion optimized around 1550 nm, in correspondence of the absolute attenuation minimum, covered by Rec. G.653 [3]; and SMFs loss minimized (but not dispersion optimized) around 1550 nm, covered by Rec. G. 654 [4], for use in the third transmission window. Up to now, dispersion flattened fibres are not considered in CCITT Recommendations, but work is in progress in IEC.

A synthetic specification of SMFs through the mode field diameter, the cutoff wavelength, the attenuation coefficient, the chromatic dispersion parameters and the geometric and dimensional parameters had been chosen. In the following some evolution trends concerning these parameters and the relative test methods are discussed. CCITT considers two categories of test methods: the Reference Test Methods (RTMs) and the Alternative Test Methods (ATMs). RTMs ensure the maximum accuracy and are directly related to the definition of the parameter. ATMs may be more practical than RTMs but unambiguously related to them.

2.1 Mode field diameter

The MFD [1] provides information about micro- and macro-bending sensitivity of the SMF and about joint performances [7,8]. Actually all standardisation bodies have adopted the MFD definition based on the inverse of the rms angular width of the far field pattern of the fibre [8,9]. Correspondingly, the recommended RTM is the far field scan of the fibre exit radiation pattern, while the variable aperture technique, the knife-edge scan and the near field scan have been considered as ATMs [1]. The transverse offset technique, once very popular, has been discarded from the set of test methods because of the intrinsically poor reliability and repeatability, as demonstrated by the results of various Round Robin Tests (RRT) [10,11].

As previously said, the MFD influences microbending losses. However, a very accurate prediction depends also on other parameters as the mode propagation constant and the statistic parameters of the microbending perturbation, which are difficult to measure. Some Committees (IEC, CECC) are considering standards on microbending loss tests directly and proposals are under study.

2.2 Cutoff wavelength

The Cutoff WaveLength (CWL) of the first higher order mode determines the spectral region of effective single-mode operation of the fibre. Its operational definition from a measurement of the power transmitted by the fibre in a given deployment condition, referenced to that of the fibre itself with a small bend inserted or a multimode fibre has been widely accepted since the middle of 80s. At first, only the uncabled CWL was considered, as measured on a fibre sample 2 m long bent on a loop of 140 mm radius [1]. Though this quantity favoured enhancement of the agreement among manufacturers and users, it was felt that this parameter only was too conservative in view of long distance applications. For this reason the cabled CWL has been introduced, as measured on a cable section 22 m long, including two uncabled fibre tails 1 meter long [1] with small loops - diameter 80 mm - to simulate the effect of splice organisers (RTM); however, the definition of this parameter raises some problems. In the first place, as far as the test method is concerned, the cabled CWL measurement is heavily destructive. To circumvent this problem, an ATM has been proposed where 22 m of uncabled fibre are suitably deployed. Some debate is in run concerning the diameter of the small loops at the fibre ends: only recently IEC and CCITT reached an agreement on the value of 80 mm. In second place, the cabled CWL can depend on the cable type and is application-dependent. A possible way out of this problem is empirical and consist of developing mapping functions relating on a statistical basis the cabled CWL for a given cable structure to the uncabled CWL of the used fibres: also this aspect is actually matter of study.

Finally, international intercomparisons have shown that the reproducibility of uncabled CWL measurements is in some cases severely affected by the presence of unpredictable humps in the spectral transmission curve [12,13] which seem to be due to coupling between the radiating higher order mode and modes of the fibre cladding. They are very much sensitive to the fibre refractive index profile and curvatures. Work is in progress to get a deeper understanding of the phenomenon so as to devise means of eliminating their uncontrollable effect on the determination of CWL. The use of suitable fitting functions is under study.

2.3 Attenuation coefficient and losses

The standardisation of SMF attenuation is generally well assessed. The RTM recommended by CCITT is the cut-back method, which is partially destructive and requires access to both fibre ends.

A very popular technique overcoming the aforementioned drawbacks is the backscattering (OTDR) technique, recommended by CCITT as an ATM, which is very practical and can also be used for routine measurements and testing of installed plants.

Presently the discussion is open on how to set properly attenuation specifications for practical system applications. While a description in terms of attenuation coefficient at the center of the various transmission windows is generally accepted, it can be of interest to consider attenuation properties over a certain spectral range around the nominal ones. This fact could permit to reach an economical trade-off between system performance and cost with reference to actual applications. This could allow, for example, to tolerate a wider spread of source emission wavelengths in short range links, such as the subscriber loop; moreover, consideration of WDM transmission systems also pushes in the direction of an attenuation standard given on a suitable range of wavelengths.

A convenient way of setting more flexible attenuation specifications in a more application-oriented form, seems to be that of spectral attenuation modelling. This should be based on the measurement of the attenuation coefficient at a given small set of predictor wavelengths (say 1300, 1330, 1370, 1380, 1550 nm) and evaluating the attenuation coefficients for a larger set of wavelengths (say 10 nm spaced wavelengths in the range 1260-1600 nm) by means of a suitable matrix (and eventually of a correction vector) whose elements have to be calculated on a statistical basis for each fibre type and manufacturer, due to the dependence of the attenuation spectra on the actual fabrication process. This procedure is actually reported as an Appendix to CCITT Rec. G. 652 [2]. Need is felt to consider a similar algorithm for G.653 fibres too.

A loss parameter of increasing importance is related to the longitudinal uniformity of the fibre. The problem of its definition and testing appears among the questions for the next CCITT/XV study period 1993-1996: a possible solution could be based on the analysis of the backscattering traces of the fibre under test. In fact, some of the fibre parameters, such as the MFD and the CWL, can be measured only at the ends of a fibre section; for some other parameters, such as attenuation and dispersion, global values on the whole length are measured: a longitudinal uniformity criterium should ensure that also these parameters are uniform all along the sample: this aspect is important when the factory lengths of fibre are much longer than the cable units obtained from them.

2.4 Dispersion

Chromatic dispersion (CD) sets a limit to the transmission capacity of a SMF. Presently it is standardised in terms of the wavelength and slope of the dispersion curve versus wavelength at the zero dispersion point. Spectral fitting functions (different for dispersion-unshifted and dispersion-shifted fibres) are also provided which give limits for the CD coefficient in terms of minimum and maximum allowable values for the zero dispersion wavelength and of maximum allowable value for the zero dispersion slope [2,3].

The recommended RTM for the determination of CD parameters is the phase shift technique, while ATMs are the pulse delay technique and the interferometric method. The latter is intrinsically the most accurate (assuring time resolution in the order of 0.1 ps) but can be applied to short fibre lengths (2-5 m) only. Therefore its reliability depends on the longitudinal uniformity of the fibre itself.

All methods giving the CD coefficient from measurements of the spectral time delay share a common delicate aspect, i. e., the choice of the fitting function to interpolate the experimental data. The various Committees have recommended standard functions such as the three-term Sellmeier expansion for dispersion-unshifted fibres and the parabolic fit for dispersion-shifted ones, to which the spectral fitting functions mentioned at the beginning of this Section are related. However, if dispersion-flattened fibres will be considered by standardisation bodies, a new suitable fitting function should be found: this question is still matter of study.

A characteristic of SMFs of special interest in long-haul high-bitrate systems for which the need for standardisation is emerging, is the Polarisation-Mode Dispersion (PMD). It originates from the fact that, contrary to what happens in ideal fibres, the two orthogonal polarisations of the fundamental mode of an actual fibre do not propagate with the same group velocity, because of fluctuations of fibre geometric and optical parameters or random stresses caused by the cabling process, which induce unwanted birefringence. The resulting statistical distribution of group velocities along the fibre causes a broadening of the launched pulse. This effect becomes relevant for long distance, high capacity systems where ultra-low chromatic dispersion fibres and very narrow linewidth laser sources are used; in this application PMD can represent the ultimate limitation to the system performance. Problems could also arise in systems making use of optical isolators, such those employing optical amplifiers, see

Sect. 3. Proposals are under study at CCITT to define proper parameters to describe PMD and suitable test methods: the question has been inserted in the list of arguments for the next study period.

2.5 Geometry

The relevant geometrical parameters of SMFs are: the MFD, the mode field concentricity error, the cladding diameter and the cladding non-circularity. Leaving aside the MFD which has been already considered in Sect. 2.1, the RTM for the other geometric parameters is the transmitted near-field technique. Actually recommended ATMs are the refracted near field, the side-view and the imaging transmitted near field. The present status of fibre geometry specifications is not yet satisfactory because both the RTM and the ATMs suffer from relatively large reproducibility errors, as demonstrated by various international measurements intercomparisons [10,14], which only in part can be attributed to local geometry fluctuations along the fibre sample. The question of fibre geometry has assumed a high level of importance for related industries, because of the wide use of mechanical connectors expected in optical links such as those involved in the project Fibre-To-The-Home (FTTH). The necessity of keeping losses and costs of connectors and mechanical splices to a minimum, pushes for a tighter tolerance of fibre geometry. Considerable efforts have been done to improve the accuracy of existing methods and look for new ones; interferometric and micrometric methods are gathering increasing interest [14,15]. Presently a new extensive RRT of geometry measurements is in run organised within CCITT/XV with the aim to identify the most reproducible methods and algorithms for experimental data analysis.

2.6 Mechanical properties

Specifications in this area are intended to characterise the in-service reliability of optical fibres with respect to environmental and deployment conditions. Because of the ever increasing use of optical fibres in aerial, buried and submarine cables, the interest for the aspect of predictability of fibre lifetime is now crucial. Test methods for strength testing have been set by IEC [5,6], and recently revised, by CCITT. A parameter measuring the fibre resistance to stress corrosion, which is empirically related to the dependence of crack growth on applied stress, has been included in CCITT Recs. G.650 to G.654. The introduction of further parameters is under study.

3. Future trends in the optical network

The development of optical amplifiers of various types has quickly led to impressive enhancements of the performance of optical communications systems. Ultimately it can be envisaged to arrive to substantially transparent and lossless links, allowing new network architectures and increased capability for provision of new services. Moreover, non linear transmission techniques, such as soliton based systems, have demonstrated their practical viability and paved the way to long-haul non-repeated links, because of the dispersion compensation provided by non linearity. Besides this, a more efficient exploitation of the huge fibre bandwidth could be achieved by means of wavelength multiplexing techniques, that would result useful also for enhancing the throughput of switches. These features strongly push towards an all-optical telecommunication network where unprecedented and unparalleled possibilities are offered to system and network designers to meet the requirements of the telecommunication market. New functionalities to the optical network could also comprehend distribution of radio-satellite signals (CATV, HDTV) and provision of a high-capacity framework for mobile radio systems, the use of which is rapidly growing world wide.

In the light of these trends, entirely new fields of activity are opened to standardisation bodies. Fig. 1 shows how CCITT is planning to face these new items in the next study period.

3.1 Standardisation of active fibre amplifiers

The standardisation activities on OFAs are worth of particular mention. In fact, in very few years, very rapid technological developments have made it possible to transform Erbium doped OFAs from laboratory to commercial devices. The enormous potentials of OFAs and their near use in telecommunication systems around 1550 nm have brought the problem of their standardisation to an international level, in order to fix uniform and homogeneous requirements on OFA performances and supply adequate informations for users in the choice of suitable devices for the various applications (in-line amp., pre-amp., booster).

In its last meeting (May 1992), CCITT has in fact prepared Rec. G.661 [16] concerning the definition of the relevant parameters of an OFA, seen as a black-box (with at least two optical ports and electrical connections for power supply), characterizing its transmission and operation properties.

As far as the test methods are concerned they will be covered together with reliability and environmental characteristics by the IEC Generic Specification on Optical Fibre Amplifiers, currently under development, to which Rec. G. 661 will make reference. IEC (TC86 - WG6) has also developed a Technical Report (not a standard) on OFA components containing the definitions of the relevant parameters of the essential components inside the OFA. As future activities, CCITT has planned to develop by 1994 two new Recommendations; the first on the generic characteristics of OFAs, the second on system aspects of OFAs. IEC will complete the aforementioned documents by 1993 and in parallel will begin to develop section and blank detail specifications, for each particular application of OFAs. Simultaneously a considerable activity is going to be developed on the system specifications in a way to take into account the introduction of OFAs.

4. Standardisation of systems and components

Because of the high flexibility of the optical network which allows its use at various levels from small private LANs to broadband services on an international scale, there will be in the immediate future an enormous demand for optical components and for standards to efficiently interface systems at different function levels. In fact, standardisation of systems and components is mandatory in order to allow users, network and service suppliers to design compatible links and system interfaces using components from a variety of unrelated suppliers. In addition to this, effective management of complex telecommunication networks requires sophisticated management systems. Again network suppliers are free to buy equipment from several manufacturers, leading to increasing demand for standardisation in the fields of operation, management and maintenance too [17]. Some examples are given by FDDI and IEEE 802 standards as regards high-speed data communication LANs, based on MM fibres. The ETSI MAN standardisation activity covers aspects of architecture and protocols within the European public networks and the specification of a public connectionless data service. ETSI has also set up a MAN Working Party with the purpose of defining MAN architectures, protocols and services suitable for an evolution towards the future B-ISDN [18]. At CCITT, standardisation activity is in progress for regulating the evolution from ISDN to B-ISDN. These efforts are very important because they are setting out the framework for the development and introduction of future broadband networks, regulating the introduction of new sets of services such as CATV or HDTV, or providing standard access to the existing ones. This would bring about cost benefits for both manufacturers and service suppliers. However, up to now this is perhaps the least mature area of the standards process. Some problems have been solved, setting some standards for digital networks, such as SONET and SDH, but analog (such as CATV) and distribution (such as PONs) network standardisation is still far behind.

At the level of single components some specification issues are still open. As far as fibre passive components are concerned, activities are in progress at IEC (SC86B), ETSI (TM1) and CECC (WG27). In particular, various subgroups of IEC-SC86B (see Fig. 2) are concerned with generic, mid-level and detailed specifications of joints and connectors (WG1), branching devices, attenuators, multiplexers (WG2), and relevant test methods, reliability and quality control (WGs 3-5). Work is also in progress to set specifications on switches and optical isolators. It is worth noting that passive optical components are extensively employed also in OFAs manufacturing.

Particular care requires the characterisation of general branching-devices that can be done in terms of the insertion loss matrix, from which parameters such as excess loss, coupling ratio, directivity, return loss and isolation can be derived. An important feature of all kinds of passive components, and particularly connectors, is the Optical Return Loss (ORL), which characterises the amount of back-reflected light; presently the specification of ORL is under study in the various Committees. Also the polarisation sensitivity of branching devices and optical isolators is of concern.

5. Conclusions

The globalisation of economy and the needs for all telecommunication actors (network operators and manufacturers) to deploy common solutions, ask for the availability of internationally recognised standards. This is becoming a precondition to be able to successfully offer new services and the corresponding equipments. Standardisation plays an important role also in the regulation process and is crucial in the evolution towards an open telecommunication market. Some criteria of non-discrimination among suppliers, international networking, uniform availability with homogeneous quality of services and interworking or interchangeability of different equipments, lead to the conclusion that larger markets are only accessible for services which are either full-standardised or, at least, make use of standardised elements necessary for compatible communications. This should

indicate a rapid introduction of standards, in order to avoid problems associated with incompatible implementations. The ISDN represents a clear case in which the lengthy process for harmonisation and standardisation is one of the factors that have so far delayed the time schedule for its availability. On the other hand there are some new technologies (e.g. the OFAs) which are still under development, although already introduced in the market. In this case a judicious, progressive setting of standards will permit an harmonised development of the application without preventing further progress of the research in the corresponding fields.

References

- [1] CCITT Recommendation G.650, "*Definition and test methods for the relevant parameters of single-mode fibres*"
- [2] CCITT Recommendation G.652, "*Characteristics of a single-mode optical fibre cable*"
- [3] CCITT Recommendation G.653, "*Characteristics of a dispersion shifted single-mode optical fibre cable*"
- [4] CCITT Recommendation G.654, "*Characteristics of a 1550 nm wavelength loss minimised single-mode optical fibre cable*"
- [5] International Standard IEC 793/1, "*Optical fibres - Part 1: Generic specifications*"
- [6] International Standard IEC 793/2, "*Optical fibres - Part 2: Product specifications*"
- [7] CSELT Technical Staff, "Fiber Optic Communications Handbook", TAB/McGraw-Hill, Blue Ridge Summit (PA), (1990).
- [8] M. Artiglia et al. , "*Mode Field Diameter Measurements in Single-Mode Optical Fibers*", J. Lightwave Technol. Vol. 7, No. 8, pp. 1139-1152, (1989).
- [9] K. Petermann, "*Constraints for fundamental-mode spot size for broadband dispersion-compensated single-mode fibres*", Electron. Lett. Vol. 19, pp. 712-714, (1983).
- [10] COST 217 Group, "*Interlaboratory measurement campaign on single-mode fibres*", IEE Proc. Pt. J, Vol. 136, No. 6, pp. 307-314, (1989).
- [11] B. Walker, COST 217 Group, "*COST 217 intercomparison and analysis of fibre mode field diameter measurements*", IEE Proc. Pt. J, Vol. 138, No. 6, pp. 373-378, (1991).
- [12] G. Kuyt, COST 217 Group, "*COST 217 interlaboratory comparison of uncabled and cabled fibre cut-off wavelength measurements*", Tech. Dig. of the Optical Fibre Measurement Conference, York (U.K.), Sept. 17-18, pp. 12-15 (1991)
- [13] S.A. Jacobs, D. W. Peckham, "*The anomalous structure observed in single-mode fiber cutoff wavelength measurements: theory and solutions*", Tech. Dig. of the Symposium on Optical Fiber Measurements, Boulder (CO), pp. 49-54, (1990).
- [14] W.T. Kane, "*The first international fibre geometry round robin*", Tech. Dig. of the Optical Fibre Measurement Conference, York (U.K.), Sept. 17-18, pp. 119-122 (1991)
- [15] M. Young, "*Fiber Cladding diameter by contact micrometry*", Tech. Dig. of the Optical Fibre Measurement Conference, York (U.K.), Sept. 17-18, pp. 123-126 (1991)
- [16] CCITT Recommendation G.661, "*Definitions and test methods for the relevant generic parameters of optical fibre amplifiers*"
- [17] CCITT Recommendation M.30, "*Principles for a Telecommunications Management Network*"
- [18] ETSI NA 5 Working Party on MAN, Report of the meeting , Stockholm, Sweden (October 28-November 2, 1990).

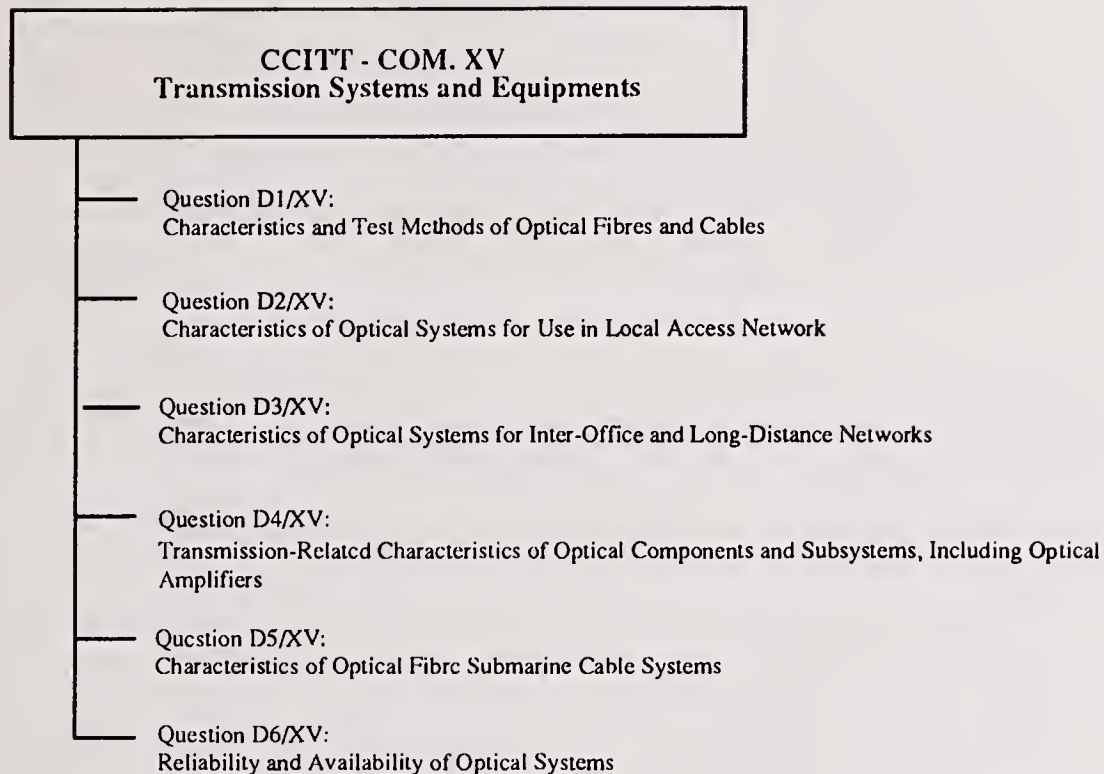


Fig. 1 - Proposed structure for Studies on Fibre Optic Communication in CCITT for the next Study period (1992-1996)

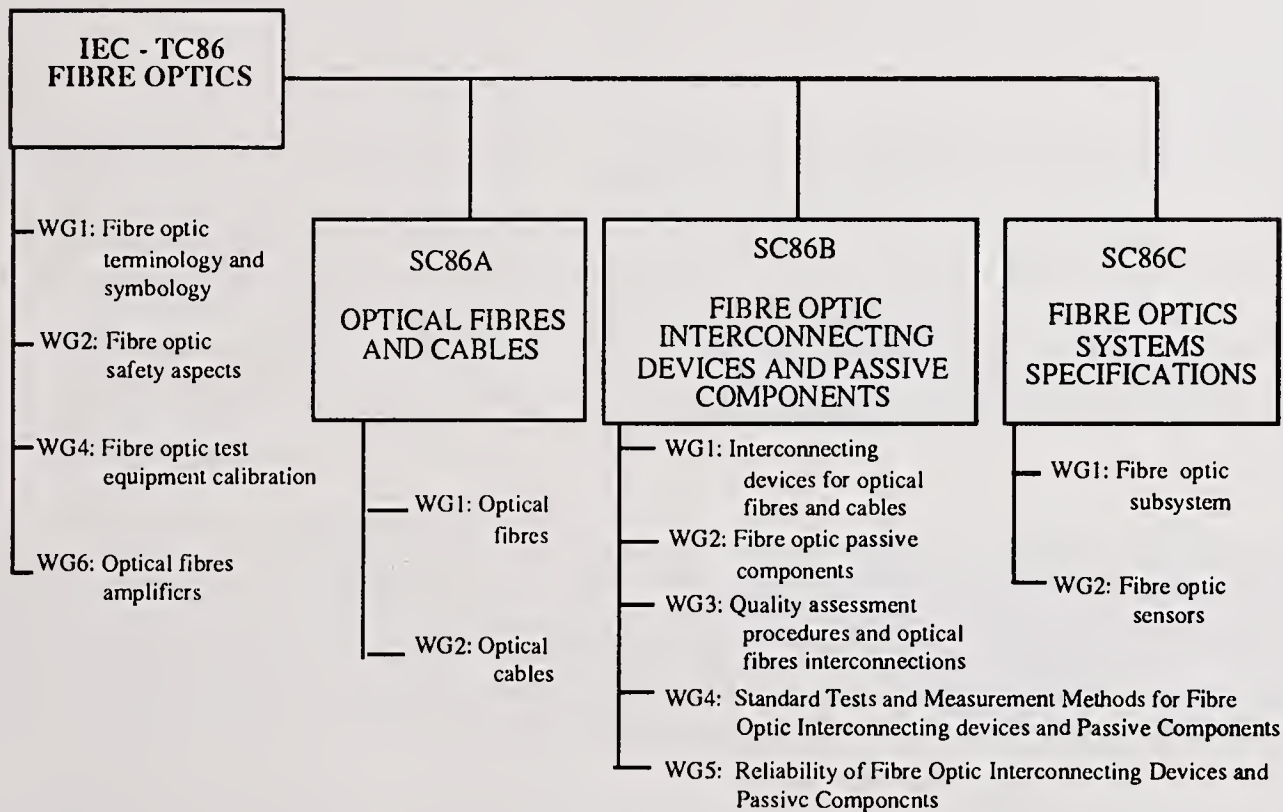


Fig. 2 - Structure of IEC Groups for standardisation on Fibre Optic Communication

COST 217 INTERCOMPARISON OF OTDR MEASUREMENTS ON SINGLE-MODE FIBRES

M.Artiglia, COST 217 Group *

Abstract

The results of an extensive intercomparison of OTDR measurements on three types of single mode fibres, organised in the framework of the European Project COST 217, are presented and discussed. Seventeen laboratories from all over Europe participated to the intercomparison. The results show an acceptable agreement, particularly in attenuation measurements. However the overall reproducibility is still too high and the need emerges of effective calibration procedures for OTDR machines.

1. Introduction

The backscattering technique, or OTDR [1], is very popular since it provides a powerful and practical tool for testing optical fibre attenuation, loss of fibre joints and for locating fibre defects or faults in an installed line. The key of its success is that OTDR is in principle very simple and suitable for field measurements, because it requires only one fibre-end access. OTDR machines are commercially available since some years and product engineering has reached an advanced degree of maturity. In view of industrial testing of SMF OTDR is expected to play a very important role; in fact it has been recommended as ATM by CCITT for attenuation measurements. In this perspective, the participants to Working Group 1 of the European Project COST 217 (*Optical measurements techniques for advanced optical fibre devices and systems*) have recently organised and carried out an extensive interlaboratory intercomparison to assess the reproducibility of OTDR measurements in the laboratories all over Europe. Twenty-three laboratories from ten Countries (B, CH, D, E, I, NL, S, SF, UK and TK) took part to the intercomparison. For the measurements two sets of three fibre bobbins and a special fibre bobbin were prepared and the participants divided in two groups so as to allow the groups to work in parallel. The fibres were provided by the participants and were: two bobbins of Matched Cladding fibre (fibres MC1 and MC2, about 10 km long), two bobbins of Dispersion Shifted fibre (fibres DS1 and DS2, about 6 km long) and two bobbins of Dispersion Flattened fibre (fibres DF1 and DF2, about 6 km long). Besides these very good quality fibres, a seventh fibre bobbin with joints, fibre disuniformities and short length samples, particularly suited to test OTDR measurement set-ups was prepared and circulated. To avoid direct handling of the fibre spools the fibres were closed in sealed boxes and the fibre ends connectorised with FC/PC connectors. The two fibre sets (circulated in March 1990) were intended to be used also for a comparison of Chromatic Dispersion measurements, the results of which have been discussed elsewhere [2]. The special bobbin (circulated in march 1991) consisted of six fibres about 3 Km long in a loose tube; two of them were joined together in order to obtain a line 6 km long (referred to in the following as the *long line*), and one was made joining together four fibre pieces about 0.8 km long (the *short line*), see Fig. 1. Presently, the CD and OTDR measurements on the two set of fibre bobbins are still in run whereas those on the special bobbin are almost concluded. The main results obtained so far will be now briefly discussed. To evaluate the quality of the measurements the Interlaboratory Reproducibility (I.L.R.) defined as the standard deviation of all the measurements in the various laboratories will be used in the following.

2. Discussion of the results

The participants were asked to provide mean value, standard deviation and maximum deviation for each measured parameter; moreover detailed information was required concerning the set-up used (assessed accuracy, type of instrument and so on) and the configuration adopted for the measurements. In all measurements described below the effective refractive index value $n_{eff} = 1.4670$ was used, independently of the fibre type. All the participants performed their measurements using commercial instruments. The average reproducibility of the used set-ups

* M. Artiglia, P. Di Vita, A. Rossaro, CSELT, Turin (I); M. Blondel, E. Jaunart, Faculté Polytechnique de Mons, Mons (B); H. Gilgen, B. Perny, Swiss PTT, Bern (CH); J.Vobian, FTZ - DBP, Darmstadt (D); P. Blasco, CCSA, Zaragoza (E); J. Atin, Telefonica, Madrid (E); G. De Marchis, F. Matera, FUB, Roma (I); D. Cuomo, FOS, Battipaglia (I); E. Uboldi, SIRTI, Milano (I); F. Esposito, Teleco Cavi, Roseto degli Abruzzi (I); G. Kuyt, Philips Optical Fibre, Eindhoven (NL); E. Sundberg, Telia, Haninge (S); K. Sjölin, Ericsson Cables, Hudiksvall (S); L. Oksanen, Nokia Cables, Vantaa (SF); B. Walker, NPL, Teddington (UK); Z. Ziya Oztürk, MRC-Tübitak, Gebze (TK)

(computed from the figures claimed by the participants) on the various parameters resulted to be as follows:

att. coeff: $\Delta\alpha = \pm 0.015$ (max values < 0.03) dB/km, fibre length: $\Delta L = \pm 5$ m,
joint loss: $\Delta\alpha_{\text{joint}} = \pm 0.015$ dB, joint location: $\Delta L_{\text{joint}} = \pm 7$ m

As far as the measurements on the two sets of fibre bobbins are concerned (23 Labs), the following parameters were to be measured:

attenuation coefficients at 1300 nm and 1500 nm (α), Fibre Length (L)

The results are summarised in Table 1. As far as the attenuation coefficient is considered a quite good agreement was found for all fibres at both wavelengths. The I.L.R. is less than 0.02 dB/km and is comparable with the average reproducibility of the used set-ups. The only exception is given by fibre DF2 at 1300 nm; in this case a laboratory measured a very high attenuation coefficient; by neglecting this value the corresponding reproducibility is substantially improved. Also for fibre length an acceptable agreement among the laboratories was found. For fibres DS1 and DF1 the I.L.R. is comparable with the claimed average reproducibility of the instruments. Worse I.L.R.s were found for fibres MC1, MC2, DS2 and DF2, due to the fact that three laboratories measured values somewhat below average. By neglecting these results the I.L.R.s becomes smaller than ± 7 m.

As far as the measurements on the fibre bobbin specially conceived for testing OTDR set-ups are concerned (17 Labs), the participant were asked to measure the following parameters:

long line: *attenuation coefficient of fibres 1 and 2 in both transmission windows, total length of the line, joint loss, joint location*

short line: *attenuation coefficient of fibres 1, 2, 3 and 4 in both transmission windows, loss of joints 1, 2 and 3, location of the three joints*

Fibres and joints were counted starting from head 1 of the lines (see Fig 1). The results are summarised in Table 2 and 3.

Considering first the results of the long line (Table 2), a fairly good agreement at both 1300 nm and 1550 nm (I.L.R. $< \pm 0.02$ dB/km for both fibres) was found for the attenuation coefficient (Figs. 2 and 3). In fact the I.L.R.s are comparable to the average reproducibility of the set-ups claimed by the participants; the I.L.R. of the second fibre seems to be slightly worse. Total length of the line results are in good agreement at 1550 nm (I.L.R. = ± 5 m); but some problems exist at 1300 nm (I.L.R. = ± 18 m) were two laboratories gave results somewhat below the average. By neglecting these results the agreement is considerably improved. Also for joint loss (Fig. 4) an acceptable I.L.R. is found at both wavelengths (note that three participants did not provide sufficient information to calculate the joint loss). Joint location measurements are in fairly good agreement at 1300 nm (I.L.R. = ± 10 m), but at 1550 nm the agreement is quite poor because one laboratory measured a value which is far below average; neglecting it the agreement becomes acceptable.

As far as the short line is considered, a slightly worse agreement is found for the attenuation coefficients at both 1300 nm and 1550 nm (Figs. 5 and 6), this could be due to the short length of the fibre samples. The I.L.R. ranges from ± 0.02 to ± 0.04 dB/km. A substantially good agreement at both wavelengths was found for the total length of the line (I.L.R. $\approx \pm 6$ m) and the joint loss, which shows I.L.R.s comparable to attenuation, see Figs. 7 and 8. For the joint location a fairly good agreement is found at 1300 nm (I.L.R. $\approx \pm 10$ m) but some problems exist at 1550 nm where one laboratory obtained values that are higher than average; by neglecting it the agreement is considerably improved.

3. Conclusions

In conclusion the OTDR instruments have reached a good level of maturity and showed a fairly good reproducibility. However, the reproducibility values obtained and those claimed by most of the participants on attenuation (around 0.02 dB/km) are too high to meet the requirements of fibre producers for quality control and of typical contractual specifications imposed by PTTs to fibre producers (< 0.005 dB/Km). Further work is therefore needed to improve the agreement. Some Laboratories have to correct their set-up for systematic errors. This issue will be the subject of scheduled activities in the framework of the recently started Project COST 241 (ideal continuation of COST 217 which expired few months ago); in particular, calibration of OTDR set-ups will be

investigated; this is a very important topic in view of the use of this technique on industrial scale for SMF characterisation.

References

- [1] CCITT Recommendation G. 650
 [2] COST 217 Group: "COST 217 intercomparison of chromatic dispersion measurements on single-mode fibres", Proc. of EFOC/LAN '92, Paris, June 24-26, 1992, Paper 12

Table 1 - OTDR measurements on long fibre bobbins: mean values and standard deviations (ILR)

$n_0 = 1.467$	MC1	MC2	DS1	DS2	DF1	DF2
$\alpha @ 1300 \text{ nm (dB/km)}$	0.366	0.363	0.425	0.405	0.433	0.458
$ILR_\alpha \text{ (dB/km)}$	0.006	0.008	0.010	0.077	0.019	0.085
$\alpha @ 1550 \text{ nm (dB/km)}$	0.223	0.227	0.255	0.253	0.270	0.271
$ILR_\alpha \text{ (dB/km)}$	0.004	0.019	0.006	0.053	0.026	0.020
$L @ 1300 \text{ nm (m)}$	10172.2	12578.1	6616.3	6382.1	6468.1	6370.9
$ILR_L \text{ (m)}$	10.8	13.7	7.3	15.2	6.4	12.6

Table 2 - OTDR measurements on the special bobbin (long line): mean values and standard deviations (ILRs)

$n=1.4670$	1300 nm	1550 nm
fibre 1 att.(dB/Km)	0.346	0.224
$ILR_1 \text{ (dB/Km)}$	0.015	0.019
fibre 2 att.(dB/Km)	0.508	0.420
$ILR_2 \text{ (dB/km)}$	0.026	0.025
Total Length (m)	6101	6104
ILR (m)	18	5
Joint Loss (dB)	0.073	0.07
ILR (dB)	0.01	0.01
(*) Joint Location (m)	3056	3064
ILR (m)	10	21

(*) Measured from head 1 of the line

Table 3- OTDR measurements on the special bobbin (short line): mean values and standard deviations (ILRs)

$n=1.4670$	1.300 nm	ILR_{1300}	1550 nm	ILR_{1550}
fibre 1 att.(dB/Km)	0.34	0.03	0.22	0.04
fibre 2 att.(dB/Km)	0.34	0.02	0.21	0.02
fibre 3 att.(dB/Km)	0.34	0.02	0.20	0.02
fibre 4 att.(dB/Km)	0.34	0.03	0.23	0.03
Total Length (m)	3055	5	3054	6
Joint 1 Loss (dB)	0.63	0.03	0.46	0.03
Joint 2 Loss (dB)	0.75	0.03	0.52	0.03
Joint 3 Loss (dB)	0.24	0.02	0.16	0.02
(*) Joint 1 Loc.(m)	746	11	746	10
(*) Joint 2 Loc.(m)	1393	10	1398 (1395 [^])	16 (7 [^])
(*) Joint 3 Loc.(m)	2299	9	2304 (2300 [^])	17 (9 [^])

(*) Measured from head 1 of the line

([^]) Worst value excluded

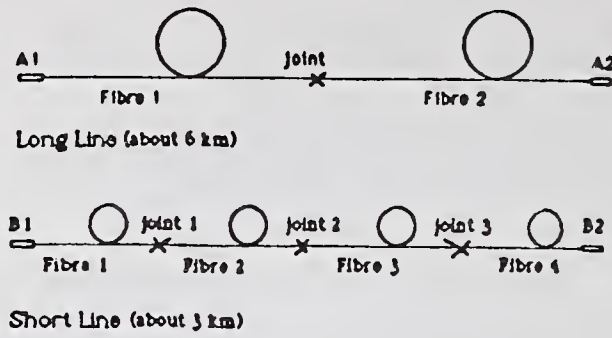


Fig.1 - Schematic of the measured fibre lines

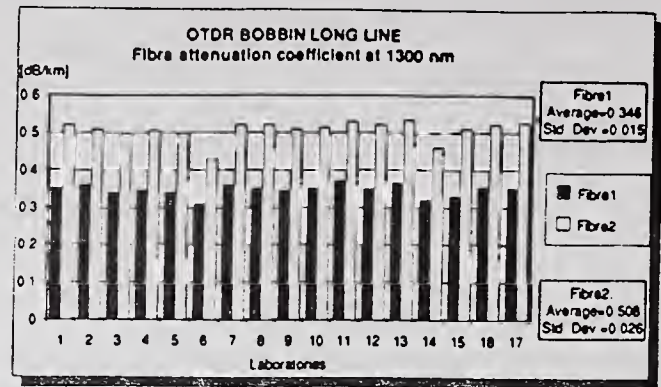


Fig 2 - Results of attenuation measurements on the long line @1300 nm (fibres 1 and 2)

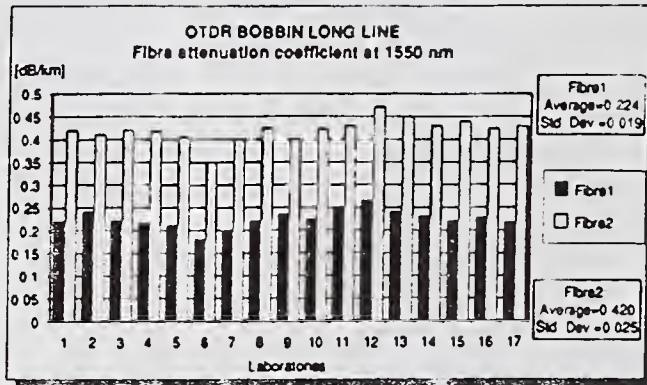


Fig 3 - Results of attenuation measurements on the long line @1550 nm (fibres 1 and 2)

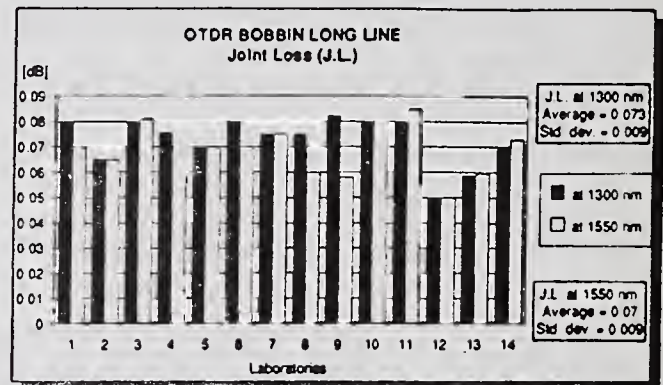


Fig 4- Results of joint loss measurements on the long line @1300 nm and 1550 nm

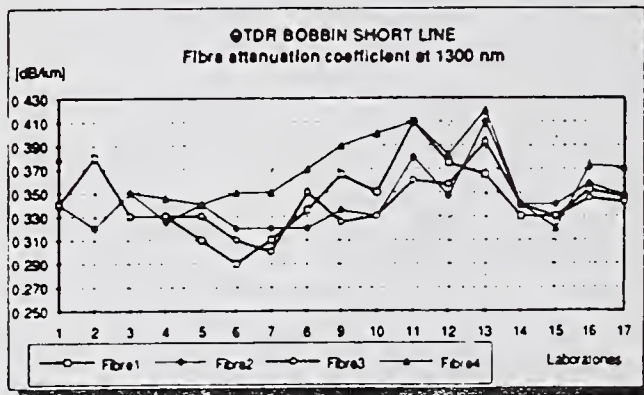


Fig 5- Results of attenuation measurements on the short line @1300 nm

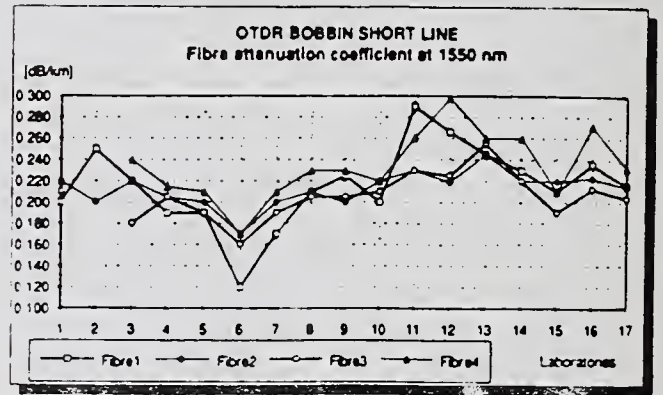


Fig 6 - Results of attenuation measurements on the short line @1550nm (fibres 1 to 4)

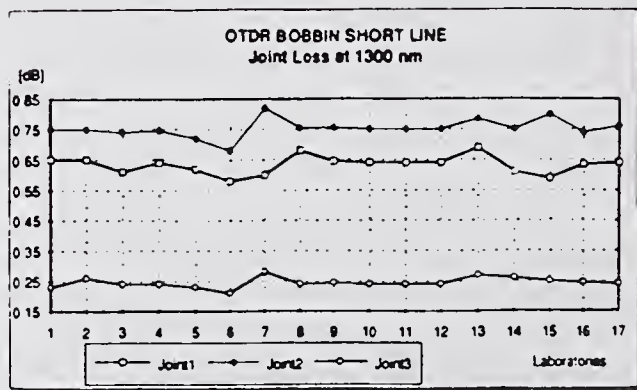


Fig 7 - Results of joint loss measurements on the short line @1300 nm (joints 1 to 3)

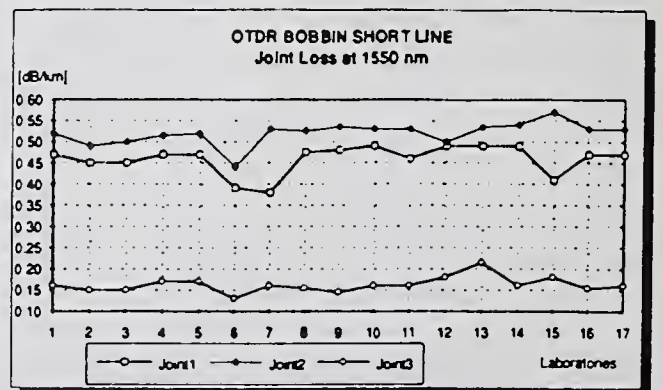


Fig 8 - Results of joint loss measurements on the short line @1550 nm (joints 1 to 3)

COST 217 INTERCOMPARISON OF MEASUREMENTS ON ER-DOPED FIBRES

P. Kiiveri, COST 217 Group (*)

VTT, Technical Research Centre of Finland, Otakaari 7B, 02150 Espoo (SF)

(*) C.A. Millar BTRL, (UK); M. Monerie, J.F. Bayon, CNET, (F); M. Artiglia, CSELT, (I); M.A. Rebolledo, University of Zaragoza, (E); M. Settembre FUB, (I); J. Vobian, FTZ, (D); K. Dybdal Jutland Telephone, (DK); B. Walker NPL, (UK); M. Babeliowsky, PTT Research, (NL); S. Wingstrand, Telia, (S); N. Gisin University of Geneva, (CH); P. Kiiveri, VTT (SF); J. Atin, Telefonica, (E); W.E. Heinlein (University of Kaiserslautern, (D))

Abstract

An intercomparison of measurements on three Er-doped fibres has been organised in the working group 3 of the European COST 217 project (optical measurement techniques for advanced optical fibre systems and devices). A set of fibre parameters, including core diameter, refractive index difference, mode field diameter, cut-off, absorption, fluorescence peak wavelength, time constant, doping concentration and gain, have been measured using samples from three fibres made by three participating laboratories. The measurement results and the properties of the three fibres with different core compositions are compared.

1 Introduction

The COST 217 group has characterized three laboratory made Er-doped fibres, of which almost no data was available before the measurement campaign. Most of the fibre parameters were measured by several participants and could be compared. Results of some parameters that were measured only by one or two participants are given to complete the fibre parameter sets. The information of the fibre parameters is needed e.g. for understanding and modelling the operation of the amplifiers, optimising the amplifier structures and for designing better active fibres.

2 Used Er-doped fibres

The measured samples were taken from three different erbium doped fibres. The long fibres were cut to short samples with original lengths of 5.5m (samples from fibre I), 14.5m (from fibre II) and 13m (from fibre III). Each of the 14 participating laboratories got a sample from every fibre. The homogeneity of the fibre III was checked using the OTDR before the fibre was cut to samples. The homogeneity of the fibre I and fibre II was not checked. The fibres were made by the British Telecom Research Laboratories BTRL (UK), Technical Research Centre of Finland VTT (SF) and Centre National d'Etudes des Telecommunications CNET (F).

2.1 Fibre compositions

The three fibres had different core compositions. The fibre I had Ge/Al/Er doped core, fibre II had Al/Er doped core and fibre III had Ge/Er doped core. One laboratory was able to measure the Er-concentrations from fibre samples using SEM/EPMA (scanning electron microscopy/electron probe micro analysis) technique (table 1).

3 Measured fibre parameters (passive)

3.1 Core diameter

The core diameter results showed that the fibre II had elliptical core (with eccentricity of about 0.6). The standard deviations (S.D.) of the core diameter results of the three fibres were about 3% of the mean values, except the S.D. of the short axis of the fibre II, which was 8.4% (tables 2-4).

3.2 Refractive index difference

The S.D. of the refractive index difference of the fibre I was 9.4%, of fibre II it was 6.8% and of fibre III 3.0% of the mean value (fig. 1., tables 2-4). It is interesting to notice that the S.D. is worse with the cores with higher Δn and Al-doping than the S.D. of the Ge-doped fibre III with lower Δn . Because the reproducibility of the cut-off measurements was good (the S.D. of all three fibres was $< 1\%$), it is probable that the high S.D. of the Δn is not only connected to the variations of the refractive index difference along the fibres but also to the accuracy of the measurements.

3.3 Mode field diameter

The mode field diameter (MFD) measurements were done using commercial devices or laboratory measurement set-ups calibrated during the earlier COST 217 standard singlemode fibre measurement campaign [1,2]. Petermann II definition was used for the mode field diameters. The MFD results of the participant N (tables 2-4) are not included in the standard deviation, because the measured values were systematically higher than the values of the other three participants. The standard deviations of the mode field diameters (excluding N results) at $1.3\mu\text{m}$ / $1.55\mu\text{m}$

wavelengths were: fibre I 2.2% / 1.4%, fibre II 2.9% / 0.0% and fibre III 1.7% / 1.9%. These values can be compared to the COST 217 dispersion shifted fibre MFD measurements, where the S.D. was 3.5% / 4.0% when several measurement methods were used [2].

3.4 Cut-off

The cut-off measurements have been made using the standard bending method. The S.D. of the cut-off wavelength measurements was less than 10 nm (<1% of the mean values) for all three fibres. The standard deviations are about the same as in previous COST 217 matched cladding fibre measurements (S.D.=11 nm), but smaller than in dispersion shifted fibre measurements (S.D.=16.7 nm) [3].

3.5 Absorption at the peak near 1.53 μm

The absorption values were measured using cut-back method. The absorption mean values and standard deviations (%) of the three fibres at 1.53 μm (fig. 2 and tables 2-4) were: 4.4 dB/m, 5.1% (fibre I); 6.3 dB/m, 2.4% (fibre II) and 12.3 dB/m, 5.8% (fibre III). These absorption results could be compared with the absorption values calculated using the measured Er-concentrations (table 1), but the accuracy of the concentration measurements is possibly too low for a meaningful comparison.

4 Measured fibre parameters (active)

4.1 Fluorescence peak wavelengths

The measured fluorescence peak wavelength mean values were: Fibre I: 1531.5 nm (number of results N=2, S.D.=0.5nm), Fibre II: 1530.9 nm (N=5, S.D.=0.9nm) and Fibre III: 1537 nm (N=4, S.D.=0.5nm). Pumping wavelengths of 514 nm, 980 nm and 1481 nm with different pumping powers and sample lengths from 0.1m to 14m were used. Due to the aluminium doping in the fibre I and II cores the fluorescence peak wavelengths of those fibres were shorter than the peak wavelength of the fibre III (fig. 2).

4.2 Fluorescence time constants

The fluorescence time constants (1/e life times) were measured by one participant and only from fibres II and III. The values were 11.5 \pm 0.2 ms (fibre II) and 12.0 \pm 0.2 ms (fibre III). Pumping wavelength was 514 nm and fibre lengths 2 cm.

4.3 Small signal gain

The gains of short fibre samples (L=2m) were measured by one participant. The gain of the fibre III (Ge-core) was smaller than the gain of the fibre I and II (Al-doped cores) at 1536 nm (fig. 4). The gain with long samples of the fibre II was measured by three participants. The signal wavelengths varied from 1536 nm to 1550 nm and the pumping wavelengths from 1478 nm to 1486 nm. Also the signal powers varied. It is obvious that the gain measurement set-ups should be standardised to get comparable results (fig. 3).

5 Summary and conclusions

A measurement campaign with three laboratory made erbium doped fibres with different core compositions has been completed. The results are summarised in the tables 1-4 and in figures 1-4. Similar measurement methods as for standard telecommunication fibres were used for MFD, cut-off, core diameter, absorption and refractive index measurements. For cut-off and absorption measurements non-destructive methods could be preferable, because active fibres are quite expensive. The interlaboratory reproducibility of the MFD, cut-off, and fluorescence peak wavelength measurements was quite good (S.D. <3%). The interlaboratory reproducibility of the refractive index, core diameter and absorption measurement results was lower (S.D. 5.8%-9.4%). There were not enough data for comparison of the Er-concentration and fluorescence time constant measurements. Er-concentration analysis from fibre samples appeared to be difficult due to the low Er-concentration levels used.

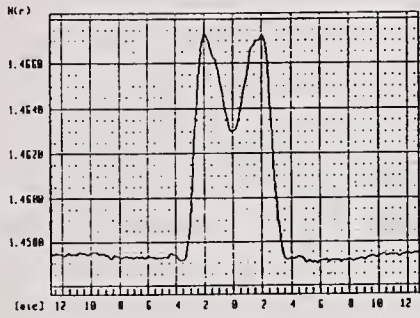
Because the gain depends on pump and signal wavelengths, standard pumping and signal wavelengths for measurement set-ups should be defined to make the gain measurements comparable.

References

- [1] COST 217 Group. "COST 217 Interlaboratory measurement campaign on single-mode fibres", IEE Proc., vol. 136. Pt. J, No 6, pp. 307-314, Dec. 1989.
- [2] COST 217 Group. "COST 217 Intercomparison and analysis of fibre mode field diameter measurements", IEE Proc., vol. 138, No 6, pp. 373-378, Dec. 1991.
- [3] G. Kuyt, COST 217 Group. "COST 217 Interlaboratory comparison of uncabled and cabled fibre cut-off wavelength measurements", Optical Fibre Measurement Conference, York, UK., 1991, pp. 12-15.

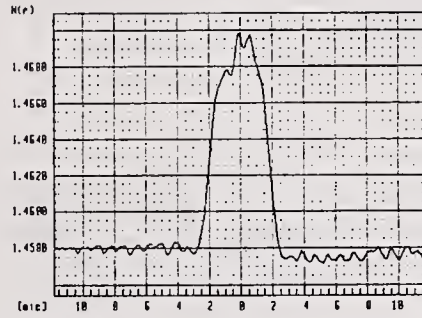
APPENDIX I

Delta N: 0.676 %



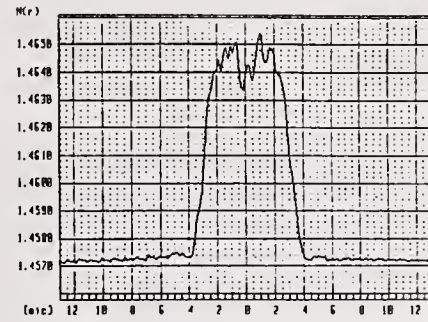
a) Fibre I

Delta N: 0.840 %



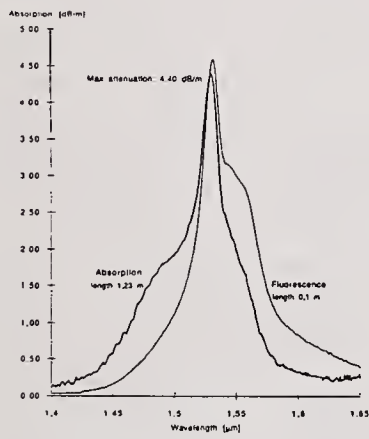
b) Fibre II

Delta N: 0.581 %

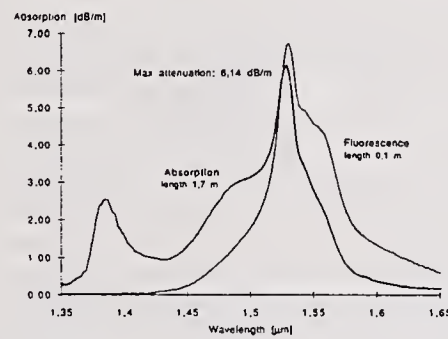


c) Fibre III

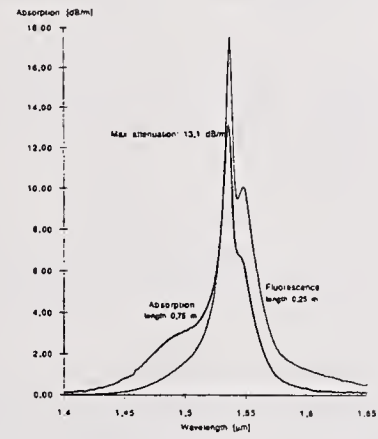
Fig. 1. Refractive index profiles of the three Er-doped fibres.



a) Fibre I



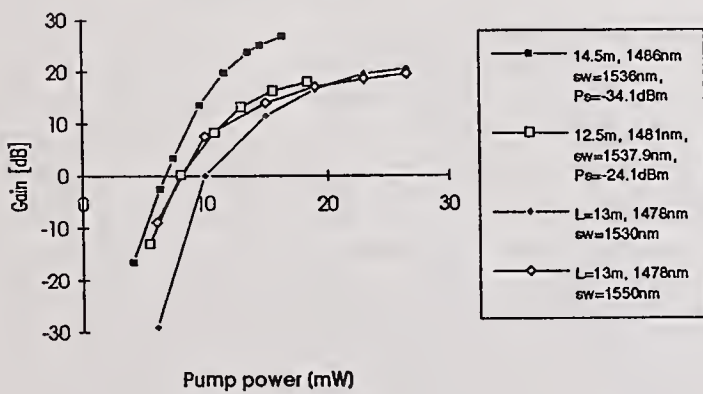
b) Fibre II



c) Fibre III

Fig. 2. Absorption and fluorescence curves of the Er-fibres.

Fibre II gain results



Gain results L=1.9...2.2 m

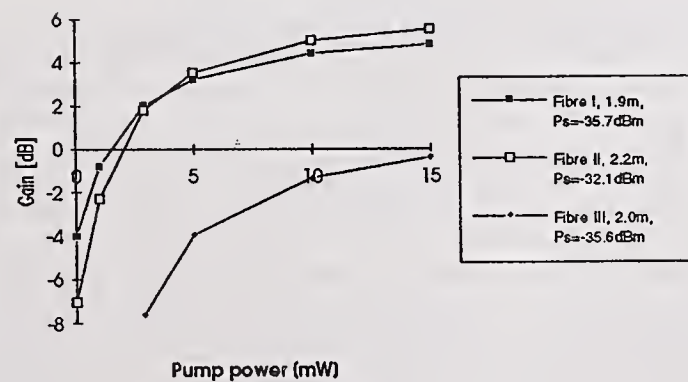


Fig. 3. Gain of the fibre II as a function of coupled pumping power.

Fig. 4. Gain of the short fibre samples as a function of coupled pumping power. Signal wavelength was 1536nm.

APPENDIX II

Table 1. Measured Er-concentrations in the fibre I, II and III cores.

Measured by	Fibre	Er ³⁺ /wt%	Er ₂ O ₃ /wt%
F	I	0.04	0.04
F	II	0.05	0.05
F	III	0.07	0.08
B *	III	-	0.13-0.20

*) Estimated from the absorption values

Table 2. Measured fibre I parameters.

MEASURED	ϕ core	MFD@1.3/1.55	Δn	Cut-off	Att @1.53
BY:	μm	μm	e(-3)	nm	dB/m
A	5.5	- -	13.5	1290	4.2
B	5.7	- -	11.0	1290	4.2
I	-	6.2 -	-	1308	4.5
K	-	6.2 7.1	-	1309	4.5
L	5.6 / 6.0	6.5 6.9	11.9	1309	4.4
M	-	- -	-	1308	4.8
N	5.5 / 5.7	[6.8] [8.0]	11.7-12.2	1290	4.1
O	5.8	- -	9.9	-	-
MEAN	5.7	6.3 7.0	11.7	1301	4.4
S.D.	0.16	0.14 0.10	1.1	9.2	0.22
S.D./mean (%)	2.9%	2.2% 1.4 %	9.4%	0.7%	5.1%

Table 3. Measured fibre II parameters.

MEASURED	ϕ_x/ϕ_y core	MFD@1.3/1.55	Δn	Cut-off	Att @1.53
BY:	μm	μm	e(-3)	nm	dB/m
M	[4.3] *	- -	11.5 - 11.8 *	-	6.1
B	[4.2]	- -	11.8 - 13.3	1086	6.3
C	-	- -	-	1100	6.3
F	4.0 / 5.1	- -	12.2	1090	-
I	-	5.6 -	-	1093	6.0
K	-	6.0 6.7	-	1090	6.4
L	4.5 / 5.5	5.7 6.7	10.5 - 12.2	1088	6.2
M	-	- -	-	1088	6.2
N	3.8 / 5.1	[6.9] [8.4]	11.7 - 12.0	1096	6.5
O	3.6 / 5.1	- -	10.4	-	-
MEAN	4.0 / 5.2	5.8 6.7	11.7	1091	6.3
S.D.	0.33 / 0.17	0.17 0.0	0.8	4.4	0.15
S.D./mean %	8.4% / 3.3%	2.9% 0.0%	6.8%	0.4%	2.4%

*) Measured from the preform

Table 4. Fibre III parameters.

MEASURED	ϕ core	MFD@1.3/1.55	Δn	Cut-off	Att @1.53
BY:	μm	μm	e(-3)	nm	dB/m
B	6.4	- -	8.0	1125	12.6
C	-	- -	-	1150	11.9
D	-	- -	-	-	12.5
F	6.0	- -	8.5	-	-
I	-	7.3 -	-	1138*	12.9
K	-	7.2 8.1	-	1142	11.3
L	6	7.0 7.8	8.8	1155	11.1
M	-	- -	-	1143	13.2
N	5.9 / 6.3	[7.4] [8.8]	8.2-8.3	1155	12.7
O	6.1	- -	8.3	-	-
MEAN	6.1	7.2 8.0	8.4	1144	12.3
S.D.	0.18	0.12 0.15	0.25	9.9	0.71
S.D./mean (%)	2.9%	1.7% 1.9%	3.0%	0.9%	5.8%

*) Bending reference $r=4\text{cm}$

SINGLE-MODE FIBER GEOMETRY AND CHROMATIC DISPERSION: RESULTS OF INTERLABORATORY COMPARISONS

Timothy J. Drapela, Douglas L. Franzen, and Matt Young
National Institute of Standards and Technology
325 Broadway
Boulder, CO 80303

The National Institute of Standards and Technology (NIST) recently completed two interlaboratory comparisons with members of the Telecommunications Industry Association (TIA). Participants included most major fiber and cable manufacturers in North America. We evaluated test procedures for geometry and chromatic dispersion. In both cases, the measurement spread in the industry was due mostly to systematic differences among laboratories. Measurement agreement would be significantly improved through the use of reference fibers.

GEOMETRY

A previous international geometry comparison (1989), organized through CCITT and coordinated in North America by NIST, gave a spread (1σ) of $0.38\ \mu\text{m}$ for cladding diameter. An interim report concluded that the agreement should be improved if the industry wanted to further reduce tolerances. Participants in the comparison received fiber samples consecutively cut from fiber spools; consequently, sample nonuniformity could have influenced the results.

In the present study, participants used the gray scale method to measure cladding diameter, noncircularity, and concentricity error. The gray scale method, based on video microscopy, is the most common method used by industry and is described in TIA test procedure FOTP-176.¹ A near-field image of a cleaved fiber end is obtained with a video microscope. The outside boundary of the cladding is digitized, and an "edge table" is compiled. Cladding diameter is then determined by curve-fitting to the edge table data. Calibration is accomplished by measuring reticles and/or reference fibers of known dimension.

Participants in the TIA comparisons measured the same cleaved fiber ends, so sample uniformity was not an issue. An individual fiber was contained in a protective metal housing designed to fit into a gray scale system, Fig. 1. In this configuration, the fiber is extended for measurement; the brass barrel can rotate and is indexed to indicate a specific angular orientation.

Results from TIA members were compared to the diameters measured at NIST with a contact micrometer and a scanning confocal microscope (SCM).² The contact micrometer measures fiber diameter approximately 1 mm from the cleaved end. The micrometer jaws consist of a fixed cylinder (the anvil) and a moveable spindle, both made of polished, hardened steel. Differential displacement of the spindle is measured by an optical interferometer. In the SCM, the fiber endface is scanned across a focused HeNe laser beam, and the location of the cladding edge is determined by observing the reflected light. The contact micrometer and SCM have been compared, and cladding diameter measurements agree within 30 nm. When measuring the comparison fibers, NIST measured cladding diameter at four angular orientations: 0° , 45° , 90° and 135° .

Comparison of cladding diameters of five fiber samples are shown in Fig. 2. The measurement spread (1σ), averaged over all fibers, for the eight participants is $0.15\ \mu\text{m}$. This is a substantial improvement over the previous comparison and reinforces the need to measure the same fiber ends. Results shown in Fig. 2 are the differences for each measured fiber with respect to the NIST contact micrometer (solid horizontal line). The NIST value for a given fiber is the average of the 0° , 45° , 90° , and 135° diameters. The square data points are the four-diameter participant averages, whereas the circular points are the participant values using the curve-fitting method described in FOTP-176. With the exception of Participant 4, there is no statistical difference between the two diameters. Figure 2 indicates that the overall measurement spread is largely due to systematic differences among participants; that is, a given participant's results are closely grouped. Table 1 is the average offset and standard deviation of the offset for each participant with respect to NIST. The average offset standard deviation among gray scale participants is $0.027\ \mu\text{m}$. If each participant's data were corrected for an offset, the overall measurement spread would dramatically decrease; this emphasizes the need for reference fibers. Comparison results were also obtained for noncircularity, with a worst-case measurement spread (1σ) of 0.07 %, and for concentricity error, with a worst-case measurement spread (1σ) of $0.04\ \mu\text{m}$.

CHROMATIC DISPERSION

The comparison of test procedures for measuring chromatic dispersion in single-mode fibers was carried out over a two-year period, from mid-1989 through late 1991. Seven fibers, donated by various fiber manufacturers, were used in the comparison. Five of the fibers were dispersion unshifted; two were dispersion shifted. The fibers were color coded for identification and put into a loose-tube buffer. This cable was then cut into 5.1 km and 2.7 km lengths. Participants were asked to measure the zero-dispersion wavelength λ_0 , the dispersion slope at that wavelength, S_0 , and the dispersion coefficient $D(\lambda)$ at 1310 nm, for both lengths of fiber.

Six participants used the differential phase shift method, in which $D(\lambda)$ is determined from the differential group delay between two closely spaced wavelengths. λ_0 and S_0 are determined by curve-fitting to the dispersion data. The source is typically one or more sinusoidally modulated LEDs filtered by a monochromator. Further details of this method are given in FOTP-175.¹

Three participants used the phase shift method, in which spectral group delay data are obtained from measuring the relative phase shifts of modulated sources at three or more wavelengths. λ_0 , S_0 , and $D(\lambda)$ are determined from equations fitted to the spectral group delay. The sinusoidally modulated source can be either multiple laser diodes or filtered LEDs. Further details of this method are given in FOTP-169.¹

Three participants used the time domain method described in FOTP-168.¹ In this method, a Nd:YAG fiber Raman laser or several laser diodes are used, and the spectral group delay data at several wavelengths are obtained directly in the time domain. Dispersion parameters are obtained by fitting to the spectral group delay data.

For dispersion-unshifted fibers, the fit to the group delay for all three methods is a 3-term Sellmeier equation; the dispersion is the first derivative of this equation.

We restrict our analysis here to the dispersion-unshifted fibers. Overall results have been calculated, in the form of mean values $\pm 1 \sigma$ for each fiber. Long and short lengths exhibit very similar behavior in these statistics. The overall measurement spreads (1σ) averaged over the five long dispersion-unshifted fibers, are 0.93 nm for λ_0 , 0.0016 ps/(nm²·km) for S_0 , and 0.08 ps/(nm·km) for $D(1310 \text{ nm})$.

We also examined the relative offsets among participants. Figure 3 shows the offsets from the average measured zero-dispersion wavelength value for each fiber, for each of the participants. Each point for a given participant represents one of the five long dispersion-unshifted fibers. Similar plots have been made for S_0 and $D(1310 \text{ nm})$. These three graphs are similar in the conclusions that can be reached. There are no readily identifiable systematic offsets between measurement methods. There are, however, clear systematic offsets among participants.

Analysis can be done on the statistics of these offsets. An average offset taken over all five dispersion-unshifted fibers and the standard deviation of the offset is calculated for each participant. This standard deviation is related to the participant's random error. Table 2 shows the average value of the zero-dispersion wavelength offset and the offset standard deviation for each participant, for the long fibers; the average offset standard deviation is 0.16 nm. For the short lengths, the corresponding value is 0.35 nm. In this case, the length of the fiber has a significant effect. The average offset standard deviations for the long fibers are 0.0004 ps/(nm²·km) for S_0 and 0.016 ps/(nm·km) for $D(1310 \text{ nm})$. For the short fibers, these values increase to 0.0008 ps/(nm²·km) for S_0 and 0.03 ps/(nm·km) for $D(1310 \text{ nm})$. The average offset standard deviations are all roughly twice as high for the short lengths than for the long lengths. This implies larger random error for shorter lengths. The main reason for including long and short lengths in this study was to verify this effect.

Analysis of the dispersion-shifted fibers is more complicated but is worth brief mention. The overall statistics for these fibers compare favorably with the previous five fibers. The offset statistics, on the other hand, are not as precise. The average offset standard deviations are roughly double.

This comparison shows acceptable overall spread in dispersion measurements by three different methods, with no apparent method-dependent offsets. Also, for these lengths of fiber, differences are due to systematic offsets among participants, with the random error small. If better agreement is desired, calibration fibers could be used to significantly reduce the offsets. This possibility is currently being examined.

ACKNOWLEDGMENTS

We thank the following organizations for their participation in these comparisons: Alcatel Cable Systems, Inc.; AT&T Bell Technologies; Bellcore; Corning, Inc.; GTE Laboratories, Inc.; Litespec, Inc.; Northern Telecom; Photon Kinetics; Raynet Corporation; Siecor Corporation; Spectran Corporation; York Technology, Inc. We thank Casey Shaar of Photon Kinetics for providing the design of the fiber housings.

REFERENCES

1. Fiberoptics Test Procedures (FOTPs) can be obtained from: Telecommunications Industry Association-Electronic Industries Association, 2001 Pennsylvania Avenue, N.W., Washington, D.C. 20006.

2. M. Young, S. E. Mechels, P. D. Hale, "Optical Fiber Geometry: Accurate Measurement of Cladding Diameter," paper presented at Conf. on Precision Electromagnetic Measurements, Paris, June 9-12, 1992; IEEE Trans. Inst. and Meas. (submitted).

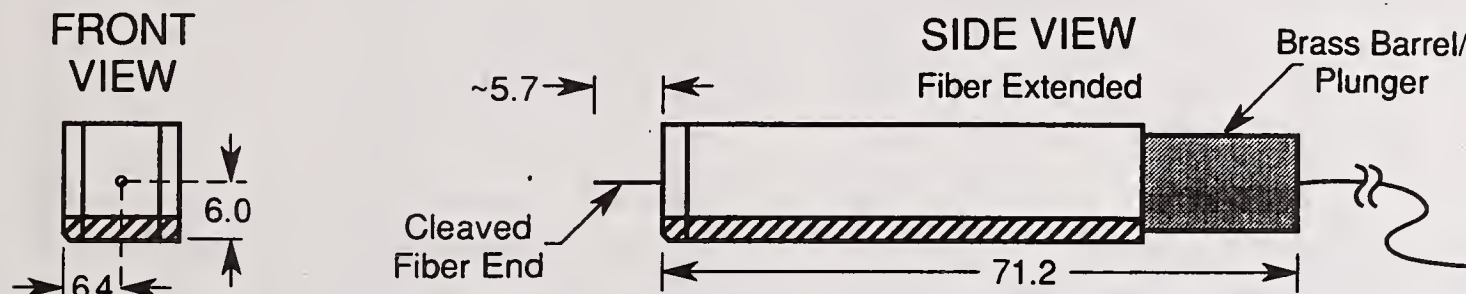


Figure 1 Diagram of fiber housing used in the geometry comparison, showing brass barrel pushed forward and hence, fiber end extended. (Dimensions are in millimeters.)

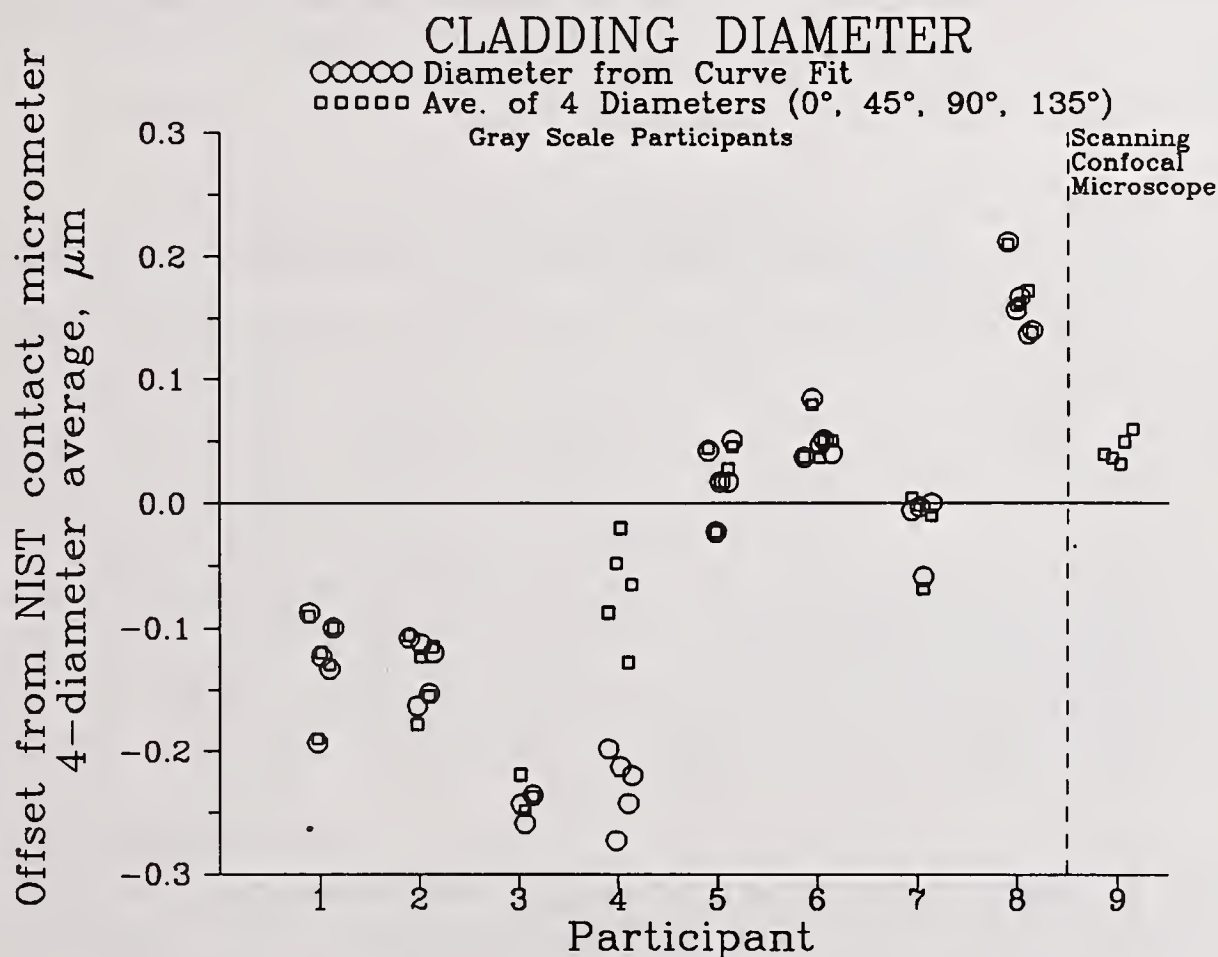


Figure 2 Participant offsets from NIST contact micrometer average values of cladding diameter, for five comparison fibers. Gray scale offsets of best-fit and 4-diameter average values are shown. SCM values are shown for comparison.

**CLADDING DIAMETER
GRAY SCALE BEST-FIT OFFSETS FROM
NIST CONTACT MICROMETER
4-DIAMETER AVERAGE**

Participant	Average Offset, μm	Standard Deviation, μm
4	-0.127	0.041
2	-0.131	0.025
3	-0.246	0.012
4	-0.229	0.029
5	+0.021	0.029
4	+0.052	0.019
7	-0.017	0.028
8	+0.163	0.030
Avg.		0.027

Table 1 Average and standard deviation of offsets of gray scale best-fit values from NIST contact micrometer four-diameter average values of cladding diameter, taken over five housed fiber samples, for each participant.

**ZERO-DISPERSION WAVELENGTH
OFFSETS FROM AVERAGE VALUES
LONG FIBERS (5.1 km)**

Participant	Average Offset, nm	Standard Deviation, nm
5	-0.86	0.08
2	+0.21	0.11
3	-0.86	0.12
5	+0.26	0.08
5	-1.10	0.15
6	+0.43	0.13
7	+1.09	0.08
8	+0.26	0.11
8	+1.04	0.06
10	-1.79	0.11
11	+0.61	0.51
12	-0.45	0.35
Ave.		0.16

Table 2 Average and standard deviation of offsets from average values of zero-dispersion wavelength, taken over five long dispersion-unshifted fibers, for each participant.

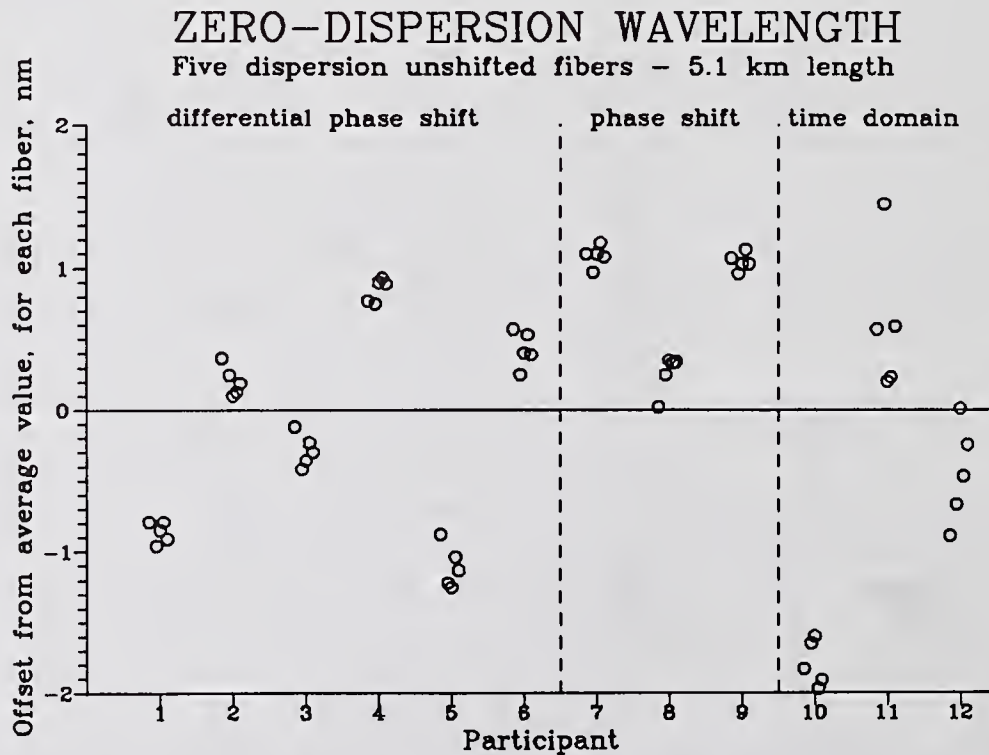


Figure 3 Participant offsets from average values of zero-dispersion wavelength, for long lengths of five dispersion-unshifted fibers. (Five points per participant correspond to measurements on five fibers.)

Moderate-Accuracy Wavelength Standards for Optical Communications

S.L. Gilbert, T.J. Drapela, and D.L. Franzen

National Institute of Standards and Technology
Electromagnetic Technology Division
325 Broadway, Boulder, Colorado 80303

INTRODUCTION

Wavelength standards in the 1.3 μm and 1.5 μm regions are important for proposed optical communication schemes involving wavelength and frequency division multiplexing. Such systems will increase the information-carrying capacity of a fiber by simultaneously transmitting many different wavelengths. The first systems that will utilize this type of multiplexing will probably have channel separations on the order of 1 nm (\approx 130 GHz). To define each channel and prevent channel overlap, a moderate-accuracy wavelength reference (accuracy of about 0.01 nm, or 7 parts in 10^6) will be needed for each channel. Such references could also be used to calibrate optical spectrum analyzers in these wavelength regions. Wavelength references with higher accuracy will be required for systems with smaller channel spacing.

We have designed an apparatus for moderate-accuracy wavelength standards which uses molecular absorption lines as references. For absolute wavelength standards, a stable, reproducible reference is necessary. Natural resonances of atoms or molecules are ideal, since their wavelengths are not subject to large variations due to environmental changes such as temperature or pressure. Unfortunately, atomic and molecular reference lines in the 1.3 μm and 1.5 μm regions are not common; atomic transitions initiate from excited states, and molecular lines are weak overtone or combination bands.

We probe molecular resonances by illuminating a gaseous sample of molecules with light from an LED and observe the characteristic absorption lines using an optical spectrum analyzer. The system is simple and compact, and provides a series of reference lines in the 1.5 μm region. We are presently working on a similar approach for the 1.3 μm region.

1.5 μm APPARATUS

Our 1.5 μm wavelength reference apparatus is based on the absorption of light by the acetylene molecule. Of the molecular absorbers identified to date, acetylene has the strongest lines in this region. The $\nu_1 + \nu_3$ vibrational-rotational band of the $^{12}\text{C}_2\text{H}_2$ acetylene molecule has a clean spectrum containing approximately 40 clearly distinguishable lines with

spacings of about 0.5 nm between 1.51 μm and 1.54 μm .¹ A similar spectrum shifted about 8 nm toward longer wavelengths can be obtained from $^{13}\text{C}_2\text{H}_2$.² If additional lines are required, the $^{12}\text{C}^{13}\text{CH}_2$ spectrum³ could also be used.

A schematic diagram of the apparatus is shown in Fig. 1. Light from a fiber-pigtailed 1550 nm edge-emitting LED is collimated and passed through a sealed absorption cell containing $^{12}\text{C}_2\text{H}_2$ acetylene gas. The transmitted light is coupled into an optical fiber and is then observed on a diffraction-grating optical spectrum analyzer. The acetylene absorption lines appear as dips on the 70 nm wide LED emission spectrum. Figure 2 shows a scan over the acetylene absorption spectrum using this apparatus. The absorption lines are labeled according to the molecule's rotational-vibrational structure. The vacuum wavelengths of these lines, given in Table 1, have been measured to an accuracy of ± 0.001 nm.³

The system was designed to be rugged, compact, and stable. With the exception of the path through the acetylene cell, the LED light was guided in single-mode fiber. Coupling of the light into and out of the acetylene cell was accomplished using fibers which were fused to graded refractive index (GRIN) rod lenses. The first lens produced a collimated beam of light which passed through the 5 cm long acetylene cell and was coupled into the output fiber by a second GRIN lens. The acetylene cell was secured in an aluminum frame, and the GRIN lenses were held in aluminum plates which were rigidly locked to the cell frame after alignment. A simple electronic circuit using 5 VDC supplies and resistance networks supplied current for the LED and its thermoelectric cooler. The cell was constructed out of glass tubing with windows fused onto the ends and a small tube on the side for filling. It was first evacuated and then filled to a pressure of 4×10^4 Pa (300 Torr).

Figure 3 shows a scan over part of the acetylene spectrum on an expanded scale. The linewidths of the absorption lines are limited by the 0.1 nm instrumental resolution. The line centers can be easily determined to an accuracy of 0.01 nm. Sakai, Sudo, and Ikegami² have studied the effect of temperature and acetylene pressure on the center wavelengths of the acetylene absorption lines. They concluded that the temperature sensitivity is less than 100 kHz/K and the pressure sensitivity is less than 1.5 kHz/Pa. This sensitivity is very small compared with the desired accuracy of 0.01 nm (~ 1.3 GHz).

1.3 μm APPARATUS

We are presently investigating the use of methane (CH_4) as a reference for the 1.3 μm region. The $\nu_2 + 2\nu_3$ band, centered at 1.33 μm , is very weak and requires a longer absorption path. We have constructed an apparatus which is very similar to that described in the previous section with the substitution of a 15 cm long absorption cell. With a methane pressure of 4×10^4 Pa, we observed an absorption of 15% on the 1.331 μm Q branch line⁴ of this band. Other molecular candidates for references in the 1.3 μm region are ammonia and hydrogen fluoride.

CONCLUSIONS

We have constructed a simple apparatus for producing a series of reference lines in the 1.5 μm region. We are investigating a similar approach for the 1.3 μm region. These LED/molecular absorber systems provide wavelength references with accuracies of 0.01 nm, which is sufficient for wavelength division multiplexed optical communication systems with channel spacings of about 1 nm.

REFERENCES

1. P. Varanasi and B.R.P. Bangaru, "Intensity and Half-Width Measurements in the 1.525 μm Band of Acetylene," *J. Quant. Spectrosc. Radiat. Transfer* **15**, 267 (1975).
2. Y. Sakai, S. Sudo, and T. Ikegami, "Frequency Stabilization of Laser Diodes Using 1.51 - 1.55 μm Absorption Lines of $^{12}\text{C}_2\text{H}_2$ and $^{13}\text{C}_2\text{H}_2$," *IEEE J. Quantum Electron.*, **28**, 75 (1992).
3. A. Baldacci, S. Ghersetti, and K. N. Rao, "Interpretation of the Acetylene Spectrum at 1.5 μm ," *J. Mol. Spectrosc.* **68**, 183 (1977).
4. K. Chan, H. Ito, and H. Inaba, "Optical Remote Monitoring of CH_4 Gas Using Low-Loss Optical Fiber Link and InGaAsP Light-Emitting Diode in 1.33- μm Region," *Appl. Phys. Lett.* **43**, 634 (1983).

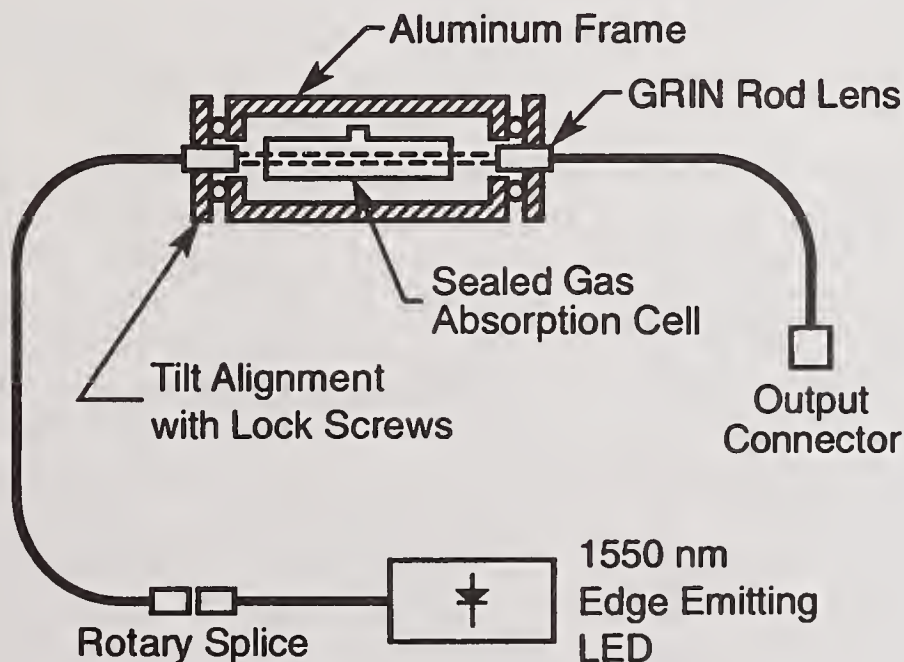


FIGURE 1 Schematic diagram of the 1.5 μm wavelength reference apparatus.

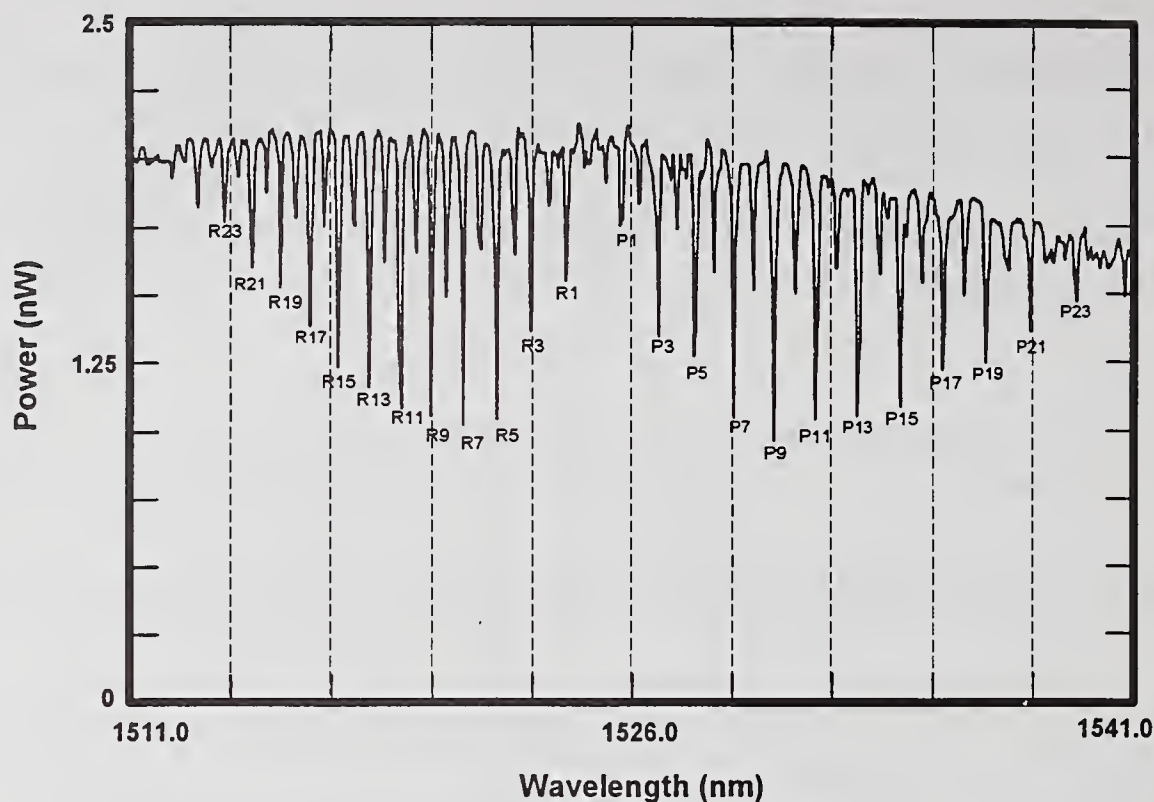


FIGURE 2 Scan over the acetylene $\nu_1 + \nu_3$ absorption band with a resolution of 0.1 nm. Wavelengths for the labeled lines are given in Table 1. The intermediate lines (R_{22} , R_{20} , ...) are also accurately measured.

Line	λ_{vac} (nm)	Line	λ_{vac} (nm)
R23	1513.97	P1	1525.76
R21	1514.78	P3	1526.87
R19	1515.59	P5	1528.01
R17	1516.44	P7	1529.18
R15	1517.31	P9	1530.37
R13	1518.22	P11	1531.59
R11	1519.14	P13	1532.83
R9	1520.08	P15	1534.10
R7	1521.06	P17	1535.39
R5	1522.06	P19	1536.71
R3	1523.09	P21	1538.06
R1	1524.14	P23	1539.43

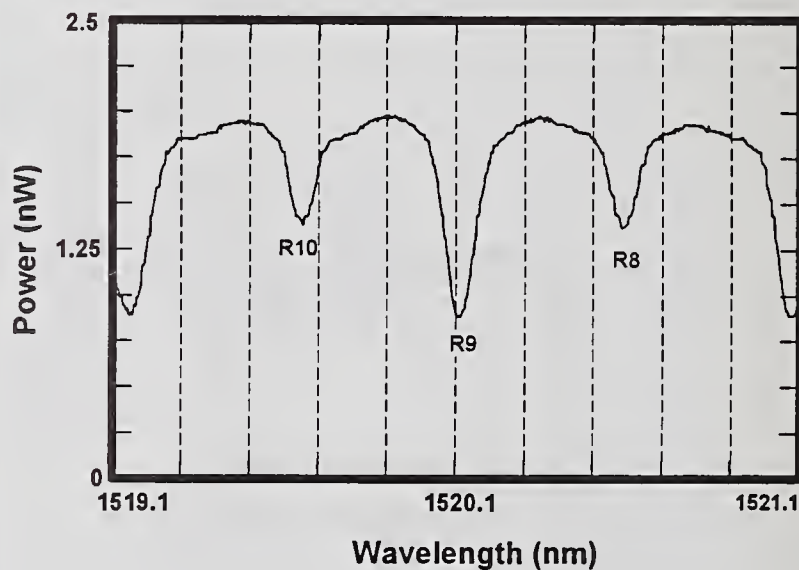


FIGURE 3 Scan in the vicinity of R9 (0.1 nm resolution).

Characterization of Fiber-Optic Amplifiers

Douglas W. Hall
Opto-Electronics Group, Corning Incorporated
Corning, NY 14831

The telecommunications industry is on the verge of a third fiber-optic revolution. The first revolution occurred in the early '70s with the invention of low-attenuation fiber itself. Multi-mode fibers, PIN detectors, and LED light sources allowed communication over guided-wave media with bandwidth-length products approaching those of free space links. Eventually, with the improvement in fibers and the advent of reliable semiconductor lasers, signal dispersion in the media, rather than attenuation, became the factor limiting increased bandwidth-length product systems. The second revolution occurred in the mid-1980s with the wide-spread deployment of single-mode fiber systems. The use of a single spatial mode reduced dispersion, making attenuation once again the limiting factor in system bandwidth-length product. The third revolution is the upcoming deployment of fiber-optic amplifiers; their use will shift the limit of a system's bandwidth-length product back to dispersion.

As with any rapidly developing technology, ideas and their scientific demonstration have outstripped the detailed study and consensual agreement of measurement techniques that is required before widespread acceptance of the technology occurs. The international standards bodies, such as CCITT and IEC, to whom we normally look for definition of standard measurement techniques, are only now defining what a fiber-optic amplifier is and what its important parameters are, let alone techniques on how to reliably obtain values of those parameters. This paper describes the Corning group's view of the state of measurement development and highlights some of the remaining challenges.

First we must define the beast we are trying to characterize. For example, an IEC subcommittee created to study optical amplifiers has preliminarily agreed to define a fiber-optic amplifier using the concept of a "black box" with two optical ports; this allows manufacturers latitude to bring different and evolving technologies to bear on solving optical, environmental, and reliability problems, without the need to specify the internal workings of their devices. The simplest manifestation of a fiber-optic amplifier consists of a pump laser, a wavelength division multiplexer (WDM) and a length of Er-doped fiber. In order to have a complete survivable amplifier, other elements are required, such as pump-laser controllers, power supplies, monitor optics (e.g. tap couplers) and control circuitry, optical isolators, telemetry circuitry and telemetry signaling method. Different manufacturers are currently offering many combinations of these elements as the market-place decides what assortment of elements it wants to define as an optical-fiber amplifier. The optical schematic diagram of one version of an amplifier specified for a power amplifier application is shown in Fig. 1.

The primary parameters that characterize the two-port black box are common to electrical as well as optical amplifiers: gain, bandwidth, noise, and distortion. Other secondary parameters of importance that must be specified to understand the impact of a fiber-optic amplifier in various applications include amplified spontaneous emission (ASE) optical power spectral density, the amount of pump-light leakage to the amplifier ports, the return loss of signal light from the input and output port, and the out-of-band insertion loss. For two of the primary parameters, gain and noise, measurements based on optical and electrical-based techniques have appeared in the literature. It is our group's opinion that all four of the primary measurements must be made in the electrical domain since the purpose of lightwave systems, amplified or not, is to transport electrical signals. In other words, measurements of optical amplifiers should employ techniques that are most directly related to what system designers need to know. Secondary parameters can be measured either optically or electrically since they may be manifestations of the uniquely optical nature of the signal transmission. All the primary amplifier parameters can, in principle, be measured using a single experimental set-up, shown schematically in Fig. 2. In practice, it is unlikely that a single laser light source will combine the features of wavelength tunability, low noise, and high-linearity required for the bandwidth, noise, and distortion measurements, respectively. In the following, issues associated with some of the primary measurements are discussed.

Gain

In a gain measurement, one must separate the optical power associated with the signal from the co-propagating ASE power. This is most easily done by modulating the input signal and determining the modulated or AC gain of the amplifier. Using the equivalence of AC and DC gain of Erbium amplifiers that occurs for modulation frequencies above 10 kHz, the average signal power out of the amplifier is the input power times the AC gain.

While the principle of a gain measurement is fairly straightforward, the high gain of fiber amplifiers can lead to erroneous results in the small-input power regime unless great care is taken to reduce reflections within the measurement system. Reflection of either signal or ASE back into the amplifier can cause saturation of the amplifier's gain with signal powers well below the saturation level. An example of the impact of reflection at the output of amplifiers with small-signal gain of 42 dB and 31 dB is shown in Fig. 3, where the apparent small-signal gain is plotted vs. reflection.

Another challenge that has not yet been addressed is the measurement of the gain of an amplifier for a specific signal wavelength in the presence of other wavelengths or bands of wavelengths. This information is necessary for the design of WDM systems and also single-wavelength systems consisting of chains of amplifiers where ASE may build up along the chain to a level where it affects gain at signal wavelength(s).

Noise

Noise measurements are perhaps the least understood and most difficult of the primary amplifier measurements. The goal is to obtain a figure-of-merit that quantifies an amplifier's contribution to a system's total noise. That figure-of-merit presently used is the amplifier's noise figure, defined as the logarithm (in dB) of the ratio of the electrical signal-to-noise ratio (SNR) at the input of an amplifier to the electrical SNR at its output. Two important caveats are often forgotten in this definition: 1) the input light source is meant to be shot-noise limited and 2) the detector is meant to be a noiseless detector with unity quantum efficiency. Part of the problem in measurement is that noise contributed by an amplifier is often so small that it is difficult to measure the noise added by the amplifier in the presence of noise from a real light source and detector.

Our preferred method for measurement involves determining the carrier-to-noise ratio (CNR) of the system in Fig. 2 with and without the device under test while changing the attenuation of the output attenuator to keep constant average signal power on the detector. This yields the noise added by the amplifier and thus enables calculation of the amplifier's noise figure.

It is well known that two types of noise added by an amplifier are signal-spontaneous (s-sp) beat noise and spontaneous-spontaneous (sp-sp) beat noise. The first results from heterodyning between the signal and spontaneous radiation at the detector, while the latter results from a similar heterodyning between various spectral components of the ASE. The electrical noise spectral density, $N(f)$ with units of A^2/Hz , resulting from these phenomena can be expressed in terms of two optically measurable quantities: the received signal power P_r , with units of W, and the ASE optical power spectral density $\rho_{ase}(\nu)$, with units of W/Hz, where f represents signal (base-band) frequencies and ν represents optical frequencies.

$$N_{s-sp} = 2 r^2 P_r \rho_{ase}(\nu)$$

$$N_{sp-sp} = r^2 \int [\rho_{ase}(\nu)]^2 d\nu$$

The danger of using an optical technique to obtain P_r and $\rho_{ase}(\nu)$ and then calculating the electrical noise spectral density is that noise contributions of the amplifier due to other phenomena are not accounted for. Examples of other phenomena that could possibly occur in an amplifier are phase-noise to intensity-noise conversion and noise resulting from leakage of light into the signal path from a nominally 1480 nm pump.

Distortion

It has been established that distortion due to gain saturation that occurs in semiconductor-optical amplifiers does not occur in fiber-optic amplifiers [1]. Distortion due to other processes can occur but at a level which does not have impact on digital systems. The distortion can have

significant impact in subcarrier multiplexed AM transmission, such as that used in transmission of CATV signals, where parts per million distortion is unacceptable. One mechanism of distortion is the interaction of laser chirp with the variation of gain with wavelength, also known as gain slope. While the gain slope of an amplifier can be quite small in a highly saturated amplifier, effects are often visible in a CATV signal's composite second-order (CSO) distortion. Since the magnitude of the effect is so dependent on the characteristics of the source, alternative techniques such as measurement of the small-signal gain spectrum in the presence of an unmodulated signal have been performed [2]. An established, reliable technique has not, however, been proposed.

Summary

While amplifier products rush through development toward deployment, measurement techniques have not kept pace; work to develop and perfect these measurements must be accelerated before widespread implementation of amplified systems takes place. Areas that need immediate attention are the measurement of gain with multiple-wavelength signals, measurement of noise properties, and measurement of distortion for AM-VSB applications.

Acknowledgment: It is a pleasure to acknowledge the contributions of R. P. Blaszyk, L. J. Button, D. R. Cole, R. A. Modavis, E. F. Murphy, and M. A. Newhouse to my understanding of optical amplifier parameters and their measurement.

References

1. R.I. Laming, L. Reekie, P.R. Morkel, and D.N. Payne, *Electron. Lett.*, **25**, p. 455 (1989).
2. N. Kwong, J. Pastaski, H. Blauvelt, and I. Ury, "Measured spectral dependence of distortion in erbium-doped fiber amplifiers," in *Digest of Conference on Optical Fiber Communication, 1992 OSA Technical Digest Series, Vol. 5* (Optical Society of America, Washington, D.C., 1992) p. 191.

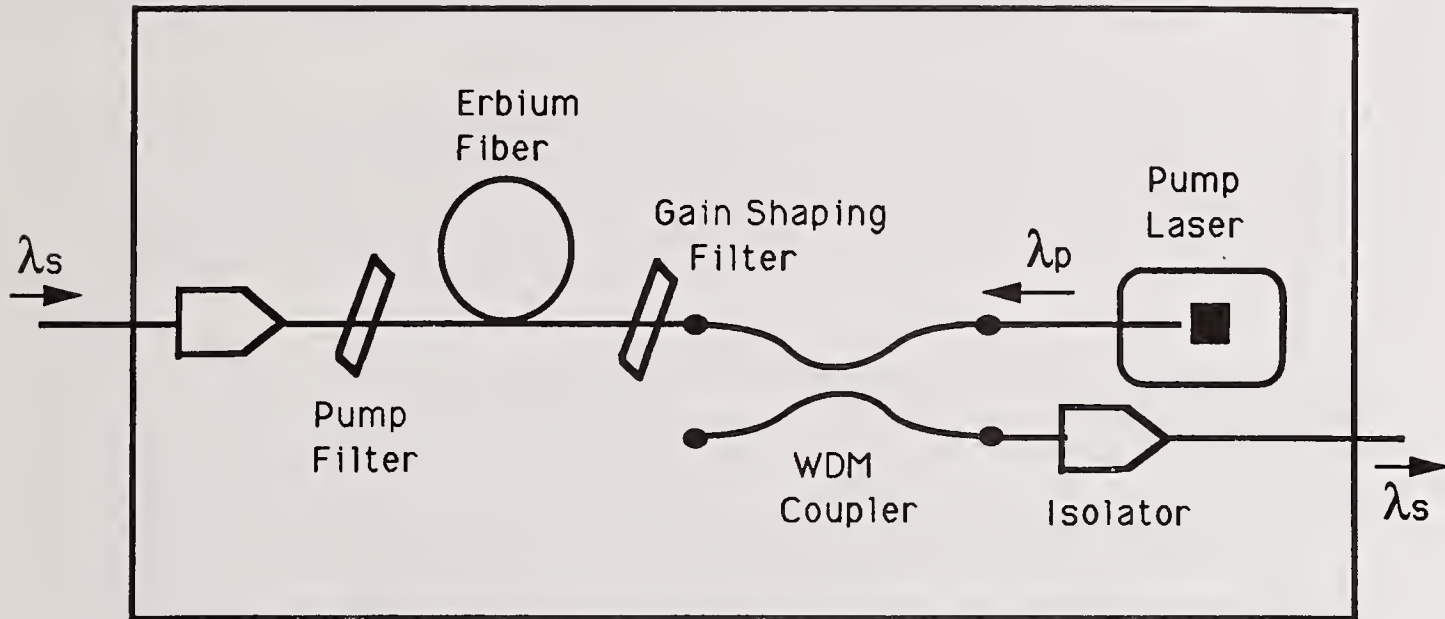


Fig. 1 Optical schematic of one implementation of a single-pumped erbium fiber-optic amplifier.

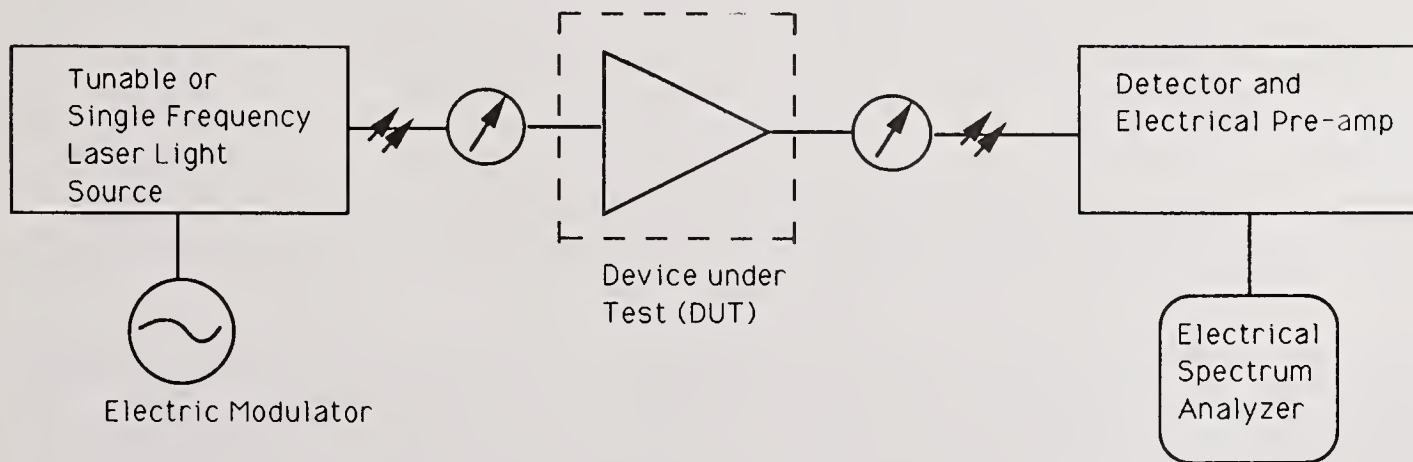


Fig. 2 Schematic of set-up required for measuring the four primary amplifier quantities: gain, bandwidth, noise, and distortion.

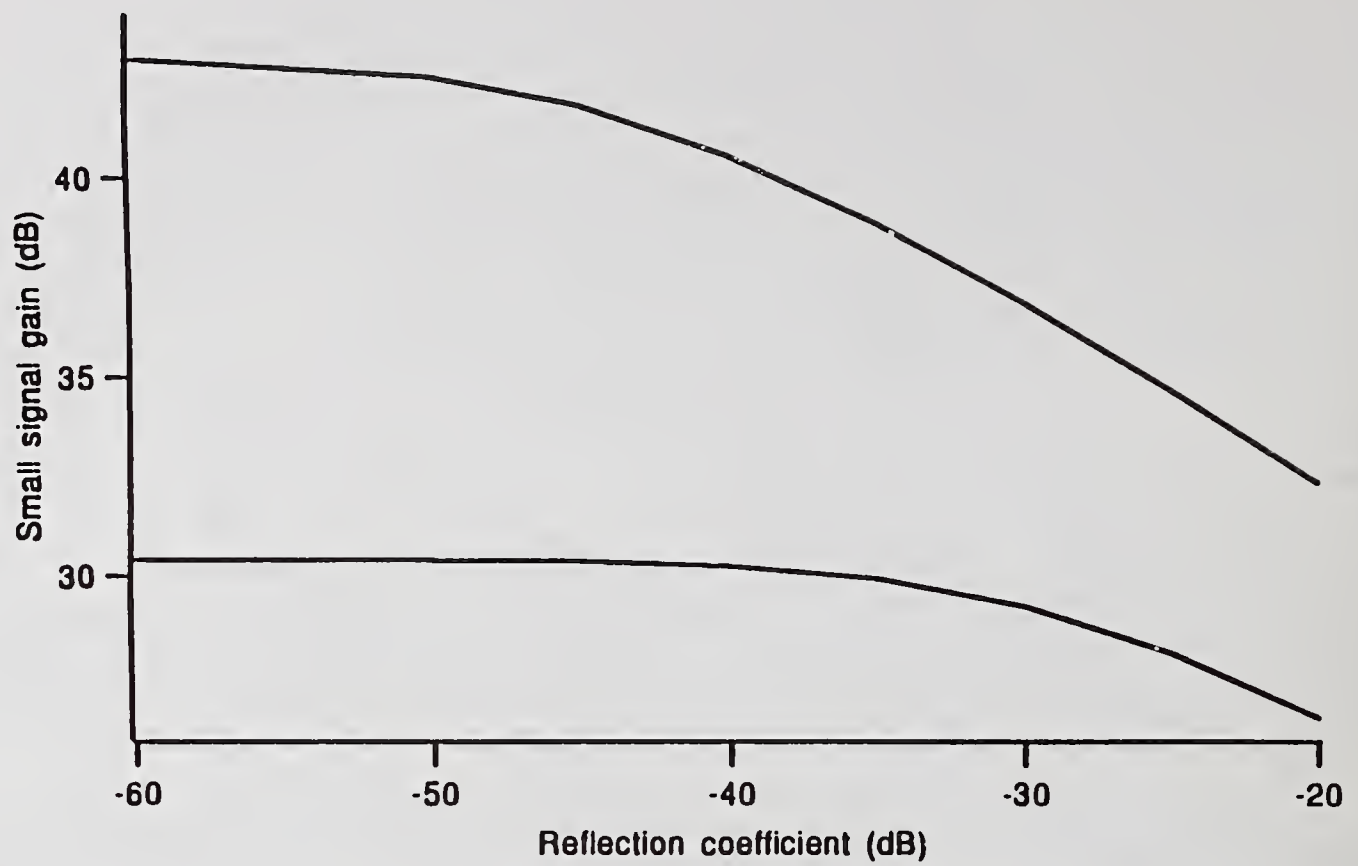


Fig. 3 Impact of back-reflection on the apparent small-signal gain of an amplifier with maximum small-signal gain of 40 dB.

Chromatic Dispersion of Erbium-doped Fiber Amplifier Measured by Fourier Transform Spectroscopy

*Robert K. Hickernell, Kazumasa Takada, Makoto Yamada, Makoto Shimizu, and Masaharu Horiguchi

NTT Opto-electronics Laboratories, Tokai, Ibaraki-ken, 319-11 Japan

*guest researcher, from National Institute of Standards and Technology, Boulder, Colorado USA

Abstract: We report the measurement of group index and chromatic dispersion in an erbium-doped fiber amplifier by Fourier transformation of low-coherence interferograms. Resonant absorption-induced changes in dispersion due to erbium ions in a germania co-doped fiber are as large as 25 ps/(km·nm), and gain-induced changes in dispersion are as large as -12 ps/(km·nm). The measurements confirm theoretical calculations based on a Kramers-Kronig transformation of measured absorption and emission spectra.

Introduction: Erbium-doped fiber amplifiers are increasingly used in a variety of components for 1.5 μm telecommunications. The dispersion changes which accompany the resonant gain and absorption in rare-earth doped fibers may have a significant effect on short pulse propagation in devices such as soliton lasers. A quasi-three-level system description has been used to model the complex susceptibility of erbium-doped fiber amplifiers, and refractive index changes were calculated from the Kramers-Kronig transformation of measured absorption and emission spectra as a function of pump power.¹ A change in phase index on the order of 10^{-7} due to pumping of a germania co-doped fiber was measured using a fiber interferometer with a tunable laser source.² Noise in the measured phase data concealed the dispersion characteristics.

Fourier transform spectroscopy is a powerful tool for measuring the absorptive and dispersive properties of bulk optical samples.³ Recently, dispersive spectroscopy has been applied to the measurement of guided-wave properties, including dispersion,⁴ the location of index discontinuities with fraction-of-a-wavelength precision,⁵ and the correction of dispersion-induced interferogram broadening.⁶

We present here the measurement of group index and dispersion in an erbium-doped fiber amplifier using dispersive spectroscopy. Resonant index perturbation is separated from resonant loss and gain by Fourier transformation, greatly simplifying the interferogram analysis. The measurements are compared with the theoretical predictions of the three-level laser system model.

Background: Consider a Mach-Zehnder interferometer with a movable reference arm and a broadband source. The phase of the Fourier transform of the interferogram with respect to the change in optical path is equal to the optical phase difference between the two arms, as a function of wavenumber.³ The phase change due to a test sample in one arm can be measured (within an unknown constant) by subtracting the phase of the interferogram with the sample removed from that of the sample interferogram. The first derivative of the phase with respect to wavenumber yields the group index of the sample, and the second derivative is proportional to the dispersion. If the length through which the scanning arm can be moved is shorter than the path delay of the sample, a calibrated reference fiber can be inserted in the scanning arm and its phase delay subtracted in the analysis.

Experimental setup: A fiber-optic Mach-Zehnder interferometer was constructed as shown in Fig. 1 and consisted primarily of standard single-mode fiber. A segment of dispersion-shifted fiber in the test arm balanced the dispersion of the two arms. The signal source was an LED having a center wavelength of 1.53 μm and a 3-dB bandwidth of 70 nm. Signal power in the erbium-doped test fiber was maintained at -30 dBm to avoid gain saturation. The scanning arm contained a polarization controller to maximize interference visibility. Optical path difference was changed by translating a linear dc-motor-driven stage on which collimating lenses and a cube-corner retroreflector were mounted. The optical phase was modulated at 40 kHz by a piezoelectric fiber stretcher in the test arm,

and lock-in detection with a 100 Hz bandwidth extracted the signal interferogram. The test arm contained a fiber wavelength-division coupler to inject 1.48 μm counter-propagating pump light into the erbium-doped test fiber. Optical isolators in each input and output port and a fiber connector return loss of greater than 45 dB prevented back-reflection of pump light and laser oscillation of the fiber amplifier.

Clock pulses for interferogram sampling were generated by the zero crossings of an ac-coupled, high coherence interference signal.⁷ Light from a stabilized 1.3197 μm DFB laser was injected into the interferometer through the second input coupler port and separated at the output with a dichroic mirror. Since the 1.3 μm reference light and 1.55 μm signal light were copropagating, distortion of the sampled interferogram due to fiber temperature changes and scanning arm vibration was minimal.

A free-space, white-light Michelson interferometer was constructed with its scanning stage in common with that of the Mach-Zehnder interferometer to provide a start trigger for each sampling run. Its fixed arm was mounted on a stepping motor to calibrate the relative position difference between sample and reference measurements, as required for the determination of group index.

Measurement and Analysis: We made initial measurements on standard single-mode, dispersion-shifted, and high-NA fibers. The maximum length of fiber for which an absolute measurement of group index could be made without a dummy reference fiber was 25 cm. The stage was scanned at a rate of 20 $\mu\text{m/s}$ through an optical path length change of 5.4 mm to sample 8192 points. Fast Fourier transformation (FFT) yielded the phase with a wavelength resolution of 0.4 nm near 1.53 μm . After subtraction of the residual system phase without the test fiber, a fourth-order polynomial fit to the sample phase as a function of wavenumber was made over the region 1.5 μm to 1.6 μm . Our measurements of 1 m lengths of fiber agreed to within ± 0.6 ps/(km·nm) with measurements by a commercial instrument.

A 729 ± 0.5 cm length of erbium-doped, germano-silicate optical fiber with a relative core index difference of 1.2% was studied.⁸ The average erbium concentration in the core was 6.8×10^{17} cm⁻³, and loss at the absorption peak was 1.16 dB/m. The 730 cm dummy reference fiber had a core index of 1.2% and a dispersion of -21 ps/(km·nm) at 1.535 μm . Figure 2 shows the sampled interferograms without pumping and for 25 mW coupled pump power. Increase in the overall magnitude of the signal due to amplifier gain is easily observed, but the complex change in shape of the interferogram is undecipherable without the use of Fourier transform analysis. After subtraction of the system phase and correction for the group index and dispersion of the reference fiber, a fourth-order polynomial fit of phase vs. wavenumber over the entire region between 1.5 μm and 1.6 μm yields only the broad spectral variation of group index and dispersion of the host fiber.

To resolve the resonant dispersive features due to the presence of erbium-induced absorption and gain, we performed a quadratic curve fit over a sliding, seven-point data window. Figure 3 is a plot of the dispersion as a function of wavelength for different coupled pump powers. The peak perturbation of dispersion of the unpumped fiber is 25 ps/(km·nm) at 1.537 μm , large enough to counteract the background dispersion of -15 ps/(km·nm), also plotted in Fig. 3. The sign of the perturbation reverses as the pump power increases through the threshold value, coincident with the transition from loss to gain. The effect of population inversion saturation is seen near the largest pump power of 25 mW, which was 9.4 times the threshold power of 2.7 mW, as calculated from gain data.⁸ Maximum pumped dispersion perturbation was 10 ps/(km·nm) at 1.535 μm and -12 ps/(km·nm) at 1.537 μm . The noise is due in part to polarization-dependent source artifacts.

We measured the emission and absorption lineshapes of the erbium fiber in the wavelength range from 1.40 μm to 1.65 μm with 0.5 nm resolution. The normalized lineshapes were used to calculate the respective cross sections, and a Kramers-Kronig transformation produced the corresponding dispersive part of the cross sections.¹ We scaled the emission and absorption spectra to the measured peak absorption coefficient to account for the overlap of the signal mode and the erbium concentration profile. Populations of the upper and lower energy levels as a function of distance in the fiber were calculated from the pump absorption and threshold power. The calculation included the saturation term due to stimulated emission,⁹ based on the average pump absorption and emission coefficients given in Ref. 8. The calculated index change integrated over the length of the fiber had peak values

of -1.1×10^{-8} and $+1.6 \times 10^{-8}$ without pumping, and -0.4×10^{-8} and $+0.8 \times 10^{-8}$ with a pump power of 25 mW.

The calculated change in dispersion, also using a sliding, seven-point quadratic fit, is shown in Fig. 4. The experimentally measured perturbation from the host fiber dispersion is plotted in the same figure for comparison. Agreement between the measurement and calculation is very good. Noise in the theoretical calculation is due to noise in the measured absorption and emission spectra. The measured and calculated perturbation of group index are plotted in Fig. 5 over a wider wavelength range than in Fig. 4. The resonance near $1.552 \mu\text{m}$ is due to the secondary erbium absorption peak.

Conclusion: We conclude that Fourier transform spectroscopy with a fiber interferometer is a powerful technique for measuring resonant dispersive changes in rare-earth-doped fibers. The change in chromatic dispersion due to absorption and gain in an erbium-doped fiber can be significant compared to the background dispersion of the host fiber, particularly in the case of a narrow gain spectrum.

Acknowledgments: The authors express their thanks to Y. Takeuchi for supplying the fiber couplers and to T. Ikegami, T. Izawa, and M. Nakahara for their support of this work. R.K. Hickernell expresses his appreciation to the NTT staff for their help during his visit.

References

1. E. Desurvire, *J. Lightwave Technol.* **8**, 1517-1527 (1990).
2. S.C. Fleming and T.J. Whitley, *Electron. Lett.* **27**, 1959-1961 (1991).
3. J. Chamberlain, *The Principles of Interferometric Spectroscopy*, John Wiley & Sons, Chichester 1979.
4. P.-L. Francois, M. Monerie, C. Vassallo, Y. Durteste, and F.R. Alard, *J. Lightwave Technol.* **7**, 500-513 (1989).
5. B.L. Danielson and C.Y. Boisrobert, *Appl. Opt.* **30**, 2975-2979 (1991).
6. A. Kohlhaas, C. Fromchen, and E. Brinkmeyer, *J. Lightwave Technol.* **9**, 1493-1502 (1991).
7. K. Takada, M. Kobayashi, and J. Noda, *Appl. Opt.* **29**, 5170-5176 (1990).
8. M. Yamada, M. Shimizu, M. Horiguchi, and M. Okayasu, *IEEE J. Quant. Electron.* **28**, 640-649 (1992).
9. E. Desurvire, *IEEE Photon. Technol. Lett.* **1**, 293-296 (1989).

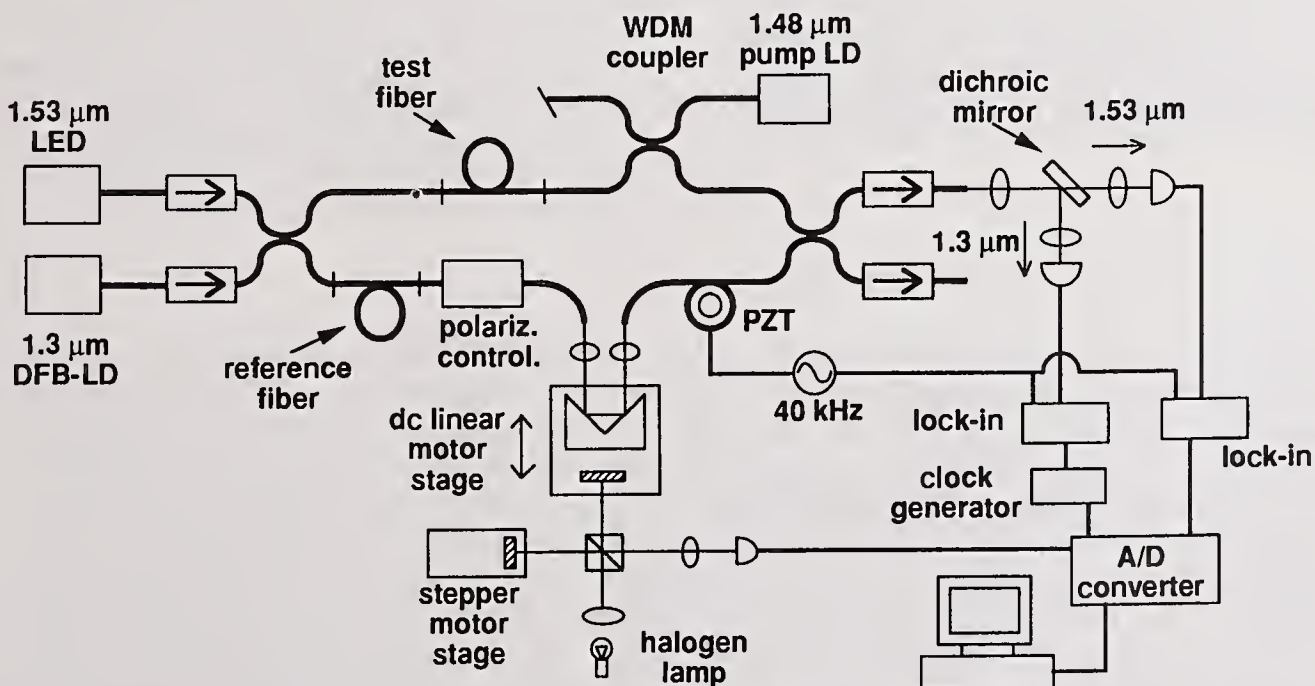


Fig. 1. Experimental setup of low-coherence interferometer.

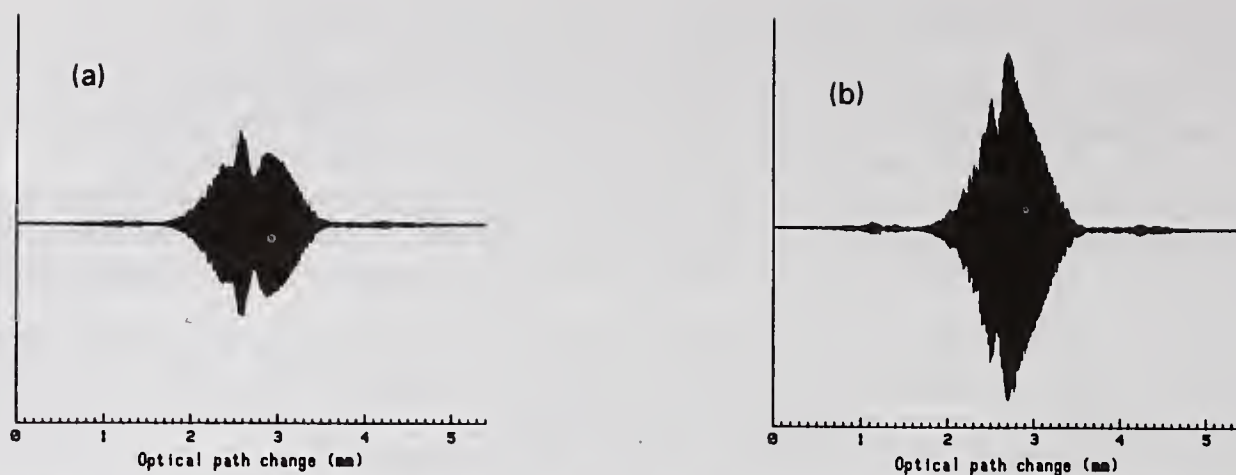


Fig. 2. Low-coherence interferogram signal as a function of optical path change: (a) unpumped; (b) pump power, 25 mW.

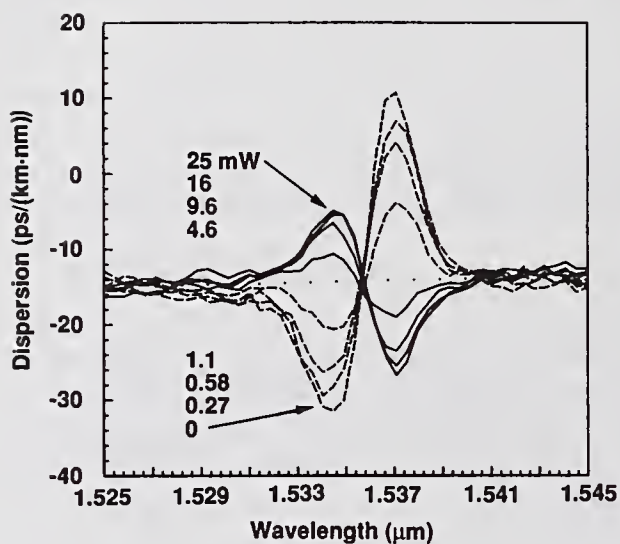


Fig. 3. Measured dispersion of erbium-doped fiber for different pump powers: below pump threshold power (dashed); above pump threshold power (solid); host fiber dispersion (dotted).

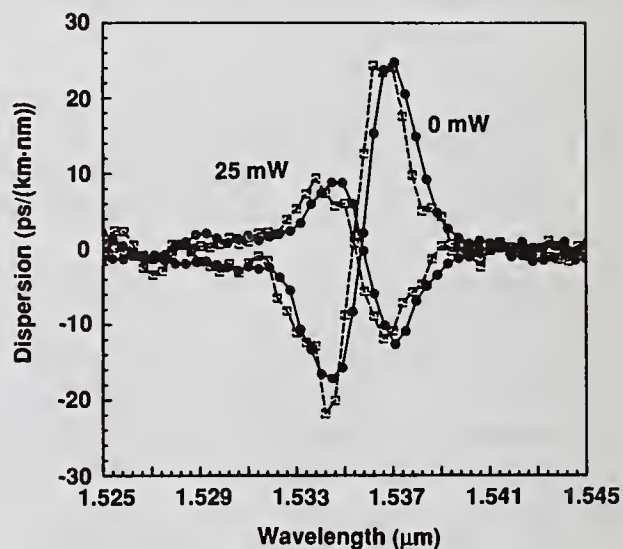


Fig. 4. Pumped and unpumped perturbation of dispersion due to erbium ions: measured (solid line, dot); calculated from Kramers-Kronig transformation of absorption and emission data (dashed line, box).

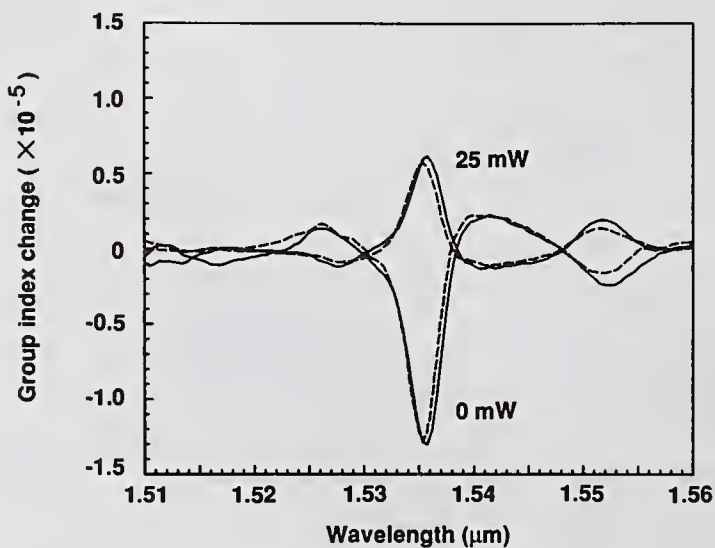


Fig. 5. Pumped and unpumped perturbation of group index due to erbium ions: measured (solid line); calculated (dashed).

NOISE MEASUREMENTS OF ERBIUM-DOPED OPTICAL FIBRE AMPLIFIERS: INFLUENCE OF SOURCE EXCESS NOISE

M. Artiglia, P. Bonanni (*), A. Cavaciuti, M. Potenza, M. Puleo, B. Sordo

CSELT - Centro Studi E Laboratori Telecomunicazioni SpA
Via G. Reiss Romoli, 274 - 10148 TORINO (Italy)
(* SIRTI - Via Vida, 19 - 20127 MILANO (Italy)

Abstract: *This paper will consider the influence that the presence of input excess noise may have on the noise degradation figure of an Erbium-doped fibre amplifier. A procedure is suggested to correct the measured data for the excess noise and relate them to the ideal noise figure.*

1. Introduction

Erbium Doped Fibre Amplifiers (EDFAs) are very attractive for use in optical telecommunication systems operating in the third window. They can in principle bring to dramatic enhancements of the performance of optical links and their potentials in various applications are being intensively explored worldwide. One aspect of EDFAs which is of great interest is the degradation of the signal to noise ratio (SNR) they cause because of the amplified spontaneous emission (ASE) generated by the device itself. In the literature this feature is characterised by the noise figure F of the amplifier, defined as the ratio of the input SNR to the output SNR [1]. A crucial assumption of this definition is that the input signal must be coherent, that is quantum noise limited. This assumption, however, does not hold true in practice where the noise figure is calculated from measured SNRs. In fact, laser diodes used as optical sources for the characterisation and the applications of EDFAs are affected by excess noise, such as the Relative Intensity Noise (RIN), back-reflection induced noise and, for external cavity lasers, the noise contributed by suppressed side-modes. This excess noise at the input is amplified too and influences both optical and electrical noise measurements since it affects the measured fluctuations and the level of noise floor. The aim of this paper is to show that this effect contributes in a non negligible way to the measured noise characteristics of the device. Throughout the attention will be focussed on the RIN of DFB lasers. In particular noise dependence on input power level will be investigated, both theoretically and experimentally. A good agreement of experimental data, measured on an EDFA pumped at 1480 nm, and theory is found. A procedure is suggested to correct the measured data for the excess noise and relate them to the ideal noise figure F . This could be useful in many practical situations, in which very low noise sources are not available.

2. Theory

The definition of the noise figure F of an optical amplifier is related to the evaluation of the intrinsic limits of the device in contributing noise to an input signal affected only by the unavoidable quantum noise [2]. For an ideal amplifier F cannot be lower than the theoretical quantum limit of 3 dB. In most practical applications, where the input signal can be not-quantum limited, F becomes unrelated to the actual situation and the degradation of the SNR is dependent on the excess noise at the input. In particular, the noise degradation of the amplifier due to spontaneous emission decreases as the excess input noise increases. Therefore, in practical applications, care must be exercised in defining the noise properties of EDFAs.

The SNR for the input signal beam can be expressed as:

$$\left(\frac{S}{N}\right)_{in} = \frac{n_{in}^2}{2B\Sigma_{in}^2} \quad (1)$$

in terms of the mean photon number n_{in} and of the relative fluctuations Σ_{in}^2 . If the noise properties of the signal are quantum limited (i.e., the signal is in a coherent state) $\Sigma_{in}^2 = n_{in}$ and (1) assumes the well-known form used to compute noise figures. In the following we will consider a laser beam affected by a non negligible RIN and calculate the SNR degradation due to the amplifier. This is considered as a cascade of an input device (characterised by a loss Γ_{in}), of an erbium-doped active fibre (characterised by its total internal gain G and spontaneous emission factor n_{sp}) and of an output device (with loss Γ_{out}). The input and output devices actually can consist of connectors, WDMs and isolators. At the end of the cascade, the SNR will be again given by (1), but with the pertaining output values, n_{out} and Σ_{out}^2 . Defining the noise degradation figure, N_F , as:

$$N_F = \frac{(S/N)_{in}}{(S/N)_{out}} \quad (2)$$

and passing to electrical quantities, we will have:

$$N_F^{(\epsilon)} = \frac{1}{1 + \eta \sigma_{RIN}^2 I_{in}} \cdot \left\{ \frac{1}{G \Gamma_{out} \Gamma_{in}} + m_t n_{sp} \Delta f_o \frac{G-1}{(G \Gamma_{in})^2 \Gamma_{out} I_{in}} + \right. \\ \left. + 2 \eta n_{sp} \frac{G-1}{G \Gamma_{in}} + m_t n_{sp}^2 \Delta f_o \left(\frac{G-1}{G \Gamma_{in}} \right)^2 + \eta \sigma_{RIN}^2 I_{in} \right\} \quad (3)$$

where the following quantities have been introduced: detector responsivity η , RIN spectral density σ_{RIN}^2 , mean input photon flux I_{in} (associated to n_{in} and the signal band), optical filter bandwidth Δf_o and number m_t of "transverse" modes contributing to ASE ($m_t = 2$ in the present case). The various terms in braces of Eq. (3) are respectively the contributions of the signal shot noise, the spontaneous emission shot noise, the signal-spontaneous emission beat noise, the spontaneous emission beat noise with itself and the excess noise to the output SNR. In particular, the latter term does not appear in formulas giving the amplifier noise figure F (where $\sigma_{RIN}^2 = 0$).

2. Experimental set-up and discussion of the results

The used experimental set-up is shown in Fig.1. The light exiting a DFB laser is passed through a pigtailed variable attenuator and then injected into the EDFA. An optical isolator prevents backward ASE to enter the DFB laser. The output of the EDFA is then sent to a PIN photodiode for detection. The average DC component of the photocurrent is measured by a calibrated picoamperometer, while the AC component, carrying the fluctuations, is amplified and fed to an electrical spectrum analyser. In the measurements discussed here no optical filter was inserted at the output of the amplifier to reduce the detected ASE; this explains the somewhat high values of the noise degradation measured at low input power but has no influence on the validity of the presented approach. The used EDFA has been developed by the authors. The active fibre, pumped at 1480 nm with a copropagating scheme, has a relatively large core radius and is a little longer than the optimal length so as to obtain a flat gain spectrum even in the small to mid signal range. Measured spectral gain curves for three different input power levels are shown in Fig. 2; gain variations are less than 4 dB even in the small-signal regime. An optical isolator is inserted internally before the output port of the amplifier. Both input and output ports are FC/PC connectorised. As a source a commercial DFB laser of very high quality was used, operated in two different conditions, such that the measured RIN values were less than -165 dB/Hz in one case and -145 dB/Hz in the other. Emission wavelength was 1530 nm. The RIN was measured using the method described in [3].

The curves in Fig. 3 a) show the behaviour of the measured noise degradation figure $N_F^{(\epsilon)}$ versus the input signal level for the two operating conditions. The high values of $N_F^{(\epsilon)}$ are due both to the absence of any optical filter to reduce ASE level and to the fact that the active fibre was not fully inverted. The lowest curve corresponds to a source RIN value of -145 dB/Hz, the other to a RIN of -165 dB/Hz. Fig. 4 shows curves as calculated from Eq. (3) for RIN equal to -170 dB/Hz, -165 dB/Hz (these cases are hardly distinguishable), -150 dB/Hz, -145 dB/Hz from top to bottom. The upper curves of Fig. 4 a) correspond to experimental conditions: no optical filter inserted, $\Gamma_{in} = \Gamma_{out} = -1$ dB, G given by the measured values of the fibre internal gain (the small-signal gain at 1530 nm signal wavelength was 25 dB for a 25 mW pump power) as a function of input power. The detector quantum efficiency was put equal to unity, according to the normalisation used to obtain the experimental curves in order to eliminate the influence of photodiode characteristics. A reasonable agreement is found between experimental data and theoretical results. An even better agreement is expected through a more accurate estimation of the behaviour of n_{sp} versus input signal level. Theoretical calculations show that the -170 dB RIN-curve practically coincides with the behaviour of the F -curve (no excess noise present). Therefore, optical sources with RIN lower than that value, can be considered as quantum limited for practical purposes.

Since so low RIN figures are not commonly encountered, attention must be paid to excess noise of optical sources. In fact, coming to Fig. 3 b), let us consider the upper (experimental) curve which represents the amplifier noise degradation figure for the -145 dB/Hz case assuming that the input signal is quantum limited. The discrepancy with the lowest curve of Fig. 3 a) is evident in the saturation region, where the corresponding behaviours are quite different. This is because also RIN contributes to both the input and the output SNRs: neglecting its presence before the amplifier necessarily leads to an overestimation of the device noise degradation figure. On the other hand, starting from the same assumption of Poissonian input signal, but correcting the measured SNR at the output by subtracting from the measured fluctuations the amplified RIN

contribution [last term in braces in Eq. (3)], one obtains a $N_F(\theta)$ (dashed line) in good agreement with that measured for the RIN equal to -165 dB/Hz [lowest curve in Fig. 3 b)] which in turn is very close to the ideal behaviour of F [see Fig. 4 a)]. To support the validity of the proposed analysis, Fig. 4 a) also shows theoretical curves in different operating conditions: the lower family of plots refers to the presence of an optical filter of 1 nm bandwidth. It is interesting to note that the behaviour of $N_F(\theta)$ is mainly influenced, besides n_{sp} , by the optical filter in the small-signal regime and by the RIN of the source in the large-signal regime. Finally, Fig 4 b) shows the noise degradation for a highly inverted fibre (small-signal n_{sp} of around 1.2) with optical filter. A considerable reduction of $N_F(\theta)$ is seen as expected, but the influence of RIN is still clearly evident.

3. Conclusions

The influence of source excess noise on SNR degradation measurements of EDFAs has been investigated experimentally. Excess noise is capable of altering considerably the behaviour of the (S/N) degradation versus input power level, with respect to the ideal case. A simple theoretical model which fits quite well the experimental data has been presented. Finally, a simple procedure for relating the measured data to the ideal noise figure has been proposed, based on the knowledge of the excess noise (RIN) of the laser diode used as an optical source for the measurements. Effectiveness of the procedure has been demonstrated.

References

- [1] See for example the Tech. Dig. of the Topical Meeting on Optical Amplifiers and applications, Snowmass (CO), July 24-26, 1991 and references therein quoted.
- [2] T. Okoshi, K. Kikuchi: "Coherent Optical Fiber Communications", KTK-Kluwer, 1988
- [3] P. Gambini et al., "Characterization of laser diode intensity noise at microwave frequencies with high sensitivity", SPIE OE/FIBERS Conf., Boston (USA), September 1989.

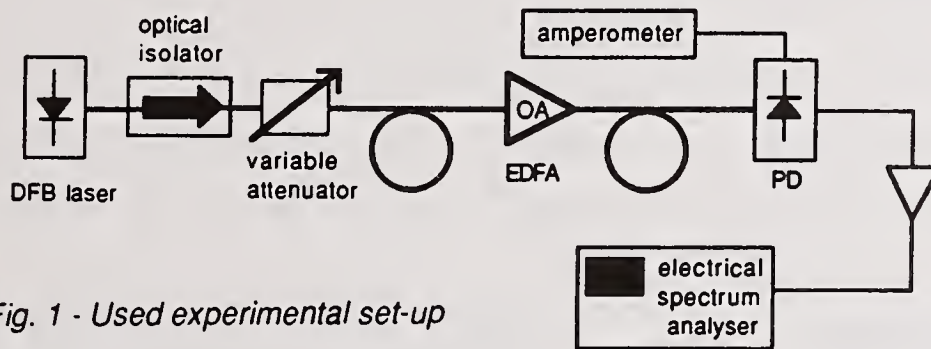


Fig. 1 - Used experimental set-up

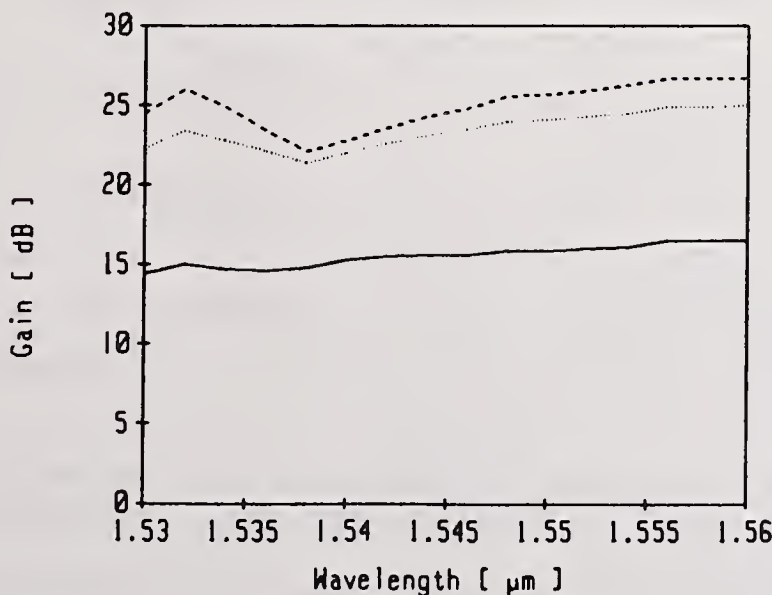


Fig. 2 - Gain spectra of the used EDFA measured at different input power levels: -30 dBm (dashed line), -20 dBm (dotted line), -8 dBm (continuous line)

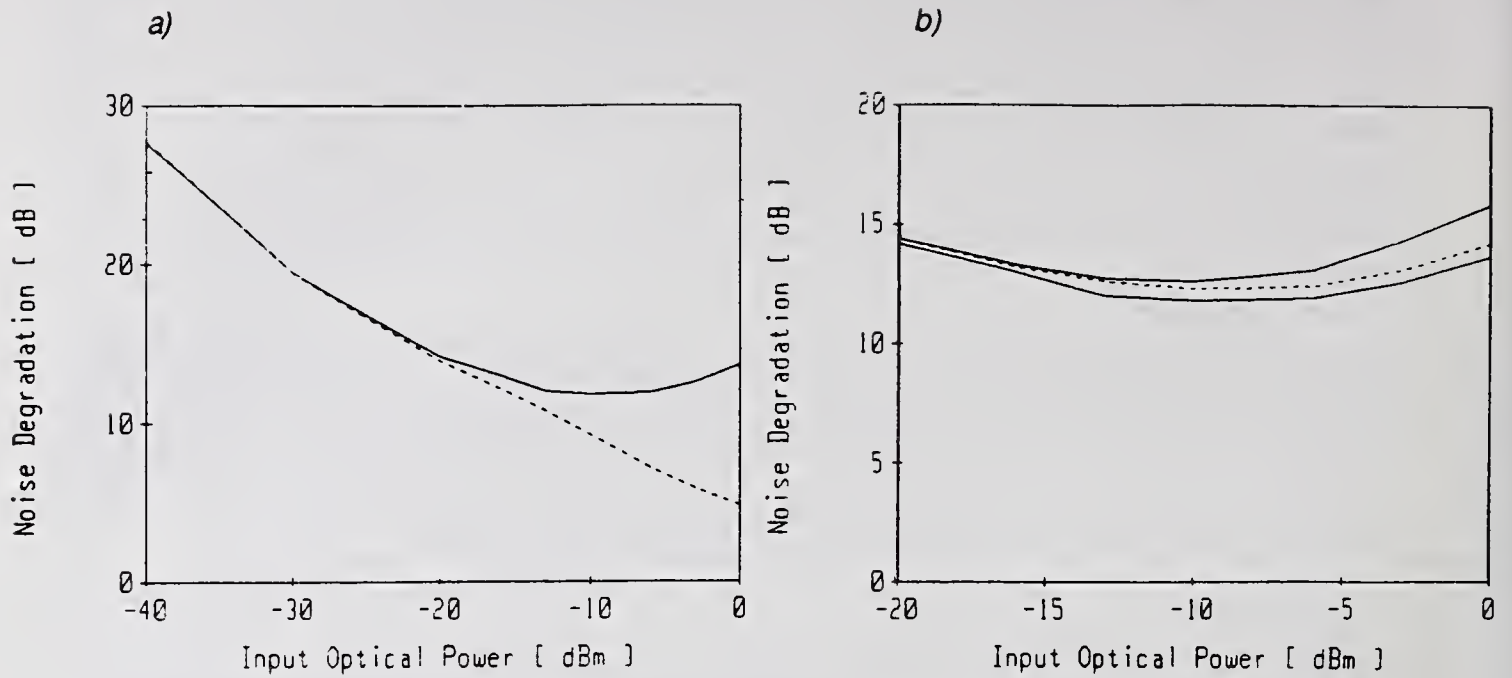


Fig.3 - a) Measured values of $N_F^{(e)}$; continuous line: source RIN -165 dB/Hz; dashed line: -145 dB/Hz;
 b) lower curve: $N_F^{(e)}$ at -165 dB/Hz; upper curve: noise figure without correction; dashed line: corrected noise figure.

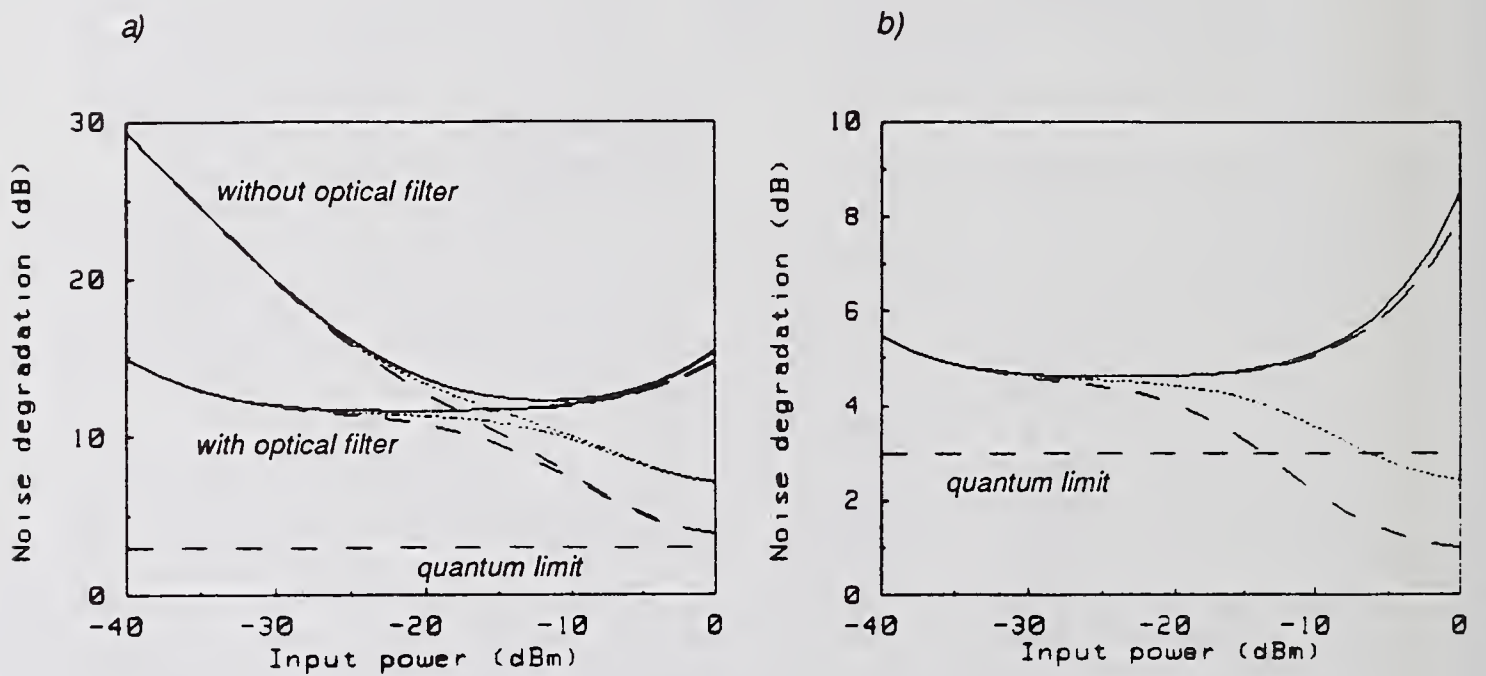


Fig.4 - a) Upper curves: calculated values of $N_F^{(e)}$ after (3) (from top to bottom: source RIN -170 dB/Hz; -165 dB/Hz; -150 dB/Hz; -145 dB/Hz); lower curves: same as before but with a 1 nm optical filter;
 b) same RIN levels as a) but with lower spontaneous emission factor (i.e. at higher pump levels) and 1 nm optical filter.

Accuracy of noise figure measurement for erbium-doped fiber amplifiers by the optical method

T. Kashiwada, M. Shigematsu and M. Nishimura

Sumitomo Electric Industries, Ltd.
1, Taya-cho, Sakae-ku, Yokohama, 244, Japan

1. Introduction

Noise figure (NF) is one of the most important parameters of Er³⁺-doped fiber amplifiers (EDFAs). In general, there are two types of techniques for measuring the NF: the optical and electrical methods.⁽¹⁾⁽²⁾ Although the optical method is relatively simple, accuracy of the NF measured in the saturation region has been questioned. Recently, a new technique was proposed to improve accuracy of the optical method by utilizing the polarization properties of the signal and the amplified spontaneous emission (ASE).⁽³⁾⁽⁴⁾ It seems, however, that the accuracy and limits of the measurements have not yet been analyzed quantitatively. In this paper, we examine the errors in the NF measurements, and determine the accuracy of each setup for measurement.

2. Optical method of NF measurement

The NF is given by the following equation, when the signal-spontaneous beat noise is dominant :

$$NF = \frac{P_{ASE}}{h\nu\Delta\nu G} \quad (1)$$

where P_{ASE} is the ASE power within the optical bandwidth of $\Delta\nu$, ν is the signal frequency and G is the gain of the EDFA. The NF can be determined by measuring P_{ASE} and G using an optical spectrum analyzer.

In the saturation region, however, the ASE power level becomes small and comparable to amplified sideband components of the signal and/or noises due to the limited dynamic range of the spectrum analyzer. Therefore, it is necessary to eliminate or suppress them for accurate measurement of P_{ASE} . Possible techniques for the purpose are (a) add a narrow spectral width bandpass filter to the light source, and (b) polarize the signal at the output port of the EDFA using a polarization controller and suppress it by an orthogonally aligned polarizer.⁽³⁾⁽⁴⁾

3. Error analysis

Each technique was tested experimentally. Figure 1 shows the experimental setup. Four cases were examined : Case 1-without a bandpass filter (BPF) or polarization control (PC), Case 2-with BPF only, Case 3-with PC only and Case 4-with both BPF and PC. The same curve fitting technique was used in all cases to interpolate P_{ASE} at the signal wavelength. The spectral resolution of the spectrum analyzer was 1nm. Figure 2 shows the gain and the NF as a function of the input signal power measured in each case. In Case 3, the NF could not be determined because of wavelength-dependent undesirable noises in the ASE measurement. In the low input signal power region, the NFs of the other three cases were in good agreement. On the other hand, in the high input signal power region, the NF measured in Case 4 was considerably smaller than those in the other cases.

In order to quantitatively determine the error in each case, the noise of the measurement system itself was examined. Figure 3 shows the measured optical spectrum for each setup with the Er^{3+} -doped fiber (EDF) replaced by a normal single mode fiber having the same length. The noise level relative to the main signal in the adjacent wavelength region could be determined from Fig.3. The signal-to-noise ratio (S/N) in Case 4 was as high as 69dB, while the S/N in Case 1 was only 39dB.

From the S/N values determined above, it was possible to predict measured values of P_{ASE} in each case by theoretically calculating G (thus the output signal power) and $P_{ASE(5)}$ and then adding the system noise, assuming that the S/N of the system was conserved with existence of the EDF. Comparison between the prediction and actual measurements is demonstrated in Fig.4. Agreement is excellent.

4. Discussion

It is worth noting that neither Case 2 nor Case 3 showed a significant improvement in the system S/N, while Case 4 was dramatic as seen in Fig.3. The polarization control is effective for suppressing the amplified main signal to substantially increase the dynamic range of the spectrum analyzer, but the amplified sideband components of the signal still remain, because their polarization state is different from that of the main signal after passing through several optical components in the EDFA. The BPF is essential for reducing those sideband components.

Measurement accuracy of the improved method was investigated based on the system S/N determined from Fig.3. Figure 5 illustrates the relation among the output signal power, the system noise and the ASE power level. In order to achieve 0.1dB accuracy of the NF measurement, the system noise must be 17dB lower than P_{ASE} or less. It can be concluded that the conventional optical method (Case 1) is accurate only when the input signal power is smaller than -20dBm, and that the improved method (Case 4) can be applied to a wide input signal power range up to nearly +10dBm.

5. Conclusion

Accuracy of the NF measurement for EDFAs by the optical technique was investigated quantitatively. The system noises of different setups were determined and the improved method employing a bandpass filter and the polarization control technique was proved to be accurate even in the deep saturation region.

References

- (1) P.R.Morkel, et al., Opt. Lett., Vol.14, pp1062-1064 (1989)
- (2) C.R.Giles, et al., Photon. Technol. Lett., Vol.1, No.11, pp367-369 (1989)
- (3) J. Aspell, et al., Technical Digest on OFC'92, paper ThA4 (1992)
- (4) T.Kashiwada, et al., IEICE National Conf., paper C-309 (in Japanese) (1992)
- (5) K.Kikuchi, Electron. Lett., Vol.26, No.22, pp1851-1853 (1990)

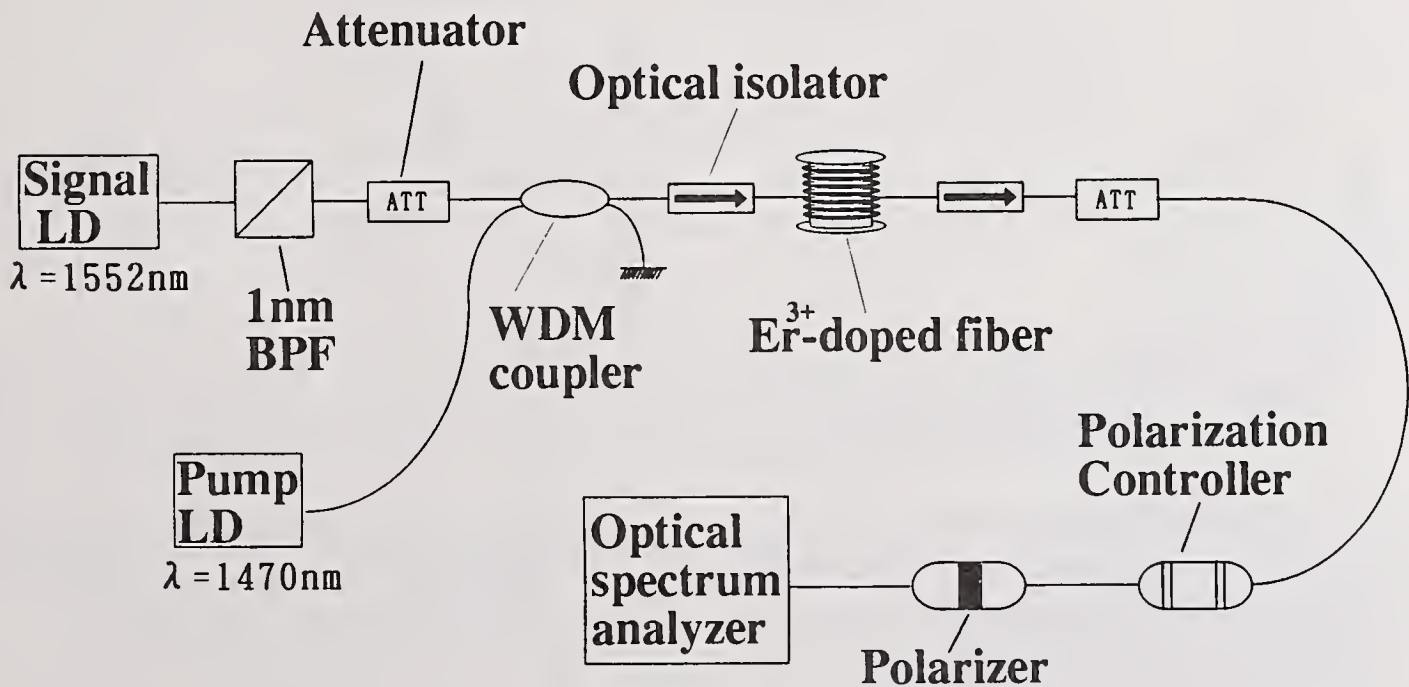


Fig.1 Measurement setup for NF

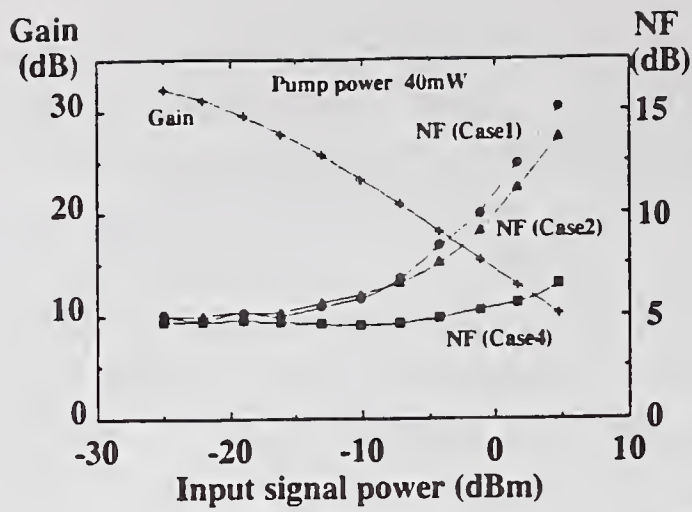


Fig.2 Gain and NF measured with different setups

Fig.3 System noise levels relative to the main signal measured for different setups

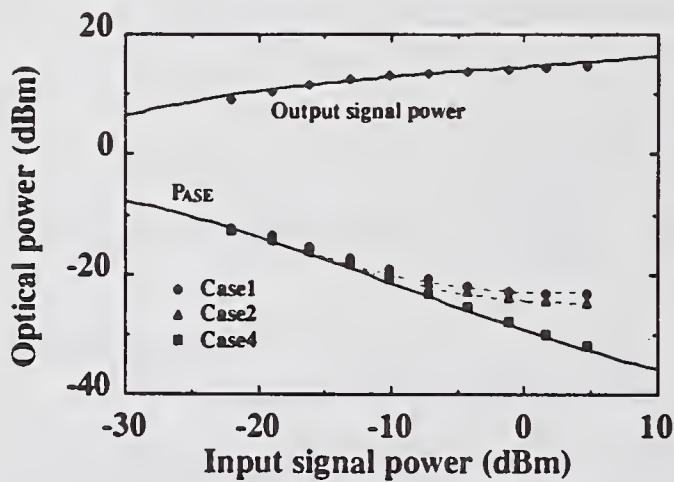
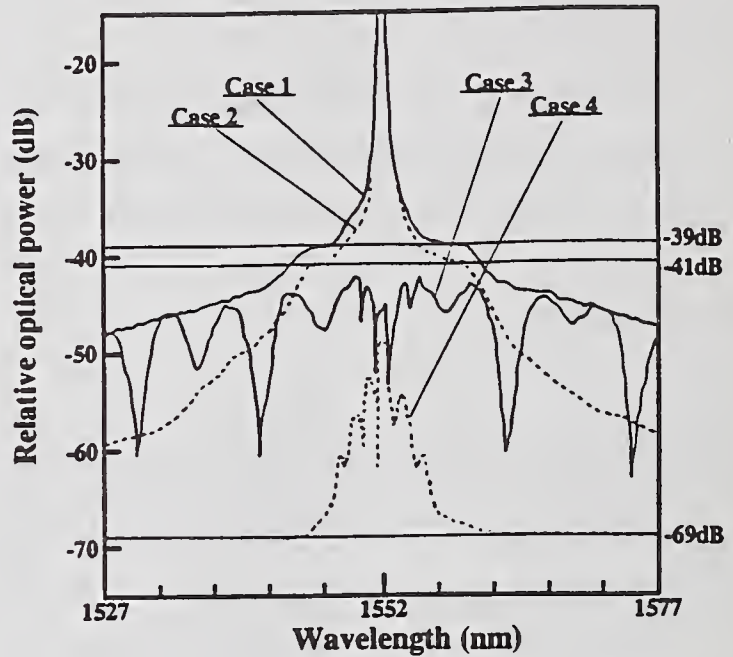


Fig.4 Comparison between the ASE power levels actually observed (marks) and theoretically predicted based on the system noises (curves)

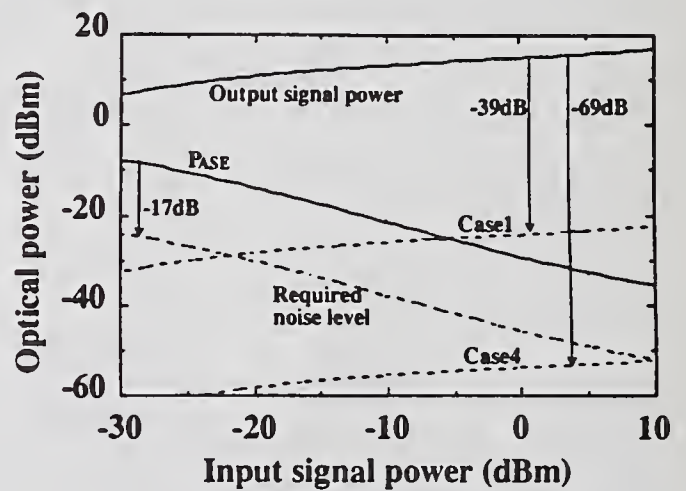


Fig.5 Relation among the output signal power, the system noise and the ASE power level

AUTOMATED MEASUREMENT OF GAIN CHARACTERISTICS OF OPTICAL FIBER AMPLIFIERS

Douglas R. Cole and Miles E. Vance
Corning Incorporated
Opto-Electronic Components
Corning, New York 14831

INTRODUCTION

In this paper we describe and evaluate an automated system for the measurement of gain, output powers, amplified spontaneous emission (ASE), and unabsorbed pump power of an erbium-doped fiber amplifier (EDFA), as a function of input power and wavelength.

In order to make accurate gain measurements it is necessary to separate the signal from the ASE. One solution to this problem is provided by intensity modulation of the signal laser followed by AC detection of the amplified output. The measurement system utilizes RF modulation and an RF spectrum analyzer, which provides the requisite accuracy and precision. We chose, wherever possible, to use commercially available measuring instruments and equipment which could be easily interfaced with the control and data processing computer.

The system obtains values of modulated input and output optical powers, as well as total average input and output optical powers. These measurements are made first on a non-amplifying standard single mode reference (REF) fiber, then on the EDFA to be tested. The optical power gain G is then given by ratios involving only the modulated powers:

$$G = (P_o^m / P_i^m)_{EDFA} / (P_o^m / P_i^m)_{REF} , \quad (1)$$

where P_i^m is the modulated input optical power and P_o^m is the modulated output optical power. The total average optical input signal power P_i is then measured and multiplied by the gain to get the average optical output signal power P_o :

$$P_o = G P_i , \quad (2)$$

Note that P_o does not include ASE, but is the true average signal power for a given average P_i . At high signal levels, P_o becomes essentially equal to the measured total average output power, since ASE becomes negligible.

OPTICAL AND ELECTRICAL HARDWARE SET-UP

The system's signal wavelength can be tuned from 1520 nm to 1550 nm. Before splicing in an EDFA at the device under test (DUT) location, as shown on Fig. 1, the input fiber is spliced to the output fiber and a REF measurement is run. Our calibration specifications require a REF gain stability of +/- 0.25 dB.

An EDFA booster amplifier is used to provide roughly 18 dB of gain for the tunable laser diode signal, thereby obtaining high input power through the entire tuning range. The tunable bandpass filter (TBF) has a FWHM bandpass of 3.5 nm and passes the signal, while blocking most of the booster amplifier's ASE. A variable optical attenuator (VOA 1) steps the attenuation of the input signal. VOA 2 and VOA 3 are appropriately adjusted to prevent signal saturation of the input and output receivers. Coupler 1 is used to tap the input signal. A ratio of the actual input signal delivered to the DUT and the input receiver signal is established. Backward ASE is also captured at this point. Couplers 2 and 3 allow unabsorbed 980 nm pump power (P_u) to be measured for either backward or forward pumping.

Reflected light traveling through the gain fiber of an EDFA reduces the overall amplification of the signal. Therefore, it is important to minimize back reflections to about -60 dB. Low back reflection devices, isolators and angled physical contact connectors (FC/APC) are used.

Polarization variations in signal light are minimized by stipulating minimum polarization sensitivity of critical optical components and placing most system fibers in a fixed position.

The signal generator provides an RF signal, at 50 MHz with 1 mW of electrical power, to the tunable laser diode. The optical signal modulation index is about 16 percent.

PINFET receivers are mounted on test fixtures which provide RF outputs to the RF switch and spectrum analyzer combination and photocurrents to picoammeters.

SOFTWARE

A General Purpose Interface Bus (GPIB) connects a Macintosh IIFX computer to the equipment. Instrument control and data acquisition are performed by a National Instruments software application called LabVIEW 2.

Each real instrument has a stand alone control program or 'virtual instrument' (VI) which writes set-up commands to and reads data from the instrument via a GPIB cable. Each instrument's operating sequence and data acquisition is governed by the main VI program which 'software wires' the devices together.

For a given signal wavelength the input signal is attenuated in 3 dB or other increments from 0 dBm to - 45 dBm. Instruments are polled at each step and data is stored in one of 21 arrays. Next, the main VI program completes the following functions. A raw data file is created in a spreadsheet format. Data is normalized to account for receiver responsivity, variable and

fixed optical insertion losses and attenuation of fixed filters. This normalized data is plotted, along with a fit curve, as shown on Fig. 2, as well as a test sheet listing pertinent test conditions and data table.

RESULTS

Typical gain curves of Fig. 2 were all obtained in 20 minutes after splicing in the DUT. Measurement time can be dramatically reduced by selecting fewer input signal values, especially at the low-input end, and by sacrificing precision.

The basic repeatability of consecutive measurements, with no changes made between measurements, was ± 0.39 dB (3 SIGMA) for small-signal gain and ± 0.25 dB (3 SIGMA) for output power.

According to Eq.(1), long-term variation of the input and output attenuations and signal-processing systems does not produce an error in G, and we thus expect day-to-day repeatability of G to be only slightly worse than ± 0.39 dB (3 SIGMA) because of small differences in splice loss when the amplifier is exchanged for the REF fiber.

From Eq.(2), long-term variation of the input attenuation and signal-processing system produces a proportional error in P_o . This variation was found to be ± 0.21 dB (3 SIGMA) over a period of 4 months. Thus we may expect long-term repeatability of ± 0.33 dB (3 SIGMA) plus the small splice-loss variations.

A test of the linearity of the RF and DC signal-processing systems is the equivalence of the calculated P_o and the measured total optical average power at high signal levels. Typically we find these to agree within 0.1 dB.

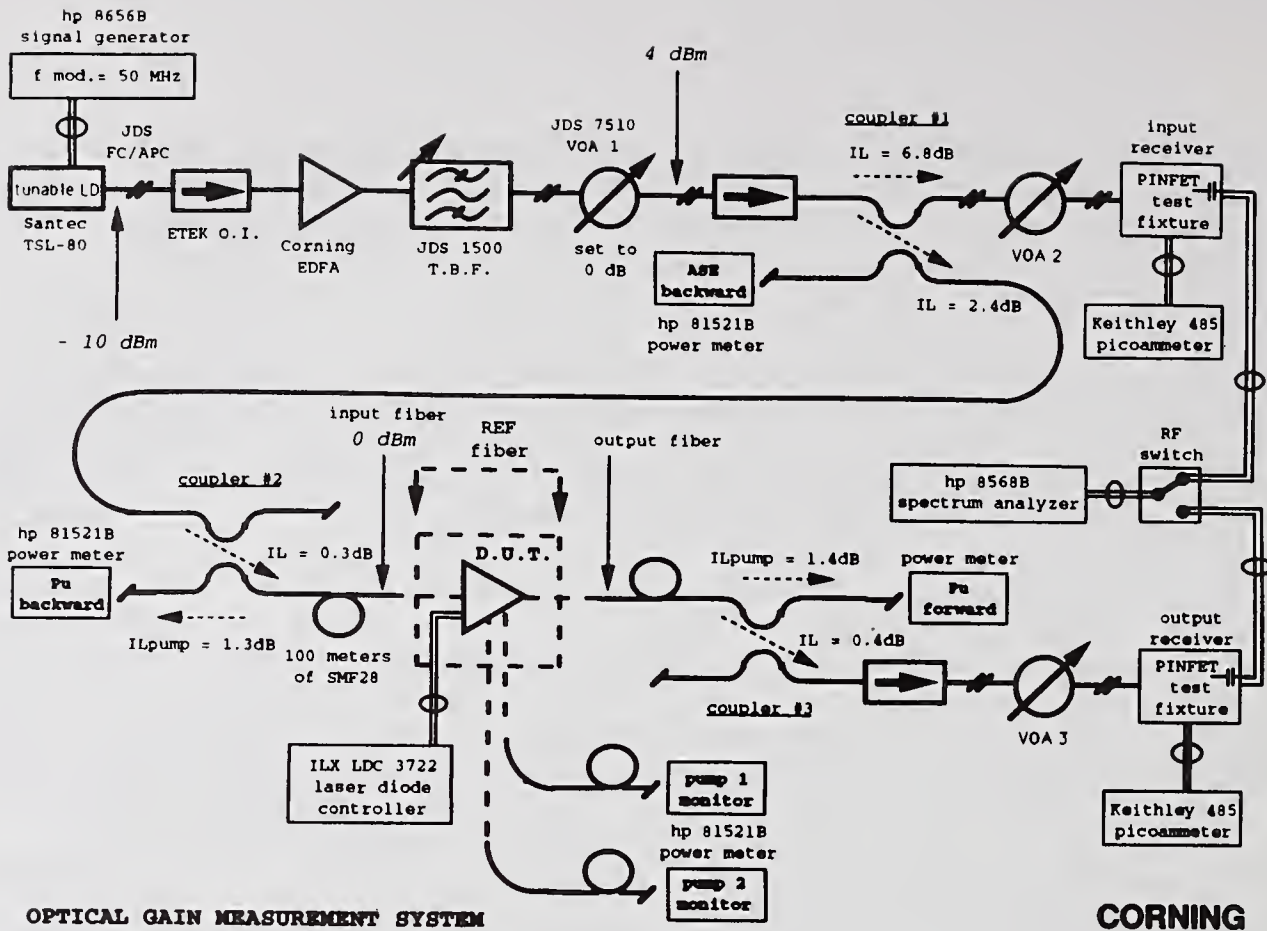
The absolute accuracy of P_o depends on that of the power meter used for calibrating the P_i measurement, stated by the manufacturer as $\pm 3.5\%$ [1].

CONCLUSIONS

We have assembled a convenient and versatile automated system for the measurement of gain, output power, ASE, and unabsorbed pump power for a wide range of input powers and wavelengths. Computer control permits data acquisition and processing that is executed with minimal operator intervention. Repeatability of the small-signal gain and the output-power measurements is about ± 0.4 dB (3 SIGMA).

REFERENCE

1. Hewlett Packard, Operating Manual Optical Head HP81521B Part No. 81522-90011, April 1989.



OPTICAL GAIN MEASUREMENT SYSTEM

CORNING

Fig. 1

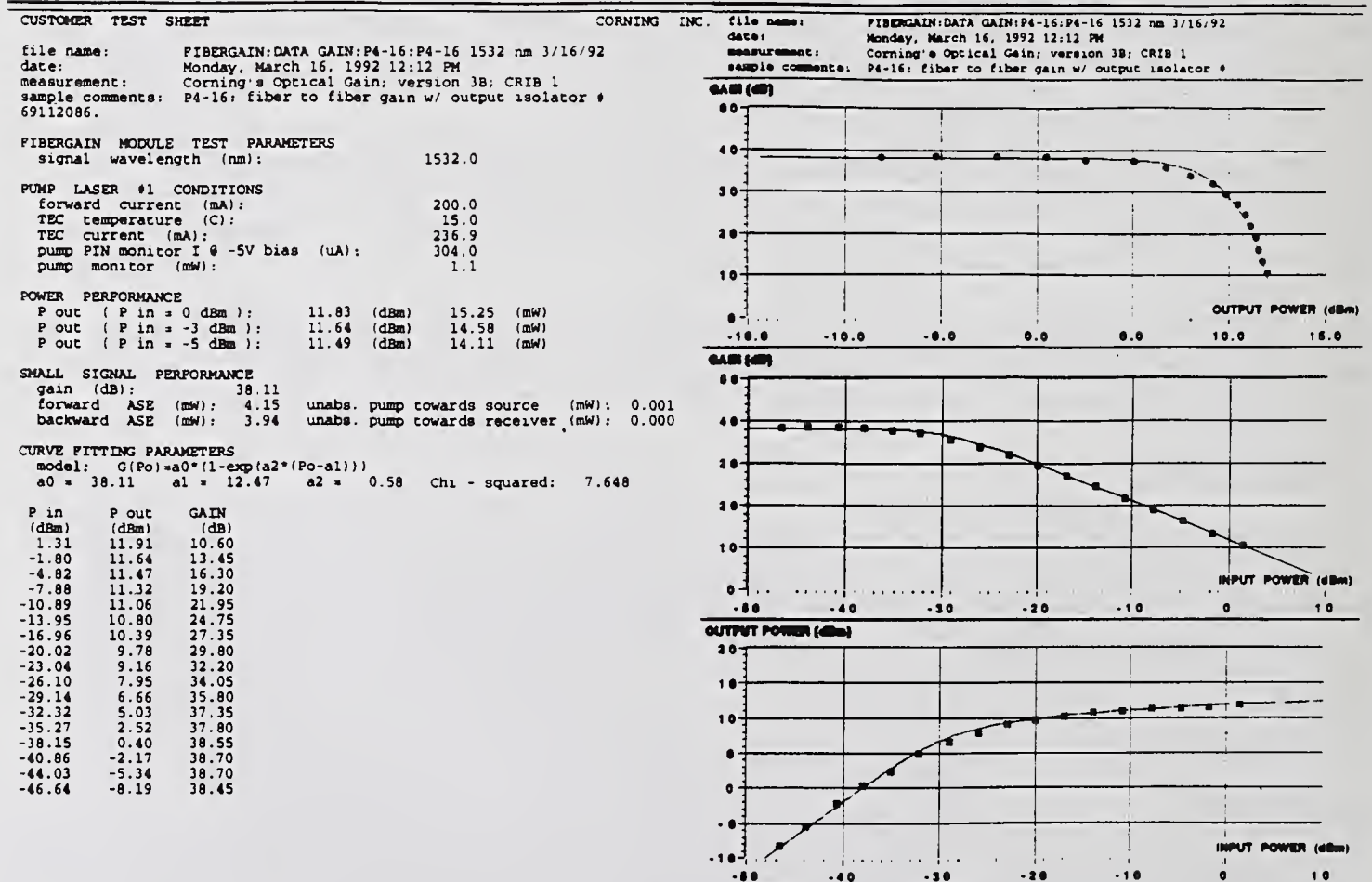


Fig. 2

Cutoff Wavelength Measurement Precision Improvement by Curve Fitting

T.A. Hanson, Corning, Inc.
K.A. Emig, Corning, Inc.
C.S. Brown, AT&T Bell Labs
R.J. Smith, AT&T Network Cable Systems

Abstract

The existence of spurious, transient, long-wavelength transition structure (humps) in transmitted cutoff wavelength measurement curves has been previously documented and well studied over the last few years. This transition structure creates a large increase in the variability of the measurement when using the present test procedure recommendations of national and international standards bodies. A method of fitting the data to a rigorous model, which minimizes the effect of the structure, is presented. Application of the fitting algorithm to two common fiber designs, and to the two most popular measurement methods, shows significant improvement in precision.

Introduction

The theoretical basis for long-wavelength transition structure in the transmitted cutoff wavelength measurement, as well as empirical methods to eliminate the structure, have been previously reported [1] [2] [3]. The general conclusions from these studies are: a) the transition structure results from coating materials which have a different refractive index than the fiber's cladding, b) small levels of microbending, index-matching the cladding, or increased sample length drastically reduces or eliminates the structure, and c) the existence of the structure is more a metrology problem than a functional one since the low levels of bending in practical applications are sufficient to eliminate the structure.

In 1988, Okafor and Peckham [3] presented a model for fitting the transmitted cutoff wavelength curve in the transition region. To accomplish this, a transform was derived which, when applied to the measurement data, forms a straight line function in wavelength:

$$1) \quad \log(\chi)(\lambda - \lambda_c) = Y = 10 \log[-(10/A) \log[(10^{(\alpha/10)} - 1)/\rho]]$$

where α is the measured attenuation
 ρ is found to be equal to 2
 $A = 10 \log[\rho / (10^{0.01} - 1)]$
 $\log(\chi)$ is unknown
and λ_c is the cutoff wavelength

The transform is constructed such that the wavelength at which the line crosses zero is the cutoff wavelength as defined by the 0.1 dB intercept definition [4] [5] [6]. By applying a linear regression to this equation, the slope, $\log(\chi)$, and the intercept, λ_c , can be determined. The recommended least-squares method of performing the regression [3] works well for cutoff wavelength curves which do not exhibit transition structure. However, since the transition structure is always positive in direction, it causes a unidirectional fit error on those cutoff plots exhibiting the structure. To deal with the transition structure, a linear regression which limits the allowable negative errors has been developed.

Algorithm

The basic idea of the algorithm proposed in this paper comes from observation that the transition structure is made up of data points with positive deviation from the ideal. To illustrate this, a 2-meter fiber sample was deployed per TIA FOTP-80, i.e., straight deployment with a single, 140-mm radius turn, and measured for cutoff wavelength. The coating was then removed and the sample remeasured in index-matching oil. The results are shown in Figures 1 and 2, respectively, and demonstrate that the transition structure consists of a positive deviation from the ideal curve causing the cutoff value to err in the direction of longer wavelength.

When the data from the above curves are plotted as $-Y$ vs. λ , after transformation according to Eq. 1, the transition structure causes positive deviations from a straight line. A method of defining this straight-line fit is to minimize the sum of the absolute values of error, subject to a constraint that all errors are positive. This is accomplished through the use of a Simplex Algorithm [7]. A further refinement of the regression is to allow for a small level of negative error equivalent to the magnitude of the electro-optic noise demonstrated in the long-wavelength portion of the curve. Appropriate formulas are applied to determine the negative error constraint. The advantage of this refinement is it minimizes overcorrection of the curve-fit by allowing an appropriate level of negative fit-error.

This model is designed to apply only to the cutoff transition region. Applied to data generated with the bend reference technique, the upper wavelength limit of the transition region is defined as the maximum wavelength at which the attenuation is greater than 0.1 dB, plus 10 nm. The lower wavelength limit is defined as the wavelength where a local maximum, less the next local minimum, is greatest.

For the multimode reference technique, a preceding step is required before the model's upper and lower limits are determined. The data from the long wavelength region beyond the transition region forms a sloped line, sometimes called the backslope. The backslope is fit by starting at the minimum attenuation wavelength and using the next 150 nm of data towards longer wavelengths. Non-negative error regression, followed by adjusting the intercept by the median value of the errors, reduces the effect of humps on the straight-line fit. The difference between the measured data points and a straight line projected from the backslope toward shorter wavelengths is calculated, yielding a data set similar to that obtained using the bend reference technique. The model limits are now determined in the same manner as described above.

Results

The measurements resulting in Figures 1 and 2 were described earlier. Cutoff values calculated from the raw data for the coated fiber and the index-matched fiber were 1200 and 1180 nm, respectively. Application of the curve-fitting algorithm to both data sets result in calculated values of 1178 nm for both measurements. In the case of the index-matched fiber, where little trace of transition structure exists, the curve-fit value is essentially the same as that obtained from the raw data. In the case of the coated fiber exhibiting significant structure, the curve-fit value is equivalent to the value obtained without structure.

Figure 3 shows a comparison of the model value vs. the standard definition on a population of depressed-clad design fibers measured by the bend reference technique. In this case, 104 samples were measured using both calculations. The average difference between the two measurements is only 4 nm. The effect of transition structure on the standard definition of cutoff is to create measurement outliers in the direction of longer wavelength.

Figure 4 shows a repeatability study for matched-clad design fiber using the multimode reference technique. A total of 64 measurements were made on 16 different fibers, and the cutoff values calculated using the standard algorithm and the proposed curve-fit algorithm. Cutoff measurements exhibiting multiple 0.1 dB crossovers were eliminated from this data set. The average difference between the two calculation methods was 3 nm. Pooled standard deviations for the standard calculation and the curve-fit were 6 nm and 2 nm, respectively, indicating a significant improvement in measurement precision.

Conclusions

The results of this work leads us to three basic conclusions. First, the effects of transition structure on the measured cutoff wavelength value can be significantly reduced or eliminated by a combination of the appropriate theoretical model and a fitting algorithm that controls the negative fit-errors. Secondly, the improved precision resulting from the use of the fitting algorithm reduces the potential for specification compliance issues, as well as decreasing the variability in a variety of cutoff-related models. Lastly, a universal method of controlling the effects of humps on the measured cutoff value by alternative deployment configurations have been sought, but no practical configuration has been found. The software solution presented here yields nearly the same value as would be reported if the structure wasn't present, but with much less measurement variability.

References

- [1] "The Anomalous Structure Observed in Single-mode Fiber Cutoff Wavelength Measurements: Theory and Solutions," S.A. Jacobs and D.W. Peckham, Symposium on Optical Fiber Measurements, NIST SP 792, 1990, pp. 49-52.
- [2] "Elimination of the Primary Sources of Measurement Variability in Single-mode Fiber Transmitted Cutoff Wavelength," K.A. Emig, Journal of Lightwave Technology, vol. 17, No. 10, Oct. 1989, pp. 1466-1472.
- [3] "An Accurate Method of Determining Single-mode Fiber Cutoff Wavelength," C.N. Okafor and D.W. Peckham, Symposium on Optical Fiber Measurements, NBS SP 748, 1988, pp. 119-122.
- [4] TIA/EIA (Telecommunications Industry Association / Electronic Industries Association), RS-455-80
- [5] CCITT (International Telegraph and Telephone Consultative Committee), Recommendation G.652.
- [6] IEC (International Electrotechnical Commission), Method IEC 793-1-C7
- [7] Linear and Nonlinear Programming, V.A. Sposito, Iowa State University Press, 1975.

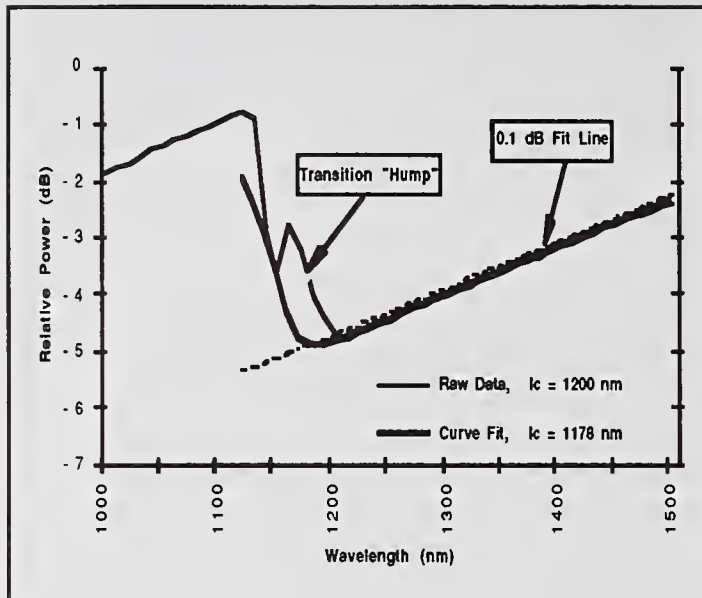


Fig. 1 - Coated Fiber Cutoff Plot

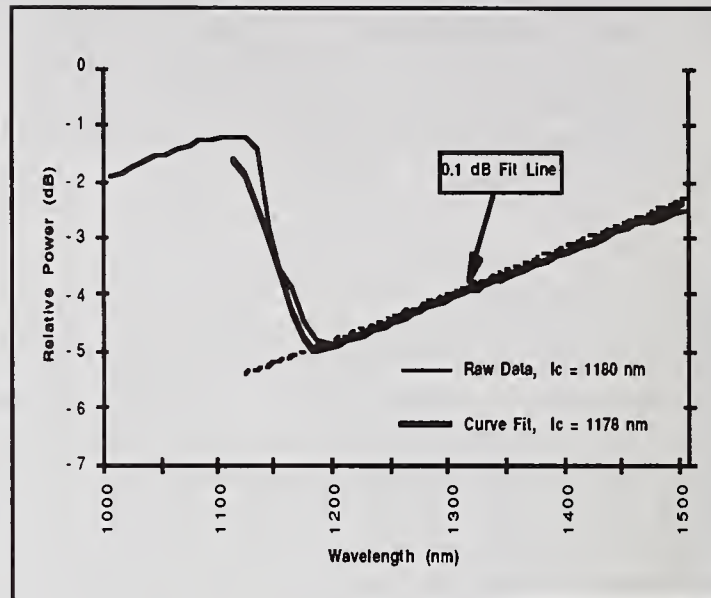


Fig. 2 - Index-matched Cutoff Plot

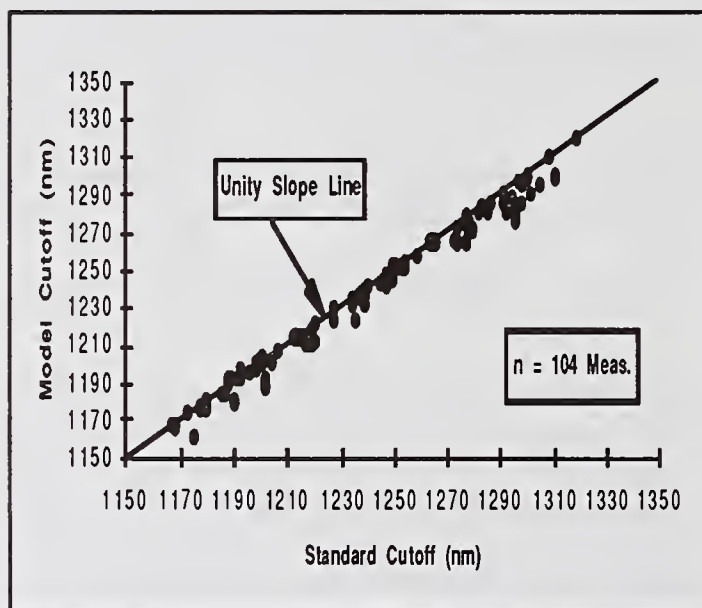


Fig. 3 - Model vs. Standard Cutoff Comparison on Depressed-clad Fiber

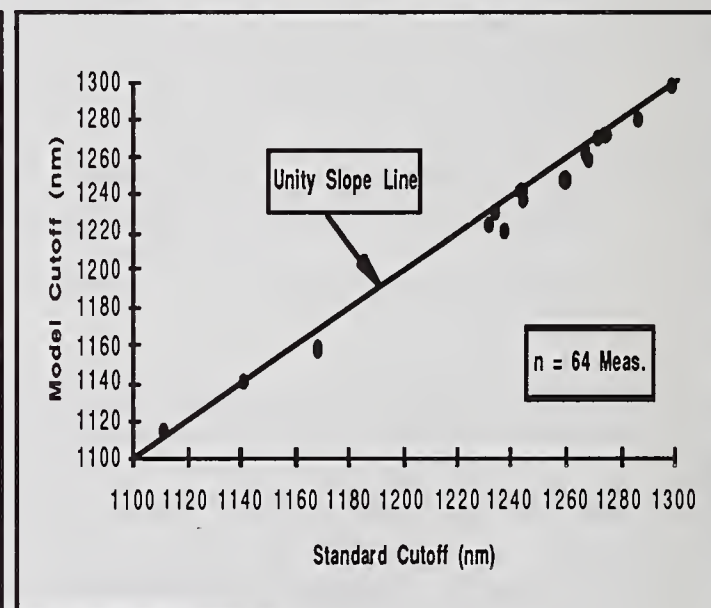


Fig. 4 - Model vs. Standard Cutoff Comparison on Matched-clad Fiber

DETERMINATION OF THE LP₁₁ MODE CUTOFF WAVELENGTH FROM THE MODAL INTERFERENCE PATTERN

K.ABE, Y.LACROIX, Y.CAI AND L.BONNELL
NATIONAL OPTICS INSTITUTE

369 RUE FRANQUET, SAINTE-FOY, QUEBEC, CANADA, G1P 4N8

INTRODUCTION

In order to eliminate the modal interference (MI) between LP₀₁ and LP₁₁ modes in the 1300 nm region [1] and the consequent system noise [2] which could be induced by a short section of fiber (e.g. stub, patchcord), it is desirable to select a fiber whose cutoff wavelength (λ_c) for the LP₁₁ mode is lower than the minimum operational wavelength. However, the rigorous definition and determination of λ_c require an accurate knowledge of the index profile which is not trivial to measure for fiber. Alternatively, attempts to measure the parameter directly have encountered difficulties due to the poorly defined LP₁₁ mode near cutoff, for example, the extreme sensitivity of the power level within the mode to the fiber lay-out condition. For the purpose of specification, the EIA cutoff wavelength ($\lambda_c(\text{EIA})$) is commonly being quoted based on the definition and the test method recommended by the EIA standards committee [3]. However, the relation between $\lambda_c(\text{EIA})$ and the real λ_c has not been established. Furthermore, measurement difficulties are often encountered with matched cladding fibers when the test method is used [4].

Instead of the direct determination of λ_c , references [5,6] suggested the measurement of the equalization wavelength (λ_e) from the MI pattern, where λ_e is the wavelength at which the wavelength derivatives of the propagation constants are equal for LP₀₁ and LP₁₁ modes. Assuming a step index profile, the following relation can be used to determine the cutoff wavelength, $\lambda_c(\text{EQ})$:

$$\lambda_c(\text{EQ})/\lambda_e = V_e/V_c \sim 1.26, \dots\dots\dots (1)$$

where the normalized frequencies $V_c=2.405$ by definition and $V_e\sim 3.03$ for a typical step index "single-mode" fiber.

During the investigations of MI for commercially available matched cladding fibers [1], it was found that equation (1) is not applicable to these fibers due to the deviation of the index profile from a step profile and also that a reasonably accurate λ_c value can be estimated from the MI pattern in the 1300 nm range without relying upon the power level in the LP₁₁ mode.

EXPERIMENTAL RESULTS

The experimental set-up consisted of a white light source, a fiber with a stub spliced in the middle, and a spectrum analyzer. The MI was measured for the stub lengths between 10 mm and 1 m over the wavelength range from 900 to 1550 nm. For long stub lengths, the coating was kept on the stub and the splice sections were immersed in an index-matching oil in order to minimize the cladding modes. For short stub lengths, the coating was stripped and the stub fiber

was immersed in an index-matching oil. An example of MI is shown in Fig.1.

The phase of MI is given by $\phi = \Delta\beta \cdot l$ [6], where $\Delta\beta = \beta_{01} - \beta_{11}$, l is the stub length, and β_{01} and β_{11} are the propagation constants for the LP_{01} and LP_{11} modes, respectively. The oscillation period ($\Delta\lambda$) provides us with the information on the wavelength derivative of $\Delta\beta$:

$$d(\Delta\beta)/d\lambda = 2\pi/\Delta\lambda \cdot l. \quad \dots\dots\dots (2)$$

The oscillation periods and the corresponding wavelengths were measured from the plot and the $-2\pi/\Delta\lambda \cdot l$ values were plotted as a function of the wavelength, as shown in Fig.2. Note that $d(\Delta\beta)/d\lambda$ is negative in the wavelength range. The measurements were repeated several times for different stub lengths and the results were combined to make the plot.

In any text books, theoretical plots of β and its wavelength derivative (or group delay) vs. V can be found for infinite cladding. As pointed out in references [1,7] however, the propagation constant near cutoff indicates a continuity to that of the cladding modes which are sensitively affected by the fiber coating and the lay-out condition. For this reason, we can not expect the abrupt termination of the propagation constant at the cutoff as the theory predicts, unless the cladding mode is totally eliminated without disturbing the LP_{11} mode. In spite of this experimental difficulty, the cutoff wavelength can be estimated with reasonable accuracy from Fig.2. As the wavelength increases, the plot indicates a monotonic downward trend with an increasing slope. The theory predicts that the plot should come to the end at cutoff. However, the effects of the residual cladding modes manifest itself as the irregular continuing points, as demonstrated in the figure. The cutoff wavelength ($\lambda_c(\text{MI})$) was estimated from the transition point. As compared to the long stub measurements, short stub lengths were found to be more convenient for the MI measurements in the wavelength range near and beyond the cutoff, because the S/N ratio could be enhanced due to the higher power level in the LP_{11} mode and the large oscillation period which allowed us to use a large slit width.

For four matched cladding fibers, the $\lambda_c(\text{MI})$ values were determined in this manner. The results are listed in Table 1 (fibers-A, B, C and D) together with other fiber parameters. In the table, the MFDs were measured by using a far-field scanning method. The $\lambda_c(\text{EIA})$ measurements encountered the problem commonly known as "bumps and humps" for all the fiber samples. Therefore, ranges of the estimated cutoff values were given. The λ_c values were measured from the MI pattern in the 1000 nm region using the stub length of 1 m, and the $\lambda_c(\text{EQ})$ values were determined using equation (1). Note that $\lambda_c(\text{MI})$ is consistently larger than $\lambda_c(\text{EQ})$ for all the sample fibers. This discrepancy was suspected as being caused by the index profile which was slightly graded, as shown in Fig.3. The refracted near-field technique was used for this measurement. In order to confirm this interpretation, similar measurements were performed for a depressed cladding fiber made by the MCVD process. The results of the MI measurements are shown in Fig.4 and the index profile in Fig.3. The cutoff parameters for this fiber are listed in Table 1 (fiber-E). With this fiber, a good agreement was found between the λ_c values estimated from the two methods due to the fact that the core-cladding boundary was step-like, a characteristic of fibers made by the MCVD process. However, the appearance of the plot shown in Fig.4 is slightly different from those for matched cladding fibers, e.g. Fig.2. Tentatively, the more straight plot of Fig.4 was interpreted as due to the high index outer cladding. Currently, an attempt is being made to fabricate a fiber with a near perfect step index profile and to compare the theoretically calculated cutoff wavelength with the measurement.

CONCLUSION

For the purpose of selecting a fiber to ensure that the LP₁₁ mode cutoff is below the operational wavelength, the EIA cutoff was found to be unreliable because of the measurement problem associated with the matched cladding fibers and because of the lack of correlation between the real cutoff and this parameter. Alternatively, the cutoff wavelength estimated from the equalization wavelength was also found to be unreliable due to the breakdown of the step index assumption for the fibers: note fiber-D which indicated relatively low $\lambda_c(\text{EQ})$ in spite of the high $\lambda_c(\text{MI})$ and fiber-A with the opposite trend. However, it has been demonstrated that the LP₁₁ cutoff wavelength can be estimated by measuring MI and plotting the $-2\pi/\Delta\lambda \cdot l$ value against λ . Even though the accuracy of the measurement is not great, the test method has the advantages of being experimentally simple and of being independent of the power level in the LP₁₁ mode which is sensitive to the fiber length and its lay-out condition. For a depressed cladding fiber made by the MCVD process, a good agreement between $\lambda_c(\text{EQ})$ and $\lambda_c(\text{MI})$ was demonstrated due to the step-like index profile in the core-cladding boundary.

REFERENCES

- [1] K.Abe, Y.Lacroix, L.Bonnell and Z.Jakubczyk, "Modal interference in a short fiber section: fiber length, splice loss, cutoff, and wavelength dependences", *J. Lightwave Tech.*, Vol.10, No.4, April 1992, pp.401-406.
- [2] D.G.Duff, F.T.Stone and J.Wu, "Measurements of modal noise in single mode lightwave systems", *Optical Fiber Communications Conference, 1985 Technical Digest*, (Optical Society of America, Washington DC), pp.52.
- [3] EIA standard, FOTP-80, "Cutoff wavelength of uncabled single-mode fiber by transmitted power", EIA-455-80, Electronic Industries Association, October 1988.
- [4] S.A.Jacobs and D.W.Peckham, "The anomalous structure observed in single mode fiber cutoff wavelength measurements: theory and solutions", *Technical Digest Symposium on Optical Fiber Measurements*, Boulder, 1990, pp.49-54.
- [5] A.C.Boucouvalas and S.C.Robertson, "Simple technique for measurement of equalization wavelength in single mode optical fibres", *Elec. Lett.*, Vol.23, 1987, pp.215-216.
- [6] J.L.Archambault, R.J.Black, H.Bures, F.Gonthier, S.Lacroix and C.Saravanos, "Fiber core profile characterization by measuring group velocity equalization wavelengths", *IEEE Photonics Tech. Lett.*, Vol.3, 1991, pp.351-353.
- [7] P.J.B.Clarricoats, "Optical fibre waveguides-a review", *Progress in Optics*, (North Holland, 1976), Vol.XIV, pp.329-400.

NOTE for Table 1

"M" and "D" for the cladding design stand for matched and depressed cladding, respectively. "Quoted" means that the values were quoted by the fiber supplier. " $\lambda_c(\text{EIA})$, $\lambda_c(\text{EQ})$, and $\lambda_c(\text{MI})$ " are the cutoff wavelengths determined by the EIA test method, the LP₀₁-LP₁₁ equalization wavelength, and the modal interference pattern in the 1300 nm range, respectively.

Table 1: LIST OF PARAMETERS FOR THE FIBERS

Fiber:	A	B	C	D	E
Cladding design:	M	M	M	M	D
MFD(quoted), μm :	-	8.96	9.44	9.32	
MFD(measured), μm :	9.40	9.32	9.42	9.40	
$\lambda_c(\text{EIA})(\text{quoted})$, nm:	-	1238	1211	1319	
λ_e , nm:	1020	1000	980	985	1150
$\lambda_c(\text{EIA})(\text{measured})$, nm:	1235	1230-60	1225	1310-40	1260
$\lambda_c(\text{EQ})$, nm:	1290	1265	1240	1246	1450
$\lambda_c(\text{MI})$, nm:	1320	1340	1310	1350	1440

Fig.1: Example of MI pattern; fiber-A, $l = 10$ cm.

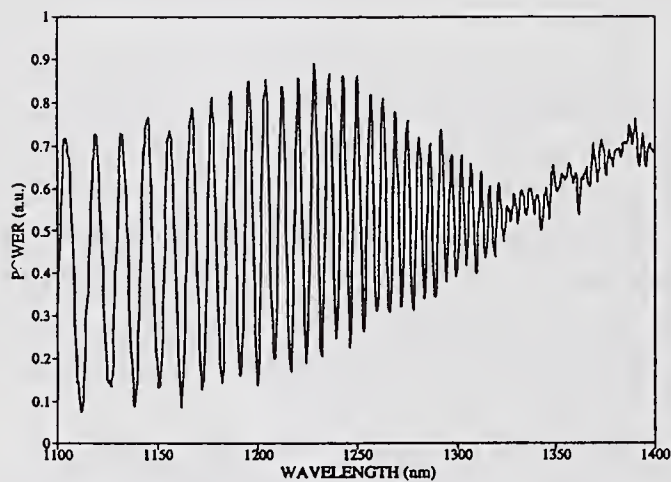


Fig.3: Fiber index profile; solid line; fiber-A, dotted line; fiber-E.

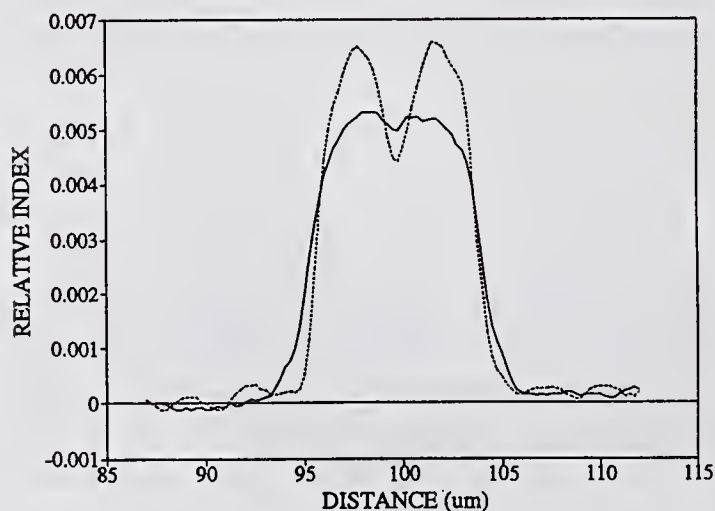


Fig.2: $-2\pi/\Delta\lambda \cdot l$ vs. λ plot; fiber-A, $l = 10$ cm (O), 1.5 cm (●).

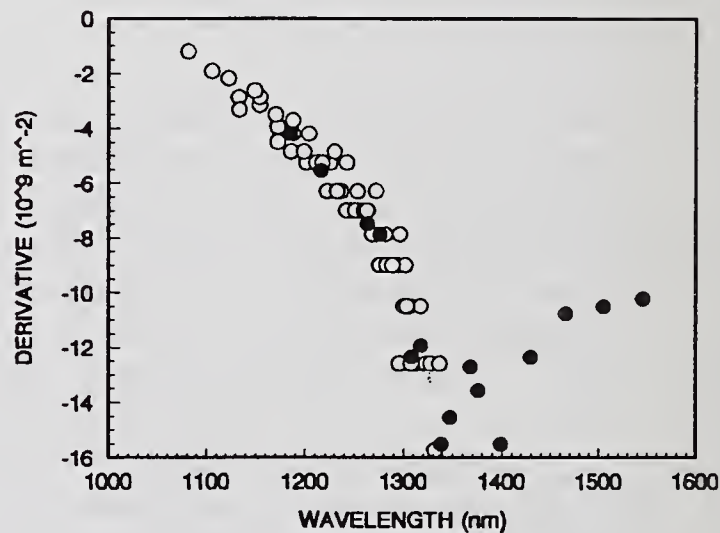
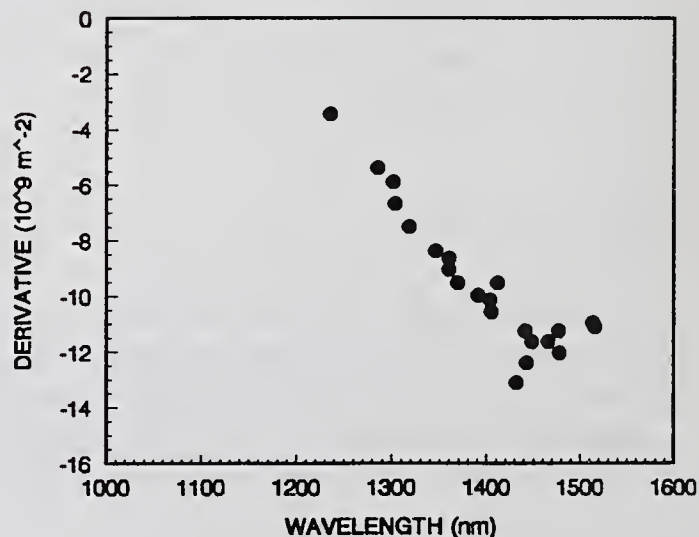


Fig.4: $-2\pi/\Delta\lambda \cdot l$ vs. λ plot; fiber-E, $l = 1.5-3.0$ cm.



**LENGTH AND CURVATURE DEPENDENCE
OF THE EFFECTIVE CUTOFF WAVELENGTH IN SINGLE-MODE FIBERS
MEASURED WITH AN AZIMUTHAL FILTERING TECHNIQUE**

D. PAGNOUX

J.M. BLONDY

Institut de Recherche en Communications Optiques et Microondes
123, avenue A. Thomas - 87 060 Limoges - FRANCE

1. Introduction

The theoretical cutoff wavelength λ_c of a single-mode fiber determines the theoretical frontier between the single-mode and the bimodal propagation regions. On the other hand, the effective cutoff wavelength λ_e is the practical limit of the single-mode operation domain of the fiber. It takes into account the effects of all the perturbation parameters (bendings, microbendings, core diameter fluctuations, etc...). λ_e also strongly depends on the length of the fiber and is always lower than λ_c .

When the operating wavelength λ is lower than λ_e , the first higher-order mode can propagate, inducing modal-noise and pulse dispersion. So, for an installed single-mode fiber, λ_e must be accurately determined. Many techniques have already been proposed, among which : the near-field shape observation method [1], the mode interference technique [2], the field coherence degree measurement [3] and the short pulses propagation experiment [4]. The technique recommended by the International Advisory Committee on Telegraph and Telephone (CCITT) is the bend loss technique [5]. Most of these previous methods need a measurement reference or can work only with specific lengths of fiber.

In this paper, we compare the length and curvature dependence of the effective cutoff wavelength for two different kinds of single-mode fibers. We make use of an azimuthal filtering self-referenced technique, allowing precise measurements of λ_e for lengths of fiber between some centimeters and several kilometers. This technique will be described in the next section, and then the experimental results will be given and analysed.

2. The azimuthal filtering technique [6]

The experimental set-up is shown in figure 1. The light beam from a 0.5 nm spectral width monochromator, chopped at a f_c frequency equal to 70 Hz, is launched into the fiber under test. The output far-field pattern of the fiber is scanned by mean of a rotating "bow-tie" slit, which is rotated at a f_s frequency equal to 4 Hz. The part of the light crossing the slit is focused by a concave mirror on the input face of a large core diameter multimode fiber. The optical power detected by a cooled Ge-detector at the output of the multimode fiber is displayed on a FFT spectrum analyser.

In the single-mode domain, the part of the optical power crossing the rotating slit is constant and a single-line spectrum at the f_c frequency is displayed by the analyser. In the bimodal region, a modulation due to the azimuthal properties of the propagating LP_{11} mode is introduced in the detected power. This modulation creates two lateral lines at the f_1 frequency, with $f_1 = f_c \pm 2f_s$, in the spectrum of the displayed signal.

P_{11} and P_{01} are the optical powers carried by the LP_{11} and the LP_{01} modes, respectively. The ratio P_{11}/P_{01}

expressed in dB is simply related to A_c and A_1 , the amplitudes of the lines at the f_c and f_1 frequencies respectively, by:

$$D(\lambda) = 10\log\left(\frac{P_{11}}{P_{01}}\right) = 10\log\left(\frac{2A_1}{A_c - 2A_1}\right) \quad (1)$$

In the monomode region, $P_{11} = 0$ and then $D(\lambda) = -\infty$. In the bimodal region, in the case of an equal repartition of the power between the LP_{01} mode and the LP_{11} mode, $D(\lambda)$ becomes equal to 0. At last, assuming no fundamental mode in the fiber, $D(\lambda)$ would tend to $+\infty$. $D(\lambda)$ exhibits very large variations when λ crosses λ_e .

In the bend loss technique, λ_e is the wavelength for which the total transmitted power level is 0.1 dB higher than the power transmitted by the pure LP_{01} mode. In our technique, this criterion corresponds to a $D(\lambda_e)$ value equal to -17dB. So, λ_e is simply determined by scanning the wavelength domain until $D(\lambda)$ reaches -17dB.

3. Experimental results

Length dependence of λ_e : The bend loss technique is not adequate in order to study the length dependence of the cut-off wavelength over approximatively 10 m. An alternative method, based on the measurement of the losses of a splice realized between the tested fiber and a monomode fiber with low λ_e , has already been used [7].

With our method, we have measured the length dependence of λ_e for a slightly depressed cladding single-mode fiber (DC fiber), from 1 meter to 2.15 kilometers. The fiber under test was submitted neither to bends with less than 200 mm radii, nor mechanical stress. The experimental results are reported in figure 2.

λ_e is a linear function of the logarithm of the length, for lengths from 1m to 2 km. For a 2 m reference sample, the value of λ_e is 1105 nm. The average shift of λ_e is approximatively 40 nm per decade. Our results are in good agreement with previously published results. Over 2 km, because of the differential attenuation, the optical power guided by the LP_{11} mode becomes negligible compared to the power guided in the LP_{01} mode, and this phenomena induces large imprecisions in the determination of λ_e . Same effects have been mentioned in [7].

A quadruple-clad dispersion flattened fiber (QC fiber) has then been tested. In order to avoid difficulties due to special propagation properties [8], we have first verified that the LP_{11} mode was the first higher-order mode in this fiber. As shown in figure 3, λ_e exhibits a remarkable linear variation versus fiber length, until 25 m. In the first 25m, the down slop of the curve is 10 nm/m. In the following 2.5 km, no significant variation can be noticed. The length dependence observed for this kind of fiber is very different from the typical variations obtained with the DC fiber. The curvature dependence of λ_e for the two different fibers is studied in the next section.

Curvature dependence of λ_e : The measurements have been made on 2m reference samples of the tested fibers. Every bend was one complete loop around a drum with a constant curvature radius. For the DC fiber, experimental results are reported in figure 4. The curve decreases linearly versus $1/R$, where R is the bend radius. λ_e falls down from 1110 nm when $R = 35$ mm to 875 nm when $R = 4$ mm. For values of R larger than 40 mm, no significant variations of λ_e have been observed, as reported in [9].

In the case of the QC fiber, λ_e is directly an increasing linear function of R up to 150 mm, as shown in figure 5. λ_e is very sensitive to large bends radii, which are somewhat slight perturbations of the guide. The losses of the LP₁₁ mode are then largely increased by small perturbations such as these bends, but also microbends or core diameter variations. This can partially explain the strong length dependence of λ_e in the QC fiber, in the very first meters of propagation. More detailed results will be presented at the conference.

4. Conclusion

The proposed azimuthal filtering technique, easy to set-up, allows a very quick and accurate determination of λ_e owing to the very abrupt variations of the parameter $D(\lambda)$ in the cutoff wavelength region. The precision of the measurement is better than 1 nm. It does not require any reference measurement and is also insensitive to source power level and detector sensitivity drifts. The method can be used for any length of fiber as well as for installed fiber links. To our knowledge, the only disadvantage of this technique is that it does not work with some special multi-clad fibers, for which the first higher-order mode is the LP₀₂ mode instead of the LP₁₁ mode.

Length and curvature effects have been measured for DC and QC fibers. Particularly in the QC fiber, the value of λ_e measured on a short reference sample is largely higher than the value measured for an operating link, due to the rapid decrease of λ_e with length and curvature. When designing the fiber, this behaviour must be taken into account in order to reduce the losses of the LP₀₁ mode by keeping the practical value of λ_e sufficiently close to the operating wavelength.

5. Acknowledgements

The authors are grateful to Pr. P.H. FACQ and M. CLAPEAU for their major contribution in the conceiving of the proposed technique, and for helpful discussions.

6. References

- [1] Y. MURAKAMI, K. KAWANA and H. TSUCHIYA : "Cutoff wavelength measurements for single-mode optical fibers", *Appl. Opt.*, 1979, **18**, pp. 1101-1105.
- [2] E. BRINKMEYER and S. HECKMANN : "Cutoff wavelength determination in single-mode fibers by mode interference", *Opt. Lett.*, 1984, **9**, pp. 28-30.
- [3] P. SPANO, G. DE MARCHIS and G. GROSSO : "Coherence properties and cutoff wavelength determination in dielectric wave-guides", *Appl. Opt.*, 1983, **22**, pp. 1915-1917.
- [4] Y. KATO, K. KITAYAMA, S. SEIKAI and N. UCHIDA : "Effective cutoff wavelength of the LP₁₁ mode in single mode fiber cables", *IEEE J, quantum Electron.*, 1981, QE-17, pp. 35-38.
- [5] Y. KATSUYAMA, M. TOKUDA, N. UCHIDA and M. NAKAHARA : "New method for measuring V-value of a single-mode optical fibre", *Electron. Lett.*, 1976, **12**, pp. 669-670.
- [6] J.M. BLONDY, A.M. BLANC, M. CLAPEAU, and P. FACQ : "Azimuthal filtering technique for effective LP₁₁ cutoff wavelength measurement in optical fibres", *Electron. Lett.*, 1987, **23**, n°10, pp. 522-523.
- [7] W.T. ANDERSON and T.A. LENAHAN : "Length dependence of the effective cutoff wavelength in single-mode fibers", *Journ. of Ligh. Techn.*, 1984, **2**, n°3, pp 238-242
- [8] P.L. FRANCOIS, J.F. BAYON, F. ALARD : "Design of monomode quadruple-clad fibres", *Electron. Lett.*, 1984, **20**, n°17, pp 688-689
- [9] V. SHAH : "Curvature dependence of the effective cutoff wavelength in single-mode fibers", *Journ. of Ligh. Techn.*, 1987, **5**, n°1, pp 35-43

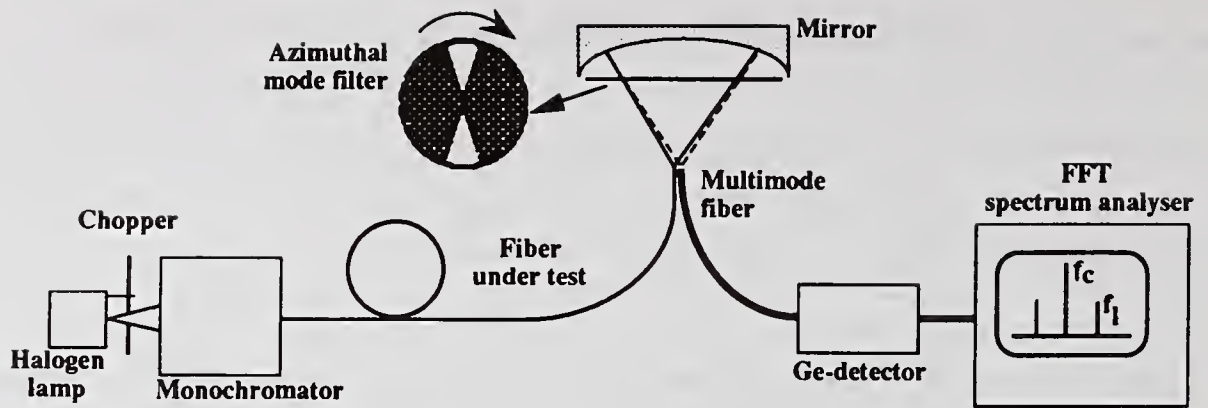


figure 1 : experimental set-up

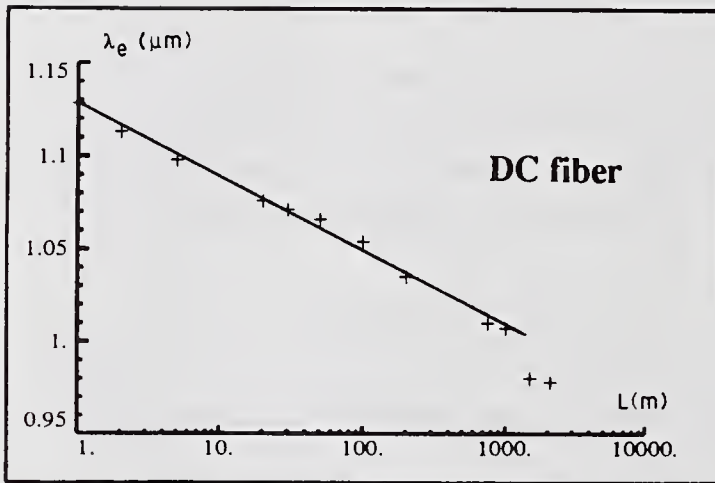


figure 2 : length dependence of the effective cutoff wavelength of a depressed clad single-mode fiber.

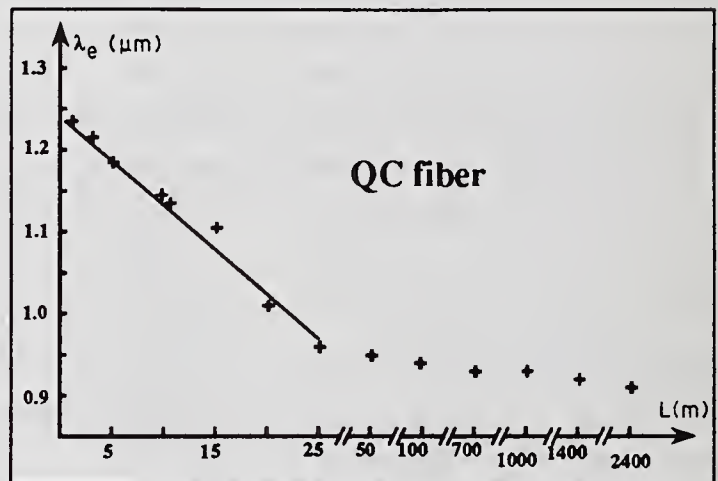


figure 3 : length dependence of the effective cutoff wavelength of a quadruple clad single-mode fiber.

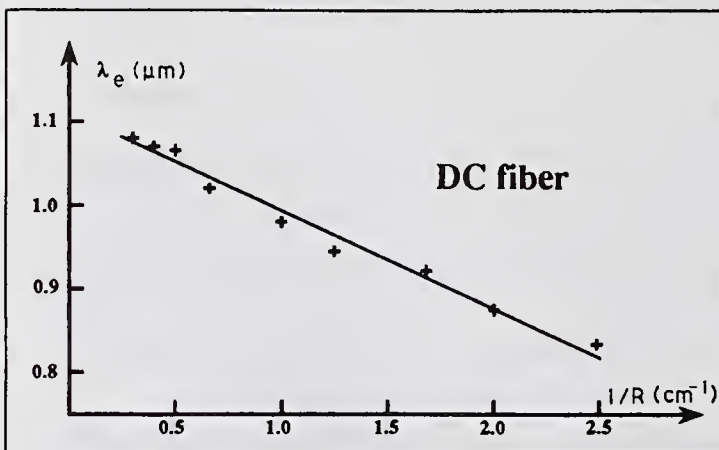


figure 4 : curvature dependence of the effective cutoff wavelength of a depressed clad single-mode fiber.

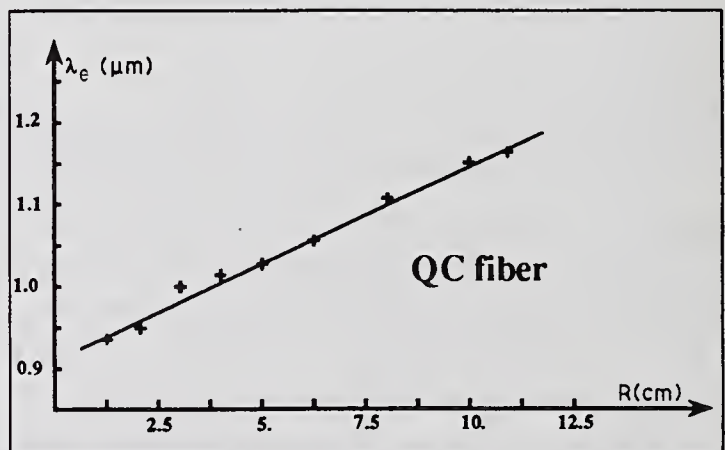


figure 5 : curvature dependence of the effective cutoff wavelength of a quadruple clad single-mode fiber.

Mode Field Diameter and Cutoff Wavelength Profile Measurement using Dual Wavelength OTDR

by James Warder and Costas Saravanos
Northern Telecom Canada Limited
Optical Cable Division
Saskatoon, Saskatchewan, Canada

Introduction

Mode field diameter and cutoff wavelength are two very important parameters in the characterization of single mode optical fibers. Currently, single mode optical fibers are characterized for mode field diameter of the fundamental (LP_{01}) mode and cutoff wavelength of the LP_{11} mode using destructive test methods in which 2 meter long fiber samples are measured from each fiber end.

The most widely used techniques for measuring mode field diameter are described in FOTP-164 (Single mode fiber, measurement of mode field diameter by far field scanning) and FOTP-167 (Mode field diameter measurement, variable aperture method in the far field). The fiber cutoff wavelength is measured according to FOTP-80 (Cutoff wavelength of uncabled single mode fiber by transmitted power). Unless a fiber is cut into many 2 meter sample lengths (a completely destructive approach), these methods yield values of mode field diameter and cutoff wavelength for the fiber ends only.

The test method presented in this paper demonstrates an approach to characterizing the absolute mode field diameter and cutoff wavelength in a single mode fiber along its entire length using a switchable, dual wavelength OTDR, with accuracies of $\pm 0.3\mu\text{m}$ and $\pm 20\text{nm}$ respectively.

The main advantages of this method are:

- non-destructive in nature
- provides measurements of mode field diameter and cutoff wavelength along the entire fiber length
- determines several parameters from the same data set, reducing the time required for fiber characterization

Principles of operation

It has been shown [1] that OTDR fiber signatures, acquired using a two direction measurement method, are separated into two constituent components, representing fiber loss and fiber imperfection. It has been further determined [2] that the fiber imperfection component, $I(\lambda)$, is related to the mode field diameter fluctuations by :

$$I(\lambda, z) = 20 \log_{10} \left(\frac{W(\lambda, z_r)}{W(\lambda, z)} \right) \quad (1)$$

The test method presented here, based on an empirical equation developed by Marcuse [3], relates the

fiber cutoff wavelength, λ_{cf} , and the ratio of mode field diameters, $W(\lambda_1)$ and $W(\lambda_2)$, measured at two distinct wavelengths, λ_1 and λ_2 , [4] :

$$R = \frac{W(\lambda_1)}{W(\lambda_2)} = \frac{0.65 + 0.434 \left(\frac{\lambda_1}{\lambda_{cf}} \right)^{(3/2)} + 0.0149 \left(\frac{\lambda_1}{\lambda_{cf}} \right)^6}{0.65 + 0.434 \left(\frac{\lambda_2}{\lambda_{cf}} \right)^{(3/2)} + 0.0149 \left(\frac{\lambda_2}{\lambda_{cf}} \right)^6} \quad (2)$$

Given the ratio of mode field diameter profiles (at two distinct wavelengths) the cutoff wavelength profile is generated. A combination of the above methods determines absolutely the profiles of mode field diameter and cutoff wavelength, along the entire fiber length, if $W(\lambda, z_r)$ is known. But because the two-direction OTDR technique provides data for the test fiber only, these profiles are relative measurements, not absolute values. To make absolute measurements of the mode field diameter and cutoff wavelength profiles an appropriate reference must be provided to determine $W(\lambda, z_r)$.

Experimental

The test method presented here provides this reference with the test setup illustrated in figure 1. In this setup the input port of a 1x2 optical switch is spliced to the dual wavelength OTDR input, while the output ports are connected to two 1.5 km long alignment fibers. When the OTDR signature is measured from both directions, each single-ended trace contains data from the alignment fiber, the alignment points, and the fiber under test. By combining the two OTDR signatures, the loss and imperfection components for the alignment fibers, alignment points and test fiber are separated. With this information we reference the imperfection profiles to a known value, that is, one of the two alignment fibers. These fibers now provide the reference from which the absolute values of mode field diameter and fiber cutoff wavelength are determined.

The test equipment used for this work included a single mode 1310/1550nm dual wavelength OTDR, a 1x2 optical switch and the two 1500 meter long alignment fibers. The OTDR is connected to a computer for data acquisition and analysis. The cutoff wavelength and mode field diameter of the alignment fibers are measured using the methods described in FOTP-80 and FOTP-167.

During data analysis it is important to be able to identify the fiber end point within the data field. This is achieved by using a highly reflective optical switch, positioned within the OTDR "dead zone" to prevent any forward reflections from appearing within the fiber span.

The ends of the test fiber are aligned to fibers A and B using an X-Y-Z positioner and index matching oil. The OTDR then acquires the fiber signatures from each direction with the aid of the optical switch. (figure 2a and 2b). Subsequently, they are analyzed for fiber loss, mode field diameter (figure 2c and 2d) and cutoff wavelength profiles (figure 2e).

To verify this technique several fiber types were analyzed, with the results tabulated in Tables 1 and 2. As can be seen, the accuracy and repeatability of this technique agrees with established methods to within $\pm 0.3\mu\text{m}$ for mode field diameter and $\pm 20\text{nm}$ for cutoff wavelength.

Conclusion

The technique outlined here provides an alternate test method for the absolute measurement of mode field diameter and cutoff wavelength profiles in single mode fibers with accuracies of $\pm 0.3\mu\text{m}$ and $\pm 20\text{nm}$ respectively.

The simplicity and relative speed of this technique, coupled with the ability to measure loss, discontinuity, mode field diameter, and cutoff wavelength with one procedure, makes this method a powerful tool for both process development and production monitoring.

Acknowledgements

The assistance received from Ming-jun Li and Ken Kowaliuk in the preparation of this paper is greatly appreciated.

References

- [1] P. Divita, V. Rossi; Backscattering Measurements in Optical Fibers: Separation of Power Decay From Imperfection Contributions, Electronic Letters 15, P.467, (1979).
- [2] M.S. O'Sullivan, R.S. Lowe; Interpretation of SM Fiber OTDR Signatures, Proceedings SPIE '86 Optical Testing and Metrology (1986).
- [3] D. Marcuse; Loss Analysis of Single Mode Fiber Splices, Bell System Technical Journal, May-June (1977).
- [4] K.W. Kowaliuk, J. Ferner; A Technique to Estimate the Cutoff Wavelength Profile in Single Mode Fibers Using a Switchable Dual Wavelength OTDR, Proceedings NIST '88 Symposium on Optical Fiber Measurements (1988).

Table 1 - Comparison of FOTP and OTDR Test Methods

Fiber Type	OTDR Cutoff	FOTP-80 Cutoff	OTDR MFD	FOTP-167 MFD
Fiber A	1288nm	1297nm	8.98 μm	8.90 μm
Fiber B	1260nm	1250nm	8.88 μm	8.69 μm
Fiber C	1222nm	1216nm	9.10 μm	9.11 μm

Table 2 - OTDR Test Method Accuracy / Repeatability

	Accuracy (3σ)	Repeatability (3σ)
MFD (1310nm)	< 0.3 μm	< 0.1 μm
Cutoff Wavelength	< 20 nm	< 10 nm

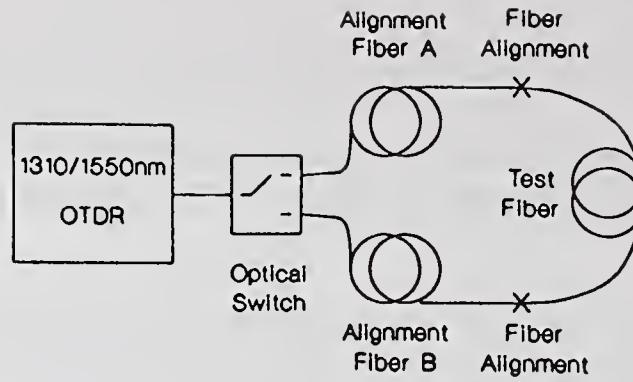


figure 1 - OTDR Test Method Setup

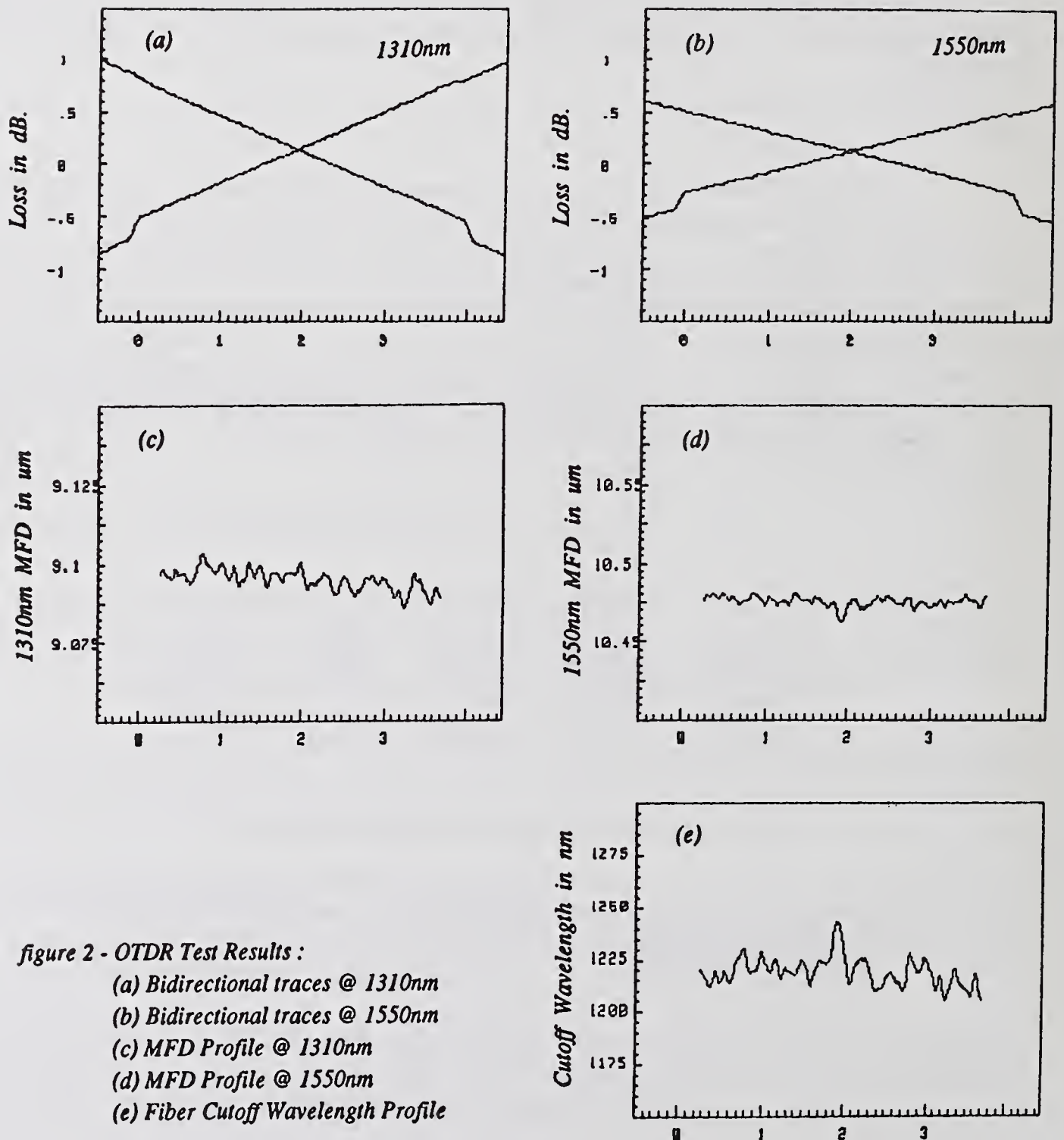


figure 2 - OTDR Test Results :
 (a) Bidirectional traces @ 1310nm
 (b) Bidirectional traces @ 1550nm
 (c) MFD Profile @ 1310nm
 (d) MFD Profile @ 1550nm
 (e) Fiber Cutoff Wavelength Profile

Far Field MFD measurements from a reduced far field pattern

A. Chiantore, F. Cocchini, D. Cuomo, G. Ferri

F.O.S. S.p.A., Battipaglia (SA), ITALY

1. Introduction

Far field technique, for Mode Field Diameter (MFD) measurements, consists in measuring the far field pattern of a fibre, i.e. measuring the radiated power from a fibre on a given (symmetric) angular range at a given distance from the output end of the fibre. From the wave propagation theory, the far field (Fraunhofer) zone is any distance greater than S^2/λ , where λ is the operating wavelength, and S is any dimension representative of the radiating object; for optical fibres $\lambda \cong 1300$ nm while S (MFD) $\cong 10$ μm , so that a distance x is in the far field zone if:

$$x \gg \frac{S^2}{\lambda} \approx 76 \mu\text{m} = 0.076 \text{ mm}$$

To fulfil this prescription, one usually choose $x \approx 1$ cm (i.e. $x \sim 100 S^2/\lambda$), not exceeding this limit in order to balance the far field request with the limited amount of power available from solid states light sources.

The receiver, at the distance x from the output end of the fibre, is capable to rotate on an angular range the amplitude of which is a function of the MFD (i.e. of the refractive index profile) of the fibre: the lower the (near field) MFD of the fibre, the greater the angular range. For instance, to reconstruct the MFD of a standard step index fibre for telecommunication an angular range of at least $\pm 22^\circ$ is necessary; moreover, this range must be spanned (in order to obtain the required accuracy) with a step of 0.5 degrees: the obtained power data (F) can be consequently used as input for the so called Petermann II definition of MFD:

$$w = \frac{1}{\pi} \left[2 \frac{\int_0^\infty q^3 F^2(q) dq}{\int_0^\infty q F^2(q) dq} \right]^{-1/2} \quad q = \frac{1}{\lambda} \sin \theta$$

The aforementioned procedure, even though accurate and easy to follow, is very expensive in terms of time, requiring the acquisition of typically 90 data per measure. This main problem could be avoided reducing the number of necessary data, i.e. trying to reconstruct the MFD from a reduced set of experimental points. The set can be identified, when the pattern to be reconstructed is very regular, following a method [1] based on a model suggested by T. Hanson for spectral attenuation modeling [2].

This paper describes the results of a study devoted to the determination of such a reduced set of data.

2. Theoretical background

Given " m " far field pattern corresponding to " m " different fibres, let a_{ij} be the data read by the receiver at the angle " i "

for the j -th fibre: for instance, $a_{(-22),1}$ is the power at -22° for the 1-st fibre. Our task is to reconstruct the whole data set a_{ij} ($j = 1$ to m , $i = -22$ to $+22$) represented by a matrix A with dimension $m \times n$ (n being the number of sampling angles for the far field pattern), through a matrix B containing the reduced set of data for the same m fibres (so that its dimension is $m \times p$, with $p \ll n$) and an unknown matrix S , the dimension of which is of course $p \times n$. In formulae:

$$A = B S$$

so that S is derived in the least squares sense as:

$$S = (B^T B)^{-1} B^T A$$

B^T being the transpose of B . Depending on the statistical significance of the matrix A from which S is obtained, the same matrix S can be used to derive the far field pattern of any other fibre, just measuring the far field in the reduced number of points " p ". The accuracy of this procedure has been inferred:

- a) a priori, choosing a data set (matrix A) the distribution of which closely resembles the distribution of the whole population;
- b) a posteriori, optimizing the prediction of the MFD's: using a linear regression technique to obtain the elements of S , the average error (measured values - simulated values) in the prediction of the MFD by definition tends to zero, so that a more appropriate parameter to be minimized is the standard deviation (σ) of those errors.

As mentioned, the s_{ij} (elements of S) were determined applying a standard linear regression technique on 50 known (measured) complete far field patterns of as many fibres. However, the identification of the s_{ij} cannot prescind from the determination of the proper number of elements of B (b_{ij}), i.e. one has to find how many and which far field data have to be in any case measured. The criterium used was, first to fix only one angle (and the symmetric one with respect to the fibre axis) and minimize σ as a function of its position; then, once the position of the first angle has been found, to look for the position of the second angle and so on, until σ reaches a given value.

3. Experimental set-up and results

In order to determine the a_{ij} 's a ("home-made") direct far field bench was used, with a dynamic range of about -60 dB, measuring 50 step index single mode OVD fibres (SM-R, with MFD's ranging between 9.0 and 9.6 μm @1300 nm) and 50 segmented core dispersion shifted OVD fibres (SM-DS, with MFD's ranging between 7.6 and 8.4 μm @1540 nm): the close similarity among the far field patterns is clearly shown in figg. 1 (SM-R) and 2 (SM-DS), also justifying the use of the method previously described.

The first step consisted in assuming that the data necessary to correctly reconstruct the MFD can be reduced to only one angle, and in determining its value: in figg. 3a, 4a, 5a the standard

deviation of the errors as a function of the angle value is given, showing that a minimum is obtained for an angle equal to $\pm 8^\circ$ for SM-R fibres (MFD @1301, fig. 3a and @1540, fig.4a), and to $\pm 14^\circ$ for SM-DS fibres (MFD @1540, fig.5a). Once the first angle was so identified, next step was to find the position of the second angle, and so on: finally, we found that using four angles (8 measured points) the standard deviation of the errors was reduced down to (or less than) 1%. This is clearly shown by figg. 3, 4, 5, which should have to be used as follows:

- 1) curves a) show the trend of σ when the MFD is reconstructed from one angle only;
- 2) once the first angle position has been fixed (e.g., for the MFD @1301 nm of a SM-R fibre, it's $\pm 8^\circ$), looking at curves b) the position of the second angle is found (in the example above, $\pm 0.5^\circ$);
- 3) at this stage, an accuracy of about 1.5 % has been achieved: depending on the target, one can continue with the same procedure, or stop; in our simulation, four angles (8 measurements) are necessary in order to obtain an accuracy of about 1%. It is clearly seen from the figures that the minima are more evident for the first angles (curves a, b, c): increasing the number of angles (curves "d" and possibly other curves for 5, 6 or more angles) one tends to the intrinsic uncertainty in MFD evaluation, so the curves become more flat; however, in these situations the minima are readily found from the numerical data, not from the graphs. Even better results than 1% of uncertainty can be achieved with five or more angles.

4. Conclusions

In this paper, a method has been suggested to obtain the MFD of SM-R and SM-DS fibres starting from a reduced set of measured far field power values: the reason for such a kind of study was in the attempt to reduce the (very long) time necessary for a direct far field measurement, which is the most accurate and reliable, without losing too much in terms of precision.

We have shown that, knowing a certain number of complete far field patterns representative of a given category of fibres, it is possible to reproduce the MFD with an accuracy of less than 1% reducing the number of necessary points from about 90 to 8. Even better accuracies can be obtained with 10, 12 or more data acquisition points: however, we point out that a precision of 1% could be accepted, if compared with the tolerance (10%) suggested by CCITT [3] on the nominal value of SM fibres.

5. References

- [1] M. Ohashi *et al.*: "Loss Model for singlemode fibres", *Elect. Lett.* 28, 6, 1992.
- [2] T.A. Hanson: "Spectral attenuation modeling with matrix methods", *OFMC Proc.*, York (UK), 1991.
- [3] CCITT Rec. G.652, Blue Book, Melbourne 1988

Acknowledgements

We gratefully acknowledge FOS General Management for the kind permission to publish this paper.

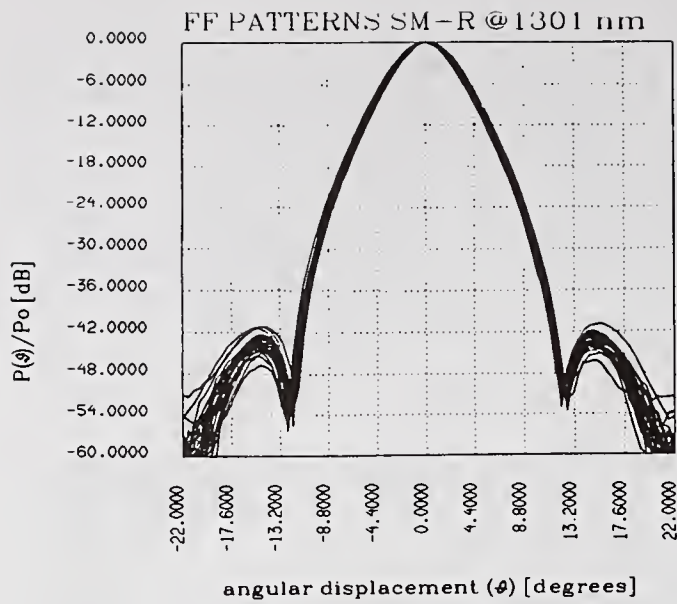


Fig. 1

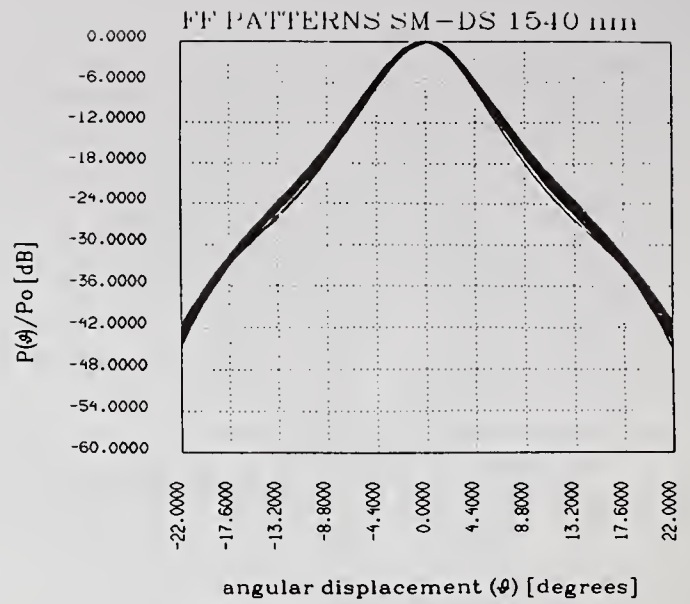


Fig. 2

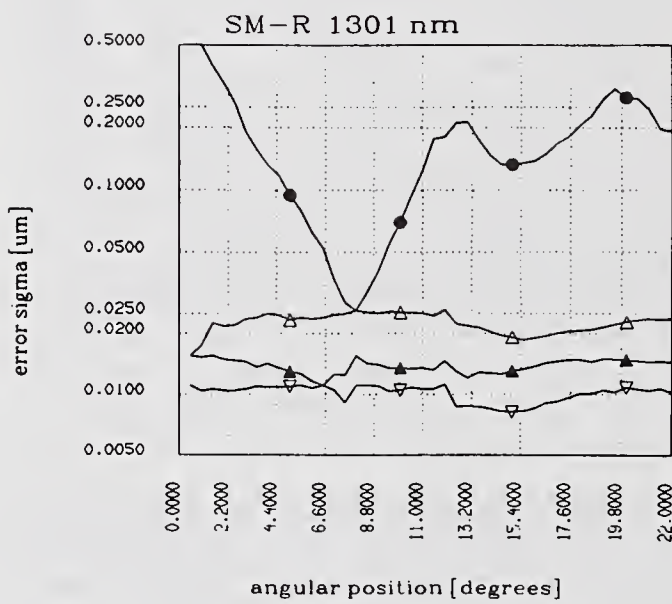


Fig. 3

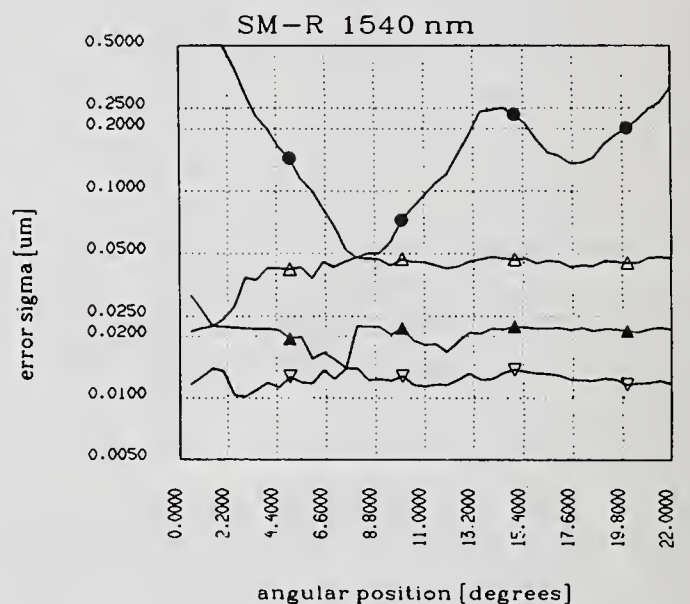


Fig. 4

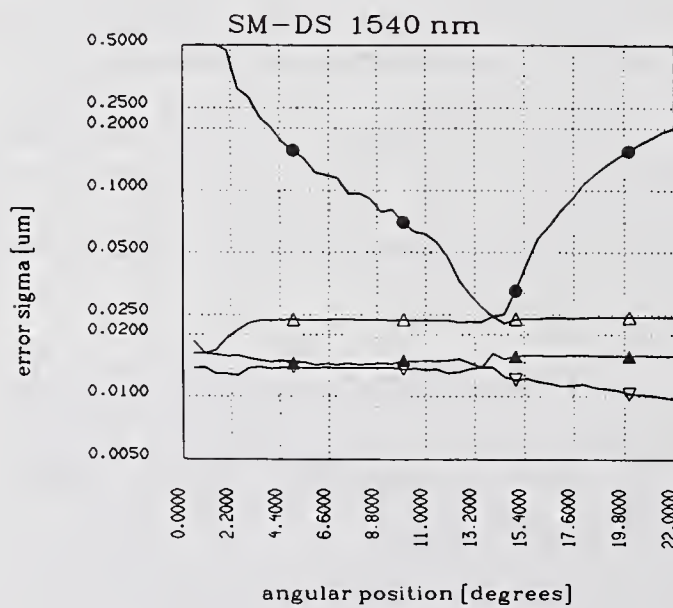


Fig. 5

Legenda for Figg. 3, 4, 5
 error σ for MFD reconstruction from:
 curve a - (●) - one angle;
 curve b - (Δ) - two angles;
 curve c - (▲) - three angles;
 curve d - (▽) - four angles.

AUTHOR INDEX

Abe, K.	221	Hale, P.D.	51,55	Potenza, M.	171,205
Antos, J.	89	Hall, D.	195	Poyntz-Wright, L.J.	137
Arai, S.	67	Hallam, A.G.	59	Pozzi, F.	95
Artiglia, M.	171,179,205	Hanson, T.A.	217	Pregibon, D.	15
Atkins, G.R.	81	Hattori, Y.	63	Puleo, M.	115,123,205
Atkins, R.M.	103	Heffner, B.	131		
		Hickernell, R.K.	201	Quoi, K.W.	71
Baines, J.	45	Horiguchi, M.	201		
Baney, D.M.	163	Horiguchi, T.	11	Raine, K.	45
Barlow, A.J.	107	Hui, R.	123	Reed, W.A.	71
Benson, J.M.	85			Robert, P.	151
Berardinelli, J.D.	7	Ingles, A.L.	15,127	Rossaro, A.	171
Blondy, J.M.	225	Inoue, A.	63		
Bonanni, P.	205	Ishida, Y.	67	Saravanos, C.	37,229
Bonnell, L.	221			Sato, T.	11
Bottanelli, M.	119	James, D.A., Jr.	15	Satoh, H.	41
Brown, C.S.	217	Judy, A.F.	19	Sceats, M.G.	81
				Schmitzer, H.	155
Cai, Y.	221	Kapron, F.P.	7,29	Shaw, Julia H.	59
Caponio, N.	123	Kashiwada, T.	209	Shigematsu, M.	209
Cavaciuti, A.	171,205	Kiiveri, P.	183	Shimizu, M.	201
Chiantore, A.	233	Kilmer, J.P.	33	Shinoki, S.	63
Chojetzki, C.	155	Kim, K.S.	71	Sikora, E.S.R.	77
Chou, H.	167	Kobayashi, Y.	63	Smith, R.J.	217
Chunnillall, C.J.	85	Kohmura, Y.	67	Sordo, B.	205
Clayton, J.B.	15	Kosiorska, H.	23	Sorin, W.V.	163
Cocchini, F.	233	Koyamada, Y.	11	Stokes, L.F.	141
Cole, D.R.	213	Kume, N.	41	Stolen, R.	71
Cuomo, D.	233			Suchoski, P.	111
		Lacroix, Y.	221		
DeBernardi, C.	95	Lewis, N.	1	Takada, K.	159,201
DiVita, P.	171			Thévenaz, L.	151
Drapela, T.J.	187,191	Maeda, J.	145		
Duca, L.	119	Matsuoka, R.	41	Vance, M.E.	213
Dultz, W.	155	Mechels, S.E.	55	Varachi, J.P.	33
		Morasca, S.	95	Vezzoni, E.	115,123
Emig, K.A.	217			Vobian, J.	155
		Namihira, Y.	145	Voots, T.	107
Ferri, G.	233	Niklès, M.	151		
Ficke, W.H.	107	Nishimura, M.	209	Warder, J.	229
Franzen, D.L.	51,187,191			Wong, B.	23
		Pagnoux, D.	225	Wright, J.V.	77
Gambini, P.	115,123	Parker, A.D.	99		
Gardner, W.B.	99	Pasturczyk, Z.	37	Yamada, M.	201
Gilbert, S.L.	191	Petersen, J.C.	85	Young, M.	55,187
Gu, Y.	137	Pitassi, S.	119	Yuce, H.H.	29,33
		Poole, S.B.	81		

BL-114A
(5-90)

U.S. DEPARTMENT OF COMMERCE
NATIONAL INSTITUTE OF STANDARDS AND TECHNOLOGY

BIBLIOGRAPHIC DATA SHEET

1. PUBLICATION OR REPORT NUMBER
NIST SP 839

2. PERFORMING ORGANIZATION REPORT NUMBER
B92-0221

3. PUBLICATION DATE
September 1992

4. TITLE AND SUBTITLE

Technical Digest -- Symposium on Optical Fiber Measurements, 1992

5. AUTHOR(S)

Gordon W. Day and Douglas L. Franzen

6. PERFORMING ORGANIZATION (IF JOINT OR OTHER THAN NIST, SEE INSTRUCTIONS)

U.S. DEPARTMENT OF COMMERCE
NATIONAL INSTITUTE OF STANDARDS AND TECHNOLOGY
BOULDER, COLORADO 80303-3328

7. CONTRACT/GRANT NUMBER

8. TYPE OF REPORT AND PERIOD COVERED
Final

9. SPONSORING ORGANIZATION NAME AND COMPLETE ADDRESS (STREET, CITY, STATE, ZIP)

Sponsored by the National Institute of Standards and Technology, in cooperation with the IEEE Laser and Electro-Optics Society and the Optical Society of America.

10. SUPPLEMENTARY NOTES

Previous symposia were held in 1980, 1982, 1984, 1986, 1988 and 1990. Technical Digests of those were published as NBS Special Publications 597, 641, 683, 720, 748 and 792.

11. ABSTRACT (A 200-WORD OR LESS FACTUAL SUMMARY OF MOST SIGNIFICANT INFORMATION. IF DOCUMENT INCLUDES A SIGNIFICANT BIBLIOGRAPHY OR LITERATURE SURVEY, MENTION IT HERE.)

This digest contains summaries of 54 papers presented at the Symposium on Optical Fiber Measurements, held September 15-17, 1992, at the National Institute of Standards and Technology, Boulder, Colorado.

12. KEY WORDS (6 TO 12 ENTRIES; ALPHABETICAL ORDER; CAPITALIZE ONLY PROPER NAMES; AND SEPARATE KEY WORDS BY SEMICOLONS)

fiber optics; instrumentation; measurements; optical fiber; reviews

13. AVAILABILITY

- | | |
|-------------------------------------|--|
| <input checked="" type="checkbox"/> | UNLIMITED |
| <input type="checkbox"/> | FOR OFFICIAL DISTRIBUTION. DO NOT RELEASE TO NATIONAL TECHNICAL INFORMATION SERVICE (NTIS). |
| <input checked="" type="checkbox"/> | ORDER FROM SUPERINTENDENT OF DOCUMENTS, U.S. GOVERNMENT PRINTING OFFICE, WASHINGTON, DC 20402. |
| <input checked="" type="checkbox"/> | ORDER FROM NATIONAL TECHNICAL INFORMATION SERVICE (NTIS), SPRINGFIELD, VA 22161. |

14. NUMBER OF PRINTED PAGES

245

15. PRICE



NIST Technical Publications

Periodical

Journal of Research of the National Institute of Standards and Technology—Reports NIST research and development in those disciplines of the physical and engineering sciences in which the Institute is active. These include physics, chemistry, engineering, mathematics, and computer sciences. Papers cover a broad range of subjects, with major emphasis on measurement methodology and the basic technology underlying standardization. Also included from time to time are survey articles on topics closely related to the Institute's technical and scientific programs. Issued six times a year.

Nonperiodicals

Monographs—Major contributions to the technical literature on various subjects related to the Institute's scientific and technical activities.

Handbooks—Recommended codes of engineering and industrial practice (including safety codes) developed in cooperation with interested industries, professional organizations, and regulatory bodies.

Special Publications—Include proceedings of conferences sponsored by NIST, NIST annual reports, and other special publications appropriate to this grouping such as wall charts, pocket cards, and bibliographies.

Applied Mathematics Series—Mathematical tables, manuals, and studies of special interest to physicists, engineers, chemists, biologists, mathematicians, computer programmers, and others engaged in scientific and technical work.

National Standard Reference Data Series—Provides quantitative data on the physical and chemical properties of materials, compiled from the world's literature and critically evaluated. Developed under a worldwide program coordinated by NIST under the authority of the National Standard Data Act (Public Law 90-396). NOTE: The Journal of Physical and Chemical Reference Data (JPCRD) is published bi-monthly for NIST by the American Chemical Society (ACS) and the American Institute of Physics (AIP). Subscriptions, reprints, and supplements are available from ACS, 1155 Sixteenth St., NW., Washington, DC 20056.

Building Science Series—Disseminates technical information developed at the Institute on building materials, components, systems, and whole structures. The series presents research results, test methods, and performance criteria related to the structural and environmental functions and the durability and safety characteristics of building elements and systems.

Technical Notes—Studies or reports which are complete in themselves but restrictive in their treatment of a subject. Analogous to monographs but not so comprehensive in scope or definitive in treatment of the subject area. Often serve as a vehicle for final reports of work performed at NIST under the sponsorship of other government agencies.

Voluntary Product Standards—Developed under procedures published by the Department of Commerce in Part 10, Title 15, of the Code of Federal Regulations. The standards establish nationally recognized requirements for products, and provide all concerned interests with a basis for common understanding of the characteristics of the products. NIST administers this program as a supplement to the activities of the private sector standardizing organizations.

Consumer Information Series—Practical information, based on NIST research and experience, covering areas of interest to the consumer. Easily understandable language and illustrations provide useful background knowledge for shopping in today's technological marketplace.

Order the above NIST publications from: Superintendent of Documents, Government Printing Office, Washington, DC 20402.

Order the following NIST publications—FIPS and NISTIRs—from the National Technical Information Service, Springfield, VA 22161.

Federal Information Processing Standards Publications (FIPS PUB)—Publications in this series collectively constitute the Federal Information Processing Standards Register. The Register serves as the official source of information in the Federal Government regarding standards issued by NIST pursuant to the Federal Property and Administrative Services Act of 1949 as amended, Public Law 89-306 (79 Stat. 1127), and as implemented by Executive Order 11717 (38 FR 12315, dated May 11, 1973) and Part 6 of Title 15 CFR (Code of Federal Regulations).

NIST Interagency Reports (NISTIR)—A special series of interim or final reports on work performed by NIST for outside sponsors (both government and non-government). In general, initial distribution is handled by the sponsor; public distribution is by the National Technical Information Service, Springfield, VA 22161, in paper copy or microfiche form.

U.S. Department of Commerce
Technology Administration
National Institute of Standards and Technology
325 Broadway
Boulder, Colorado 80303-3328

**OFFICIAL BUSINESS
PENALTY FOR PRIVATE USE, \$300**